Relaxation par RMN multi-champs dans les biomolécules

Nicolas Bolik-Coulon

PSL
UNIVERSITÉ PARIS

THÈSE DE DOCTORAT
DE L'UNIVERSITÉ PSL

Préparée à l'École Normale Supérieure

NMR relaxation in biomolecules over orders of magnitude of magnetic field

Soutenue par
Nicolas Bolik-Coulon
Le 28 juin 2021

École doctorale n°388
Chimie Physique et Chimie Analytique de Paris-Centre

Composition du jury :

Dr. Carine van Heijenoort CNRS, ICSN, Gif-sur-Yvette	*Présidente*
Prof. Arthur G. Palmer III Columbia University, New York	*Rapporteur*
Prof. Malcolm H. Levitt University of Southampton	*Rapporteur*
Prof. Sereina Riniker ETH, Zürich	*Examinatrice*
Dr. Jean-Nicolas Dumez CNRS, Université de Nantes	*Examinateur*
Prof. Fabien Ferrage CNRS, École Normale Supérieure, Paris	*Directeur de thèse*

1794
ENS | PSL

Acknowledgments

I want to start by thanking all the members of the jury committe, Sereina Riniker, Carine van Heijenoort, Jean-Nicolas Dumez and in particular Arthur G. Palmer and Malcolm H. Levitt for being the rapporteurs of this thesis. I am gratefull different experts in the field accepted to review my PhD work.

Fabien, je te remercie pour ta confiance et ton encadrement, et ce bien avant que je ne démarre ma thèse. La liberté quasi-totale que tu m'as accordée pour partir dans les axes de recherche que nous avons choisis m'a permis d'explorer des aspects de la théorie de la relaxation que je n'aurais pas imaginer il y a plus de 5 ans à mon arrivée au laboratoire. Merci pour ton soutien dans mon projet professionnel et tes conseils pour me permettre de le réaliser.

Je tiens à remercier tout particulièrement Philippe Pelupessy qui, en plus de son soutien sans faille dans les moments compliqués, a su répondre à mes nombreuses questions sur des aspects de la RMN tout aussi variés. Je remercie également Guillaume Bouvignies pour les conversations toujours très agréables, et pour m'avoir initié à la simulation de séquence d'impulsions et leur compréhension d'une manière générale. Son aide a été très précieuse et m'a sans aucun doute sauvé de longues heures à chercher des erreurs de codes...

Ces travaux de thèse ont été réalisés en collaboration avec de nombreuses personnes, certaines du laboratoire et d'autres non, et que je tenais à mentioner ici: Diego Carnevale, Fabio Sterpone, Guillaume Bouvignies, Jean-Nicolas Dumez, Milan Zachrdla, Olivier Languin-Cattöen, Pavel Kadeřávek, Philippe Pelupessy, Samuel Cousin. Je remercie également toutes les personnes du laboratoire, qui ont contribué indirectement *via* une discussion autour d'un café, ou simplement pour les bons moments partagés ensembles: Behdad, Daniel, David, Dennis, Duy, Edward, Emeric, Geoffrey, Isabelle, Jean-Jacques, Jessie, Lucie, Ludovic, Paula, Mathieu, Milan, Nicolas, Olivier, Patrick, Rachel, Simone, Soha, Sina, Vineeth, Ziqing.

Mes travaux de thèse auraient dû comprendre une part significative liée à l'étude de la protéine Artemis. Ce manuscript ne mentionne pas ces travaux que j'ai arrêté relativement tôt. Malgré tout, cela m'a permis d'acquérir de l'expérience en RMN biomoléculaire et la préparation d'échantillon. Pour cela, je souhaite remercier Ludovic Carlier pour avoir su être à mes côtés à la paillasse quand j'en avais besoin, sa patience sans borne, mais aussi pour nos longues

discussions autour d'un café.

Anne Halloppé, Éliane Moulinie, Karine Gherdi et Pauline Barjolin m'ont assisté dans les taches administratives et en cela m'ont permis de me focaliser pleinement sur la recherche. Je les remercie pour leur efficacité et bonne humeur quotidienne.

Mon séjour au laboratoire a débuté dès le début de l'année 2016, et m'a conduit à travailler avec un thésard et un post-doctorant qui ont quitté le laboratoire avant que je ne démarre ma thèse. Samuel Cousin et Pavel Kadeřávek, merci pour ces formidables moments passés en votre companie au laboratoire (entre autre) et qui m'ont permis de commencer mes projets de thèse sereinement. Vous retrouver lors d'une conférence est toujours un plaisir.

Il va de soit que cette aventure n'aurait pas été la même sans un groupes d'amis proches et soudés. Ces trois années de recherche ont semblé bien courte en leur companie. Je tiens a mentionner tout particulièrement mes collocs avec qui les confinements ont fait que la moitié de ma thèse s'est faite en leur compagnie (Antoine, Christelle, Sébastian et Thomas), les membres assidus des 'Thursday Seminars', devenus récemment les 'Week-End Seminars' (Bahar, Behdad, David, Duy, Jessie, Rachel, Simone et Ziqing), et tous ceux avec qui j'ai passés des moments mémorables (Alexandre, Anna, Hakim, Huitong, Mélanie, Pépé, Rosie pour n'en nommer que quelques uns). Un immense merci à Christelle et Thomas pour m'avoir aidé à relâcher la pression pendant la phase finale de l'écriture.

Même si nos différents projets nous ont éloignés les uns des autres, retrouver, à diverses occasions, ce groupe d'amis formés au cours de notre formation à l'ENS est irremplaçable. Je ne saurais tous les mentionner ici, mais je tenais a remercier particulièrement Alia, Alice, Antoine, Aurélien, Benoît, Charline, Étienne, Julien, Louise, Marius, Gaëtan, Pierre, Thomas J., Thomas M., Valérie.

L'éloignement et différents confinements ont fait que je n'ai pu passer autant de temps avec ma famille que je ne l'aurais souhaité. Je les remercie du fond du cœur pour leur compréhension, mais surtout pour leur soutien sans faille. Votre fierté envers ce que vous m'avez vu accomplir n'a pas de prix.

Contents

List of Acronyms

2F Two-Field

BMRB **B**iological **M**agnetic **R**esonance data **B**ank

BWR **B**loch-**W**angsness-**R**edfield

CSA **C**hemical **S**hift **A**nisotropy

DD **D**ipole-**D**ipole

DFT **D**ensity **F**unctional **T**heory

DNP **D**ynamic **N**uclear **P**olarization

dDNP **d**issolution **D**ynamic **N**uclear **P**olarization

DQ **D**ouble **Q**uantum

EFG **E**lectric **F**ield **G**radient

EMF **E**xtended **M**odel **F**ree

ESR **E**lectron **S**pin **R**esonance

FFC **F**ast **F**ield **C**ycling

FID **F**ree **I**nduction **D**ecay

GIAO **G**auge-**I**ndependent **A**tomic **O**rbital

GUI **G**raphical **U**ser **I**nterface

HMQC **H**eteronuclear **M**ultiple **Q**uantum **C**oherence

HRR **H**igh-**R**esolution **R**elaxometry

HZQC **H**eteronuclear **Z**ero **Q**uantum **C**oherence

ICARUS **I**terative **C**orrection for the **A**nalysis of **R**elaxation **U**nder **S**huttling

IFIM **I**nfinitely **F**ast **I**nternal **M**otions

IFMR **I**nfinitely **F**ast **M**ethyl **R**otation

IMPACT **I**nterpretation of **M**otions by a **P**rojection onto an **A**rray of **C**orrelation **T**imes

IDP **I**ntrinsically **D**isordered **P**roteins

IDR **I**ntrinsically **D**isordered **R**egions

LLPS **L**iquid-**L**iquid **P**hase **S**eparation

LLS **L**ong-**L**ived **S**tates

MBP **M**altose **B**inding **P**rotein

MCMC **M**arkov-**C**hain **M**onte-**C**arlo

MD **M**olecular **D**ynamic

MF **M**odel **F**ree

MFM **M**odel **F**ree for **M**ethyl

MINOTAUR **M**atching **I**ntensities to **O**ptimize **T**imescales and **A**mplit**U**des of motions from **R**elaxometry

MQ **M**ultiple **Q**uantum

NMR **N**uclear **M**agnetic **R**esonance

NOESY **N**uclear **O**verhauser **E**ffect **S**pectroscop**Y**

NUS **N**on **U**niform **S**ampling

PAS **P**rincipal **A**xis **S**ystem

PDB **P**rotein **D**ata **B**ank

PES **P**otential **E**nergy **S**urface

RDC **R**esidual **D**ipolar **C**oupling

S3E **S**pin **S**tate **S**elective **E**xcitation

SF **S**ystem **F**rame

SNR **S**ignal-to-**N**oise **R**atio

SRLS **S**lowly **R**elaxing **L**ocal **S**tructure

ST2-PT **S**ingle **T**ransition-to-**S**ingle **T**ransition **P**olarization **T**ransfer

TMS **T**etra**M**ethyl**S**ilane

TOCSY **TO**tal **C**orrelation **S**pectroscop**Y**

TROSY **T**ransverse **R**elaxation-**O**ptimized **S**pectroscop**Y**

ZQ **Z**ero **Q**uantum

Résumé en Français

La Résonance Magnétique Nucléaire (RMN) est une spectroscopie permettant l'analyse de la matière sur un large panel d'applications, allant de l'étude de piles à combustibles (RMN solide) [1] à l'imagerie biomédicale (Imagerie par Résonance Magnétique, IRM) [2], en passant par l'analyse de produits agroalimentaires [3]. Quel que soit son domaine d'application, la RMN consiste à mesurer un signal produit par des spins après avoir appliqué une série d'impulsions radio-fréquences et de délais, et en présence d'un champ magnétique intense généré par l'aimant du spectromètre RMN. Plus ce dernier est intense, plus le signal detecté est intense et résolu, c'est-à-dire plus les signaux qui émanent de spins distincts peuvent être distingués. Avec le gain de sensibilité apporté par l'augmentation des champs magnétiques produits par les aimants, ainsi que grâce aux progrès électroniques qui ont permis le développement de sondes RMN plus sensibles [4], la RMN a trouvé sa place parmi les méthodes de tout premier plan pour l'étude de la structure, dynamique et fonction des biomolécules [5, 6, 7].

RMN et dynamique des biomolécules

À ce jour, la diffraction des rayons-X, et, plus récemment, la cryomicroscopie électronique (Cryo-EM), se sont imposées comme les techniques de choix pour la détermination de la structure de biopolymères (protéines et acides nucléiques) [8]. Pour ces deux techniques, la mesure se fait dans un état figé (le crystal en diffraction des rayons-X, une glace amorphe en Cryo-EM), à la différence de la RMN qui permet de sonder les molécules notamment en solution, une caractéristique particulièrement intéressante car plus proche de leur environnement natif. Il est aujourd'hui généralement admis que la fonction des biomolécules, et en particulier celle des protéines, ne peut être totalement comprise à l'aide de la structure tri-dimensionelle, et que la dynamique des atomes qui la composent est essentielle aux phénomènes biologiques en jeu [9]. Dès lors, la RMN constitue une méthode de choix pour l'étude de biomolécules complexes.

En RMN, c'est l'étude de l'évolution des spins vers leur état d'équilibre thermique, phénomène appelé relaxation des spins nucléaires, qui permet de sonder les mouvements des liaisons chimiques [10, 11]. Ces mouvements peuvent être de plusieurs natures et avoir différentes échelles de temps : quelques picosecondes pour la rotation d'un groupe méthyle, quelques centaines de picoseconde à quelques nanosecondes pour les mouvements locaux de chaines latérales

dans les protéines, plusieurs nanosecondes pour la diffusion rotationnelle, microsecondes et plus pour les réarrangements conformationnels, la liaison d'un ligand, etc... Pour chacune de ces échelles de temps, la RMN offre une ou plusieurs expériences permettant de les caractériser au moyen de vitesses de relaxation. Dès lors, la compréhension du processus de relaxation des spins est essentielle pour interpréter les résultats RMN en terme de dynamique.

Les vitesses de relaxation peuvent s'exprimer analytiquement en utilisant la théorie Bloch-Wangsness-Redfield (BWR) comme des combinaisons linéraires de la fonction de densité spectrale évaluée à différentes fréquences [12, 13, 14]. La fonction de densité spectrale est une densité de probabilité de mouvement pour une fréquence donnée et s'écrit, en général, comme une somme de fonctions Lorentziennes [15]. Lors de la mesure de la vitesse longitudinale d'auto-relaxation (R_1) d'un azote-15 dans une paire ^{15}N-^{1}H d'une liaison peptidique, la fonction de densité spectrale est "mesurée" simultanément aux fréquences $\omega_H - \omega_N$, ω_N et $\omega_H + \omega_N$, avec $\omega_X = \gamma_X B_0$ la fréquence de Larmor au champ magnétique B_0 de la mesure et γ_X le rapport gyromagnétique du noyau X [16]. Aux champs magnétiques couramment utilisés en RMN des biomolécules ($B_0 > 9\,\mathrm{T}$), la fonction de densité spectrale n'est donc pas caractérisée à des fréquences non nulles inférieures à 40 MHz (on note que les vitesses de relaxation transversales dépendent de la fonction de densité spectrale en $\omega = 0$). Or, de nombreux mouvements internes dans les biomolécules ont des fréquences plus basses. La plupart de la variation de la fonction de densité spectrale n'est pas déterminée par des mesures à haut champs, comme le montre la fonction de densité spectrale en Figure 1 (trait plein) et calculée en utilisant un exemple très simple et l'approche Model Free (MF) [15]:

$$\mathcal{J}(\omega) = \frac{2}{5}\left[\mathcal{S}^2 \frac{\tau_c}{1+(\omega\tau_c)^2} + (1-\mathcal{S}^2)\frac{\tau_i'}{1+(\omega\tau_i')^2}\right], \tag{1}$$

où τ_c est le temps caractéristique pour la diffusion rotationelle, $\tau_i'^{-1} = \tau_c^{-1} + \tau_i^{-1}$ avec τ_i le temps caractéristique pour le mouvement de la liaison N-H avec une amplitude du mouvement reliée au paramètre d'ordre $\mathcal{S}^2$. Ainsi, la mesure de vitesses de relaxation aux champs utilisés en RMN des biomolécules offre *a priori* une faible précision quant à la caractérisation des mouvements internes. Une solution serait de réaliser la mesure à des champs plus faibles, comme suggéré par la Figure 1. Cependant, jusqu'à très récemment, la très faible sensibilité et résolution liée à l'utilisation de tels champs magnétiques pour la détection du signal en RMN biomoléculaire rendaient ces mesures impossibles.

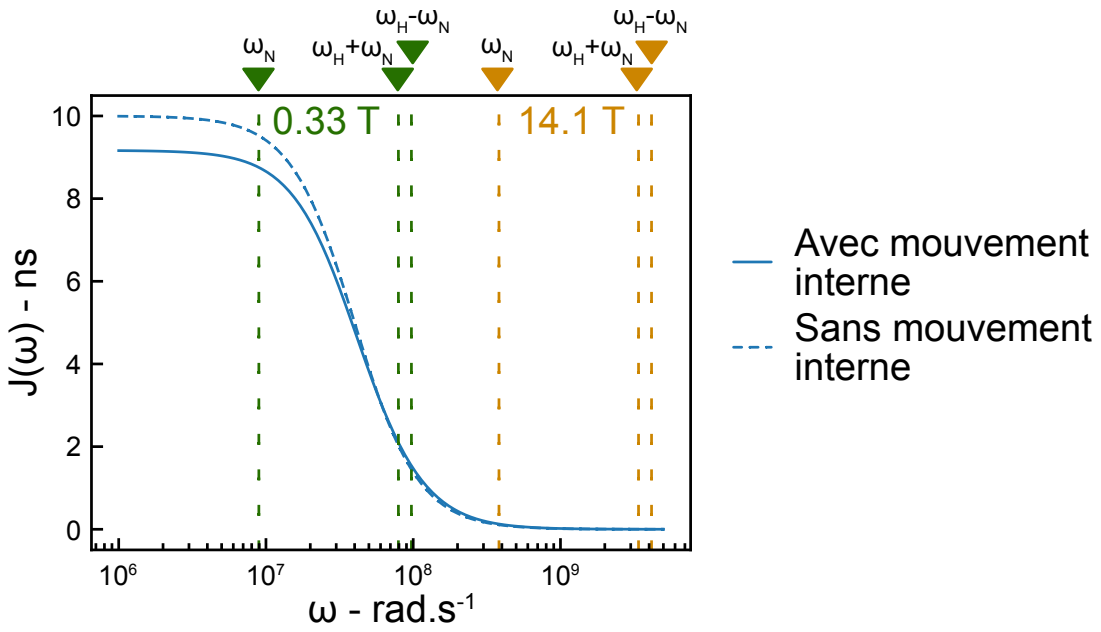

Figure 1: Fonction de densité spectrale et fréquences sondées par la vitesse de relaxation R_1 de l'azote-15 dans une paire de spins ^{15}N-^{1}H. Les fonctions de densité spectrale sont calculées en utilisant Eq. 1 et un temps de corrélation pour la diffusion rotionnelle $\tau_c = 25\,\text{ns}$. Dans le cas où un mouvement interne est considéré (trait plein), on a $\mathcal{S}^2 = 0.8$ et $\tau_i = 20\,\text{ns}$. Dans le cas où le mouvement interne n'est pas inclu (pointillés), on a $\mathcal{S}^2 = 1$. Les fréquences qui contribuent à la vitesse de relaxation longitudinale R_1 de l'azote-15 sont indiquées par les lignes verticales pointillées pour deux champs magnétiques: 14.1 T (fréquence de Larmor du proton de 600 MHz) en orange, et 0.33 T (fréquence de Larmor du proton de 14 MHz) en vert.

Une solution à ce problème de sensibilité a été apportée par le laboratoire et consiste à déplacer l'échantillon le long du champ de fuite produit par l'aimant : l'échantillon est déplacé vers le haut et stabilisé à une certaine position pendant le délais de relaxation, puis ramené au cœur de l'aimant pour la détection du signal [17]. Ainsi, les propriétés de relaxation peuvent être mesurées à bas champ, tout en conservant une bonne sensibilité pour la mesure du signal. Les vitesses de relaxation mesurées par cette méthode, appelée relaxométrie à haute résolution (RHR), contiennent des contributions d'autres chemins de relaxation qui sont habituellement supprimées par l'utilisation d'impulsions radio-fréquences dans les expériences de relaxation classiques. Dès lors, comment prendre en compte ces contributions pour obtenir une analyse fine de la dynamique des biomolécules ?

Nous avons mis en place une feuille de calcul MATHEMATICA [18, 19] appelée REDKITE et utilisant des fonctions implémentées dans SPINDYNAMICA [20]. Cet outil a été mis à profit

pour l'étude de la dynamique des groupes méthyles $\delta 1$ des isoleucines marqués sélectivement $^{13}C^1H^2H_2$ dans la protéine Ubiquitine [21]. RedKite nous a permis de calculer analytiquement les vitesses de relaxation pour le système de spin d'intérêt (*i.e.* $^{13}C^1H^2H_2$) comme une combinaison linéaire de la fonction de densité spectrale évaluée à différentes fréquences. RedKite peut également être utilisé pour l'étude d'un grand nombre de système de spins. Une fois les expressions des vitesses de relaxation obtenues, nous étions en mesure d'analyser les données de relaxation mesurées : les vitesses de relaxation du carbone-13 longitudinale (R_1), transverse (R_2), et les vitesses de relaxation croisée carbone-proton enregistrées à l'aide de spectromètres conventionnels à 4 champs magnétiques différents, ainsi que 27 données de RHR enregistrées à bas champs. Afin d'analyser précisément les vitesses de relaxation enregistrées en déplaçant l'échantillon au-dessus de l'aimant, il nous faut prendre en compte les effets de la relaxation croisée lorsque les chemins de relaxation ne sont plus contrôlés par l'application d'impulsion radio-fréquence.

Pour cela, nous avons développé une première approche, appelée ICARUS (Iterative Correction for the Analysis of Relaxation Under Shuttling), qui repose sur la correction des données de relaxométrie au moyen d'une successions d'itérations. Pour se faire, les données de relaxation enregistrées de façon conventionnelles, dites 'exactes', sont analysées afin d'extraire un premier jeu de paramètres pour la dynamique (*i.e.* paramètre de la fonction de densité spectrale) qui va être utile à l'initialisation des itérations. Ce premier jeu de paramètres est utilisé pour simuler les expériences de relaxométrie et ainsi calculer une décroisance de l'intensité du signal selon une vitesse de relaxation dite 'simulée'. Ces simulations consistent à calculer l'évolution du système pendant le déplacement de l'échantillon vers la position du bas champ, pendant le délai de relaxation, puis le retour vers le cœur de l'aimant avant la détection, ainsi que toutes les périodes de stabilisation de l'échantillon. Les vitesses simulées sont comparées aux vitesses calculées aux bas champs auxquels la relaxation a lieu. En l'abscence de relaxation croisée, les vitesses simulées et calculées seraient identiques. Le ratio des vitesses calculées et simulées défini un facteur de correction pour chaque bas champ auquel une vitesse de relaxation a été mesurée. Le facteur de correction est appliqué aux données expérimentales pour générer des données 'corrigées' qui sont analysées, avec les données exactes, pour conduire à un deuxième jeu de paramètres pour la dynamique. Celui-ci sera utilisé dans la deuxième itération de la boucle, pour conduire à un troisième jeu de paramètres. La convergence des facteurs de correction permet l'arrêt de la boucle, et ainsi d'obtenir des données corrigées pour les bas champs. L'utilisation de la méthode de Monte-Carlo par chaînes de Markov (MCMC) sur les données

exactes et corrigées conduit à des distributions pour les paramètres de la fonction de densité spectrale et permet une interprétation biophysique et fonctionnelle des mouvements dans la biomolécule d'intérêt.

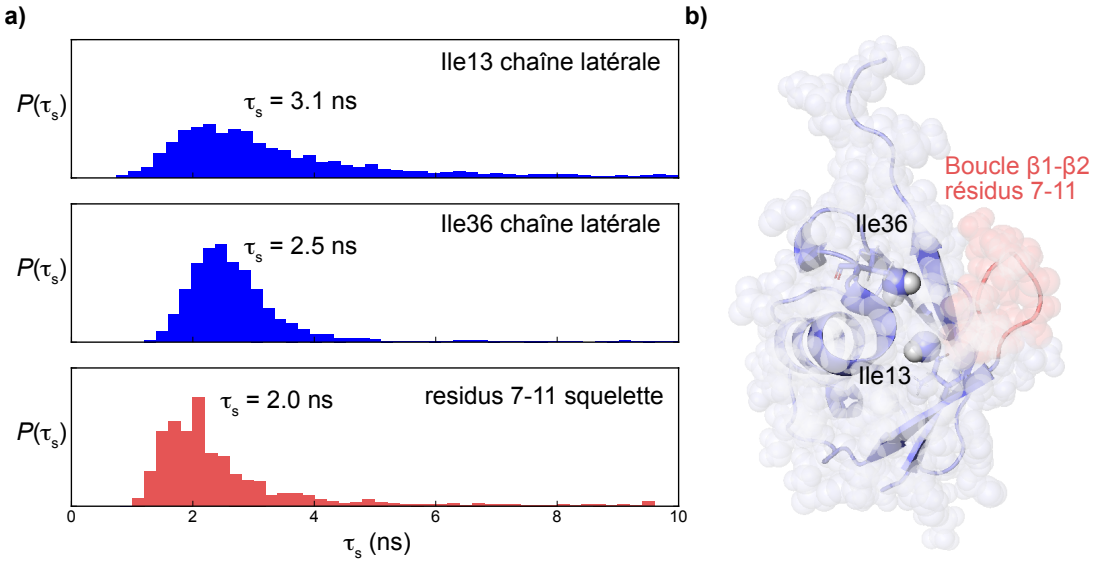

Figure 2: Mouvements nanosecondes dans l'Ubiquitine. **a)** Distributions du temps de corrélation τ_s décrivant les mouvements lents et obtenues après analyse avec la méthode MCMC de données de RHR sur les groupes méthyles $\delta 1$ de l'isoleucine 13 (haut), 36 (milieu) et sur les groupes N-H du squelette peptidique pour les résidues 7 à 11 (bas). La moyenne des distributions est indiquée sur chaque panel. La distribution pour les résidues 7 à 11 est obtenue selon $P_{7-11}(\tau_s) = \prod_{i=7}^{i=11} P_i(\tau_s)$ avec $P_i(\tau_s)$ la distribution de temps de corrélation pour le résidue i. **b)** Structure de l'Ubiquitine montrant la boucle $\beta 1$-$\beta 2$ (rouge) et les chaînes latérales des isoleucines 13 et 36. Figure adaptée de [21].

Nous présentons ici des résultats obtenus pour l'analyse des isoleucines 13 et 36 de l'Ubiquitine. Ces isoleucines sont soumises à des mouvements complexes sur des échelles de temps variant de la pico-seconde (rotation du groupe méthyle autour de son axe de symmétrie) à plusieurs nanosecondes (mouvements des liaisons C-C) [21]. En particulier, la relaxométrie permet de détecter un mouvement nanoseconde pour ces deux résidus sur des échelles de temps similaires (Fig. 2a). De plus, l'analyse des données de relaxométrie enregistrées précédemment sur les paires ^{15}N-^{1}H des liaisons peptidiques montre que les résidus 7 à 11 de la boucle $\beta 1$-$\beta 2$ (Fig. 2b) adoptent également un mouvement lent avec un temps caractéristique global du même ordre que ceux des groupes méthyles des isoleucines 13 et 36 (Fig. 2a). Des données de RMN et de dynamique moléculaire (MD) ont suggéré que ces deux régions (la boucle $\beta 1$-$\beta 2$

et la boucle α1-β3 à laquelle appartient Ile36) ont des mouvements concertés, ce que semblent corroborer nos résultats, même si nous ne pouvons pas, par notre analyse, clairement indiquer si les distributions de temps de corrélations similaires sont une coincidence ou réellement dûes à des mouvements concertés.

L'approche ICARUS présente néanmoins deux défauts. Le premier réside dans le fait qu'il n'est à ce jour possible de vérifier expérimentalement la qualité de la correction qu'à une poignée de champs magnétiques. Une seule mesure de vitesse de relaxation 'exacte' a été réalisée à bas champ dans le laboratoire en utilisant un spectromètre à deux champs [22], ce qui a permis de vérifier l'accord entre les vitesses corrigées et exactes à 0.33 T, mais rien n'a été fait aux champs intermédiaires (de 9.4 T à 0.33 T). Le second provient de l'hypothèse que les décroissances en intensité mesurées expérimentalement en RHR peuvent être reproduites par une fonction mono-exponentielle pour obtenir une vitesse de relaxation. Sur les données que nous avons enregistrées, nous n'avons pas observé de déviations entre ce type de modèle et les mesures expérimentales, mais il est possible que pour des systèmes de spin avec une forte relaxation croisée, des déviations significatives soient obtenues. Pour ces raisons, nous avons développé une autre approche pour l'analyse des données de relaxométrie.

Cette deuxième méthode, appelée MINOTAUR (Matching INtensities to Optimize Timescales and AmplitUdes of motions from Relaxometry) ne repose pas sur l'utilisation de vitesses de relaxation à bas champ. MINOTAUR est un programme utilisant la méthode de MCMC sur les vitesses de relaxation exactes (enregistrées avec des spectromètres conventionnels) et les décroissances en intensité obtenues par RHR pour conduire à des distributions pour les paramètres de la fonction de densité spectrale. Ainsi, alors que dans ICARUS les décroissances simulées étaient utilisées pour simuler une vitesse de relaxation, dans MINOTAUR elles sont utilisées directement pour reproduire les données expérimentales. Cette approche n'est donc pas itérative (ormis pour les itérations de la méthode MCMC), et permet une analyse immédiate des données en terme de dynamique (pas d'intermédiaire entre les données et la méthode MCMC).

Modèles de mouvements atomiques

La RMN, tout comme la diffraction des rayons-X et récemment la Cryo-EM, offrent une résolution atomique de l'information : un pic dans un spectre RMN correspond à un nombre limité de noyaux de la molécule étudiée. Il est donc *a priori* possible de caractériser avec précision

les mouvements de chaque résidue d'une protéine, et relier ces informations à des propriétés thermodynamiques telles que l'entropie conformationnelle [23, 24]. Pourtant, les modèles de mouvements utilisés restent basés sur l'approche MF (Eq. 1) [15], qui ne donne aucune information sur le type de mouvement en jeu. De plus, ce modèle de fonction de densité spectrale et ceux qui en ont découlé ont été sujets à de nombreuses controverses en lien avec leur simplicité mathématique [25, 26, 27, 28, 29]. Cependant, choisir un modèle pour analyser des données de RMN nécessite une connaissance de la nature des mouvements. Les simulations de MD permettent d'aller en ce sens, pour obtenir une description plus précise de la dynamique interne des biomolécules par l'analyse simultanée des trajectoires de MD et des vitesses de relaxation [30, 31, 32]. De plus, l'utilisation de la RHR permet d'étendre les échelles de temps accessibles par la RMN [33] et ainsi avoir une description plus fine et plus complètes des mouvements. Dès lors, pouvons-nous étudier la dynamique des chaînes latérales des protéines en utilisant des modèles de mouvements plus explicites que les approches de type MF et des informations tirées de la dynamique moléculaire ?

La fonction de densité spectrale, composante décrivant la dynamique des atomes dans la théorie BWR, est la transformée de Fourier de la fonction de corrélation pour l'orientation des interactions participant à la relaxation. Nous avons repris l'approche initialement proposée pour le calcul de ces fonctions de corrélation [34] et qui consiste à résoudre l'équation de diffusion adaptée au modèle de mouvement considéré. Pour les 4 types de mouvement étudiés (diffusion rotationelle, échange entre conformères, diffusion sur un cône, diffusion dans un cône), les équations de diffusion ont déjà été résolues. Nous avons donc repris ces résultats pour les combiner et former des modèles de mouvement incluant plusieurs composantes. Seules les équations pour la diffusion dans un cône ont dû être modifiées pour les rendre généralisables à des cas plus complexes que ceux pour lesquels elles ont été initialement développées.

Nous avons ensuite questionné la capacité du MF à évaluer les temps caractéristiques et amplitudes de mouvement avec exactitude. Pour cela, nous avons utilisé des données synthétiques, ce qui nous a permis de montrer que le MF constitue une bonne approximation pour les fonctions de corrélation des mouvements de type diffusif (diffusion sur un cône, diffusion dans un cône). La correspondance entre temps de corrélation (obtenu *via* l'analyse MF) et coefficient de diffusion (la grandeur physique décrivant la dynamique du système) peut néanmoins être complexe. De plus, les fonctions de corrélation de type MF ne permettent pas, en général, de décrire correctement la dynamique des sytèmes dans le cas de transition entre po-

sitions discrètes, c'est-à-dire *la dynamique des chaînes latérales qui s'échangent entre rotamères.*

Avant d'analyser les données de RHR enregistrées sur les groupes méthyles $\delta 1$ des isoleucines de l'Ubiquitine, nous avons obtenu des informations sur le type de mouvement de ces chaînes latérales grâce à une simulation de MD. Les diagrammes de Ramachandran extraits de la MD montrent que les liaisons C-C adoptent des conformations privilégiées qui changent au cours de la trajectoire. Au sein de la protéines, les isoleucines se distinguent de part le nombre, la nature et les distributions de population des conformations qu'elles adoptent. Dans l'analyse des données de RHR, nous avons donc opté pour un mouvement d'échange entre rotamères en plus de la rotation du groupe méthyle autour de son axe de symmétrie, modélisée en utilisant les équations de diffusion sur un cône. Nous nous sommes également intéressé à l'évolution des tenseurs de déplacement chimiques pour chacun des 9 rotamères du diagramme de Ramachandran des isoleucines, et en particulier l'anisotropie de déplacement chimique (CSA) qui constitue un mécanisme de relaxation. Nous avons donc calculé ces CSA en utilisant la DFT (Théorie Fonctionnellle de la Densité) pour les 9 géométries possibles. Nous avons ainsi pu constater que les CSA des carbones $\delta 1$ pouvaient varier jusqu'à 10 ppm d'un conformère à l'autre, ce qui représente des variations significatives alors que la moyenne est à 19 ppm. En conséquence, nous avons modifié la fonction de corrélation modélisant les mouvements des chaînes latérales des isoleucines pour inclure, en plus de la variation des orientations des liaisons chimiques, la variation de l'intensité des interactions conduisant à un mécanisme de relaxation et en particulier du CSA. Nous avons également pu montrer que le fait de considérer un CSA moyen et des CSA distincts conduit à des différences importantes dans les vitesses de corrélations croisées entre le CSA du carbone et l'intéraction dipolaire entre le carbon et le proton.

L'analyse des données de relaxation avec des modèles de mouvement explicites s'est faite en utilisant les vitesses de relaxation R_1 et R_2 du carbon-13 et les vitesses de relaxation dipolaire carbon-proton enregistrées à haut champ, et les données de RHR corrigées par ICARUS. Les modèles de mouvement utilisent les informations obtenues de la MD de telle sorte que seuls les rotamères peuplés au cours de la trajectoire ont été considérés pour construire la matrice d'échange. Ainsi, la MD indique que pour l'isoleucine 61, seuls les rotamères 6 et 9 sont significativement peuplés (Fig. 3a). Un modèle d'échange à 2 états à donc été utilisé pour reproduire les vitesses de relaxation du carbone-13 par la méthode MCMC (Fig. 3b,c). Les paramètres obtenus ont des distributions étroites et bien définies (Fig. 3d), et les vitesses de relaxation sont bien reproduites par ce modèle à 4 paramètres libres (dans l'analyse MF, 6

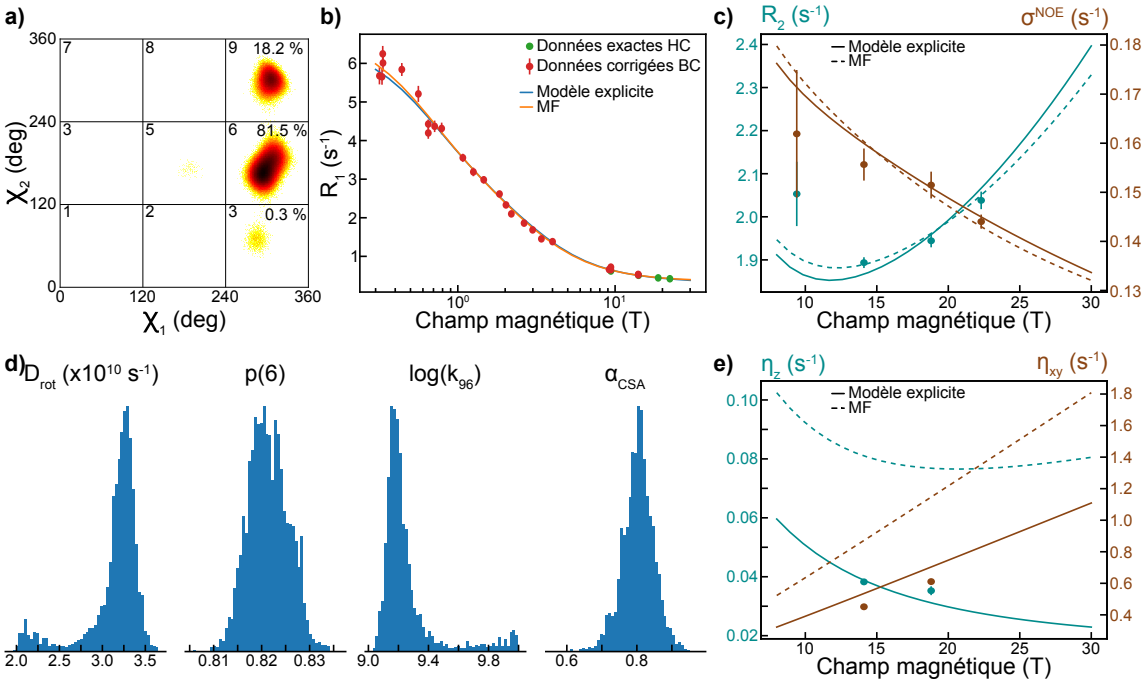

Figure 3: Résultats pour l'analyse de la dynamique de l'isoleucine 61 par RMN et MD. **a)** Diagramme de Ramachandran de Ile-61 obtenu après analyse de la trajectoire de dynamique moléculaire sur l'Ubiquitine. Les 9 rotamères sont numérotés comme indiqué sur chaque cadran, ainsi que la population (en pourcentage) observée au cours de la MD. Reproduction des données de relaxation longitudinale (**b**), transverse pour le carbone (**c**, bleu) et de relaxation croisée carbon-proton (**c**, marron) apres analyse par la méthode de MCMC. Les résultats de l'analyse MF précédemment publiés sont également indiqués [21]. HC: Haut Champs. BC: Bas Champs. **d)** Histogrammes des paramètres libres au cours du MCMC. D_{rot} est le coefficient de diffusion pour la rotation du groupe méthyle autour de son axe de symmétrie, p(6) la population du rotamère 6, $\log(k_{96})$ le logarithme de la constante d'échange (exprimée en s^{-1}) du rotamère 6 au rotamère 9 et α_{CSA} un coefficient de mise à l'échelle pour les CSA calculés en DFT. **e)** Vitesse de corrélation croisée longitudinale (blue) et transverse (marron) entre le CSA du carbone-13 et l'interaction dipolaire carbone-proton. Ces vitesses ne sont pas inclues dans la méthode de MCMC.

paramètres étaient laissés libres). Le coefficient de diffusion pour la rotation du groupe méthyle est de $3.2 \times 10^{10}\,s^{-1}$ ce qui correspond à un temps caractéristique de l'ordre de 15 ps, en accord avec les résultats obtenus par analyse MF [21]. Les populations pour le rotamère 6 obtenues par l'analyse de la trajectoire de MD et des données de relaxation sont en très bon accord (0.815 et 0.82 respectivement), et la vitesse d'échange du rotamère 6 à 9 est de $10^{9.2}\,s^{-1}$. Pour prendre en compte l'écart entre les CSA calculés par DFT et déterminé expérimentalement, un facteur commun pour les tenseurs de CSA des deux rotamères a été introduit (paramètre α_{CSA}

dans la Fig. 3d). De façon remarquable, ce modèle nous a permis de reproduire les vitesses de corrélation croisée CSA-dipole du carbone-13, alors que les vitesses obtenues à partir de la fonction de corrélation de type MF présentaient un écart significatif par rapport aux données expérimentales (Fig. 3e).

La RMN multi-champs comme alternative aux très hauts champs

La relaxation des spins est un phénomène inévitable qui renseigne sur la dynamique globale (diffusion) et locale des liaisons chimiques, et qui affecte le signal mesuré en RMN. Du fait qu'elle induit le retour des spins vers leur état d'équilibre, elle conduit à une diminution de l'intensité du signal mesuré, jusqu'à ce qu'il ne puisse plus être distingué du bruit lié à la mesure. Chaque état d'un système de spin donné a ses propres propriétés de relaxation, si bien qu'il est possible d'optimiser les expériences RMN pour ne sélectionner que ceux qui ont des propriétés de relaxation favorables. C'est dans cette optique que les expériences de type TROSY (Transverse Relaxation Optimised SpectroscopY) ont été développées, dans un premier temps pour les paires de spins ^{15}N-^{1}H des liaisons peptidiques [35], puis pour les groupes méthyles $^{13}C^{1}H_3$ des chaînes latérales aliphatiques [36]. Au-dela de l'intérêt particulier d'étudier la dynamique des molécules, l'étude de la relaxation des spins trouve donc également des applications dans le développement d'expériences plus sensibles. En particulier, certains noyaux, comme le carbon-13 dans les groupes carbonyles des liaisons peptidiques, ont des propriétés de relaxation très défavorables à haut champs magnétiques, au point qu'il est probable que les expériences multi-dimensionnelles mettant en jeu ces noyaux devront être revisitées sur les nouvelles génération d'aimants actuellement accessibles (1.2 GHz). Le mécanisme de relaxation associé est l'anisotropie de déplacement chimique (CSA), dont la contribution à la relaxation transversale augmente quadratiquement avec le champ magnétique, si bien que certains noyaux ayant des CSA élevés peuvent avoir des propriétés de relaxation favorables à des champs très faibles, comme c'est le cas du fluor-19.

Afin d'apporter une solution aux propriétés de relaxation pouvant être défavorables à haut champ, le laboratoire a récemment introduit le concept de spectroscopie à deux champs [39, 37]. Tout comme pour la RHR, son principe repose sur le déplacement de l'échantillon au sein du spectromètre, la différence majeure étant que la position d'arrivée au champ plus faible est fixe et se fait dans une deuxième sonde placée au-dessus de l'appareil (Fig. 4a). Cela permet de contrôler les systèmes de spin à bas champ, et de réaliser des expériences multi-

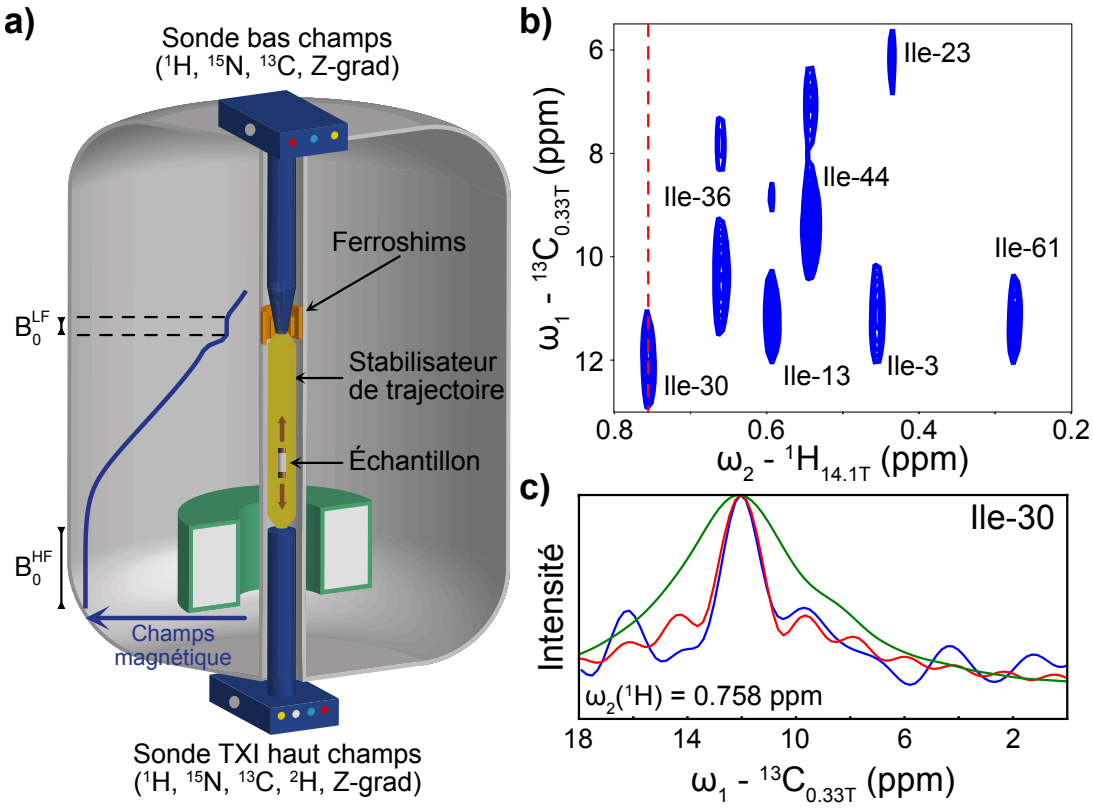

Figure 4: Principe de la spectroscopie RMN à deux champs. **a)** Schéma montrant le fonctionement d'un spectromètre à deux champs. Deux sondes sont placées de telle sorte à pouvoir appliquer des implulsions radio-fréquences aux niveaux des régions de champ magnétique homogène créées par l'aimant (vert) du spectromètre et les ferroshims (orange). L'échantillon est déplacé d'un point à l'autre *via* le stabilisateur de trajectoire (jaune) à des vitesses pouvant aller jusqu'à 10 m.s^{-1} grâce à de l'air comprimé. **b)** Spectre des groupes méthyles $\delta 1$ des isoleucines de l'Ubiquitine avec un marquage isotopique $^{13}C^{1}H_3$. Sur ce spectre, le déplacement chimique du carbone a été édité à bas champ (0.33 T) par une évolution zéro quantum alors que la dimension associée au déplacement chimique du proton a été détectée à haut champ (14.1 T). Les artefacts apparaissant à 2.7 ppm des pics principaux ne sont pas compris à ce jour. **c)** Section du spectre montré en **b** selon la ligne pointillée rouge montrant le spectre enregistré (blue), le spectre simulé en utilisant la théorie du méthyle-TROSY pré-existente (vert) et la théorie du méthyle-TROSY que nous avons généralisé (rouge). Figure adaptée de [37] et [38].

dimensionnelles où l'une des dimensions est associée à un bas champ tout en concervant la sensibilité du haut champ de l'aimant sur une autre dimension (Fig. 4b). Sur ce spectre de groupes méthyle $^{13}C^{1}H_3$, la bonne résolution obtenue dans la dimension du bas champ était particulièrement surprenante car en désaccord avec les prédictions que nous pouvions faire en utilisant la théorie du méthyle-TROSY [36]. C'est seulement en s'affranchissant des hypothèses

avec lesquelles cette théorie a été intialement développée, et en considérant toutes les transitions entre niveaux d'énergie indépendamment les unes des autres, que nous avons pu généraliser la théorie du méthyle-TROSY dans les conditions dans lesquelles le spectre à deux champ a été enregistré [38] (Fig. 4c).

Aucune des expériences existantes à ce jour ne permettent de résoudre le problème de la relaxation liée aux grands CSA à hauts champs magnétiques. Peut-on utiliser la spectroscopie RMN à deux champs pour enregistrer le spectre de noyaux ayant des CSA élevés tout en préservant la sensibilité des hauts champs ? Nous avons mené une étude théorique en prenant pour système modèle une paire de spin ^{13}C-^{19}F pour une tyrosine sur laquelle un des protons en position 3 du cycle a été remplacé par un fluor-19. Une expérience TROSY a récemment été développée pour ce type de système, mais la forte valeur du CSA du fluor conduit néanmoins à des raies larges [40]. Nous avons proposé une expérience alternative où la dimension associée au déplacement chimique du fluor est éditée à bas champs et la composante TROSY du carbon-13 est détectée à haut champ [41]. Nos simulations ont suggéré qu'un bas champ de 2.5 T et une détection à 21.15 T conduisent à une intensité optimale dans le cadre d'une expérience à deux champs. À ce bas champ, la relaxation liée au CSA est significativement réduite par rapport à une expérience réalisée à haut champ. Afin de déterminer si la perte de polarisation liée au fait que les spins sont soumis à un champ faible pendant une partie de l'expérience ne se fait pas au détriment de la qualité du spectre, nous avons comparé les spectres simulées pour les expériences un champ et deux champs. Que ce soit en terme de résolution dans la dimension fluor ou en terme de rapport signal sur bruit, nous prédisons que l'expérience à deux champs conduit à des spectres de meilleure qualité. En l'état, nous n'avons cependant pas les moyens de vérifier ces préfictions : en effet, notre système à deux champs opère à des champs trop faibles (0.33 et 14.1 T). Cela nous a néanmoins permis d'introduire le concept de TROSY à deux champs. Dans le TROSY tel qu'il a été initialement développé, les transitions ayant des propriétés de relaxation favorables sont sélectionnées au cours de l'expérience. Ici, nous proposons également de sélectionner le champ magnétique pour l'évolution de ces opérateurs, ceux-ci pouvant être différent d'une dimension de l'expérience à l'autre.

Conclusion et perspectives

Ma thèse a tourné constamment autour d'une équation : l'équation du super-opérateur de relaxation donnée par la théorie BWR. Cette équation en a constitué la pierre angulaire, que ce soit pour comprendre des propriétés de relaxation favorables sur des expériences multi-champs, calculer des vitesses de relaxation pour analyser des données expérimentales, ou encore mettre au point des modèles pour l'analyse des mouvements de chaînes latérales aliphatiques dans les protéines. À mon sens, ma thèse montre deux choses. La première, et cela a déjà été souligné dans d'autres thèses du laboratoire et les papiers qui en ont découlés, la RMN à deux champs peut s'imposer comme une alternative à la RMN 'conventionnelle' face aux problématiques que la RMN à très hauts champs posent dans l'étude de systèmes biomoléculaires complexes. Pour atteindre cet objectif, il faudra néanmoins qu'un effort soit fourni dans le développement d'une nouvelle génération d'instruments. La seconde est plus nuancée et réside dans le fait que la relaxométrie haute résolution telle que pratiquée dans le laboratoire a effectivement cette capacité de sonder les mouvements atomiques avec une grande précision, mais que l'extraction de paramètres biophysiques pertinents peut s'avérer (très) complexe. L'accès aux bas champs magnétiques tout en concervant la sensibilité et résolution des hauts champs magnétiques a néanmoins conduit à de nouvelles découvertes et ont montré que l'édifice que constitue la théorie de la relaxation est perfectible.

Pendant ces 3 années de recherche, j'ai cherché à répondre à des questions en lien avec des problèmes très spécifiques et liés au phénomène de relaxation. La plupart des travaux sont à ce jour publiés si bien qu'il serait tentant de déclarer que ces questions ont été répondues. Pourtant, un certain nombre de points restent encore en suspens ; les pics additionels observés sur le spectre des groupes méthyles des isoleucines de l'Ubiquine (Fig. 4b) sont-ils des artefacts liés au système expérimental ? Les prédictions faites quant aux bénéfices de la RMN à deux champs pour les paires de spins ^{13}C-^{19}F dans les résidus aromatiques sont-elles exactes ? Comment concilier MD et relaxation ? Ce dernier point me parait critique. La MD et la RMN apportent des informations à la fois complémentaires et similaires, et pourtant il n'est pas rare d'observer des différences significatives entre les résultats obtenus par l'une ou l'autre de ces techniques. Les calculs que j'ai menés recemment m'ont convaincu que les approches MF ne peuvent permettre de caractériser la dynamique des chaînes latérales aliphatiques pour lesquelles des modèles complexes doivent être utilisés. Poursuivre ces travaux préliminaires permettra d'aboutir à des modèles plus adaptés pouvant fournir des interprétations en terme de propriétés biophysiques.

General introduction

Structure and dynamics of biopolymers

Proteins and nucleic acids are the main actors in performing cellular activity, together with other small molecules (lipids, metabolites,...). Studying their functions and regulatory pathways not only helps in understanding how living organisms function and interact with their environment, but also how to design therapeutic agents to treat potential miss-functions and deseases. These molecules have been studied with atomic details, primarily by X-ray diffraction of the crystallized sample [42] but also with **N**uclear **M**agnetic **R**esonance (NMR) (both in liquid and solid states) [43] and cryogenic electron microscopy of the sample in vitreous water [44]. Obtaining the tri-dimensional organisation of the atoms that constitute the molecule has been of great interest in the frame of the "structure-function" paradigm: the function of a protein can be determined from its structure.

The structure-function paradigm has been challenged as it became clear that proteins and nucleic acids exhibit dynamic properties, and that every protein functions requires protein motions. In addition to performing critical catalitic activity in the cell [45, 46, 47], nucleic acids and associated proteins can triger **L**iquid-**L**iquid **P**hase **S**eparation (LLPS) [48], an important process in regulating gene expression for example [49, 50]. Some proteins contain elements of few tens up to hundreds of amino acids, called **I**ntrinsically **D**isordered **R**egions (IDR), and characterized by the abscence of a stable tri-dimensional structure which can be involved in a wide range of functions [51]. Folded proteins also undergo motions, other than the overall rotational diffusion that is characteristic of the hydrodynamic properties of the molecule: domain-domain motions can be triggered by the binding of ligand and change the shape of the protein, flexible parts of the protein (loops and turns) can wobble in the low nano-second range, hydrogen bonds and salt bridges can be broken and replaced in the range of micro-seconds to seconds, side chains can adopt different rotamer conformations and exchange between each of them in the tens of pico- to nano-seconde range, chemical bonds adopt libration motions,... These dynamic features are reporters of the energy landscapes of the biomolecules. These cannot be fully characterized by a single or limited set of static structures.

NMR is a versatile technique that offers information at atomic resolution, can be per-

formed in solution, *i.e* in conditions close to the native state of the biomolecule, and can report on timescales ranging from the low pico-seconds to seconds and more. As such, NMR has established itself as a powerful tool for the study of the dynamic and function of biomolecules. The constant increase in magnetic field strength [4], has lead to an increase in sensitivity and resolution of the recorded spectra, while isotope specific labeling strategies [36, 52, 53] allowed the study of larger and more challenging biomolecular assemblies [54, 55].

Studying dynamics with nuclear magnetic resonance

In NMR, radio-frequency pulses are used to create coherences and perturb the system from its equilibrium state [56]. The evolution of these coherences can produce the NMR signal and give information about the chemical environment through the chemical shifts, but also always includes the irreversible return of the spin system to its equilibrium state. This process is called *relaxation* and relies on the local interaction of nuclear spins [57, 58, 16]. In biomolecular NMR, these interactions are the dipolar interaction between a pair of spins (nuclear spins or unpaired electrons), the interaction with the ensemble of electrons around the nucleus (called chemical shift) and the interaction with the quadrupolar moment of the nucleus for isotopes with spin quantum number higher than 1/2. Due to the re-orientations of chemical bonds originating from the internal dynamics of the molecule, the interactions fluctuate. Thus, measuring the relaxation properties of nuclear spins allows one to characterize these fluctuations, that is dynamic properties of the molecule under study [10, 59].

A time correlation-function $\mathcal{C}(t)$ can be defined for these interactions, which usually corresponds to the re-orientation of the bond vectors. Its limit at infinite time relates to the amplitudes of motions, while the decay rates inform on the associated time-scales of motions. The Fourier transform of $\mathcal{C}(t)$, $\mathcal{J}(\omega)$, is the density probability of motions at frequencies ω, and is of great interest in NMR spectroscopy. Indeed, relaxation rates can be analytically expanded in linear combinations of $\mathcal{J}(\omega)$ at a limited set of frequencies [12, 13, 14]. Thus, the measurement of relaxation rates at multiple magnetic fields can lead to the characterization of the spectral density function over a wide range of frequencies and give great insights on molecular motions [60, 61]. However, at the high magnetic fields required to obtain sufficient sentivity for biomolecular NMR (typically higher than 9.4 T), the spectral density function is probed only at rather high frequencies, mostly corresponding to low pico- to low nano-seconds time-scales.

High-**R**esolution **R**elaxometry (HRR) has been developped to extend the range of frequencies that are probed by NMR relaxation rate measurements, and thus the time-scales of internal motions that can be characterized [33]. It relies on moving the sample above the magnet to use the stray field as a variable field while preserving the high-field sensivity and resolution for detection [62, 63]. This methodology has been applied to the study of phospholipids [64], DNA [65], and proteins backbone [66, 17] and side chains [21]. HRR relaxation rates require a careful analysis [67] since nuclear spins are not controlled during the relaxation delays by the use of radio-frequency pulses as in standard relaxation experiments [68]. A reliable description of the dynamic properties thus requires an accurate understanding of the active cross-relaxation pathways while the sample is outside of the NMR probe. The past few years have seen the popularization of a number of tools for the study of relaxation processes [69, 70, 20], but analytical tools for use in HRR and with applications to a broad range of situation are still missing.

Different models have been proposed to analyze NMR relaxation rates recorded on biomolecules [71, 25, 27, 72, 73], but the most popular one in biomolecular NMR remains the **M**odel **F**ree (MF) [15]. In this approach, the dynamic properties are characterized by an order parameter, that relates to the amplitude of motion and conformational entropy [23, 24], and one effective correlation time. A second time scale and order parameter were later included [74] to yield the **E**xtended **M**odel **F**ree (EMF) approach and account for the deviations observed when reproducing experimental data with the MF spectral density function. However, models based on the MF approach do not give any information about the nature of motions. NMR measurements have to be combined with **M**olecular **D**ynamic (MD) simulations to obtain a mechanistic description of dynamics [75, 21, 31, 32]. Relaxation rates measured using HRR can *a priori* lead to a better characterization of the motions [33]. Today, MD simulations can be used to identify which model is best to describe the dynamic properties of the system of interest. Thus, MD can be used to build explicit models of motions [34] that can be used to analyse HRR relaxation data in order to build a realistic picture of the motions in a combined NMR and MD analysis.

Increasing sensitivity and resolution in NMR

Although it reports on motional properties, relaxation also leads to polarization losses in the course of a pulse sequence that can translate into poor signal quality. During an NMR experiment, different coherences can be created, each of them potentially having different relaxation

rates and manipulating only spin coherences with favorable relaxation properties can lead to better signal quality. **T**ransverse **R**elaxation-**O**ptimized **S**pectroscop**Y** (TROSY) type of experiments were developped in this logic, first on ^{15}N-^{1}H spin pairs of the protein backbone [35, 76], and then on aromatic ^{13}C-^{1}H pair of aromatic rings [77] and ^{13}C^{1}H$_3$ methyl groups [36], and all rely on interferences between relaxation mechanisms [78, 79, 80]. The ^{15}N-^{1}H TROSY has allowed the study of a 900-kDa GroEL-GroES chaperone complex [81], while the 1 MDa hsp60 chaperonin was amenable to NMR studies with the methyl-TROSY approach [54]. Thus, understanding relaxation properties can help designing more sensitive experiments for the study of challenging systems.

The increase in magnetic field strength commercially available has been justified by the constant need for better sensitivity, in particular in biomolecular NMR experiments. However, the **C**hemical **S**hift **A**nisotropy (CSA) contribution to transverse relaxation quadratically scales with the magnetic field, leading to line broadening that can dramatically deteriorate the spectrum quality at high magnetic-fields. The carbonyl-^{13}C of peptide bonds has a high CSA value of about 140 ppm [82] and recording standard multi-dimensional experiments involving this nucleus will most likely become challenging at the highest available magnetic field (1.2 GHz at the time of writing). This contribution to relaxation can potentially be decreased by recording the spectra of high-CSA nuclei at lower magnetic fields, but this comes at the price of dramatic loss of sensitivity. A solution could potentially consist in using a Two-Field (2F) NMR spectrometer for the measurement [39, 37]: the dimension associated to the high-CSA nucleus could be edited at low field while the signal generated by another type of nuclear spin would be detected at high field. This would ensure high sensitivity during the detection, and high resolution in both dimension. Applications of 2F-NMR have been proposed to overcome the effect of line broadening due to chemical exchange [37], to record **TO**tal **C**orrelation **S**pectroscop**Y** (TOCSY) spectrum with broadband isotropic mixing [83] and measure low-field relaxation rates [22]. An application to multi-dimensional experiments to overcome the unfavorable high-field CSA relaxation is missing and can be considered.

Thesis outline

In the first chapter, the fundamentals of the **B**loch-**W**angsness-**R**edfield (BWR) relaxation theory will be introduced, and its implementation in a MATHEMATICA notebook will be presented with an example on the ^{15}N-^{1}H spin pair. This notebook, called REDKITE, is intended to be

as general as possible for a broad range of applications and was used throughout the projects conducted during this PhD.

In Chapter 2, we will investigate relaxation properties of $^{13}C^{1}H_3$ methyl groups in a two-field version of the high-field methyl-TROSY pulse-sequence. We will provide an explanation to the narrow linewidths that were experimentally obtained by generalizing the methyl-TROSY theory ouside the conditions for which it was initially developped (*i.e* high molecular-weight proteins and high magnetic-fields) [36]. We will then propose a 2F-TROSY experiment to record the spectrum of pairs of spin with one high-CSA nucleus. These experiments rely on the use of a 2F-NMR spectrometer to edit the chemical shift of such nuclei at low field while detecting the signal from the spin evolution of the other nucleus at high field.

Chapter 3 is dedicated to the analysis of HRR data, with two tools that were developped and can be used in a wide range of situations: **I**terative **C**orrection for the **A**nalysis of **R**elaxation **U**nder **S**huttling (ICARUS) and **M**atching **I**ntensities to **O**ptimize **T**imescales and **A**mplit**U**des of motions from **R**elaxometry (MINOTAUR). These tools are used to characterize the dynamic properties of isoleucine-δ1 methyl groups in the protein Ubiquitin.

In the last chapter of this thesis, we will review models of motions that were introduced in the 1960s and 1970s, and use them in combination with a MD simulation on Ubiquitin to re-analyse our HRR collected on isoleucine-δ1 methyl groups using explicit models of motions. In addition, we will evaluate relaxation when changes of CSA tensors are correlated with jumps between rotamer states of the isoleucine side-chains, and show that this relaxation mechanism is relevant to reproduce the measured relaxation rates.

Chapter 1

Theory of nuclear spin relaxation

Contents

1.1 Introduction

Standard **N**uclear **M**agnetic **R**esonance (NMR) experiments consist in using radiofrequency pulses to manipulate nuclear spins in a sample experiencing an intense, stable and homogenous magnetic field [16]. NMR experiments are built using three successive steps: (1) a polarization step which ensures the nuclear spins return towards their equilibrium state so the maximum magnetization, hence maximum signal, can be obtained for a given experimental time; (2) a pulse sequence step which contains radiofrequency pulses and delays designed to transfer the polarization from one spin quantum state to another; (3) a detection step during which signal is acquired. Each of these steps is influenced by the rates and pathways at which the spins return to their equilibrium state, a process called relaxation: a long polarization step is necessary when

the relaxation rates are small, lengthening the experimental time; fast relaxation properties of coherences and spin orders during the preparation step can lead to dramatic signal losses with detrimental consequences on the recorded spectra; fast relaxation properties of the coherence producing the detected signal lead to peak broadening and, consequently, a decrease in spectrum quality. The understanding of nuclear-spin relaxation is essential to interpret potential poor spectrum quality, improve already existing NMR experiments, and design new pulse-sequences. For example, the introduction of the Ernst angle [84] has lead to increased signal-to-noise ratio by using partial excitation before detection (leading to lower signal) to significantly shorten the polarization step allowing efficient signal-accumulation per unit of time. More recently, resolution and sensitivity gains were reached by exploiting relaxation interferences [78, 85, 79, 80] in **T**ransverse **R**elaxation-**O**ptimized **S**pectrosco**P****Y** (TROSY) type of pulse sequences [35, 36].

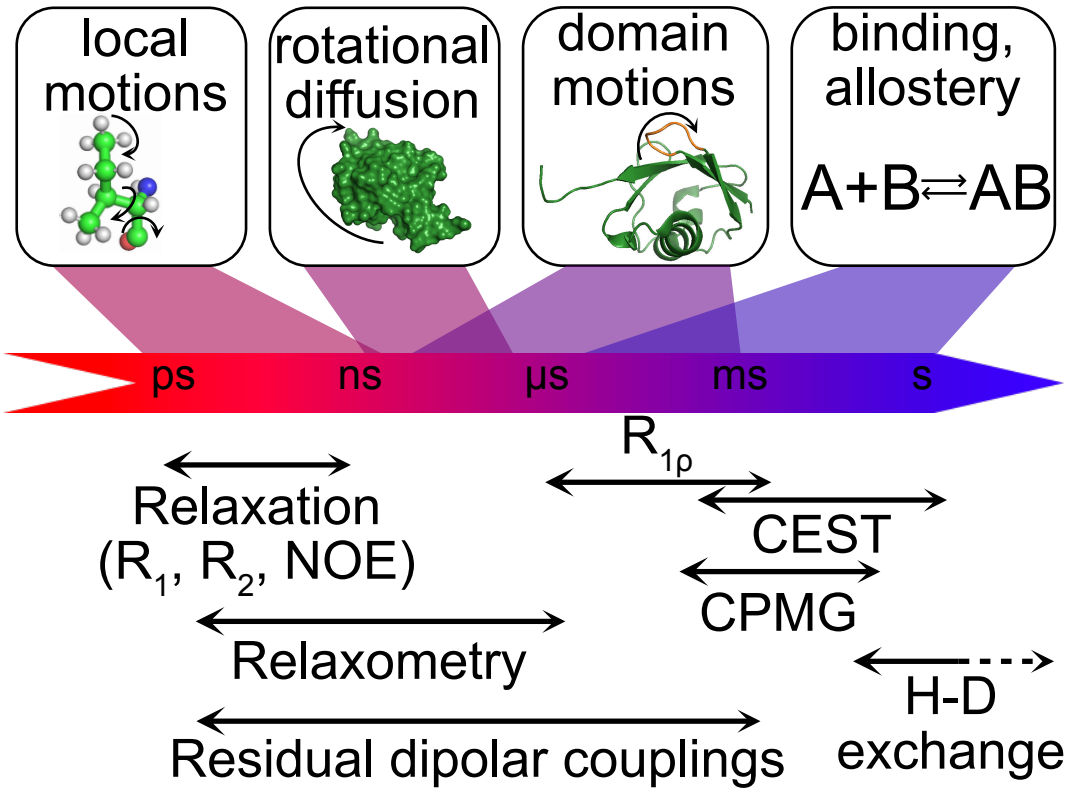

Figure 1.1: Timescales of motions in proteins and NMR experiments to probe these motions. Local motions include both side-chains (methyl rotation, C-C bond libration, rotamer jumps) and backbone motions. The dash arrow indicates that H-D exchange techniques can probe slower motions. The list of experimental techniques and type of motions shown here are non-exhaustive. CEST: Chemical Exchange Saturation Transfer. CPMG: Carr-Purcell-Meiboom-Gill. H-D exchange: Hydrogen-Deuterium exchange. NOE: Nuclear Overhauser Effect.

Relaxation of one nuclear spin is induced by the interaction of this spin with a fluctuating magnetic field. Thermal energy allows molecular motions, such as global rotational diffusion or internal chemical-bond motions, which change the orientation of the spin interactions with respect to the static field of the spectrometer magnet, and, in its turn, changes the local field experienced by the spins. Thus, the relaxation properties of nuclear spins are not only dertermerminant for the quality of the recorded spectrum, they are also reporters on the structural and dynamics characteristics of the molecule under study [10, 86]. The local fluctuations of the magnetic fields can occur on timescale varying from the picosecond to seconds and more, making NMR a perfect tool to study a broad range of dynamic processes in biomolecules, such as fast sub-nanosecond side-chain and slower backbone motions in the hundreds of nanosecond range, domain-domain reorientations and chemical reactions.

A wide range of NMR experiments has been developped to measure specific relaxation rates that report on different types of information (Fig. 1.1). In the frame of this thesis, we were essentially interested in side-chain motions in proteins, as revealed by relaxation and relaxometry types of experiments. The analysis of the collected relaxation rates allows an interpretation in terms of the internal dynamics of the system under investigation. In this chapter, the **B**loch-**W**angsness-**R**edfield (BWR) theory will be presented. This semi-classical approach allows one to treat relaxation processes in solution [12, 13, 14]. The BWR theory has been implemented in a MATHEMATICA [18] notebook which will be presented next and has been used to carry most of the calculations presented in this PhD (chapters 2 and 3).

1.2 Fundamentals of the Bloch-Wangsness-Redfield relaxation theory

We will review here the most important steps and approximations leading to the calculation of the time-evolution of the density operator. More detailled descriptions of the BWR theory can be found elsewhere [57, 79, 87, 58, 59].

1.2.1 Master equation

The evolution of the density operator $\hat{\sigma}(t)$ is described by the Liouville-von Neumann equation, in units of $\hbar$:

$$\frac{\mathrm{d}\hat{\sigma}(t)}{\mathrm{d}t} = -i[\hat{\mathcal{H}}(t), \hat{\sigma}(t)], \tag{1.1}$$

where the commutator operator applied on two operators $\hat{A}$ and $\hat{B}$ is defined as:

$$[\hat{A}, \hat{B}] = \hat{A}\hat{B} - \hat{B}\hat{A}. \tag{1.2}$$

The Hamiltonian $\hat{\mathcal{H}}$ of the system can be expressed as the sum of a stationary part $\hat{\mathcal{H}}_0$ and a smaller fluctuating part $\hat{\mathcal{H}}_1(t)$:

$$\hat{\mathcal{H}}(t) = \hat{\mathcal{H}}_0 + \hat{\mathcal{H}}_1(t). \tag{1.3}$$

This equation can be transformed in the interaction frame of the stationary Hamiltonian $\hat{\mathcal{H}}_0$. An operator $\hat{\mathcal{O}}$ transformed into the interaction frame is labeled with a tilde:

$$\tilde{\hat{\mathcal{O}}}(t) = \exp\Big\{i\hat{\mathcal{H}}_0 t\Big\}\hat{\mathcal{O}}(t)\exp\Big\{-i\hat{\mathcal{H}}_0 t\Big\}. \tag{1.4}$$

The frame transformation of the full Hamiltonian $\hat{\mathcal{H}}$ requires the subtraction of the static Hamiltoniean $\hat{\mathcal{H}}_0$, so that the Liouville-von Neumann equation (Eq. 1.1) now reads:

$$\frac{\mathrm{d}\tilde{\hat{\sigma}}(t)}{\mathrm{d}t} = i[\tilde{\hat{\sigma}}(t), \tilde{\hat{\mathcal{H}}}_1(t)]. \tag{1.5}$$

We will develop a second-order time-dependent perturbation to solve Eq. 1.5. After integration, we obtain:

$$\tilde{\hat{\sigma}}(t) = \tilde{\hat{\sigma}}(0) + i\int_0^t [\tilde{\hat{\sigma}}(t'), \tilde{\hat{\mathcal{H}}}_1(t')]\mathrm{d}t', \tag{1.6}$$

which can be inserted into Eq. 1.5 to yield the Liouville-von-Neumann equation, in the interaction frame:

$$\frac{\mathrm{d}\tilde{\hat{\sigma}}(t)}{\mathrm{d}t} = i[\tilde{\hat{\sigma}}(0), \tilde{\hat{\mathcal{H}}}_1(t)] - \int_0^t [[\tilde{\hat{\sigma}}(t'), \tilde{\hat{\mathcal{H}}}_1(t')], \tilde{\hat{\mathcal{H}}}_1(t)]\mathrm{d}t'. \tag{1.7}$$

1.2.2 Hypotheses in the BWR theory

In the frame of the BWR theory, the following hypotheses are made to calculate the ensemble average of the evolution of the density operator:

- for an ensemble average, denoted by the horizontal bar, $\overline{[\tilde{\hat{\sigma}}(0), \tilde{\hat{\mathcal{H}}}_1(t)]}$ averages to zero;
- a time t can be found that is short enough such that the evolution of the spin system is negligible on the interval $[0, t]$ but that is much larger than the typical correlation times for the fluctuations of $\tilde{\hat{\mathcal{H}}}_1(t)$.

The consequences of the second hypothesis in Eq. 1.7 are that the integration can be extended to $+\infty$, and the density operator does not depend on the variable of integration and we can perform the change $t' \to t$. The evolution of the density matrix $\tilde{\hat{\sigma}}(t)$ over time for an ensemble average, under a perturbation Hamiltonian $\tilde{\hat{\mathcal{H}}}_1(t)$, can now be expressed as:

$$\overline{\frac{\mathrm{d}\tilde{\hat{\sigma}}(t)}{\mathrm{d}t}} = -\int_0^\infty \overline{\left[\tilde{\hat{\mathcal{H}}}_1(t), [\tilde{\hat{\mathcal{H}}}_1(t+\tau), \tilde{\hat{\sigma}}(t)]\right]}\mathrm{d}\tau. \tag{1.8}$$

The second hypothesis implies that Eq. 1.8 is valid only for system close to equilibrium. In his seminal papers [13, 14], A. Redfield identifies this limitation and notes that his development is valid in the high-temperature limit for systems with weak order (*i.e.* liquid with weak collisions between particles). These conditions apply in almost all biomolecular liquid-state NMR studies. Recently, Bengs and Levitt used Lindblad operators to introduce a new form of master equation [88] that applies to systems far from their equilibium state, such as encountered in **D**ynamic **N**uclear **P**olarization (DNP) experiments [89].

1.2.3 Irreducible tensor representation

The master equation Eq. 1.8 can be further simplified using the irreducible tensor representation in order to separate the angular and spin parts of the Hamiltonian. The perturbation Hamiltonian $\tilde{\hat{\mathcal{H}}}_1(t)$ may include several interactions, identified by the label i. Each of them can be written as the sum of the product of time-dependent spatial variables $V_{l,-q}(t)$ and tensor spin

operators $\hat{T}_{l,q}$ of rank l and coherence order q (which is usually simply called order):

$$\hat{\mathcal{H}}_1(t) = \sum_i \zeta_i \sum_l \sum_{q=-l}^{l} (-1)^q V^i_{l,-q}(t) \hat{T}^i_{l,q}, \tag{1.9}$$

where ζ_i is the amplitude of the interaction i. The irreducible tensor $\hat{T}^i_{l,q}$ can be expressed as a linear combination of eigenoperators $\{\hat{A}^i_{l,q,p}\}$ of the superoperator $[\hat{H}_0, \cdot]$, with eigenvalues $\omega^{(i)}_{l,q,p}$:

$$\hat{T}^i_{l,q} = \sum_p \hat{A}^i_{l,q,p}. \tag{1.10}$$

These eigenoperators can be written in the interaction frame as:

$$\tilde{\hat{A}}^i_{l,q,p}(t) = \exp\Big\{(i\hat{\mathcal{H}}_0 t)\Big\} \hat{A}^i_{l,q,p} \exp\Big\{(-i\hat{\mathcal{H}}_0 t)\Big\} = e^{i\omega^{(i)}_{l,q,p} t} \hat{A}^i_{l,q,p}. \tag{1.11}$$

In the interaction frame, we now have:

$$\tilde{\hat{\mathcal{H}}}_1(t) = \sum_i \zeta_i \sum_l \sum_{q=-l}^{l} \sum_p (-1)^q e^{i\omega^{(i)}_{l,q,p} t} V^i_{l,-q}(t) \hat{A}^i_{l,q,p}. \tag{1.12}$$

Since $\tilde{\hat{\mathcal{H}}}_1$ is Hermitian, we can also write:

$$\tilde{\hat{\mathcal{H}}}_1(t) = \sum_i \zeta_i \sum_l \sum_{q=-l}^{l} \sum_p (-1)^q e^{-i\omega^{(i)}_{l,q,p} t} V^{i,*}_{l,-q}(t) \hat{A}^{i,\dagger}_{l,q,p}, \tag{1.13}$$

where $(\dagger)$ denotes the hermitian conjugate of the operator, and $(*)$ the complex conjugate. Substituting Eq. 1.12 and 1.13 into Eq. 1.8 gives:

$$\begin{aligned} \overline{\frac{\mathrm{d}\tilde{\hat{\sigma}}(t)}{\mathrm{d}t}} = -\sum_{i,j} \zeta_i \zeta_j \sum_{l,l'} \sum_{q=-l}^{l} \sum_{q'=-l'}^{l'} \sum_{p,p'} (-1)^{q+q'} e^{i(\omega^{(i)}_{l,q,p} - \omega^{(j)}_{l',q',p'})t} \times \\ \Big[\hat{A}^i_{l,q,p}, [\hat{A}^{j,\dagger}_{l',q',p'}, \tilde{\hat{\sigma}}(t)]\Big] \int_0^\infty \langle V^i_{l,-q}(t) V^{j,*}_{l',-q'}(t+\tau)\rangle e^{-i\omega^{(j)}_{l',q',p'}\tau} \mathrm{d}\tau, \end{aligned} \tag{1.14}$$

The correlation function $C_{i,j}$ between the interations i and j is defined as:

$$\langle V^i_{l,-q}(t) V^{j*}_{l',-q'}(t+\tau)\rangle = \delta_{q,q'} \delta_{l,l'} C_{i,j}(\tau), \tag{1.15}$$

where δ is the Kronecker delta, such that:

$$\overline{\frac{\mathrm{d}\tilde{\hat{\sigma}}(t)}{\mathrm{d}t}} = -\sum_{i,j}\zeta_i\zeta_j\sum_{l}\sum_{q=-l}^{l}\sum_{p,p'}e^{i(\omega^{(i)}_{l,q,p}-\omega^{(j)}_{l,q,p'})t}\left[\hat{A}^{i}_{l,q,p},[\hat{A}^{j,\dagger}_{l,q,p'},\tilde{\hat{\sigma}}(t)]\right]\int_0^\infty C_{i,j}(\tau)e^{-i\omega^{(j)}_{l,q,p'}\tau}\mathrm{d}\tau. \quad (1.16)$$

We assume that the functions $V^i_{l,-q}$ and $V^i_{l,-q'}$ are statistically independent unless their coherence orders are equal, which yields to the condition $q = q'$. The functions $V^i_{l,-q}$ are related to spherical harmonics (details on spherical harmonics are given in Appendix A.2). The irreducible representations of three interaction Hamiltonians are given below.

Dipole-dipole interaction The magnetic moment of a spin has an effect on the relaxation of the neighbouring spins through its local magnetic field. This dipolar coupling decreases as a function of r^3 with r the distance between the two coupled spins, and is used in NMR spectroscopy to obtain distance contrains, for example when solving protein structures [90, 91]. The dipolar coupling Hamiltonian between two spins I and S is given by [56, 92]:

$$\hat{\mathcal{H}}^{I,S}_{DD} = -\frac{\mu_0\hbar\gamma_I\gamma_S}{4\pi r^3_{IS}}\left[3\left(\vec{I}\cdot\frac{\vec{r}_{IS}}{r_{IS}}\right)\left(\vec{S}\cdot\frac{\vec{r}_{IS}}{r_{IS}}\right)-\vec{I}\cdot\vec{S}\right], \quad (1.17)$$

where μ_0 is the permeability of free space, $\hbar$ is the Planck constant divided by 2π, γ_X the gyromagnetic ratio of nucleus X and r_{IS} the internuclear distance. The Hamiltonian can be decomposed as a product of rank-2 spherical harmonics and rank-2 tensors:

$$\hat{\mathcal{H}}^{I,S}_{DD} = d_{IS}\sqrt{6}\sum_{q=-2}^{2}\sum_{p}(-1)^q\mathrm{Y}_{2q}(\Omega_{L,IS})\hat{A}^{DD}_{2,q,p}, \quad (1.18)$$

where $d_{IS} = -\frac{\mu_0}{4\pi}\frac{\hbar\gamma_I\gamma_S}{r^3_{IS}}$ is the dipolar constant, Y_{2p} are rank-2 spherical harmonics, the rank-2 tensors $\hat{A}^{DD}_{2,q,p}$ are given in Table. 1.1 together with their eigenvalues $\omega^{DD}_{2,q,p}$, and $\Omega_{L,IS}$ is the set of Euler angles for transformation from the laboratory frame to the frame of the interaction (whose main axis points along the internuclear vector).

Chemical-shift anisotropy interaction Electrons around the nucleus act as conducting coils generating a small magnetic field that adds to the external field. Thus, depending on their position on the molecules, nuclear spins are submitted to a more or less intense magnetic field compared to the static field of the NMR spectrometer. This effect, known as chemical shift, leads to peak separation in NMR spectra, and is associated to the chemical shift interaction

Table 1.1: Rank-2 tensors ($\hat{A}^{DD}_{2,q,p}$) and associated eigenvalues ($\omega^{DD}_{2,q,p}$) for the decomposition of the dipolar coupling Hamiltonian [16]. q is the coherence order of the tensor, p an index for the decomposition, $\omega_X = -\gamma_X B_0$ the Larmor frequency of spin X at magnetic field B_0. Details on spin angular momentum operators can be found in Appendix A.1.

q	p	$\hat{A}^{DD}_{2,q,p}$	$\hat{A}^{DD}_{2,-q,p} = (-1)^q \hat{A}^{DD,\dagger}_{2,q,p}$	$\omega^{DD}_{2,q,p}$
0	0	$(2/\sqrt{6})\hat{I}_z\hat{S}_z$	$(2/\sqrt{6})\hat{I}_z\hat{S}_z$	0
0	1	$-1/(2\sqrt{6})\hat{I}^-\hat{S}^+$	$-1/(2\sqrt{6})\hat{I}^+\hat{S}^-$	$\omega_S - \omega_I$
0	2	$-1/(2\sqrt{6})\hat{I}^+\hat{S}^-$	$-1/(2\sqrt{6})\hat{I}^-\hat{S}^+$	$\omega_I - \omega_S$
1	0	$-(1/2)\hat{I}_z\hat{S}^+$	$(1/2)\hat{I}_z\hat{S}^-$	ω_S
1	1	$-(1/2)\hat{I}^+\hat{S}_z$	$(1/2)\hat{I}^-\hat{S}_z$	ω_I
2	0	$(1/2)\hat{I}^+\hat{S}^+$	$(1/2)\hat{I}^-\hat{S}^-$	$\omega_I + \omega_S$

Hamiltonian [56, 93]:

$$\hat{\mathcal{H}}^I_{CS} = \gamma_I \vec{\sigma}_I \cdot \vec{B} \cdot \vec{I}, \tag{1.19}$$

where $\vec{\sigma}_I$ is the chemical shift tensor of spin I and $\vec{B}$ the magnetic field. The chemical shift tensor is written, in matrix representation:

$$\sigma_I = \begin{pmatrix} \sigma_{11} & \sigma_{12} & \sigma_{13} \\ \sigma_{21} & \sigma_{22} & \sigma_{23} \\ \sigma_{31} & \sigma_{32} & \sigma_{33} \end{pmatrix}. \tag{1.20}$$

The tensor can be split into an isotropic (rank $l = 0$), anisotropic antisymmetrical (rank $l = 1$) and anisotropic symmetric (rank $l = 2$) parts [94]:

$$\sigma_I = \sigma_{iso} \begin{pmatrix} 1 & 0 & 0 \\ 0 & 1 & 0 \\ 0 & 0 & 1 \end{pmatrix} + \begin{pmatrix} 0 & \sigma^{(a)}_{12} & \sigma^{(a)}_{13} \\ -\sigma^{(a)}_{12} & 0 & \sigma^{(a)}_{23} \\ -\sigma^{(a)}_{13} & -\sigma^{(a)}_{23} & 0 \end{pmatrix} + \begin{pmatrix} \sigma_{11} - \sigma_{iso} & \sigma^{(s)}_{12} & \sigma^{(s)}_{13} \\ \sigma^{(s)}_{12} & \sigma_{22} - \sigma_{iso} & \sigma^{(s)}_{23} \\ \sigma^{(s)}_{13} & \sigma^{(s)}_{23} & \sigma_{33} - \sigma_{iso} \end{pmatrix}, \tag{1.21}$$

where $\sigma_{iso} = \sum_{i=1}^{3} \sigma_{ii}/3$, and $\sigma^{(a)}_{ij}$ and $\sigma^{(s)}_{ij}$ refer respectively to the antisymmetric and symmetric components of the chemical shift tensor and are defined as $\sigma^{(a)}_{ij} = (\sigma_{ij} - \sigma_{ji})/2$ and $\sigma^{(s)}_{ij} = (\sigma_{ij} + \sigma_{ji})/2$. The isotropic part (rank $l = 0$) is independent from the molecular orientations and does not contribute to the relaxation (unless it is affected by conformational changes [95, 96]): it is affecting the Zeeman Hamiltonian to yield observable site-specific chemical shift in solution NMR. The anisotropic parts (rank $l = 1$ and $l = 2$) depend on the molecular orientations and contribute to the relaxation as the **C**hemical **S**hift **A**nisotropy (CSA) interaction.

The rank-1 tensor part (antisymmetric) is usually neglected. Note that, in the presence of highly anisotropic motions, the contribution of the antisymmetric CSA (rank-1 tensors) may account for up to 10 % of the contribution of the CSA rank-2 tensors to auto-relaxation [97, 98].

The rank-2 tensor part (symmetric, $\sigma_I^{(2)}$) can be diagonalized:

$$\sigma_I^{(2)} = \mathcal{R}_{CSA} \begin{pmatrix} \sigma_x - \sigma_{iso} & 0 & 0 \\ 0 & \sigma_y - \sigma_{iso} & 0 \\ 0 & 0 & \sigma_z - \sigma_{iso} \end{pmatrix} \mathcal{R}_{CSA}^{-1}, \tag{1.22}$$

where the $\sigma_i, i \in \{x, y, z\}$ are the principal components of the chemical shift tensor, and $\mathcal{R}_{CSA}$ contains the eigenvectors associated to the three eigenvalues and corresponds to the rotation matrix from the frame where σ_I was initially written (for example, the molecular frame) to the frame defined by the principal axes of the interaction. In this frame, the CSA Hamiltonian is written:

$$\begin{aligned} \hat{\mathcal{H}}_{CSA}^I = & \frac{1}{3}\gamma_I \left(\sigma_z - \sigma_x\right) \left(B_z \hat{I}_z + B_y \hat{I}_y - 2B_x \hat{I}_x\right) \\ & + \frac{1}{3}\gamma_I \left(\sigma_z - \sigma_y\right) \left(B_z \hat{I}_z + B_x \hat{I}_x - 2B_y \hat{I}_y\right). \end{aligned} \tag{1.23}$$

Three cases appear.

Isotropic chemical shift tensor In its simplest case, all components of the chemical shift are equal, and there is no CSA contribution to relaxation.

Axially symmetric chemical-shift tensor When two eigenvalues are degenerate, the CSA is axially symmetric. Let us assume $\sigma_x = \sigma_y$ (a frame transformation can always be applied to reach this particular situation). The anisotropy of the CSA is defined as:

$$\Delta\sigma_{axial} = \sigma_z - \sigma_x. \tag{1.24}$$

The CSA Hamiltonian is decomposed as:

$$\hat{\mathcal{H}}_{CSA,axial}^I = \Delta\sigma_{axial}\omega_I \sqrt{\frac{2}{3}} \sum_{q=-2}^{2} (-1)^q \mathrm{Y}_{2q}(\Omega_{L,CSA}) \hat{A}_{2,q,0}^{CSA}, \tag{1.25}$$

where $\omega_I = -\gamma_I B_0$ is the Larmor frequency of spin I at magnetic field B_0, Y_{2p} are rank-2 spherical harmonics, the rank-2 tensors $\hat{A}_{2,q,0}^{CSA}$ are given in Table. 1.2 together with their

Table 1.2: Rank-2 tensors ($\hat{A}^{CSA}_{2,q,0}$) and associated eigenvalues ($\omega^{CSA}_{2,q,0}$) for the decomposition of the CSA interaction Hamiltonian [16]. q is the coherence order of the tensor, p an index for the decomposition, $\omega_I = -\gamma_I B_0$ the Larmor frequency of spin X at magnetic field B_0. Details on spin angular momentum operators can be found in Appendix A.1.

q	$\hat{A}^{CSA}_{2,q,0}$	$\hat{A}^{CSA}_{2,-q,0} = (-1)^q \hat{A}^{CSA,\dagger}_{2,q,0}$	$\omega^{CSA}_{2,q,0}$
0	$(2/\sqrt{6})\hat{I}_z$	$(2/\sqrt{6})\hat{I}_z$	0
1	$-(1/2)\hat{I}^+$	$(1/2)\hat{I}^-$	ω_I
2	-	-	-

eigenvalues $\omega^{CSA}_{2,q,0}$, and $\Omega_{L,CSA}$ is the set of Euler angles for transformation from the laboratory frame to the CSA frame.

Asymmetric chemical-shift tensor When the three eigenvalues of the CSA tensors are different, Eq. 1.25 is not valid. Without loss of generality (a frame rotation would be sufficient to obtain such situation), we impose that $\sigma_x < \sigma_y < \sigma_z$. In order to write an equation of the form of Eq. 1.25, we write the diagonalized rank-2 tensor part of the CSA (Eq. 1.22):

$$\sigma_I^{(2)} = \mathcal{R}_{CSA} \left[\begin{pmatrix} \sigma_x - \sigma_{iso} & 0 & 0 \\ 0 & \sigma_x - \sigma_{iso} & 0 \\ 0 & 0 & \sigma_z - \sigma_{iso} \end{pmatrix} + \begin{pmatrix} 0 & 0 & 0 \\ 0 & \sigma_y - \sigma_x & 0 \\ 0 & 0 & 0 \end{pmatrix} \right] \mathcal{R}^{-1}_{CSA}, \tag{1.26}$$

From this equation, the longitudinal ($\Delta\sigma_\parallel$) and orthogonal ($\Delta\sigma_\perp$) components of the CSA tensor are defined:

$$\Delta\sigma_\parallel = \sigma_z - \sigma_x, \quad \Delta\sigma_\perp = \sigma_y - \sigma_x. \tag{1.27}$$

The CSA Hamiltonian for asymmetric chemical shift tensors is then:

$$\hat{\mathcal{H}}^I_{CSA,asym} = \omega_I \sqrt{\frac{2}{3}} \sum_{q=-2}^{2} (-1)^q \hat{A}^{CSA}_{2,q,0} \left(\Delta\sigma_\parallel \mathrm{Y}_{2q}(\Omega_{L,\sigma_\parallel}) + \Delta\sigma_\perp \mathrm{Y}_{2q}(\Omega_{L,\sigma_\perp}) \right), \tag{1.28}$$

with the same definitions as above, and $\Omega_{L,\sigma_\parallel}$ and $\Omega_{L,\sigma_\perp}$ being the Euler angles for transformation from the laboratory frame to the longitudinal and orthogonal component of the CSA frames respectively.

Quadrupolar interaction Isotopes with a quantum magnetic number higher than 1/2 possess a quadrupolar moment. The quadrupolar interaction leads often to fast relaxation at stan-

dard magnetic fields so that such spins are rarely used in solution-states biomolecular NMR. The quadrupolar interaction Hamiltonian is [56, 99]:

$$\hat{\mathcal{H}}_Q^I = \frac{e\mathcal{Q}}{6\hbar m_s^I(2m_s^I-1)} \sum_{\alpha,\beta=x,y,z} V_{\alpha\beta}\left[\frac{3}{2}\left(\hat{I}_\alpha\hat{I}_\beta + \hat{I}_\beta\hat{I}_\alpha\right) - \delta_{\alpha\beta}m_s^I(m_s^I+1)\hat{E}\right], \tag{1.29}$$

where e is the electronic charge, $\mathcal{Q}$ is the quadrupole moment, m_s^I is the quantum spin number of spin I, $V_{\alpha\beta}$ are elements of the **E**lectric **F**ield **G**radient (EFG) tensor, δ is the Kronecker delta and $\hat{E}$ is the identity operator. The Hamiltonian is decomposed using products of spherical harmonics and rank-2 tensors as [99]:

$$\hat{\mathcal{H}}_Q^I = \frac{e^2q\mathcal{Q}}{4\hbar m_s^I(2m_s^I-1)} \sum_{q=-2}^{2} (-1)^q V_q^{PAS} \mathrm{Y}_{2q}(\Omega_{L,\mathcal{Q}})\hat{A}_{2,q,0}^{\mathcal{Q}}, \tag{1.30}$$

where q is the nuclear charge, Y_{2q} are rank-2 spherical harmonics, $\Omega_{L,\mathcal{Q}}$ is the set of Euler angles for transformation from the laboratory frame to the main axis of the frame of the quadrupolar interaction, the rank-2 tensors $\hat{A}_{2,q,0}^{\mathcal{Q}}$ are given in Table. 1.3 together with their eigenvalues $\omega_{2,q,0}^{\mathcal{Q}}$, and V_q^{PAS} are components of the EFG expressed in the **P**rincipal **A**xis **S**ystem (PAS) of the quadrupolar interaction and are given by [99]:

$$V_0^{PAS} = \sqrt{6}, \quad V_{\pm1}^{PAS} = 0, \quad V_{\pm2}^{PAS} = \eta, \tag{1.31}$$

where η is the asymmetry of the EFG:

$$\eta = \left|\frac{V_{yy} - V_{xx}}{V_{zz}}\right|. \tag{1.32}$$

The value of $e^2\mathcal{Q}q/h$ has been measured in partially deuterated methyl groups of small molecules [100] and proteins with residue-specific resolution [101], and has a value of around 168 kHz.

1.2.4 The secular approximation

Oscillating terms can be neglected when they average to zero much faster than the evolution of the density operator under relaxation. This is the secular approximation. Thus, only secular terms for which $\omega_{l,q,p}^{(i)} = \omega_{l,q,p'}^{(j)}$ contribute to Eq. 1.16. In addition, only rank-2 ($l = 2$) tensors are relevant to describe dipole-dipole, CSA (*vide supra* for a discussion on the rank-1 part of

Table 1.3: Rank-2 tensors ($\hat{A}^{\mathcal{Q}}_{2,q,0}$) and associated eigenvalues ($\omega^{\mathcal{Q}}_{2,q,0}$) for the decomposition of the quadrupolar interaction Hamiltonian [16]. q is the coherence order of the tensor, p an index for the decomposition, $\omega_I = -\gamma_I B_0$ the Larmor frequency of spin X at magnetic field B_0. Details on spin angular momentum operators can be found in Appendix A.1.

q	$\hat{A}^{\mathcal{Q}}_{2,q,0}$	$\hat{A}^{\mathcal{Q}}_{2,-q,0} = (-1)^q \hat{A}^{\mathcal{Q},\dagger}_{2,q,0}$	$\omega^{\mathcal{Q}}_{2,q,0}$
0	$(1/\sqrt{6})\left(2\hat{I}_z^2 - \hat{I}_x^2 - \hat{I}_y^2\right)$	$(1/\sqrt{6})\left(2\hat{I}_z^2 - \hat{I}_x^2 - \hat{I}_y^2\right)$	0
1	$-(1/2)\left(\hat{I}_z\hat{I}^+ + \hat{I}^+\hat{I}_z\right)$	$(1/2)\left(\hat{I}_z\hat{I}^- + \hat{I}^-\hat{I}_z\right)$	ω_I
2	$(1/2)\hat{I}^+\hat{I}^+$	$(1/2)\hat{I}^-\hat{I}^-$	$2\omega_I$

the CSA) and quadrupolar interactions.

$$\overline{\frac{\mathrm{d}\tilde{\hat{\sigma}}(t)}{\mathrm{d}t}} = -\sum_{i,j}\zeta_i\zeta_j \sum_{q=-2}^{2}\sum_{p,p'} \delta_{\omega^{(i)}_{2,q,p},\omega^{(j)}_{2,q,p'}} \left[\hat{A}^i_{2,q,p}, [\hat{A}^{j,\dagger}_{2,q,p'}, \tilde{\hat{\sigma}}(t)]\right] \int_0^\infty C_{i,j}(\tau) e^{-i\omega^{(j)}_{2,q,p'}\tau}\mathrm{d}\tau. \tag{1.33}$$

This equation includes the Fourier tranform of the correlation function, called the spectral density function:

$$\mathcal{J}_{i,j}(\omega) = 2\int_0^\infty C_{i,j}(\tau)e^{-i\omega\tau}\mathrm{d}\tau. \tag{1.34}$$

Finally, the Master equation reads:

$$\overline{\frac{\mathrm{d}\tilde{\hat{\sigma}}(t)}{\mathrm{d}t}} = -\frac{1}{2}\sum_{i,j}\zeta_i\zeta_j \sum_{q=-2}^{2}\sum_{p,p'} \delta_{\omega^{(i)}_{2,q,p},\omega^{(j)}_{2,q,p'}} \mathcal{J}_{i,j}\left(\omega^{(i)}_{2,q,p}\right) \left[\hat{A}^i_{2,q,p}, [\hat{A}^{j,\dagger}_{2,q,p'}, \tilde{\hat{\sigma}}(t)]\right]. \tag{1.35}$$

Discussion on the secular approximation The secular approximation neglects the contribution from eigentensors which have different eigenfrequencies, based on the assumption that the resulting fast oscillating term average out. This holds true for eigentensors with largely different eigenfrequencies, but not necessarily for those which are close to one another without being exactly equal. We illustrate this here with the relaxation of the **Z**ero **Q**uantum (ZQ) operator $Z\hat{Q}_x$ in a two spin-1/2 system (labelled here I and S). The relaxation rate for this operator, without applying the secular approximation, can be calculated using Eq. 1.16:

$$\begin{aligned}\mathcal{R}(Z\hat{Q}_x, t) = \frac{d_{IS}^2}{8}(&2\mathcal{J}(\omega_I - \omega_S) + 3\mathcal{J}(\omega_I) + 3\mathcal{J}(\omega_S) \\ &- 2\cos(2(\omega_I - \omega_S)t)\mathcal{J}(\omega_I - \omega_S)),\end{aligned} \tag{1.36}$$

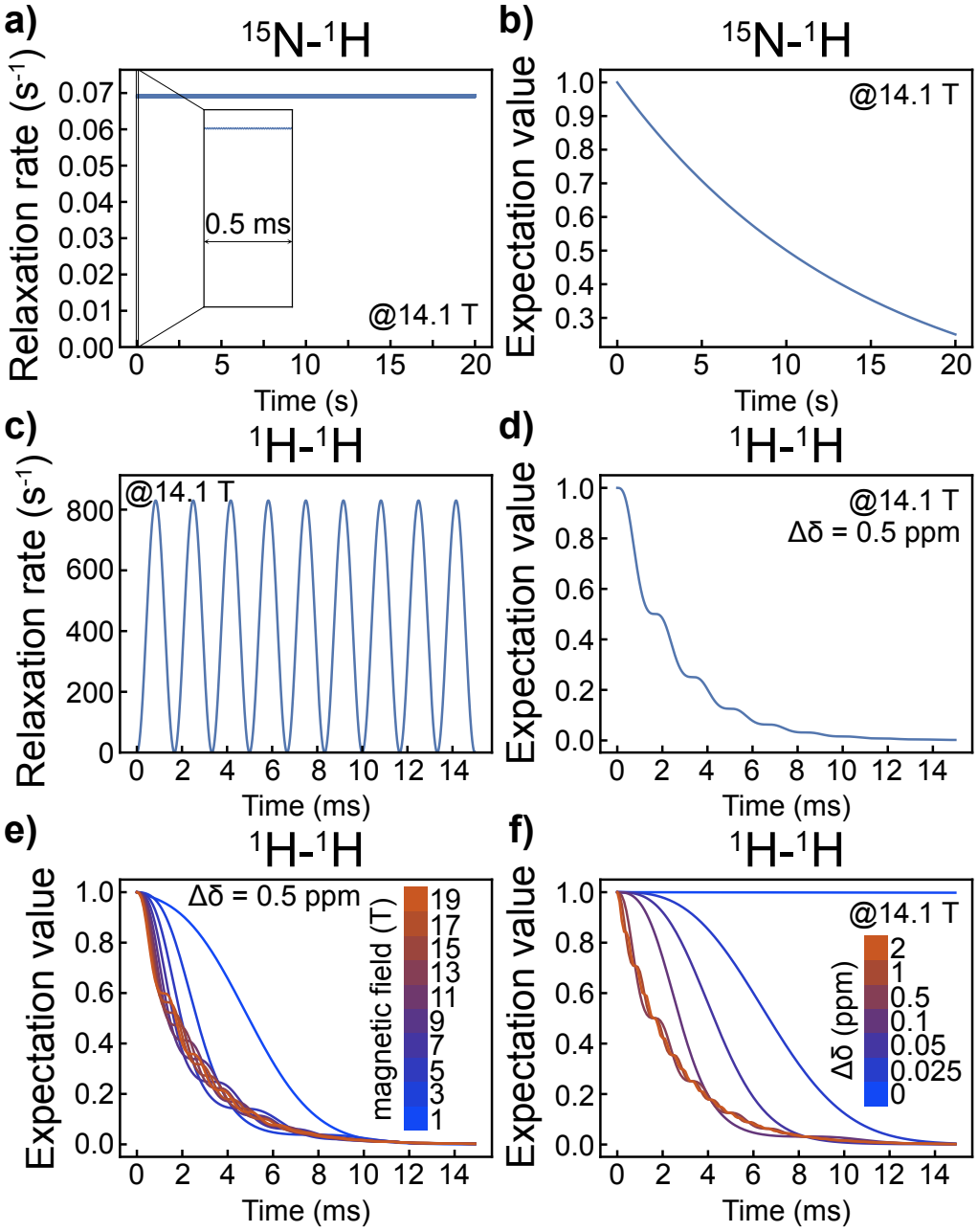

Figure 1.2: Illustration of the secular approximation effects. Relaxation rate (**a**, **c**) and expectation value (Eq. 1.38, **b**, **d**) of the $Z\hat{Q}_x$ operator for a ^{15}N-^{1}H (**a**,**b**) and two non-equivalent protons (**c**,**d**) spin pairs as a function of time at 14.1 T. A zoom over the first 10 ms of the evolution is shown in **a**. Expectation value of the $Z\hat{Q}_x$ operator in a non-equivalent ^{1}H-^{1}H spin system as a function of time for different value of magnetic field (**e**) and chemical shift difference $\Delta\delta$ between the two protons (**f**). In both the ^{15}N-^{1}H and ^{1}H-^{1}H cases, the internuclear distance is the same and set to 1.02 Å. This accentuates the effects in the homonuclear spins system case.

where the time-dependence arises from the last term, $\omega_X = -\gamma_X B_0$ is the Larmor frequency of spin X at magnetic field B_0, d_{IS} is the dipolar constant and $\mathcal{J}$ the spectral density function which, here, comes solely from the global tumbling:

$$\mathcal{J}(\omega) = \frac{2}{5}\frac{\tau_c}{1+(\omega\tau_c)^2}, \tag{1.37}$$

where τ_c is the global tumbling correlation time (choosen in the simulations presented here to be 25 ns, which rougly corresponds to the global tumbling correlation time of a 50 kDa protein at 298 K). Without the time dependent term, Eq. 1.36 is in agreement with reported rates for ZQ operators [16]. The expectation value $\langle Z\hat{Q}_x\rangle(t)$ of the operator $Z\hat{Q}_x$ can be computed using:

$$\langle Z\hat{Q}_x\rangle(t+\delta t) = \langle Z\hat{Q}_x\rangle(t) e^{-\delta t \mathcal{R}(Z\hat{Q}_x,t)}, \tag{1.38}$$

where δt is sufficiently small so that we can approximate the decay of $\langle Z\hat{Q}_x\rangle$ to be mono-exponential with a unique rate over the time δt. In the simulations presented here, δt is set to 1 μs.

First, let us consider a ^{15}N-^{1}H spin system, as can be found in the peptide plane of proteins. The Larmor frequency of the proton is about 10 times higher (in absolute value) than the nitrogen-15 Larmor frequency so that the oscillating term in Eq. 1.36 varies extremely fast and does not affect significantly the value of the relaxation rate (Fig. 1.2a), and the decay of the expectation value for the operator $Z\hat{Q}_x$ is mono-exponential (Fig. 1.2b). In this case, the secular approximation is justified.

Let us now consider a spin system composed of two non-equivalent protons. We will first consider a 0.5 ppm chemical shift different between them. The relaxation rate at 14.1 T shows large-amplitude variations, on timescales similar to relaxation (Fig. 1.2c,d). During the relaxation decay, the relaxation rate changes, leading to oscillations in the decay of the expectation value. These are particularly significant since the oscillating part involves the spectral density function evalutaed at $\omega_I - \omega_S$ and, for two non-equivalent protons, $\mathcal{J}(\omega_I - \omega_S) \gg \mathcal{J}(\omega_I) \approx \mathcal{J}(\omega_S)$. The difference frequency between the two protons depends on the magnetic field, and the frequency of these oscilations decreases when the magnetic field decreases. The relaxation being faster at lower magnetic fields, the oscillations in the expectation value are not visible (Fig. 1.2e) since the polarization decays to 0 in a time-scale much smaller than the oscillation

period, but the decays show clear deviations from a mono-exponential behavior. These conclusions also apply when, instead of changing the magnetic field, the difference in chemical shift in changed (Fig. 1.2f). When the two protons have the same chemical shift ($\Delta\delta = 0\,\text{ppm}$), the relaxation is mono-exponential and occurs on a timescale three orders of magnitude longer than the one shown in Fig. 1.2f.

In the case of non-equivalent homonuclear spin systems, the systematic use of the secular approximation can miss some important features of the relaxation process. Such situation presented here do not occur for the longitudinal and transverse relaxation, dipole-dipole cross-relaxation or two-spin order relaxation. It can only be expected when the operator of interest is expressed as a sum of operators, such as $\hat{ZQ}_x$, $\hat{ZQ}_y$, and their **D**ouble **Q**uantum (DQ) counterparts $\hat{DQ}_x$ and $\hat{DQ}_y$.

1.2.5 Relaxation in the laboratory frame

The final step consists in transforming Eq. 1.8 from the interaction representation back to the Schrödinger representation given in Eq. 1.1. For this, we invert Eq. 1.4:

$$\hat{\sigma}(t) = \exp\Big\{-i\hat{\mathcal{H}}_0 t\Big\}\tilde{\hat{\sigma}}(t)\exp\Big\{i\hat{\mathcal{H}}_0 t\Big\}, \tag{1.39}$$

with time-derivative:

$$\frac{\mathrm{d}\hat{\sigma}(t)}{\mathrm{d}t} = -i[\hat{\mathcal{H}}_0, \hat{\sigma}(t)] + \exp\Big\{-i\hat{\mathcal{H}}_0 t\Big\}\frac{\mathrm{d}\tilde{\hat{\sigma}}(t)}{\mathrm{d}t}\exp\Big\{i\hat{\mathcal{H}}_0 t\Big\}. \tag{1.40}$$

Inserting Eq. 1.35 into Eq. 1.40 leads to:

$$\overline{\frac{\mathrm{d}\hat{\sigma}(t)}{\mathrm{d}t}} = -i\overline{[\hat{\mathcal{H}}_0, \hat{\sigma}(t)]} - \frac{1}{2}\sum_{i,j}\zeta_i\zeta_j\sum_{q=-2}^{2}\sum_{p,p'}\delta_{\omega^{(i)}_{2,q,p},\omega^{(j)}_{2,q,p'}}\mathcal{J}_{i,j}\Big(\omega^{(i)}_{2,q,p}\Big)\Big[\hat{A}^{i}_{2,q,p}, [\hat{A}^{j,\dagger}_{2,q,p'}, \hat{\sigma}(t)]\Big]. \tag{1.41}$$

We now define the relaxation super-operator $\hat{\hat{\mathcal{R}}}$ as:

$$\hat{\hat{\mathcal{R}}} = \frac{1}{2}\sum_{i,j}\zeta_i\zeta_j\sum_{q=-2}^{2}\sum_{p,p'}\delta_{\omega^{(i)}_{2,q,p},\omega^{(j)}_{2,q,p'}}\mathcal{J}_{i,j}\Big(\omega^{(i)}_{2,q,p}\Big)\Big[\hat{A}^{i}_{2,q,p}, [\hat{A}^{j,\dagger}_{2,q,p'}, \cdot]\Big]. \tag{1.42}$$

The relaxation rate between operators $\hat{A}$ and $\hat{B}$ is:

$$\mathcal{R}(\hat{A},\hat{B}) = \frac{\langle \hat{B}|\hat{\hat{\mathcal{R}}}|\hat{A}\rangle}{\sqrt{\langle \hat{A}|\hat{A}\rangle\langle \hat{B}|\hat{B}\rangle}}. \tag{1.43}$$

If $\hat{A} = \hat{B}$, the rate $\mathcal{R}(\hat{A},\hat{B})$ is called an auto-relaxation rate, while if $\hat{A} \neq \hat{B}$, the rate $\mathcal{R}(\hat{A},\hat{B})$ is refered to as a cross-relaxation rate, if $i = j$, it is an auto-correlated relaxation rate, and if $i \neq j$ a cross-correlated relaxation rate. These rates can easily be calculated analytically using the BRW engine [70]. This tool calculates the double commutator for each pair of spin tensors with identical eigenfrequencies and multiplies them by the spectral density function evaluated at this frequency. The implementation of this algorithm in MATHEMATICA [18] is detailed in section 1.3.

1.2.6 Models of correlation function

The correlation function reports on the local and global fluctuations of the Hamiltonian operators of interactions, and hence often reorientations of bond vectors, in the fixed laboratory frame. Analytical models to describe the correlation function are of great interest to interpret NMR relaxation data in terms of dynamics of the molecules under investigation. Depending on the type of motions, different forms of correlation functions have been derived from the Master equation of diffusion in the 1960's-1970's, with applications in both NMR and fluorescence spectroscopy. Luginbühl and Wüthrich published a survey on the most important types of motions and their associated correlation functions [34], and these will be discussed in details in chapter 4. In the early 80's, Lipari and Szabo pointed out that using these models to the study of biomolecules can lead to overinterpretation of data as the analysis requires a *a priori* knownledge or physical intuition of the model of motions [15]. Following their argument that 'models cannot be proven; they can only be eliminated' (quoted from [15]), they introduced the **M**odel **F**ree (MF) approach, which is now widely used in biomolecular NMR, either as it was originially proposed [15, 102] or as a basis for more complex correlation functions [74, 103, 21]. It must be noted that even if without internal motional model assumptions [15, 104], the MF approach is not free of any hypothesis. One of them is the factorisation of the global rotational diffusion and internal motion correlation functions. This is mathematically rigorous when the global tumbling is isotropic and uncorrelated with internal motions. Lipari and Szabo proposed an approximated form of the correlation function when the tumbling is anisotropic and uncorrelated from the internal motions [15] which has been used in a number of studies [105, 106, 107, 108, 109].

The MF approach leads to satisfactory results for the analysis of folded proteins, but a single effective correlation time for internal motion cannot accurately reproduce relaxation data of **I**ntrinsically **D**isordered **P**roteins (IDP) for which dynamics occur over a wide range of timescale. An approach, called **I**nterpretation of **M**otions by a **P**rojection onto an **A**rray of **C**orrelation **T**imes (IMPACT) [110], as been proposed to write the correlation function of IDPs as a distribution of correlation times. It does neither assume any particular type of motion, nor a decorrelation of global tumbling and internal motions, nor a intra-residue correlation/decorrelation of motions.

The independence of the rotational diffusion and internal motions has been questionned in folded proteins: for example, loop motions or inter-domain motions can affect the overall shape of the molecule and thus, the diffusion tensor. The **S**lowly **R**elaxing **L**ocal **S**tructure (SRLS) model aims at taking such correlations into account by modeling the interaction frame motions as a diffusion in a potential which depends on the molecular environment [71, 25, 27]. Correlation functions in the presence of correlated global tumbling and conformers exchange (*i.e.* domain jump motions) have also been proposed, for both isotropic [111] and anisotropic [112, 113] tumbling diffusion tensors.

1.3 Implementation of the Bloch-Wangsness-Redfield theory in RedKite

The computation of the relaxation rates is highly efficient with the formalism of the BRW engine [70] which does not require an explicit expression of the spherical harmonics defining the correlation function (Eq. 1.15). Relaxation rates are first expressed as a function of the spectral density function $\mathcal{J}_{i,j}(\omega, \theta_i, \theta_j)$ where θ_k is the orientation of the interaction k in the **S**ystem **F**rame (SF) of the chemical moiety. This frame corresponds to an arbitrary frame in which the orientation of the interactions are calculated. The different steps of RedKite are presented in the flowchart shown in Fig. 1.3. We will illustrate the use of RedKite on an isolated pair of spin-1/2 nuclei: a ^{15}N-^{1}H pair. RedKite notebooks for an isolated ^{15}N-^{1}H spin pair and $^{13}C^{1}H^{2}H_{2}$ methyl group with a vicinal deuterium can be found at: `https://figshare.com/articles/software/RedKite/11745111`. As will become clear in the follwing sections, RedKite consists in a succession of commands imported from the SpinDynamica package [20]. This section is largely based on the associated published work [19].

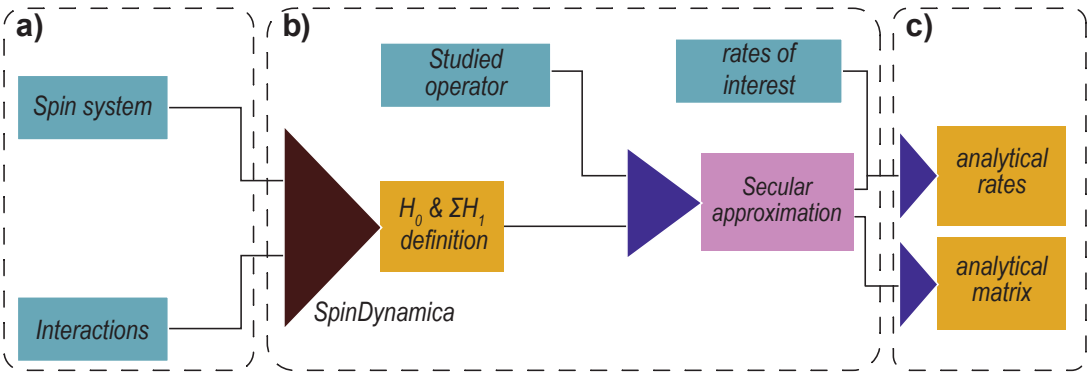

Figure 1.3: Schematic representation of the RedKite calculation, describing input information and the output of the Mathematica notebook. **a)** Initial inputs from the user are the spin system (isotopes and geometry) and CSA and quadrupolar interactions properties. **b)** After definition of the operator basis, Hamiltonian operators are defined. After indicating the operator of the basis studied during the experiment, a reduction of the size of the basis is performed. Rates of interest that will be calculated are defined as well. **c)** Calculations produce analytical expressions for the relaxation rates and the relaxation matrix. Blue rectangles: user inputs. Yellow rectangles: calculated outputs. Pink rectangle and purple triangles: tasks performed by RedKite. Figure reproduced from [19].

1.3.1 Definition of the spin system

The first step is to define the spin system by specifying for each nuclear spin the nucleus type with its isotopic number, and a unique label for each spin which is used for identification. We present as an illustration the example of a simple spin system composed of an isolated ^{15}N-^{1}H pair. The spin system is therefore defined as:

$$\text{Nuclei} = \{\{\text{"15N","NA"}\}, \{\text{"1H", "HA"}\}\};$$

where "NA" and "HA" refer to the Nitrogen-15 and Proton respectively, before running the SpinDynamica [20] SetSpinSystem command.

The geometry of the spin system is defined next. We define an array of size $n \times 3$ (where n is the number of nuclei in the spin system, in our case 2) containing the position of each atom in a Cartesian axis system. In our example, we set the nitrogen nucleus at the origin of the axis system and the proton 1.02 Å away from the nitrogen in the z-direction:

$$\text{Coordinates} = \{\{0, 0, 0\}, \{0, 0, 1.02 \times 10^{-10}\}\};$$

To complete the definition of the spin system, the CSA and quadrupolar properties have to be defined. The nuclei for which the CSA will be considered must be defined as such. In our example, we will only consider the nitrogen CSA:

$$\text{CSAConsidered} = \{1, 0\};$$

It is possible to give a numerical value to the CSA or keep its value as an analytical parameter. We will consider this latter case here:

$$\delta_{csa}[1] = \Delta\sigma_N;$$

Note that defining $\delta_{csa}[2]$ is not necessary since the proton CSA is neglected in our example. Similarly, the strength of the quadrupolar interaction does not need to be defined (see Appendix B.4 for an example that includes quadrupolar interactions).

The orientations of the CSA tensor have to be given (either numerically or analytically) as projections on the 3 axes of the molecular frame. For the sake of simplicity, we choose an alignement along the N-H axis:

$$\text{vectorNum}_1^{\text{"CSA"}} = \{0,\ 0,\ 1\};$$

The index 1 refers to the first spin in the spin system (*i.e.* the nitrogen-15). There is also a possibility to consider asymmetric CSA tensors. In this case, the asymmetric CSA tensor is decomposed in two axially symmetric components. The longitudinal and orthogonal component of the CSA have to be defined using the variables names σlong[i] and σperp[i] for the longitudinal and orthogonal values of the CSA tensors of isotope i, and vectorNuml$_i^{\text{"CSA"}}$ and vectorNump$_i^{\text{"CSA"}}$ for the associated orientations. Table B.1 contains the definitions of the different variables of RedKite.

1.3.2 Definition of spin tensors and Hamiltonian

Three different types of interactions are considered in RedKite: the dipolar couplings, the CSA (in the case where at least one spin has a CSA) and the quadrupolar couplings (in the case where spins with $m_s > 1/2$ are present in the spin system). Analytical forms of these Hamiltonian operators are calculated automatically. Other Hamiltonian operators can be defined and added if other interactions or effects are considered.

Calculation of Hamiltonian operators requires the definition of spin-tensor operators. SpinDynamica already contains their definition, but each tensor of coherence order-q is given as a linear combination of eigentensors [20]. Consequently, SpinDynamica tensors can be linear combinations of eigenvectors with different eigenfrequencies, which is an inappropriate basis to perform the secular approximation (based on the equality of eigenfrequencies of two eigenvectors). The secular approximation is better performed with complete separation of the tensor operators. The definition of each tensor is given in Table 1.1, 1.2 and 1.3, and their definition in Mathematica can be found in Appendix B.2. In the case of non-equivalent homonuclear spin systems, performing the secular approximation is more complex, as shown in previous section. RedKite performs the secular approximation, even in these situations. Numerical tools, such as Spinach [70], are available to study such systems. The Hamiltonian, as written in RedKite, can be found in Appendix B.3.

In the definitions of the Hamiltonians, we introduce the function **M**, similarly to the BRW engine [70], which depends on the operator coherence order m being considered, its associated eigenfrequency, a time t at which the Hamiltonian is calculated, and the orientation of the interactions. The function **M** is useful when calculating the double commutators to obtain relaxation rates (as detailed in the previous section). Products of the function **M** appear, which

are simplified according to:

M[l_, f1_, 0, i_]Conjugate[M[k_, f2_, t_, j_]] := KroneckerDelta[l, k] KroneckerDelta[f1, f2] G[t, i, j];

where KroneckerDelta$[x, y] = 1$ if $x = y$ and 0 otherwise, l and k are associated to tensor coherence order, *f1* and *f2* to the tensor eigenfrequencies, t the time at which the Hamiltonian is calculated, and i and j are the orientation of the interactions in the molecular frame. *G[t, f1, i, j]* is the correlation function evaluated at time t and is further replaced by the spectral density function evaluated at frequency $f1$ by using the function *BRWIntegrate*:

BRWIntegrate[$e^{\text{Times[Complex[0,}a\text{_],}t,f1\text{]}}$G[t, i_, j_]] := J[a×f1, i, j] ;

where the coefficients a are obtained from the eigenvalues of the eigentensors. For auto-correlation, $i = j$, while cross-correlation is obtained when $i \neq j$.

1.3.3 Analytical and numerical spin state restriction

The number of operators in the basis is equal to 4^n for n spin-1/2 nuclear spins. Hence, in a two spin-1/2 system there are 16 operators, which is still a workable number. For more complex spin systems, reducing the size of the basis to keep only terms relevant for the analysis of an experiment is essential. We only keep the terms contributing to the relaxation of the operator of interest (that is the operator for which the evolution of the expectation value with time needs to be carefully evaluted) following the scheme of Fig. 1.4. First, only terms with the same coherence order as the operator of interest are selected (indicated in blue in Fig. 1.4a). Then, the secular approximation is involved to average out all non-secular terms in the interaction frame (Fig. 1.4b). Cross-relaxation rates with the operator of interest in this reduced basis are calculated (Fig. 1.4c) and the operators with no cross-relaxation with the operator of interest are discarded from the basis (here this last step only removes the identity operator $\hat{E}$, Fig. 1.4d). This step is basis-dependent and some indirect cross-relaxation pathways affecting the operator of interest may be suppressed. An additional step can be applied for large spin systems to sort and select only major cross-relaxation pathways. In our example of an isolated ^{15}N-^{1}H spin pair with a CSA on the nitrogen-15 and the $\hat{N}_z$ operator defined as the operator of interest, only 3 terms remain in the basis:

$$\text{ReducedBasis} = \{\text{NA}_\text{z}, \text{HA}_\text{z}, 2\text{NA}_\text{z}\text{HA}_\text{z}\};$$

The user can also manually define its own basis.

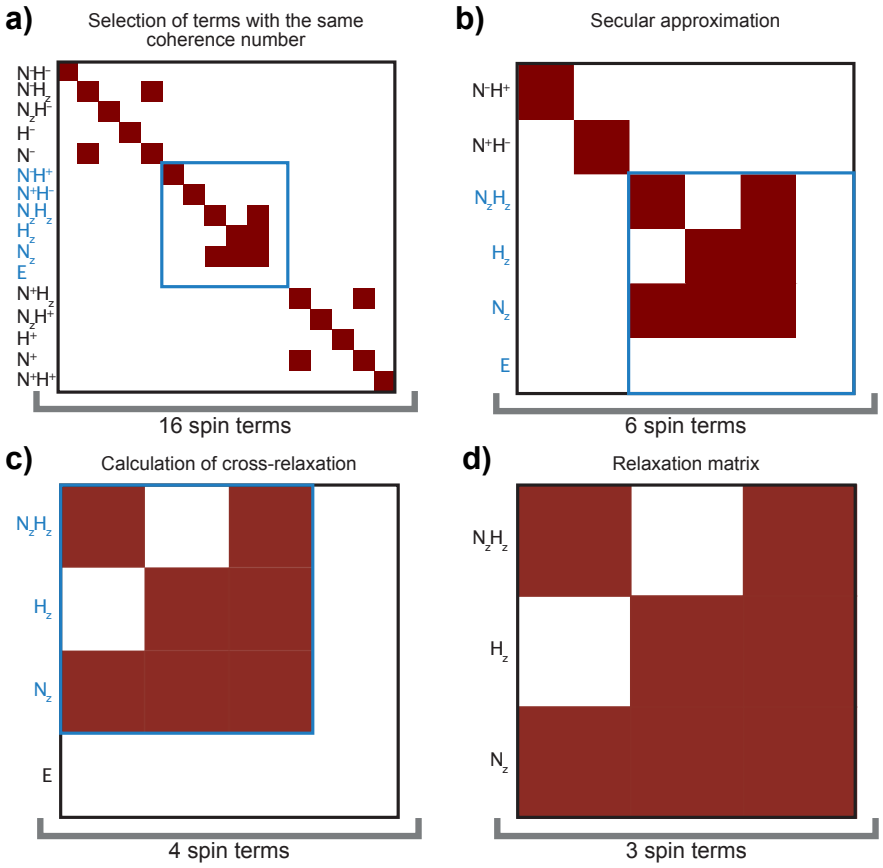

Figure 1.4: Reduction of the matrix size for our case example of a ^{15}N-^{1}H spin system. **a)** A ^{15}N-^{1}H isolated spin pair has 16 operators in its basis. **b)** The first step of the matrix reduction size consists in keeping only terms that have the same coherence order as the spin-term of interest, leading to 6 terms in the basis. **c)** The secular approximation allows another level of size reduction: only terms that are secular with the Zeeman Hamiltonian are kept in the basis. Two zero-quantum operators are removed at this stage. **d)** In the absence of cross-relaxation with the spin term of interest N_z, the identity operator is removed from the basis and the final basis contains 3 operators. In this graphical representation of the relaxation matrices, a red square indicates a non-zero value for the corresponding relaxation rate. The blue rectangles contain the selected part of the relaxation matrix after each steps of the size reduction. Normalization factors for the spin operators have been omitted for clarity. Figure reproduced from [19].

1.3.4 Calculations

Once the basis has been defined, the relaxation matrix can be calculated:

$$\mathrm{RM} = \begin{pmatrix} R_1^{\mathrm{N}} & \sigma_{\mathrm{NH}} & \delta_{\mathrm{N}} \\ \sigma_{\mathrm{NH}} & R_1^{\mathrm{H}} & 0 \\ \delta_{\mathrm{N}} & 0 & R_{\mathrm{NH}} \end{pmatrix},$$

where R_1^{N} and R_1^{H} refer to the nitrogen-15 and proton longitudinal relaxation rates respectively, R_{NH} to the auto-relaxation rate of the two-spin order $2\hat{N}_z\hat{H}_z$, σ_{NH} to the dipole-dipole cross-relaxation rate between nitrogen-15 and proton and δ_{N} to the cross-relaxation rate due to the cross-correlation of the nitrogen-15 CSA and the **D**ipole-**D**ipole (DD) coupling with the proton:

$$R_1^{\mathrm{N}} = \frac{d_{\mathrm{NH}}^2}{4}(\mathcal{J}(\omega_{\mathrm{N}} - \omega_{\mathrm{H}}) + 6\mathcal{J}(\omega_{\mathrm{N}} + \omega_{\mathrm{H}}) + 3J(\omega_{\mathrm{N}})) + \frac{1}{3}\Delta\sigma_{\mathrm{N}}^2\omega_{\mathrm{N}}^2\mathcal{J}(\omega_{\mathrm{N}}), \quad (1.44)$$

$$R_1^{\mathrm{H}} = \frac{d_{\mathrm{NH}}^2}{4}(\mathcal{J}(\omega_{\mathrm{N}} - \omega_{\mathrm{H}}) + 6\mathcal{J}(\omega_{\mathrm{N}} + \omega_{\mathrm{H}}) + 3\mathcal{J}(\omega_{\mathrm{H}})), \quad (1.45)$$

$$R_{\mathrm{NH}} = \frac{d_{\mathrm{NH}}^2}{4}(3\mathcal{J}(\omega_{\mathrm{N}}) + 3\mathcal{J}(\omega_{\mathrm{H}})) + \frac{1}{3}\Delta\sigma_{\mathrm{N}}^2\omega_{\mathrm{N}}^2\mathcal{J}(\omega_{\mathrm{N}}), \quad (1.46)$$

$$\sigma_{\mathrm{NH}} = \frac{d_{\mathrm{NH}}^2}{4}(-\mathcal{J}(\omega_{\mathrm{N}} - \omega_{\mathrm{H}}) + 6\mathcal{J}(\omega_{\mathrm{N}} + \omega_{\mathrm{H}})), \quad (1.47)$$

$$\delta_{\mathrm{N}} = \Delta\sigma_{\mathrm{N}}\omega_{\mathrm{N}}d_{\mathrm{NH}}\mathcal{J}(\omega_{\mathrm{N}}), \quad (1.48)$$

with $d_{\mathrm{NH}} = -\frac{\mu_0}{4\pi}\frac{\hbar\gamma_{\mathrm{H}}\gamma_{\mathrm{N}}}{r_{\mathrm{NH}}^3}$ the dipolar coefficient between the proton and the nitrogen-15, r_{NH} the distance separating the two nuclei, γ_X the gyromagnetic ratio of nucleus X, $\hbar$ the Plank constant divided by 2π, μ_0 the permeability of free space, and $\Delta\sigma_{\mathrm{N}} = \sigma_{\mathrm{zz}} - \frac{\sigma_{\mathrm{xx}}+\sigma_{\mathrm{yy}}}{2}$ the CSA of the nitrogen-15 with σ_{kk} the k^{th} diagonal element of the chemical shift tensor. $\mathcal{J}$ is the spectral density function and is expressed as a function of the proton (ω_{H}) and nitrogen-15 (ω_{N}) Larmor frequencies.

All types of relaxation rates in this spin system can be calculated. In such a spin system, it is relatively easy to record longitudinal and transverse relaxation rates for the nitrogen-15 nucleus, as well as the cross-relaxation rate with the proton. These rates are calculated by:

```
RatesOfInterest = {
{Rate[opI["NA", "z"], opI["NA", "z"]], "R1N"},
{Rate[opI["NA", "+"], opI["NA", "+"]], "R2N"},
{Rate[opI["NA", "z"], opI["HA", "z"]], "Sigma"}};
```

where Rate is the implemented command to calculate relaxation rates as described in the section 1.2. This leads to the expression of transverse relaxation rate for nitrogen-15:

$$\begin{aligned} R_2^{\mathrm{N}} =& \frac{d_{\mathrm{NH}}^2}{8}(\mathcal{J}(\omega_{\mathrm{N}} - \omega_{\mathrm{H}}) + 6\mathcal{J}(\omega_{\mathrm{N}} + \omega_{\mathrm{H}}) + 3\mathcal{J}(\omega_{\mathrm{N}}) + 6\mathcal{J}(\omega_H) + 4\mathcal{J}(0)) \\ &+ \frac{1}{18}\Delta\sigma_{\mathrm{N}}^2\omega_{\mathrm{N}}^2(3\mathcal{J}(\omega_{\mathrm{N}}) + 4\mathcal{J}(0)). \end{aligned} \tag{1.49}$$

1.3.5 Model free spectral density function

The user has to provide at least one definition of spectral density function in order to have a model for the dynamics of the system. In our case, we can use a model-free approach [15] with a correlation time for global tumbling τ_c, one order parameter S^2 and an effective correlation time for internal motions τ_{int}:

$$\mathcal{J}(\omega) = \frac{2}{5}\left(\frac{S^2\tau_c}{1+(\omega\tau_c)^2} + \frac{(1-S^2)\tau'_{int}}{1+(\omega\tau'_{int})^2}\right), \tag{1.50}$$

where $\tau_{int}'^{-1} = \tau_c^{-1} + \tau_{int}^{-1}$. This function is implemented in RedKite as:

$$\begin{aligned} \mathrm{JNH}[\omega\_, i\_, j\_] :=& \mathrm{Module}[\{\mathrm{spec}, \tau 1\}, \\ \tau 1 =& \tau_c\tau_{int}/(\tau_c + \tau_{int}); \\ \mathrm{spec} =& \frac{2}{5}\left(S2\frac{\tau_c}{1+(\omega\tau_c)^2} + \right. \\ & \left. (1-S2)\frac{\tau 1}{1+(\omega\tau 1)^2}\right)] \end{aligned}$$

Other models of spectral density function can be used as well. At this point, the relaxation rates seen above can be expressed as a function of the parameters of the dynamics of the system (order parameter and correlation times). Numerical calculations can be performed if values for the parameters of the spectral density function are provided.

1.4 Conclusion

The basis of the BWR relaxation theory [12, 13, 14] was introduced in this chapter, and some of its main hypotheses were discussed. The secular approximation may lead to substantial deviations form the expected evolution of the spin system under relaxation only in particular situations. The range of applicability of the theory to high-temperature and weak-order solution is not limitting in the context of biomolecular liquid-state NMR where they are fullfilled [13, 14].

The BWR theory has been implemented in a MATHEMATICA [18] notebook using the SPINDYNAMICA package [20]. This program, called REDKITE, is applicable to a wide range of spin systems. An illustration of its usuage has been detailed for an isolated ^{15}N-^{1}H spin pair. REDKITE has been used by others to help designing experiments to improve the sensitivity of **N**uclear **O**verhauser **E**ffect **S**pectroscop**Y** (NOESY) experiments [114] and analyse quadrupole relaxation in methyl groups [115]. Three applications of REDKITE will be detailed in this manuscript: understanding experimental spectra recorded under unsual conditions (chapter 2), and calculating relaxation matrix for systems of interest to design new experiment (chapter 2) or analyse relaxation data (chapter 3). In the frame of the BWR relaxation theory, the relaxation super-operator (Eq. 1.42) shows two distinct elements:

- The tensor part. It is determined by the spin system. During the course of an experiment, the proper selection of coherence pathway can lead to relaxation-optimized pulse sequence. The TROSY types of pulse sequences [35, 36] apply this idea to select slowly relaxing-operators. In chapter 2 we will use these aspects to rationalize the observation of a methyl-TROSY effect in a situation where it is not expected.

- The lattice part. This is the spectral density function, which is determined by the dynamics of the molecule. Its dependence on the Larmor frequency leads to a magnetic field dependence of the relaxation. In chapter 2, we will show how we can use this aspect to develop multiple-field NMR spectroscopy with improved sensitivity compared to single-field experiments. In addition, the measurement of relaxation rates at different fields allows a mapping of the spectral density function and an interpretation in terms of dynamics. These aspects will be investigated in chapter 3. In the chapter 4, we will review and analyze some models of correlation function to study the dynamics of biomolecules, and propose new correlation functions for the analysis of side-chain dynamics.

Chapter 2

Two-field NMR and TROSY

Contents

2.1 Introduction

Structural biology aims at describing the intricate relationship between the structure, dynamics and function of biomolecules. Among all the techniques brought by decades of methodological developments, **N**uclear **M**agnetic **R**esonance (NMR) is the only one with the ability to provide direct information on all these three aspects. However, NMR suffers from a limited sensitivity which significantly decreases as the size of the molecule increases. Consequently, until the very end of the 20$^{\text{th}}$ century, biomolecular NMR rarely focussed on systems exceeding 30 kDa. The progress of NMR over the last decades was made possible by the constant development of magnets with higher magnetic fields [4], the availability of more sensitive probes, especially cryogenic probes, as well as countless innovative methodological developments. A major breakthrough

for the investigation of large biomolecules has been the introduction of **T**ransverse **R**elaxation-**O**ptimized **S**pectroscop**Y** (TROSY) [35]. In the ^{15}N-^{1}H spin pair present in peptide bonds, the TROSY effect relies on the selection of a coherences that benefit from destructive interference between the **C**hemical **S**hift **A**nisotropy (CSA) and **D**ipole-**D**ipole (DD) relaxation mechanisms [78, 79, 80], leading to a dramatic decrease of their transverse relaxation rates [35, 116]. The improvement in resolution and sensitivity has made possible the study of large biomolecular systems up to about 1 MDa [81].

Relaxation interference also gives rise to a TROSY effect in $^{13}C^{1}H_3$ methyl groups in macromolecules. Tugarinov *et al.* [36] described the **H**eteronuclear **M**ultiple **Q**uantum **C**oherence (HMQC) experiment and associated methyl-TROSY effect using two main assumptions: the slow-tumbling approximation and infinitely fast methyl-group rotation. The slow-tumbling approximation is suitable to describe relaxation properties in high molecular-weight proteins on high-field magnets (10 to 25 T). In addition, rotation of methyl groups can be considered infinitely fast since it is much faster than the slow global tumbling of large proteins. Under these assumptions, the contributions of all intra-methyl DD couplings for the relaxation of the central line of the triplet are exactly zero in an HMQC experiment [36, 117]. This major discovery hand in hand with the development of schemes for protein $^{13}C^{1}H_3$ labeling at specific positions, both in proteins [52, 118, 119] and nucleic acids [55], has opened new perspectives to study high-molecular weight biomolecules with NMR [120] as was shown by several studies of large molecular machines, such as the proteasome [121, 122], a 1 MDa-chaperone [54] or the nucleosome core particle [55, 123].

The need for higher magnetic-field has been justified by the need for higher sensitivity which would allow the study of always more challenging systems. Undoubtedly of great interest for the biomolecular NMR community, such high-field magnets (as high as 1.2 GHz at the time of writing) can also have detrimental effects on the quality of the recorded spectra. For example, the CSA interaction scales linearly with the magnetic field (Eq. 1.25 and Eq. 1.28) so that the relaxation rates of nuclei with large CSA can lead to dramatic polarization losses at high magnetic fields. The carbonyl carbon-13 nucleus present in peptide bonds has a high CSA ($\sigma_z \approx 250$ ppm, $\sigma_y \approx 170$ ppm and $\sigma_z \approx 80$ ppm) [82], leading to relaxation rates higher than $600\,s^{-1}$ for protein assemblies with the size of the nucleosome at 1.2 GHz. Such a high relaxation rate would make most of the multi-dimensional NMR experiments with transfer trough the carbonyl function challenging, if not impossible, decreasing the attractivity for higher magnetic

fields.

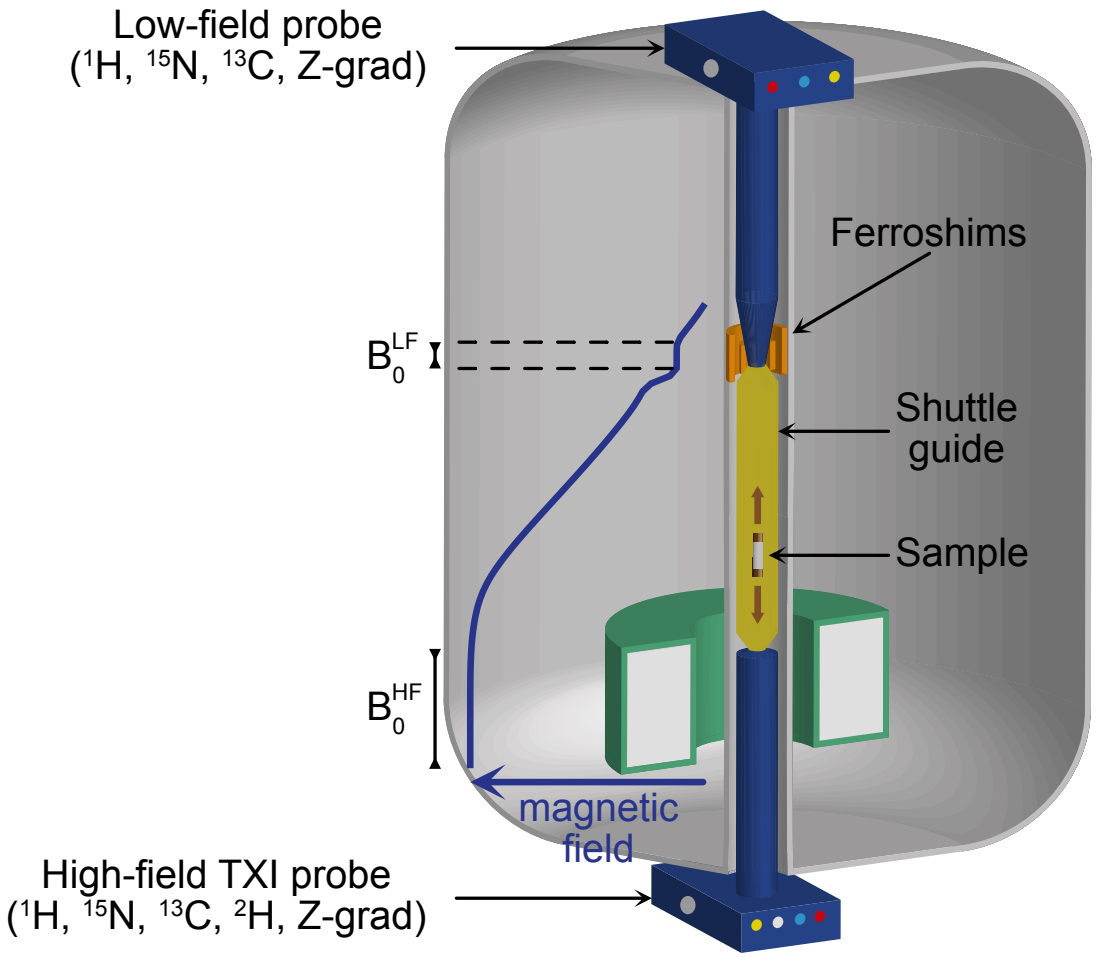

Figure 2.1: Schematic of a 2F-NMR spectrometer. The magnet shown in green operating at $B_0^{\mathrm{HF}} = 14.1\,\mathrm{T}$ produces a stray field (blue line). The ferroshims (orange) create a plateau of magnetic field at $B_0^{\mathrm{LF}} = 0.33\,\mathrm{T}$. The sample shuttle (yellow) moves the sample between the two positions at up to $10\,\mathrm{m.s^{-1}}$. Two probes are placed at the two magnetic centers. The high-field probe is used for signal detection. Figure reproduced and edited from [37].

Two-Field NMR (2F-NMR) spectroscopy has been recently proposed to overcome the challenges brought by very high-field NMR [39]. The laboratory is equipped with a propotype of 2F-NMR spectrometer. It consists in a commercial 600 MHz spectrometer where a pneumatic sample shuttle couples the high-field position with a low-field position placed around 1 m higher, in the stray-field gradient produced by the high-field magnet (Fig. 2.1). The low-field position has a value of 0.33 T (14 MHz proton Larmor frequency) and ferroshims provide a *c.a.* 10 ppm field homogeneity [39]. A second probe is placed on top of the spectrometer to manipulate the

spins at low-field. The coupling between the two positions allows one to polarize and detect the signal at high field to maximize the signal intensity while monitoring specific spin properties at low field. Our prototype has been used to overcome chemical exchange broadening [37], obtain broad-band correlations throughout aliphatic and aromatic ^{13}C resonances [83], and measure accurate relaxation rates at low field on Ubiquitin isoleucine methyl-groups [22] and on the backbone of an **I**ntrinsically **D**isordered **P**roteins (IDP) using pseudo-four-dimensional NMR and **N**on **U**niform **S**ampling (NUS) [124].

Our 2F-NMR spectrometer was also used to record a **H**eteronuclear **Z**ero **Q**uantum **C**oherence (HZQC) experiment of the isoleucines methyl-group of the protein Ubiquitin. This experiment is the 2F equivalent of the HMQC pulse-sequence to record methyl-TROSY spectra [36]. It combines detection at 14.1 T and evolution of multiple-quantum coherences at 0.33 T [37]. Narrow linewidths were obtained in the indirect low-field dimension suggesting a TROSY effect at low field, well outside the slow-tumbling regime where the initial methyl-TROSY theory was introduced [36]. Understanding this observation requires a formal description of methyl group relaxation in all motional regimes. In the first part of this chapter, we extend the methyl-TROSY theory to situations ouside the slow-tumbling regime. This first part is based on an already published experiment which revealed an unexpected spin property.

In the second part of this chapter, we propose a new type of TROSY experiment. Currently, TROSY-types of pulse sequences aim at selecting slowing relaxing coherences [35, 36]. Here, we propose to optimize transverse-relaxation rates by optimizing the magnetic field for spin evolution and detection, the two being potentially different. We refer to this class of experiment as 2F-TROSY. Our prototype of 2F-spectrometer does not permit us to record such experiments yet. This part will aim at showing the potential of 2F-NMR spectroscopy for biomolecular NMR.

2.2 Understanding the methyl-TROSY over a wide range of magnetic field

This section is largely based on the associated published work [38].

2.2.1 Experimental evidence

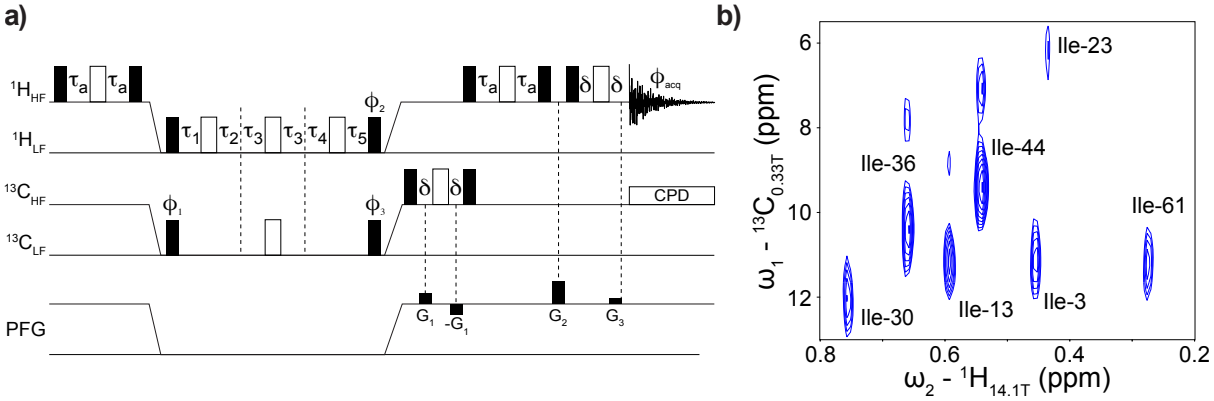

Figure 2.2: Two-field HZQC experiment recorded on U-[^{2}H, ^{15}N], Ile-δ_1[^{13}CH$_3$]-ubiquitin. **a)** Pulse sequence for the 2F-HZQC [37]. All pulses are applied along the x-axis of the rotating frame, unless specified otherwise. The phases are cycled as $\phi_1 = x, -x$, $\phi_2 = 4\{x\}, 4\{y\}$ and $\phi_3 = 2\{x\}, 2\{-x\}, 2\{y\}, 2\{-y\}$ with a receiver phase $\phi_{acq} = \{x, -x, -x, x\}$. The phase cycling ensures that the spin system evolves under ZQ coherences during $\tau_1 = (\tau_0 + n_1\Delta t_1)c$ and $\tau_5 = \tau_0 c$, and under DQ coherences during $\tau_2 = (\tau_0 + n_1\Delta t_1)(1-c)$, $2\tau_3 = 2\tau_0(2c-1) + 2n_1\Delta t_1(c-0.5)$ and $\tau_4 = \tau_0(1-c)$ with $c = (\gamma_C/\gamma_H + 1)/2$, Δt_1 the time increment and n_1 the index of the time increment. The other delays are $\tau_a = 1/(4J_{CH})$ with $J_{CH} = 125$ HZ and δ comprising the length of the gradient (0.9 ms) and the recovery delay. The gradients G_1, G_2 and G_3 are applied along the z axis with amplitudes 10 G.cm^{-1}, 15 G.cm^{-1} and $2(\gamma_C/\gamma_H)G_1$ respectively. Carbon-13 decoupling during acquisition is achieved using the GARP composite pulse with $\omega_{1\mathrm{GARP}}/2\pi = 2.08$ kHz [125]. HF: High Field. LF: Low Field. **b)** 2D-correlation spectrum of the seven isoleucines recorded on U-[^{2}H, ^{15}N], Ile-δ_1[^{13}CH$_3$]-ubiquitin [37]. A shearing transformation allows the display of ^{13}C-chemical shifts in the indirect dimension. Figure adapted from [38].

The experiment suggesting the persistence of the methyl-TROSY effect at low field has been published recently by our group [37]. It was recorded in 9 hours on a sample of 1.5 mM specifically labeled U-[^{2}H, ^{15}N], Ile-δ_1[^{13}CH$_3$]-ubiquitin, expressed and purified as detailed in the original publication, and using the pulse sequence shown in Fig. 2.2. The seven peaks corresponding to the seven isoleucine of Ubiquitin are clearly identified. The additional artifacts *c.a.* 2.7 ppm away from the most intense peak are still unexplained. The surprisingly narrow

linewidth in the carbon low-field dimension were originally hypothesized to arise from a methyl-TROSY effect [37], but the small size of the protein (8.5 kDa) and the low field for spin evolution make that the system is outside of the slow tumbling motional regime for which the existing methyl-TROSY theory was developped [36]. Here we propose a general analysis of the relaxation properties of ZQ and DQ coherences in methyl groups, which goes beyond the main hypotheses of the original methyl-TROSY work: slow tumbling and fast methyl rotation [36].

2.2.2 Theoretical framework

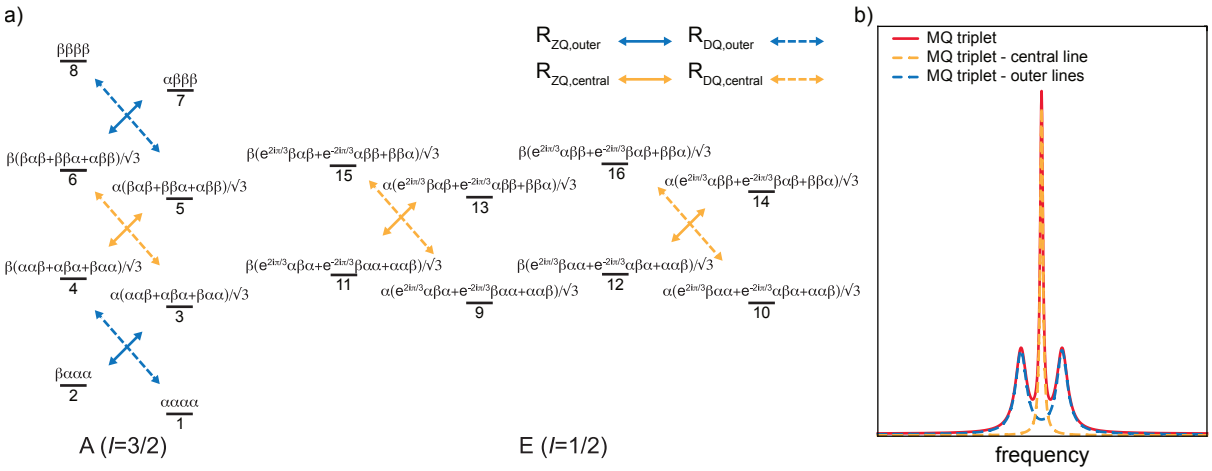

Figure 2.3: Description of the methyl-TROSY multiple-quantum spectrum and associated spin transitions. **a)** Energy level diagram of a $^{13}C^{1}H_3$ spin system using symmetry-adapted states for the point group C_3. In the state labels, the first spin state corresponds to the ^{13}C nuclear spin, and the others to the three ^{1}H spins, *i.e.* each spin state can be written as $|CH_1H_2H_3\rangle$ where C and H_i refer to the spin states of the carbon and proton i respectively (either α or β). Each state is associated with a number in order to simplify the description. Transitions of interest have been highlighted with solid (resp. dashed) arrows for the ZQ (resp. DQ) coherences. Transitions giving rise to the outer (resp. central) component of the triplet are colored in blue (resp. orange). **b.** Simulated multiple-quantum methyl-TROSY triplet showing the contributions from the outer and central lines. Figure reproduced from [38].

2.2.2.1 Spin system

Many studies have focussed on the relaxation properties of H_3 and $^{13}C^{1}H_3$ spin systems in methyl groups [126, 92, 93, 127, 128, 129]. Here, we consider a $^{13}C^{1}H_3$ spin system of an isolated methyl group for which tetrahedral geometry is assumed, that is the carbon nucleus occupies the center of a tetrahedron, three corners of which are occupied by the protons. This

Table 2.1: Single-transition operator basis used for the study of the relaxation properties of ZQ and DQ coherences. The numbers in the bra and ket refer to the states as shown in Fig. 2.3.

$\mathcal{B}_{ZQ}$		$\mathcal{B}_{DQ}$	
$ZQ^{\mathrm{A}}_{\mathrm{outer},1}$	$\|3\rangle\langle 2\|$	$DQ^{\mathrm{A}}_{\mathrm{outer},1}$	$\|4\rangle\langle 1\|$
$ZQ^{\mathrm{A}}_{\mathrm{outer},2}$	$\|7\rangle\langle 6\|$	$DQ^{\mathrm{A}}_{\mathrm{outer},2}$	$\|8\rangle\langle 5\|$
$ZQ^{\mathrm{A}}_{\mathrm{central}}$	$\|5\rangle\langle 4\|$	$DQ^{\mathrm{A}}_{\mathrm{central}}$	$\|6\rangle\langle 3\|$
$ZQ^{\Sigma\mathrm{E}}_{\mathrm{central}}$	$\frac{1}{\sqrt{2}}(\|13\rangle\langle 11\| + \|14\rangle\langle 12\|)$	$DQ^{\Sigma\mathrm{E}}_{\mathrm{central}}$	$\frac{1}{\sqrt{2}}(\|15\rangle\langle 9\| + \|16\rangle\langle 10\|)$

nuclear spin system is characterized by sixteen energy levels, direct product of the spin states of a ^{13}C spin with a $^{1}H_3$ spin system. Mathematically, the relevant symmetry group to describe this system of three protons is the alternating group A_3. The point group C_3 is isomorphic to A_3 and more commonly used when refering to symmetry properties in physical sciences. An equivalent theoretical description could be built on the irreducible representation of the point group C_{3v}. The energy levels are then separated into two manifolds based on their spin quantum number: A ($I = \frac{3}{2}$) and E ($I = \frac{1}{2}$). A schematic representation is shown in Fig. 2.3.a where the ZQ and DQ coherences are highlighted in solid and dashed arrows respectively.

2.2.2.2 Operators

We will use the following convention: in the abscence of indices to ^{1}H operators, the sum over the three protons is implicit, *i.e.* $\hat{\mathrm{H}}^{\pm} = \sum_{i=1}^{3} \hat{\mathrm{H}}_i^{\pm}/\sqrt{3}$ where $\hat{\mathrm{H}}_i$ is the operator for proton i. Note that in the following, the operator-sign "^" is ommited. The product operators that are relevant to the present analysis are the ZQ ($2\mathrm{C}^{+}\mathrm{H}^{-} \pm 2\mathrm{C}^{-}\mathrm{H}^{+}$) and DQ ($2\mathrm{C}^{+}\mathrm{H}^{+} \pm 2\mathrm{C}^{-}\mathrm{H}^{-}$) coherence operators of a $^{13}\mathrm{C}^{1}\mathrm{H}_3$ spin system. The analysis performed here only considers the $2\mathrm{C}^{+}\mathrm{H}^{-}$ and $2\mathrm{C}^{+}\mathrm{H}^{+}$ transition operators, but can be performed similarly for the corresponding $2\mathrm{C}^{-}\mathrm{H}^{+}$ and $2\mathrm{C}^{-}\mathrm{H}^{-}$ transition operators. A symmetry analysis shows that the subspace of operators for which: i) the point group is C_3 (i.e., the operators are unchanged by a circular permutation of the three protons) and ii) the coherence orders are $\mathrm{m_C} = +1$ and $\mathrm{m_H} = -1$ for ZQ transitions, or $\mathrm{m_C} = +1$ and $\mathrm{m_H} = +1$ for DQ transitions has dimension five. All transitions are shown in Fig. 2.3.a. As explained below, defining the sums and the differences of the transitions in the E-manifold allows a size-reduction of the basis to four terms. A suitable basis for the study of the considered single-transition operators expressed in terms of the transitions shown in Fig. 2.3.a

is presented in Table 2.1.

The expansion of the two **M**ultiple **Q**uantum (MQ) transition operators relevant for the study of the pulse sequence in the respective bases defined in Table 2.1 is:

$$\begin{aligned} 2\mathrm{C}^{+}\mathrm{H}^{-} =& \frac{1}{4} ZQ^{\mathrm{A}}_{\mathrm{outer},1} + \frac{1}{4} ZQ^{\mathrm{A}}_{\mathrm{outer},2} + \frac{1}{2\sqrt{3}} ZQ^{\mathrm{A}}_{\mathrm{central}} + \frac{1}{2\sqrt{6}} ZQ^{\Sigma\mathrm{E}}_{\mathrm{central}}, \\ 2\mathrm{C}^{+}\mathrm{H}^{+} =& \frac{1}{4} DQ^{\mathrm{A}}_{\mathrm{outer},1} + \frac{1}{4} DQ^{\mathrm{A}}_{\mathrm{outer},2} + \frac{1}{2\sqrt{3}} DQ^{\mathrm{A}}_{\mathrm{central}} + \frac{1}{2\sqrt{6}} DQ^{\Sigma\mathrm{E}}_{\mathrm{central}}. \end{aligned} \tag{2.1}$$

The single-transition operators $ZQ^{\Delta\mathrm{E}} = (|13\rangle\langle 11| - |14\rangle\langle 12|)/\sqrt{2}$ and $DQ^{\Delta\mathrm{E}} = (|15\rangle\langle 9| - |16\rangle\langle 10|)/\sqrt{2}$ need not to be included in the basis, as they are found to be in independent subspaces for the evolution analysed here: they do not contribute to the expansion of the studied ZQ and DQ transitions and they do not cross-relax with the other terms.

In the slow-tumbling approximation, the methyl-TROSY spectrum can be studied using two single-transition operators, equivalent to those described by Tugarinov *et al.* [36] for the description of the central and outer lines of the triplet (Fig. 2.3.b):

$$\begin{aligned} T_{\mathrm{outer}} &= \frac{1}{4}\left(ZQ^{\mathrm{A}}_{\mathrm{outer},1} + DQ^{\mathrm{A}}_{\mathrm{outer},1} + ZQ^{\mathrm{A}}_{\mathrm{outer},2} + DQ^{\mathrm{A}}_{\mathrm{outer},2}\right), \\ T_{\mathrm{central}} &= \frac{1}{2\sqrt{3}}\left(ZQ^{\mathrm{A}}_{\mathrm{central}} + DQ^{\mathrm{A}}_{\mathrm{central}} + \frac{1}{\sqrt{2}}\left(ZQ^{\Sigma\mathrm{E}}_{\mathrm{central}} + DQ^{\Sigma\mathrm{E}}_{\mathrm{central}}\right)\right). \end{aligned} \tag{2.2}$$

2.2.2.3 Relaxation mechanisms

Nuclear spin relaxation is described using the **B**loch-**W**angsness-**R**edfield (BWR) (chapter 1) relaxation theory. Calculations were performed using the framework of SpinDynamica [20] as implemented in RedKite [19]. We considered the three ^{1}H-^{1}H and three ^{13}C-^{1}H DD interactions, as well as the ^{13}C-CSA interaction, when mentioned.

2.2.2.4 Spectral density functions

To take into account the methyl rotation around its symmetry axis, the **M**odel **F**ree (MF) approach [15] has been modified to include three types of motions, considered to be uncorrelated: the global tumbling, motions of the methyl symmetry axis occuring on the nano- to sub-nanosecond time scales [74], and the rotation of the methyl group, resulting in a correlation

function similar to a form previously introduced for methyl groups [109]:

$$C(t,\theta_{\vec{i},\vec{j}}) = \frac{1}{5}e^{-t/\tau_c}(S_f^2 + (1-S_f^2)e^{-t/\tau_f})(S_m^2(\theta_{\vec{i},\vec{j}}) + (\mathcal{P}_2(\cos(\theta_{\vec{i},\vec{j}})) - S_m^2(\theta_{\vec{i},\vec{j}}))e^{-t/\tau_m}), \quad (2.3)$$

where τ_c is the overall global tumbling correlation time, S_f^2 and τ_f are the order parameter and correlation time for the motions of the symmetry axis aligned with the CC bond, and τ_m is the correlation time for the rotation of the methyl group. $S_m^2(\theta_{\vec{i},\vec{j}})$ is the order parameter of the methyl group which can be expressed as $S_m^2(\theta_{\vec{i},\vec{j}}) = \mathcal{P}_2[\cos\left(\theta_{\vec{i},\vec{CC}}\right)] \times \mathcal{P}_2[\cos\left(\theta_{\vec{j},\vec{CC}}\right)]$ [130], where $\mathcal{P}_2$ is the second order Legendre polynomial and $\vec{CC}$ is the vector aligned along the CC bond and associated with the symmetry axis of the system. $\theta_{\vec{i},\vec{j}}$ defines the angle between the vectors i and j formed by the two pairs of nuclei involved in the considered DD interactions, or the symmetry axis of the CSA tensor, and allows for possible cross-correlation. The Fourier transform of the correlation function gives the following spectral density function for the **M**odel **F**ree for **M**ethyl (MFM) model:

$$\begin{aligned}\mathcal{J}_{MFM}(\omega,\theta_{\vec{i},\vec{j}}) =& \frac{2}{5}[S_m^2(\theta_{\vec{i},\vec{j}})(S_f^2 L(\omega,\tau_c) + (1-S_f^2)L(\omega,\tau_f')) \\ &+ (\mathcal{P}_2(\cos(\theta_{\vec{i},\vec{j}})) - S_m^2(\theta_{\vec{i},\vec{j}}))(S_f^2 L(\omega,\tau_m') + (1-S_f^2)L(\omega,\tau_f''))],\end{aligned} \quad (2.4)$$

where ω is the Larmor frequency, effective correlation times are expressed as $\tau_k'^{-1} = \tau_k^{-1} + \tau_c^{-1}$, $(k \in \{f, \text{met}\})$ and $\tau_f''^{-1} = \tau_f^{-1} + \tau_c^{-1} + \tau_m^{-1}$, and $L(\omega,\tau) = \tau/(1+(\omega\tau)^2)$ stands for the Lorentzian function. This spectral density function will be used throughout this section, unless otherwise specified. For the sake of simplicity, a compact notation is used in the rest of the manuscript. Spectral density functions are labeled with indices referring to the auto- and cross-correlated interactions following a notation suggested by Werbelow and Grant [126]. Notations used for the spectral density functions and values of $S_m^2(\theta_{\vec{i},\vec{j}})$ and $\mathcal{P}_2(\cos\theta_{\vec{i},\vec{j}})$ are listed in Table C.1.

In the hypothesis of an **I**nfinitely **F**ast **M**ethyl **R**otation (IFMR) the second line in Eq. 2.4 vanishes, leading to the spectral density function $\mathcal{J}_{MFM}^{IFMR}$:

$$\begin{aligned}\mathcal{J}_{MFM}^{IFMR}(\omega,\theta_{\vec{i},\vec{j}}) &= \lim_{\tau_m \to 0} \mathcal{J}_{MFM}(\omega,\theta_{\vec{i},\vec{j}}) \\ &= \frac{2}{5}\left[S_m^2(\theta_{\vec{i},\vec{j}})S_f^2 L(\omega,\tau_c) + S_m^2(\theta_{\vec{i},\vec{j}})(1-S_f^2)L(\omega,\tau_f')\right].\end{aligned} \quad (2.5)$$

Importantly, under the IFMR approximation, the dependence on the relative orientation of all interactions vanishes, leading to $\mathcal{J}_{\text{HCH}} = \mathcal{J}_{\text{CH}}$ and $\mathcal{J}_{\text{HHH}} = \mathcal{J}_{\text{HH}}$ which is important for relax-

ation interference (see below). Finally, the slow tumbling approximation implies $\mathcal{J}(\omega) = 0$ for $\omega \neq 0$.

Tugarinov *et al.* used a simpler form of spectral density function adapted to slow tumbling for the overall rotational diffusion and **I**nfinitely **F**ast **I**nternal **M**otions (IFIM), in which all internal correlation times are zero [36]:

$$\mathcal{J}^{IFIM}_{MFM}(\omega, \theta_{\vec{i},\vec{j}}) = \frac{2}{5} S^2_m(\theta_{\vec{i},\vec{j}}) S^2_f L(\omega, \tau_c). \tag{2.6}$$

In the analysis presented here, the following parameters $S^2_f = 0.5$, τ_c=10 ns, τ_f=100 ps and τ_m=5 ps will be used, if not specified otherwise [21]. Introducing the additional correlation time τ_f for internal motions does not change the general features of methyl-TROSY.

2.2.3 Methyl-TROSY at high field

In the absence of the proton refocusing pulse during the indirect evolution period of the HMQC pulse-sequence, the coupling between the evolving ^{13}C-^{1}H spin pair and the passive ^{1}H-^{1}H spin pair leads to a triplet arising from the different spin states of the passive protons (Fig. 2.3.b). The central line of the triplet is much sharper than the outer lines (for a detailed description of the HMQC spectrum, see Tugarinov *et al.* [36]). The dipolar contributions to the transverse relaxation rates for the outer and central single-transition operators (T_{outer} and $T_{central}$ defined in Eq. 2.2) can be expressed as general (gen) expressions $R^{\text{gen}}_{\text{MQ,outer}}$ and $R^{\text{gen}}_{\text{MQ,central}}$:

$$\begin{aligned} R^{\text{gen}}_{\text{MQ,outer}} = & \frac{1}{8} d^2_{\text{CH}} \left[8\mathcal{J}_{\text{CH}}(0) + 9\mathcal{J}_{\text{CH}}(\omega_{\text{C}}) + 3\mathcal{J}_{\text{CH}}(\omega_{\text{C}} - \omega_{\text{H}}) + 9\mathcal{J}_{\text{CH}}(\omega_{\text{H}}) \right. \\ & \left. + 18\mathcal{J}_{\text{CH}}(\omega_{\text{C}} + \omega_{\text{H}}) \right] \\ & + \frac{1}{4} d^2_{\text{CH}} \left[4\mathcal{J}_{\text{HCH}}(0) + 3\mathcal{J}_{\text{HCH}}(\omega_{\text{C}}) + \mathcal{J}_{\text{HCH}}(\omega_{\text{C}} - \omega_{\text{H}}) + 3\mathcal{J}_{\text{HCH}}(\omega_{\text{H}}) \right. \\ & \left. + 6\mathcal{J}_{\text{HCH}}(\omega_{\text{C}} + \omega_{\text{H}}) \right] \\ & + \frac{3}{4} d^2_{\text{HH}} \left[3\mathcal{J}_{\text{HH}}(0) + 4\mathcal{J}_{\text{HH}}(\omega_{\text{H}}) + 2\mathcal{J}_{\text{HH}}(2\omega_{\text{H}}) \right] \\ & + \frac{3}{4} d^2_{\text{HH}} \left[3\mathcal{J}_{\text{HHH}}(0) + 2\mathcal{J}_{\text{HHH}}(\omega_{\text{H}}) - 2\mathcal{J}_{\text{HHH}}(2\omega_{\text{H}}) \right], \end{aligned} \tag{2.7}$$

$$
\begin{aligned}
R^{\text{gen}}_{\text{MQ,central}} =& \frac{1}{8} d^2_{\text{CH}} \left[8\mathcal{J}_{\text{CH}}(0) + 9\mathcal{J}_{\text{CH}}(\omega_{\text{C}}) + 3\mathcal{J}_{\text{CH}}(\omega_{\text{C}} - \omega_{\text{H}}) + 9\mathcal{J}_{\text{CH}}(\omega_{\text{H}})\right. \\
&\left. + 18\mathcal{J}_{\text{CH}}(\omega_{\text{C}} + \omega_{\text{H}})\right] \\
&+ \frac{1}{4} d^2_{\text{CH}} \left[-4\mathcal{J}_{\text{HCH}}(0) - 3\mathcal{J}_{\text{HCH}}(\omega_{\text{C}}) + \mathcal{J}_{\text{HCH}}(\omega_{\text{C}} - \omega_{\text{H}}) + 3\mathcal{J}_{\text{HCH}}(\omega_{\text{H}})\right. \\
&\left. + 6\mathcal{J}_{\text{HCH}}(\omega_{\text{C}} + \omega_{\text{H}})\right] \\
&+ \frac{3}{4} d^2_{\text{HH}} \left[3\mathcal{J}_{\text{HH}}(0) + 4\mathcal{J}_{\text{HH}}(\omega_{\text{H}}) + 2\mathcal{J}_{\text{HH}}(2\omega_{\text{H}})\right] \\
&+ \frac{3}{4} d^2_{\text{HH}} \left[-3\mathcal{J}_{\text{HHH}}(0) + 2\mathcal{J}_{\text{HHH}}(2\omega_{\text{H}})\right],
\end{aligned}
\tag{2.8}
$$

where d_{ij} are dipolar coefficients for the DD interaction between nuclei i and j, $d_{ij} = -\frac{\mu_0 \hbar}{4\pi} \frac{\gamma_i \gamma_j}{r^3_{ij}}$ with μ_0 the permeability of free space, $\hbar$ the Planck's constant divided by 2π, γ_n the gyromagnetic ratio of nucleus n, and r_{ij} the distance between nuclei i and j. Importantly, the rates $R^{\text{gen}}_{\text{MQ,central}}$ and $R^{\text{gen}}_{\text{MQ,outer}}$ are not equal due to different cross-correlated contributions depending on $\mathcal{J}_{\text{HCH}}$ and $\mathcal{J}_{\text{HHH}}$. Using the slow tumbling approximation, we only retain terms of the spectral density function evaluated at 0 frequency, leading to:

$$
\begin{aligned}
R^{ST}_{\text{MQ,outer}} =& d^2_{\text{CH}} \left[\mathcal{J}_{\text{CH}}(0) + \mathcal{J}_{\text{HCH}}(0)\right] + \frac{9}{4} d^2_{\text{HH}} \left[\mathcal{J}_{\text{HH}}(0) + \mathcal{J}_{\text{HHH}}(0)\right], \\
R^{ST}_{\text{MQ,central}} =& d^2_{\text{CH}} \left[\mathcal{J}_{\text{CH}}(0) - \mathcal{J}_{\text{HCH}}(0)\right] + \frac{9}{4} d^2_{\text{HH}} \left[\mathcal{J}_{\text{HH}}(0) - \mathcal{J}_{\text{HHH}}(0)\right].
\end{aligned}
\tag{2.9}
$$

As explained in the previous section, under IFMR, the spectral density functions for auto- and cross-correlation are equal, $\mathcal{J}_{\text{CH}} = \mathcal{J}_{\text{HCH}}$ and $\mathcal{J}_{\text{HH}} = \mathcal{J}_{\text{HHH}}$, so that:

$$
\begin{aligned}
R^{ST,IFR}_{\text{MQ,outer}} &= 2d^2_{\text{CH}} \mathcal{J}_{\text{CH}}(0) + \frac{9}{2} d^2_{\text{HH}} \mathcal{J}_{\text{HH}}(0), \\
R^{ST,IFR}_{\text{MQ,central}} &= 0.
\end{aligned}
\tag{2.10}
$$

The complete cancellation of the relaxation rate of the central line arises from the combination of two approximations: slow tumbling and IFMR. A similar cancellation of auto- and cross-correlated relaxation terms is responsible for the existence of long-lived nuclear spin states in methyl groups [129]. Introducing the spectral density function $\mathcal{J}^{IFIM}_{MFM}$ (Eq. 2.6), we obtain:

$$
\begin{aligned}
R^{ST,IFIM}_{\text{MQ,outer}} &= \frac{\mu_0}{4\pi} \left(2\frac{2}{5} \frac{S^2_m(\theta_{\vec{CH},\vec{CH}}) S^2_f \gamma^2_{\text{H}} \gamma^2_{\text{C}} \hbar^2 \tau_c}{r^6_{\text{HC}}} + \frac{9}{2}\frac{2}{5} \frac{S^2_m(\theta_{\vec{HH},\vec{HH}}) S^2_f \gamma^4_{\text{H}} \hbar^2 \tau_c}{r^6_{\text{HH}}} \right), \\
R^{ST,IFIM}_{\text{MQ,central}} &= 0.
\end{aligned}
\tag{2.11}
$$

Replacing S^2_m according to Table C.1, we obtain the same expressions as reported in Tugarinov

et al. [36]:

$$R^{ST,IFIM}_{\mathrm{MQ,outer}} = \frac{\mu_0}{4\pi}\left(\frac{4}{45}\frac{S_f^2\gamma_{\mathrm{H}}^2\gamma_{\mathrm{C}}^2\hbar^2\tau_c}{r_{\mathrm{HC}}^6} + \frac{9}{20}\frac{S_f^2\gamma_{\mathrm{H}}^4\hbar^2\tau_c}{r_{\mathrm{HH}}^6}\right), \qquad (2.12)$$
$$R^{ST,IFIM}_{\mathrm{MQ,central}} = 0.$$

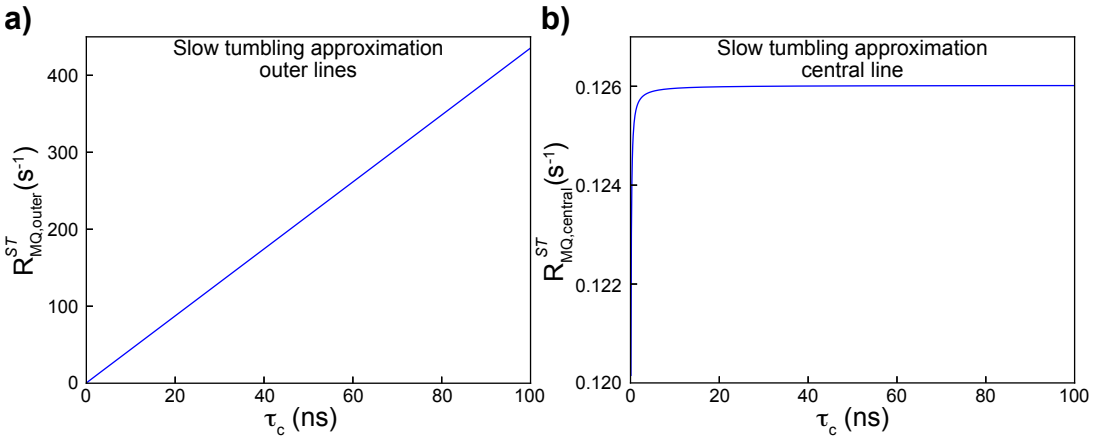

Figure 2.4: Variation of the DD contributions to auto-relaxation rates in the slow-tumbling approximation with the correlation time τ_c for the outer lines (**a**) and the central line (**b**). Relaxation rates were calculated using the spectral density function $\mathcal{J}_{MFM}$. The non-zero rates predicted for the central line are due to finite speed of methyl rotation. Figure reproduced from [38].

The relaxation rate of the outer lines calculated using the general expression $R^{\mathrm{gen}}_{\mathrm{MQ,outer}}$ (Eq. 2.8) and in the slow tumbling approximation $R^{ST}_{\mathrm{MQ,outer}}$ (Eq. 2.9) and using the spectral density function $\mathcal{J}_{MFM}$ compare well for magnetic fields higher than 5 T, both of them being independent of the magnetic field and proportional to the global tumbling correlation time τ_c (Fig. 2.4.a and Fig. 2.5.a). The value of the relaxation rate of the central line $R^{ST}_{\mathrm{MQ,central}}$ approaches zero in the slow tumbling approximation (Eq. 2.9 and Fig. 2.4.b), as analytically calculated in the case of the IFMR (Eq. 2.10). In the general case, the central line relaxation rate $R^{\mathrm{gen}}_{\mathrm{MQ,central}}$ has a non-zero value. For magnetic fields higher than 5 T, it is small and can be considered independent of the magnetic field and global tumbling correlation time τ_c (Fig. 2.5.b), thus reproducing the expected behavior predicted by the slow tumbling approximation. These calculations show that in the frame of the operator expansion introduced by Tugarinov *et al.* [36] (Eq. 2.2), the slow tumbling approximation allows an accurate description of the relaxation rates of the triplet at moderate and high magnetic fields.

However, using this operator expansion, calculation of the relaxation rate of the central

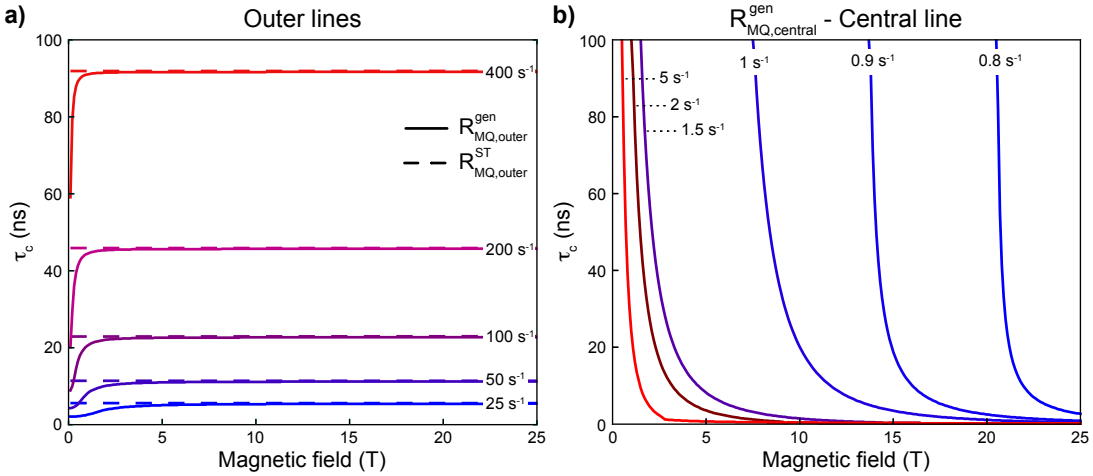

Figure 2.5: Domain of validity of the slow-tumbling regime. **a)** Contour plot of the relaxation rate of the outer lines of the triplet as a function of the magnetic field and the correlation time τ_c and calculated using Eq. 2.8 ($R^{\text{gen}}_{\text{MQ,outer}}$, solid line) and Eq. 2.9 ($R^{ST}_{\text{MQ,outer}}$, dashed line). The slow-tumbling approximation holds when the dashed and solid lines coincide. **b)** Contour plot of the relaxation rate of the central line of the triplet as a function of the magnetic field and the correlation time τ_c and calculated using Eq. 2.8 ($R^{\text{gen}}_{\text{MQ,central}}$). By comparison, the expected relaxation rate for the central single-transition operator T_{central} in the slow-tumbling approximation is $R^{ST}_{\text{MQ,central}} \approx R^{ST,IFR}_{\text{MQ,central}} = 0$ (Fig. 2.4.b). Figure reproduced from [38].

line of the triplet shows a rapid increase of $R^{\text{gen}}_{\text{MQ,central}}$ at low magnetic fields (Fig. 2.6). Such an increase is in contradiction with the experimental observation of favorable relaxation properties of MQ coherences at 0.33 T in the 2F-HZQC experiment recorded on a sample of Ubiquitin [37]. As $R^{\text{gen}}_{\text{MQ,central}}$ is calculated without making the initial hypotheses of slow tumbling and infinitely fast rotation of the methyl group, this discrepancy between theory and experiment cannot be attributed to the expression of the spectral density function but to the expansion of operators employed. In the following section, we will show that the expansion of operators introduced in the theoretical framework section allows us to understand the relaxation properties of MQ coherences at low magnetic fields.

2.2.4 Methyl-TROSY beyond the slow tumbling limit

2.2.4.1 Definition of a suitable basis

So far, calculations were done using an expansion of the single-transition operators between those contributing to the sharp central line, and those contributing to the broad outer lines of the triplet. Here, we suggest to calculate independentely the relaxation properties of each

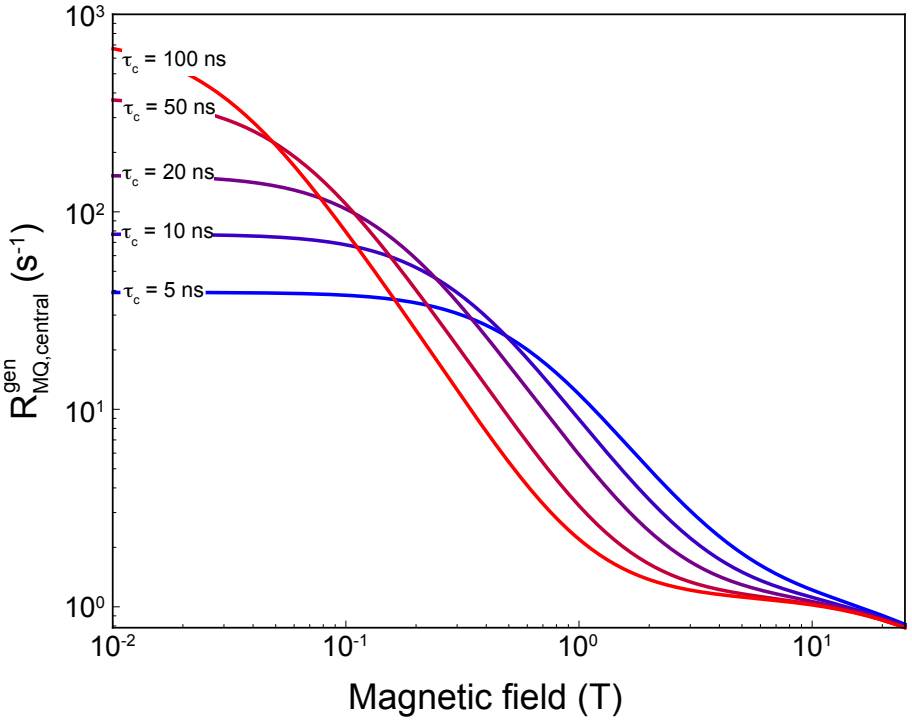

Figure 2.6: Variation of the general expression of the central line relaxation rate $R^{gen}_{\mathrm{MQ,central}}$ with respect to the magnetic field for different values of the overall corelation time τ_c. Relaxation rates were calculated using the spectral density function $\mathcal{J}_{MFM}$ and Eq. 2.8. The contribution of the CSA to the relaxation is not included. Figure reproduced from [38].

single-transition operator in order to identify slowly relaxing components. Suitable bases for the expansion of the $2C^+H^-$ and $2C^+H^+$ coherences are presented in the theoretical framework section (Table 2.1 and Eq. 2.1).

2.2.4.2 Identification of a slowly relaxing term in the new operator basis

The contribution of the carbon-13 CSA is included in the following analysis. It is assumed to be axially symmetric with anisotropy $\Delta\sigma = \sigma_{zz} - (\sigma_{xx} + \sigma_{yy})/2 = 20\,\mathrm{ppm}$ and aligned with the direction of the C-C bond. The proton CSA is expected to be approximately 1 ppm [131] and is neglected in our analysis. Relaxation rates for the zero- and double-quantum single-transition operators forming the bases $\mathcal{B}_{ZQ}$ and $\mathcal{B}_{DQ}$ are shown in Fig. 2.7. The single-transition operators contributing to the outer lines of the triplet relax faster than the single-transition operators of the central line, at all magnetic fields (between 0.01 T and 25 T), in agreement with the previous analysis [36]. Interestingly, the two operators corresponding to the outer lines do not have the same relaxation properties at high fields. This effect arises from the CSA/DD contributions to

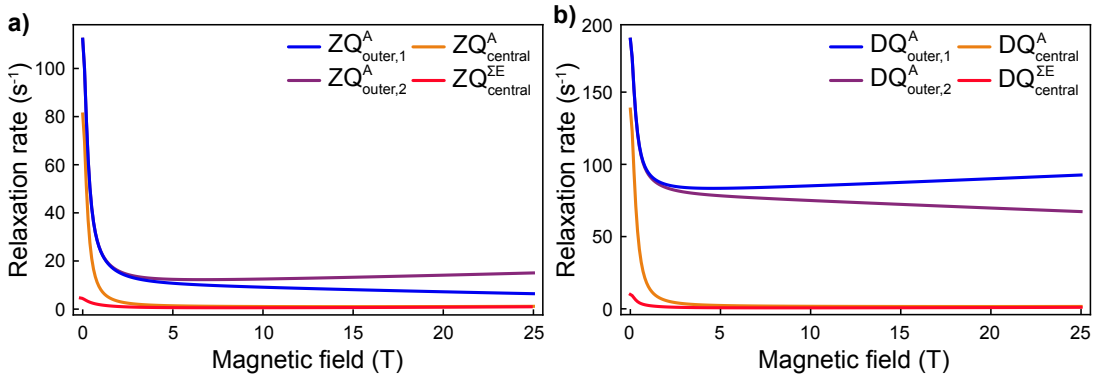

Figure 2.7: Magnetic field variation of the relaxation rates of the four single-transition operators of the MQ triplet in the ZQ basis (**a**) $\mathcal{B}_{ZQ}$ and the DQ basis (**b**) $\mathcal{B}_{DQ}$. Relaxation rates were calculated using the spectral density function $\mathcal{J}_{MFM}$. Figure reproduced from [38].

relaxation, which are negligible at low field (see Appendix C.1 for expressions of the relaxation rates).

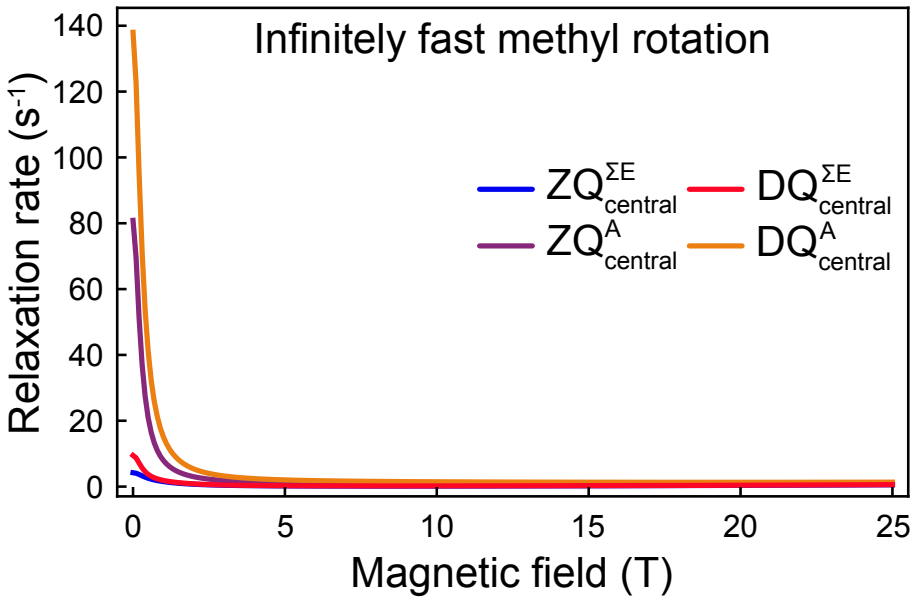

Figure 2.8: Auto-relaxation rates of the operators $ZQ^{\Sigma E}_{central}$, $ZQ^{A}_{central}$, $DQ^{\Sigma E}_{central}$ and $DQ^{A}_{central}$ from 0.1 to 25 T. Relaxation rates were calculated using the spectral density function $\mathcal{J}^{IFR}_{MFM}$. Figure reproduced from [38].

The two operators that describe the central line have comparable relaxation properties at high fields (higher than ca. 5 T). This is consistent with the treatment proposed by Tugarinov

et al. in the slow-tumbling regime with IFMR [36]. At lower fields, the two single-transition operators of the central line have drastically different relaxation behaviors. This difference arises even in the IFMR limit (Fig. 2.8). The A-manifold operators contributing to the central line $ZQ^{\mathrm{A}}_{\mathrm{central}}$ and $DQ^{\mathrm{A}}_{\mathrm{central}}$ relax much faster while the sums of the E single-transition operators still relax slowly. It would be possible to verify these predictions experimentally by separating the ^{1}H transitions of the two manifolds using a two-field version of the approach described in Tugarinov and Kay [132] or Tugarinov *et al.* [133].

The ratio of the relaxation rates of the two operators corresponding to the central line is around 10 in the ZQ and DQ cases at 0.33 T with the parameters for dynamics used here (see theoretical framework section). Similar conclusions can be drawn in the case of large proteins ($\tau_c = 100\,\mathrm{ns}$) where the slow-tumbling approximation is almost justified at 0.33 T: the sums of the E single-transition operators have small relaxation rates around $4\,\mathrm{s}^{-1}$ in $\mathcal{B}_{ZQ}$ and $5\,\mathrm{s}^{-1}$ in $\mathcal{B}_{DQ}$ at 0.33 T. The A-manifold central MQ transition operators $ZQ^{\mathrm{A}}_{\mathrm{central}}$ and $DQ^{\mathrm{A}}_{\mathrm{central}}$ have relaxation rates higher but comparable to their E-manifold equivalents at 0.33 T ($11\,\mathrm{s}^{-1}$ in $\mathcal{B}_{ZQ}$ and $20\,\mathrm{s}^{-1}$ in $\mathcal{B}_{DQ}$). This shows that the combined operators approach [36] is still valid at relatively low magnetic fields for high molecular-weight proteins.

Taken together, these results suggest that the methyl-TROSY effect is retained at low fields for only one of the two single-transition operators that contribute to the central line of the triplet, while both single-transition operators relax slowly at high field.

2.2.4.3 Cross relaxation between and within the lines

Slowly relaxing single-transition coherences lead to an efficient TROSY effect if they are good approximations of the eigenvectors of the relaxation matrix. Here, we studied the cross-relaxation pathways related to the slow-relaxing terms. This requires a full treatment of the relaxation matrix in the considered basis. Two types of cross-relaxation pathways have to be considered: cross-relaxation between the slowly relaxing single-transition operator of the central line and the fast relaxing single-transition operator of the central line (intra-line transfer) or cross-relaxation between the central line of the triplet and the outer lines (inter-line transfer). Percentage of intra- and inter-line cross-relaxation with respect to the auto-relaxation of the $MQ^{\Sigma\mathrm{E}}_{\mathrm{central}}$ operators are shown in Fig. 2.9.

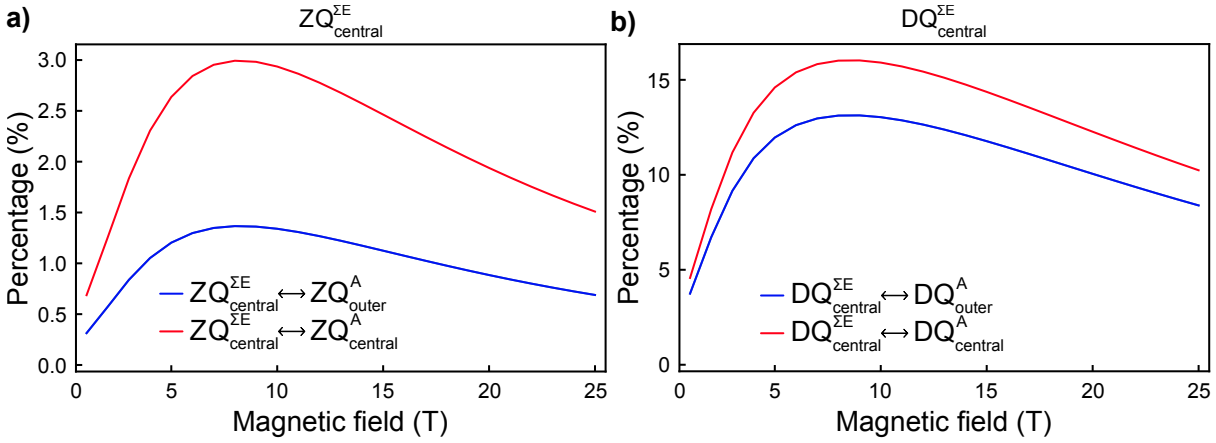

Figure 2.9: Magnetic field variation of the cross-relaxation rate between the E- and A-manifolds of the MQ triplet in the ZQ basis (**a**) $\mathcal{B}_{ZQ}$ and the DQ basis (**b**) $\mathcal{B}_{DQ}$. The cross-relaxation rates are expressed as the percentage of the auto-relaxation rate of the (**a**) $ZQ^{\Sigma E}_{central}$ and (**b**) $DQ^{\Sigma E}_{central}$ transition operators. Relaxation rates were calculated using the spectral density function $\mathcal{J}_{MFM}$. The two single-transition operators contributing to the outer lines of the triplet have the same cross-relaxation rates with the E-manifold in both the ZQ and DQ cases. Figure reproduced from [38].

Inter-line cross-relaxation rates appear as non-secular in the interaction frame of ^{13}C-^{1}H scalar-coupling interactions (they oscillate at the angular frequency 2πJ with J the scalar coupling constant). Thus the predicted cross-relaxation rates with the single-transition operators contributing to the outer lines of the triplet (blue curves in Fig. 2.9) have no effect on the relaxation of the term contributing to the central line. On the other hand, intra-line cross-relaxation is always secular. At high fields (higher than 5 T) cross-relaxation has no effect as the A- and E-manifold central coherences have the same relaxation rates (Fig. 2.7). At low fields (lower than 1 T), the $ZQ^{A}_{central}$ and $DQ^{A}_{central}$ terms relax much faster than the sums of the E single-transition operators. The $ZQ^{\Sigma E}_{central}$ cross-relaxation rate with $ZQ^{A}_{central}$ ranges from 0.5 to 3% of the auto-relaxation of the slowly relaxing $ZQ^{\Sigma E}_{central}$ from 1 to 5 T so that cross-relaxation effects can be neglected (red curve in Fig. 2.9.a). The intra-line cross-relaxation rate represents 5 to 15% of the auto-relaxation rate in the DQ case (Fig. 2.9.b), and may have a small effect on the decay of the polarization. Interestingly, intra-line cross-relaxation rates are independent of the magnetic field as they only depend on spectral density function evaluated at zero-frequency and originate from dipolar interactions (see Appendix C.1 for detailed relaxation rate expressions). Moreover, the percentage of cross-relaxation is independent of the global tumbling correlation time τ_c and our conclusions can be extended to large proteins.

2.2.4.4 Fast methyl rotation is important for a TROSY effect

As discussed in the previous section, the theory of methyl-TROSY proposed by Tugarinov *et al.* is based on the hypotheses of slow tumbling of the protein and infinitely fast rotation of the methyl group [36]. We investigated the effect of the finite speed of rotation of the methyl group on both auto- and cross-relaxation rates.

Fast rotation of the methyl group is essential for favorable auto-relaxation rates as even the previously identified slowly relaxing terms have significantly higher relaxation rates for rotation correlation times τ_m values larger than 1 ns, especially at low fields (Fig. 2.10.a and b). At 0.33 T, the auto-relaxation rates of the operators for the central line of the triplet are mostly independendent of the correlation time τ_m in the range from 0.1 ps (close to the IFMR) to 100 ps, *i.e.* the chosen value for the correlation time τ_f (Fig. 2.10.c). This correlates with a higher loss of polarization through intra-line cross-relaxation as the slow and fast relaxing terms are mixed rapidely for $\tau_m > 100$ ps (Fig. 2.10.d). In agreement with the initial treatment of Tugarinov *et al.*, a fast rotating group on the pico-second to few tens of pico-second time scales ensures an efficient methyl-TROSY effect at high fields as well as the ability to record a methyl-TROSY spectrum at low magnetic fields (below 1 T). The same conclusions can be drawn for larger proteins (Fig. 2.10.e-h).

In the case of protein NMR, isoleucine is a favorable methyl group-bearing residue with low energy barriers for methyl group rotation [21]. The rotation of the methyl group in alanine can be significantely affected by interactions with the protein backbone, leading to a higher τ_m [134]. Hence, signals from $^{13}C^{1}H_3$ groups in alanine side-chains are expected to be broader than signals of isoleucines, or even leucines or valines.

2.2.4.5 What happens at very high fields

The contribution of the CSA to relaxation is negligible at the low fields considered so far. CSA contributions to the relaxation of MQ transition operators increase with the magnetic field. At the highest currently commercially available magnetic field ($B_0 = 28.2$ T), this contribution to relaxation is not negligible but is still small. We have investigated how relaxation due to the CSA interaction would alter HMQC spectra of methyl groups at magnetic fields that may be commercially available in the future ($B_0 > 30$ T). As discussed above, the proton CSA is neglected.

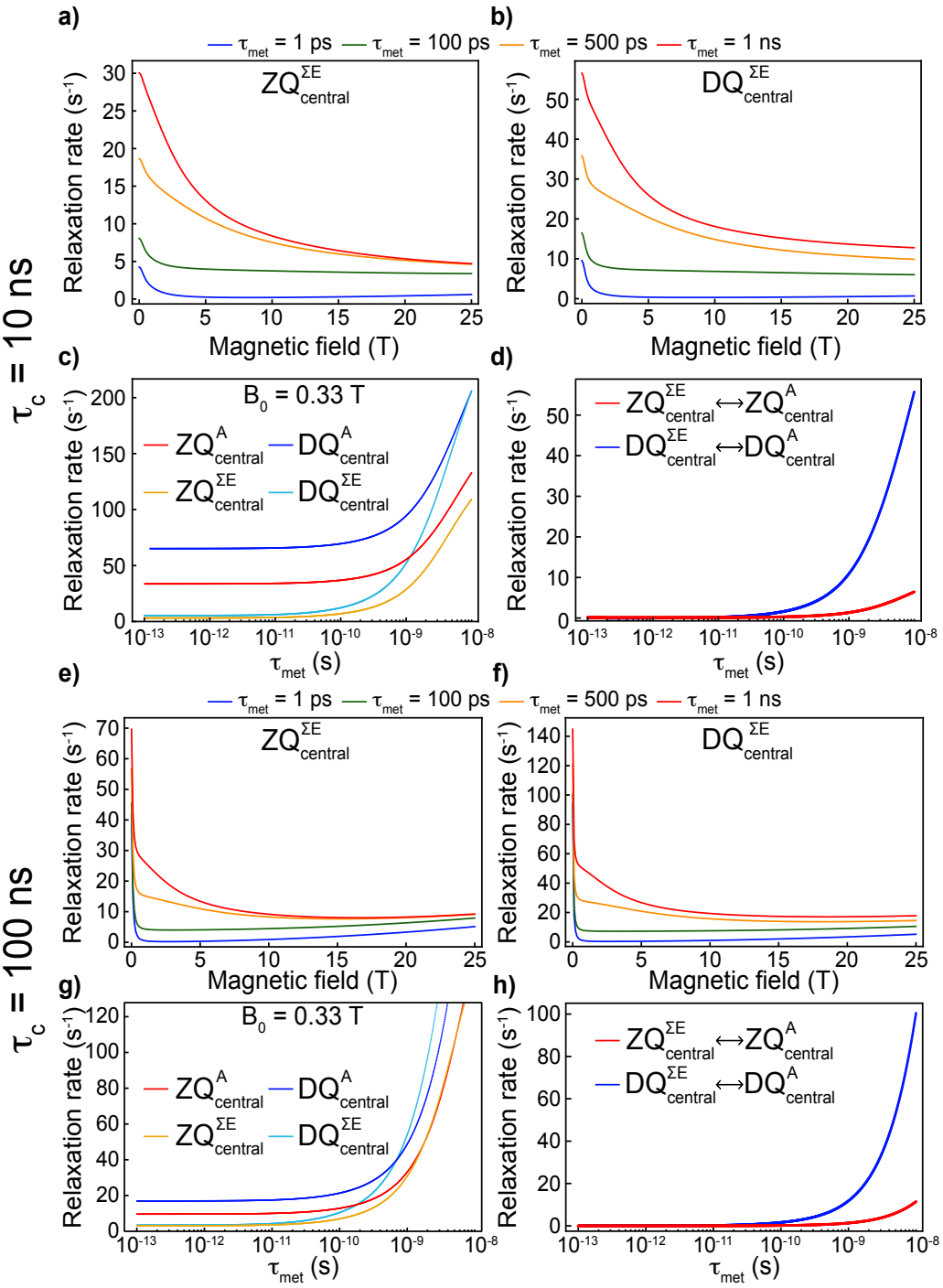

Figure 2.10: Effect of methyl group rotation on methyl relaxation properties. Evolution of the relaxation rates for the operators $ZQ^{\Sigma E}_{\text{central}}$ ($\tau_c = 10\,\text{ns}$, **a** and $\tau_c = 100\,\text{ns}$, **e**) and $DQ^{\Sigma E}_{\text{central}}$ ($\tau_c = 10\,\text{ns}$, **b** and $\tau_c = 100\,\text{ns}$, **f**) from 0.1 to 25 T with τ_m values ranging from 1 ps to 1 ns. Evolution of the auto-relaxation rates of the operators contributing to the central line of the triplet as a function of the correlation time for methyl group rotation τ_m at 0.33 T for $\tau_c = 10\,\text{ns}$ (**c**) and $\tau_c = 100\,\text{ns}$ (**g**). Evolution of the intra-line cross-relaxation rates as a function of the correlation time for methyl group rotation τ_m for $\tau_c = 10\,\text{ns}$ (**d**) and $\tau_c = 100\,\text{ns}$ (**h**). These rates are independent of the magnetic field as can be seen in the expressions in Appendix C.1. Relaxation rates were calculated using the spectral density function $\mathcal{J}_{MFM}$. Figure adapted from [38].

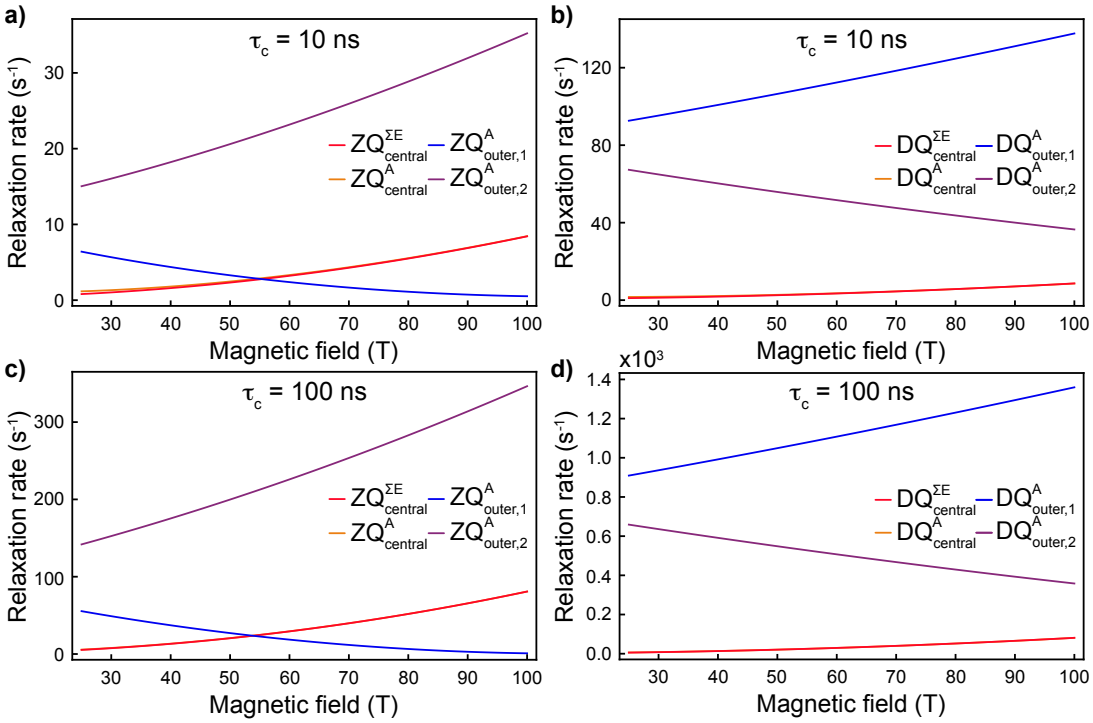

Figure 2.11: Effect of the ^{13}-CSA contribution on the auto-relaxation rates. Depence of the auto-relaxation rates of the single-transition operators contributing to the central and outer lines of the triplet on the magnetic field for very high fields (from 25 to 100 T) in the basis $\mathcal{B}_{ZQ}$ ($\tau_c = 10$ ns, **a** and $\tau_c = 100$ ns, **c**) and $\mathcal{B}_{DQ}$ ($\tau_c = 10$ ns, **b** and $\tau_c = 100$ ns, **d**). Relaxation rates were calculated using the spectral density function $\mathcal{J}_{MFM}$. Figure reproduced from [38].

The contribution of the CSA leads to a small but significant increase of the auto-relaxation rates for the single-transition operators of the central line (Fig. 2.11). Such increase is expected to moderately deteriorate the quality of HMQC spectra.

By contrast, the relaxation rates of the outer lines of the triplet change dramatically with the magnetic field in both the ZQ and DQ cases. When the magnetic field increases, if the passive spins (^{1}H) are in the α state (operators $\mathrm{MQ}^A_{\mathrm{outer},1}$), auto-relaxation rates decrease for ZQ transition operators but increase for DQ transition operators. On the other hand, when passive protons spins are in the β state (operators $\mathrm{MQ}^A_{\mathrm{outer},2}$), the auto-relaxation rates increase for ZQ transition operators but decrease DQ transition operators. The magnetic-field variation of relaxation rates is dominated by the interference between the ^{13}C-CSA and the ^{1}H-^{1}H DD interactions. The additional ^{13}C-CSA/^{13}C-^{1}H DD cross-correlated contribution leads

to a stronger field-dependence of relaxation rates for DQ transition operators than for ZQ transition operators as can be infered from analytical expressions (Appendix C.1, remembering that $\mathcal{J}_{\mathrm{CCH}}$ and $\mathcal{J}_{\mathrm{CCHH}}$ are negative at all magnetic fields). The overall effect of CSA/DD cross-correlated relaxation leads to a crossing of the field-dependence of relaxation rates for ZQ transition operators at very high fields: the single-transition operators $\mathrm{ZQ}^{A}_{\mathrm{outer},1}$ (passive spins in α state) becomes the single-transition operator with the smallest auto-relaxation rate for magnetic fields higher than ca. 55 T (2.3 GHz). For the central line, the sum of the CSA/DD cross-correlations vanishes so that the field variation of CSA constributions to relaxation is only due to the auto-correlation (see Appendix C.1 for expressions of relaxation rates). For large proteins at very high fields, recording a HZQC spectrum [135] on the $\mathrm{ZQ}^{A}_{\mathrm{outer},1}$ appears to be more favorable, introducing a new form of methyl TROSY based on cancellation between CSA and DD contributions to relaxation. This prediction suggests that transverse relaxation-optimized spectroscopy due to CSA/DD interference should be investigated in aliphatic groups at fields $B_0 > 30$ T.

2.2.5 Two-field HZQC analysis

At the end of the evolution at low field (Fig. 2.2.a), ZQ coherences are selected by phase cycling. Importantly, the selected ZQ terms have evolved half of the time as ZQ and half of the time as DQ coherences to simultaneously scale down the ^{1}H offset and suppress the evolution due to ^{13}C-^{1}H scalar couplings. It allows the correlation between a ZQ ^{13}C-^{1}H coherence at 0.33 T and a single-quantum proton coherence at 14.1 T (Fig. 2.2.b) [37].

2.2.5.1 Methods: simulation of the HZQC spectrum

Relaxation The propagator for an evolution of the spin system during the delay $\tau = \tau_1 + \tau_2 + 2\tau_3 + \tau_4 + \tau_5$, where the times τ_i are defined in Fig. 2.2.a, at low field is (without considering evolution under the chemical shifts):

$$\mathcal{P}(\tau) = e^{-\tau/4\left(\hat{\hat{\mathcal{R}}}_{ZQ}+\hat{\hat{\mathcal{H}}}_J\right)}\mathcal{F}_{ZD}^{-1}e^{-\tau/4\left(\hat{\hat{\mathcal{R}}}_{DQ}+\hat{\hat{\mathcal{H}}}_J\right)}\mathcal{U}e^{-\tau/4\left(\hat{\hat{\mathcal{R}}}_{DQ}+\hat{\hat{\mathcal{H}}}_J\right)}\mathcal{F}_{ZD}e^{-\tau/4\left(\hat{\hat{\mathcal{R}}}_{ZQ}+\hat{\hat{\mathcal{H}}}_J\right)}, \quad (2.13)$$

where $\hat{\hat{\mathcal{R}}}_{ZQ}$ (resp. $\hat{\hat{\mathcal{R}}}_{DQ}$) is the relaxation matrix superoperator in the ZQ (resp. DQ) operator bases $\mathcal{B}_{ZQ}$ (resp. $\mathcal{B}_{DQ}$, see Table 2.1), $\mathcal{U}$ the matrix accounting for the effect of the simultaneous

π-pulses:

$$\mathcal{U} = \begin{pmatrix} -1 & 0 & 0 & 0 \\ 0 & -1 & 0 & 0 \\ 0 & 0 & 0 & -1 \\ 0 & 0 & -1 & 0 \end{pmatrix}, \tag{2.14}$$

in basis $\{DQ^{\Sigma\mathrm{E}}_{\mathrm{central}}, DQ^{\mathrm{A}}_{\mathrm{central}}, DQ^{\mathrm{A}}_{\mathrm{outer},1}, DQ^{\mathrm{A}}_{\mathrm{outer},2}\}$, $\hat{\hat{\mathcal{H}}}_J$ accounts for the scalar coupling:

$$\hat{\hat{\mathcal{H}}}_J = \begin{pmatrix} 0 & 0 & 0 & 0 \\ 0 & 0 & 0 & 0 \\ 0 & 0 & 2i\pi J & 0 \\ 0 & 0 & 0 & -2i\pi J \end{pmatrix}, \tag{2.15}$$

in both the ZQ and DQ subspaces spanned by the bases $\hat{\hat{\mathcal{R}}}_{ZQ}$ and $\hat{\hat{\mathcal{R}}}_{DQ}$ respectively, with J the scalar coupling constant, set to 130 Hz, and $\mathcal{F}_{ZD}$ the bijection function from $\mathcal{B}_{ZQ}$ to $\mathcal{B}_{DQ}$ accounting for the first and third proton π-pulses:

$$\mathcal{F}_{ZD} \begin{pmatrix} ZQ^{\Sigma\mathrm{E}}_{\mathrm{central}} \\ ZQ^{\mathrm{A}}_{\mathrm{central}} \\ ZQ^{\mathrm{A}}_{\mathrm{outer},1} \\ ZQ^{\mathrm{A}}_{\mathrm{outer},2} \end{pmatrix} = - \begin{pmatrix} DQ^{\Sigma\mathrm{E}}_{\mathrm{central}} \\ DQ^{\mathrm{A}}_{\mathrm{central}} \\ DQ^{\mathrm{A}}_{\mathrm{outer},2} \\ DQ^{\mathrm{A}}_{\mathrm{outer},1} \end{pmatrix}. \tag{2.16}$$

The expected value at the end of the low-field evolution is obtained by:

$$\mathcal{E}_{2\hat{C}_y\hat{H}_y}(\tau) = \rho_{2\hat{C}_y\hat{H}_y \to \mathcal{B}_{ZQ}} \mathcal{P}(\tau) \rho^{\mathrm{T}}_{2\hat{C}_y\hat{H}_y \to \mathcal{B}_{ZQ}}, \tag{2.17}$$

where $\rho_{2\hat{C}_y\hat{H}_y \to \mathcal{B}_{ZQ}}$ is the projection of the operator monitored during the evolution period (*i.e.* $2\hat{C}_y\hat{H}_y$) on $\mathcal{B}_{ZQ}$ and the superscript T refers to the transpose operation:

$$\begin{aligned} \rho_{2\hat{C}_y\hat{H}_y \to \mathcal{B}_{ZQ}} &= \left(\frac{1}{2\sqrt{6}}, \frac{1}{2\sqrt{3}}, \frac{1}{4}, \frac{1}{4} \right), \\ \rho^{\mathrm{T}}_{2\hat{C}_y\hat{H}_y \to \mathcal{B}_{ZQ}} &= \begin{pmatrix} 1/(2\sqrt{6}) \\ 1/(2\sqrt{3}) \\ 1/4 \\ 1/4 \end{pmatrix}. \end{aligned} \tag{2.18}$$

Detection The entire spectrum was simulated by including the chemical shift evolution, with the same sweep width and number of points as in the recorded 2F-HZQC to provide a reliable comparison. Both simulated and measured spectra were processed with the same parameters for zero-filling. No apodisation function was used in the indirect dimension. The individual free induction decays were simulated and fast Fourier transformation was applied using the Python scipy.fftpack library [136]. Spectra were created using the Python nmrglue library [137]. All extracted cross-sections were further normalized independantely to the maximum peak intensity.

2.2.5.2 Validation of the methyl-TROSY theory

In order to confirm our treatment of relaxation in methyl groups during MQ evolution, we simulated the spin evolution (relaxation, chemical shift and scalar coupling) at the low magnetic field center ($B_0 = 0.33\,\mathrm{T}$) and calculated the corresponding spectrum. We used a spectral density function that accounts for the global tumbling of the protein (correlation time τ_c), the rotation of the methyl group (order parameter S_m^2 and correlation time τ_m), and two modes of motion of the C-C bond within the protein: fast (order parameter S_f^2 and correlation time τ_f) and slow (order parameter S_s^2 and correlation time $\tau - s$). The spectral density function is written as:

$$\begin{aligned}\mathcal{J}_{Ubi}(\omega,\theta_{\vec{i},\vec{j}}) = \frac{2}{5}\Big[&S_m^2(\theta_{\vec{i},\vec{j}})(S_f^2S_s^2L(\omega,\tau_c) + (1-S_f^2)L(\omega,\tau_f') + S_f^2(1-S_s^2)L(\omega,\tau_s')) \\ &+(\mathcal{P}_2[\cos(\theta_{\vec{i},\vec{j}})] - S_m^2(\theta_{\vec{i},\vec{j}}))(S_f^2S_s^2L(\omega,\tau_m') + (1-S_f^2)L(\omega,\tau_f'') + S_f^2(1-S_s^2)L(\omega,\tau_s''))\Big],\end{aligned} \tag{2.19}$$

using the same definition as above. The values of the motional parameters used in the simulation of the spectrum were obtained in an independant study [21] based on high-resolution NMR relaxometry of U-[^{2}H, ^{15}N], Ile-δ_1[^{13}C^{1}H^{2}H$_2$]-ubiquitin and are reported in Appendix Table E.1.

Cross-section of the 2F-HZQC along the carbon dimension and simulated spectra are shown in Fig. 2.12. Using a single relaxation rate $R^{\mathrm{gen}}_{\mathrm{MQ,central}}$ (Eq. 2.8) cannot explain the relatively sharp peaks at low field but is in perfect agreement with the HZQC spectrum recorded at a single high field ($\mathrm{B_0} = 14.1\,\mathrm{T}$) (Fig. 2.13). Our model, which considers the individual relaxation rates of the two contributions to the central line, reproduces well the linewidth of the peaks in both spectra. The low intensity observed for Ile-23 (Fig. 2.2.b) may be due to slower rotation of the methyl group (Table E.1) as would be expected from Fig. 2.10.

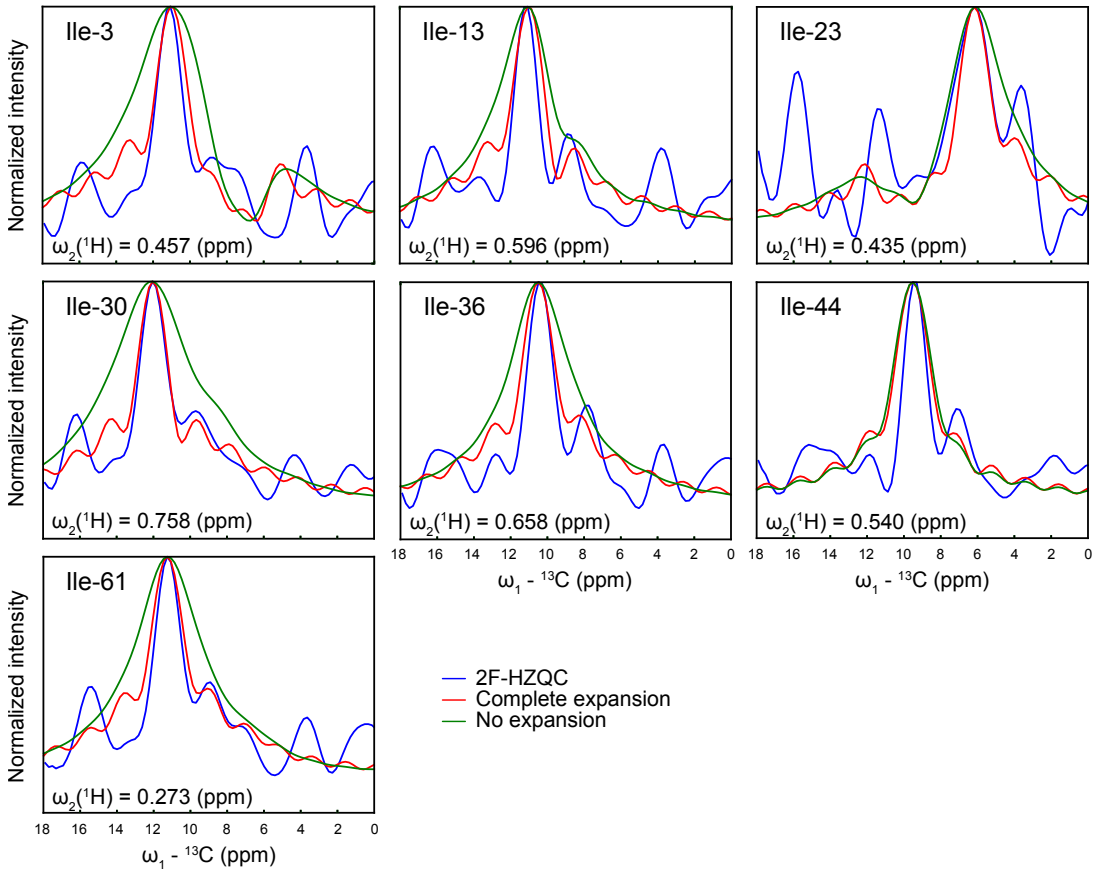

Figure 2.12: Simulation of the 2F-HZQC spectrum at 0.33 T of U-[^{2}H, ^{15}N], Ile-δ_1[^{13}CH$_3$]-ubiquitin. Simulation of cross-sections along the indirect dimension of the 2F-HZQC spectrum for the seven isoleucine residues of Ubiquitin measured with t_1 evolution at 0.33 T. The cross-sections from the experimental spectra (blue) are compared with a simulation using our approach (red) or using the previously reported expression of relaxation rates for the central lines of the triplets (green). All cross-sections are normalized independently so that each of them have the same maximum intensity. We applied an apodization function to the experimental and simulated FIDs of the form: $sp(x) = \sin^2 \frac{\pi/2+0.48\pi n}{N-1}$, with n the data index and N the number of points in the proton dimension. Figure reproduced from [38].

2.2.6 Conclusion

A general analysis of the relaxation properties of zero- and double-quantum coherences in methyl groups has been described, without invoking two key hypotheses of the original methyl-TROSY work [36]: slow tumbling and fast methyl rotation, which are appropriate for large macromolecules at high fields. Symmetry considerations show that the free evolutions of ZQ (or DQ) coherences occur in a subspace of dimension 4. A numerical analysis shows that one component of this subspace relaxes slowly at all magnetic fields where the Redfield treatment of relaxation

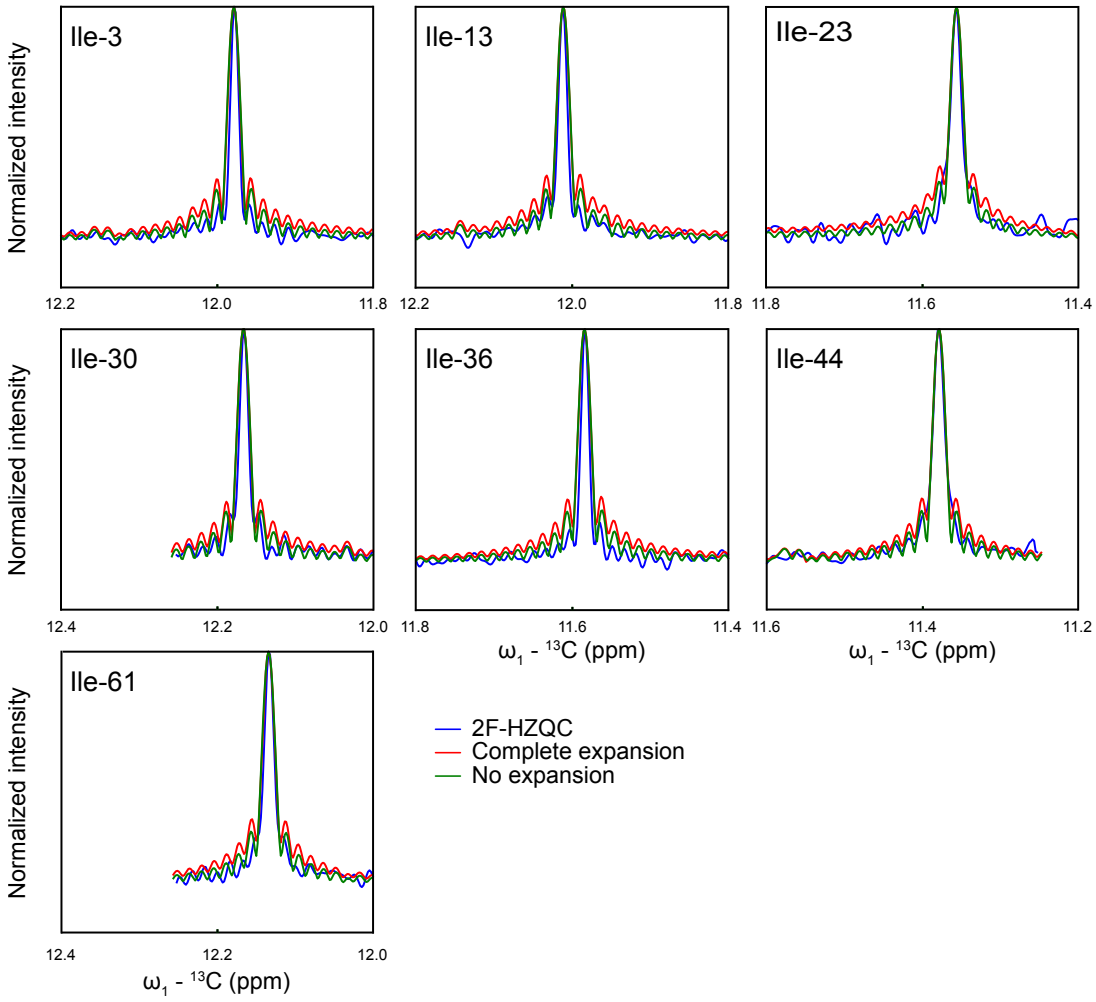

Figure 2.13: Simulation of the HZQC spectrum at 14.1 T of U-[^{2}H, ^{15}N], Ile-δ_1[^{13}CH$_3$]-ubiquitin. Simulation of cross-sections along the indirect dimension of the HZQC spectrum for the seven isoleucine residues of Ubiquitin measured with t_1 evolution at 14.1 T. The cross-sections from the experimental spectra (blue) are compared with simulations using our approach (red) or using the previously reported expression of relaxation rates for the central lines of the triplets (green). All cross-sections are normalized independently so that all spectra have the same maximum intensity. We applied an apodization function to the experimental and simulated FIDs of the form: $sp(x) = \sin^2 \frac{\pi/2+0.48\pi n}{N-1}$, with n the data index and N the number of points in the proton dimension. Figure reproduced from [38].

is valid. At high field, two operators relax slowly and correspond to the central lines of the methyl triplet. Analytical calculations with our model are then equivalent to the conventional methyl-TROSY theory. At low field, where the slow-tumbling approximation is not valid anymore, a single component relaxes slowly, preserving the methyl-TROSY effect for a third of the polarization. A detailed analysis of the spectral density functions that describe relaxation prop-

erties of multiple-quantum coherences confirmed that the TROSY effect is optimal under fast rotation of the methyl group from the pico- to few tens of pico-second time scales. This limits optimal TROSY conditions to un-constrained methyl groups with a free rotation around the symmetry axis. This particularity may hinder the observation of some conformationally constrained methyl-groups. Our comprenhensive approach shows that CSA/DD cross-correlated relaxation leads to more favorable relaxation properties for one component of the outer lines of the triplet at very high fields ($B_0 > 50\,T$). At these magnetic fields, recording an HZQC exploiting the interference between the DD and CSA relaxation mechanisms will lead to a new type of methyl TROSY. This new development sheds light on the 2F-HZQC experiment performed on Ubiquitin [37]. It shows that the manipulation of ZQ coherences can be used to observe methyl groups of large macro-molecules at low magnetic fields where contributions of chemical exchange line broadening are dramatically reduced [37].

2.3 Two-field TROSY for the study nuclei with high CSA in large proteins

This section is largely based on the associated published work [41].

2.3.1 Motivation

The NH- and methyl-TROSY both rely on interference between relaxation mechanisms. The methyl-TROSY experiment is based on the cancellation between intra-methyl DD interactions while the NH-TROSY exploits interference between DD and CSA interactions [78, 79, 80, 36]. The amplitude of the dipolar interaction is field-independent so that the methyl-TROSY effect is ubiquitous at conventional magnetic fields ($B_0 > 9\,T$) and even at lower magnetic fields, down to a fraction of a Tesla, as shown in the previous section and Ref. [38]. The CSA interaction scales linearly with the magnetic field and, consequently, TROSY effects based on DD/CSA interference mechanisms are optimal at magnetic fields where the CSA interactions has a magnitude similar to the DD interactions [35]. However, recent theoretical work showed that the optimal field in terms of **S**ignal-to-**N**oise **R**atio (SNR) for NH-TROSY is 1.5 GHz proton Larmor frequency, whereas optimal DD/CSA interference is around 950 MHz, as higher fields lead to better intrinsic sensitivity [138]. In two-spin systems, an essential component to obtain increased resolution is the selection of the appropriate operator (the TROSY single-transition operator) at the optimal field.

The set of two-spin TROSY pulse sequences used for the study of biomolecules has mainly been applied on pairs of the type X-^{1}H (X=backbone-^{15}N in proteins or aromatic-^{15}N and ^{13}C in proteins and nucleic acids) [35, 77, 139, 140]. In these spin systems, the CSA of the protons is either small or comparable to the amplitude of the DD interaction at magnetic fields currently accessible for biomolecular NMR (between 9 and 28 T) and leads to field-dependence of the proton transverse relaxation rate usually less pronounced than for the relaxation of backbone-^{15}N and aromatic-^{13}C nuclei [138], with the exception of imino protons in nucleic acids [141]. Thus, the optimal field for the associated TROSY experiment depends mostly on the relaxation properties of the heteronucleus. This is not the case in the recently developed two-dimensional ^{13}C-^{19}F-TROSY experiment for the study of specifically ^{19}F-labeled protein aromatic side-chains and nucleic acid bases [40, 142]. The potential of this approach cannot

be overstated, as the study of aromatic side-chains by NMR is one of the biggest challenges in large biomolecules. The interference between the ^{13}C-^{19}F DD and the ^{13}C-CSA relaxation mechanisms is strong, leading to favorable relaxation properties of the TROSY component of the ^{13}C polarization. On the other hand, because of the large ^{19}F-CSA, the interference between the ^{13}C-^{19}F DD and the ^{19}F-CSA relaxation mechanisms is far from optimal at conventional magnetic fields for biomolecular NMR (higher than 9.4 T). The unfavorable ^{19}F relaxation properties originating from its large CSA lead to two drastically different optimal fields for the relaxation of ^{19}F and ^{13}C coherences [40]. Is it nevertheless possible to define a magnetic field that would be a good compromise for aromatic ^{13}C-^{19}F-TROSY experiments in large proteins (with a correlation time for overall rotational diffusion $\tau_c > 25$ ns) ? Numerical simulations (see below) show that there will likely be no good single magnetic field compromise for the investigation of large systems by ^{13}C-^{19}F-TROSY. Then, would it be possible to exploit the optimal relaxation properties of both ^{13}C and ^{19}F within the same experiment? Here, we introduce the concept of two-field transverse relaxation-optimized spectroscopy (2F-TROSY) where we exploit the different optimums for the transverse relaxation in multiple-spin systems by visiting two vastly different magnetic fields within a single experiment.

2.3.2 Theory and calculations

2.3.2.1 Relaxation theory

We considered pairs of directly bound ^{13}C and ^{19}F nuclei separated by 133.8 picometers, with the physical properties of a specifically labelled side chain of 3-Fluorotyrosine (3F-Tyr) as previously used [40]. Analytical calculations of the relaxation rates (see Appendix C.2) for an isolated ^{13}C-^{19}F spin pair were performed using RedKite [19] in the basis formed by the 16 terms:

$$\mathcal{B}_{CF} = \{\hat{\mathbb{1}}, \hat{\mathrm{F}}_\mathrm{x}, \hat{\mathrm{F}}_\mathrm{y}, \hat{\mathrm{F}}_\mathrm{z}, \hat{\mathrm{C}}_\mathrm{x}, \hat{\mathrm{C}}_\mathrm{y}, \hat{\mathrm{C}}_\mathrm{z}, 2\hat{\mathrm{F}}_\mathrm{x}\hat{\mathrm{C}}_\mathrm{z}, 2\hat{\mathrm{F}}_\mathrm{y}\hat{\mathrm{C}}_\mathrm{z}, 2\hat{\mathrm{F}}_\mathrm{z}\hat{\mathrm{C}}_\mathrm{x}, 2\hat{\mathrm{F}}_\mathrm{z}\hat{\mathrm{C}}_\mathrm{y}, 2\hat{\mathrm{F}}_\mathrm{x}\hat{\mathrm{C}}_\mathrm{x}, 2\hat{\mathrm{F}}_\mathrm{x}\hat{\mathrm{C}}_\mathrm{y}, 2\hat{\mathrm{F}}_\mathrm{y}\hat{\mathrm{C}}_\mathrm{x}, 2\hat{\mathrm{F}}_\mathrm{y}\hat{\mathrm{C}}_\mathrm{y}, 2\hat{\mathrm{F}}_\mathrm{z}\hat{\mathrm{C}}_\mathrm{z}\}, \tag{2.20}$$

where $\hat{\mathbb{1}}$ is the identity operator. The ^{13}C- and ^{19}F-CSA tensors from Ref.[40] were used and are given in Appendix Table C.3. We used the MF approach [15] for the spectral density function, which includes the effect of internal motions and global tumbling:

$$\mathcal{J}_{i,j}(\omega) = \frac{2}{5}\mathcal{P}_2(\cos\theta_{i,j})\left(S^2\frac{\tau_c}{1+(\omega\tau_c)^2} + (1-S^2)\frac{\tau_i'}{1+(\omega\tau_i')^2}\right), \tag{2.21}$$

where i and j are vectors pointing along the principal axes of interactions i and j in the molecular frame, $\mathcal{P}_2$ is the second order Legendre polynomial $\mathcal{P}_2(x) = (3x^2 - 1)/2$, $\tau_i'^{-1} = \tau_c^{-1} + \tau_i^{-1}$ with τ_c the isotropic global tumbling correlation time and τ_i the correlation time associated with local motions of order parameter S^2. We set the parameters of local dynamics to those of a rigid side chain, with $S^2 = 0.8$ and $\tau_i = 100\,\text{ps}$. The evolution of all the relaxation rates with the magnetic field are shown in Appendix Fig. C.1.

2.3.2.2 Simulation, processing and analysis of a spectrum

Theory To accurately account for polarization losses, lineshapes, and pathways, the evolution of the magnetization throughout the full pulse sequence was simulated by integrating the complete master equation [143] and generate the FID using Python and the numpy [144, 145] and scipy [136] packages. The free-evolution Liouvillian for a ^{13}C-^{19}F group written in the basis $\mathcal{B}_{CF}$ (Eq. 2.20) is:

$$\mathcal{L} = \begin{pmatrix}
0 & 0 & 0 & 0 & 0 & 0 & 0 & 0 & 0 & 0 & 0 & 0 & 0 & 0 & 0 & 0 \\
0 & \mathcal{R}_2(\text{F}) & \Omega_F & 0 & 0 & 0 & 0 & \eta_F & \pi J_{CF} & 0 & 0 & 0 & 0 & 0 & 0 & 0 \\
0 & -\Omega_F & \mathcal{R}_2(\text{F}) & 0 & 0 & 0 & 0 & -\pi J_{CF} & \eta_F & 0 & 0 & 0 & 0 & 0 & 0 & 0 \\
\theta_F & 0 & 0 & \mathcal{R}_1(\text{F}) & 0 & 0 & \sigma & 0 & 0 & 0 & 0 & 0 & 0 & 0 & 0 & \delta_F \\
0 & 0 & 0 & 0 & \mathcal{R}_2(\text{C}) & \Omega_C & 0 & 0 & 0 & \eta_C & \pi J_{CF} & 0 & 0 & 0 & 0 & 0 \\
0 & 0 & 0 & 0 & -\Omega_C & \mathcal{R}_2(\text{C}) & 0 & 0 & 0 & -\pi J_{CF} & \eta_C & 0 & 0 & 0 & 0 & 0 \\
\theta_C & 0 & 0 & \sigma & 0 & 0 & \mathcal{R}_1(\text{C}) & 0 & 0 & 0 & 0 & 0 & 0 & 0 & 0 & \delta_C \\
0 & \eta_F & \pi J_{CF} & 0 & 0 & 0 & 0 & \rho_F & \Omega_F & 0 & 0 & 0 & 0 & 0 & 0 & 0 \\
0 & -\pi J_{CF} & \eta_F & 0 & 0 & 0 & 0 & -\Omega_F & \rho_F & 0 & 0 & 0 & 0 & 0 & 0 & 0 \\
0 & 0 & 0 & 0 & \eta_C & \pi J_{CF} & 0 & 0 & 0 & \rho_C & \Omega_C & 0 & 0 & 0 & 0 & 0 \\
0 & 0 & 0 & 0 & -\pi J_{CF} & \eta_C & 0 & 0 & 0 & \Omega_C & \rho_C & 0 & 0 & 0 & 0 & 0 \\
0 & 0 & 0 & 0 & 0 & 0 & 0 & 0 & 0 & 0 & 0 & \lambda_{mq} & \Omega_C & \Omega_F & -\mu_{mq} & 0 \\
0 & 0 & 0 & 0 & 0 & 0 & 0 & 0 & 0 & 0 & 0 & -\Omega_C & \lambda_{mq} & \mu_{mq} & \Omega_F & 0 \\
0 & 0 & 0 & 0 & 0 & 0 & 0 & 0 & 0 & 0 & 0 & -\Omega_F & \mu_{mq} & \lambda_{mq} & \Omega_C & 0 \\
0 & 0 & 0 & 0 & 0 & 0 & 0 & 0 & 0 & 0 & 0 & -\mu_{mq} & -\Omega_F & -\Omega_C & \lambda_{mq} & 0 \\
\theta_{CF} & 0 & 0 & \delta_F & 0 & 0 & \delta_C & 0 & 0 & 0 & 0 & 0 & 0 & 0 & 0 & \mathcal{R}_{CF}
\end{pmatrix} \tag{2.22}$$

where $J_{CF} = -240\,\text{Hz}$ is the scalar coupling constant between the ^{13}C and ^{19}F nuclei [40], Ω_i is the offset for nucleus i and the thermal correction is defined by [146, 147]:

$$\begin{aligned}
\theta_F &= -\,2 \times 10^{-10}\,(\omega_F \mathcal{R}_1(\text{F}) + \omega_C \sigma)\,, \\
\theta_C &= -\,2 \times 10^{-10}\,(\omega_C \mathcal{R}_1(\text{C}) + \omega_F \sigma)\,, \\
\theta_{CF} &= -\,2 \times 10^{-10}\,(\omega_C \delta_C + \omega_F \delta_F)\,,
\end{aligned} \tag{2.23}$$

Thus, the effect of the magnetic field on the available polarization is included in the Liouvillian. The scaling factor 10^{-10} is used to avoid calculations overflow.

The propagator during a free evolution period is calculated as:

$$\mathcal{P}_{free}(\tau) = e^{-\tau\mathcal{L}}, \tag{2.24}$$

with τ being the evolution delay. The propagator during an rf pulse is:

$$\mathcal{P}_{rot}(\tau_{pulse}) = e^{-\tau_{pulse}(\mathcal{L}+\mathcal{L}_{pulse})}, \tag{2.25}$$

with τ_{pulse} being the pulse length and the Liouvillian for the pulse is:

$$\mathcal{L}_{pulse} = \begin{pmatrix}
0 & 0 & 0 & 0 & 0 & 0 & 0 & 0 & 0 & 0 & 0 & 0 & 0 & 0 & 0 & 0 \\
0 & 0 & 0 & -\omega_y^F & 0 & 0 & 0 & 0 & 0 & 0 & 0 & 0 & 0 & 0 & 0 & 0 \\
0 & 0 & 0 & \omega_x^F & 0 & 0 & 0 & 0 & 0 & 0 & 0 & 0 & 0 & 0 & 0 & 0 \\
0 & \omega_y^F & -\omega_x^F & & 0 & 0 & 0 & 0 & 0 & 0 & 0 & 0 & 0 & 0 & 0 & 0 \\
0 & 0 & 0 & 0 & 0 & 0 & -\omega_y^C & 0 & 0 & 0 & 0 & 0 & 0 & 0 & 0 & 0 \\
0 & 0 & 0 & 0 & 0 & 0 & \omega_x^C & 0 & 0 & 0 & 0 & 0 & 0 & 0 & 0 & 0 \\
0 & 0 & 0 & 0 & \omega_y^C & -\omega_x^C & 0 & 0 & 0 & 0 & 0 & 0 & 0 & 0 & 0 & 0 \\
0 & 0 & 0 & 0 & 0 & 0 & 0 & 0 & 0 & 0 & 0 & \omega_y^C & -\omega_x^C & 0 & 0 & -\omega_y^F \\
0 & 0 & 0 & 0 & 0 & 0 & 0 & 0 & 0 & 0 & 0 & 0 & 0 & \omega_y^C & -\omega_x^C & \omega_x^F \\
0 & 0 & 0 & 0 & 0 & 0 & 0 & 0 & 0 & 0 & 0 & \omega_y^F & 0 & -\omega_x^F & 0 & -\omega_y^C \\
0 & 0 & 0 & 0 & 0 & 0 & 0 & 0 & 0 & 0 & 0 & 0 & \omega_y^F & 0 & -\omega_x^F & \omega_x^C \\
0 & 0 & 0 & 0 & 0 & 0 & 0 & -\omega_y^C & 0 & -\omega_y^F & 0 & 0 & 0 & 0 & 0 & 0 \\
0 & 0 & 0 & 0 & 0 & 0 & 0 & \omega_x^C & 0 & 0 & 0-\omega_y^F & 0 & 0 & 0 & 0 & 0 \\
0 & 0 & 0 & 0 & 0 & 0 & 0 & 0 & -\omega_y^C & \omega_x^F & 0 & 0 & 0 & 0 & 0 & 0 \\
0 & 0 & 0 & 0 & 0 & 0 & 0 & 0 & \omega_x^C & 0 & \omega_x^F & 0 & 0 & 0 & 0 & 0 \\
0 & 0 & 0 & 0 & 0 & 0 & 0 & \omega_y^F & -\omega_x^F & \omega_y^C & -\omega_x^C & 0 & 0 & 0 & 0 & 0
\end{pmatrix}, \tag{2.26}$$

with:

$$\begin{aligned}
\omega_x^F &= \frac{\pi}{\tau_\pi^F}\cos\left(\frac{\pi}{2}\phi_F\right) \quad \omega_y^F = \frac{\pi}{\tau_\pi^F}\sin\left(\frac{\pi}{2}\phi_F\right), \\
\omega_x^C &= \frac{\pi}{\tau_\pi^C}\cos\left(\frac{\pi}{2}\phi_C\right) \quad \omega_y^C = \frac{\pi}{\tau_\pi^C}\sin\left(\frac{\pi}{2}\phi_C\right),
\end{aligned} \tag{2.27}$$

with τ_π^{i} being the pulse length for a 180°-pulse on nucleus i with phase ϕ_{i}. ϕ_{i} equals 0, 1, 2 or 3 for a pulse along x, y, -x or -y respectively. Pulse lengths used in the simulations are reported in Table 2.2.

The gradients used during the **S**ingle **T**ransition-to-**S**ingle **T**ransition **P**olarization **T**ransfer (ST2-PT) block [148] of the single-field experiment [40] were simulated by separating the sample into 10,000 slices over 2 cm, modifying the Liouvillian for free evolution in each slice according to the associated magnetic field, and taking the average signal over the whole sample.

The simulation of the evolution of the density operator during the shuttle transfers was performed as previously described [19]. Briefly, we used the existing prototype of a 2F-NMR

Table 2.2: Pulse lengths used in the simulation of the experiments. The values of the pulse-lengths at low-field are based on the existing two-field system [37, 39].

	Two-field TROSY		Single-field TROSY	
	Carbon 90°-pulse	Fluorine 90°-pulse	Carbon 90°-pulse	Fluorine 90°-pulse
Low field	10 μs	6 μs	-	-
High fields	12 μs	10 μs	12 μs	10 μs

spectrometer operating at 14.1 T and 0.33 T to model the design of other 2F-NMR systems. The field profiles were assumed to be identical to the one of our current system apart from a scaling factor $\alpha(B_0)$ where B_0 is the high-field value and α is a dimensionless function of the magnetic field B: $\alpha(B_0) = B_0/(14.1\,\mathrm{T})$ (Fig. 2.14). In this design, the sample is shuttled at constant speed until it reaches the desired low field. The computation of the density operator is performed every 1 ms during the transfers of the sample shuttle.

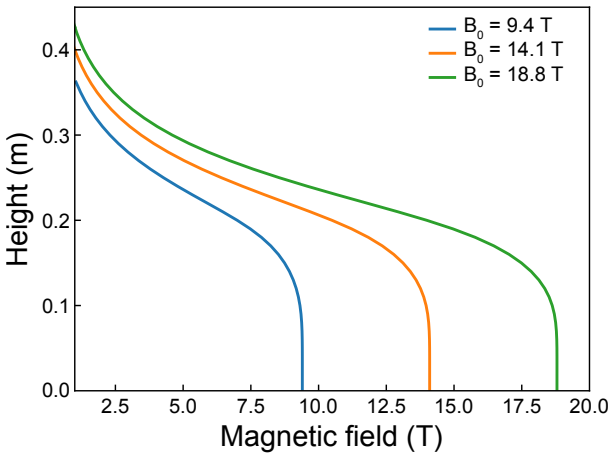

Figure 2.14: Examples of scaled magnetic field profiles used in the simulations. The field profile for a spectrometer operating at 14.1 T (orange) is taken as a reference and matches the existing 600 MHz/14 MHz 2F-NMR spectrometer. The magnetic field profiles for spectrometers operating at 9.4 T (blue) and 18.8 T (green) are calculated by multiplying the reference profile (orange) by a factor $\alpha(B_0) = B_0/14.1$ where B_0 is the operating magnetic field. Figure reproduced from [41].

Acquisition details When acquiring a spectrum, different user-defined parameters affect the signal intensity and SNR (acquisition time, sweep width, number of points in the indirect di-

mension, etc...). In order to obtain relevant comparisons between the simulated pulse sequences, and the range of magnetic fields evaluated in this study, we considered that:

- the spectral width is constant to 10 ppm in both dimensions. The number of points is then automatically calculated based on the maximum acquisition time of the associated dimension. Note that in the case of the indirect fluorine dimension, a very low number of points sometimes leads to a slightly different spectral width.
- the maximum acquisition time for the direct carbon dimension is $t_{2,max} = 3 \times T_2(^{13}\mathrm{C} - \mathrm{TROSY})$ where $T_2(^{13}\mathrm{C} - \mathrm{TROSY})$ is the relaxation rate of the TROSY ^{13}C single transition coherence.

We also considered the pulse lengths to be the same at different magnetic fields (see Table 2.2).

Optimization of the recycling delays and simulation of dummy scans We define the recycling delay as the sum of the acquisition time and inter-scan delay (d_1 in Bruker pulse programs). This delay allows the longitudinal polarization to evolve towards its equilibrium value and determines the available polarization at the beginning of the next scan. Having a long recycling delay maximizes the amount of polarization at the expense of experimental time. We optimized the inter-scan delay at each magnetic field for both experiments when the acquisition time is set to $t_{2,max}$. For this, we simulated 10 scans, without indirect dimension editing, and compared the value of $\frac{F_z(d_1)}{\sqrt{t_{2,max}+d_1}}$ of the 11^{th} scan for different values of inter-scans delays. We devide by $\sqrt{t_{2,max}+d_1}$ since the signal-to-noise ratio evolves as the square-root of the experimental time and the duration of the pulse sequence is negligible. In all the simulations presented here, the inter-scan delays were the optimized delays, and 10 dummy scans were simulated prior to detection to obtain the steady-state fluorine polarization.

Extracting peak heights from noise-free spectra The comparison of the peak heights from one field to the other was used to optimize the magnetic field to record each experiment (see below). The height of a Lorentzian-shaped peak is proportional to:

$$\mathrm{H} = \frac{\mathrm{FID}(t=0)}{R_2(^{19}\mathrm{F})R_2(^{13}\mathrm{C} - \mathrm{TROSY})}, \tag{2.28}$$

where $\mathrm{FID}(t=0)$ is the signal at time 0 (*i.e.* the peak area), $R_2(^{13}\mathrm{C} - \mathrm{TROSY})$ is the carbon-TROSY relaxation rate and $R_2(^{19}\mathrm{F})$ is either the fluorine-TROSY single-transition coherence (for the single-field experiment) or the fluorine transverse (for the 2F experiment) relaxation

rate. This relationship assumes perfect sampling in both dimensions, which is a good approximation for the direct dimension, but not necessarily in the indirect dimension.

The definition of the Liouvillian (Eq. 2.22) already takes into account the proportionality of the polarization to the magnetic field through a field-dependent thermal correction [146]. However, it does not consider the proportionality of the detected signal to the resonance frequency from Faraday's law. Likewise, the noise increases with the square root of the resonance frequency. In addition, at high magnetic fields, the recycling delay becomes longer, leading to potentially longer experimental times and lower peak heights per units of time. In order to include these effects, we multiplied the peak height H by $\sqrt{\frac{\alpha(B_{0,i})}{\beta(t_{PS,i})}}$ with $B_{0,i}$ the magnetic field of detection for the experiment i, $t_{PS,i}$ the time for one scan of the experiment i without indirect dimension editing and:

$$\alpha(B) = \frac{B}{B_{0,ref}},$$
$$\beta(t) = \frac{t}{t_{PS,ref}},$$

with $B_{0,ref}$ and $t_{PS,ref}$ the magnetic field and experimental time for one scan of the reference experiment without indirect dimension editing. We consider as reference experiment the single-field pulse sequence recorded at 14.1 T on 3F-Tyr with a global tumbling correlation time $\tau_c = 25\,\text{ns}$ (in these conditions, $t_{PS,ref} = 1.52\,\text{sec}$). This scaling factor does not consider the effect of accumulating different number of points in the indirect dimension in order to reach a fixed spectral width at different fields. An accurate estimate of the noise level is performed by simulating spectra with noise.

Processing of the spectra The simulated FIDs were processed using the nmrglue Python library [137]. All processing parameters were the same for all spectra (except phases which were adapted from one pulse sequence to the other):

- zero-filling to double the number of points in both dimensions,
- apodization function using the shifted sine-bell function: $sp(n) = \sin^2 \frac{\pi/2+0.48\pi n}{N-1}$ with n the data index and N the number of points in the associated dimension.

Simulation with noise and assessment of the signal-to-noise When spectra with noise were simulated, a Gaussian-shaped noise centered on 0 was generated using the *random.normal* function from the Python numpy library [144, 145] and was added to the FID before process-

ing. In each simulation, the same width for the Gaussian distribution was given as input to the *random.normal* function. In order to consider the effect of the magnetic field on the level of noise when comparing experiments recorded over different durations, the noise-free FID and the noise were scaled with $\alpha(B_{0,i})$ and $\sqrt{\alpha(B_{0,i})}$ respectively. This accounts for the proportionality of the noise to $\sqrt{B_{0,i}}$, and the proportionality of the detected signal to $B_{0,i}^2$ (note that the effect of the magnetic field on the polarization is already accounted for in the Liouvillian with the thermal correction so that we do not scale the noise-free FID with $\alpha^2(B_{0,i})$). In order to take into account the effect of the experimental time on the level of noise, the noise-free FID and the noise were also scaled with $t_{exp,i}/t_{exp,ref}$ and $\sqrt{t_{exp,i}/t_{exp,ref}}$ respectively, with $t_{exp,i}$ ($t_{exp,ref}$) the total experimental time for the experiment i (for the reference experiment). Here, the reference experiment is the single-field TROSY pulse sequence used to record spectra of 3F-Tyr at 14.1 T with global tumbling correlation time $\tau_c = 25$ ns and an indirect dimension aquisition time $t_{1,max} = 1.25 \times T_2(^{19}\text{F} - \text{TROSY})$ with $T_2(^{19}\text{F} - \text{TROSY})$ the relaxation time for the fluorine-TROSY component (experimental time of 4.9 hours).

Evaluation of the signal-to-noise ratio was done using two spectra:

- the spectrum corresponding to the sum of the FID and the noise. This spectrum was used to extract the peak height I;
- the spectrum of the noise only. This spectrum was generated by processing the random noise using the same parameters as for the complete FID. This spectrum was used to extract the standard deviation of the noise σ_{noise}.

The SNR is then given by:

$$\text{SNR} = \frac{I}{\sigma_{noise}}.$$

This computational procedure ensures that no parts of the peak are considered in the estimation of the noise (which is particularly critical when the TROSY selection is not optimal) and that sufficient points are included to obtain an accurate estimate of σ_{noise} (which is important when a low number of points is used in the indirect dimension).

The level of noise was choosen such that it would visually reproduce the noise in spectra already published [40]. We simulated the single-field experiment using the same experimental parameters as the ones used to record the spectrum of **M**altose **B**inding **P**rotein (MBP) until the noise was visually similar to the one reported in the original paper (signal-to-noise ratio of

25, Fig. 2.15 and [40]). Since the MBP spectrum was recorded with 80 scans [40], the spectra and noise level were scaled with 80 and $\sqrt{80}$ respectively. Thus, the scaling of the FID and noise level by $80 \times t_{exp,i}/t_{exp,ref}$ and $\sqrt{80 \times t_{exp,i}/t_{exp,ref}}$ respectively leads to spectra with a number of scans leading to the same experimental time for each of them.

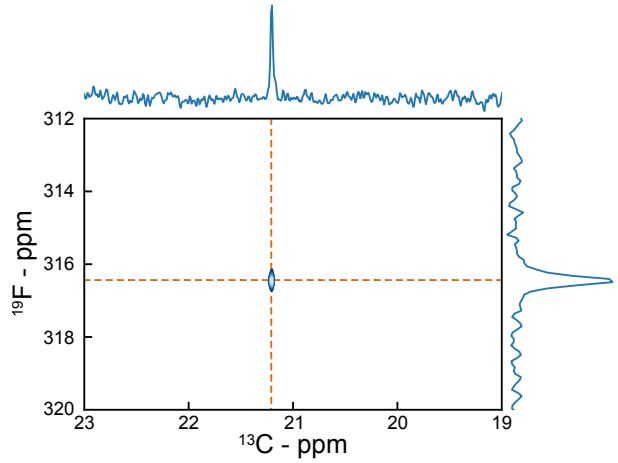

Figure 2.15: Simulation of the spectrum of MBP labeled on 3F-Tyr using the single-field TROSY pulse sequence with experimental parameters identical to Ref. [40]: B_0 = 14.1 T, 80 scans, recycling delay of 2 sec, $t_{1,max}$=10 ms, $t_{2,max}$=348 ms, 116 (4,096) complex points in the indirect (direct) dimension. Noise was added in this simulation. We show 10 contour levels starting from the highest intensity and with a factor 1.2 between two consecutive levels. The SNR is equal to 25.1. Figure reproduced from [41].

2.3.3 Results and discussion

2.3.3.1 Relaxation properties of aromatic ^{13}C-^{19}F groups

The large CSA (Table C.3) is the dominant source of ^{19}F nuclear spin relaxation at high magnetic fields (i.e. higher than 10 T). The CSA contribution to transverse relaxation scales with the square of the magnetic field and becomes a minor contribution at fields lower than a few Tesla (7 % at 1 T vs 95 % at 14.1 T for the 3F-Tyr and τ_c = 25 ns) where relaxation is mainly caused by the DD interaction. Fast ^{19}F transverse relaxation, both for an in-phase coherence and TROSY single-transition, precludes the observation of intense and well-resolved peaks at magnetic fields that are commonly used for biomolecules (Fig. 2.16a). The ^{13}C-TROSY component displays very favorable relaxation properties at high-field: at 14.1 T, the TROSY effect is strong with a relaxation rate for the TROSY component about 6 times lower than the in-phase transverse relaxation rate (Fig. 2.16b). The most favorable transverse relaxation properties are found at low

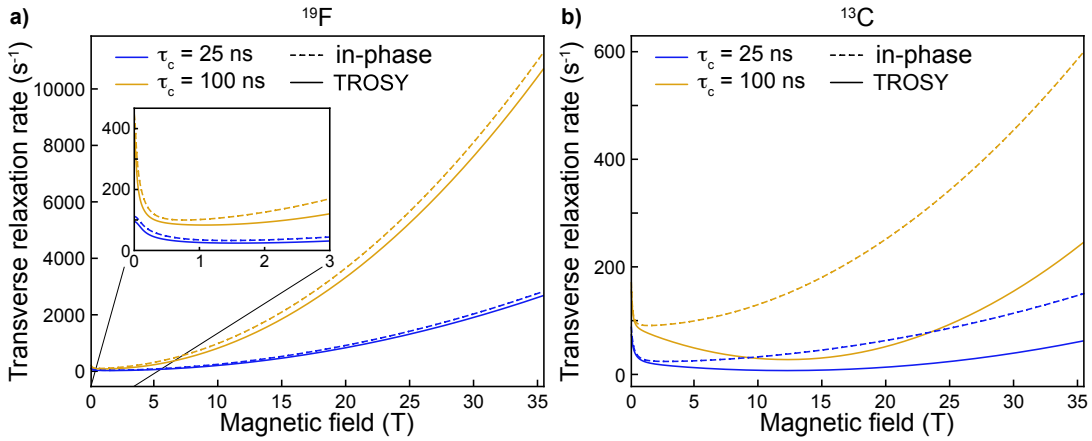

Figure 2.16: Transverse relaxation rates of an isolated ^{13}C-^{19}F aromatic spin pair. Fluorine-19 (**a**) and carbon-13 (**b**) relaxation rates of the in-phase coherences (dash) and TROSY single transition (plain) for $\tau_c = 25\,\text{ns}$ (blue) and $\tau_c = 100\,\text{ns}$ (orange). Calculations were performed using the parameters for the CSA tensors of 3F-Tyr. Figure reproduced from [41].

magnetic fields ($B_0 \approx 1\,\text{T}$) for ^{19}F and at high magnetic field ($B_0 \approx 15\,\text{T}$) for ^{13}C for proteins with correlation times for overall tumbling in the range 1 to 200 ns. These two drastically different optimal magnetic fields suggest that any single field for the ^{13}C-^{19}F TROSY single-field experiment [40] (hereafter referred to as 1F-TROSY) will likely be a poor compromise between irreconcilable constraints (Fig. 2.17) [138]. By contrast, 2F-NMR offers in principle the possibility to reach two independently optimized magnetic fields within the course of a single experiment. This approach should be particularly well suited to record the spectra of aromatic ^{13}C-^{19}F groups.

2.3.3.2 Pulse sequence for two-field TROSY

The 2F-TROSY pulse sequence proposed here is presented in Fig. 2.18. Nuclear spin systems are controlled using radiofrequency pulses and pulsed field gradients at both high- and low-field magnetic centers. Additional delays corresponding to sample shuttle transfers from one magnetic center to the other (τ_{Sh}) and waiting delays needed by the shuttle apparatus before ($\tau_{\text{HF},1}$ and $\tau_{\text{LF},2}$) and after shuttling ($\tau_{\text{LF},1}$ and $\tau_{\text{HF},2}$) were included when simulating the pulse sequence [39].

The sample is polarized at high field before shuttling to low field. At point **a** of the pulse-sequence, $\hat{F}_z$ is the only operator with a non-zero expectation value. The ^{19}F chemical shift is labeled at low field in a semi-constant time fashion [149] with an effective evolution

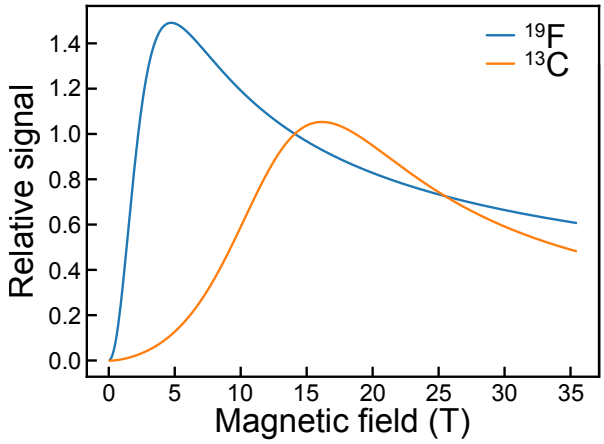

Figure 2.17: Field optimization following the approach of Ref. [138]. The relative signal for a nucleus X at a magnetic field B_0 is given by $B_0^{3/2} \times T_2(X)$ where $T_2(X)$ is the TROSY transverse relaxation time of X and scaled so that the relative signal is 1.0 at 14.1 T. These calculations have been performed for a global tumbling correlation time of 25 ns and the CSA tensor parameters of 3F-Tyr. Figure reproduced from [41].

under the ^{13}C-^{19}F scalar-coupling for a duration $T = (2|J_{CF}|)^{-1}$. Depending on the phase φ_1, either the cosine or sine t_1-evolving components are stored as a two-spin order $2\hat{F}_z\hat{C}_z$ (point **b**) and preserved during the transfer from low to high magnetic field (from **b** to **c**). The **S**pin **S**tate **S**elective **E**xcitation (S3E) block [150] allows for efficient selective excitation of the ^{13}C-TROSY component at high field (point **d**). The use of two inversion pulses on ^{19}F at high field preserves the longitudinal magnetization recovered between points **b** and **c**. This scheme allows to reduce the subsequent recycling delay and make the experiment more time efficient. When ^{19}F broadband excitation is needed, composite π-pulses can be used, keeping in mind that transverse relaxation may not be negligible during ^{19}F pulses (Fig. 2.16a).

Throughout the phase cycle, the nature of the evolving operators during the S3E element [150] is the same, ensuring identical relaxation properties of the different pathways during the S3E block [150] and the effective cancellation of undesired components of the density operator. This is not the case for the 1F-TROSY pulse sequence [40] for which the ST2-PT block [148] creates alternatively a single-quantum anti-phase ^{13}C coherence and a multiple-quantum transition coherence which relax with drastically different rates at high fields because of the strong ^{19}F-CSA (see Appendix D, sections D.1 and D.2). This leads to imperfect selection of the TROSY line in the original ^{13}C-^{19}F TROSY experiment (Fig. D.2). Similarly, an alternative 2F-TROSY pulse sequence could select the ^{19}F-TROSY component with an ST2-PT block [148]

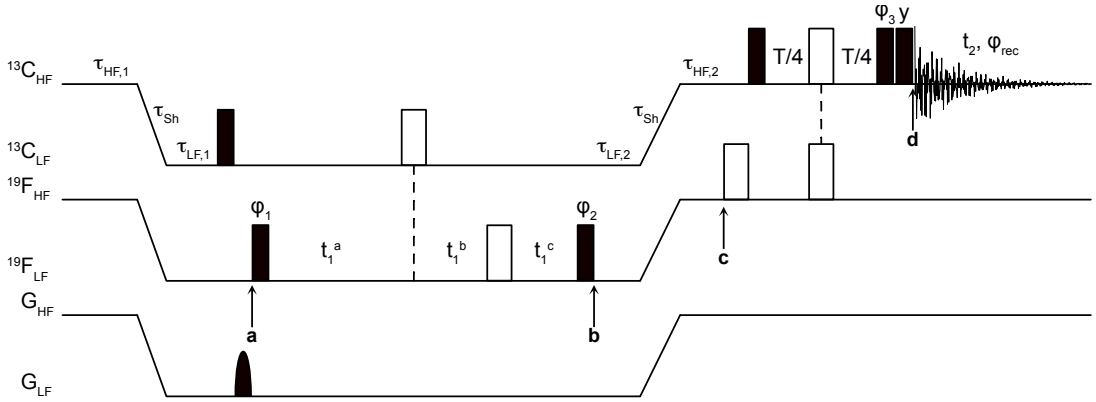

Figure 2.18: 2F-TROSY pulse sequence for the study of aromatic ^{13}C-^{19}F groups. Black narrow (respectively wide white) rectangles represent 90° (respectively 180°) pulses. Phases are aligned along the x-axis of the rotating frame unless otherwise stated. Phase cycles are as follows: φ_1=(x,-x,x,-x,x,-x,x,-x), φ_2=(y,y,y,y,-y,-y,-y,-y), φ_3=($\pi/4$,$\pi/4$,5$\pi/4$,5$\pi/4$,$\pi/4$,$\pi/4$,5$\pi/4$,5$\pi/4$) and φ_{rec}=(x,-x,-x,x,- x,x,x,-x). The sign discrimination of the frequency in the indirect dimension is achieved using the States method by changing the phase cycle for φ_1 to (y,-y,y,-y,y,-y,y,-y). For the semi-constant time indirect evolution period, $t_1^a = \frac{T}{2} + \frac{n_1}{N-1}\frac{t_{1,max}}{2}$, $t_1^b = \frac{n_1}{2(N-1)}(t_{1,max} - T)$ and $t_1^c = \frac{T}{2}\frac{N-n_1-1}{N-1}$, with $T = 1/2|J_{CF}|$, N and $t_{1,max}$ the number of points and maximum evolution delay in the indirect dimension respectively, n_1 the increment number. The pulse sequence can be modified to include proton decoupling during the t_1 and t_2 evolution periods. The horizontal line breaks represent the shuttling transfers from one field to the other. τ_{Sh} is the shuttling delay to and from the desired position. $\tau_{HF,1}$ and $\tau_{HF,2}$ are waiting delays at high field, respectively before and after shuttling. $\tau_{LF,1}$ and $\tau_{LF,2}$ are waiting delays at low field, respectively after and before shuttling. In our simulations, we set $\tau_{Sh} = 100\,ms$, $\tau_{HF,1} = 25\,ms$, $\tau_{LF,1} = 40\,ms$, $\tau_{LF,2} = 5\,ms$ and $\tau_{HF,2} = 350\,ms$. Figure reproduced from [41].

at low field (Fig. D.3). Cross-relaxation between the two ^{13}C single-transition longitudinal polarization operators during the shuttle transfer and stabilization delays would lead to imperfect TROSY selection and thus the use of ST2-PT block [148] for 2F-TROSY is not recommended (Fig. D.4 and D.5).

2.3.3.3 What are the optimal fields to record the TROSY experiments?

In order to account for all sources of polarization loss in the course of an experiment, accurate determination of the optimal magnetic fields requires the full simulation of the pulse-sequences. We compared the expected peak height at each magnetic field (or pairs of magnetic fields in the case of the 2F-TROSY sequence) assuming ideal sampling in both dimensions so that the linewidth in both dimensions is directly linked to their associated transverse relaxation rate and does not depend on the number of points in the time dimensions and apodization func-

tion (see section 2.3.2.2 for more details). In these calculations, peak heights are scaled by $\sqrt{\alpha(B_0)t_{PS}/t_{ref}}$, a factor proportional to the expected evolution of the SNR with the magnetic field and experimental time [56]. Note that the effect of signal accumulation arising from indirect dimension acquisition is not taken into account and, therefore, peak heights do not fully reproduce expected SNR variations.

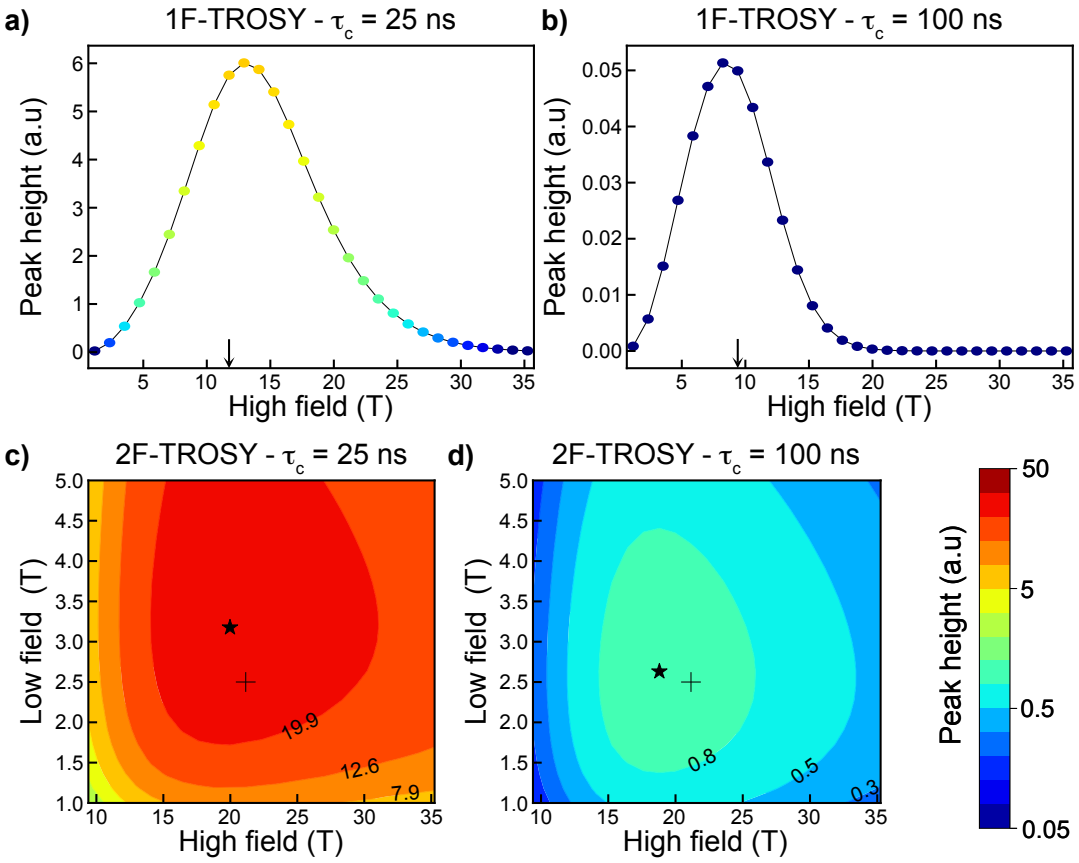

Figure 2.19: Magnetic field optimization of the 1F-TROSY and 2F-TROSY experiments. Expected peak heights for the 1F-TROSY (**a**, **b**) and 2F-TROSY (**c**, **d**) experiments, for 3F-Tyr and a global tumbling correlation time $\tau_c = 25$ ns (**a**, **c**) and $\tau_c = 100$ ns (**b**, **d**). The color scale is identical for all pannels. The conventional magnetic fields closest to the optimal fields are indicated with an arrow (**a**, **d**) or a cross (**c**, **d**). The highest peak-height position is indicated with a star in pannels **c** and **d**. In pannels **a** and **b**, points are connected by a solid line for visual clarity. Figure reproduced from [41].

The optimal field for the 1F-TROSY is lower than the optimal field for the relaxation of the single-transition ^{13}C-TROSY (Fig. 2.19a,b) because of the losses from fast relaxation of ^{19}F-coherences during the ST2-PT block [148], as well as the broadening in the fluorine dimen-

sion caused by fast relaxation of the TROSY single-transition ^{19}F-coherence (Fig. 2.16a). The optimal conventional fields are predicted to be 11.75 T for medium sized proteins ($\tau_c = 25$ ns), and 9.4 T for larger systems ($\tau_c = 100$ ns). The optimal magnetic field for detection of the ^{13}C-TROSY operator is higher in the 2F-TROSY experiment (Fig. 2.19c,d) since no fluorine coherence is generated at high field. For this experiment, we recommend a high field in the vicinity of 21.15 T and a low field close to 2.5 T for the 3F-Tyr.

In the 2F-TROSY experiment, the optimal high-field strongly correlates with the orientation of the ^{13}C-CSA tensor with respect to the C-F bond (Fig. 2.20). A perfect alignment of the ^{13}C-CSA with the C-F bond leads to an optimal interference between the CSA and DD interactions. In this case, the ^{13}C-TROSY effect is strong at moderate magnetic fields (*ca.* $10 < B_0 < 15$ T). Increased equilibrium polarization and higher sensitivity of signal detection at higher magnetic field does not counter-balance the less efficient ^{13}C-TROSY effect. The optimal low field for ^{19}F chemical shift evolution inversely correlates with the value of the orthogonal component of the ^{19}F-CSA tensor (i.e. the larger component of the tensor). Lower magnetic fields lead to a higher reduction of the ^{19}F-CSA contribution to the relaxation of the evolving fluorine in-phase coherence for compounds having the larger orthogonal component of the ^{19}F-CSA tensor.

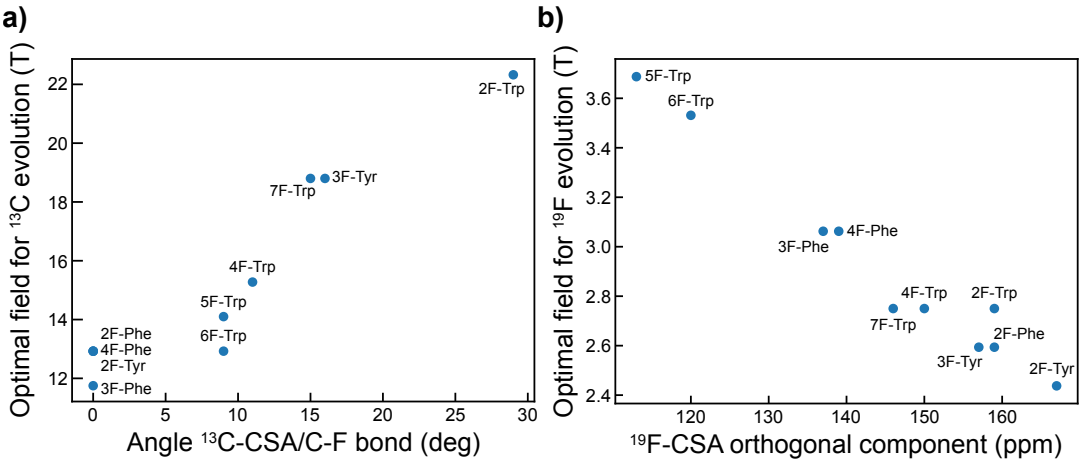

Figure 2.20: Correlation plots (**a**) between the angle between the principal axis of the ^{13}C-CSA and the C-F bond and the optimal field for carbon-detection in the 2F-TROSY experiment, and (**b**) between the orthogonal component of the ^{19}F-CSA ($\sigma_\perp^F$) and the optimal field for fluorine chemical shift evolution in the 2F-TROSY experiment. Optimal fields are obtained for $\tau_c = 100$ ns. Figure reproduced from [41].

2.3.3.4 Two-field TROSY offers increased sensitivity and resolution

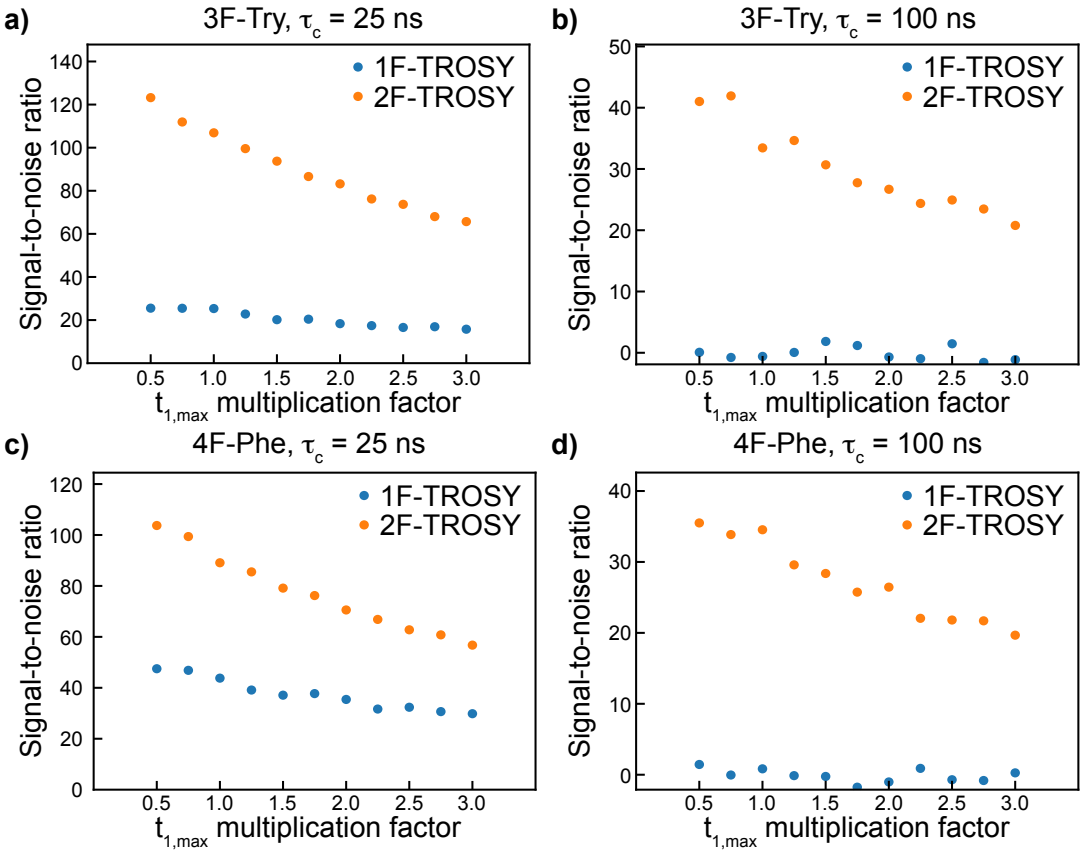

Figure 2.21: Expected SNR for the 1F-TROSY and 2F-TROSY experiments. The SNR was estimated for proteins with global tumbling correlation times $\tau_c = 25$ ns (**a** and **c**) and $\tau_c = 100$ ns (**c** and **d**) labeled with 3F-Tyr (**a** and **b**) or 4F-Phe (**c** and **d**). The value of $t_{1,max}$ is calculated as $t_{1,max}(C) = C \times T_2(^{19}F)$ where C is a multiplication factor, ranging from 0.5 to 3.0, and $T_2(^{19}F)$ is the transverse relaxation time for the fluorine TROSY single-transition coherence (resp. the in-phase single-quantum coherence) in the 1F-TROSY (resp. 2F-TROSY) experiment. The experimental time is the same for each simulated experiment (4.9 hours), leading to a higher number of scans for experiments with shorter $t_{1,max}$. Figure reproduced from [41].

We compared the expected SNR from the 1F-TROSY and 2F-TROSY experiments at their optimal magnetic field(s) by simulating the full two-dimensional spectra with Gaussian noise with scaled intensity from one field to the other (see section 2.3.2.2). The level of noise was chosen to approximately reproduce the SNR on MBP spectra already published (SNR 25 for 80 scans of 700 μM MBP, recycling delay of 2 sec, 116 complex points in the indirect dimension and $t_{1,max} = 10$ ms, see Fig. 2.15) [40]. Peak intensities depend, among other parameters, on

the number of points in the indirect time dimension, which is usually set to reach a desired resolution for a given spectral width. To take different options into account, we simulated the pulse sequences for different values of $t_{1,max}$. For moderate protein sizes ($\tau_c = 25\,\text{ns}$), the 2F-TROSY experiment offers better sensitivity by a factor ca. 5 for $t_{1,max} = T_2(^{19}F)$ (Fig. 2.21a). For a large system ($\tau_c = 100\,\text{ns}$), no visible peak is expected at the chosen level of noise for the 1F-TROSY experiment, while good SNR for the 2F-TROSY experiment can be achieved in similar experimental time (Fig. 2.21b). Similar results are obtained for compounds with better ^{13}C-TROSY efficiency (i.e. lower optimal field for carbon detection) such as the 4F-Phe (Fig. 2.21c,d). In the following, we consider $t_{1,max} = 1.25 \times T_2(^{19}F)$ [151].

Having two distinct magnetic centers allows one to carry the evolution of the ^{19}F and ^{13}C-TROSY coherences where their respective relaxation properties are most favorable. We have chosen conventional magnetic fields that lead to near-optimal sensitivity ($B_{low} = 2.5\,\text{T}$ and $B_{high} = 21.15\,\text{T}$). The 2F-TROSY experiment not only leads to better sensitivity but also to better resolution in both dimensions as compared to the 1F-TROSY experiment (Fig. 2.22). The resolution in the carbon dimension is the same for the two experiments if the detection is done at the same field. However, recording both experiments at 14.1 T to obtain a strong ^{13}C-TROSY effect leads to losses in intrinsic sensitivity (initial polarization and signal detection) compared to situations where the experiments are recorded at their optimal field(s). The sub-optimal TROSY relaxation interference in the 1F-TROSY leads to large carbon linewidth in the spectra of large protein ($\tau_c = 100\,\text{ns}$). For a medium-size system ($\tau_c = 25\,\text{ns}$), the 1F-TROSY experiment provides good peak separation in spite of the broadening in the fluorine dimension, but the spectra of larger proteins ($\tau_c = 100\,\text{ns}$) show ca. 2 ppm broad peaks. The 2F-TROSY experiment gives rise to a lower fluorine linewidth in spite of the lower magnetic field, even for large systems (ca. 1 ppm). Combined with the optimal ^{13}C-TROSY detection, satisfactory peak separation can be obtained in situations where peak overlap and a low SNR would prevent quantitative analysis in the 1F-TROSY pulse sequence.

2.3.4 Conclusion

We have introduced the concept of two-field transverse relaxation-optimized spectroscopy (2F-TROSY). It takes advantage of the development in 2F-NMR spectroscopy [37, 39] to increase the sensitivity in multidimensional spectra. By optimizing the magnetic field of different parts of the pulse sequence, the transverse relaxation rates of the evolving operators are decreased to

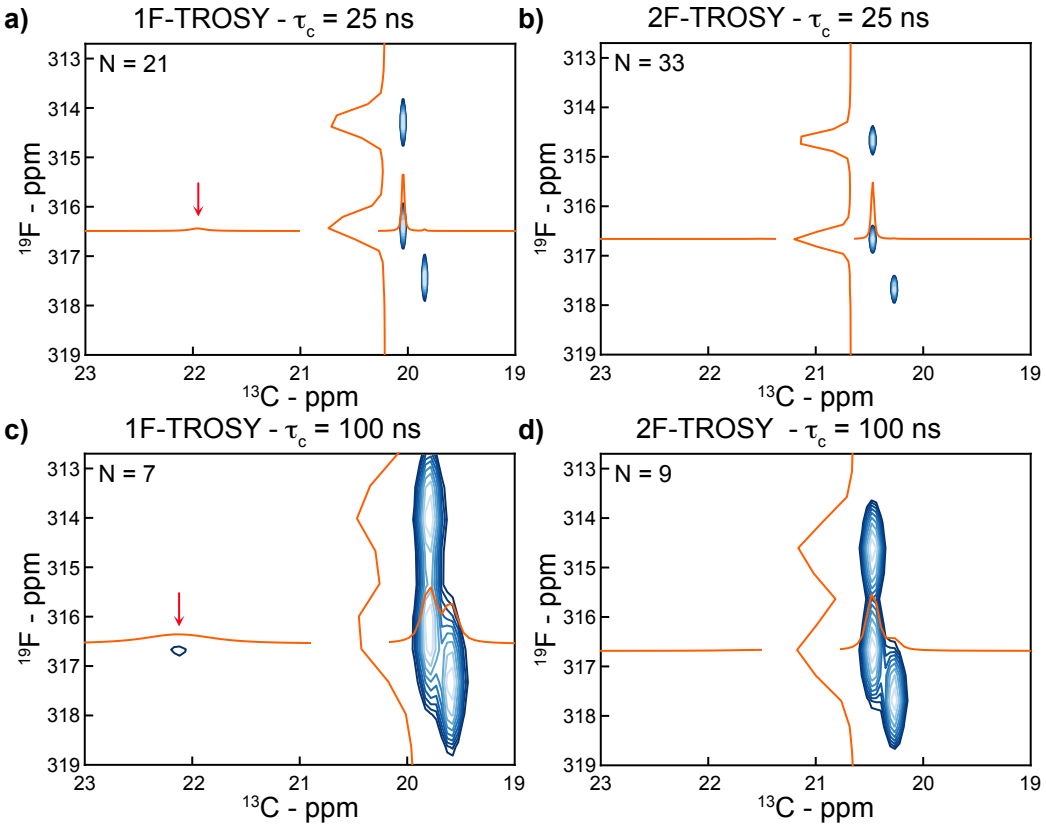

Figure 2.22: Simulated noise-free two-dimensional ^{13}C-^{19}F TROSY spectra with 3 peaks. Spectra for the 1F-TROSY (**a**, **c**) and 2F-TROSY (**b**, **d**) experiments simulated with global tumbling correlation times $\tau_c = 25\,\text{ns}$ (**a**, **b**) and $\tau_c = 100\,\text{ns}$ (**c**, **d**) for $t_{1,max} = 1.25 \times T_2(^{19}F)$ where $T_2(^{19}F)$ is the transverse relaxation time of the coherence edited in the indirect dimension. In each spectrum, 10 contour levels are shown, starting from the maximum intensity and with a factor 1.2 between two consecutive levels. Spectra were simulated without noise. Cross-sections for one peak are shown in orange. In panels **a** and **b**, the carbon anti-TROSY peak is shown with the red arrow. The number of recorded points in the indirect dimension is indicated on the top left corner of each panel. Figure reproduced from [41].

their minimal values. We have illustrated the potential of this new type of pulse sequences on ^{13}C-^{19}F aromatic spin pairs, where optimal magnetic fields are in a range that will be accessible in future designs of 2F-NMR spectrometers.

We expect a new generation of 2F-NMR spectrometers to offer sufficiently high homogeneity to allow the evolution of single-quantum coherences at low field, an essential feature to obtain high-resolution spectra and develop a new toolbox of pulse sequences. We expect ^{19}F aromatic side-chain specific labeling [40] combined with 2F-TROSY will open the way for the

investigation of structure, dynamics and function of aromatic side chains in proteins, as well as purine and pyrimidine bases in nucleic acids [142]. This would provide new probes for NMR of large proteins and nucleic acids. Further benefits are expected in systems with line broadening due to chemical exchange [37, 152]. Beyond the scope of ^{13}C-^{19}F, 2F-NMR approaches that exploit favorable relaxation properties at low field can be adapted to the NMR investigation of a variety of nuclei with large CSAs to increase the sensitivity and resolution in NMR spectra of large systems. These include nuclei such as the carbonyl carbon of peptide bonds or ^{19}F in the context of ^{13}C-^{19}F$_3$ groups, where significant TROSY-type interference was not found at high field [153] but the field-dependence of TROSY in ^{13}C-^{19}F$_3$ groups has not been explored as much as for ^{13}C-^{1}H$_3$ groups [38] yet.

2.4 Conclusion

In the first part of this chapter, we used RedKite and a complete expansion of the Hilbert space for an isolated $^{13}C^{1}H_3$ methyl group to understand linewidths in two dimensional 2F-HZQC spectrum obtained on the protein Ubiquitin specifically labeled at its isoleucine-δ_1 methyl groups. We explained the unexpected persistence of signal in the two-field HZQC experiment by showing that an excited coherence has favourable relaxation properties, even at low fields. This showed that the methyl-TROSY effect still exists at low fields beyond the slow tumbling motional regime.

In addition to revealing a spin property, this experiment paves the way for a new class of pulse sequences with spin evolution at multiple fields. In the second part of this chapter, we introduced the concepts of two-field TROSY: slowly relaxing operators are selected and chemical shift editing is performed at the optimal field for resolution and sensitivity. We illustrated this approach computationaly on aromatic ^{13}C-^{19}F groups for which the carbon and fluorine chemical shift evolution are optimal at two very distinct fields. With the constant increase in available magnetic fields, high-CSA nuclei (such as the carbon-13 in carbonyl groups of peptide bonds) might become an impediment to record many multi-dimensional experiments. Coupling a high-magnetic center to a low-field has the potential to offer high sensitivity and resolution for these spin groups.

Historically, investiments to increase the available magnetic-field stength has been justified by the need for higher sensitivity. Undeniably, these technological developments will make a number of challenging sytems amenable to NMR studies. The work presented in this chapter suggests however that a number of studies will not be possible at very high magnetic fields. As much as increased magnetic fields are of great interest for the biomolecular community, we argue that the ability to shuttle the sample from a high to low field and back will become equally important. This will require solving a number of technological challenges, starting with obtaining a highly homogeneous low-field to allow single-quantum coherence evolution.

Chapter 3

Relaxation in field-varying experiments

Contents

3.1 Introduction

Several clases of experiments are based on either moving the sample through a broad range of magnetic fields or switching rapidly the magnetic field between two extreme values. An in depth investigation of relaxation processes is particularly critical to design and interpret a

selection of experiments which have been designed recently: (1) The existence of **L**ong-**L**ived **S**tates (LLS) [154, 155] was revealed by the combination of high-field coherent evolution and low-field relaxation; (2) In **d**issolution **D**ynamic **N**uclear **P**olarization (dDNP) [89, 156, 157], the hyperpolarized sample is transferred back and forth between the polarizing magnetic center and the high-field spectrometer through magnetic fields that can be as low as the earth magnetic field; (3) Multi-scale dynamics can be characterized with **F**ast **F**ield **C**ycling (FFC) relaxometry [158] where the magnetic field is switched from *ca.* 1 T down to *ca.* 100 μT; (4) A sample-shuttle apparatus can be used to combine relaxometry experiments with high-field **N**uclear **M**agnetic **R**esonance (NMR) [62, 63, 159, 17] to gain atomic resolution description of molecular dynamics; (5) This kind of device can also be used to investigate relaxation properties of spin terms that are only relevant at low fields [160]; (6) A sample shuttle may couple two magnetic centers in a Two-Field (2F) NMR spectrometer [39] to record multi-dimensional experiments where spins are manipulated at two vastly different fields [39, 37, 22, 124].

Sample-shuttling experiments have been used to measure longitudinal relaxation rates over orders of magnitude of magnetic fields and characterize the dynamics of membrane vesicules [64], protein backbone [66, 17] and side-chains [21]. This type of experiments, called **H**igh-**R**esolution **R**elaxometry (HRR), consists in the measurement of relaxation rates over a broad range of magnetic field while preserving the high resolution of conventional high-field magnets (*i.e.* higher than 9 T) [62, 63]. This approach relies on moving the NMR sample in the stray field of a commercial magnet to measure longitudinal relaxation rates over orders of magnitude of magnetic field. The sample is transfered back in the high-field magnetic center for detection, thus ensuring high sensitivity and resolution.

During a HRR experiment, the sample is moved outside of the magnetic center where no radiofrequency pulse can be applied. Thus, relaxation decays acquired using HRR deviate from ideal decays with the longitudinal relaxation rate for two reasons. First, the effective density operator at the beginning of the relaxation delay is usually different from the desired longitudinal operator due to cross-relaxation during the sample transfers. Second, cross-relaxation pathways during the relaxation delay may lead to multi-exponential polarization decays. Therefore, the analysis of experimental HRR rates requires to account for these systematic deviations in order to accurately determine the motional parameters of the system under study. We introduced an iterative correction procedure called **I**terative **C**orrection for the **A**nalysis of **R**elaxation **U**nder **S**huttling (ICARUS) [17, 67] for the correction of HRR relaxation rates. Using symbolic expres-

sions of magnetic-field dependent relaxation matrices, the HRR experiments are simulated and measured relaxometry relaxation rates are corrected so that a reliable analysis of the dynamic properties of the system under study can be performed. These aspects will be detailed with application on $\{^{13}C^{1}H^{2}H_{2}\}$-labeled methyl-groups on the protein Ubiquitin.

We later developped a new approach to analyze HRR relaxation data without the need for correction. Instead of extracting parameters for the dynamics of the system from relaxation rates, we reproduce relaxation decays from the relaxometry experiment. The fourth section of this chapter introduces this approach, with a comparison with results obtained from the analysis using ICARUS. This new method for quantitative analysis of HRR relaxation data is presumably more rigorous as (i) it does not require fitting potentially multi-exponential decay to extract a single longitudinal relaxation rate and (ii) is free from any correction procedure that can only be verified experimentally using 2F NMR spectroscopy [22].

The first two sections of this chapter are largely based on the associated published work [21, 19]. ICARUS is available here: `https://figshare.com/articles/software/ICARUS/9893912`.

3.2 High-resolution relaxometry and protein dynamics

The spectral density function has been used extensively to describe motional properties of molecular systems [15, 102, 11, 16]. Having a proper definition of the spectral density function, and more specifically of its parameters, is essential in order to understand the dynamics of these systems: order parameters reflect on the rigidity of the system and can be related to conformational entropy [161, 162, 163, 164]; correlation times reflect on the time-scales of the different types of internal motions of the system under study. Expressed as linear combination of the spectral density function evaluated at different frequencies, relaxation rates are direct probes of the spectral density function [16, 58, 59].

Until recently, the analysis of dynamic modes in proteins was restricted to the measurement of relaxation rates on standard high-field magnets (typically higher than 9.4 T, corresponding to a proton Larmor frequency of 400 MHz). At these magnetic fields and for standard biomolecular nuclear-spin labels (^{1}H, ^{13}C, ^{15}N), the spectral density function is only probed at frequencies higher than 40 MHz (as well as at 0 for transverse auto-relaxation rates). On molecular systems such as proteins, the spectral density function varies more between 0 and 40 MHz than at all frequencies above 40 MHz, *i.e.* complex motions occur at lower frequencies. This leads to two major issues: relaxation rates recorded at high magnetic fields are potentially poor reporters for the complexity of motions; and the deconvolution of overall rotational diffusion and internal motion can appear to be complex as they can occur on similar timescales. An elegant solution has recently been proposed to overcome the later difficulty by weak interactions of the protein of interest to nanoparticules, thus artificially changing the global tumbling correlation times by orders of magnitude [165, 166].

One way to extend the range of frequencies where the spectral density is probed is to record relaxation rates at lower fields. This approach suffers from loss of sensitivity and resolution. This limitation is overcome by shuttling the sample in the stray field of the magnet, inside the bore of a standard high-field spectrometer, while still detecting the signal at the high-field position [62, 63, 17]. This methodology has been used in the group to study the dynamics of backbone [17] and side-chains [21] of Ubiquitin over two orders of magnitude of magnetic fields and allowing the quantitative characterization of motions from pico- to nanosecond time-scales.

3.2.1 Theoretical framework for the dynamics of methyl groups

3.2.1.1 Model of correlation function

Different models of correlation function for a wide variety of molecular systems have been suggested in the past [15, 74, 27, 29, 11, 72, 110, 167]. In our analysis of high field and relaxometry relaxation rates on $\{^{13}C^1H^2H_2\}$-methyl group of Ubiquitin, the data recorded at low fields (lower than 5 T) allowed a better characterization of the complexity of motions that can occur in a methyl-bearing side-chain, in particular χ_1/χ_2 rotameric transitions in isoleucine residues on nanosecond timescales [21]. The analysis was based on the **E**xtended **M**odel **F**ree (EMF) description of the CC bond motions [74]. Assuming (i) isotropic tumbling of the protein characterized by a correlation time τ_c, (ii) EMF for CC bonds motions, (iii) perfect tetrahedral symmetry for the methyl group with a characteristic correlation time for the methyl group rotation τ_{met} associated to an order parameter $S^2_{met}(\theta_{i,j})$ [130] and (iv) statistical independence between methyl group rotation, motions of the methyl group axis and overall rotational diffusion, the correlation function can be modeled by:

$$C^{\text{met}}_{i,j}(t) = C_g(t)C_{\text{axis}}(t)C^{i,j}_{\text{met}}(t), \tag{3.1}$$

where:

$$\begin{aligned} &C_g(t) = e^{-t/\tau_c}, \quad C_{\text{axis}}(t) = S^2 + (1-S^2_f)e^{-t/\tau_f} + S^2_f(1-S^2_s)e^{-t/\tau_s}, \\ &C^{i,j}_{\text{met}}(t) = S^2_{met}(\theta_{i,j}) + \left(\mathcal{P}_2(\cos\theta_{i,j}) - S^2_{met}(\theta_{i,j})\right)e^{-t/\tau_{met}}, \end{aligned} \tag{3.2}$$

with $S^2_{met}(\theta_{i,j}) = \mathcal{P}_2(\cos\theta_i)\mathcal{P}_2(\cos\theta_j)$ and $\mathcal{P}_2$ is the second order Legendre polynomial function, $\mathcal{P}_2(x) = (3x^2-1)/2$, θ_k is the angle between the principal axis of an axially symmetric interaction k vector and the CC-axis (methyl group symmetry axis) and $\theta_{i,j}$ the angle between the principal axes of two (possibly identical) axially symmetric interactions i and j. The order parameters S^2_f and S^2_s characterize motions of the system frame and are associated with the correlation times τ_f and τ_s, respectively. The overall order parameter is defined as $S^2 = S^2_f S^2_s$. The corresponding spectral density function is:

$$\begin{aligned} \mathcal{J}_{i,j}(\omega) = \frac{2}{5}\Bigg[& S^2_{met}(\theta_{i,j})\left(S^2_f S^2_s \frac{\tau_c}{1+(\omega\tau_c)^2} + (1-S^2_f)\frac{\tau'_f}{1+(\omega\tau'_f)^2} + \right. \\ & \left. S^2_f(1-S^2_s)\frac{\tau'_s}{1+(\omega\tau'_s)^2}\right) + (\mathcal{P}_2(\cos\theta_{i,j}) - S^2_{met}(\theta_{i,j}))\times \\ & \left(S^2_f S^2_s \frac{\tau'_{met}}{1+(\omega\tau'_{met})^2} + (1-S^2_f)\frac{\tau''_f}{1+(\omega\tau''_f)^2} + S^2_f(1-S^2_s)\frac{\tau''_s}{1+(\omega\tau''_s)^2}\right)\Bigg], \end{aligned} \tag{3.3}$$

where $\tau_a'^{-1} = \tau_a^{-1} + \tau_c^{-1}$ and $\tau_a''^{-1} = \tau_a^{-1} + \tau_c^{-1} + \tau_{met}^{-1}$.

In the following, $\mathcal{J}_{\mathrm{AB}}$ will be used to denote the **D**ipole-**D**ipole (DD) auto-correlation between nuclei A and B, $\mathcal{J}_A$ for the **C**hemical **S**hift **A**nisotropy (CSA) auto-correlation of nucleus A, $\mathcal{J}_{\mathrm{AB,CD}}$ for the DD cross-correlation between the spin pairs AB and CD, $\mathcal{J}_{\mathrm{A,BC}}$ for the cross-correlation between the CSA of nucleus A and the DD interaction between nuclei B and C. Finally, the index $\mathcal{Q}$ will be used to denote the quadrupolar interactions. These notations follow conventions proposed by Werbelow and Grant [126].

As detailed bellow, in our treatment of the relaxometry data, the effects of the surrounding deuterium nuclei arising from the labelling of the protein have to be considered. These have been taken into account by adding a single additional deuterium nucleus in the spin system. For simplicity, while we consider the additional dipolar contributions to relaxation rates of the $\{^{13}\mathrm{C}^1\mathrm{H}^2\mathrm{H}_2\}$ spin system, we do not include this additional nucleus in our basis. We approximated the spectral density function for the correlations involving this vicinal deuterium $\mathrm{D}_{\mathrm{vic}}$ to be described by Eq. 3.3, although it is not part of the methyl group.

3.2.1.2 Relaxation rates

In our analysis of high-field and relaxometry relaxation rates of $\{^{13}\mathrm{C}^1\mathrm{H}^2\mathrm{H}_2\}$-methyl groups of Ubiquitin, longitudinal and transverse carbon-13 autorelaxation rates, longitudinal proton autorelaxation rates and dipolar cross-relaxation rates were used. Dipolar relaxation with an effective vicinal deuterium was considered. The set-up of RedKite for such a spin system is detailed in Appendix B.4. The contribution of the proton CSA to relaxation is expected to be negligible [131], and is not considered in the following. The CSA tensor of the carbon-13 nucleus is assumed to be symmetric and aligned with the CC bond. Expressions of the relaxation rates are given in the following equations:

$$\begin{aligned} R_1(^{13}C) =& \frac{1}{3}\Delta\sigma_C^2\omega_{\mathrm{C}}^2\mathcal{J}_{\mathrm{C}}(\omega_{\mathrm{C}}) \\ &+ \frac{1}{4}d_{\mathrm{CH}}^2\left(\mathcal{J}_{\mathrm{CH}}(\omega_{\mathrm{C}}-\omega_{\mathrm{H}}) + 3\mathcal{J}_{\mathrm{CH}}(\omega_{\mathrm{C}}) + 6\mathcal{J}_{\mathrm{CH}}(\omega_{\mathrm{C}}+\omega_{\mathrm{H}})\right) \\ &+ \frac{4}{3}d_{\mathrm{CD}}^2\left(\mathcal{J}_{\mathrm{CD}}(\omega_{\mathrm{C}}-\omega_{\mathrm{D}}) + 3\mathcal{J}_{\mathrm{CD}}(\omega_{\mathrm{C}}) + 6\mathcal{J}_{\mathrm{CD}}(\omega_{\mathrm{C}}+\omega_{\mathrm{D}})\right) \\ &+ \frac{2}{3}d_{\mathrm{CD_{vic}}}^2\left(\mathcal{J}_{\mathrm{CD_{vic}}}(\omega_{\mathrm{C}}-\omega_{\mathrm{D}}) + 3\mathcal{J}_{\mathrm{CD_{vic}}}(\omega_{\mathrm{C}}) + 6\mathcal{J}_{\mathrm{CD_{vic}}}(\omega_{\mathrm{C}}+\omega_{\mathrm{D}})\right), \end{aligned} \tag{3.4}$$

$$
\begin{aligned}
R_1(^1\mathrm{H}) =& \frac{1}{4} d_{\mathrm{CH}}^2 (\mathcal{J}_{\mathrm{CH}}(\omega_{\mathrm{C}} - \omega_{\mathrm{H}}) + 3\mathcal{J}_{\mathrm{CH}}(\omega_{\mathrm{H}}) + 6\mathcal{J}_{\mathrm{CH}}(\omega_{\mathrm{C}} + \omega_{\mathrm{H}})) \\
&+ \frac{4}{3} d_{\mathrm{HD}}^2 (\mathcal{J}_{\mathrm{HD}}(\omega_{\mathrm{D}} - \omega_{\mathrm{H}}) + 3\mathcal{J}_{\mathrm{HD}}(\omega_{\mathrm{H}}) + 6\mathcal{J}_{\mathrm{HD}}(\omega_{\mathrm{D}} + \omega_{\mathrm{H}})) \\
&+ \frac{2}{3} d_{\mathrm{HD_{vic}}}^2 (\mathcal{J}_{\mathrm{HD_{vic}}}(\omega_{\mathrm{D}} - \omega_{\mathrm{H}}) + 3\mathcal{J}_{\mathrm{HD_{vic}}}(\omega_{\mathrm{H}}) + 6\mathcal{J}_{\mathrm{HD_{vic}}}(\omega_{\mathrm{D}} + \omega_{\mathrm{H}})), \\
\sigma_{\mathrm{CH}} =& \frac{1}{4} d_{\mathrm{CH}}^2 (-\mathcal{J}_{\mathrm{CH}}(\omega_{\mathrm{C}} - \omega_{\mathrm{H}}) + 6\mathcal{J}_{\mathrm{CH}}(\omega_{\mathrm{C}} + \omega_{\mathrm{H}})), \\
R_2(^{13}C) =& \frac{1}{18} \Delta\sigma_C^2 \omega_{\mathrm{C}}^2 \, (4\mathcal{J}_{\mathrm{C}}(0) + 3\mathcal{J}_{\mathrm{C}}(\omega_{\mathrm{C}})) \\
&+ \frac{1}{8} d_{\mathrm{CH}}^2 (4\mathcal{J}_{\mathrm{CH}}(0) + \mathcal{J}_{\mathrm{CH}}(\omega_{\mathrm{C}} - \omega_{\mathrm{H}}) + 3\mathcal{J}_{\mathrm{CH}}(\omega_{\mathrm{C}}) + 6\mathcal{J}_{\mathrm{CH}}(\omega_{\mathrm{H}}) \\
&+ 6\mathcal{J}_{\mathrm{CH}}(\omega_{\mathrm{C}} + \omega_{\mathrm{H}})) \\
&+ \frac{2}{3} d_{\mathrm{CD}}^2 (4\mathcal{J}_{\mathrm{CD}}(0) + \mathcal{J}_{\mathrm{CD}}(\omega_{\mathrm{C}} - \omega_{\mathrm{D}}) + 3\mathcal{J}_{\mathrm{CD}}(\omega_{\mathrm{C}}) + 6\mathcal{J}_{\mathrm{CD}}(\omega_{\mathrm{D}}) \\
&+ 6\mathcal{J}_{\mathrm{CD}}(\omega_{\mathrm{C}} + \omega_{\mathrm{D}})) \\
&+ \frac{1}{3} d_{\mathrm{CD_{vic}}}^2 (4\mathcal{J}_{\mathrm{CD_{vic}}}(0) + \mathcal{J}_{\mathrm{CD_{vic}}}(\omega_{\mathrm{C}} - \omega_{\mathrm{D}}) + 3\mathcal{J}_{\mathrm{CD_{vic}}}(\omega_{\mathrm{C}}) \\
&+ 6\mathcal{J}_{\mathrm{CD_{vic}}}(\omega_{\mathrm{D}}) + 6\mathcal{J}_{\mathrm{CD_{vic}}}(\omega_{\mathrm{C}} + \omega_{\mathrm{D}})),
\end{aligned}
$$

where d_{AB} is the dipolar coefficient between atoms A and B and equals $-(\mu_0 \hbar \gamma_A \gamma_B)/(4\pi r_{AB}^3)$ with μ_0 the permeability of free space, $\hbar$ the Planck's constant divided by 2π, γ_X the gyromagnetic ratio of nucleus X and r_{AB} the internuclear distance between nuclei A and B, $\Delta\sigma_C$ is the CSA of the carbon-13 nucleus and $\omega_X = -\gamma_X B_0$ is the Larmor frequency for the nuclei X at a magnetic field B_0. The geometry of the methyl group was assumed to be tetrahedral with $r_{\mathrm{CH}} = r_{\mathrm{CD}} = 111.5\,\mathrm{pm}$ leading to $r_{\mathrm{HD}} = 182\,\mathrm{pm}$. The distance $r_{\mathrm{CD_{vic}}}$ is determined during the ICARUS analysis as described below.

3.2.1.3 Relaxation matrix

The secularized basis for the subspace that includes $\hat{\mathrm{C}}_z$ in a $\{^{13}\mathrm{C}^1\mathrm{H}^2\mathrm{H}_2\}$-methyl group contains 14 terms:

$$
\begin{aligned}
\mathcal{B}_{\mathrm{secularized}} = \Bigg\{ & \frac{\hat{C}_z}{3\sqrt{3}}, \frac{\hat{H}_z}{3\sqrt{3}}, \frac{\hat{D}_{1,z}}{6\sqrt{2}}, \frac{\hat{D}_{2,z}}{6\sqrt{2}}, \frac{2\hat{C}_z\hat{H}_z}{3\sqrt{3}}, \frac{\hat{C}_z\hat{D}_{1,z}}{3\sqrt{3}}, \frac{\hat{C}_z\hat{D}_{2,z}}{3\sqrt{3}}, \frac{\sqrt{2}\hat{C}_z\hat{H}_z\hat{D}_{1,z}}{3}, \\
& \frac{\sqrt{2}\hat{C}_z\hat{H}_z\hat{D}_{2,z}}{3}, \frac{\hat{C}_z\hat{D}_{1,z}\hat{D}_{2,z}}{2\sqrt{3}}, \frac{\hat{C}_z\hat{D}_1^+\hat{D}_2^-}{4\sqrt{3}}, \frac{\hat{C}_z\hat{D}_1^-\hat{D}_2^+}{4\sqrt{3}}, \\
& \frac{3\hat{C}_z\hat{D}_{1,z}\hat{D}_{1,z} - 2\hat{C}_z}{3\sqrt{6}}, \frac{3\hat{C}_z\hat{D}_{2,z}\hat{D}_{2,z} - 2\hat{C}_z}{3\sqrt{6}} \Bigg\},
\end{aligned}
\tag{3.5}
$$

where C, H, D_1 and D_2 refer to the carbon, proton, deuterium 1 and deuterium 2, respectively, as defined in the spin system in RedKite. The deuterium 1 and 2 are considered magnetically

equivalent and can be exchanged by symmetry.

As shown below, the analysis of the relaxation properties of the $\{^{13}C^1H^2H_2\}$-methyl groups of Ubiquitin during a relaxometry experiment can be performed with satisfactory accuracy in the subspace spanned by the three operators:

$$\mathcal{B}_{reduced,3} = \left\{ \frac{\hat{C}_z}{3\sqrt{3}}, \frac{\hat{H}_z}{3\sqrt{3}}, \frac{2\hat{C}_z\hat{H}_z}{3\sqrt{3}} \right\}, \tag{3.6}$$

leading to the following relaxation matrix:

$$\mathcal{R}_3 = \begin{pmatrix} R_1(^{13}\mathrm{C}) & \sigma_{\mathrm{CH}} & \eta_z^{\mathrm{C}} \\ \sigma_{\mathrm{CH}} & R_1(^1\mathrm{H}) & 0 \\ \eta_z^{\mathrm{C}} & 0 & R_{\mathrm{CH}} \end{pmatrix}, \tag{3.7}$$

where $R_1(^{13}\mathrm{C})$, $R_1(^1\mathrm{H})$ and σ_{CH} are defined above and:

$$\begin{aligned} R_{\mathrm{CH}} =& \frac{1}{3}\Delta\sigma_C^2\omega_{\mathrm{C}}^2\mathcal{J}_{\mathrm{C}}(\omega_{\mathrm{C}}) + \frac{3}{2}d_{\mathrm{CH}}^2\left(\mathcal{J}_{\mathrm{CH}}(\omega_{\mathrm{C}}) + \mathcal{J}_{\mathrm{CH}}(\omega_{\mathrm{H}})\right) \\ &+ \frac{4}{3}d_{\mathrm{CD}}^2\left(\mathcal{J}_{\mathrm{CD}}(\omega_{\mathrm{C}} - \omega_{\mathrm{D}}) + 3\mathcal{J}_{\mathrm{CD}}(\omega_{\mathrm{C}}) + 6\mathcal{J}_{\mathrm{CD}}(\omega_{\mathrm{C}} + \omega_{\mathrm{D}})\right) \\ &+ \frac{4}{3}d_{\mathrm{HD}}^2\left(\mathcal{J}_{\mathrm{HD}}(\omega_{\mathrm{H}} - \omega_{\mathrm{D}}) + 3\mathcal{J}_{\mathrm{HD}}(\omega_{\mathrm{H}}) + 6\mathcal{J}_{\mathrm{HD}}(\omega_{\mathrm{H}} + \omega_{\mathrm{D}})\right) \\ &+ \frac{2}{3}d_{\mathrm{CD_{vic}}}^2\left(\mathcal{J}_{\mathrm{CD_{vic}}}(\omega_{\mathrm{C}} - \omega_{\mathrm{D}}) + 3\mathcal{J}_{\mathrm{CD_{vic}}}(\omega_{\mathrm{C}}) + 6\mathcal{J}_{\mathrm{CD_{vic}}}(\omega_{\mathrm{C}} + \omega_{\mathrm{D}})\right) \\ &+ \frac{2}{3}d_{\mathrm{HD_{vic}}}^2\left(\mathcal{J}_{\mathrm{CD_{vic}}}(\omega_{\mathrm{H}} - \omega_{\mathrm{D}}) + 3\mathcal{J}_{\mathrm{CD_{vic}}}(\omega_{\mathrm{H}}) + 6\mathcal{J}_{\mathrm{HD_{vic}}}(\omega_{\mathrm{H}} + \omega_{\mathrm{D}})\right), \\ \eta_z^{\mathrm{C}} =& \Delta\sigma_C\omega_{\mathrm{C}}d_{\mathrm{CH}}\mathcal{J}_{\mathrm{CCH}}(\omega_{\mathrm{C}}). \end{aligned} \tag{3.8}$$

The expression of the secularized relaxation matrix in the basis $\mathcal{B}_{\mathrm{secularized}}$ can be found in Appendix section C.3.

3.2.2 Simulating sample-shuttling relaxometry experiments

3.2.2.1 Expectation value of spin operators

The expectation value of a specific operator after an evolution period t is obtained from the calculation of the propagator:

$$\hat{\hat{\mathcal{P}}}(t) = e^{-\hat{\hat{\mathcal{L}}}t}, \tag{3.9}$$

with $\hat{\hat{\mathcal{L}}}$ the Liouvillian. Eq. 3.9 assumes a constant Liouvillian over the interval t, including a constant Hamiltonian. This assumption does not hold when pulses are applied, or in field-varying experiments. In a relaxometry experiment, the fields during the polarization, relaxation and detection periods are potentially all different [158, 63]. In these cases, the evolution time t is decomposed in delays δt_i that are small enough so that the field can be considered constant:

$$\hat{\hat{\mathcal{P}}}(t) = d\hat{\hat{\mathcal{P}}}_n(\delta t_n, B_n) \times ... \times d\hat{\hat{\mathcal{P}}}_1(\delta t_1, B_1), \tag{3.10}$$

where $d\hat{\hat{\mathcal{P}}}_i$ is the propagator during the interval δt_i for which the magnetic field has a constant value B_i.

When pulses are applied, which is the case in standard pulse sequences for the measurement of relaxation rates [68], cross-relaxation pathways may no longer be active and Eq. 3.10 can be simplified using averaged Liouvillian theory [146, 168]. For example, for the measurement of longitudinal relaxation rates of nitrogen-15 in a ^{15}N-^{1}H spin pair, proton π-pulses are applied during the relaxation delay. In the abscence of such pulses, the Liouvillian reads:

$$\hat{\hat{\mathcal{L}}} = \begin{pmatrix} R_1^{\mathrm{N}} & \sigma_{\mathrm{NH}} & \delta_{\mathrm{N}} \\ \sigma_{\mathrm{NH}} & R_1^{\mathrm{H}} & \delta_{\mathrm{H}} \\ \delta_{\mathrm{N}} & \delta_{\mathrm{H}} & R_{\mathrm{NH}} \end{pmatrix}, \tag{3.11}$$

where the relaxation matrix has been written in the basis of the spin operators $\{\hat{\mathrm{N}}_z, \hat{\mathrm{H}}_z, 2\hat{\mathrm{N}}_z\hat{\mathrm{H}}_z\}$ and R_1^{N} (respectively R_1^{H}) refers to nitrogen-15 (respectively proton) longitudinal relaxation rate, R_{NH} to the two-spin order relaxation rate, σ_{NH} to the DD cross-relaxation rate between the nitrogen-15 and proton, and δ_{N} (respectively δ_{H}) to the CSA-DD cross-correlated cross-relaxation rate involving the nitrogen-15 (respectively proton) CSA. After applying a proton π-pulse, the Liouvillian is transformed according to:

$$\hat{\hat{\mathcal{L}}}' = \hat{\hat{P}}_\pi \hat{\hat{\mathcal{L}}} \hat{\hat{P}}_\pi, \tag{3.12}$$

where $\hat{\hat{P}}_\pi$ is the propagator for an ideal proton π-pulse:

$$\hat{\hat{P}}_\pi = \begin{pmatrix} 1 & 0 & 0 \\ 0 & -1 & 0 \\ 0 & 0 & -1 \end{pmatrix}. \tag{3.13}$$

When the evolution delay before and after the pulse are equal, the proton inversion pulse leads to the following average Liouvillian over the whole relaxation period:

$$\hat{\hat{\mathcal{L}}}_{av} = \begin{pmatrix} R_1^{\mathrm{N}} & 0 & 0 \\ 0 & R_1^{\mathrm{H}} & \delta_{\mathrm{H}} \\ 0 & \delta_{\mathrm{H}} & R_{\mathrm{NH}} \end{pmatrix}. \tag{3.14}$$

Over this time period, the spin operator $\hat{\mathrm{N}}_z$ is an eigenvector of the relaxation matrix, and the time-evolution of its expectation value is given by:

$$\langle \hat{\mathrm{N}}_z \rangle(t) = e^{-R_1^{\mathrm{N}} t}, \tag{3.15}$$

which is the usual mono-exponential decay used for the analysis of relaxation rates measurements (note that the evolution towards an effective saturated state is obtained from the averaging of consecutive scans [146, 169]). By constrast, an accurate analysis of relaxation properties in the abscence of radio-frequency pulses, or in field-varying experiments, requires the full relaxation matrix.

3.2.2.2 Propagator decomposition in a high-resolution relaxometry experiment

High-resolution relaxometry can be used to obtain a precise description of the dynamics of spin systems over orders of magnitude of timescales [17, 21, 67]. The analysis is based on the measurement of longitudinal relaxation rates over a broad range of magnetic fields (typically from a few tenths of Tesla up to about 20 T). A reliable description of the motions requires accurate estimates of the relaxation rates.

During each HRR experiment, the sample is transferred outside of the magnetic center to a defined position z_{relax} in the stray field above the magnet (Fig. 3.1). During the two transfers (from high to low field, and back) and the relaxation delay, all relaxation pathways are active. In contrast to the example presented above, measured polarization decays can be affected by cross relaxation and therefore cannot be used as is to determine longitudinal relaxation rates accurately (this is true for any relaxation experiment where pulses can not be applied during the relaxation period). Doing so would lead to systematic deviations in the parameters used to describe the dynamics of the system. Simulating the experiment including the time when the sample is outside the superconducting coil allows one to take into account cross-relaxation

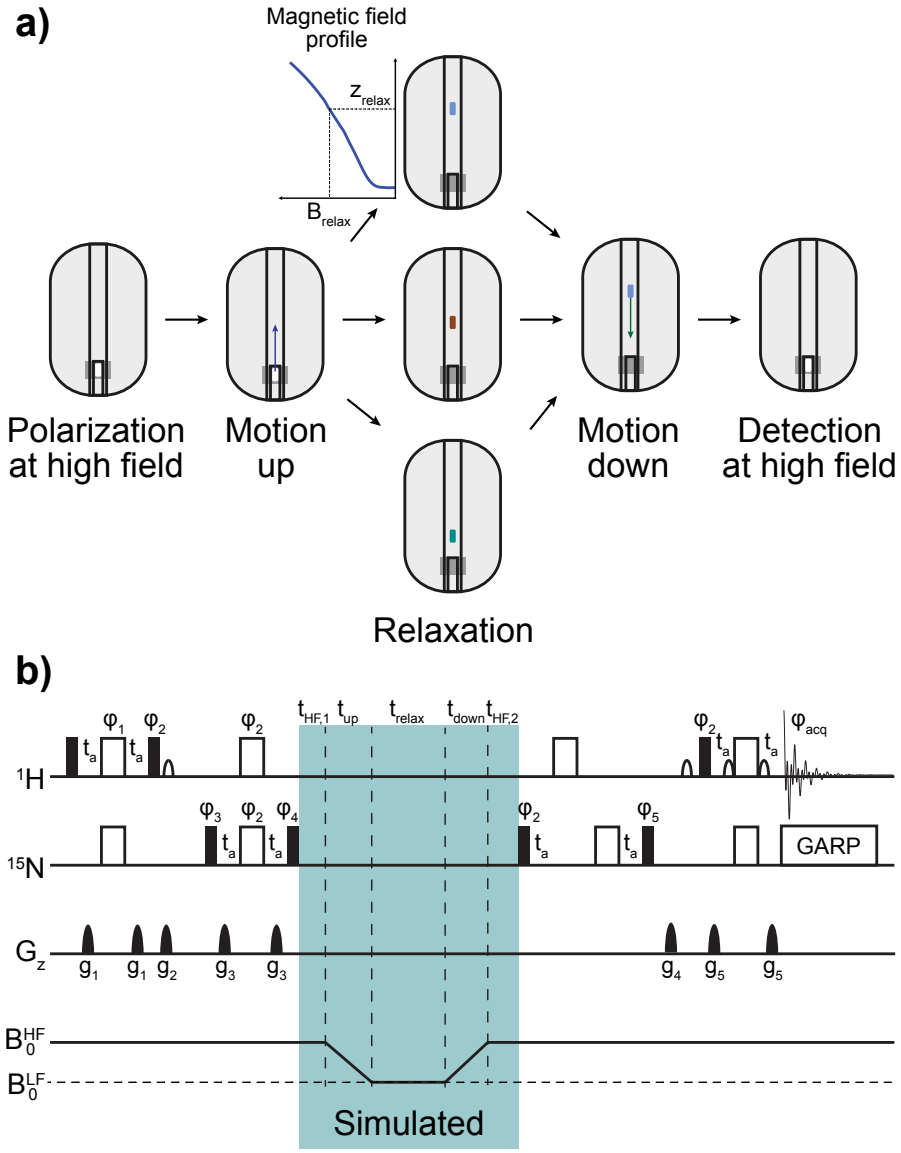

Figure 3.1: Description of an HRR scheme. **a)** The position of the sample is changed during the course of the experiment. It is first polarized at high field, and transfered to a chosen position in the stray field of the superconducting magnet, characterized by a lower magnetic field, for relaxation. The sample is then moved back to the high-field position for detection. Pannel adapted from [21]. **b)** A typical pulse sequence used to record HRR experiment. During the analysis of HRR rates, the highlighted part of the pulse sequence (blue) is simulated. Black narrow (respectively wide empty) rectangles represent $\pi/2$-pulses (respectively π-pulses). Pulses are applied along the x-axis of the rotating frame if not otherwise stated (by the φ_i). The amplitude of pulse field gradients are labeled g_i. Additional experimental details can be found in [67]. Figure reproduced from [19].

pathways and to estimate accurate relaxation rates. The complete relaxation period in a high-resolution relaxometry experiment includes three delays at constant fields and two transfers through a strong gradient of magnetic field.

The simulation of the experiment is performed by calculating the propagator during the highlighted part of the pulse sequence in Fig. 3.1b. For convenience, it is written as a product of individual propagators:

$$\begin{aligned}\hat{\hat{\mathcal{P}}}_{tot}(t_{\mathrm{HF},1}, t_{\mathrm{up}}, t_{\mathrm{relax}}, t_{\mathrm{down}}, t_{\mathrm{HF},2}) =& \hat{\hat{\mathcal{P}}}^{\mathrm{HF},2}(t_{\mathrm{HF},2}) \cdot \hat{\hat{\mathcal{P}}}^{\mathrm{down}}(t_{\mathrm{down}}) \cdot \hat{\hat{\mathcal{P}}}^{\mathrm{LF}}(t_{\mathrm{relax}}) \cdot \\ & \hat{\hat{\mathcal{P}}}^{\mathrm{up}}(t_{\mathrm{up}}) \cdot \hat{\hat{\mathcal{P}}}^{\mathrm{HF},1}(t_{\mathrm{HF},1}),\end{aligned} \tag{3.16}$$

where $\hat{\hat{\mathcal{P}}}^{\mathrm{HF},1}$ and $\hat{\hat{\mathcal{P}}}^{\mathrm{HF},2}$ are the propagators calculated at high field, respectively before and after shuttling, $\hat{\hat{\mathcal{P}}}^{\mathrm{LF}}$ is the propagator calculated at the low field position and $\hat{\hat{\mathcal{P}}}^{\mathrm{up}}$ (respectively $\hat{\hat{\mathcal{P}}}^{\mathrm{down}}$) is the propagator calculated during the motion up (respectively down) from the high-field to the low-field position (respectively from the low-field to the high-field position). This decomposition allows the calculation of the segmental propagators using either Eq. 3.9 (for constant Liouvillian superoporators) or Eq. 3.10 (for time-dependent Liouvillian superoporators). The propagators for constant-field positions (*i.e.* $\hat{\hat{\mathcal{P}}}^{\mathrm{HF},1}$, $\hat{\hat{\mathcal{P}}}^{\mathrm{LF}}$ and $\hat{\hat{\mathcal{P}}}^{\mathrm{HF},2}$) are calculated using Eq. 3.9 and the relaxation matrix calculated at either high field ($\hat{\hat{\mathcal{R}}}_{\mathrm{HF}}$) or low field ($\hat{\hat{\mathcal{R}}}_{\mathrm{LF}}$):

$$\begin{aligned}\hat{\hat{\mathcal{P}}}^{\mathrm{HF,i}}(t_{\mathrm{HF,i}}) &= e^{-t_{\mathrm{HF,i}}\hat{\hat{\mathcal{R}}}_{\mathrm{HF}}}, \\ \hat{\hat{\mathcal{P}}}^{\mathrm{LF}}(t_{\mathrm{relax}}) &= e^{-t_{\mathrm{relax}}\hat{\hat{\mathcal{R}}}_{\mathrm{LF}}}.\end{aligned} \tag{3.17}$$

The simulation of the transfers through the magnetic field gradient is performed by subdividing the experiment into intervals of few milli-seconds δt that still fulfill the conditions of Redfield theory. In order to stay in the Redfield hypothesis, δt must be large compared to the correlation time of the system to extend the integration to infinity in Eq. 1.7. In addition, δt must be sufficiently small in order to perform a discretization of the integral over the full sample trajectory. In the case of high-resolution relaxometry with a sample traveling at $\approx$10 m.s^{-1} over at most 1 m, we considered a δt of 1 ms, which corresponds, at most, to a change of about 10 % of the magnetic field between two consecutive steps. The propagators $\mathrm{d}\hat{\hat{\mathcal{P}}}(\delta t, z(t))$ for these small steps are obtained following Eq. 3.9:

$$\mathrm{d}\hat{\hat{\mathcal{P}}}(\delta t, z(t)) = e^{-\delta t \hat{\hat{\mathcal{R}}}(z(t))}, \tag{3.18}$$

where $\hat{\hat{\mathcal{R}}}(z(t))$ is the relaxation matrix evaluated at the position $z(t)$ along the bore of the magnet and characterized by its magnetic field. The experimental field profile is fitted to a polynomial expansion during the analysis of HRR data. Each propagator $\mathrm{d}\hat{\hat{\mathcal{P}}}(\delta t, z(t))$ is field dependent due to the field dependence of the relaxation matrix. The propagator for the motions up to and down from the position z_{relax} are defined as the ordered products of the infinitesimal propagators $\mathrm{d}\hat{\hat{\mathcal{P}}}$:

$$\begin{aligned}\hat{\hat{\mathcal{P}}}^{\mathrm{up}} &= \prod_{n=0}^{n_{\mathrm{max}}^{\mathrm{up}}} \mathrm{d}\hat{\hat{\mathcal{P}}}^{\mathrm{up}}(\delta t, (z(n \times \delta t))), \\ \hat{\hat{\mathcal{P}}}^{\mathrm{down}} &= \prod_{n=0}^{n_{\mathrm{max}}^{\mathrm{down}}} \mathrm{d}\hat{\hat{\mathcal{P}}}^{\mathrm{down}}(\delta t, (z(n \times \delta t))),\end{aligned} \tag{3.19}$$

where n_{max}^{up} (respectively n_{max}^{down}) is defined by $t_{\mathrm{transfer}}^{\mathrm{up}} = n_{max} \times \delta t$ (respectively $t_{\mathrm{transfer}}^{\mathrm{down}} = n_{max}^{\mathrm{down}} \times \delta t$) with $t_{\mathrm{transfer}}^{\mathrm{up}}$ (respectively $t_{\mathrm{transfer}}^{\mathrm{down}}$) the delay of transfer to the top (respectively down) position. In these calculations, the relaxation matrix is derived using the analytical expression obtained from RedKite and compiled in a Python script called FunctionsFile.py, a model of motions and a set of parameters of dynamics. We will detail applications to the dynamics of $\{^{13}\mathrm{C}^1\mathrm{H}^2\mathrm{H}_2\}$-methyl groups. The set-up of RedKite for this spin system in given in Appendix B.4.

3.3 Analysis of the relaxation in methyl groups using ICARUS

3.3.1 Principle of the iterative correction for the analysis of relaxation under shuttling

The expectation value for the operator of interest at the end of the full relaxation period (delays at high field and low field as well as the two transfers in between) can be extracted from the calculated propagator for each relaxation delay. The simulated decay as a function of the relaxation time is fitted with a mono-exponential decay function with an effective longitudinal relaxation rate $R_{sim}(\mathcal{E}_j, B_{\mathrm{LF}}^{(j)}, \mathcal{D}_i)$ where $\mathcal{E}_j$ are the experimental parameters (shuttling times and relaxation delays) for the experiment j, $B_{\mathrm{LF}}^{(j)}$ is the associated low field, and $\mathcal{D}_i$ are the parameters of dynamics for the amino acid i (Table 3.1 sums up our nomenclature for the different calculated and measured relaxometry relaxation rates). All relaxation pathways are active during the transfers between high and low-field positions. The initial density operator is partially projected onto the eigenvectors of the relaxation matrix (relaxation modes) of lowest eigenvalues. Thus, the simulated decay rate R_{sim} is *a priori* lower than the pure longitudinal relaxation rate R_{calc} calculated using the parameters of dynamics. We define the correction factor $\mathcal{C}(\mathcal{E}_j, B_{\mathrm{LF}}^{(j)}, \mathcal{D}_i)$ for each relaxometry experiment as the ratio between these two rates for an experiment j (corresponding to a specific low field $B_{\mathrm{LF}}^{(j)}$) and a residue i:

$$\mathcal{C}(\mathcal{E}_j, B_{\mathrm{LF}}^{(j)}, \mathcal{D}_i) = \frac{R_{calc}(B_{\mathrm{LF}}^{(j)}, \mathcal{D}_i)}{R_{sim}(\mathcal{E}_j, B_{\mathrm{LF}}^{(j)}, \mathcal{D}_i)}. \tag{3.20}$$

The correction factor is applied to each corresponding measured relaxometry data $R_{meas}(\mathcal{E}_j, B_{\mathrm{LF}}^{(j)})$:

$$R_{corr}(\mathcal{E}_j, B_{\mathrm{LF}}^{(j)}, \mathcal{D}_i) = \mathcal{C}(\mathcal{E}_j, B_{\mathrm{LF}}^{(j)}, \mathcal{D}_i) \times R_{meas}(\mathcal{E}_j, B_{\mathrm{LF}}^{(j)}). \tag{3.21}$$

The correction is performed iteratively (Fig. 3.2). The set of parameters $\mathcal{D}_i$ for the first iteration is obtained from the analysis of the accurate relaxation rates, *i.e* measured with the use of tailored pulse sequences, typically on high-field magnets. Then corrected relaxometry relaxation rates are analyzed alongside high-field relaxation rates from the second iteration. A new set of parameters of dynamics is extracted from this ensemble of relaxation rates. In the next iteration, these parameters of dynamics are used to simulate the experiment and compute improved corrections of experimental rates to estimate the accurate low-field relaxation rates. This is repeated until the correction factors converge. The final set of high-field and corrected relaxometry relaxation rates can then be used to extract the distribution of the parameters

Table 3.1: Nomenclature for the relaxometry relaxation rate labels and parameters determining their values. $\{\mathcal{E}_j\}$ are the experimental parameters for the experiment j, $B_{\mathrm{LF}}^{(j)}$ is the low field chosen for relaxation and $\mathcal{D}_i$ are the parameters of the spectral density function used to describe the dynamics of residue i in the simulation.

Label	Parameters	Description
R_{sim}	$\mathcal{E}_j$, $B_{\mathrm{LF}}^{(j)}$ and $\mathcal{D}_i$	Relaxation rate extrated from the fitting of the simulated polarization decay
R_{calc}	$B_{\mathrm{LF}}^{(j)}$ and $\mathcal{D}_i$	Relaxation rate calculated from the parameters of dynamics
R_{meas}	$\mathcal{E}_j$ and $B_{\mathrm{LF}}^{(j)}$	Measured relaxation decay rate
R_{corr}	$\mathcal{E}_j$, $B_{\mathrm{LF}}^{(j)}$ and $\mathcal{D}_i$	Corrected relaxation decay rate

of local motions in a **M**arkov-**C**hain **M**onte-**C**arlo (MCMC) procedure and thus evaluate the median value and uncertainty of these parameters (see below).

In the following, we will investigate the validity of key hypothesis made for the analysis of the dynamics of $\{^{13}\mathrm{C}^1\mathrm{H}^2\mathrm{H}_2\}$-methyl groups in the protein Ubiquitin for which we collected HRR on the carbon, as well as high-field longitudinal and transverse relaxation rates and carbon-proton cross-relaxation rates [21].

3.3.2 Size of the relaxation matrix

The ICARUS protocol aims at obtaining accurate estimates of low-field relaxation rates by accounting for the effects of cross-relaxation on the longitudinal relaxation decays during a HRR experiment. This estimate is based on the simulation of the relaxometry experiments, where the sample travels through a broad range of magnetic fields. In order to obtain a reliable description of relaxation over orders of magnitude of magnetic fields, simulations must use appropriate relaxation matrices as well as expressions of relaxation rates, with accurate parameters for the amplitudes of interactions and the description of the spectral density function. The full Liouville space for a $\{^{13}\mathrm{C}^1\mathrm{H}^2\mathrm{H}_2\}$ spin system is spanned by a large basis of $(2 \times \frac{1}{2} + 1)^{2\times n_{1/2}} \times (2 \times 1 + 1)^{2\times n_1} = 1296$ spin terms, with $n_{1/2} = 2$ and $n_1 = 2$ the number of spin-half and spin-one respectively (Fig. 3.3a). An efficient calculation requires to minimize the size of the Liouville space where the evolution of the density operator is calculated. We

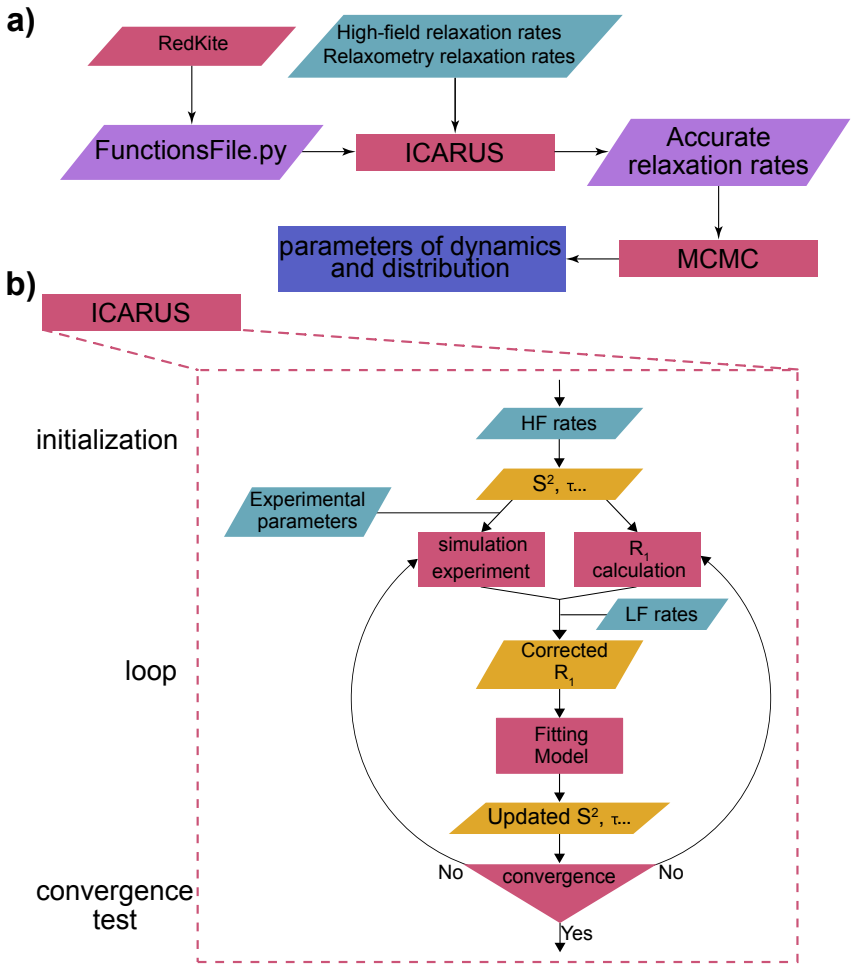

Figure 3.2: Flow chart for the analysis of high-resolution relaxometry data with ICARUS. **a)** After a FunctionsFile has been obtained from RedKite, ICARUS can be run, using, among other inputs, relaxation rates recorded on standard high-field spectrometers and the high-resolution relaxometry data. Accurate relaxometry relaxation rates are obtained, and an MCMC analysis of these corrected rates and high-field relaxation rates leads to values of parameters describing the dynamics of the system and their distribution. **b)** Flow chart of the ICARUS procedure. Accurate high-field (HF) relaxation rates are used to obtain an initial set of parameters for the dynamics of the system. These parameters are used to simulate the high-resolution relaxometry experiments (using the same experimental set up, *i.e.* shuttling time, delays, magnetic fields) from which biased simulated R_1 are extracted, and also to calculate the accurate expected R_1. The ratios of these two calculated rates are called correction factors. The product of experimental decay rates and correction factors are corrected experimental low field (LF) relaxometry relaxation rates. Together with the high-field relaxation data, the corrected rates are used to determine a new set of parameters of dynamics, further used in the next correction iteration. Convergence is not evaluated within ICARUS and the number of iterations remains a choice of the user. However, we recommend to verify the convergence of the correction factors, as these ones are essential in the determination of the final parameters of the dynamics. Typically three or four iterations are sufficient. Figure reproduced from [19].

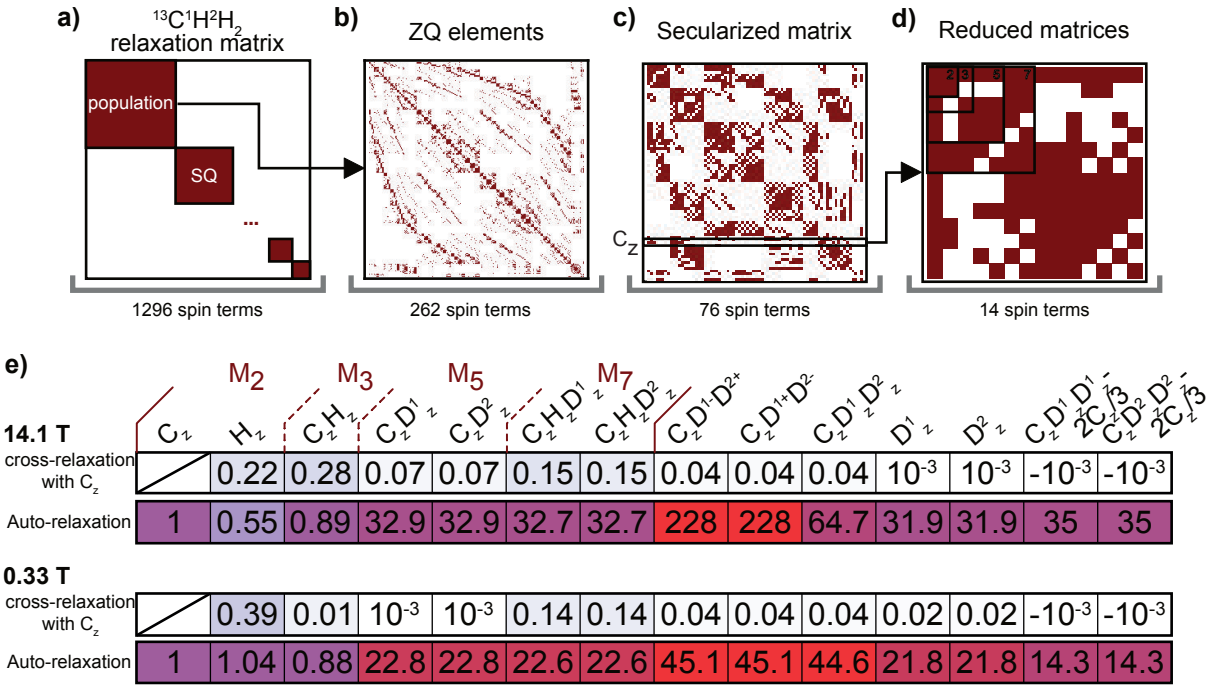

Figure 3.3: Relaxation matrix size-reduction in a $\{^{13}C^1H^2H_2\}$-methyl group. **a)** Full relaxation matrix of a $\{^{13}C^1H^2H_2\}$-methyl group. **b)** Relaxation matrix of the ZQ coherences and populations are selected. At this stage, the matrix has a 262x262 size. **c)** Secularized relaxation matrix containing 76 secular terms in the Zeeman interaction frame. The line corresponding to the operator of interest ($\hat{C}_z$) is highlighted. **d)** Relaxation matrix containing only terms cross-relaxing with the operator of interest ($\hat{C}_z$). Evaluating the cross-relaxation rates allows another level of size reduction. **e)** Numerical values of the diagonal terms of the relaxation matrix shown in **d)** (auto-relaxation, bottom row) and cross-relaxation rates with $\hat{C}_z$ (top row) for the motional parameters of the δ-1 methyl-group of Ile-3 in U-[^{2}H, ^{15}N], Ile-δ_1[$^{13}C^2H_2^1H$]-Ubiquitin at 14.1 T and 0.33 T (reported in Ref. [21], see Table E.1). Relaxation rates are normalized to the auto-relaxation rate of $\hat{C}_z$ at each magnetic field. Figure reproduced from [19].

have reduced the size of the subspace using the steps described in Section 1.3.3 for ^{15}N-^{1}H spin systems. First, we have considered the subspace only spanned by zero-quantum coherences and population operators (Fig. 3.3b). We then applied the secular approximation, and calculated all cross-relaxation terms with the $\hat{C}_z$ operator, in order to keep only non zero terms, *i.e.* terms that cross-relax with $\hat{C}_z$, reducing the size of the basis to 14 terms (Fig. 3.3d). Cross-relaxation and autorelaxation rates in this 14-element basis have been calculated at the lowest and highest magnetic fields used during our HRR experiments, *i.e* 0.33 T and 14.1 T, using parameters obtained after a preliminary ICARUS analysis (for isoleucine 3) performed using $\mathcal{B}_{reduced,3}$ (Eq. 3.6, Fig. 3.3e).

The inspection of these two relaxation matrices justifies the use of a basis containing only 3 operators as cross-relaxation rates involving other operators are either negligible (cross-relaxation from $\hat{C}_z$ to another operator can be neglected if the ratio of this cross-relaxation rate to the auto-relaxation rate of $\hat{C}_z$ is small) or involve an operator with an auto-relaxation rate much larger than the auto-relaxation rate of $\hat{C}_z$ and the cross-relaxation rate with $\hat{C}_z$ (see Appendix E.3 for the proof that cross-relaxation with fast relaxing operator do not contribute to the polarization decay of slowly relaxing operators). At both magnetic fields, the largest cross-relaxation rate with the carbon-13 longitudinal polarization is the dipolar cross-relaxation with the proton longitudinal polarization. At low magnetic field (0.33 T), even a 2-operator basis $\{\frac{1}{3}\hat{C}_z, \frac{1}{3}\hat{H}_z\}$ would be sufficient to describe the relaxation properties of a $\{^{13}C^1H^2H_2\}$-methyl group as cross-relaxation towards other terms is either very small or towards fast-relaxing terms. However, the subspace should include the two-spin order $2\hat{C}_z\hat{H}_z$ at high fields (14.1 T). Thus, HRR experiments in $\{^{13}C^1H^2H_2\}$-methyl groups have been simulated in the small subspace spanned by the three operators ($\hat{C}_z$, $\hat{H}_z$ and $2\hat{C}_z\hat{H}_z$). This subspace was used throughout our analysis of carbon-13 HRR in $\{^{13}C^1H^2H_2\}$ methyl groups.

3.3.3 Proton relaxation and surrounding deuterium

Proton longitudinal relaxation rates $R_1(^1H)$ were measured at three magnetic fields (0.33, 14.1 and 18.8 T) using standard high-field magnets (18.8 T and 14.1 T) and our 2F-NMR spectrometer operating at 14.1 T and 0.33 T [22] (see Chapter 2 for a description of 2F-NMR). These rates were also calculated after an ICARUS analysis of high-field and HRR rates considering intra-methyl group interactions only. The predicted relaxation rates are systematically lower than those measured at 0.33 T, 14.1 T and 18.8 T (Fig. 3.4a, b). Thus, even if relaxation rates in a $\{^{13}C^1H^2H_2\}$-methyl group are dominated by the contributions of internal interactions, another contribution to relaxation has to be taken into account to describe proton relaxation. The differences between the measured and calculated $R_1(^1H)$ rates were assigned to the effect of the neighbouring deuterium nuclei.

Adding the dipolar interactions with surrounding deuterium nuclei leads to non-negligible contributions to relaxation to both the proton and the carbon-13. The closest neighbouring deuterium nuclei are the $^2H\gamma_1$ and $^2H\gamma_2$ sites of the isoleucine side-chain, but other deuterium nuclei may also be in close proximity to the methyl group. The correlation function for the fluctuations

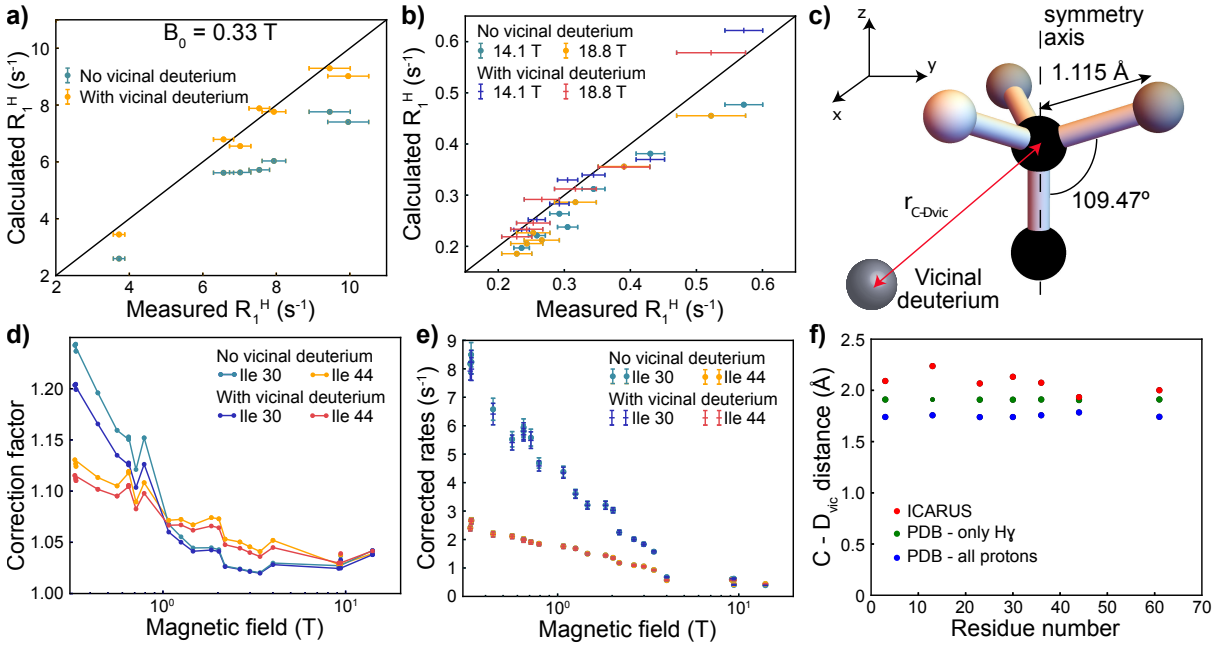

Figure 3.4: Including the effect of an effective vicinal deuterium nucleus on the analysis of HRR data of U-[^{2}H, ^{15}N], Ile-δ_1[^{13}C^{2}H$_2^1$H]-Ubiquitin. **a)** Correlation plot of the calculated proton longitudinal relaxation rate R_1 at 0.33 T with (orange) and without (blue) including the effect of the vicinal deuterium, with the experimental R_1 at 0.33 T, for the seven isoleucines of Ubiquitin. The black line is shown as a guide for perfect equality between the two rates. **b)** Correlation plots of the calculated proton longitudinal relaxation rate R_1 at 14.1 T and 18.8 T with and without including the effect of the vicinal deuterium, with the experimental R_1 at 14.1 T and 18.8 T, for the seven isoleucines of Ubiquitin. The black line is shown as a guide for perfect equality between the two rates. **c)** Geometry of the methyl group and position of the effective neighbouring deuterium. The distance $r_{\mathrm{C-D_{vic}}} = \sqrt{r^2_{\mathrm{y,D_{vic}}} + r^2_{\mathrm{z,D_{vic}}}}$ is determined using additional relaxation rates as explained in the main text. **d)** Correction factors as a function of the magnetic field for Ile-30 and Ile-44 with and without an effective vicinal deuterium nucleus. **e)** Corrected relaxometry relaxation rates for Ile-30 and Ile-44 with and without including an effective vicinal deuterium nucleus. **f)** Comparison of the distance of the vicinal deuterium with the carbon-13 nucleus obtained from the analysis of proton relaxation (red, ICARUS) to the calculated distance to an effective deuterium nucleus that accounts for either only the ^{2}Hγ_1 and ^{2}Hγ_2 nuclei of the isoleucine residue (green) or all the hydrogens (blue) in the structure of Ubiquitin, PDB 1D3Z. In these NMR derived structures, the distances were averaged over the 10 models present in the PDB file. In each model, the distance equals $r_{\mathrm{C-D_{vic}}} = \left(\sum_i \frac{1}{d_i^6}\right)^{-1/6}$ with d_i the distance of the carbon-13 to proton i (excluding intra-methyl group proton). Figure reproduced from [19].

of the corresponding internuclear vectors are expected to vary. In particular, these interactions are expected to be affected in different ways by the fast rotation of the methyl group. We mod-

eled the surrounding deuterium nuclei by a single deuterium at an effective distance $r_{C-D_{vic}}$ (Fig. 3.4.). The interaction of the proton and carbon-13 nuclei of the methyl group with this deuterium accounts for the interaction with all the other deuterium nuclei of the protein. We used two adjustable parameters to describe its position, defining its coordinates in the Cartesian axis system: the y- and z-coordinate were fitted while the x-coordinate was fixed to 0. The position of the effective surrounding deuterium nucleus is determined independently for each residue using proton relaxation rates as well as all relaxation rates used in the ICARUS iterations (accurate and corrected) and keeping the other parameters constant (*i.e.* the parameters describing the dynamics). When fitting the parameters of the model during further ICARUS analysis, the effective position of the surrounding deuterium is kept constant. Introducing the contribution of the surrounding deuterium and performing the whole ICARUS analysis again preserves the agreement between the measured and calculated proton longitudinal relaxation rates (Fig. 3.4a, b).

The surrounding deuterium has an effect on the correction factors (Fig. 3.4d) which leads to differences of corrected HRR rates between 0 and 4 % (Fig. 3.4e). Correction factors depend on the magnetic field and generally increase with decreasing magnetic field. It must be pointed out that non-monotonous changes in the correction factors profiles in Fig. 3.4d are due to differences in shuttling and waiting delays at low magnetic fields (Fig. E.4).

The effective distances with the surrounding deuterium nucleus are close to extracted distances from the NMR structure of Ubiquitin (Fig. 3.4f, PDB 1D3Z). The dipolar interaction between the methyl group and the effective deuterium is included in the following iterations of the ICARUS analysis.

3.3.4 Convergence of the iterative correction

The number of iteration steps is expected to be dependent on the spin system under study. In the case of the $\{^{13}C^1H^2H_2\}$-spin system, the convergence was reached after 2 iterations (Fig. 3.5a) for all residues except residue 44. Some slight instability in the convergence of the correction at low field is observed for this residue (Fig. 3.5b) but the amplitude of change (1-2 % at most) has a negligible effect on the values of the corrected relaxation rates (Fig. 3.5c).

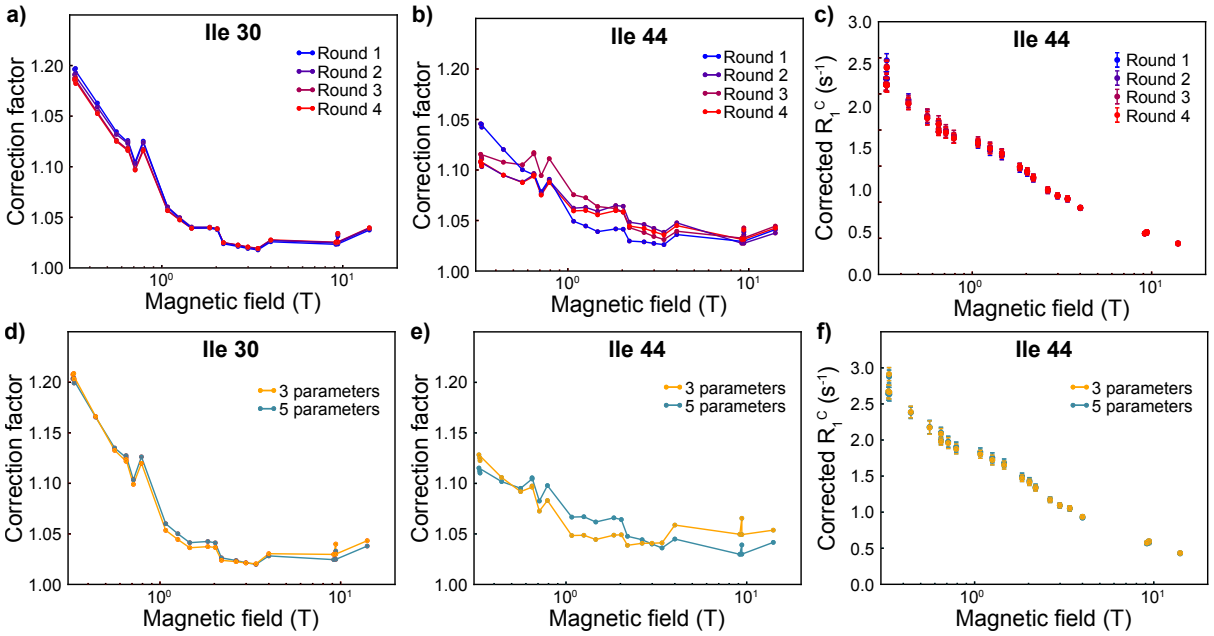

Figure 3.5: Evolution of the correction with the number of iterations of ICARUS and the selected model of motions. Correction factors as a function of the magnetic field for (**a**) Ile-30 and (**b**) Ile-44 after 1 to 4 rounds of ICARUS. **c)** Evolution of the corrected relaxation rates of Ile-44 after 1 to 4 rounds of ICARUS. Correction factors as a function of the magnetic field for (**d**) Ile-30 and (**e**) Ile-44 using a model of spectral density function with 3 (Eq. 3.22 ,orange) or 5 (Eq. 3.3, blue) parameters to describe internal dynamics. **f)** Corrected relaxation rates of Ile-44 obtained with a model with 3 (Eq. 3.22, orange) or 5 (Eq. 3.3, blue) parameters to describe internal dynamics.

3.3.5 Influence of the model of spectral density function on the correction

Different models can be used to describe the motions in a methyl group. Eq. 3.3 gives a rather complex description of the motion, but a simpler model can be tested by reducing the number of internal dynamics parameters to 3 by only considering the global tumbling, the methyl-group rotation with one fitted correlation time and C-C axis motions with only one fitted correlation time and one order parameter. The spectral density function for this model is:

$$\begin{aligned}\mathcal{J}_{i,j}^{(3)}(\omega) =& \frac{2}{5}\left[S_{met}^2(\theta_{i,j})\left(S^2\frac{\tau_c}{1+(\omega\tau_c)^2}+(1-S^2)\frac{\tau'_{int}}{1+(\omega\tau'_{int})^2}\right)\right.\\ &\left.+(\mathcal{P}_2\cos(\theta_{i,j})-S_{met}^2(\theta_{i,j}))\left(S^2\frac{\tau'_{met}}{+}(1-S^2)\frac{\tau''_{int}}{1+(\omega\tau''_{int})^2}\right)\right],\end{aligned} \tag{3.22}$$

with the same definitions as above and where τ_{int} is an internal correlation time for the motion of the C-C axis. Correction factors obtained for the two spectral density functions are shown

in Fig. 3.5d and e. They are identical for Ile-30 where both models fit the experimental data well. In contrast, the correction is slightly different for the two models of motion for Ile-44 (Fig. 3.5e), where the 5-parameters model is in better agreement with the experiments [21]. Yet, the variation on the corrected rates is small (between 1 and 2 %, Fig. 3.5f) with equally small effects on the analysis. The ICARUS analysis requires a model that accounts for the overall changes of the spectral density function on the range of frequencies probed during the experiments but it does not require that the used model reproduces all subtle details of the spectral density function: small variations of the value of the spectral density function at a specific frequency have negligible effects on the correction.

3.3.6 Scaling of the CSA/DD cross-correlated cross-relaxation rates

Our combined analysis of low-field longitudinal and high-field transverse relaxation allows us to obtain the value of the CSA for each residue in addition to parameters of internal motions, except for Ile-44 for which chemical exchange prevented the analysis of the carbon-13 transverse relaxation rates (Fig. E.1) [21]. In order to validate our analysis, a series of relaxation rates were measured as detailed hereafter: accurate low-field carbon longitudinal relaxation-rates recorded with our 2F-NMR spectrometer [22] as well as high-field longitudinal CSA/DD cross-correlated cross-relaxation rates (cross-relaxation between $\hat{C}_z$ and $2\hat{C}_z\hat{H}_z$ referred to as η_z^C). These relaxation rates were not used during the analysis of the relaxometry relaxation rates, but calculated using the set of motional parameters obtained after correction of the relaxometry data.

The calculated longitudinal CSA/DD cross-relaxation rates were strongly correlated to measurements at 14.1 T and 18.8 T but significantely overestimated (Fig. 3.6a). Our goal here is to effectively describe cross relaxation, so we decided to introduce an *ad hoc* scaling factor, applied directly to this term in the relaxation matrix. The scaling factor was calculated as the averaged inverse correlation coefficient between the unscaled and measured η_z^C at 14.1 T and 18.8 T and equals 0.505. A number of hypothesis can be made to explain the origin of the scaling factor: i) the carbon-13 CSA may be overestimated since it is determined essentially from transverse relaxation rates, which may suffer from small chemical exchange contributions; ii) the carbon-13 CSA may not be perfectly alligned with the C-C bond; iii) the form of the spectral density function may not describe correctly the motions of the methyl group; iv) the amplitude of the carbon-13 CSA may be rotamer-dependent (see section 4.6).

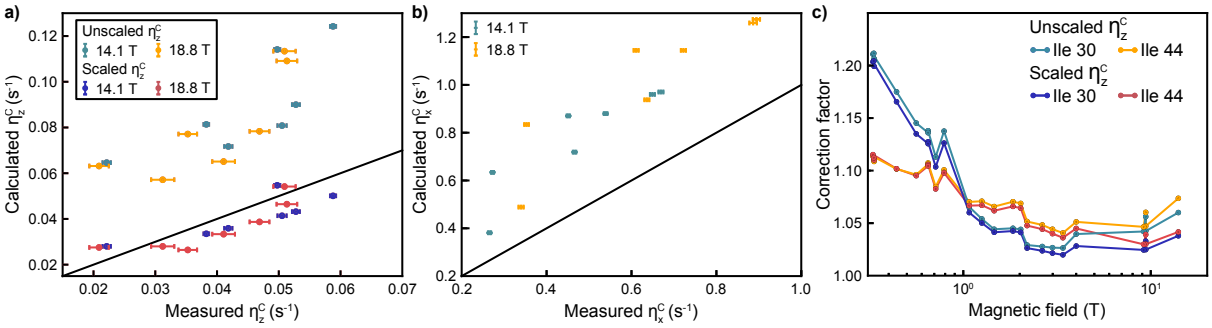

Figure 3.6: Scaling the CSA/DD cross-correlated cross-relaxation rates. **a)** Correlation plot between the calculated unscaled and scaled longitudinal CSA/DD cross-correlated cross-relaxation rates with the measured rates at 14.1 T and 18.8 T. The black line is shown as a guide for perfect equality between the two rates. **b)** Correlation plot between the calculated (without scaling) trasnverse CSA/DD cross-correlated cross-relaxation rates with the measured rates at 14.1 T and 18.8 T. The black line is shown as a guide for perfect equality between the two rates. **c)** Correction factors as a function of the magnetic field for Ile-30 and Ile-44 with or without scaling of the longitudinal CSA/DD cross-correlated cross-relaxation rate. Figure edited from [19].

To understand the origin of this scaling factor, we also measured the carbon transverse CSA/DD cross-correlated cross-relaxation rates (η_{xy}^C). The calculated relaxation rates correlate with the measurement, with an averaged inverse correlation coefficient between the calculated and measured η_{xy}^C at 14.1 T and 18.8 T of 0.629 (Fig. 3.6b). The discrepency between the scaling factors of the longitudinal and transverse CSA/DD cross-correlated cross-relaxation rates can not be accounted for only from a miss-evaluation of the carbon-13 CSA (under our assumptions of axially symmetry and perfect alignment allong the CC bond). Thus, it is likely that the model of correlation function does not describe entirely the complexity of the motions in the methyl group (see Chapter 4).

The analysis of the relaxometry relaxation data was performed again after applying the scaling factor to longitudinal CSA/DD relaxation rates. As expected, the agreement between calculated and measured CSA/DD cross-relaxation rates is significantly improved by the use of a scaling factor (Fig. 3.6a). Low-field correction factors are not sensitive to the scaling of a CSA-dependent relaxation rate (Fig. 3.6c). At moderate and high field, the effect is larger with a reduction of the correction by about 2 % which has limited impact on the analysis.

3.3.7 Validation of the correction with the suppression of cross-relaxation pathways at low field

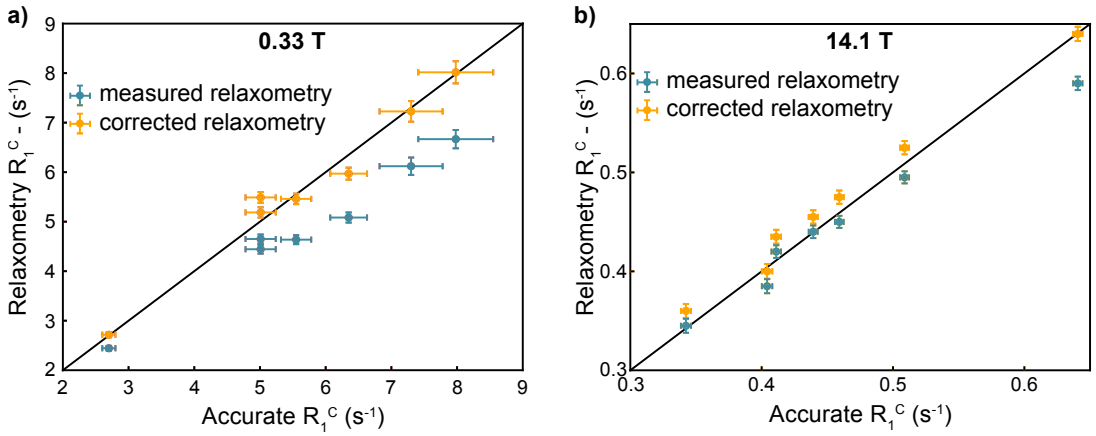

Figure 3.7: Validation of the correction protocol. **a)** Correlation plot between the relaxometry uncorrected (blue) and corrected (orange) carbon R_1 at 0.33 T with the measured two-field $R_1(^{13}C)$. **b)** Correlation plot between the pseudo-relaxometry uncorrected (blue) and corrected (orange) $R_1(^{13}C)$ with the accurate relaxation rates measured at 14.1 T. The black line is shown as a guide for perfect equality between the two rates.

Using our 2F-NMR spectrometer [37, 39], we measured, among other relaxation rates, the longitudinal carbon-13 relaxation rates at 0.33 T with suppression of cross-relaxation pathways [22]. The rates of the seven isoleucines acquired at 0.33 T have been compared to measured and corrected relaxometry relaxation rates at the same magnetic field (Fig. 3.7a). The uncorrected relaxometry rates $R_1(^{13}C)$ are systematically lower than the accurate relaxation rates. This stresses the fact that the relaxometry relaxation rates have to be corrected in order to reach a reliable analysis of the dynamics of the system. Corrected rates are in excellent agreement with the accurate $R_1(^{13}C)$ rates measured with the 2F system. This comparison validates the ICARUS approach on this spin system. In addition, experiments have been recorded at 14.1 T with and without pulses during the relaxation delay. Corresponding relaxation rates are displayed in Fig. 3.7b. The high-field experiment recorded without control of cross-relaxation pathways is similar to a shuttling experiments. Correction factors seem to be slightly overestimated at 14.1 T, but corrected rates are in better agreement with accurate rates than uncorrected rates (r.m.s.d of $3.8 \times 10^{-2}\,s^{-1}$ versus $5.7 \times 10^{-2}\,s^{-1}$, respectively), which is mostly due to the better estimation of the longitudinal relaxation rate of isoleucine-23.

3.3.8 Biophysical analysis of ICARUS results

The ICARUS corrected HRR rates were analysed together with the accurate high-field relaxation rates in a MCMC procedure using the *emcee* Python library [170] to obtain parameters distributions for the two order parameters and correlation times associated to the C-C bond motions, the correlation time for methyl rotation, and the carbon-CSA. Parameters for the dynamics and width of the associated distribution are reported in Appendix Table E.1. It must be noted that an initial analysis of the relaxation data without the carbon transverse relaxation rate $R_2(^{13}\mathrm{C})$ allowed us to identify a chemical exchange contribution to the $R_2(^{13}\mathrm{C})$ of isoleucine 44 (Appendix Fig. E.1). These rates were not considered in the analysis for this residue and its carbon-CSA was kept constant at 25 ppm.

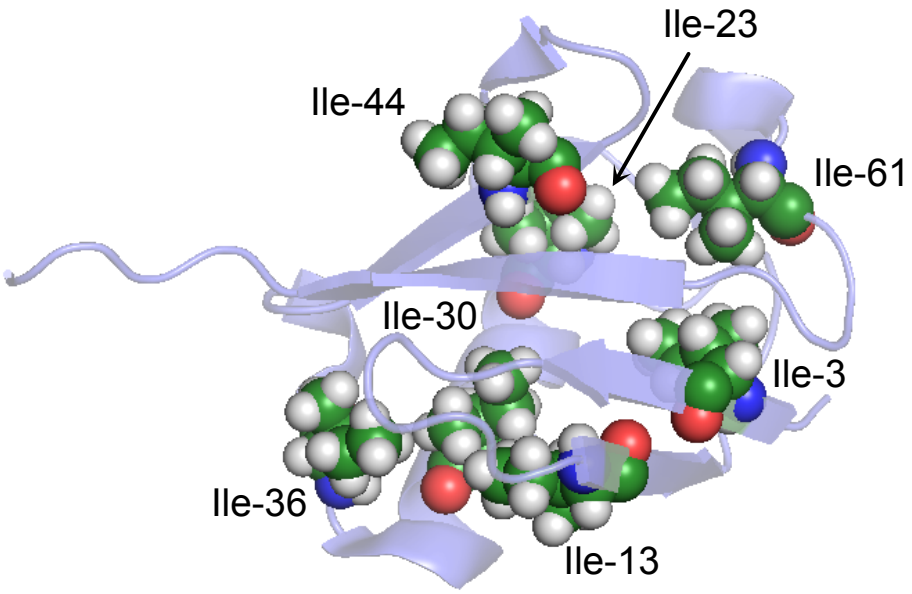

Figure 3.8: Structure of Ubiquitin showing the 7 Isoleucine residues. PDB 1D3Z.

The correlation times for methyl rotation all fall within a rather narrow range between 5.5 and 22 ps. The variations of τ_{met} correlates with the structure: the shortest value is found for the only isoleucine with its side chain at the surface of the protein, that is isoleucine 44 (Fig. 3.8). Isoleucine 23 (Ile-23) has the largest value of τ_{met} ($\tau_{met} = 22$ ps), which can be explained by the close proximity of the H_α of Ile-23 from its $\delta 1$ methyl group.

We can distinguish three groups of residues from our analysis of HRR data (see Appendix Fig. E.2 for the distribution of parameters after the MCMC procedure). Ile-44 is the

only isoleucine residue with a side chain being totally exposed to the solvent (Fig. 3.8). Its dynamic properties lead to chemical exchange affecting the values of the carbon-R_2, but HRR identifies a slow motion with a correlation time in the low nanosecond range ($\tau_s = 1.3\,\text{ns}$). On the other hand, we cannot detect motions in the nanosecond range for residues 3, 23, 30 and 61 with ill-defined order parameters $\mathcal{S}_s^2$ and associated correlation time τ_s. The apparent simplicity of motions for these residues can be explained by the fact that they are located in the hydrophobic core of the protein where the packing can hinder the motions. For Ile-30, the broad distributions for τ_s with relatively high order parameter is likely due to the fact that we consider an isotropic global tumbling tensor despite the small anisotropy that have already been reported for Ubiquitin [106]. Finally, the last group consists of Ile-13 and Ile-36 for which we can clearly identify two correlation times for internal motions in the tens of picosecond range for fast motions and in the low nanosecond range for slow motions. The two isoleucines are located at the edge of the hydrophobic core such that they are not as affected by the proximity of other hydrophobic residues as the second group of isoleucines.

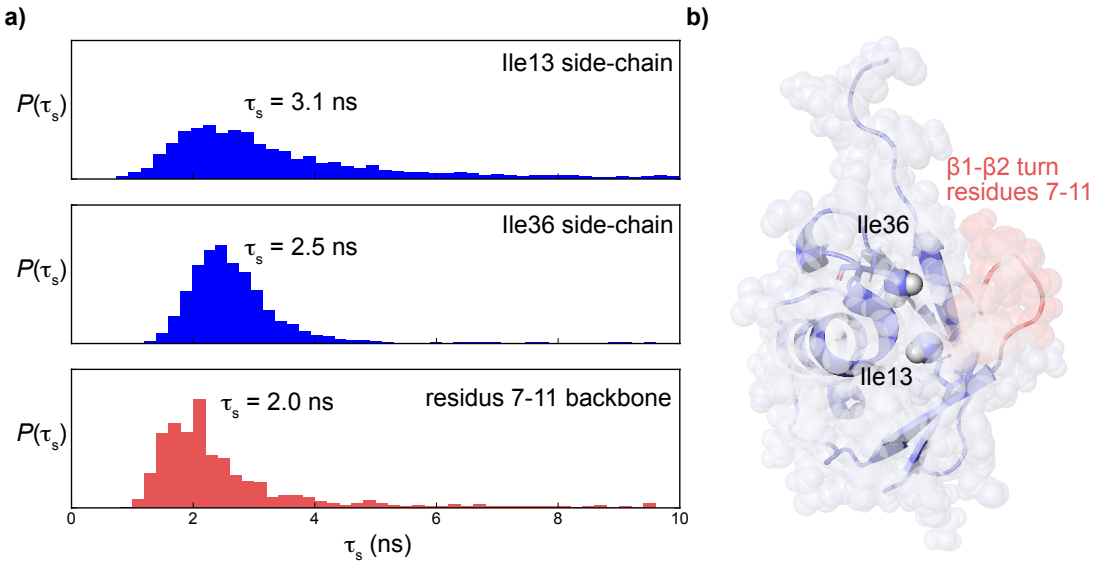

Figure 3.9: Nanosecond side chains and backbone motions in Ubiquitin. **a)** Distribution of corretaiton time τ_s from an MCMC analysis of HRR data recorded on $\delta 1$ methyl groups for Ile-13 (top) and Ile-36 (middle), and on ^{15}N-^{1}H of the backbone from residues 7-11 (bottom). The average value of τ_s is indicated on each pannel. The resulting distribution for residues 7 to 11 is given by $P_{7-11}(\tau_s) = \prod_{i=7}^{i=11} P_i(\tau_s)$ where $P_i(\tau_s)$ is the distribution of τ_s for residue i. **b)** Structure of Ubiquitin (PDB 1D3Z) showing the Ile-13 and Ile-36 $\delta 1$ methyl group and $\beta 1$-$\beta 2$ turn corresponding to residues 7 to 11. Figure reproduced from [21].

The case of Ile-13 and Ile-36 is particularly interesting as not only are they close in the protein structure, but their distributions of correlation time for slow motion also overlap (Fig. 3.9a, top and middle pannels). Ile-13 flanks the β1-β2 turn (residues 7 to 11) while Ile-36 belongs to the α1-β3 loop (residues 34 to 40) (Fig. 3.9b). These two regions have been shown to undergo substantial motions in the main conformational mode detected by a combination of **R**esidual **D**ipolar **C**oupling (RDC) and **M**olecular **D**ynamic (MD) simulations analysis [171]. In order to better evalute the correlation time for motions in the β1-β2 turn, we reanalyzed the backbone nitrogen-15 HRR data recorded for Ubiquitin [17] using ICARUS and the same procedure as for isoleucine δ1 methyl groups. The resulting distribution of correlation time overlaps with the ones of Ile-13 and Ile-36 (Fig. 3.9a). Our analysis of relaxation data cannot unambiguously identify concerted motions and the similar distribution of correlation times in the nanosecond range may be a coincidence. However, this work demonstrates how the analysis of HRR dataset can provide insights into interal motions and point at regions potentially undergoing correlated motions.

3.4 MINOTAUR: a correction-free analysis of relaxometry experiments

So far, the analysis of relaxation rates recorded under shuttling was based on an iterative correction of the relaxometry relaxation rates as implemented in ICARUS [17, 67]. As explained in the previous section, the free evolution parts of the experiment are simulated and extracted relaxation rates are compared to the calculated pure relaxation rates to obtain a correction factor applied to the measured relaxation rates. This approach suffers from two major limitations. First, the measured intensity decays are fitted with a mono-exponential decay to extract relaxation rates, but strong cross-relaxation may lead to clear deviations from a mono-exponential behavior making it impossible to extract a single relaxation rate. Second, it is possible to evaluate the quality of the correction only in particular cases, for instance with measurements performed on a 2F-NMR spectrometer (see section 3.3.7) [22].

However, this somewhat convoluted approach is not the only possible way to analyze relaxometry data and account for cross-relaxation pathways. Here, we introduce a correction-free analysis to overcome these two limitations. Accurate high-field relaxation rates and low-field intensity decays are all used together in a MCMC sampling in order to extract distributions of dynamic parameters of the spectral density function, as well as other relevent parameters of the spin system (such as CSA for example). This approach of the analysis of relaxometry data does not require to approximate the intensity decay to a mono-exponential function. In addition, data are not transformed during the analysis as would be the case with a correction factor. It has been implemented in a Python program called **M**atching **I**ntensities to **O**ptimize **T**imescales and **A**mplit**U**des of motions from **R**elaxometry (MINOTAUR) for use over a wide range of spin systems and dynamic models. In the following, we review some of the key elements of the program, re-analyse our high-resolution relaxometry methyl-group relaxation rates and compare these results with our previously reported analysis [21].

3.4.1 Computational features of MINOTAUR

MINOTAUR and ICARUS [67] are very similar in terms of usage. The **G**raphical **U**ser **I**nterface (GUI) and outputs remain essentially the same. However, ICARUS is used to correct relaxometry relaxation rates rather than extract dynamic parameters or their distribution. This was performed through the use of a different program directely reading ICARUS output folders

and running a MCMC sampling on the accurate and corrected relaxation data. MINOTAUR does not minimize a χ^2 but directly provides parameters distribution, using the same MCMC approach from the emcee Python library [170]. A drawback of the MINOTAUR approach is the handling of potentially large amount of data (all the accurate relaxation rates and all the intensities for all the low magnetic fields), which may dramatically increase the time spent in the MCMC loops. Different solutions have been implemented to overcome this limitation and are listed below.

The calculation of the relaxation rates and relaxation matrix has been implemented in C-language. The C-language is particularly efficient to perform calculations compared to Python. For example, we have seen a factor 10 difference for the evaluation of the relaxation matrix using Python and C. In practice, the gain is not as high as expected because C outputs have to be converted into Python objects. Expressions of the relaxation matrix and relaxation rates have to be compiled in the C-language. The synthax is close to the Python synthax, and expressions obtained from RedKite can be exported as C-expressions using the Mathematica command *CForm* [18]. In addition, as no χ^2 minimization is performed, first derivatives are no longer needed. Compilation of the C-scripts is directly implemented in MINOTAUR.

The increment time for the calculation of the propagator during the shuttling (from the high-field to low-field positions and back to high field) is no longer a user-defined variable but its value is optimized. The default lowest value is 1 ms. The increment is then gradually increased by 1 ms steps until a difference of the expectation value of the operator of interest (e.g. $\hat{C}_z$) higher than 1% is observed compared to the default value (calculated with the 1 ms increment). The comparison is made over 20 different simulations with 20 different and random dynamic parameters, at the lowest recorded field. The optimization is stoped when at least one of the simulations leads to a significant difference of the expected value (*i.e.* higher than 1%). For a 100 ms shuttling trajectory, increasing the increment from 1 ms to 5 ms has no effect on the expected value of the $\hat{C}_z$ operator of a $\{^{13}C^1H^2H_2\}$-methyl group in Ubiquitin and decreases the number of calculated relaxation matrix from 100 to 20 in each direction of the shuttling, significantely decreasing the calculation time.

In order to calculate the propagators during the relaxation delays, the exponential of the Liouvillian has to be calculated [67, 19]. Two methods can be used to calculate the exponential of a matrix in Python: directely computing the exponential using the *linalg.expm* function

implemented in the scipy Python library [136], or diagonalizing the matrix and calculating the exponential of the diagonalized matrix. Relaxation matrices are symmetric and can always be diagonalized. In the case where the system undergoes chemical exchange, the relaxation matrix is no longer symmetric (because of the exchange contribution) but can still be diagonalized [16]. In the case of the 3x3 relaxation matrix of $\{^{13}C^1H^2H_2\}$-methyl group, calculating the matrix exponential by diagonalization is faster by a factor 2 to 3, but this may not be true for larger matrices. The choice of the calculation method is made by calculating 10,000 random relaxation matrix exponentials and comparing the time spent to calculate them. This step takes just a few seconds to perform.

The MCMC is now paralelized over the CPUs, reducing in theory the calculation time by a factor equal to the number of CPU present on the computer. It is lower in practice, especially if the computer is being used for other tasks. In addition, we do not recommend using as many steps as what was recommended in the case of corrected relaxation rates. In the analysis of Ubiquitin $\{^{13}C^1H^2H_2\}$-methyl group, we used 20 chains of 10,000 steps after ICARUS [21]. As what will be seen later, 20 chains of 3,000 steps reproduce well the results published earlier.

As a result, the MCMC analysis of U-[^{2}H, ^{15}N], Ile-δ_1[$^{13}C^2H_2^1H$]-Ubiquitin [21] and containing 12 accurate relaxation rates and 22 relaxometry experiments, each containing at least 6 relaxation delays, is conducted within approximately 30 min for each isoleucine residues with 3,000 steps and 20 chains on a MacBook Pro (2016) with a 2.9 GHz Intel Core i5 processor and 4 CPUs.

3.4.2 Scaling intensities

One major difference between using relaxation rates extracted from fitting simulated intensity decays, and directly using these intensity decays is the need to scale the simulated intensities to the measured ones. This scaling depends on various parameters of the system (concentration of the spins, probe sensitivity, number of scans,...). For each relaxometry experiments, a unique scaling factor is applied to each simulated intensity. The scaling factors are in theory parameters of the system and should be variables of the MCMC. However, their definition makes them strictly dependent on the other parameters of the system which are constraining them as shown below.

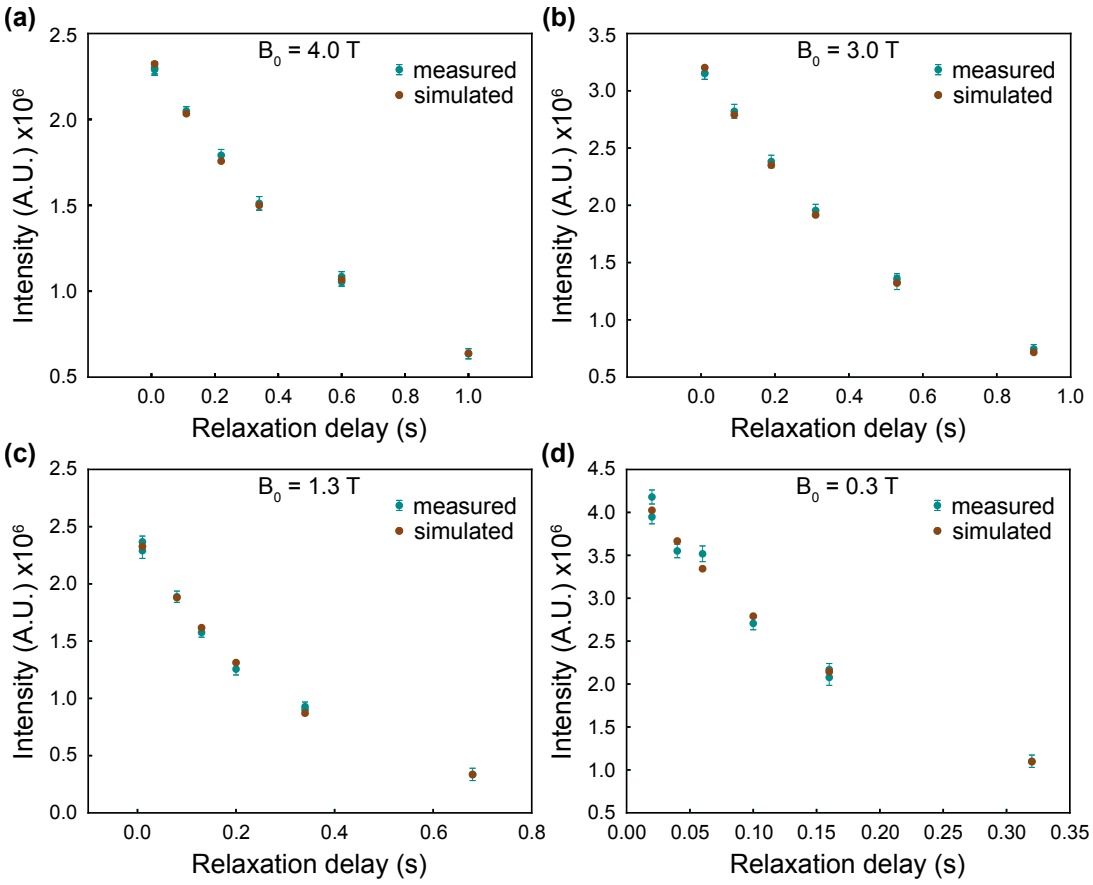

Figure 3.10: Intensity decays for Isoleucine-36 of U-[^{2}H, ^{15}N], Ile-δ_1[^{13}C^{2}H$_2$^{1}H]-Ubiquitin at four low magnetic fields (**(a)** 4.0 T, **(b)** 3.0 T, **(c)** 1.3 T and **(d)** 0.3 T). Turquoise circles are measured relaxometry intensities, brown circles are back-calculated scaled intensities using the mean dynamic parameters and Eq. 3.24 for scaling.

The χ^2_I for the intensities can be written:

$$\chi^2_I = \sum_{i=0}^{\mathrm{N}_{LF}} \sum_{j=0}^{\mathrm{N}_{VC_i}} \frac{(\mathrm{I}^{\mathrm{meas}}_{i,j} - \alpha_i \mathrm{I}^{\mathrm{sim}}_{i,j})^2}{\sigma^2_{i,j}} \tag{3.23}$$

where N_{LF} and N_{VC_i} are respectively the number of relaxometry experiments and the number of delays in the relaxometry experiment number i, $\mathrm{I}^{\mathrm{meas}}_{i,j}$, $\mathrm{I}^{\mathrm{sim}}_{i,j}$ and $\sigma^2_{i,j}$ are the measured and simulated (respectively) intensities and the experimental error (*i.e.* noise level) for the experiment i and delay j, and α_i the scaling factor for experiment i.

Derivating Eq. 3.23 with respect to α_i and cancelling the derivative to 0 leads to the

optimal value for the scaling factor of experiment i:

$$\alpha_i = \sum_{j=0}^{\mathrm{N}_{VC_i}} \frac{\mathrm{I}_{i,j}^{\mathrm{sim}} \mathrm{I}_{i,j}^{\mathrm{meas}}}{\sigma_{i,j}^2} \Bigg/ \sum_{j=0}^{\mathrm{N}_{VC_i}} \left(\frac{\mathrm{I}_{i,j}^{\mathrm{sim}}}{\sigma_{i,j}} \right)^2 \tag{3.24}$$

At each MCMC iterations, it is then possible to calculate the scaling factors as a function of the set of dynamic parameters. Fig. 3.10 shows selected simulated decays obtained after re-analysing our high-resolution relaxometry data recorded on methyl groups of U-[^{2}H, ^{15}N], Ile-δ_1[^{13}C^{2}H$_2^1$H]-Ubiquitin. The agreement between the scaled simulated intensities and the measured decay is excellent.

3.4.3 Comparison between MINOTAUR and ICARUS analysis

We analyzed the same data as the ones reported in the previous study [21], but we used intensity decays instead of HRR relaxation rates. The same form of spectral density function was used to calculate the relaxation rates and the relaxation matrices (Eq. 3.3). The optimization of the increment time for the calculation of the propagator during the shuttling period leads to an increment of 5 ms. The diagonalization methods leads to faster calculation of the matrix exponential. The MCMC was run with 20 chains and 3,000 steps each. The carbon-CSA was among the free parameters during the MCMC sampling, except for residue 44 for which carbon-13 transverse relaxation rates have been shown to be affected by chemical exchange and were discared from the analysis and its CSA was fixed to 25 ppm [21].

As reported earlier [19], the contribution from the surrounding deuterium of the protein to the relaxation has to be taken into account. In ICARUS, the procedure consisted in first not considering the effect of these deuterium, then determine the position of an effective deuterium that would reproduce proton longitudinal auto-relaxation rates, and perform the correction procedure again. Two major differences compared to our previous method of analysis have been implemented: the distance is now determined from a MCMC procedure and error evaluation can be performed; the evaluation of other defined parameters extends to any user-defined variable, which constitutes a major improvement compared to the previous situation where a methyl-adapted version of ICARUS had to be written. In short, expressions of relaxation rates and relaxation matrices accept as input four entries: the magnetic field, parameters of the systems that are to be determined using the HRR experiments (dynamic parameters, CSA for example), the global tumbling correlation time, and an array containing any other variables of the sys-

tems (loaded by the user in the GUI) and that can be residue-specific information. MINOTAUR keeps these later parameters constant throughout the program. In addition to MINOTAUR, we wrote a program called ACTEON that uses MINOTAUR outputs (*i.e.* parameters that had to be determined), accepts additional informations (*i.e.* relaxation rates) to run a MCMC on user-selected parameters that used to be kept constant. MINOTAUR can be run again using the newly determined parameters by ACTEON. In our example of the position of the vicinal deuterium, MINOTAUR is run first using intensity decays from HRR experiments, longitudinal and transverse carbon auto-relaxation rates and carbon-proton cross-relaxation rates. S_f^2, S_s^2, τ_{met}, τ_f, τ_s and the carbon-CSA (except for Ile-44) are determined. ACTEON is run using these values, the same relaxation rates and decays, and longitudinal proton auto-relaxation rates to determine the position of the vicinal deuterium, for each residue. This position is kept fixed in the final MINOTAUR run (where proton relaxation rates are not included). This procedure keeps the exact same principle as before, but has been generalized to any situations a user might encounter.

Overall, 198 data for each residue were used in MINOTAUR: 12 relaxation rates at diffrerent high magnetic fields (17 total with the repeats), and 177 intensities (22 decays). For each residue, the MCMC sampling (20 chains of 3,000 steps) took between 30 min and 40 min on a MacBook Pro (2016) with a 2.9 GHz Intel Core i5 processor and 4 CPUs. It must be noted that in order to keep a relatively equal contribution for each each experiments in the MCMC procedure, the difference between the experimental and simulated intensities in the MCMC iterations are devided by the number of relaxation delays in the associated experiments.

Parameters obtained after the analysis with MINOTAUR are reported in Appendix Table E.2. Overall, they agree well with the ICARUS analysis of the relaxometry relaxation rates (Fig. 3.11) [21]. Thus, even if imperfect, the correction procedure provides accurate estimates of low-field relaxation rates in the case of $\{^{13}C^1H^2H_2\}$-methyl groups in Ubiquitin. It must be noted that the EMF correlation function for the C-C motion is not adapted for residues 3, 23, 30 and 61, and the simpler **M**odel **F**ree (MF) correlation function [15] reproduces well the relaxation data [21]. This explains the large standard deviations for the parameters $\mathcal{S}_2^2$ and τ_s for these residues. Increasing the number of MCMC steps to 10,000 does not significantely alter the distributions (Appendix Fig. E.3).

A new method to analyse HRR experiments has been presented and implemented in

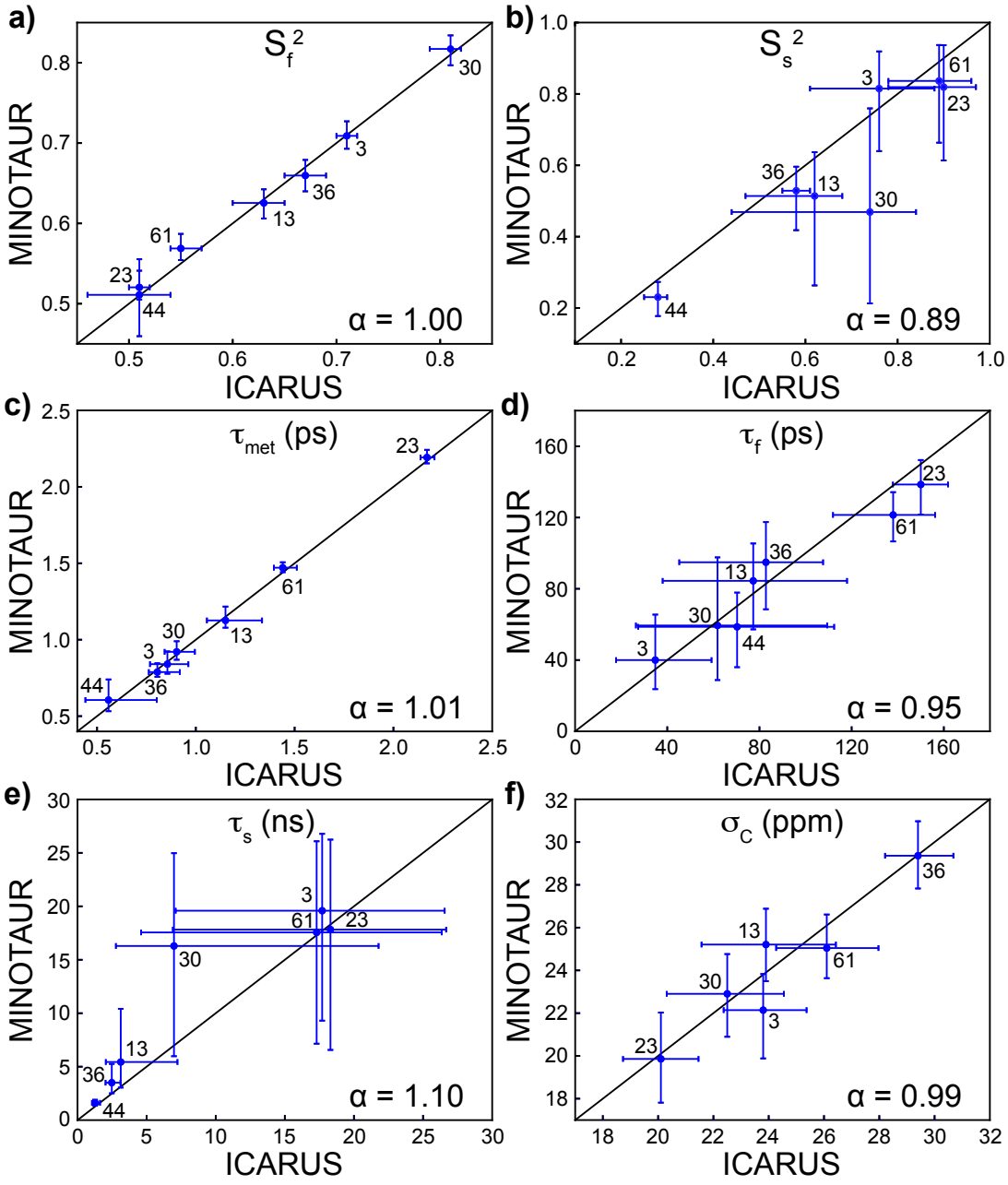

Figure 3.11: Correlation between ICARUS and MINOTAUR analysis. Correlation plot between S_f^2 (**a**), S_s^2 (**b**), τ_{met} (**c**), τ_f (**d**), τ_s (**e**) and the carbon-CSA (**f**) obtained after the ICARUS analysis [21] and MINOTAUR. The solid black lines correspond to perfect correlation. α is the slope of the linear correlation function.

a program called MINOTAUR. Relaxometry decay rates are no longer fitted and thus do not need to be corrected to take into account cross-relaxation effects. Rather, the intensity decays are reproduced after simulation of the free relaxation periods. We re-analyzed our data

recorded on isoleucine methyl groups of Ubiquitin [21] and did not see significant deviations in the description of the dynamics. This observation was expected since the experimental intensity decays did not show obvious deviation from a mono-exponential decay, justifying the correction procedure.

3.5 Conclusion

In this chapter, the basics of high-resolution relaxometry were introduced, with applications to the study of protein dynamics. The theoretical framework for the analysis of sample-shuttling experiments recorded on side-chains $\{^{13}C^{1}H^{2}H_{2}\}$ methyl-groups was presented. Two programs were used for the accurate description of isoleucine $\delta 1$-methyl groups: ICARUS and MINOTAUR. The first one uses accurate high-field relaxation rates and relaxometry decay rates to perform an iterative correction on the later. It was used to analyse several aspects of the relaxation in methyl groups. In combination with accurate low-field relaxation data, it suggested that neighbouring deuteron significantly contribute to relaxation at low fields. The second generation approach, called MINOTAUR, uses accurate high-field relaxation rates and relaxometry relaxation decays to directly obtain values for the parameters of the spectral density function. It is thus free of the correction procedure and we believe has a wider range of application than ICARUS, in particular when strong cross-relaxation leads to a clear multi-exponential relaxation decays in relaxometry experiments.

Chapter 4

Models for protein site-specific side-chains dynamics

Contents

4.1 Introduction

With the development of sample-shuttling experiments (both relaxometry and Two-Field (2F) **N**uclear **M**agnetic **R**esonance (NMR)), the range of timescales that can be probed with high accuracy using relaxation experiments is potentially extended to the tens to hundreds of nanoseconds [33]. In order to separate different timescales of motions, the initial **M**odel **F**ree (MF) correlation function have been complefixied to introduce an additional correlation time and order parameter to yield the **E**xtended **M**odel **F**ree (EMF) correlation function for internal motions [74]:

$$C_{EMF}(t) = \mathcal{S}_1^2\mathcal{S}_2^2 + (1-\mathcal{S}_1^2)e^{t/\tau_1} + \mathcal{S}_1^2(1-\mathcal{S}_2^2)e^{-t/\tau_2}, \tag{4.1}$$

where τ_1 and τ_2 are two correlation times associated respectively to squared order parameters $\mathcal{S}_1^2$ and $\mathcal{S}_2^2$. In effect, relying the analysis of relaxation data recorded over 2 orders of magnitude of magnetic fields on MF [15] or EMF [74] models is unlikely the best route towards a better understanding of protein backbone and side-chains motions [17, 21, 22]. Indeed, no information on the type of motions involved can be obtained, unless complemented with **M**olecular **D**ynamic (MD) simulations [75, 30, 21, 31, 32].

In MF type of analysis, the global tumbling is often supposed to be isotropic, which is the frame in which it was originially presented [15], with an approximated correlation function for overall diffusion when the diffusion tensor is anisotropic. This limitation has raised a number of questions regarding the relevance of the analysis of relaxation data with MF type of correlation functions in the case of couplings between global (*i.e* overall diffusion) and local motions [25, 26], and has lead to the development of the **S**lowly **R**elaxing **L**ocal **S**tructure (SRLS) approach for the analysis of NMR relaxation data. The SRLS models were initially proposed to analyze **E**lectron **S**pin **R**esonance (ESR) spectra [71, 172]. In ESR, a nitroxide tag is attached on the surface of a biomolecule, so that fluctuations in the shape of the overall diffusion tensor can have strong effects on the orientation of the spin interactions in the laboratory frame. With the exception of paramagnetic experiments, NMR spin relaxation probes bond motions in the biomolecules, for which only domain-domain reorientations are expected to lead to a coupling between global and local motions. In this case, alternative solutions to the SRLS models have also been proposed [111, 173, 174]. In addition, and as suggested by Freed and coworkers, the assumptions of simple local geometry and motions with axial symmetry have to be invoked in the frame of the MF [15] and EMF [74] approaches [27, 28, 29]. This aspect is particularly

critical as MF order parameters have been shown to be related to conformational entropy, both for protein backbone [23] and side-chains [24], and a miss-characterization of the motions will inevitably lead to a miss-characterization of the thermodynamics.

In this chapter, we will write correlation functions as obtained by solving diffusion equations. The mathematical treatment presented here follows approaches published between the 1960s and 1980s. We will then investigate how the factorization of the global tumbling correlation function and the MF approximation affects the dynamic parameters using synthetic data. We will briefly look at the effect of correlated motions in the case of methyl groups undergoing rotamer exchange. Finally, we will use our newly developped models of motion, and insights obtained from MD simulations, to analyse our relaxation data recorded on isoleucine-δ_1 methyl groups of Ubiquitin. We will show that a relaxation mechanism is associated to the change of **C**hemical **S**hift **A**nisotropy (CSA) tensors as one isoleucine jumps from one conformer to the other. This will allow us to reproduce cross-correlated cross-relaxation rates, which was not possible with the MF approach (Fig. 3.6a,b), an aspect that was already identified by Freed and coworkers [26].

4.2 General approach to calculate correlation functions

The correlation function between two interactions i and j has been defined in Chapter 1 by Eq. 1.15:

$$C_{i,j}(t) = \langle V^i_{2,q}(0) V^{j*}_{2,q}(t) \rangle, \tag{4.2}$$

where $\langle \cdots \rangle$ denotes ensemble average, $*$ stands for complex conjugate and the function V is related to rank-2 Wigner matrices by:

$$V^i_{2,q} = \mathcal{D}^{(2)*}_{q0}(\alpha_{L,i}, \beta_{L,i}, 0), \tag{4.3}$$

where $\alpha_{L,i}$ and $\beta_{L,i}$ are Euler angles for transformation from the laboratory to interaction frame. In the following, we will use the compact notation for the set of three Euler angles (see Appendix A.2 for more details on Wigner matrices):

$$\Omega_{L,i} = \{\alpha_{L,i}, \beta_{L,i}, \gamma_{L,i}\}. \tag{4.4}$$

The correlation function can then be written:

$$C_{i,j}(t) = \langle \mathcal{D}^{(2)*}_{q0}(\Omega_{L,i}, 0) \mathcal{D}^{(2)}_{q0}(\Omega_{L,j}, t) \rangle. \tag{4.5}$$

The approach to calculate the ensemble average in Eq. 4.5 is detailed in [34]. If we write:

$$C(t) = \langle A^*(\Omega(0)) B(\Omega(t)) \rangle, \tag{4.6}$$

with A and B two Wigner rotation matrices with potentially different indices, the ensemble average expands into:

$$C(t) = \int d\Omega_0 \int d\Omega P(\Omega_0) P(\Omega, t|\Omega_0, 0) A^*(\Omega_0) B(\Omega), \tag{4.7}$$

where $P(\Omega)$ is the probability that the Euler angles for frame transformation is Ω, and $P(\Omega, t|\Omega_0, 0)$ is the conditional probability that the Euler angles for frame transformation is Ω at time t when it was Ω_0 at time $t = 0$. In the following, we will calculate the ensemble averages using a Master equation for the description of relaxation-inducing rate processes:

$$\frac{\partial}{\partial t} P(\Omega, t) = -K P(\Omega, t), \tag{4.8}$$

which is a Fokker-Planck diffusion equation and where $P(\Omega, t)$ is the probability of finding the Euler angles Ω for frame transformation, at time t, and K is a model-dependent operator describing the motions of interest. The initial step is to diagonalize the operator K, with eigenvalues E_n and eigenvectors ψ_n:

$$K\psi_n = E_n\psi_n \tag{4.9}$$

The conditional probability is then:

$$P(\Omega, t|\Omega_0, 0) = \sum_n \psi_n^*(\Omega_0)\psi_n(\Omega)e^{-E_n t}, \tag{4.10}$$

and:

$$P(\Omega_0) = \lim_{t\to\infty} P(\Omega, t|\Omega_0, 0). \tag{4.11}$$

$P(\Omega_0)$ can sometimes be evaluated by simple probabilistic and geometric considerations.

The probability $P(\Omega_0)$ and conditional probability $P(\Omega, t|\Omega_0, 0)$ can be inserted in Eq. 4.7 to yield an expression of the correlation function as a sum of decaying exponential terms:

$$C(t) = \sum_i a_i e^{-t/\tau_i}. \tag{4.12}$$

It is then straightforward to calculate the spectral density functions, which are defined as the Fourier transform of correlation functions and are usefull to express relaxation rates as a function of parameters describing the dynamics (see Chapter 1):

$$\mathcal{J}(\omega) = \mathrm{Re}\left(2\int_0^{+\infty} C(t)e^{-i\omega t}dt\right) = 2\sum_i a_i \frac{\tau_i}{1+(\omega\tau_i)^2}. \tag{4.13}$$

4.3 Correlation functions for four types of motions

In this section, we will detail how the correlation function can be computed for different motions: the global rotation diffusion, the instantaneous jumps between different conformations, the diffusion on a cone and the wobbling in a cone. The correlation functions for these motions have already been reviewed [34], so that this mathematical introduction essentially consists in a review of the associated litterature. The order parameter associated to each motion will also be calculated.

4.3.1 Global tumbling

In this section, we will only consider the rotational diffusion of the protein: all interactions are fixed in the molecular frame. The correlation function describes the motions of the interactions in the laboratory frame, which is equivalent to the motions of the protein in the laboratory frame. Appendix F.1 follows the thorough treatment of this situation presented by Werbelow *et al.* [175], but other approaches can be found elsewhere [176, 177, 178, 179].

The correlation function can be decomposed using properties of the Wigner matrices $\mathcal{D}^{(2)}_{ij}(\Omega, t)$ (Eq. A.11):

$$\begin{aligned} C_{i,j}(t) =& \langle \mathcal{D}^{(2)*}_{q0}(\Omega_{L,i}, 0) \mathcal{D}^{(2)}_{q0}(\Omega_{L,j}, t) \rangle \\ =& \sum_{a,a'=-2}^{2} \langle \mathcal{D}^{(2)*}_{qa}(\Omega_{L,D}, 0) \mathcal{D}^{(2)}_{qa'}(\Omega_{L,D}, t) \mathcal{D}^{(2)*}_{a0}(\Omega_{D,i}, 0) \mathcal{D}^{(2)}_{a'0}(\Omega_{D,j}, t) \rangle, \end{aligned} \tag{4.14}$$

where D is the frame associated to the diffusion tensor, $\Omega_{L,D}$ is the time-dependent Euler angle set for the orientation of the diffusion tensor in the laboratory frame and $\Omega_{D,k}$, $k = \{i, j\}$, are the Euler angle sets for orientation of the interactions-i and -j in the diffusion frame. Since the angles $\Omega_{D,k}$, $k = \{i, j\}$, are time-independent, they can be taken out of the ensemble average. In the following, we define:

$$C_{aa'}(t) = \langle \mathcal{D}^{(2)*}_{qa}(\Omega_{L,D}, 0) \mathcal{D}^{(2)}_{qa'}(\Omega_{L,D}, t) \rangle, \tag{4.15}$$

so that we can write:

$$C_{i,j}(t) = \sum_{a,a'=-2}^{2} C_{aa'}(t) \mathcal{D}^{(2)*}_{a0}(\Omega_{D,i}) \mathcal{D}^{(2)}_{a'0}(\Omega_{D,j}). \tag{4.16}$$

Table 4.1: Values of the coefficients $a_{\kappa,a}$ and eigenvalues E_κ appearing in the global tumbling correlation function (Eq. 4.18), where $\beta = \tan^{-1}\frac{\sqrt{3}D_-}{D_{zz}-D_+}$, $D_\pm = \frac{1}{2}(D_{xx} \pm D_{yy})$, $D = \frac{1}{3}(D_{xx} + D_{yy} + D_{zz})$ and $\mathcal{L}^2 = \frac{1}{3}(D_{xx}D_{yy} + D_{xx}D_{zz} + D_{yy}D_{zz})$.

		a					E_κ
		-2	-1	0	1	2	
κ	1	0	$\frac{1}{\sqrt{2}}$	0	$\frac{1}{\sqrt{2}}$	0	$4D_{xx} + D_{yy} + D_{zz}$
	2	0	$-\frac{1}{\sqrt{2}}$	0	$\frac{1}{\sqrt{2}}$	0	$D_{xx} + 4D_{yy} + D_{zz}$
	3	$-\frac{1}{\sqrt{2}}$	0	0	0	$\frac{1}{\sqrt{2}}$	$D_{xx} + D_{yy} + 4D_{zz}$
	4	$\frac{1}{\sqrt{2}}\cos\frac{\beta}{2}$	0	$\sin\frac{\beta}{2}$	0	$\frac{1}{\sqrt{2}}\cos\frac{\beta}{2}$	$6(D + \sqrt{D^2 - \mathcal{L}^2})$
	5	$-\frac{1}{\sqrt{2}}\sin\frac{\beta}{2}$	0	$\cos\frac{\beta}{2}$	0	$-\frac{1}{\sqrt{2}}\sin\frac{\beta}{2}$	$6(D - \sqrt{D^2 - \mathcal{L}^2})$

The Master equation for global tumbling, written in a frame where the rotational diffusion tensor is diagonal, is:

$$\frac{\partial}{\partial t}P(\Omega_{L,D}, t) = -\sum_{j=x,y,z} D_{jj}L_j^2 P(\Omega_{L,D}, t), \tag{4.17}$$

where D_{jj} is the jth component of the diagonalized diffusion tensor and L_j are the associated angular momentum operators. The detailled calculation of the eigenfunctions and eigenvalues required to express the conditional probability (Eq. 4.10) can be found in the Appendix F.1. It leads to the following expression for the global tumbling correlation function:

$$\boxed{C_{aa'}(t) = \frac{1}{5}\sum_{\kappa=1}^{5} a_{\kappa,a}a_{\kappa,a'}e^{-E_\kappa t}}, \tag{4.18}$$

where the coefficients $a_{\kappa,a}$ and eigenvalues E_κ are reported in Table 4.1.

The correlation function can now be written:

$$C_{i,j}(t) = \frac{1}{5}\sum_{\kappa=1}^{5}\sum_{a=-2}^{2}\sum_{a'=-2}^{2} a_{\kappa,a}a_{\kappa,a'}e^{-E_\kappa t}\mathcal{D}^{(2)*}_{a,0}(\Omega_{D,i})\mathcal{D}^{(2)}_{a',0}(\Omega_{D,j}). \tag{4.19}$$

Special case 1: axial symmetry In this case, the Wigner matrices $\mathcal{D}^{(2)}_{\mu,k}(\Omega), k \in [-2, 2]$ are eigenfunctions of the diffusion operator with associated eigenvalue $6D_\perp + k^2\left(D_\parallel - D_\perp\right)$ where

we define $D_\perp = D_{xx} = D_{yy}$ and $D_\parallel = D_{zz}$. It follows:

$$C^{aa'}(t) = \delta_{aa'}\frac{1}{5}e^{-(6D_\perp + a^2(D_\parallel - D_\perp))t}, \tag{4.20}$$

and the total correlation function is:

$$C_{i,j}(t) = \frac{1}{5}\sum_{a=-2}^{2} e^{-(6D_\perp + a^2(D_\parallel - D_\perp))t} d_{a,0}(\beta_{D,i}) d_{a,0}(\beta_{D,j}) \cos(a(\alpha_{D,i} - \alpha_{D,j})), \tag{4.21}$$

where $\Omega_{D,k} = \{\alpha_{D,k}, \beta_{D,k}, 0\}$, $k = \{i, j\}$ are the Euler angles for orientation of the interaction frames in the diffusion frame and $d_{a,0}$ are small Wigner matrices (Appendix Table A.1).

Special case 2: isotropic tumbling In this case as well, the Wigner matrices $\mathcal{D}^{(2)}_{\mu,k}(\Omega), k \in [-2, 2]$ are eigenfunctions of the diffusion operator with degenerate eigenvalue of $6D_{rot}$. The well-known result immediately follows:

$$C^{aa'}(t) = \delta_{aa'}\frac{1}{5}e^{-t/\tau_c}, \tag{4.22}$$

where the global tumbling correlation time is defined as:

$$\tau_c = \frac{1}{6D_{rot}}. \tag{4.23}$$

The total correlation function is:

$$C_{i,j}(t) = \frac{1}{5}e^{-t/\tau_c}\mathcal{P}_2(\cos\theta_{i,j}), \tag{4.24}$$

where $\theta_{i,j}$ is the angle between interactions i and j and $\mathcal{P}_2$ is the second-order Legendre polynomial $\mathcal{P}_2(x) = (3\cos^2(x) - 1)/2$.

Graphical representations The analysis of ^{15}N-backbone relaxation data has been of great interest in the late 1990s and early 2000s to obtain information about the anisotropy of the overall diffusion tensor [106, 107, 180, 181, 182, 183, 184, 185, 186]. We will show here how assuming symmetry properties of the diffusion tensor affects the correlation function, the spectral density function, and some relaxation rates for a ^{15}N-^{1}H spin pair. We impose the interaction frame to be fixed in the diffusion frame, with Euler angles given by $\Omega_{D,i} = \{70\,\text{deg}, 60\,\text{deg}, 0\}$. The values of the diffusion tensors components are chosen to be $D_{xx} = 1.5 \times 10^7\,\text{s}^{-1}$, $D_{yy} = 2.0 \times 10^7\,\text{s}^{-1}$ and $D_{zz} = 2.5 \times 10^7\,\text{s}^{-1}$. Although the correlation functions calculated assuming partial or

complete symmetry of the diffusion tensor are almost indistinguishable from the accurate correlation function (Fig. 4.1a), the spectral density functions show some deviations at low frequencies (Fig. 4.1b).

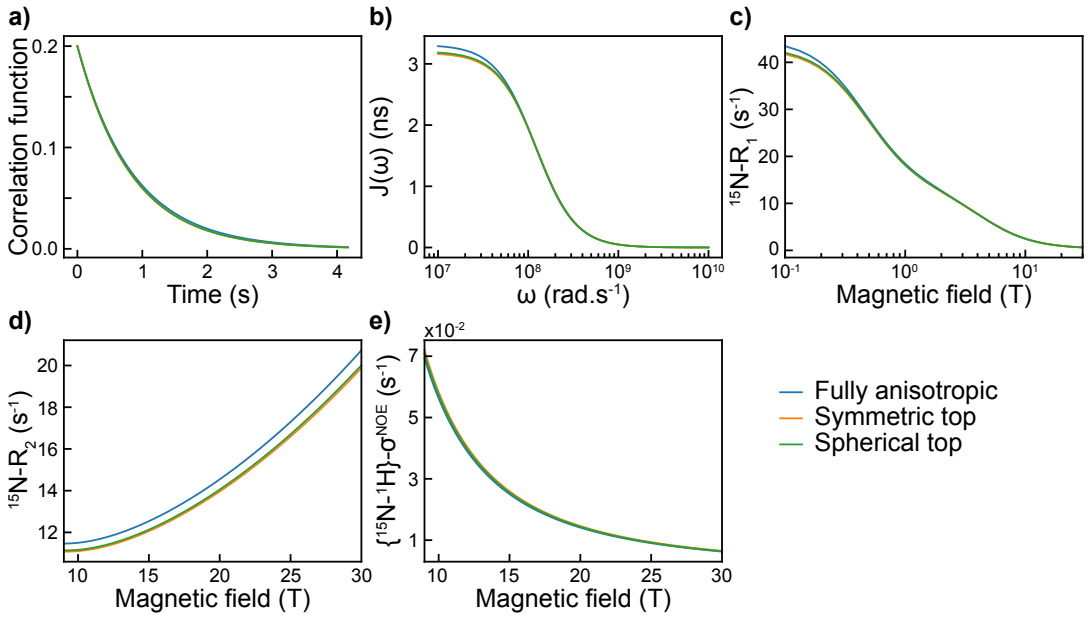

Figure 4.1: Effect of partial or full symmetry of the diffusion tensor assumption. **a)** Global tumbling auto-correlation function for a diffusion tensor with components $D_{xx} = 1.5 \times 10^7\, s^{-1}$, $D_{yy} = 2.0 \times 10^7\, s^{-1}$ and $D_{zz} = 2.5 \times 10^7\, s^{-1}$ and interaction orientation $\Omega_{D,i} = \{70°, 60°, 0\}$. The assymetric tumbling (blue) correlation function is calculated using Eq. 4.19, the symmetric top (orange) correlation function using Eq. 4.21 and the spherical top (green) correlation function using Eq. 4.24. The symmetric top correlation function was calculated using $D_{\parallel} = D_{zz}$ and $D_{\perp} = (D_{xx} + D_{yy})/2$. The spherical top correlation function was calculated using $D_{rot} = (D_{xx} + D_{yy} + D_{zz})/3$. **b)** Spectral density function associated to the correlation functions shown in **a**. Field-variation of the (**c**) nitrogen longitudinal relaxation rate, (**d**) nitrogen transverse relaxation rate and (**e**) nitrogen-proton cross-relaxation rate calculated using the spectral density function shown in **b**. The hydrogen-nitrogen distance is set to 1.02 Å and the ^{15}N-chemical shift anisotropy tensor was assumed to be axially symmetric with value 150 ppm and aligned along the N-H vector.

In order to evaluate the effect of these deviations on calculated relaxation rates, we considered an isolated ^{15}N-^{1}H spin pair, and calculated the nitrogen-15 longitudinal (R_1) and tranverse (R_2) relaxation rates as well as the proton-nitrogen-15 cross-relaxation rate (σ^{NOE}). Not surprisingly, at high magnetic fields, R_1 and σ^{NOE}, which only depend on the spectral density function evaluated at high frequencies, are not affected by assumming partial or full

symmetry of the diffusion tensor (Fig. 4.1c,e). However, deviations in R_1 profiles appear at very low field (lower than 0.5 T) which are now accessible with **H**igh-**R**esolution **R**elaxometry (HRR) [17]. Transverse relaxation rates are also dependent on the spectral density function evaluated at zero frequency, and show variations depending on the assumption being made (Fig. 4.1d). The extent of the variations depends on the orientation of the interaction in the diffusion tensor and the anisotropy of the tensor. Some of these aspects in the presence of an internal motion were discussed by J. Tropp [187].

4.3.2 Rotamer jumps

In this section, we will add one internal motion on top of the global tumbling. We will assume the interactions can adopt a finite number of fixed conformations and that they can exchange between one another. Moreover, it is assumed that the transition events are infinitely fast, that is, the system can always be found in one particular conformation. This model can be used to study side-chain motions, as revealed by MD simulations (*vide infra*): in the example presented in Fig. 4.2a, the side chain of isoleucine 36 of Ubiquitin is found in a limited number of conformations during the MD trajectory, each of them being caracterized by a pair of dihedral angles χ_1 and χ_2.

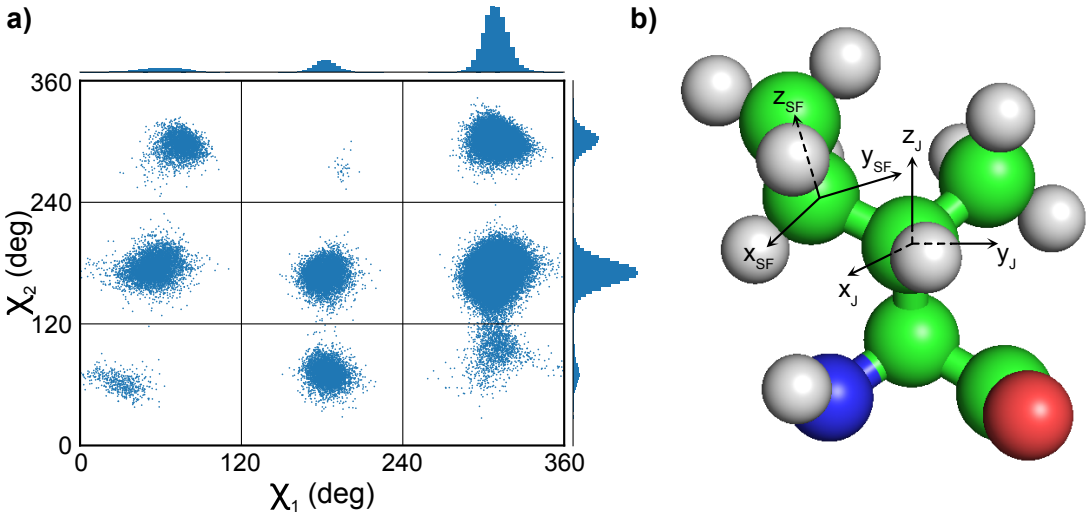

Figure 4.2: Side-chain motions and jump frames. **a)** Ramachandran diagram for isoleucine 36 obtained from a MD simulation on Ubiquitin. **b)** Structure of an isoleucine residue showing the jump frame and the system frame in one particular conformation. The parts of the frame axis that are hidden by the atoms are shown in dash lines.

The treatment of rotameric jumps in this section is based on the work of Witterbort and Szabo [188]. We will use the result from the previous section and write the correlation as:

$$C_{i,j}(t) = \frac{1}{5}\sum_{\kappa=1}^{5}\sum_{a=-2}^{2}\sum_{a'=-2}^{2} a_{\kappa,a}a_{\kappa,a'}e^{-E_\kappa t}\langle \mathcal{D}^{(2)*}_{a,0}(\Omega_{D,i},0)\mathcal{D}^{(2)}_{a',0}(\Omega_{D,j},t)\rangle, \tag{4.25}$$

where the ensemble average $\langle ...\rangle$ accounts for the presence of internal motions. This equation is valid only under the assumption that global tumbling and internal motions are uncorrelated. The Wigner matrices can be split into successive frame transformations:

- from the diffusion frame to the jump frame, with Euler angle $\Omega_{D,J}$. This transformation allows a facilitated description of the jumps. For example, in the case of isoleucine χ_1 and $\chi 2$ rotameric jumps (corresponding to different orientations of the $C_{\gamma 1}$-$C_{\delta 1}$ axis), the jump frame main axis (z_J) points along the C_α-C_β bond, with origin corresponding to the C_β (Fig. 4.2b). The orientation of x_J axis is arbitrary. This frame is fixed in the diffusion frame, and the transformation is time-independent.

- from the jump frame to the system frame (SF), with Euler angle $\Omega_{J,SF}$. From the definition of the jump frame, we have $\Omega_{J,SF} = \{\alpha_{J,SF}, \beta_{J,SF}, 0\}$. The system frame has main axis pointing along the chemical bond defining the conformation. In the case of isoleucine residues, it is the $C_{\gamma 1}$-$C_{\delta 1}$ bond (Fig. 4.2b). This transformation is time-dependent.

- from the system frame to the interaction frame. The interaction frame has its main axis pointing along the direction of the interaction. This is a time-independent transformation, with Euler angle $\Omega_{SF,i}$.

These additional frames lead to the decomposition:

$$\mathcal{D}^{(2)}_{a,0}(\Omega_{D,i},t) = \sum_{b=-2}^{2}\sum_{c=-2}^{2}\mathcal{D}^{(2)}_{a,b}(\Omega_{D,J})\mathcal{D}^{(2)}_{b,c}(\Omega_{J,SF},t)\mathcal{D}^{(2)}_{c,0}(\Omega_{SF,i}). \tag{4.26}$$

The correlation function can be written:

$$\begin{aligned} C_{i,j}(t) = \frac{1}{5}\sum_{\kappa=1}^{5}\sum_{a,a'=-2}^{2}\sum_{b,b'=-2}^{2}\sum_{c,c'=-2}^{2} & a_{\kappa,a}a_{\kappa,a'}e^{-E_\kappa t}\langle \mathcal{D}^{(2)*}_{b,c}(\Omega_{J,SF},0)\mathcal{D}^{(2)}_{b',c'}(\Omega_{J,SF},t)\rangle \times \\ & \mathcal{D}^{(2)*}_{a,b}(\Omega_{D,J})\mathcal{D}^{(2)}_{a',b'}(\Omega_{D,J})\mathcal{D}^{(2)*}_{c,0}(\Omega_{SF,i})\mathcal{D}^{(2)}_{c',0}(\Omega_{SF,j}), \end{aligned} \tag{4.27}$$

where $a_{\kappa,a}$ and E_κ are given in Table 4.1. The conditional probability (Eq. 4.10) is found by

solving the Master equation:

$$\frac{\partial}{\partial t}p_\alpha(t) = \sum_{\beta=1}^{N} \mathcal{R}_{\alpha\beta}p_\beta(t), \tag{4.28}$$

where $p_\alpha(t)$ is the population of state α at time t and $\mathcal{R}_{\alpha\beta}$ is an element of the exchange matrix $\mathcal{R}$ and corresponds to the exchange rate from state β to α. Solving for the eigenfunctions and eigenvalues (as shown in Appendix F.2) leads to the following expression of the correlation function that appears in the sum defined in Eq. 4.27:

$$\boxed{\langle \mathcal{D}^{(2)*}_{b,c}(\Omega_{J,SF},0)\mathcal{D}^{(2)}_{b',c'}(\Omega_{J,SF},t)\rangle = \sum_{\alpha=1}^{N}\sum_{\beta=1}^{N}\sum_{n=0}^{N-1} \mathcal{D}^{(2)*}_{b,c}(\Omega_{J,SF_\alpha})\mathcal{D}^{(2)}_{b',c'}(\Omega_{J,SF_\beta})\sqrt{p^{eq}_\alpha p^{eq}_\beta}\tilde{X}^{(n)}_\alpha \tilde{X}^{(n)}_\beta e^{\lambda_n t}}, \tag{4.29}$$

where $\tilde{X}^{(n)}_\alpha$ is the α^{th} value of eigenvector associated to the eigenvalue λ_n. The total correlation function is:

$$\begin{aligned} C_{i,j}(t) = \frac{1}{5}\sum_{\kappa=1}^{5}\sum_{a,a'=-2}^{2}\sum_{b,b'=-2}^{2}\sum_{c,c'=-2}^{2}\sum_{\alpha,\beta=1}^{N}\sum_{n=0}^{N-1} a_{\kappa,a}a_{\kappa,a'}\sqrt{p^{eq}_\alpha p^{eq}_\beta}\tilde{X}^{(n)}_\alpha\tilde{X}^{(n)}_\beta e^{-E_\kappa t}e^{\lambda_n t}\times \\ \mathcal{D}^{(2)*}_{a,b}(\Omega_{D,J})\mathcal{D}^{(2)}_{a',b'}(\Omega_{D,J})\mathcal{D}^{(2)*}_{b,c}(\Omega_{J,SF_\alpha})\mathcal{D}^{(2)}_{b',c'}(\Omega_{J,SF_\beta})\mathcal{D}^{(2)*}_{c,0}(\Omega_{SF,i})\mathcal{D}^{(2)}_{c',0}(\Omega_{SF,j}). \end{aligned} \tag{4.30}$$

We can recognize that the sums over b and b' are associated with decomposition of Wigner matrices. We can write in a more compact form (suppression of the sums over b and b' are associated with the variable name changes $c \to b$ and $c' \to b'$):

$$\begin{aligned} C_{i,j}(t) = \frac{1}{5}\sum_{\kappa=1}^{5}\sum_{a,a'=-2}^{2}\sum_{b,b'=-2}^{2}\sum_{\alpha,\beta=1}^{N}\sum_{n=0}^{N-1} a_{\kappa,a}a_{\kappa,a'}\sqrt{p^{eq}_\alpha p^{eq}_\beta}\tilde{X}^{(n)}_\alpha\tilde{X}^{(n)}_\beta e^{-E_\kappa t}e^{\lambda_n t}\times \\ \mathcal{D}^{(2)*}_{a,b}(\Omega_{D,SF_\alpha})\mathcal{D}^{(2)}_{a',b'}(\Omega_{D,SF_\beta})\mathcal{D}^{(2)*}_{b,0}(\Omega_{SF,i})\mathcal{D}^{(2)}_{b',0}(\Omega_{SF,j}). \end{aligned} \tag{4.31}$$

In the case of an isotropic global diffusion tensor, we can use Eq. A.10 and Eq. A.11 to simplify:

$$C_{i,j}(iso,t) = \frac{1}{5}e^{-t/\tau_c}\sum_{\alpha,\beta=1}^{N}\sum_{n=0}^{N-1}\sqrt{p^{eq}_\alpha p^{eq}_\beta}\tilde{X}^{(n)}_\alpha\tilde{X}^{(n)}_\beta \mathcal{P}_2(\cos\theta_{i_\alpha,j_\beta})e^{\lambda_n t}, \tag{4.32}$$

where $\theta_{i_\alpha,j_\beta}$ is the angle between the main axis of interaction i in rotamer α and the main axis of interaction j in rotamer β.

Order parameter for rotamer jumps The internal correlation function for rotamer jumps in Eq. 4.29 does not cancel out when $t \to \infty$ only for $n = 0$ so that the squared order parameter

for rotamer jumps is:

$$\mathcal{S}^2_{jumps}(i,j) = \sum_b \sum_{c,c'} \sum_{\alpha=1}^{N} \sum_{\beta=1}^{N} p_\alpha^{eq} p_\beta^{eq} \mathcal{D}^{(2)*}_{b,c}(\Omega_{J,SF_\alpha}) \mathcal{D}^{(2)}_{b,c'}(\Omega_{J,SF_\beta}) \mathcal{D}^{(2)*}_{c,0}(\Omega_{SF_\alpha,i}) \mathcal{D}^{(2)}_{c',0}(\Omega_{SF_\beta,j}). \tag{4.33}$$

Using Eq. A.10 and Eq. A.11, we can write the compact expression:

$$\mathcal{S}^2_{jumps}(i,j) = \sum_{\alpha=1}^{N} \sum_{\beta=1}^{N} p_\alpha^{eq} p_\beta^{eq} \mathcal{P}_2(\cos\theta_{i_\alpha,j_\beta}). \tag{4.34}$$

4.3.3 Diffusion on a cone

The diffusion on a cone can be used, for example, to model the rotation of a methyl group around its symmetry axis under the assumption that the rotation is not hindered by the proximity of other atoms that can potentially lead to a non-uniform probability distribution for each position of the protons. Methyl groups are now widely used in biomolecular NMR for their favorable relaxation properties that precisely originate from the fast rotation around their symmetry axis [36, 52, 53]. In this context, force fields used in MD simulations of proteins have been modified using NMR experimental data to correctly account for the energy barrier for the rotation [189, 190]. The solution of the Master equation (Eq. 4.8) has first been published by D. Wallach [191].

In order to describe the diffusion on a cone motion, an additional frame needs to be introduced on top of the diffusion and interaction frames. Similarly to the rotamer jumps, we call this frame the system frame (SF). The main axis is pointing along the axis of rotation, with arbitrary orientation of the x- and y-axis. The Euler angle for transformation from the diffusion frame to the system frame is $\Omega_{D,SF} = \{\alpha_{D,SF}, \beta_{D,SF}, \gamma_{D,SF}(t)\}$ where only the third angle is time-dependent in the context of this type of motion. The correlation function is then:

$$\begin{aligned} C_{i,j}(t) = \frac{1}{5} \sum_{\kappa=1}^{5} \sum_{a,a'} \sum_{b,b'} a_{\kappa,a} a_{\kappa,a'} e^{-E_\kappa t} e^{i\alpha_{D,SF}(a-a')} d_{a,b}(\beta_{D,SF}) d_{a',b'}(\beta_{D,SF}) \times \\ \langle e^{i(b\gamma_{D,SF}(0) - b'\gamma_{D,SF}(t))} \rangle \mathcal{D}^{(2)*}_{b,0}(\Omega_{SF,i}) \mathcal{D}^{(2)}_{b',0}(\Omega_{SF,j}). \end{aligned} \tag{4.35}$$

The Master equation is written using the angular momentum operator L^2_{rot}:

$$\frac{\partial}{\partial t} p(\gamma,t) = -D_{rot} L^2_{rot} p(\gamma,t) = D_{rot} \frac{\partial^2}{\partial \gamma^2} p(\gamma,t), \tag{4.36}$$

where D_{rot} is the rotational diffusion coefficient. Solving for the eigenfunctions and eigenvalues (see Appendix. F.3) leads to the rotation correlation function:

$$\boxed{\langle e^{i(b\gamma_{D,SF}(0)-b'\gamma_{D,SF}(t))}\rangle = \delta_{bb'}e^{-D_{rot}b^2t}}, \tag{4.37}$$

and the total correlation function is:

$$C_{i,j}(t) = \frac{1}{5}\sum_{\kappa=1}^{5}\sum_{a,a'}\sum_{b} a_{\kappa,a}a_{\kappa,a'}e^{-E_\kappa t}e^{-D_{rot}b^2t}e^{i\alpha_{D,SF}(a-a')}d_{a,b}(\beta_{D,SF})d_{a',b}(\beta_{D,SF})\times \\ \mathcal{D}^{(2)*}_{b,0}(\Omega_{SF,i})\mathcal{D}^{(2)}_{b,0}(\Omega_{SF,j}). \tag{4.38}$$

In the case of an isotropic global tumbling diffusion tensor, it simplifies to:

$$C_{i,j}(iso,t) = \frac{1}{5}e^{-t/\tau_c}\sum_{b=-2}^{2} e^{-D_{rot}b^2t}\mathcal{D}^{(2)*}_{b,0}(\Omega_{SF,i})\mathcal{D}^{(2)}_{b,0}(\Omega_{SF,j}). \tag{4.39}$$

Order parameter for rotation on a cone The only non-vanishing term in Eq. 4.37 is obtained for $b = 0$, so that the squared order-parameter for rotation on a cone is:

$$\mathcal{S}^2_{rot}(i,j) = \mathcal{P}_2(\cos\beta_{SF,i})\mathcal{P}_2(\cos\beta_{SF,j}). \tag{4.40}$$

In the case of methyl-group rotation, with ideal tetrahedral geometry, it leads to the well-known result $\mathcal{S}^2_{met}(\mathrm{dd_{CH}}, \mathrm{dd_{CH}}) = 1/9$, where $\mathrm{dd_{CH}}$ stands for the C-H **D**ipole-**D**ipole (DD) interaction.

4.3.4 Wobbling in a cone

The last type of motion that we will consider here is the wobbling in a cone. In this model, the bond vector undergoes restricted diffusion inside a volume that is associated to a cone. It can be usefull to model the motion of any bonds such as the ^{15}N-^{1}H pair, or C-C side-chains bonds. The correlation function for this type of motion was initially introduced in fluorescence [192] and dielectric spectroscopy [193]. As will be seen bellow, and in details in the Appendix F.4, the Master equation can be solved analytically, but the complexity of the solution has led to the introduction of approximated forms for the correlation function by the group of A. Ikegami [192], and later obtained similarly by G.Lipari and A. Szabo [194, 195], which led them to present the MF correlation function [15]. However, the initial treatment of this model and the following studies were performed under the assumption that the interaction of interest was undergoing the wobbling motion [192, 194, 195, 196], which makes it *a priori* not applicable to the study

of the motion of side-chains. A. Kumar solved the master equation when the frame undergoing the diffusion in a cone is not the interaction frame [197, 198]. We will follow his approach, as well as the one of C. Wang and R. Pecora [196] who extended the work of M. Warchol and W. Vaughan [193]. In the construction of this model, the diffusing bond vector also undergoes rotation around itself, which is not likely to correctly reproduce motions of side-chains C-C bond vectors. We present here a way to overcome this difficulty.

For the description of this motion, we introduce the Wobbling Frame (WF) which main axis points along the axis of the cone, and x-axis can point in any direction. Similarly to what was presented in the previous sections, we also include a System Frame (SF) which undergoes the diffusion motion. Assuming the wobbling and global tumbling are uncorrelated, the correlation function is written:

$$C_{i,j}(t) = \frac{1}{5}\sum_{\kappa=1}^{5}\sum_{a,a'}\sum_{b,b'}\sum_{c,c'} a_{\kappa,a}a_{\kappa,a'}e^{-E_\kappa t}\langle \mathcal{D}^{(2)*}_{b,c}(\Omega_{WF,SF},0)\mathcal{D}^{(2)}_{b',c'}(\Omega_{WF,SF},t)\rangle \times \\ \mathcal{D}^{(2)*}_{a,b}(\Omega_{D,WF})\mathcal{D}^{(2)*}_{c,0}(\Omega_{SF,i})\mathcal{D}^{(2)}_{a',b'}(\Omega_{D,WF})\mathcal{D}^{(2)}_{c',0}(\Omega_{SF,j}). \tag{4.41}$$

The Master equation that solves the conditional probability is given by:

$$\frac{\partial}{\partial t}p(\Omega,t) = -D_W L_W^2 p(\Omega,t), \tag{4.42}$$

where D_W is the diffusion coefficient for the wobble motion and L_W^2 is the angular momentum operator:

$$L_W^2 = -\frac{1}{\sin\theta}\frac{\partial}{\partial\theta}\left(\sin\theta\frac{\partial}{\partial\theta}\right) - \frac{1}{\sin^2\theta}\frac{\partial^2}{\partial\varphi^2}, \tag{4.43}$$

with reflecting boundary condition at $\theta = \beta_{cone}$, with β_{cone} the cone semi-angle opening:

$$\frac{\partial}{\partial\theta}p(\Omega,t)|_{\theta=\beta_{cone}} = 0. \tag{4.44}$$

Solving Eq. 4.42 is rather tedious, and presented in Appendix F.4. It leads to the following expression for the conditional probability:

$$p(\Omega,t|\Omega_0,0) = \sum_{m=-\infty}^{+\infty}\sum_{n=0}^{+\infty} e^{-D_W\nu_{m,n}(\nu_{m,n}+1)t}Y^m_{\nu_{m,n}}(\Omega)Y^{m*}_{\nu_{m,n}}(\Omega_0), \tag{4.45}$$

where:

$$Y^m_{\nu_{m,n}}(\Omega) = \frac{1}{\sqrt{2\pi H_{m,n}(\mu_{cone})}}P^m_{\nu_{m,n}}(\mu)e^{im\varphi}, \tag{4.46}$$

and:

$$\begin{aligned} H_{m,n}(\mu_{cone}) &= \int_{\mu_{cone}}^{1} \left(P^m_{\nu_{m,n}}(\mu)\right)^2 d\mu, \\ \mu_{cone} &= \cos\beta_{cone}, \end{aligned} \tag{4.47}$$

$P^m_{\nu_{m,n}}$ is the Legendre associated function (Appendix A.3) with degree $\nu_{m,n}$ and order m [196, 199, 200, 201]. The initial angle probability is:

$$\begin{cases} p(\Omega_0) = \dfrac{1}{2\pi(1-\mu_{cone})}, \quad \theta_0 \in [0, \beta_{cone}], \\ p(\Omega_0) = 0, \quad \theta_0 > \beta_{cone}. \end{cases} \tag{4.48}$$

The correlation function for wobbling in a cone then reads:

$$\begin{aligned} &\langle \mathcal{D}^{(2)*}_{b,c}(\Omega_{WF,SF},0)\mathcal{D}^{(2)}_{b',c'}(\Omega_{WF,SF},t)\rangle = \frac{1}{4\pi^2(1-\mu_{cone})} \sum_{m=-\infty}^{+\infty}\sum_{n=0}^{+\infty} \frac{e^{-D_W\nu_{m,n}(\nu_{m,n}+1)t}}{H_{m,n}(\mu_{cone})} \times \\ &\int_0^{\beta_{cone}} \sin\theta_0 d\theta_0 \int_0^{\beta_{cone}} \sin\theta d\theta \int_0^{2\pi} d\varphi_0 \int_0^{2\pi} d\varphi \mathcal{D}^{(2)*}_{b,c}(\varphi_0,\theta_0,-\varphi_0)\mathcal{D}^{(2)}_{b',c'}(\varphi,\theta,-\varphi) \times \\ &P^m_{\nu_{m,n}}(\cos\theta_0)P^m_{\nu_{m,n}}(\cos\theta)e^{im(\varphi-\varphi_0)}. \end{aligned} \tag{4.49}$$

The third Euler angles in the Wigner matrices equal the opposite of the first Euler angles in order for this correlation function to only account for the motion of the C-C bond in a cone, and not any rotational motions: if the third angle was set to 0, the orientation of the x-axis of the system frame with respect to the wobbling frame would not change upon diffusion in the cone. When it was initially developped, this model was accounting for motions of the interaction of interest [192, 193]. In this situation, the second index of the Wigner matrices equals 0, and the third Euler angle does not play any role. This is not the case when the interaction frame is not the one undergoing the wobbling motion, and introducing this angle is essential to best describe the motions.

Expanding the expression of the Wigner matrices and performing the integration on φ_0 and φ leads to the condition $m = b-c = b'-c'$. Note that in the previous models, the condition $m = b = b'$ was obtained, which is correct when the interaction frame is the diffusing frame since $c = c' = 0$ [196, 197, 198]. We finally can write:

$$\boxed{\langle \mathcal{D}^{(2)*}_{b,c}(\Omega_{WF,SF},0)\mathcal{D}^{(2)}_{b',c'}(\Omega_{WF,SF},t)\rangle = \frac{\delta_{b-c,b'-c'}}{1-\mu_{cone}} \sum_{n=0}^{+\infty} \frac{e^{-D_W\nu_{b-c,n}(\nu_{b-c,n}+1)t}}{H_{b-c,n}(\mu_{cone})} I^n_{b,c}(\beta_{cone})I^n_{b',c'}(\beta_{cone})},$$

(4.50)

where:

$$I^n_{b,c}(\beta_{cone}) = \int_0^{\beta_{cone}} \sin\theta d_{b,c}(\theta) P^{b-c}_{\nu_{b-c,n}}(\cos\theta) d\theta. \tag{4.51}$$

The total correlation function is then:

$$C_{i,j}(t) = \frac{1}{5}\sum_{\kappa=1}^{5}\sum_{a,a'}\sum_{b,b'}\sum_{c,c'} a_{\kappa,a}a_{\kappa,a'}e^{-E_\kappa t}\mathcal{D}^{(2)*}_{a,b}(\Omega_{D,WF})\mathcal{D}^{(2)*}_{c,0}(\Omega_{SF,i})\mathcal{D}^{(2)}_{a',b'}(\Omega_{D,WF})\mathcal{D}^{(2)}_{c',0}(\Omega_{SF,j})\times$$
$$\sum_n \frac{\delta_{b-c,b'-c'}}{1-\mu_{cone}} \frac{e^{-D_W\nu_{b-c,n}(\nu_{b-c,n}+1)t}}{H_{b-c,n}(\mu_{cone})} I^n_{b,c}(\beta_{cone}) I^n_{b',c'}(\beta_{cone}). \tag{4.52}$$

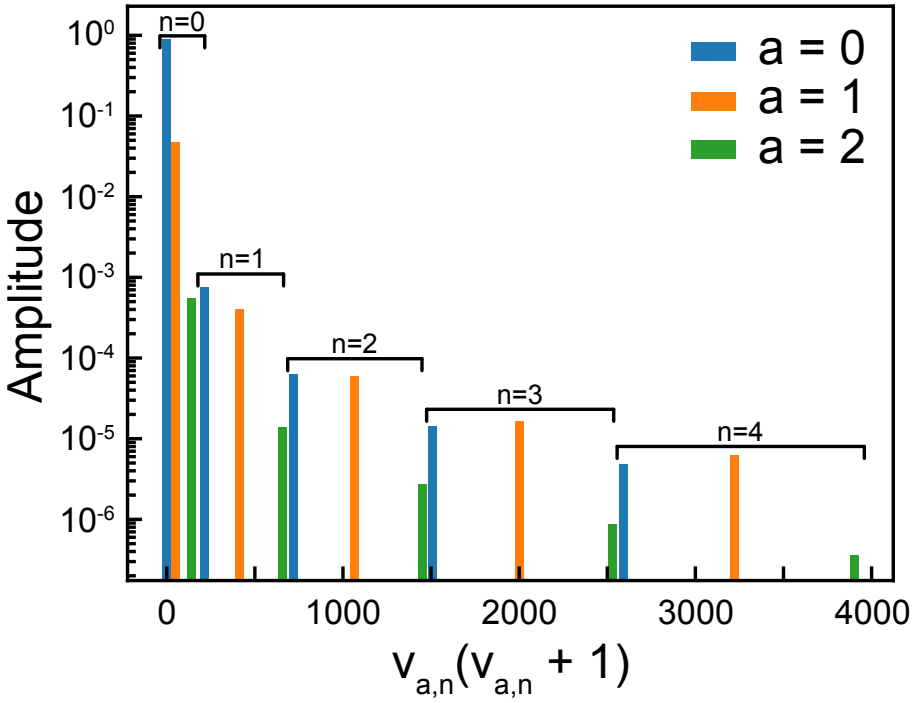

Figure 4.3: Value of $\nu_{a,n}(\nu_{a,n}+1)$ and associated pre-exponential factor for values of $a = 0, 1, 2$ and n ranging form 0 to 4 and cone semi-angle opening $\beta_{cone} = 15\,\text{deg}$. In the condition where the interaction frame is the interaction frame, cases where $a = -1$ and $a = -2$ are identical to $a = 1$ and $a = 2$ respectively.

In the following numerical evalutations of the correlation function for wobbling in a cone, the integrals $I^n_{b,c}(\beta_{cone})$ and $H_{b-c,n}(\mu_{cone})$ were computed using the Python Scipy library [136] with a limit of 30 in the sum of the Hypergeometric function part of the Legendre associated function (see Eq. A.18), a point at which the Hypergeometric function reached convergence in the conditions considered here. In addition, the sum limit over n has been set to 3 (only 4 eigenvalues for each values of $b-c$ are calculated) as the pre-exponential factor $\frac{I^n_{b,c}(\beta_{cone})I^n_{b',c'}(\beta_{cone})}{(1-\mu_{cone})H_{b-c,n}(\mu_{cone})}$

calculated for an interaction frame undergoing the wobbling motion (leading to $c = 0$) quickly drops, even for values of n higher than 2 (Fig. 4.3).

Wobbling in a cone order parameter The correlation function Eq. 4.50 is non-zero when $t \to +\infty$ for $b - c = n = 0$. Thus, we have:

$$\mathcal{S}^2_W(i,j) = \sum_b \sum_{c,c'} \frac{\delta_{b-c,0}\delta_{b-c',0}}{1-\mu_{cone}} \frac{I^0_{b,c}(\beta_{cone}) I^0_{b,c'}(\beta_{cone})}{H_{0,0}(\mu_{cone})} \mathcal{D}^{(2)*}_{c,0}(\Omega_{SF,i}) \mathcal{D}^{(2)}_{c',0}(\Omega_{SF,j}), \tag{4.53}$$

which, after using Eq. A.28, leads to:

$$\mathcal{S}^2_W(i,j) = \sum_b \left(\frac{I^0_{b,b}(\beta_{cone})}{1-\mu_{cone}} \right)^2 \mathcal{D}^{(2)*}_{b,0}(\Omega_{SF,i}) \mathcal{D}^{(2)}_{b,0}(\Omega_{SF,j}). \tag{4.54}$$

In the particular case where the interactions are undergoing the wobbling motions, we have $\Omega_{SF,i} = \Omega_{SF,j} = \{0,0,0\}$ and the order parameter simplifies into:

$$\mathcal{S}^2_W(i_W, j_W) = \left(\frac{I^0_{0,0}(\beta_{cone})}{1-\mu_{cone}} \right)^2, \tag{4.55}$$

where we write i_W and j_W to indicate that the interactions i and j are diffusing in a cone. Calculating $I^0_{0,0}$ is straightforward from Eq. 4.51:

$$I^0_{0,0}(\beta_{cone}) = \frac{1}{2} \cos\beta_{cone} \sin^2\beta_{cone}, \tag{4.56}$$

which leads to the order parameter reported by K. Kinosita *et al.* [192]:

$$\mathcal{S}^2_W(i_W, j_W) = \frac{1}{4} \cos^2\beta_{cone} (1 + \cos\beta_{cone})^2. \tag{4.57}$$

The general expression of the order parameter for interaction frames not necessarily aligned with the diffusing frame, and for the auto-correlation functions is:

$$\begin{aligned} \mathcal{S}^2_W(i,i) = & \frac{1}{(1-\cos\beta_{cone})^2} \left[\frac{1}{16} \cos^2\beta_{cone} \sin^4\beta_{cone} (3\cos^2\theta_{SF,i} - 1)^2 \right. \\ & + \frac{1}{12} \sin^4\frac{\beta_{cone}}{2} (3 + 7\cos\beta_{cone} + 2\cos 2\beta_{cone})^2 \sin^2\theta_{SF,i} \cos^2\theta_{SF,i} \\ & \left. \frac{1}{192} \sin^4\frac{\beta_{cone}}{2} (15 + 8\cos\beta_{cone} + \cos 2\beta_{cone})^2 \sin^4\theta_{SF,i} \right], \end{aligned} \tag{4.58}$$

which, in the case of interaction frames aligned with the diffusing frame, equals Eq. 4.57. The

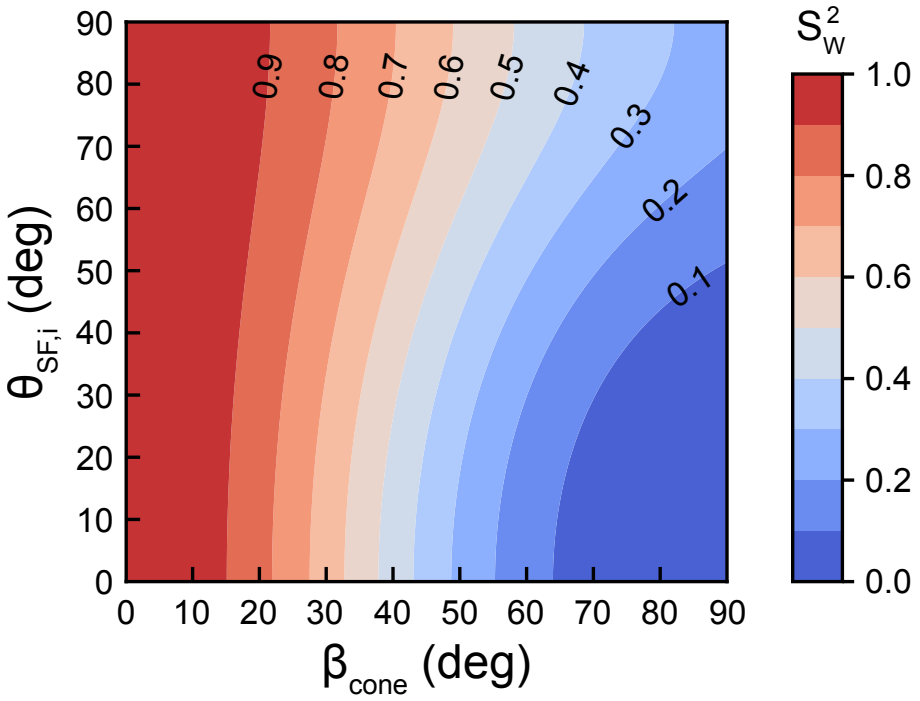

Figure 4.4: Wobbling in a cone order parameter (Eq. 4.58) as a function of the cone semi-angle opening (β_{cone}) and the angle between the interaction frame and the diffusing frame ($\theta_{SF,i}$). The order parameter is calculated assuming the two interactions have the same orientation with the diffusing frame.

evolution of the order parameter as a function of β_{cone} and $\theta_{SF,i}$ is shown in Fig. 4.4. As expected, for a fixed $\theta_{SF,i}$, it decreases when the amplitude of motions increases (*i.e.* when β_{cone} increases).

Discussion on the wobbling in a cone model The wobbling in a cone correlation function was built under the assumption of uniform probability distribution for the bond vector within the cone. This can be considered a strong hypothesis, in particular for amino-acid side-chains pointing toward the hydrophobic core of the protein where nearby atoms can hinder motions. Our MD simulation on Ubiquitin (*vide infra* for more details on the simulation) allows us to evaluate the amplitude of motions and obtain a direct measure of the density probability distributions for bond vectors. The probability density for Euler angles $\varphi_{WF,SF}$ and $\theta_{WF,SF}$ for transformation from the wobbling frame to the system frame (with main axis aligned along the

bond vector) are determined by:

$$\begin{aligned} p_{\varphi_{WF,SF}}(\varphi) &= \frac{n(\varphi,\delta\varphi)}{N\delta\varphi}, \\ p_{\theta_{WF,SF}}(\theta) &= \frac{n(\theta,\delta\theta)}{N\delta\theta\sin\theta}, \end{aligned} \tag{4.59}$$

where $n(\varphi,\delta\varphi)$ and $n(\theta,\delta\theta)$ are the number of Euler angles with values in the range $\varphi \pm \delta\varphi/2$ and $\theta \pm \delta\theta/2$ respectively, N is the number of frames in the MD simuations that were used for this calculation. The values of $\delta\varphi$ and $\delta\theta$ were set to 0.01 rad. To calculate the probability density for N-H bond motion and before calculating the Euler angles, the N-C_α and N-CO bond vectors were aligned to the first structure in the MD trajectory. Similarly, to calculate the probability density for $C_{\gamma 1}$-$C_{\delta 1}$ Euler angles, the C_β-$C_{\gamma 1}$ and $\overrightarrow{C_\alpha C_\beta} \wedge \overrightarrow{C_\beta C_{\gamma 1}}$ vectors were aligned to the corresponding vectors in the first MD frame. The main axis of the wobbling frame is defined as the averaged orientatation of the bond vector of interest in the MD. Probability densities are shown in Fig. 4.5a,b for the N-H and $C_{\gamma 1}$-$C_{\delta 1}$ bond vectors of isoleucine 30 of Ubiquitin, and clearly suggest that a uniform density probability distribution for the two Euler angles is not suitable to describe accurately the motions of these bond vectors. This can be better visualized in Fig. 4.5c where the carbon-$\delta 1$ does not sample the entire surface of a cone. Thus, studying bond libration motions using the wobbling in a cone model is not accurate, and introducing a MD-derived potential in the Master equation (Eq. 4.42) can potentially lead to a better description of this type of motion.

4.3.5 Contribution of each motion to relaxation

Now, we will evaluate here how each motion contribute to relaxation. Having an exhaustive analysis is not feasible and we will focus on typical relaxation rates: ^{13}C-R_1, ^{13}C-R_2 and ^{13}C-^{1}H-σ^{NOE} in a $^{13}C^1H^2H_2$ methyl group as encountered in a valine side-chain. The overall diffusion will be supposed to be isotropic with global tumbling correlation time $\tau_c = 10$ ns. The methyl rotation diffusion coefficient will be set to $D_{rot} = 5 \times 10^{10}\,\mathrm{s}^{-1}$, which leads to a correlation time for rotation of $\tau_{rot} = 6.1$ ps assuming the angle between the C-C and C-H bond is $\beta_{CCH} = 109.47$ deg:

$$\tau_{rot} = \frac{1}{1-\mathcal{S}^2_{rot}} \sum_{\substack{b=-2 \\ b\neq 0}}^{2} \frac{1}{b^2 D_{rot}} \left[d_{b,0}(\beta_{CCH})\right]^2, \tag{4.60}$$

where $\mathcal{S}^2_{rot} = [d_{0,0}(\beta_{CCH})]^2 = \left(\frac{3\cos^2\beta_{CCH}-1}{2}\right)^2$ is the methyl rotation squared order parameter. When a jump-type of motion is added, we will suppose that the valine side-chain can jump be-

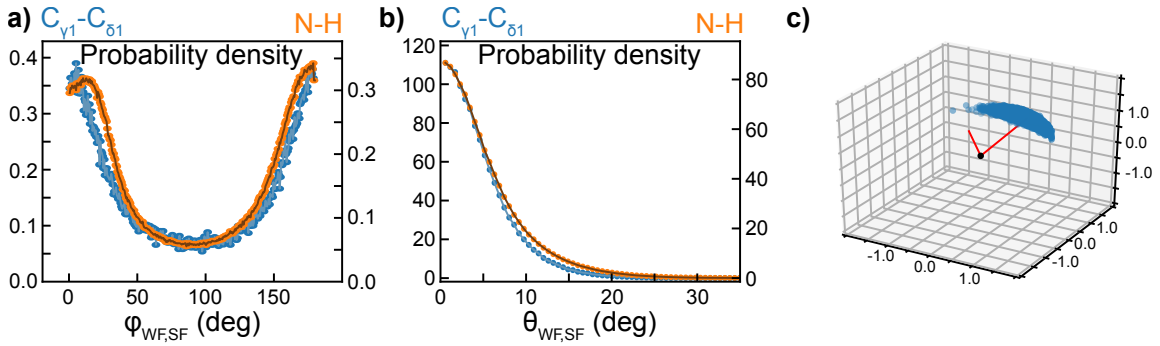

Figure 4.5: Local librations motions of selected bond vectors of isoleucine 30 from the MD simulation. Probability density for Euler angles $\varphi_{WF,SF}$ (**a**) and $\theta_{WF,SF}$ (**b**) for the $C_{\gamma 1}$-$C_{\delta 1}$ (blue) and N-H (orange) bond vectors. Points are connected by a line for visual clarity. **c)** Positions of the $C_{\delta 1}$ (blue dots) in the molecular frame. The $C_{\gamma 1}$ is shown as a black ball. The main axis of the wobbling frame is the red line pointing along the direction of the $C_{\gamma 1}$-$C_{\delta 1}$ bonds. The x-axis of the wobbling frame is also shown as a red line. Units of the axis of the molecular frames are Å.

tween three possible rotamer states, and we will distinguish the situation where each rotamers are equaly populated with equal exchange rate $k_{ex}^{sym} = 1/3 \times 10^{10}\,\mathrm{s}^{-1}$ between the different conformers (which leads to a correlation time for exchange of $\tau_{ex}^{sym} = 0.1\,\mathrm{ns}$), from the situation where $p_1 = 0.7$, $p_2 = 0.2$ and $p_3 = 0.1$ (the state numerotation is irrelevant since the global diffusion tensor is isotropic) and all exchange rates $k_{ij}^{asym} = 1/3 \times 10^{9}\,\mathrm{s}^{-1}$ with $i < j$ and k_{ij}^{asym} with $i > j$ is calculated to satisfy the microscropy reversibility condition (Eq. F.27) (which leads to a correlation time for exchange of $\tau_{ex}^{asym} = 0.18\,\mathrm{ns}$). The Euler angles associated to the jump motion are $\Omega_J = \{2n\pi/3, \beta_{CC}, 0\}$ where $n = 0, 1, 2$ and $\beta_{CC} = 76\,\mathrm{deg}$, which is typical for carbon side-chains. A wobbling in a cone motion of the $C_{\gamma 1}$-$C_{\delta 1}$ bond will also be considered, when mentioned. The cone semi-angle opening is set to 15 deg (results for opening angles of 5, 30 and 60 deg are shown in Appendix Fig. F.1), and the associated diffusion constant D_W is varied from 10^6 to $10^{10}\,\mathrm{s}^{-1}$, leading to variation of the wobbling correlation time from 1 ps to 10 ns approximately for this cone angle opening. Relaxation rates are calculated at a magnetic field of 14.1 T, and the carbon-13 CSA is set to 20 ppm.

The rotamer exchange contributes significantly to the relaxation (compare dash lines in Fig. 4.6), with an R_1 and σ^{NOE} increase by a factor 1.5 approximately, while R_2 decrease by a factor up to 3.8 when rotamer jumps motion with equal populations is introduced. The effect of the exchange is reduced for R_2 and σ^{NOE} when the populations are not equal, and increased for

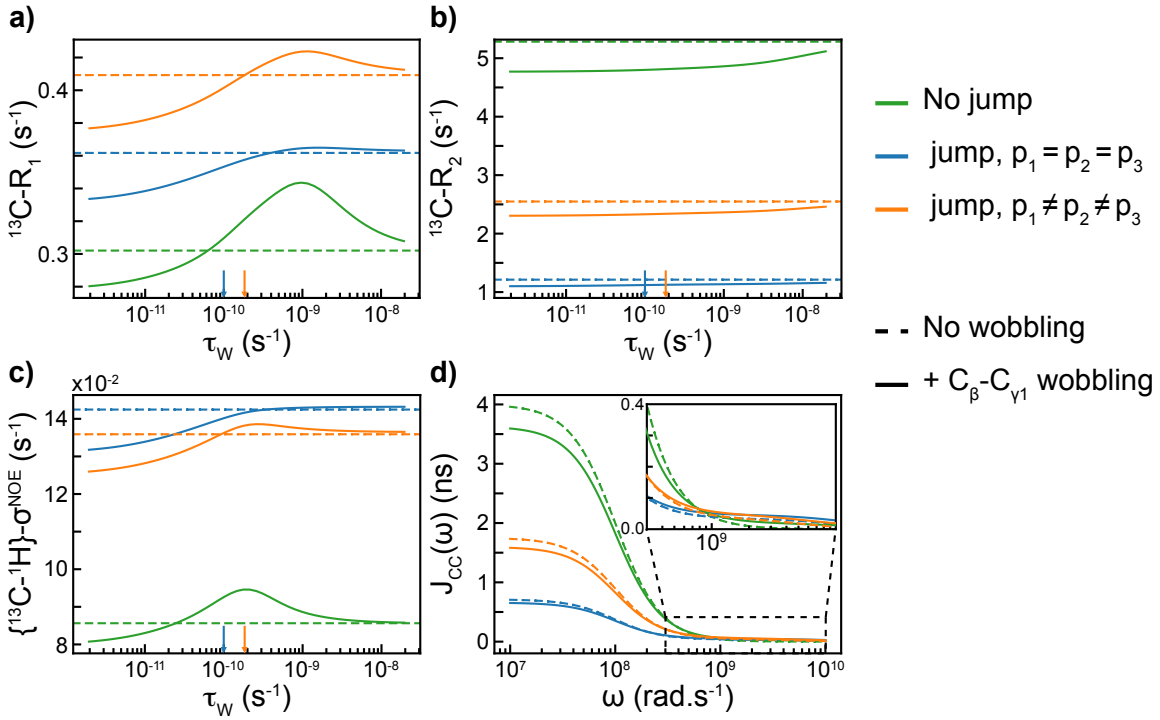

Figure 4.6: Contribution of rotamer jump and wobbling in a cone motions to relaxation. Carbon R_1 (**a**), R_2 (**b**) and carbon-proton σ^{NOE} (**c**) at 14.1 T in a $^{13}C^1H^2H_2$ valine methyl group, and associated spectral density funtion for the C_β-$C_{\gamma 1}$ bond auto-correlations. Dash lines show the value of the relaxation rates and spectral density function without wobbling. Relaxation rates (**a**-**c**) and spectral density function (**d**) calculated in the abscence of rotamer jump are shown in green. In the presence of rotamer jump, the case where all rotamer populations are equal (blue) and unequal (orange) are distinguished. In this later case, populations are $p_1 = 0.7$, $p_2 = 0.2$ and $p_1 = 0.1$. Calculations are shown as a function of the correlation time for wobbling, a function of the wobbling diffusion constant and cone semi-angle opening, set here to $\beta_{cone} = 15$ deg, while the diffusion constant D_W is varied from 10^6 to 10^{10} s^{-1}. The blue and orange vertical arrows indicate the values of the correlation time for rotamer jump, respectively when populations are equal and unequal. The spectral density functions are shown for $D_W = 10^8$ s^{-1}.

R_1. These effects can be rationalized by looking at the spectral density functions (Fig. 4.6d). In the presence of internal motions, the spectral density function tends to be higher at frequencies in the range 10^9-10^{10} rad.s^{-1}, which are frequencies R_1 and σ^{NOE} are sensitive to, leading to an increase of these rates. The higher contribution of medium-frequency motions to the spectral density function goes in pair with a decrease in the contribution of low-frequency motions, which is the main determinant in the value of the transverse relaxation rate R_2, explaining the large effects calculated in the presence of rotamer exchange.

On the other hand, the wobbling of the C_β-$C_{\gamma 1}$ bond has smaller effects on relaxation (Fig. 4.6) for the choosen cone semi-angle opening. It decreases the R_2, but the effect on longitudinal relaxation rates depends on the value of the diffusion constant D_W with fast diffusion (low τ_W) leading to a decrease in R_1 and σ^{NOE}, an increase for lower values of D_W (higher values of τ_W), and hardly any effects for very slow diffusion. These results can be rationalized using the same arguments as for the rotamer jump by analyzing the evolution of the spectral density function and the relative contribution of each frequency range to the value of the relaxation rates. These observations can be extended to proteins with higher global tumbling correlation time (Appendix Fig. F.2). It is interesting to notice the similarities between the evolution of the R_1 as a function of τ_W and the sensitivies calculated in the detector approach which characterizes the amount of motions in a given range of correlation times [202, 203, 31, 33].

The contribution of the wobbling motions increases with increasing cone semi-angle opening and can even become larger than the contribution of the rotamer jump (Appendix Fig. F.1). This can be explained by the value of order parameters, which act as weights for the Lorentzian terms of the spectral density containing contribution only from the global tumbling. The order parameters for rotamer exchange when population are equal and unequal are 0.17 and 0.43 respectively. In comparison, the wobbling order parameter equals 0.99, 0.90, 0.65 and 0.14 for values of cone semi-angle opening of 5, 15, 30 and 60 deg. Thus, for $\beta_{cone} = 60\,\mathrm{deg}$, the decreases in R_2 from either a rotamer exchange with equal population or the wobbling are similar for $\tau_W \approx \tau_{ex}^{sym}$ (Appendix Fig. F.1.h).

As a general rule of thumb, one can reasonably expect rotamer jump to be the major source of relaxation for methyl groups in aliphatic side-chains, since the amplitudes of wobbling are usually limited to small cone angle openings. This of course has to be carefully investigated before neglecting one motion, for example with the use of MD simulations.

4.4 Comparison with Model-Free correlation functions

The models presented in the previous section all share one property: they are complex. Up to 3 correlation times might be necessary to model the global tumbling; the number of decaying exponential describing rotamer jumps quickly increases as the number of accessible states increases; modeling the wobbling in a cone motion involves complex integral evaluations. Out of the 4 considered motions, the rotation on a cone seems the most simple one. In addition to their intrinsic complexity, another difficulty arises when analyzing data, in particular NMR relaxation rates: how to choose one model over the other without *a priori* knowledge of the type of motions involved? These aspects naturally led to the popularization of the Model-Free correlation function [15, 102] to model internal motions:

$$C_{MF}^{(i)}(t) = \mathcal{S}_{MF}^2 + (1 - \mathcal{S}_{MF}^2)e^{-t/\tau_{MF}}, \tag{4.61}$$

where $\mathcal{S}_{MF}^2$ is the squared order parameter and τ_{MF} an effective correlation time. The simplicity of this model makes it particularly attractive, and has indeed led to a number of successful analyses of NMR relaxation experiments [102, 204, 105, 106, 205, 206, 107, 108, 207, 109]. Over the past few decades, the MF has been modified in order to include the effect of cross correlation [103], or to include more than one correlation time and study more complex systems [74, 208, 72, 73], in particular **I**ntrinsically **D**isordered **P**roteins (IDP) [209, 210, 110, 167].

However, a series of question arises on this simple form of correlation function:

- The total correlation function results from the multiplication of the correlation functions accounting for internal motions (Eq. 4.61) and global tumbling. It is clear from section 4.3.1 that such factorization is possible only in the case of an isotropic diffusion tensor, which is the frame in which the MF was initially presented. An approximated form for the global tumbling correlation function in the case of an axially symmetric diffusion tensor was proposed as well, and consists in the sum of two decaying exponential, with decay constants and relative weights that can be determined experimentally [15]. Then, how is the factorization of the global tumbling and internal motion correlation functions affecting the fitted values of $\mathcal{S}_{MF}^2$ and τ_{MF}? It must be noted that the SRLS model of correlation function was introduced in part as an attempt to overcome this difficulty [71, 25, 27].

- The squared order parameter is of great interest as it relates NMR data to thermodynamic

quantities. M. Akke *et al.* initially related changes of order parameters to changes in free energy [161]. A relationship between order parameter and conformational entropy was later suggested and rationalized using a one-dimensional harmonic model [211]. An analytical relationship was proposed by D. Yang and L. Kay based on the wobbling in a cone model for backbone N-H^N and C^α-H^α, as well as side-chains N-H^N groups [23]. D.-W. Li and R. Brüschweiler extended the equation to side-chains C-C and C-H bonds motions by introducing amino-acid dependent parameters [24]. Recently, the group of J. Wand proposed an 'entropy meter' [212] to relate the order parameters to entropy changes empirically, assuming a linear relationship between the two. For all these different approaches, the analysis of NMR relaxation rates was essentially performed using the MF correlation function [213, 214, 212, 215, 216, 163, 217]. Then, do the MF order parameters accurately reflect on the amplitude of motions and can they be related to conformational entropy *quantitatively*?

- Only one of the presented internal motions can be modelled with a correlation function written as a mono-exponential decay: the instantaneous jumps between two rotamers. It is clear that the MF correlation time is effective and is more difficult to interpret than the order parameter when analyzing relaxation data since it contains contribution from multiple time constants. However, can it still represent approximately the time-scales for the motions involved? And is one decay time constant enough to analyze recorded relaxation rates?

- The MF correlation function contains only one order parameter and correlation time, such that it cannot accurately report on the amplitudes and time-scale of bonds undergoing more than one internal motion, such as a combination of a rotamer jump and a rotation on a cone. Modified versions of the MF correlation function has been suggested to take into account the complexity of motions in biomolecules, in particular for aliphatic side-chains [74, 21]. Then, are the fitted parameters of these models accurately reporting on the timescales and amplitudes of the motions involved?

These questions might be combined into a single one: are the parameters of the MF correlation function accurately reflecting the dynamic properties of the system under study? Here, we evaluate the accuracy of the MF to describe the parameters of the explicit models presented in preceding sections.

4.4.1 Global tumbling in the Model-Free correlation function

Here, we will evaluate the effect of the factorization of the global tumbling correlation function on the value of the fitted MF parameters. We will focus on auto-correlation only:

$$C(t) = \sum_{a,a'}\sum_{b,b'}\langle \mathcal{D}^{(2)*}_{q,a}(\Omega_{L,D},0)\mathcal{D}^{(2)}_{q,a'}(\Omega_{L,D},t)\rangle \mathcal{D}^{(2)*}_{a,b}(\Omega_{D,M})\mathcal{D}^{(2)}_{a'b'}(\Omega_{D,M})\times \\ \langle \mathcal{D}^{(2)*}_{b,0}(\Omega_{M,i},0)\mathcal{D}^{(2)}_{b',0}(\Omega_{M,i},t)\rangle, \tag{4.62}$$

where M denotes the frame in which the motion is best described, $\langle \mathcal{D}^{(2)*}_{q,a}(\Omega_{L,D},0)\mathcal{D}^{(2)}_{q,a'}(\Omega_{L,D},t)\rangle$ accounts for overall rotational diffusion, $\Omega_{D,SF}$ is the angle orienting the diffusing frame in the global diffusion tensor frame, and $\langle \mathcal{D}^{(2)*}_{b,0}(\Omega_{M,i},0)\mathcal{D}^{(2)}_{b',0}(\Omega_{M,i},t)\rangle$ accounts for internal motions. The MF correlation function is written as:

$$C_{MF}(t) = \left(\mathcal{S}^2_{MF} + (1-\mathcal{S}^2_{MF})e^{-t/\tau_{MF}}\right)\times \\ \sum_{a,a'}\langle \mathcal{D}^{(2)*}_{q,a}(\Omega_{L,D},0)\mathcal{D}^{(2)}_{q,a'}(\Omega_{L,D},t)\rangle \mathcal{D}^{(2)*}_{a,0}(\Omega_{D,M})\mathcal{D}^{(2)}_{a'0}(\Omega_{D,M}). \tag{4.63}$$

4.4.1.1 Details on the simulations

The order parameters and correlation times are fitted to the simulated accurate correlation function using the *scipy.optimize.curve_fit* function [136]. We detail here the value of the parameters for the accurate correlation function in the following simulations.

Global tumbling The global tumbling diffusion tensor eigenvalues have been set to $D_{xx} = 10^7\, s^{-1}$, $D_{yy} = 5\times 10^7\,\mathrm{s}^{-1}$ and $D_{zz} = 10^8\,\mathrm{s}^{-1}$. When the symmetric top model is used, the eigenvalues are $D_{\parallel} = D_{zz}$ and $D_{\perp} = \frac{1}{2}(D_{xx}+D_{yy})$. When the isotropic model is used, the global tumbling correlation time is equal to $\tau_c^{-1} = \frac{1}{3}(D_{xx}+D_{yy}+D_{zz})$. The two Euler angles defining $\Omega_{D,M} = \{\varphi_{D,M}, \theta_{D,M}, 0\}$ will each be incremented from 0 to π.

Jump model When modeling internal motions with the jump model, all populations will be considered equal. We will simulate a 2-state and 3-state jump model, with all exchange rates equal to $k_{ex} = 10^9\, s^{-1}$. In the 2-state jump model, the Euler angles orienting the interaction in the jump frame will be equal to $\Omega_{J,i} = \{\pm\frac{\pi}{2}, \beta_{CC}\}$ where $\beta_{CC} = 76\,\mathrm{deg}$, which is typical for carbon chains. In the 3-state jump model, the Euler angles are equal to $\Omega_{J,i} = \{\pm 2n\frac{\pi}{3}, \beta_{CC}\}$,

where $n = 0, 1, 2$. The internal correlation function is written as:

$$\langle \mathcal{D}^{(2)*}_{b,0}(\Omega_{M,i}, 0)\mathcal{D}^{(2)}_{b',0}(\Omega_{M,i}, t)\rangle = \sum_{\alpha,\beta}\sum_{n}\sqrt{p_\alpha p_\beta}\tilde{X}^{(n)}_{\alpha}\tilde{X}^{(n)}_{\beta}e^{\lambda_n t}\mathcal{D}^{(2)*}_{b,0}(\Omega_{M,i_\alpha})\mathcal{D}^{(2)}_{b',0}(\Omega_{M,i_\beta}), \quad (4.64)$$

where the same notations as in Section 4.3.2 are used.

Diffusion on a cone model In this case, the diffusion coefficient for rotation on the cone will be set to $D_{rot} = 10^{11}\,\mathrm{s}^{-1}$ and the cone semi-angle opening will be chosen so as to model a methyl group geometry $\beta_{cone} = 180 - 109.47 = 70.53\,\mathrm{deg}$. The internal correlation function is:

$$\langle \mathcal{D}^{(2)*}_{b,0}(\Omega_{M,i}, 0)\mathcal{D}^{(2)}_{b',0}(\Omega_{M,i}, t)\rangle = \delta_{bb'}e^{-b^2 D_{rot}t}\left[d_{b,0}(\beta_{cone})\right]^2. \quad (4.65)$$

Wobbling in a cone model In this last model, the diffusion coefficient will be equal to $D_W = 10^8\,\mathrm{s}^{-1}$ and the cone semi-angle opening is chosen to be $\beta_{cone} = 20\,\mathrm{deg}$. The interaction frame will be supposed to be aligned with the diffusing frame so that the correlation function for internal motions reads:

$$\langle \mathcal{D}^{(2)*}_{b,0}(\Omega_{M,i}, 0)\mathcal{D}^{(2)}_{b',0}(\Omega_{M,i}, t)\rangle = \delta_{bb'}\frac{1}{1-\mu_{cone}}\sum_{n}e^{-D_W\nu_{b,n}(\nu_{b,n}+1)t}\frac{\left[I^n_{b,0}(\beta_{cone})\right]^2}{H_{b,n}(\mu_{cone})}, \quad (4.66)$$

where the same notations as in Section 4.3.4 are used.

4.4.1.2 Isotropic global tumbling

In this simple case, the factorization of the global tumbling correlation function is exact and the correlation functions are written:

$$\begin{aligned} C(t) &= \frac{1}{5}e^{-t/\tau_c}\sum_{b=-2}^{2}\langle \mathcal{D}^{(2)*}_{b,0}(\Omega_{M,i}, 0)\mathcal{D}^{(2)}_{b,0}(\Omega_{M,i}, t)\rangle, \\ C_{MF}(t) &= \frac{1}{5}e^{-t/\tau_c}\left(\mathcal{S}^2_{MF} + (1-\mathcal{S}^2_{MF})e^{-t/\tau_{MF}}\right). \end{aligned} \quad (4.67)$$

Since the factorization is exact, the fitted parameters can be used as reference for the parameters fitted in the case of an asymmetric overall diffusion tensor. Fitted parameters are reported in Table 4.2. We will evaluate whether or not they correctly represent the internal dynamics in the following sections.

4.4.1.3 Asymmetric rotational diffusion tensor

In this case, the factorization of the global tumbling correlation function is not mathematically rigorous. The two correlation functions for the symmetrical top diffusion tensor read [15, 218]:

$$\begin{aligned} C(t) &= \frac{1}{5}\sum_{a=-2}^{2}\sum_{b,b'=-2}^{2} e^{-(6D_\perp+a^2(D_\parallel-D_\perp))t} d_{a,b}(\theta_{D,M}) d_{a,b'}(\theta_{D,M}) \times \\ &\qquad \langle \mathcal{D}^{(2)*}_{b,0}(\Omega_{M,i},0)\mathcal{D}^{(2)}_{b,0}(\Omega_{M,i},t)\rangle, \\ C_{MF}(t) &= \frac{1}{5}\left(\mathcal{S}^2_{MF} + (1-\mathcal{S}^2_{MF})e^{-t/\tau_{MF}}\right)\sum_{a=-2}^{2} e^{-(6D_\perp+a^2(D_\parallel-D_\perp))t}\left[d_{a,0}(\theta_{D,M})\right]^2, \end{aligned} \tag{4.68}$$

and for the fully asymmetric tensor [106]:

$$\begin{aligned} C(t) &= \frac{1}{5}\sum_{a,a'=-2}^{2}\sum_{b,b'=-2}^{2}\sum_{\kappa=1}^{5} a_{\kappa,a}a_{\kappa,a'}e^{-E_\kappa t}e^{i\varphi_{D,M}(a-a')} d_{a,b}(\theta_{D,M}) d_{a,b'}(\theta_{D,M}) \times \\ &\qquad \langle \mathcal{D}^{(2)*}_{b,0}(\Omega_{M,i},0)\mathcal{D}^{(2)}_{b,0}(\Omega_{M,i},t)\rangle, \\ C_{MF}(t) &= \frac{1}{5}\left(\mathcal{S}^2_{MF} + (1-\mathcal{S}^2_{MF})e^{-t/\tau_{MF}}\right) \times \\ &\qquad \sum_{a,a'=-2}^{2}\sum_{\kappa=1}^{5} a_{\kappa,a}a_{\kappa,a'}e^{-E_\kappa t}e^{i\varphi_{D,M}(a-a')}\left[d_{a,0}(\theta_{D,M})\right]^2. \end{aligned} \tag{4.69}$$

We can note here that, the MF correlation function cannot distinguish the orientation of the interaction frames in the diffusion frame, which is particularly critical in the presence of a rotamer jump motion. The fitted MF parameters agree well with the ones obtained when simulating an isotropic global tumbling, except in the case of the two-state jump model where large deviations of the fitted parameters are obtained when $\Omega_{D,M}$ is changed (Table 4.2, top). J. Wand and co-workers already distinguished the 2-state and 3-state jump models by considering the resulting symmetry [219]. In the case of 3 exchanging states with equal populations, the motions is azymutal symmetric, that is:

$$\langle x^2\rangle = \langle y^2\rangle, \;\; \langle x\rangle = \langle y\rangle = 0, \;\; \text{and} \;\; \langle xy\rangle = 0, \tag{4.70}$$

where $\langle\cdots\rangle$ denotes an ensemble average, and x and y are the x- and $y-$coordinates of the interaction frame in the jump frame (labelled M in this section). In the case of the 2-state jump model presented here, the first condition in Eq. 4.70 is not fulfilled. It is not fulfilled neither when populations in the 3-state jump model are not equal, in which case the factorization of the asymmetric global tumbling correlation functions does not accurately reproduces MF

Table 4.2: Values of the fitted MF parameters (correlation function Eq. 4.63) for 4 types of internal motions and the three possible symmetry property of the overal diffusion tensor. In the case of the symmetric top and fully asymmetric overal diffusion tensor, the reported values and errors correspond to the average and standard deviation over the simulations with different values of $\theta_{D,M}$ and $\{\varphi_{D,M}, \theta_{D,M}\}$ respectively. The 3-state jump model with unequal populations (bottom row) was simulated with $p_1 = 0.7$, $p_2 = 0.2$ and $p_3 = 0.1$.

	Isotropic		Symmetric top		Fully asymmetric	
	$\mathcal{S}^2_{MF}$	τ_{MF} (ps)	$\mathcal{S}^2_{MF}$	τ_{MF} (ps)	$\mathcal{S}^2_{MF}$	τ_{MF} (ps)
2-state jump $p_1 = p_2$	0.82	612	0.56 ± 0.24	$1,368 \pm 709$	0.52 ± 0.29	$1,840 \pm 1,181$
3-state jump $p_1 = p_2 = p_3$	0.16	319	0.16 ± 0.01	331 ± 21	0.17 ± 0.00	329 ± 20
rotation	0.12	4.5	0.12 ± 0.00	4.7 ± 0.0	0.11 ± 0.00	4.9 ± 0.0
wobbling	0.83	340	0.83 ± 0.00	348 ± 27	0.83 ± 0.00	351 ± 27
3-state jump $p_1 \neq p_2 \neq p_3$	0.43	153	0.43 ± 0.11	188 ± 117	0.42 ± 0.12	186 ± 169

parameters obtained in the isotropic tumbling case, and show large deviations depending on the orientation in the diffusion tensor frame (Table 4.2, bottom).

These simulations suggest that the factorization of the global tumbling correlation function does not affect the value of the fitted parameters in the presence of a diffusing-type of internal motions (that is diffusion on a cone or wobbling in a cone). When the sampling of the conformational space is discrete (jump model), the factorization does not affect the value of the MF fitted parameters when the motion has azymutal symmetry, a strong condition that may not be met in most cases. This result is in contradiction with results of J. Wand and co-workers who concluded that the MF correlation function is robust in the 3-state jump model, even if populations are not equal [219]. A strong difference between our simulations and their study is the fact that the conclusion of the authors is based only on simulations of the internal correlation function. In this subsection, we did not compare the values of the fitted parameters with the ones choosen for the simulations such that MF fitted parameters might reproduce expected ones, as suggested by the authors [219]. The conclusions brought here only concern

the factorization of the global tumbling correlation function, which in the case of a jump-like motion without azymutal symmetry in an asymmetric diffusion tensor affects the value of the fitted parameters. These aspects were not investigated in the original paper [219].

4.4.2 Accuracy of the Model-Free fitted parameters

Here, we will evaluate if the MF order parameter matches the expected one, and if the MF correlation time reports on the correct time-scales for the internal motions. Based on the previous conclusions, we will only consider the diffusing-like motions and a jump motion with azymutal symmetry. In addition, for the sake of simplicity, we will consider that the global tumbling is isotropic. In this case, we will not simulate the decay associated with the overall diffusion so that the time-scales of each motion can arbitrarily be set to unity.

4.4.2.1 Jump model

Since we only consider azymutal symmetric motion, we will restrict ourselves here to a 3-state jump model with equal equilibrium population for each state, and equal exchange rate between each state. The global tumbling motion is not considered in the simulations so that the exchange rate will be taken equal to $k_{ex} = 1\,\text{a.u.}$ without loss of generality. In addition, we will consider the case where the interaction frame is not necessarily aligned with the rotamer frame (*i.e.* the frame undergoing the jump motions), and is oriented with Euler angles $\Omega_{R,i} = \{\varphi_{R,i}, \theta_{R,i}\}$ in the rotamer frame. The correlation function is then written as:

$$C(t) = \sum_{b} \sum_{c,c'} \sum_{\alpha,\beta} \sum_{n} \sqrt{p_\alpha p_\beta} \tilde{X}_\alpha^{(n)} \tilde{X}_\beta^{(n)} e^{\lambda_n t} \times \mathcal{D}_{b,c}^{(2)*}(\Omega_{J,R_\alpha}) \mathcal{D}_{b,c'}^{(2)}(\Omega_{J,R_\beta}) \mathcal{D}_{c,0}^{(2)*}(\Omega_{R,i}) \mathcal{D}_{c,0}^{(2)}(\Omega_{R,i}), \tag{4.71}$$

which is can be compacted into:

$$C(t) = \sum_{\alpha,\beta} \sum_{n} \sqrt{p_\alpha p_\beta} \tilde{X}_\alpha^{(n)} \tilde{X}_\beta^{(n)} e^{\lambda_n t} \mathcal{P}_2(\cos\theta_{i_\alpha, i_\beta}), \tag{4.72}$$

where $\theta_{i_\alpha, i_\beta}$ is the angle between the interaction-i main axis in rotamers α and β. We will compare the expected and fitted MF order parameter and correlation time as a function of the angles $\varphi_{R,i}$ and $\theta_{R,i}$. First, we can show that the expected correlation time is independent from

the internal geometry of the system:

$$\tau_{MF} = \frac{1}{1-\mathcal{S}^2} \sum_{n>0} \sum_{\alpha,\beta} \frac{-1}{\lambda_n} \sqrt{p_\alpha p_\beta} \tilde{X}_\alpha^{(n)} \tilde{X}_\beta^{(n)} \mathcal{P}_2(\cos\theta_{i_\alpha,i_\beta}). \tag{4.73}$$

In this particular case where all populations are equal, the eigenvalues $\lambda_n, n > 0$ are degenerate and equal to $-3k_{ex}$ such that:

$$\tau_{MF} = \frac{1}{3k_{ex}} \frac{1}{1-\mathcal{S}^2} \sum_{n>0} \sum_{\alpha,\beta} \sqrt{p_\alpha p_\beta} \tilde{X}_\alpha^{(n)} \tilde{X}_\beta^{(n)} \mathcal{P}_2(\cos\theta_{i_\alpha,i_\beta}). \tag{4.74}$$

The sum over the variable n can be extended to $n = 0$, provided the order parameter is then substracted (the element of the sum evaluated for $n = 0$ equals the order parameter, see section 4.3.2):

$$\tau_{MF} = \frac{1}{3k_{ex}} \frac{1}{1-\mathcal{S}^2} \left(\sum_{n} \sum_{\alpha,\beta} \sqrt{p_\alpha p_\beta} \tilde{X}_\alpha^{(n)} \tilde{X}_\beta^{(n)} \mathcal{P}_2(\cos\theta_{i_\alpha,i_\beta}) - \mathcal{S}^2 \right). \tag{4.75}$$

We can now recognize that the sum equals the correlation function at $t = 0$, which, for auto-correlation of internal motions, equals to 1, such that we finally obtain:

$$\tau_{MF} = \frac{1}{3k_{ex}}. \tag{4.76}$$

In the case presented here, the MF correlation time is equal to 1/3 a.u..

Simulating and fitting 400 different correlation functions calculated for 20 angles $\varphi_{R,i}$ and $\theta_{R,i}$ varying from 0 to $\pi/2$ leads to a fitted MF correlation time of $\tau_{ex}^F = 0.33 \pm (4.9 \times 10^{-7})$ a.u. (average and standard deviation calculated for the 400 cases), which is in perfect agreement with the expected correlation time, and is indeed independent from the internal geometry. This result shows that the MF correlation function can accurately report on the exchange rate of an azymutal symmetric jump motion. It can also perfectly reproduce the expected order parameter (Fig. 4.7a). However, its value strongly depends on the orientation of the interaction frame in the rotamer frame (Fig. 4.7b). Indeed, it does not report on the amplitude of motions of the bond undergoing the jumps, but on the amplitude of motions of the interaction frame, bound to the jumping frame. Note that in the simple case presented here, the interaction frame is fixed in the rotamer frame such that a change of jump frame can lead to $\Omega_{R,i} = \{0, 0\}$. When other motions are involved, this might not be possible.

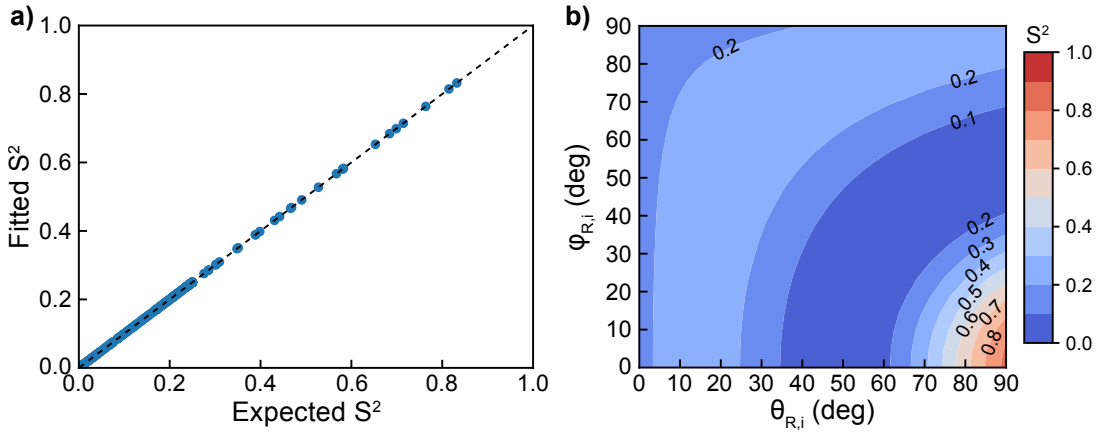

Figure 4.7: Comparison between the expected and fitted MF order parameters in the case of a 3-state jump model with azymutal symmetry. **a)** Correlation plot between the expected (Eq. 4.34) and fitted order parameters for different Euler angles $\Omega_{R,i} = \{\varphi_{R,i}, \theta_{R,i}\}$ orienting the interaction frame in the rotamer frame. The dash line is shown as a guide for perfect equality between the two order parameters. **b)** Contour plot of the expected order parameter as a function of the Euler angles orienting the interaction frame in the rotamer frame $\Omega_{R,i} = \{\varphi_{R,i}, \theta_{R,i}\}$.

4.4.2.2 Methyl rotation

Here, we will consider the diffusion on a cone motion, applied to methyl group rotation around the C-C symmetry axis. The restriction to this particular moiety is not strongly limitting: this model does not apply to other common chemical bond motions in biomolecules which are *a priori* better modeled with the wobbling in a cone type of correlation functions. Following the approach presented for the jump motion, we will consider the overall tumbling to be isotropic and it will not be simulated. The diffusion constant for rotation on the cone will be taken equal to $D_{rot} = 1\,\text{a.u.}$, and the angle between the C-C and C-H bonds is $\beta_{cone} = 109.47\,\text{deg}$. We can calculate the correlation function for motions of the C-H and H-H dipolar interactions:

$$\begin{aligned} C_{CH}(t) &= \sum_{b=-2}^{2} e^{-b^2 D_{rot} t} \left[d_{b,0}(\beta_{cone})\right]^2, \\ C_{HH}(t) &= \frac{1}{4}\left(1 + 3e^{-4D_{rot}t}\right) = \frac{1}{4} + \left(1 - \frac{1}{4}\right) e^{-4D_{rot}t}, \end{aligned} \tag{4.77}$$

where we have used the fact that the H-H and C-C bond are orthogonal to write C_{HH}. As can be seen in Eq. 4.77, the correlation function for H-H motions is already written in the form of a MF type of correlation function, with order parameter 1/4 and correlation time $1/(4D_{rot})$. Nor surprisingly, it is perfectly fitted with a MF correlation function, and the fitted parameters

correspond to the expected ones (Fig. 4.8a). However, a single exponential decay does not perfectly reproduce the simulated correlation function for C-H motions (Fig. 4.8b). The order parameter is slightly overestimated and the correlation time underestimated by 20 %. The methyl-group order parameter is well-described for each type of possible interactions, and is usually not fitted. Critically however, a unique motion (the rotation of a methyl group) leads to *two distinct correlation times* depending on whether C-H or H-H motions are probed. These results show that:

- since order parameters for methyl-groups rotation are of little interest and usually never fitted, an MF correlation function can be used to model methyl group rotation. The fitted correlation time is underestimated, but the order of magnitude will be correct.

- for the analysis of methyl-groups relaxation properties, a single MF spectral density function can not be used for C-H and H-H dipolar interactions associated spectral density functions. A scaling factor of 2 has to be applied to the correlation time for C-H motions.

- the analysis of MF correlation time for methyl rotation can easily be interpreted to extract the diffusion constant for methyl rotation.

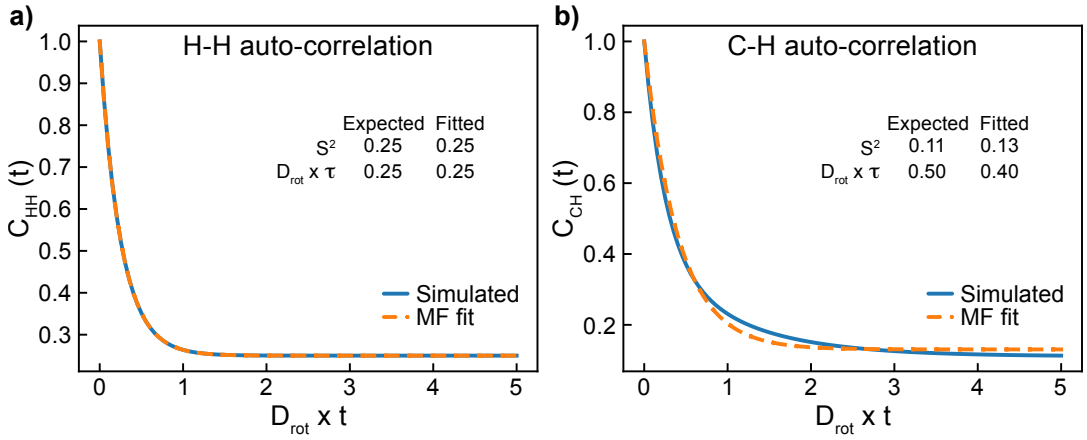

Figure 4.8: Correlation function for methyl group rotation. Auto-correlation function for H-H (**a**) and C-H (**b**) motions. Simulated correlation function are shown in blue, and MF fit in dash orange. The correlation functions are shown as a function of $D_{rot} \times t$ such that they are independent of the diffusion constant D_{rot}. The expected and fitted MF parameters are shown on each pannel.

4.4.2.3 Wobbling in a cone

We now turn to the last internal motion considered in this section: diffusion in a cone. Again, and without loss of generality, the diffusion constant will be supposed to be equal to $D_W = 1$ a.u.. We will only consider cone semi-angle opening lower than $\pi/3$ which covers most of the bond motions in folded biomolecules.

Interaction frame aligned with the diffusing frame We first consider the simpler case where the interaction frame is the diffusing frame. The correlation function simulated here is written as:

$$C(t) = \frac{1}{1-\mu_{cone}} \sum_{b=-2}^{2} \sum_{n} \frac{\left[I^n_{b,0}(\beta_{cone})\right]^2}{H_{b,n}(\mu_{cone})} e^{-D_W \nu_{b,n}(\nu_{b,n}+1)t}, \tag{4.78}$$

using the same notations as in section 4.3.4. Fitting the simulated correlation functions reproduces well the expected values for the order parameter and correlation time for cone semi-angle opening lower than 30 deg (Fig. 4.9). The agreement between the expected and fitted order parameter is still satisfactory for larger cone opening, and the correlation time can still report on the order of magnitude for the time scale of motion, provided the dependence in cone semi-angle opening is taken into account (see y-scale in Fig. 4.9b).

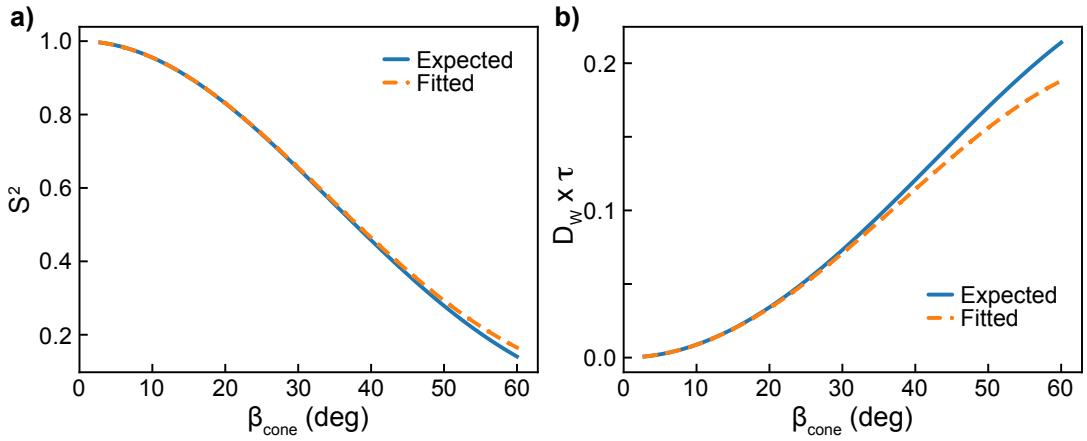

Figure 4.9: Order parameter (**a**) and correlation time (**b**) as a function of the cone semi-angle opening for an interaction frame undergoing a wobbling in a cone type of motion. The expected values are shown as a solid blue line and the fitted ones as a dashed orange line.

Interaction frame not aligned with the diffusing frame In the case where the interaction frame is not aligned with the diffusing frame but is oriented with Euler angles

$\Omega_{SF,i} = \{\varphi_{SF,i}, \theta_{SF,i}\}$, the correlation function reads:

$$C(t) = \frac{1}{1-\mu_{cone}} \sum_{b=-2}^{2} \sum_{c=-2}^{2} \sum_{n} \frac{\left[I^n_{b,c}(\beta_{cone})\right]^2}{H_{b-c,n}(\mu_{cone})} e^{-D_W \nu_{b-c,n}(\nu_{b-c,n}+1)t} \left[d_{c,0}(\theta_{SF,i})\right]^2 , \tag{4.79}$$

which is independent from the first Euler angle $\varphi_{SF,i}$. The expected order parameters and correlation time are well reproduced by the MF correlation function (Fig. 4.10). For large cone semi-angle opening ($\beta_{cone} = 60\,\text{deg}$), a small deviation in the order parameter is observed, and the correlation time still reports on the order of magnitude of the time-scales involved with a systematic error lower than 10 %. It can also be noted that while the order parameter shows a dependence in Euler angle $\theta_{SF,i}$, the correlation time has only a small dependence in internal geometry.

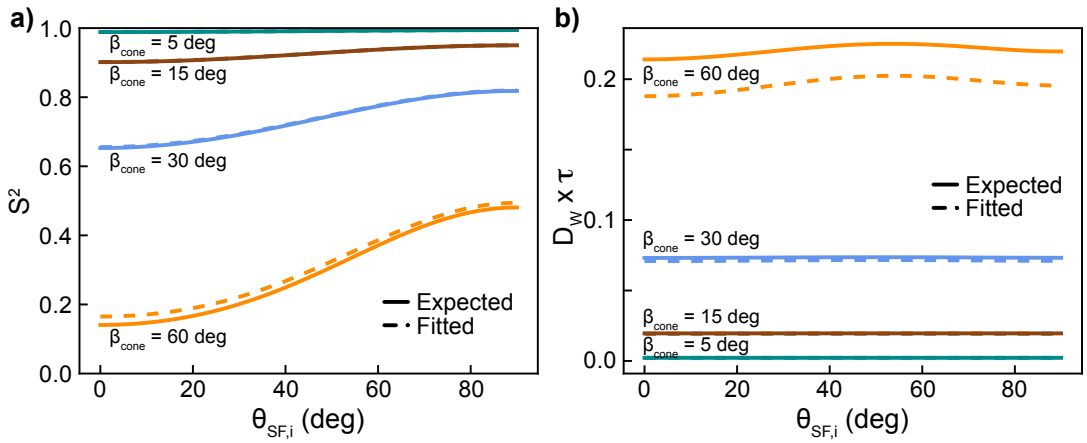

Figure 4.10: Order parameter (**a**) and correlation time (**b**) as a function of the cone semi-angle opening for an interaction frame attached to a frame diffusing in a cone. The expected values are shown in solid lines and the fitted ones in dash lines. Calculations were performed for 4 cone semi-angles opening.

4.4.3 Model-Free in the presence of uncorrelated motions

Motions in biomolecules can be far more complex than the superposition of one of the aforementioned internal motions and global tumbling. We will investigate here to what extend MF correlation functions accurately report on order parameters and correlation times for the motions involved. Instead of fitting simulated correlation functions, we will here calculate and fit relaxation rates for a $^{13}C^1H^2H_2$ methyl group of a valine in a protein. We will only consider carbon longitudinal and transverse auto-relaxation rates, as well as the ^{13}C-^1H DD cross-relaxation

rate, at magnetic fields of 9.4, 14.1, 18.8, 23.5 and 28.2 T. Equations for the relaxation rates can be found in Appendix C.3. The ^{13}C-CSA is supposed to be axially symmetric with value 20 ppm.

4.4.3.1 Method

The protein will be suposed to tumble isotropically, with a global tumbling correlation time of $\tau_c = 10\,\text{ns}$. The methyl rotation is included, with a diffusion coefficient $D_{rot} = 5 \times 10^{10}\,\text{s}^{-1}$ and a cone opening for the rotation of $\beta_{CCH} = 70.53\,\text{deg}$. We will first consider only one additional internal motion, and the three following cases will be simulated:

- a wobbling in a cone motion, with cone semi-angle opening of $\beta_{cone} = 15\,\text{deg}$ and diffusion cofficient $D_W = 10^7\,\text{s}^{-1}$;
- a 3-state rotamer exchange motion with azymutal symmetry and exchange rate between each state equal to $k_{ex} = 1/3 \times 10^9\,\text{s}^{-1}$;
- a 3-state rotamer exchange motion with same geometric parameters, but with $p_1 = 0.7$, $p_2 = 0.2$ and $p_3 = 0.1$ (the state labelling is irrelevant since the global tumbling is isotropic) and $k_{ij} = 1/3 \times 10^9\,\text{s}^{-1}$, $i < j$.

The spectral density functions for the C-H and C-C auto-correlation when the wobbling is included are:

$$\begin{aligned}
\mathcal{J}^W_{CH}(\omega) &= \frac{2}{5}\sum_{b=-2}^{2}\sum_{c=-2}^{2}\sum_{n}\frac{\tau^W_{b,c,n}}{1+(\omega\tau^W_{b,c,n})^2}\frac{1}{1-\mu_{cone}}\frac{\left[I^n_{b,c}(\beta_{cone})\right]^2}{H_{b-c,n}(\mu_{cone})}\left[d_{c,0}(\beta_{CCH})\right]^2, \\
\mathcal{J}^W_{CC}(\omega) &= \frac{2}{5}\sum_{b=-2}^{2}\sum_{n}\frac{\tau^W_{b,0,n}}{1+(\omega\tau^W_{b,0,n})^2}\frac{1}{1-\mu_{cone}}\frac{\left[I^n_{b,0}(\beta_{cone})\right]^2}{H_{b,n}(\mu_{cone})}
\end{aligned} \tag{4.80}$$

and when the rotamer exchange is included:

$$\begin{aligned}
\mathcal{J}^{Ex}_{CH}(\omega) =& \frac{2}{5}\sum_{b=-2}^{2}\sum_{c=-2}^{2}\sum_{\alpha,\beta}\sum_{n=0}^{2}\frac{\tau^{Ex}_{b,c,n}}{1+(\omega\tau^{Ex}_{b,c,n})^2}\sqrt{p_\alpha p_\beta}\tilde{X}^{(n)}_\alpha\tilde{X}^{(n)}_\beta\mathcal{D}^{(2)*}_{b,c}(\Omega_{J,R_\alpha})\mathcal{D}^{(2)}_{b,c}(\Omega_{J,R_\beta})\times \\
& \left[d_{c,0}(\beta_{CCH})\right]^2, \\
\mathcal{J}^{Ex}_{CC}(\omega) =& \frac{2}{5}\sum_{b=-2}^{2}\sum_{\alpha,\beta}\sum_{n=0}^{2}\frac{\tau^{Ex}_{b,0,n}}{1+(\omega\tau^{Ex}_{b,0,n})^2}\sqrt{p_\alpha p_\beta}\tilde{X}^{(n)}_\alpha\tilde{X}^{(n)}_\beta\mathcal{D}^{(2)*}_{b,0}(\Omega_{J,R_\alpha})\mathcal{D}^{(2)}_{b,0}(\Omega_{J,R_\beta}),
\end{aligned} \tag{4.81}$$

with the same notations as above and:

$$\begin{aligned}(\tau^{W}_{b,c,n})^{-1} &= \tau_c^{-1} + D_W\nu_{b-c,n}(\nu_{b-c,n}+1) + c^2 D_{rot},\\ (\tau^{Ex}_{b,c,n})^{-1} &= \tau_c^{-1} - \lambda_n + c^2 D_{rot}.\end{aligned} \tag{4.82}$$

When three motions are included, we will consider that the wobbling affects the rotamer frame which exchanges between 3-states. The same parameters as before will be used such that two cases will be distinguished (exchange with or without azymutal symmetry), except that the coefficient for diffusion in a cone will be increased to $D'_W = 10^8\,\mathrm{s}^{-1}$. The spectral density functions are written:

$$\begin{aligned}\mathcal{J}^{Ex,W}_{CH}(\omega) =& \frac{2}{5}\sum_{b,c,d}\sum_{\alpha,\beta}\sum_{n=0}^{2}\sum_{m}\frac{\tau^{n,m}_{b,c,d}}{1+(\omega\tau^{n,m}_{b,c,d})^2}\sqrt{p_\alpha p_\beta}\tilde{X}^{(n)}_{\alpha}\tilde{X}^{(n)}_{\beta}\frac{1}{1-\mu_{cone}}\frac{\left[I^m_{c,d}(\beta_{cone})\right]^2}{H_{c-d,m}(\mu_{cone})}\times\\ & \mathcal{D}^{(2)*}_{b,c}(\Omega_{J,R_\alpha})\mathcal{D}^{(2)}_{b,c}(\Omega_{J,R_\beta})\left[d_{d,0}(\beta_{CCH})\right]^2,\\ \mathcal{J}^{Ex,W}_{CC}(\omega) =& \frac{2}{5}\sum_{b,c}\sum_{\alpha,\beta}\sum_{n=0}^{2}\sum_{m}\frac{\tau^{n,m}_{b,c,0}}{1+(\omega\tau^{n,m}_{b,c,0})^2}\sqrt{p_\alpha p_\beta}\tilde{X}^{(n)}_{\alpha}\tilde{X}^{(n)}_{\beta}\frac{1}{1-\mu_{cone}}\frac{\left[I^m_{c,0}(\beta_{cone})\right]^2}{H_{c,m}(\mu_{cone})}\times\\ & \mathcal{D}^{(2)*}_{b,c}(\Omega_{J,R_\alpha})\mathcal{D}^{(2)}_{b,c}(\Omega_{J,R_\beta}),\end{aligned} \tag{4.83}$$

with:

$$(\tau^{n,m}_{b,c,d})^{-1} = \tau_c^{-1} - \lambda_n + D'_W\nu_{c-d,m}(\nu_{c-d,m}+1) + d^2 D_{rot}. \tag{4.84}$$

A **M**arkov-**C**hain **M**onte-**C**arlo (MCMC) analysis is used to obtain MF [15] and EMF [74] parameters for the internal motions. The associated following spectral density functions are [15, 74, 130, 21]:

$$\begin{aligned}\mathcal{J}^{MF}_{CH}(\omega) =& \frac{2}{5}\mathcal{S}^2_m\left(\mathcal{S}^2\frac{\tau_c}{1+(\omega\tau_c)^2} + (1-\mathcal{S}^2)\frac{\tau'_i}{1+(\omega\tau'_i)^2}\right)\\ & + \frac{2}{5}(1-\mathcal{S}^2_m)\left(\mathcal{S}^2\frac{\tau'_m}{1+(\omega\tau'_m)^2} + (1-\mathcal{S}^2)\frac{\tau''_i}{1+(\omega\tau''_i)^2}\right),\\ \mathcal{J}^{MF}_{CC}(\omega) =& \frac{2}{5}\left(\mathcal{S}^2_{MF}\frac{\tau_c}{1+(\omega\tau_c)^2} + (1-\mathcal{S}^2_{MF})\frac{\tau'_i}{1+(\omega\tau'_i)^2}\right),\end{aligned} \tag{4.85}$$

Table 4.3: Values of MF parameters obtained from fitting carbon-13 longitudinal and transverse relaxation rates and ^{13}C-^{1}H DD cross-relaxation rates at 5 different fields compared with the expected parameters for a $^{13}C^{1}H^{2}H_{2}$ methyl group on a protein with isotropic global tumbling correlation time $\tau_c = 10\,$ns, undergoing rotation and one of the 3 considered motions. The error is obtained from the parameters distribution following the MCMC analysis of the simulated relaxation rates.

	$\mathcal{S}^2$		τ_i (ns)		τ_m (ps)	
	expected	fitted	expected	fitted	expected	fitted
C-C wobbling	0.90	0.87 ± 0.04	1.96	4.75 ± 3.03	10.0	10.1 ± 0.24
Symmetric jump	0.17	0.17 ± 0.01	1.00	1.02 ± 0.13	10.0	9.89 ± 0.35
Asymmetric jump	0.43	0.43 ± 0.03	1.84	1.82 ± 0.38	10.0	9.94 ± 0.34

$$
\begin{aligned}
\mathcal{J}_{CH}^{EMF}(\omega) =& \frac{2}{5}\mathcal{S}_m^2\left(\mathcal{S}_1^2\mathcal{S}_2^2\frac{\tau_c}{1+(\omega\tau_c)^2} + (1-\mathcal{S}_1^2)\frac{\tau_1'}{1+(\omega\tau_1')^2} + \mathcal{S}_1^2(1-\mathcal{S}_2^2)\frac{\tau_2'}{1+(\omega\tau_2')^2}\right) \\
& \frac{2}{5}(1-\mathcal{S}_m^2)\left(\mathcal{S}_1^2\mathcal{S}_2^2\frac{\tau_m'}{1+(\omega\tau_m')^2} + (1-\mathcal{S}_1^2)\frac{\tau_1''}{1+(\omega\tau_1'')^2} + \right. \\
& \left. \mathcal{S}_1^2(1-\mathcal{S}_2^2)\frac{\tau_2''}{1+(\omega\tau_2'')^2}\right), \\
\mathcal{J}_{CC}^{EMF}(\omega) =& \frac{2}{5}\left(\mathcal{S}_1^2\mathcal{S}_2^2\frac{\tau_c}{1+(\omega\tau_c)^2} + (1-\mathcal{S}_1^2)\frac{\tau_1'}{1+(\omega\tau_1')^2} + \mathcal{S}_1^2(1-\mathcal{S}_2^2)\frac{\tau_2'}{1+(\omega\tau_2')^2}\right),
\end{aligned}
\tag{4.86}
$$

where $\mathcal{S}_m = \mathcal{P}_2(\cos\beta_{CCH})$ is the methyl rotation order parameter, $\mathcal{S}$ is the order parameter associated to the correlation time τ_i in the MF, $\mathcal{S}_1$ (respectively $\mathcal{S}_2$) is the order parameter for the motion associated to the correlation time τ_1 (respectively τ_2), and $\tau_k'^{-1} = \tau_c^{-1} + \tau_k^{-1}$ and $\tau_k''^{-1} = \tau_c^{-1} + \tau_m^{-1} + \tau_k^{-1}$ with $k = i, 1, 2, m$. The MCMC is performed using the emcee Python library [170] with 15 chains of 15,000 steps (only the last 10,000 are kept for analysis). The error for the calculated relaxation rates is set to 5 % of their value.

4.4.3.2 Model Free and two internal motions

In the case where only one additional internal motion is considered, on top of the methyl rotation, the MF spectral density function can perfectly fit the simulated relaxation rates (Appendix Fig. F.3). The comparison of the MF fitted and expected parameters (Table 4.3) shows that the fitted order parameters and correlation times are in very good agreement with the expected values. Among the MF parameters, the order parameter is of particular interest since it can be used to calculate conformational entropy [23, 24], heat capacity [213] or changes in entropy

upon binding of a drug for example [214, 212]. Thus, a MF analysis of $^{13}C^{1}H^{2}H_2$ methyl groups relaxation rates undergoing rotation and one additional motion on top of an isotropic overall tumbling can *a priori* still report accurately on the thermodynamic properties.

4.4.3.3 Model Free and three internal motions

We will here investigate the case where the methyl group of a Valine side-chain still undergoes a rotation around the C_β-$C_{\gamma 1}$ bond, but two additional internal motions are considered: the wobbling of the C_β-$C_{\gamma 1}$ bond (with a diffusion constant 10 times higher than in the previous section) and the rotamer exchange between each rotamer positions. Relaxation rates are fitted using the MF [15] and EMF [74] correlation functions (Appendix Fig. F.4). The EMF correlation function better reproduces the simulated relaxation rates than the MF correlation function.

The fitted correlation time for methyl rotation perfectly reproduces the correlation time obtained when only one additional internal motion was considered (compare Table 4.3 and Table 4.4). Since the C_β-$C_{\gamma 1}$ wobbling diffusion coefficient was increased by a factor 10, this suggests the fitted value for the correlation time of methyl-rotation is independent from the time-scale of the other motions. This is consistent with the variations of τ_m that do not exceed 0.1 ps when the diffusion coefficient for wobbling is changed over 4 orders of magnitude (Appendix Fig. F.5e,k).

When analyzing relaxation data with the EMF spectral density function [74], we can wonder if the two sets of fitted order parameters and correlation times can report on the motions involved, that is wether each of them can be associated to one particular motion. With the new diffusion constant for wobbling, the associated expected correlation time is 197 ps, which is in the same order of magnitude as the fitted correlation time τ_2, while τ_1 can correspond to the correlation time for rotamer jumps (compare Table 4.3 and Table 4.4). However, the fitted correlation times τ_1 and τ_2 show negligeable variations when the wobbling diffusion coefficient spans 4 orders of magnitude (Appendix Fig. F.5) which suggest that neither of them report on this motion. This is likely due to the fact that for the chosen cone semi-angle opening, the contribution of the wobbling to relaxation is small compared to the rotamer exchange (Fig. 4.6). Critically, the fitted order parameters are far from any of the expected ones (compare Table 4.3 and Table 4.4) which also indicates the the EMF correlation function does not allow to identify

Table 4.4: Values of EMF parameters obtained from fitting ^{13}C longitudinal and transverse relaxation rates and ^{13}C-^{1}H DD cross-relaxation rates at 5 different fields for a $^{13}C^{1}H^{2}H_{2}$ methyl group on a protein with isotropic global tumbling correlation time $\tau_c = 10$ ns, undergoing rotation, wobbling of the C-C bond holding the methyl group, and a rotamer exchange process with azymutal or non-azymutal symmetry. The error is obtained from the parameters distribution following the MCMC analysis of the simulated relaxation rates.

	$\mathcal{S}_1^2$	τ_1 (ns)	$\mathcal{S}_2^2$	τ_2 (ps)	τ_m (ps)
Symmetric jump	0.64 ± 0.24	2.39 ± 1.56	0.18 ± 0.15	703 ± 185	10.1 ± 0.42
Asymmetric jump	0.54 ± 0.10	3.42 ± 1.07	0.62 ± 0.11	656 ± 238	10.2 ± 0.39

the parameters describing each motions individually.

4.4.4 Conclusion

In this section, we have shown that the MF correlation function reproduces the accurate correlation function for the models considered here. When two internal motions are considered, on top of an isotropic overall tumbling, fitted MF parameters agree well with the expected ones. Deviations are noticed in three cases. (1) The methyl rotation seems to be ill-characterized by a MF correlation function, but fitted correlation times still report correctly on the order of magnitude for the time-scales involved. However, the value of the MF correlation time for rotation depends on wether C-H or H-H correlation are probed (that is depending on wheter carbon or proton relaxation rates are analyzed). If such correlations are analyzed together, the spectral density function has to be adapted to each correlation. (2) When more than two internal motions are considered, the deconvolution of each contribution to the relaxation rates is not trivial from fitted EMF parameters as each individual parameters can not be assigned to one particular motion. (3) When the overall tumbling is not isotropic, which concerns the large majority of biomolecules, the MF correlation function miss-characterizes rotamer exchange processes which do not have azymutal symmetry. This condition on the symmetry property of the exchange is very strong and is unlikely to hold often, so that MF-type of correlation functions might lead to a miss-characterization of rotamer-jump processes that, when present, mostly dominate the relaxation of side-chains (see previous section).

4.5 Correlation functions in the presence of correlated internal motions

So far, correlation functions were written assuming statistical independence between each motions. In the case of methyl groups in aliphatic side-chains, it is relatively easy to imagine that the methyl rotation or C-C wobbling depend on the rotameric state. Here, we present the correlation functions for correlated rotamer jumps and methyl rotation. This section is based on the treatment of correlated overal tumbling and rotamer jumps which was initially presented in the late 2000s [111, 173].

4.5.1 Analytical treatment for correlated rotamer jumps and methyl rotation

We will treat the case where a methyl group jumps between rotameric states with different rotation properties in each of them. The correlation function is:

$$\begin{aligned} C_{i,j}(t) =& \frac{1}{5}\sum_{\kappa=1}^{5}\sum_{a,a'=-2}^{2}\sum_{b,b'=-2}^{2}\sum_{c,c'=-2}^{2} a_{\kappa,a}a_{\kappa,a'}e^{-E_\kappa t}\mathcal{D}^{(2)*}_{a,b}(\Omega_{D,J})\mathcal{D}^{(2)}_{a',b'}(\Omega_{D,J})\times \\ & \langle\mathcal{D}^{(2)*}_{b,c}(\Omega_{J,SF},0)\mathcal{D}^{(2)}_{b',c'}(\Omega_{J,SF},t)\rangle\mathcal{D}^{(2)*}_{c,0}(\Omega_{SF,i})\mathcal{D}^{(2)}_{c',0}(\Omega_{SF,j}), \end{aligned} \tag{4.87}$$

where the same notations as above have been used. The correlation function for overall tumbling is already expanded as presented in the previous sections. In the Euler angle set $\Omega_{J,SF} = \{\varphi_{J,SF}, \theta_{J,SF}, \phi_{J,SF}\}$, $\varphi_{J,SF}$ orients the jump frame in the direction of the populated rotamer and is thus time dependent, $\theta_{J,SF}$ rotates the jump frame to align it on the rotamer frame (which was introduced in the previous sections), and $\phi_{J,SF}$ rotates the resulting frame to align its x-axis along the direction of one C-H bond and is thus time dependent. The ensemble average can be expressed:

$$\langle\mathcal{D}^{(2)*}_{b,c}(\Omega_{J,SF},0)\mathcal{D}^{(2)}_{b',c'}(\Omega_{J,SF},t)\rangle = \sum_{\alpha,\beta} p^{eq}_{\alpha}\langle\mathcal{D}^{(2)*}_{b,c}(\Omega_{J,SF},0)\mathcal{D}^{(2)}_{b',c'}(\Omega_{J,SF},t)\rangle_{\beta\alpha}, \tag{4.88}$$

where the sums run over all accessible states, and the notation $\langle\cdots\rangle_{\beta\alpha}$ indicates that the ensemble average is calculated with initial state α and final state β. It can be calculated as follows:

$$\begin{aligned} \langle\cdots\rangle_{\beta\alpha} =& \int_0^{2\pi} d\phi_0 \int_0^{2\pi} d\phi p(\phi_0)\mathcal{D}^{(2)*}_{b,c}(\{\varphi_{J,SF_\alpha}, \theta_{J,SF_\alpha}, \phi_0\})\times \\ & p(\{\varphi_{J,SF_\beta}, \theta_{J,SF_\beta}, \phi\}, t|\{\varphi_{J,SF_\alpha}, \theta_{J,SF_\alpha}, \phi_0\}, 0)\mathcal{D}^{(2)}_{b',c'}(\{\varphi_{J,SF_\beta}, \theta_{J,SF_\beta}, \phi\}), \end{aligned} \tag{4.89}$$

where φ_{J,SF_k} and θ_{J,SF_k} are the values of the Euler angles to transform from the jump frame to the **S**ystem **F**rame (SF) in rotamer k. The probability $p(\phi_0)$ is:

$$p(\phi_0) = \frac{1}{2\pi}, \tag{4.90}$$

and in order to calculate the conditional probability, we will use the notation:

$$p(\{\varphi_{J,SF_\beta}, \theta_{J,SF_\beta}, \phi\}, t|\{\varphi_{J,SF_\alpha}, \theta_{J,SF_\alpha}, \phi_0\}, 0) = p(\beta, \phi, t|\alpha, \phi_0, 0). \tag{4.91}$$

The Master equation that solves the conditional probability is a combination of the Master equations for rotamer exchange and diffusion on a cone:

$$\frac{d}{dt}p(\beta, \phi, t|\alpha, \phi_0, 0) = \sum_{\gamma=1}^{N} \mathcal{R}_{\beta\gamma} p(\gamma, \phi, t|\alpha, \phi_0, 0) - D_{rot,\beta} L_{rot}^2 p(\beta, \phi, t|\alpha, \phi_0, 0), \tag{4.92}$$

where $\mathcal{R}_{ij}$ are elements of the exchange matrix $\mathcal{R}$ (*i.e.* exchange rate from state j to state i) and $D_{rot,\beta}$ is the diffusion constant for diffusion on a cone in state β. We solve Eq. 4.92 by writting the conditional probability in terms of eigenfunctions of the angular momentum operator L_{rot}^2 (see Appendix F.3):

$$p(\beta, \phi, t|\alpha, \phi_0, 0) = \sum_n \frac{1}{2\pi} e^{in(\phi-\phi_0)} c_n^{\beta\alpha}(t), \tag{4.93}$$

which, after insertion and identification in Eq. 4.92, leads to the following differential equation for the functions $c_n^{\beta\alpha}$:

$$\frac{d}{dt}c_n^{\beta\alpha}(t) = -D_{rot,\beta} n^2 c_n^{\beta\alpha}(t) + \sum_{\gamma=1}^{N} \mathcal{R}_{\beta\gamma} c_n^{\beta\alpha}(t). \tag{4.94}$$

It can be written in matrix form as:

$$\frac{d}{dt}C_n^{\alpha}(t) = \sum_{\gamma=1}^{N} \mathcal{R}_{n,\beta\gamma} C_n^{\alpha}(t), \tag{4.95}$$

where $C_n^{\alpha}(t)$ is a column vector containing the elements $c_n^{\mu\alpha}(t)$ for all states μ and $\mathcal{R}_{n,\mu\nu}$ are elements of the matrix $\mathcal{R}_n$ defined as:

$$\mathcal{R}_{n,\mu\nu} = \begin{cases} \mathcal{R}_{\mu\nu} & \mu \neq \nu \\ \mathcal{R}_{\mu\nu} - n^2 D_{rot,\mu} & \mu = \nu \end{cases}. \tag{4.96}$$

Similarly to the treatment of rotamer jumps, we define the symmetrized pseudo-exchange matrix as:

$$\tilde{\mathcal{R}}_{rot,n} = \tilde{\mathcal{R}} - n^2\mathcal{D}_{rot}, \tag{4.97}$$

wherer $\mathcal{D}_{rot}$ is a diagonal matrix containing the methyl rotation diffusion coefficient as diagonal elements, and $\tilde{\mathcal{R}}$ is the symmetrized exchange matrix (Eq. F.31). Then, the functions $c_n^{\beta\alpha}$ can be explicitely written as:

$$c_n^{\beta\alpha}(t) = \sqrt{\frac{p_\beta^{eq}}{p_\alpha^{eq}}} \sum_{m=1}^{N} \tilde{X}_\alpha^{(n,m)} \tilde{X}_\beta^{(n,m)} e^{\lambda_{n,m}t}, \tag{4.98}$$

where N is the number of states and $\tilde{X}_\zeta^{(m,n)}$ is the value ζ of the eigenvector $\tilde{X}^{(n,m)}$ for the symmetrized exchange matrix associated to the eigenvalue $\lambda_{n,m}$. The ensemble average in Eq. 4.89 can now be expressed as:

$$\begin{aligned}\langle\cdots\rangle_{\beta\alpha} =& \frac{1}{2\pi} e^{i(b\varphi_{J,SF_\alpha} - b'\varphi_{J,SF_\beta})} d_{b,c}(\theta_{J,SF_\theta}) d_{b',c'}(\beta_{J,SF_\beta}) \times \\ & \sum_n \int_0^{2\pi} d\phi_0 \int_0^{2\pi} d\phi e^{i(c\phi_0 - c'\phi)} \frac{1}{2\pi} e^{in(\phi-\phi_0)} c_n^{\beta\alpha}(t) \\ =& \delta_{cc'} e^{i(b\varphi_{J,SF_\alpha} - b'\varphi_{J,SF_\beta})} d_{b,c}(\theta_{J,SF_\alpha}) d_{b',c}(\theta_{J,SF_\beta}) c_c^{\beta\alpha}(t),\end{aligned} \tag{4.99}$$

which leads to the correlation function for correlated rotamer jumps and methyl rotation:

$$\begin{aligned}C_{i,j}(t) =& \frac{1}{5} \sum_{\kappa=1}^{5} \sum_{a,a'=-2}^{2} \sum_{b=-2}^{2} \sum_{\alpha,\beta} \sum_n a_{\kappa,a} a_{\kappa,a'} e^{-E_\kappa t} \mathcal{D}_{a,b}^{(2)*}(\Omega_{D,SF_\alpha}) \mathcal{D}_{a',b}^{(2)}(\Omega_{D,SF_\beta}) \times \\ & \sqrt{p_\alpha^{eq} p_\beta^{eq}} \tilde{X}_\alpha^{(b,n)} \tilde{X}_\beta^{(b,n)} e^{\lambda_{b,n}t} \mathcal{D}_{b,0}^{(2)*}(\Omega_{SF,i}) \mathcal{D}_{b,0}^{(2)}(\Omega_{SF,j}).\end{aligned} \tag{4.100}$$

4.5.2 Effect of correlated motions on relaxation rates

We investigate here how the correlation of motions affects relaxation rates in a $^{13}C^1H^2H_2$ methyl group. We restrict the calculations to a 2-state exchange, with Euler angles for jumps of $\{\pm\pi/2, \beta_{J,CC}, 0\}$, where $\beta_{JCC} = 76\,\text{deg}$ is typical for aliphatic carbon chains. The exchange rate k_{12} is fixed to $k_{12} = 0.5 \times 10^9\,\text{s}^{-1}$, and k_{21} is calculated using Eq. F.27 to satisfy the miscroscopic reversibility condition. We impose an isotropic overall diffusion tensor with global tumbling correlation time $\tau_c = 25\,\text{ns}$. Relaxation rates are calculated for three distributions of rotamers: $p_1 = 0.3$, $p_1 = 0.5$ and $p_1 = 0.7$. Finally, the population average methyl rotation diffusion coefficient is set to $10^{11}\,\text{s}^{-1}$, and the difference of diffusion coefficients between the two states is $\Delta D_{rot} = 5 \times 10^{10}\,\text{s}^{-1}$, with the highest diffusion coefficient being associated to rotamer

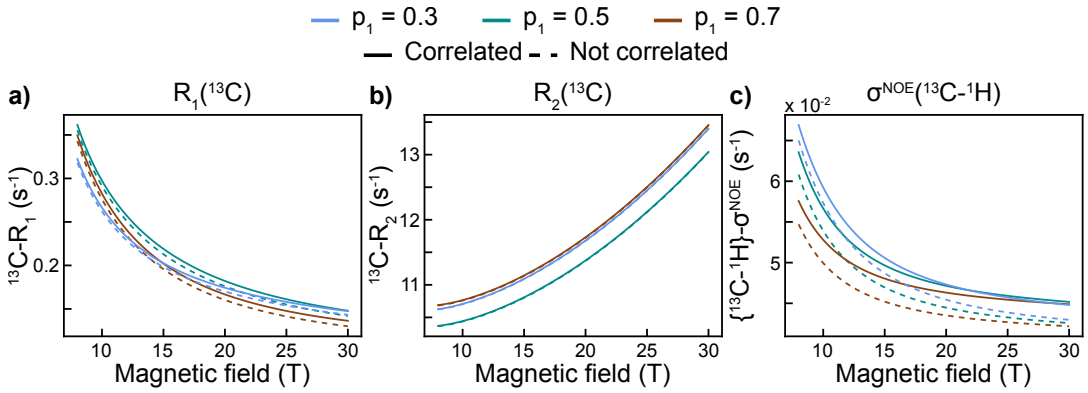

Figure 4.11: Contribution of correlated rotamer jumps and methyl rotation to relaxation. Magnetic field variations of carbon R_1 (**a**), R_2 (**b**) and carbon-proton DD cross-relaxation rate (**c**) in a $^{13}C^1H^2H_2$ methyl group exchanging between two rotamers states and calculated for three distributions of populations. Relaxation rates calculated with a unique diffusion coefficient for methyl rotation are shown in dash, and relaxation rates calculated by considering the correlation between rotamer jumps and methyl rotation motions are shown in plain lines.

1. We impose an axially symmetric CSA tensor for the ^{13}C nucleus with an anisotropy of 20 ppm.

Transverse relaxation rates calculated with the same properties for methyl rotation in both rotamers are indistinguishable from the rates where the correlation between motions are taken into account (Fig. 4.11b). This is due to the fact that the main contribution to these rates is the CSA, which does not report on methyl rotation. However, longitudinal auto-relaxation rates (Fig. 4.11a) and DD cross-relaxation rates (Fig. 4.11c) show significant deviations depending on wether correlated motions are considered or not.

4.6 Unravelling a CSA rotamer-dependent relaxation mechanism

When we introduced the **B**loch-**W**angsness-**R**edfield (BWR) relaxation theory (Chapter 1), we implicitly assumed that the strengths of the interactions were time independent. Chemical bonds vibrates in the femtosecond range by a few picometers, so that it is a valid approximation in the case of the DD interactions between directly bonded nuclei, even if its effective strength needs to be carefully set [220]. Similarly, bonds vibrations lead to slight variations in CSA tensors for the nitrogen and carbonyl carbon-13 of peptide planes [221]. In this later study, S. Tang and D. Case indicate that the use of a scaling factor for the CSA when analyzing relaxation data is a way to take into account the motional averaging of the CSA tensor. However, to the best of our knowledge, no study focused on the variations of CSA tensors in protein side-chains and their effect on relaxation.

Our initial NMR and MD analyses of isoleucine-δ_1 methyl groups (Ile-δ_1) dynamics in Ubiquitin showed that isoleucine side-chains undergo instantaneous (that is faster than the sampling of the MD, *i.e.* time difference between two saved frames) jumps between different rotameric states [21], with a retention time of a few nanoseconds in each conformers. For each of the orientation of the carbon chain, it is reasonable to expect a significantly different CSA tensor such that the strength of the CSA interaction cannot be considered time-independent on the timescales of the relaxation. In this section, we show that the difference in CSA between conformers contributes to relaxation. Then, we calculate the CSA tensors of Ile-δ_1 for different conformation of an isoleucine side-chain in water. We re-analyze our relaxometry data recorded on Ile-δ_1 of Ubiquitin and show that the models of correlation function introduced in the previous sections can reproduce CSA-DD cross-correlated cross-relaxation rate much better than the MF analysis (Fig. 3.6a,b). This analysis is performed using results from MD simulations, in particular to limit the size of the exchange matrix to the sole populated states.

4.6.1 Relaxation with a time-dependent CSA tensor

In this section, we restrict ourselves to the simple case of a methyl group exchanging between two rotamers in a protein undergoing isotropic overall diffusion with correlation time $\tau_c = 25\,\text{ns}$. We asume perfect tetrahedral geometry for the methyl group, and a diffusion coefficient for the rotation $D_{rot} = 5 \times 10^{10}\,\text{s}^{-1}$. The set of Euler angles for transformation from the jump

frame to the rotamer frame is $\Omega_{J,R} = \{\pm\pi/2, \beta_J, 0\}$ with $\beta_J = 76\,\text{deg}$, which is typical for carbon chains. The carbon CSA tensors is considered axially symmetric and aligned along the C-C bond of the methyl group. The proton CSA is neglected. We set the exchange rate from state 1 to 2 to $k_{21} = 0.5 \times 10^9\,\text{s}^{-1}$ and the exchange rate k_{21} is calculated to satisfy the microreversibility condition (Eq. F.27) depending on the three situations we consider for the population of state 1: $p_1 = 0.3$, $p_1 = 0.5$ and $p_1 = 0.7$. Finally, the population average of the CSA value is set to $\sigma_{av} = 18.2\,\text{ppm}$ which corresponds to the value of the carbon-δ1 in isoleucine side-chains determined from cross-correlated cross-relaxation rates [131]. We evaluate the effect of $\Delta\sigma = \sigma_2 - \sigma_1$, the difference in CSA between the two states. The individual CSAs are calculated using:

$$\begin{aligned} \sigma_1 &= \sigma_{av} - p_2\Delta\sigma, \\ \sigma_2 &= \sigma_{av} + p_1\Delta\sigma, \end{aligned} \tag{4.101}$$

where σ_i is the value of the CSA in state i. We focus on carbon-R_1, carbon-R_2 and the carbon CSA/DD cross-correlated cross-relaxation rates η_z and η_{xy} in a $^{13}C^1H^2H_2$ spin system for a magnetic field $B_0 = 14.1\,\text{T}$:

$$\begin{aligned} R_1(^{13}\text{C}) =& \frac{1}{4}(\mathcal{J}^{(I)}_{CH}(\omega_H - \omega_C) + 3\mathcal{J}^{(I)}_{CH}(\omega_C) + 6\mathcal{J}^{(I)}_{CH}(\omega_\text{H} + \omega_C)) \\ &+ \frac{4}{3}(\mathcal{J}^{(I)}_{CD}(\omega_C - \omega_D) + 3\mathcal{J}^{(I)}_{CD}(\omega_C) + 6\mathcal{J}^{(I)}_{CD}(\omega_C + \omega_D)) \\ &+ \mathcal{J}^{(I)}_{C}(\omega_C), \\ R_2(^{13}\text{C}) =& \frac{1}{8}(4\mathcal{J}^{(I)}_{CH}(0) + \mathcal{J}^{(I)}_{CH}(\omega_H - \omega_C) + 3\mathcal{J}^{(I)}_{CH}(\omega_C) + 6\mathcal{J}^{(I)}_{CH}(\omega_H) + \\ &6\mathcal{J}^{(I)}_{CH}(\omega_H + \omega_C)) \\ &+ \frac{2}{3}(4\mathcal{J}^{(I)}_{CD}(0) + \mathcal{J}^{(I)}_{CD}(\omega_C - \omega_D) + 3\mathcal{J}^{(I)}_{CD}(\omega_C) + 6\mathcal{J}^{(I)}_{CD}(\omega_D) + \\ &6\mathcal{J}^{(I)}_{CD}(\omega_C + \omega_D)) \\ &+ \frac{1}{6}(4\mathcal{J}^{(I)}_{C}(0) + 3\mathcal{J}^{(I)}_{C}(\omega_C)), \\ \eta_z(^{13}\text{C}) =& \sqrt{\frac{3}{2}}\mathcal{J}^{(I)}_{C,CH}(\omega_C), \\ \eta_{xy}(^{13}\text{C}) =& \frac{1}{2}\sqrt{\frac{1}{6}}(4\mathcal{J}^{(I)}_{C,CH}(0) + 3\mathcal{J}^{(I)}_{C,CH}(\omega_C)), \end{aligned} \tag{4.102}$$

where the superscript (I) indicates that the strengths of the interactions are included in the spectral density functions which are written (using the same notations as in the previous sec-

tions):

$$\begin{aligned}
\mathcal{J}^{(I)}_{CH}(\omega) =& d^2_{CH}\frac{2}{5}\sum_{a,b=-2}^{2}\sum_{\alpha,\beta=1}^{2}\sum_{n=0}^{1}\frac{\tau_{b,n}}{1+(\omega\tau_{b,n})^2}\sqrt{p_\alpha p_\beta}\tilde{X}^{(n)}_\alpha\tilde{X}^{(n)}_\beta\times \\
& \mathcal{D}^{(2)*}_{a,b}(\Omega_{J,R_\alpha})\mathcal{D}^{(2)}_{a,b}(\Omega_{J,R_\beta})d_{b,0}(\beta_{CCH})^2, \\
\mathcal{J}^{(I)}_{CD}(\omega) =& d^2_{CD}\frac{2}{5}\sum_{a,b=-2}^{2}\sum_{\alpha,\beta=1}^{2}\sum_{n=0}^{1}\frac{\tau_{b,n}}{1+(\omega\tau_{b,n})^2}\sqrt{p_\alpha p_\beta}\tilde{X}^{(n)}_\alpha\tilde{X}^{(n)}_\beta\times \\
& \mathcal{D}^{(2)*}_{a,b}(\Omega_{J,R_\alpha})\mathcal{D}^{(2)}_{a,b}(\Omega_{J,R_\beta})d_{b,0}(\beta_{CCH})^2, \\
\mathcal{J}^{(I)}_{C}(\omega) =& \frac{2}{3}\omega^2_C\frac{2}{5}\sum_{\alpha,\beta=1}^{2}\sum_{n=0}^{1}\sigma_\alpha\sigma_\beta\frac{\tau_{0,n}}{1+(\omega\tau_{0,n})^2}\sqrt{p_\alpha p_\beta}\tilde{X}^{(n)}_\alpha\tilde{X}^{(n)}_\beta\mathcal{P}_2(\cos\theta_{\alpha,\beta}), \\
\mathcal{J}^{(I)}_{C,CH}(\omega) =& d_{CH}\sqrt{\frac{2}{3}}\omega_C\frac{2}{5}\mathcal{P}_2(\cos\beta_{CCH})\sum_{\alpha,\beta=1}^{2}\sum_{n=0}^{1}\sigma_\alpha\frac{\tau_{0,n}}{1+(\omega\tau_{0,n})^2}\sqrt{p_\alpha p_\beta}\tilde{X}^{(n)}_\alpha\tilde{X}^{(n)}_\beta\times \\
& \mathcal{P}_2(\cos\theta_{\alpha,\beta}),
\end{aligned} \tag{4.103}$$

where $\beta_{CCH} = 180 - 109.47 = 70.53\,\text{deg}$ is the angle between the C-H bond and the methyl group symmetry axis, $\theta_{\alpha,\beta}$ is the angle between the vectors pointing along the directions of the C-C bonds in rotamers α and β (that is 0 when $\alpha = \beta$ and $2\beta_{CC}$ when $\alpha \neq \beta$), and:

$$\tau^{-1}_{b,n} = \tau^{-1}_c - \lambda_n + b^2 D_{rot}, \tag{4.104}$$

where λ_n is the n^{th} eigenvalue of the symmetrized exchange matrix (see Section 4.3.2).

The carbon auto-relaxation rates show very small deviations depending on whether distinct CSA values are considered or not (Fig. 4.12a,b), which most likely arrives from the relatively small contribution of the CSA (about 1.5 % for the carbon-R_1 and 5 % for the carbon-R_2) compared to the DD interactions. The cross-correlated cross-relaxation rates calculated with distinct CSA tensors show a linear variation with the difference in anisotropy between the two states (Fig. 4.12c,d). This can be understood by expanding the spectral density function for cross-correlation between the carbon-CSA and carbon-proton DD interactions:

$$\begin{aligned}
\mathcal{J}^{(I)}_{C,CH}(\omega) =& d_{CH}\sqrt{\frac{2}{3}}\omega_C\frac{2}{5}\mathcal{P}_2(\cos\beta_{CCH})\left[\sigma_{av}\left(\frac{\tau_c}{1+(\omega\tau_c)^2}(p_1^2+p_2^2+2p_1p_2\mathcal{P}_2(\cos\beta_J))\right.\right. \\
& \left.+\frac{2\tau_{0,1}}{1+(\omega\tau_{0,1})^2}p_1p_2(1-\mathcal{P}_2(\cos\beta_J))\right) \\
& \left.+\Delta\sigma p_1p_2(p_1-p_2)(1-\mathcal{P}_2(\cos\beta_J))\left(\frac{\tau_{0,1}}{1+(\omega\tau_{0,1})^2}-\frac{\tau_c}{1+(\omega\tau_c)^2}\right)\right],
\end{aligned} \tag{4.105}$$

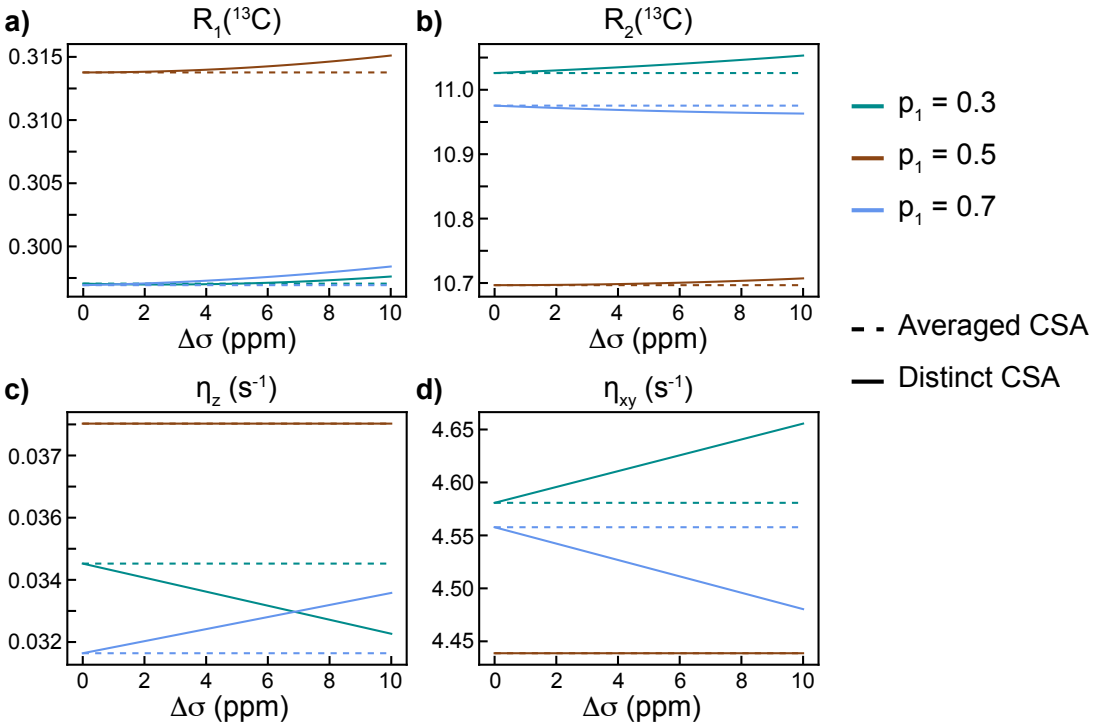

Figure 4.12: Highlighting the CSA rotamer-dependent relaxation mechanism. Evolution of the carbon-R_1 (**a**), carbon-R_2 (**b**), and carbon longitudinal (**c**) and transverse (**d**) cross-correlated cross-relaxation rate for a methyl group exchanging between two rotamer positions as a function of the difference between the CSA of the two rotamers. Calculations are performed for three equilibrium position for the state 1 and by either considering a population-averaged CSA value (dash) or distinct CSA tensors (solid).

where the last line contains the $\Delta\sigma$-dependent part of the spectral density function and highlights the linear variation of the cross-correlated cross-relaxation rates when the difference of CSA is changed. For the chosen geometry, we have:

$$\begin{aligned} &d_{CH}\mathcal{P}_2(\cos\beta_{CCH}) > 0, \\ &1 - \mathcal{P}_2(\cos\beta_J) > 0. \end{aligned} \tag{4.106}$$

In addition, we have chosen $\Delta\sigma = \sigma_2 - \sigma_1 > 0$ and:

$$\begin{aligned} &\tau_{0,1} - \tau_c = -\tau_c^2 \frac{k_{12} + k_{21}}{1 + \tau_c(k_{12} + k_{21})} < 0, \\ &\frac{\tau_{0,1}}{1 + (\omega_C \tau_{0,1})^2} - \frac{\tau_c}{1 + (\omega_C \tau_c)^2} > 0, \end{aligned} \tag{4.107}$$

such that, when calculations are performed with distinct CSA tensors, η_z increases when $p_1 > p_2$

and decreases otherwise, and since $J^{(I)}_{C,CH}(0) \gg J^{(I)}_{C,CH}(\omega_C)$, η_{xy} decreases when $p_1 > p_2$ and increases otherwise. Finally, when $p_1 = p_2$, the $\Delta\sigma$-dependent term in Eq. 4.105 vanishes and the cross-correlated cross-relaxation rates are independent of the difference in CSA value between the two states. In can be noted that the effect of this relaxation mechanism increases with the magnetic field, as expected for a CSA-dependent relaxation mechanism (Appendix Fig. F.6).

Conclusion In this initial section, we used a simple model to highlight the contribution of internal dynamics to relaxation when a spin system exchanges between discrete positions with distinct CSA tensors. In particular, CSA/DD cross-correlated cross-relaxation rates seem to be affected by this mechanism. These rates were poorly reproduced by our analysis of HRR data of Ile-δ1 methyl groups of Ubiquitin using an MF-type of correlation function (Fig 3.6 of chapter 3) [19]. We re-analyse these data using the models developped in this chapter to potentially explain these differences.

4.6.2 Computation of CSA tensors for an isoleucine side-chain

Geometry optimization of the rotamers The conformation of an isoleucine side-chain is defined by the pair of dihedral angles (χ_1, χ_2), with χ_1 being associated to the C_α-N and C_β-$C_{\gamma 1}$ bonds, and χ_2 to the C_α-C_β and $C_{\gamma 1}$-$C_{\delta 1}$ bonds. Both of these dihedral angles can identify 3 staggered conformations, for values expected to be close to 60 deg, 180 deg and 300 deg, thus leading to 9 possible rotamer states. In order to obtain a structure for the 9 rotamers, an initial structure of isoleucine in zwitterionic form was optimized with **D**ensity **F**unctional **T**heory (DFT) methods as implemented in Gaussian 09 Revision A.01 [222]. All DFT calculations were realized by Diego Carnevale, and I analyzed the results obtained directly from Gaussian. The B3LYP [223, 224] hybrid functional and 6-311++G(2d,p) Pople basis set were chosen [225], with solvent effects due to water implicitly taken into account by means of the polarizable continuum model [226]. The local minimum produced by this geometry optimization resulted in χ_1 and χ_2 values of –63.05 and –64.85 deg, respectively. Subsequently, this structure was utilized to perform a relaxed **P**otential **E**nergy **S**urface (PES) scan at the same level of theory by varying independently the two dihedral angles in steps of 30 deg over 360 deg, so as to generate 144 conformers. The 9 rotamers were thus identified as local minima of the cost function defined as:

$$f(\chi_1, \chi_2, r) = \sqrt{(\chi_{1,r} - \chi_1)^2 + (\chi_{2,r} - \chi_2)^2}, \tag{4.108}$$

were $\chi_{1,r}$ and $\chi_{2,r}$ are the theoretical χ_1 and χ_2 angles in rotamer r. The values of the χ_1 and χ_2 angles for the selected structures are reported in Appendix Table F.3. These rotamers also correspond to local minima of the PES, or are close to local minima, and fall within an energy window of *ca.* 10.5 kJ.mol^{-1} (Appendix Fig. F.7). The global minimum is characterized by $\chi_1 = 59.88$ deg and $\chi_2 = 173.85$ deg.

CSA calculation The CSA tensors of the selected rotamers were calculated by means of the **G**auge-**I**ndependent **A**tomic **O**rbital (GIAO) method [227, 228] at the same level of theory as for the geometry optimizations. The CSA tensors were then diagonalized to extract the principal components and orientations of the 3 main axes in the molecular frame, and define the longitudinal and orthogonal components of the CSA interaction as we decompose the fully asymmetric CSA tensors into two axially symmetric interactions (see Chapter 1 for more details). In order to calculate the relaxation rates, the set of Euler angles for the orientation of the CSA components in the rotamer frame has to be determined. In order to do so, we first defined the jump frame, as explained in section 4.3.2, with main axis pointing along the C_α-C_β bond, and the x-axis defined as:

$$\vec{x}_J = \frac{\overrightarrow{C_\alpha N} \wedge \vec{z}_J}{\|\overrightarrow{C_\alpha N}\|}, \tag{4.109}$$

where $\overrightarrow{C_\alpha N}$ is the vector pointing in the direction of the C_α-N bond, and $\vec{x}_J$ and $\vec{z}_J$ are the normalized vectors defining the x- and z-axes of the jump frame. From this frame, the Euler angles $\varphi_{J,R}$ and $\theta_{J,R}$ defining the orientation of the rotamer frame in the jump frame can be calculated, and are reported in the last columns of Appendix Table F.3. In each rotamer frames, defined after applying transformations of the jump frame with the corresponding Euler angles, the orientation of the CSA components can be calculated. The amplitude of the CSA components and their respective set of Euler angles for orientation in the rotamer frames are given in Table 4.5.

From these DFT calculations, it is clear that the strength of the CSA interaction depends on which rotamer is populated. In particular, rotamer 9 stands out with longitudinal and orthogonal components of the CSA tensor that are 15 % to 75 % lower than the CSA components of the other rotamers. Thus, if isoleucine side-chains undergo fast transitions between rotamers, the amplitude of the interaction is time-dependent. It must be noted that on top of having different anisotropy of chemical shift, each rotamer have different isotropic chemical shift, a property that can be used to obtain the distribution of rotamer populations [229].

Table 4.5: Amplitude (σ) and orientation (Euler angles $\varphi_{R,\sigma}$ and $\theta_{R,\sigma}$) of the longidutinal (denoted by the subscript $\|$) and orthogonal (denoted by the subscript $\perp$) components of the CSA tensor for each rotamers, and isotropic chemical shift referenced against the TMS isotropic chemical shift. The rotamers are labelled from 1 to 9 (label r)

	Longidutinal			Orthogonal			
r	$\sigma_{\|}$ (ppm)	$\varphi_{R,\sigma_{\|}}$ (deg)	$\theta_{R,\sigma_{\|}}$ (deg)	$\sigma_{\perp}$ (ppm)	$\varphi_{R,\sigma_{\perp}}$ (deg)	$\theta_{R,\sigma_{\perp}}$ (deg)	$\delta(r)$ (ppm)
1	23.61	103.08	39.66	6.03	163.24	118.11	12.99
2	26.32	253.69	47.17	6.74	157.87	73.93	13.77
3	22.69	226.33	151.17	6.63	166.75	93.24	15.09
4	25.81	176.84	9.59	7.11	100.69	95.61	13.57
5	27.48	166.95	163.57	9.21	97.39	97.41	14.23
6	25.58	172.60	24.43	8.25	229.37	69.59	13.54
7	21.15	156.81	8.15	11.03	156.91	79.80	10.1
8	17.25	248.01	157.41	6.55	131.90	107.37	7.49
9	14.17	138.63	119.87	2.56	220.43	139.87	7.06

CSA tensors were also calculated for TMS using the same level of theory to reference carbon isotropic chemical shifts as:

$$\delta(r) = \overline{\delta_{iso}(\text{TMS})} - \delta_{iso}(r), \tag{4.110}$$

where r denotes the rotamer number, δ_{iso} is the isotropic chemical shift calculated as the average of the tensor eigenvalues and $\overline{\delta_{iso}(\text{TMS})}$ is the average of the isotropic chemical shift of the 4 carbons of TMS.

4.6.3 Using molecular dynamics simulations to build motional models

An isoleucine side-chain can adopt 9 different conformers, such that analyzing relaxation data with a jump model would require determining 8 populations and 36 rate constants. We used a MD simultion to get more insights into the relevant conformations to describe the motions of isoleucines side-chains in Ubiquitin and decrease the number of free parameters.

Methods Our collaborators at the Institut de Biologie Physico-Chimique (IBPC) performed a 1 μs MD simulation using the **P**rotein **D**ata **B**ank (PDB) structure 1UBI of Ubiquitin in Gromacs 2018.4 [230, 231, 232, 233, 234] and the Amber ff99SB*-ILDN force field [235, 236] modified with accurate methyl rotation energy barriers [190]. The structure is solvated at 300 K and 1 bar in a 65 Å box neutralized and enriched with *ca.* 0.05 mol.L^{-1} NaCl using the TIP4P/2005 water model. The integration step is 2 fs while the protein coordinates are saved every 0.5 ps. When building the Ramachandran plots, only frames saved every 10 ps were used.

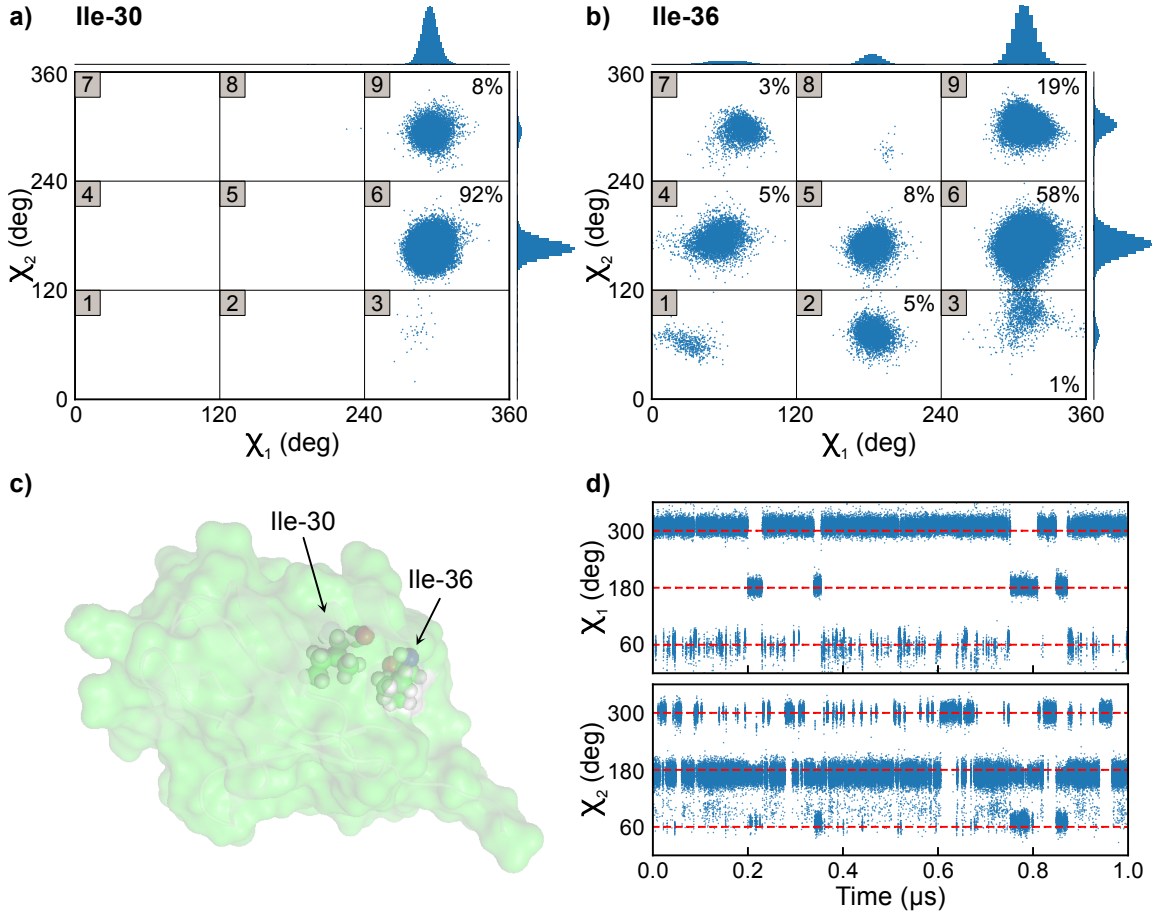

Figure 4.13: Priviledged conformations for isoleucine side-chains in Ubiquitin from MD simulations. Ramachandran plot for isoleucines 30 (**a**) and 36 (**b**) where each dots correspond to one set of angles (χ_1, χ_2) for a snapshot in the MD trajectory. Histograms of χ_1 and χ_2 angles are shown on the side of each Ramachandran plots. Each cadrans delimit the 9 rotamers (numbered from 1 to 9). **c)** Structure of Ubiquitin (PDB: 1D3Z) showing the buried isoleucine 30 and isoleucine 36 which is closer to the surface. **d)** Variations of the χ_1 and χ_2 angles over the course of the MD trajectory for isoleucine 36. The values for the angles χ_1 and χ_2 at the center of each cadrans of the Ramachandran plot are shown with the horizontal red dash lines.

Analysis of conformer distribution In order to identify the conformation or set of conformers the isoleucines of Ubiquitin are sampling during the MD simulation, we computed the set of angles (χ_1, χ_2) at each 10 ps interval. We present here the examples of isoleucines 30 and 36 which have very distinct dynamic behaviour as shown by their Ramachandran plots (Fig. 4.13a,b). Isoleucine 30 (Ile-30) exchanges between one major conformation and a less populated conformation (less than 10 %). Both conformations have the same χ_1 angle. On the other hand, Ile-36 adopts two majors conformations (the same as Ile-30) that account for 78 % of the whole MD trajectory, and 5 other minor conformations (we neglect rotamers that have populations lower than 1 %). The difference in number of populated states can be explained by the position of the two residues in the structure (Fig 4.13c): Ile-30 is buried and faces the β-sheet, leading to restriction on the angle χ_1; on the contrary, Ile-36 is in the α1-β3 loop with a prefered orientation toward the hydrophobic core constraining the value of χ_1 to a value close to 300 deg but with other accessible states with a different χ_1, where the side chain points towards the surface, are possible. The distributions of rotamers for all Ile residues in the MD trajectory are given in Appendix Table F.4 and the histograms in Appendix Fig. F.8. It is worth noticing that the transition between each states is faster than 0.5 ps (Fig. 4.13d), except between rotamers 3 and 6 for Ile-36 for which intermediate states can be detected. This suggests that a model of instantaneous jumps between discrete states as presented in the previous sections is suitable to describe the motions of the C-C bonds of isoleucine side-chains in Ubiquitin.

The widths of the distribution of χ_1 and χ_2 angles indicate that the C-C bonds also undergo libration motions around their equilibrium positions. Modeling these motions could potentially be achieved with the wobbling in a cone model, although we noticed that the full cone surface is not sampled (see Fig. 4.5). In addition to considerably complexify the correlation functions, doing so would add four unknown parameters (two cone semi-angles opening and two diffusion constants) for each populated rotamers. Extracting these parameters from relaxation data only, on top of exchange rates and populations of the rotamers, seems an impossible task. Using the result from section 4.3.5, we will neglect these motions in the analysis of HRR data.

For all isoleucines, the rotamer with lowest CSA (rotamer 9) is observed during the MD trajectory, while other states with larger CSA values are populated as well (Appendix Table F.4). The exchange between these states will thus contribute to relaxation through the correlation between the CSA tensors of each rotamer state. Before analyzing the relaxation data, we can calculate the expected chemical shifts of the isoleucine residues using the DFT

results and the population of the rotamers from the MD simulation as:

$$\delta_{\mathrm{MD}}(\mathrm{Ile}) = \sum_{r=1}^{9} p(r, \mathrm{Ile})\delta(r), \tag{4.111}$$

where the sum runs over each rotamer states, $p(r, \mathrm{Ile})$ is the population of rotamer r for the considered isoleucine and $\delta(r)$ is the isotropic chemical shift for rotamer r (Table 4.5). The predicted and experimental chemical shift obtained from the **B**iological **M**agnetic **R**esonance data **B**ank (BMRB) (entry 6466) and referenced against the TMS agree very well with one another. It must be noted that the experimental chemical shift were shifted by 2.86 ppm compared to the reported values to have a TMS carbon chemical shift set at 0 [237].

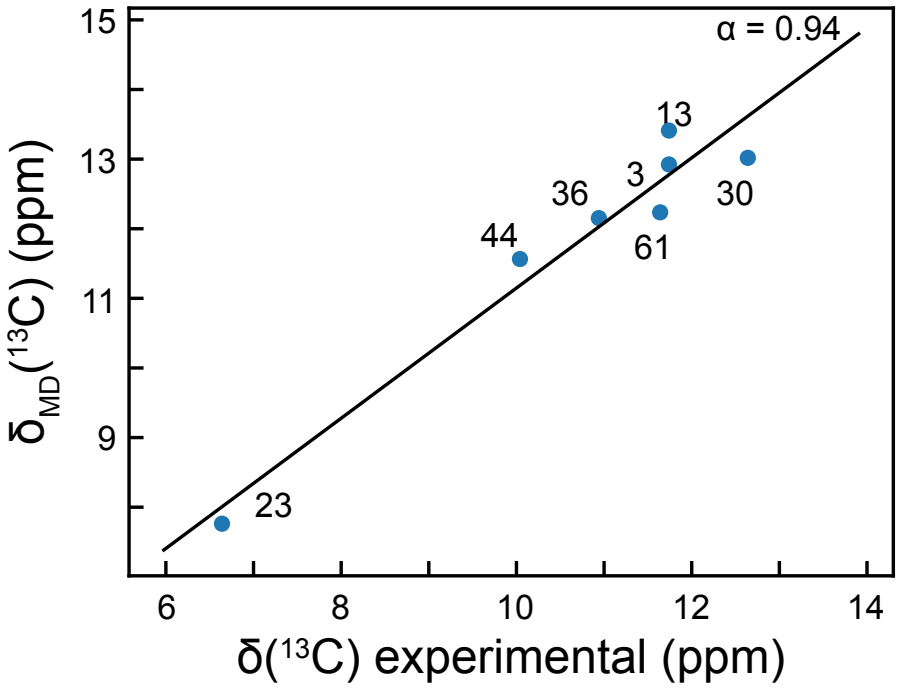

Figure 4.14: Correlation plot between the experimental and predicted carbon chemical shift of Ile-δ1 methyl group of Ubiquitin. The slope of the dark line is $\alpha = 0.94$.

4.6.4 Analysis of relaxation data using explicit models of motions

We present here the results of the analysis of Ile-δ1 methyl groups relaxation data in Ubiquitin. We first re-analysed backbone nitrogen-15 high-field R_1 and R_2 and nitrogen-proton σ^{NOE} [17] to obtain an accurate estimate of hydrodynamic properties. The RotDiff analysis [181, 238, 184, 185] indicates that an axially symmetric overall diffusion tensor best reproduces the

experimental data, with principal values $D_{\parallel} = 3.99 \times 10^7\,\mathrm{s}^{-1}$ and $D_{\perp} = 3.39 \times 10^7\,\mathrm{s}^{-1}$. We used an axially symmetric model of rotational diffusion in the following analysis.

Ile-30 and Ile-61 In order to first test our approach on systems that can be characterized with a minimal set of parameters, we primarily focused on isoleucine residues which showed only two populated rotamers throughout the MD trajectory: Ile-30 and Ile-61. We analyzed the four carbon R_1 and R_2, the four DD cross-relaxation rates σ^{NOE} recorded at 9.4, 14.1, 18.8 and 22.3 T, and the HRR corrected rates using **I**terative **C**orrection for the **A**nalysis of **R**elaxation **U**nder **S**huttling (ICARUS). For these two residues, only 4 parameters need to be determined, which we did using an MCMC procedure (compared to 6 free parameters in the initial EMF analysis [21]): the diffusion constant for methyl rotation, which was supposed to be the same in the two rotamer states, the population of rotamer 6, the logarithm of the exchange rate from state 6 to 9 and a scaling constant applied to the CSA values (α_{CSA}). This scaling factor accounts for the difference between experimentally determined and DFT-predicted CSA tensors [131] which, in our case, can originate from the fact that CSA tensors were computed for an isoleucine amino acid dissolved in implicit water. The MCMC was performed with 10 chains of 1,500 steps using the emcee Python library [170]. Only the last 1,000 steps of each MCMC chain were kept for analysis.

Despite the smaller number of free parameters in the model, relaxation rates are well reproduced by the MCMC procedure for these two residues (Fig. 4.15a,b,d,e). Only σ^{NOE} of Ile-30 are better reproduced with the EMF type of spectral density function (Fig. 4.15b). The distributions of parameters obtained from the MCMC analysis are well defined (Fig. 4.15g,h). In particular, the populations p_6 are in perfect agreement with the MD simulation. We calculated the magnetic field evolution of the CSA/DD cross-correlated cross-relaxation rates with the two models and using the results of the analysis of the carbon R_1, R_2 and carbon-proton σ^{NOE}. For Ile-30, the agreement between the experimental and predicted values is slightly improved by the use of an explicit model of motions, and is excellent for Ile-61 (Fig. 4.15c,f).

In order to evaluate the effect of the CSA rotamer-dependent relaxation mechanism, we analyzed the same relaxation data using the same models of explicit motions, but with a CSA equal to the population averaged CSA. In this model, the CSA interaction is constant. The effect on the carbon R_1, R_2 and carbon-proton σ^{NOE} is negligible (Appendix Fig. F.9), in agreement with the simple case investigated above (Fig. 4.12). Cross-correlated cross-relaxation

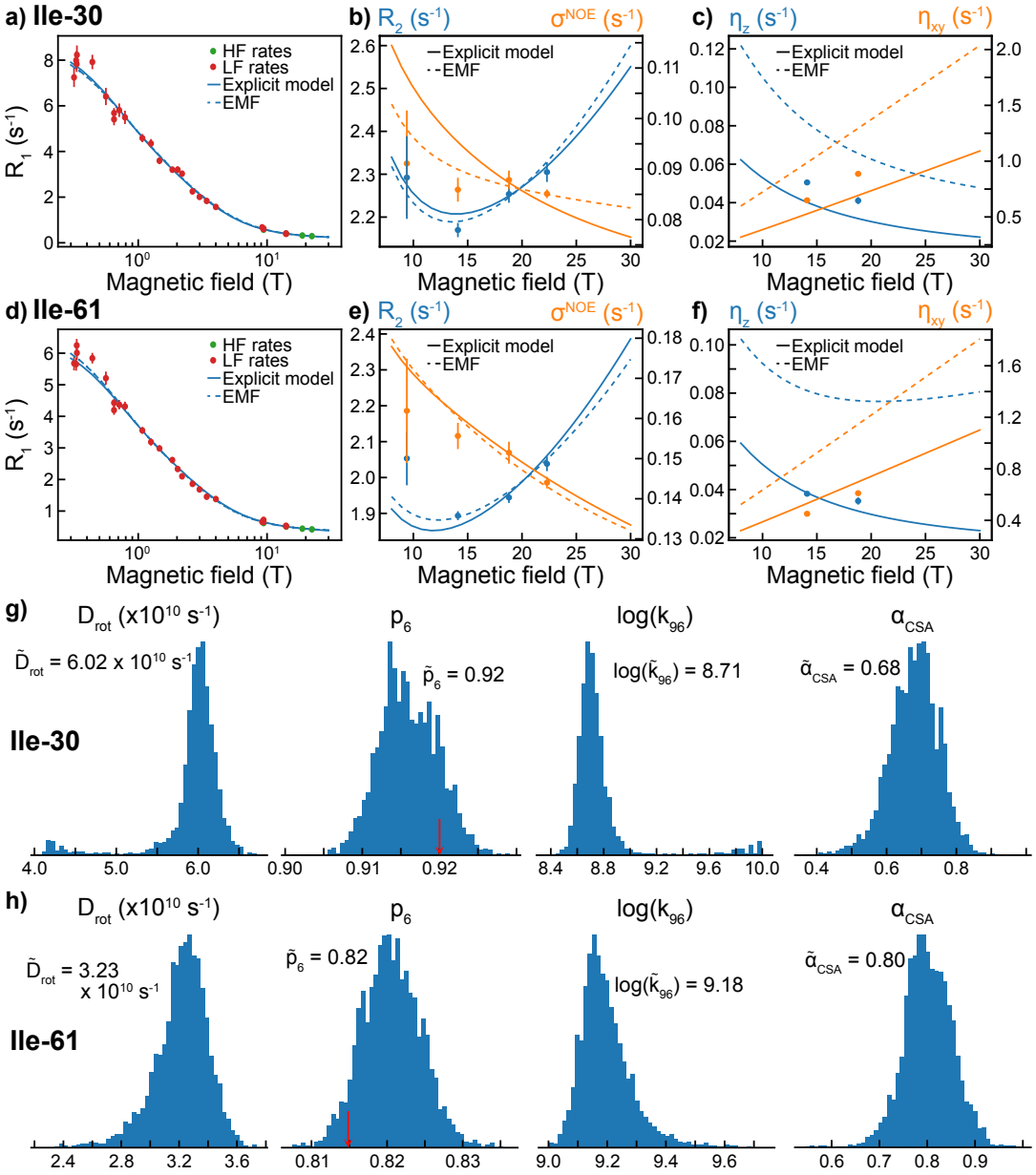

Figure 4.15: Analysis of relaxation rates for Ile-30 and Ile-61 using an explicit model of motion. Carbon R_1 (**a** and **d**), R_2 and carbon-proton σ^{NOE} (**b** and **e**), and longitudinal and transverse cross-correlated cross-relaxation rates (**c** and **f**) for Ile-30 (**a**-**c**) and Ile-61 (**d**-**f**) as a function of the magnetic field. The results from the EMF analysis are shown in dash lines in each panel. Only carbon R_1, R_2 and carbon-proton σ^{NOE} were used in each analysis while η_z and η_{xy} were calculated for validation using the obtained results. Distribution of parameters for the explicit model of motions for Ile-30 (**g**) and Ile-61 (**h**). The mean values of parameters are given on every panels. Populations obtained from the MD analysis are indicated by the red arrows. The exchange rate k_{96} is expressed in s^{-1}.

rates show slight variations depending on wheter distinct CSAs are considered or not (Appendix Fig. F.9), in particular η_z which better reproduces experimental data when correlation between CSA tensors are included in the correlation function.

Table 4.6: Parameters of the explicit model of motions using ICARUS corrected rates with the EMF spectral density function of MINOTAUR. The exchange rate k_{96} is expressed in s^{-1}.

		D_{rot} ($\times 10^{10}\,s^{-1}$)			p_6		
		Median	$+\sigma$	$-\sigma$	Median	$+\sigma$	$-\sigma$
Ile-30	ICARUS	6.02	0.17	0.18	0.92	0.01	0.00
	MINOTAUR	5.87	0.18	0.49	0.92	0.01	0.01
Ile-61	ICARUS	3.23	0.15	0.19	0.82	0.00	0.00
	MINOTAUR	3.24	0.06	0.06	0.83	0.00	0.00
		$\log k_{96}$			α_{CSA}		
		Median	$+\sigma$	$-\sigma$	Median	$+\sigma$	$-\sigma$
Ile-30	ICARUS	8.71	0.11	0.08	0.68	0.07	0.07
	MINOTAUR	8.75	0.12	0.13	0.66	0.07	0.08
Ile-61	ICARUS	9.18	0.09	0.06	0.80	0.05	0.04
	MINOTAUR	9.14	0.04	0.03	0.74	0.03	0.03

This re-analysis of the HRR dataset was performed with ICARUS corrected rates using the EMF spectral density function. We have shown in the previous sections that the EMF correlation function can reproduce carbon R_1, R_2 and carbon-proton σ^{NOE}. Thus, we can still expect to obtain an accurate description of the dynamics from the use of HRR corrected rates with the EMF type of correlation function. In order to confirm this hypothesis, the intensity decays and the accurate relaxation rates were analyzed using MINOTAUR. The good agreement between the parameters determined from the two methods indicates that ICARUS corrected rates can indeed be used here (Table 4.6). The main difference between the two approaches is the computational time: one MINOTAUR run for one residue exchanging between two rotamer positions took *ca.* 1 hour on a MacBook Pro (2016) with a 2.9 GHz Intel Core i5 processor and 4 CPUs while the analysis using reported ICARUS corrected rates took *ca* 2 min. In the following analysis, we used ICARUS corrected rates in the MCMC procedure.

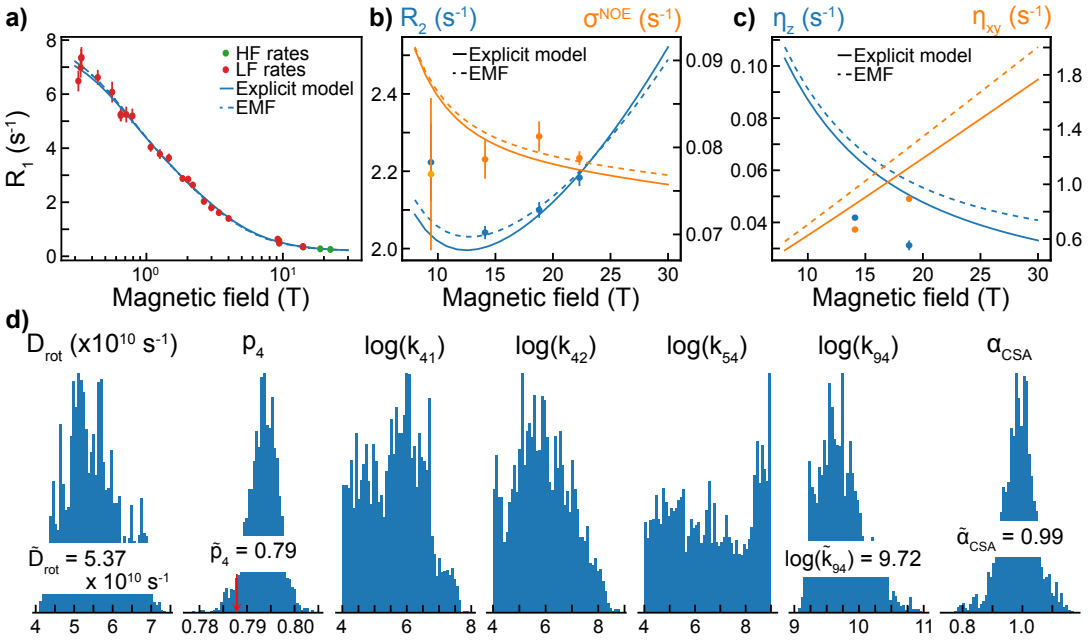

Figure 4.16: Analysis of relaxation rates for Ile-3 using a 5-rotamer jump model. Carbon R_1 (**a**), R_2 and carbon-proton σ^{NOE} (**b**) and longitudinal and transverse cross-correlated cross-relaxation rates (**c**) as a function of the magnetic field. The results from the EMF analysis are shown as dash lines in each panel. Only carbon R_1, R_2 and carbon-proton σ^{NOE} were used in each analysis while η_z and η_{xy} were calculated using the obtained results for cross-validation. **d)** Distributions of parameters for the explicit model of motions. The mean values of parameters are given on every panels when relevant. The populations p_4 obtained from the MD analysis is indicated by the red arrow. The exchange rates are expressed in s^{-1}.

Ile-3 Ile-3 is predicted to mainly sample rotamer 4 and 9, while rotamers 1, 2 and 5 have small populations that account for 10 % of the whole trajectory (Appendix Table F.4). The population of these later 3 states were set to the values obtained from the MD analysis while we only considered exchange between rotamer 4 (the most populate state) and the other four. This reduction in the number of free parameters in the MCMC procedure relies on the assumption that NMR relaxation data are mostly sensitive to exchange involving the most populated rotamer. The carbon R_1, R_2 and σ^{NOE} are well reproduced with a 5-rotamer state exchange model (Fig. 4.16a,b). Exchange rates are ill-defined except between the two most populated states (Fig. 4.16d). However, the 5-rotamer state exchange model reproduces the cross-correlated cross-relaxation rates slightly better than the 2-rotamer state model (Fig. 4.16c and Appendix Fig. F.10). The population of rotamer 4 obtained from the analysis of the NMR data matches the one from the MD simulation (which is not the case for the 2-rotamer state rotamer model, see Appendix Fig. F.10), which might indicate that the well-defined parameters in Fig. 4.16 are

accurately reporting on the internal dynamics of the portein.

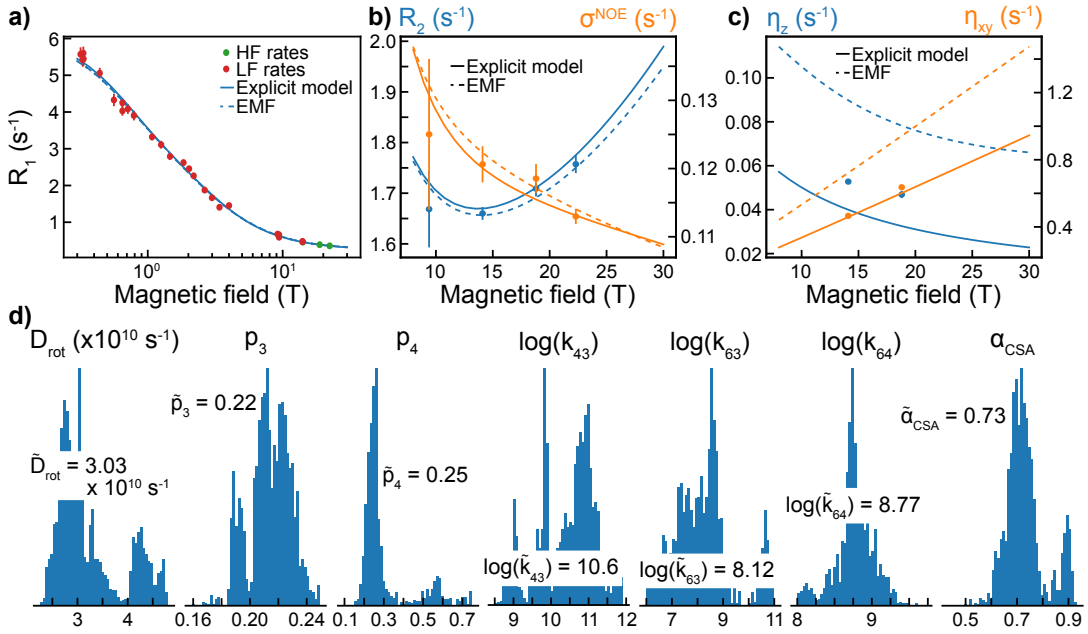

Figure 4.17: Analysis of relaxation rates for Ile-13 using a 3-rotamer jump model. Carbon R_1 (**a**), R_2 and carbon-proton relaxation rates (**b**) and longitudinal and transverse cross-correlated cross-relaxation rates (**c**) as a function of the magnetic field. The results from the EMF analysis are shown in dash lines in each pannel. Only carbon R_1, R_2 and carbon-proton σ^{NOE} were used in each analysis while η_z and η_{xy} were calculated using the obtained results for cross-validation. **d)** Distributions of parameters for the explicit model of motions. The mean values of parameters are given on every panels. The exchange rates are expressed in s^{-1}.

Ile-13 The MD simulation analysis reveals that rotamers 3, 4 and 6 are the main form of Ile-13, while rotamers 1, 5 and 9 are populated by up to 3 % each. For this reason, we initially analyzed the NMR relaxation data using the 3-rotamer state exchange model. Carbon R_1, R_2 and σ^{NOE} are well-reprocuded by this model (Fig. 4.17a,b). The exchange rate distributions obtained from the MCMC analysis are broad but an average value can be identified (Fig. 4.17d). The populations of rotamer 3 and 4 are well defined but not in the range of the MD trajectory (0.22 *vs* 0.12 for p_3 and 0.25 *vs* 0.55 for p_4). This might indicate that the sampling in the MD simulation is not representative of the behaviour of this side-chain and, consequently, that this analysis using rotamer 3, 4 and 6 to build the model of motions might not correctly describe the dynamic features of this side chain. However, the agreement between the calculated and measured cross-correlated cross-relaxation rates is improved compared to the EMF analysis, in particular for η_{xy} (Fig. 4.17c). The use of a more complex model of motions involving the 6

rotamer states does not significantly improve the agreement (Appendix Fig. F.11).

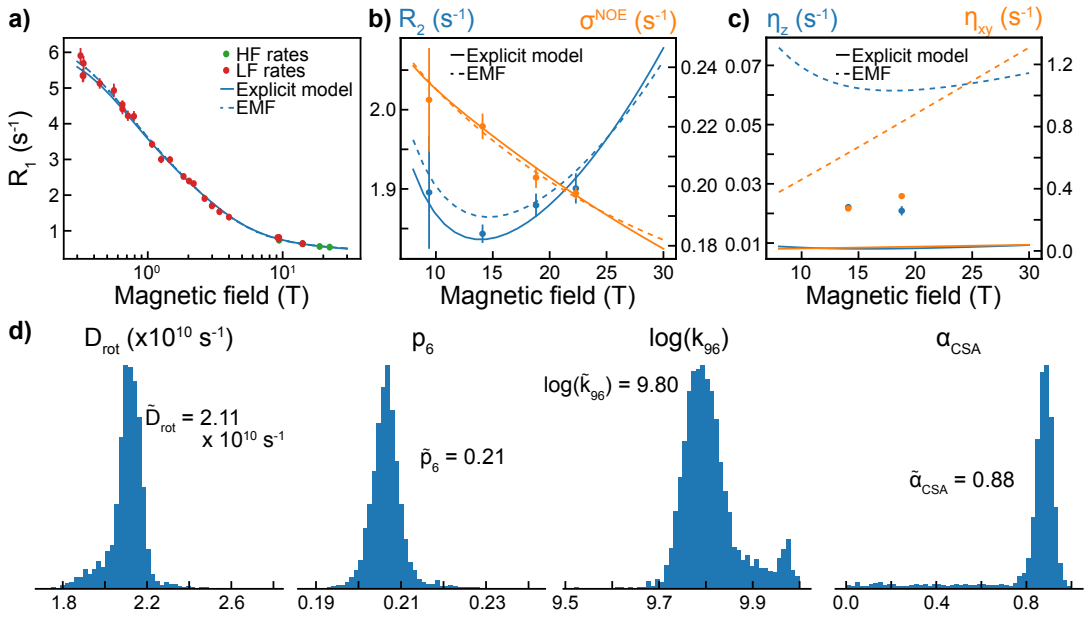

Figure 4.18: Analysis of relaxation rates for Ile-23 using a 2-rotamer jump model. Carbon R_1 (**a**), R_2 and carbon-proton σ^{NOE} (**b**) and longitudinal and transverse cross-correlated cross-relaxation rates (**c**) as a function of the magnetic field. The results from the EMF analysis are shown in dash lines in each pannel. Only carbon R_1, R_2 and carbon-proton σ^{NOE} were used in each analysis while η_z and η_{xy} were calculated using the obtained results for cross-validation. **d)** Distributions of parameters for the explicit model of motions. The mean values of parameters are given on every panels. The exchange rate k_{96} is expressed in s^{-1}.

Ile-23 According to the MD simulation, Ile-23 exists in 3 rotamer states that differ only by their χ_2 dihedral angle. The population of rotamer 3 is predicted to be very small (3 %) so that we initially analyzed the relaxation data with a 2-rotamer jump model. Carbon R_1, R_2 and carbon-proton σ^{NOE} are nicely reproduced with this model, but calculated η_z and η_{xy} still show significant deviations compared to experimental values (Fig. 4.18). The 3-rotamer exchange model leads to broad distributions of parameters associated to rotamer 3 (population and exchange rates), and the calculated η_z and η_{xy} do not better reproduce the measured rates (Appendix Fig. F.12). The significant difference between the populations of rotamer 6 determined from the NMR data and MD trajectory (0.21 *vs* 0.06), added to the disagreement in cross-correlated cross-relaxation rates, can be interpreted as the sign that a conformation of Ile-23 is not well sampled during the MD trajectory.

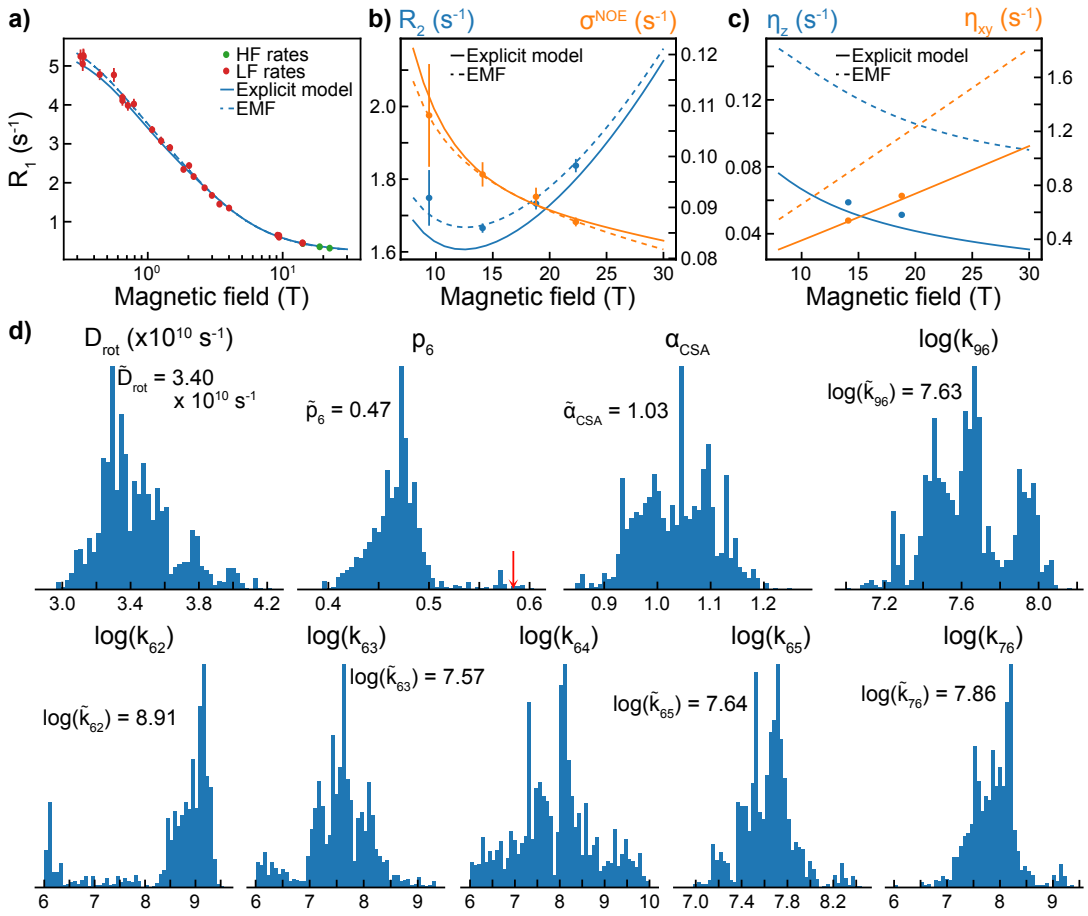

Figure 4.19: Analysis of relaxation rates for Ile-36 using a 7-rotamer jump model. Carbon R_1 (**a**), R_2 and carbon-proton σ^{NOE} (**b**) and longitudinal and transverse cross-correlated cross-relaxation rates (**c**) as a function of the magnetic field. The results from the EMF analysis are shown in dash lines in each panel. Only carbon R_1 and carbon-proton σ^{NOE} were used in each analysis while carbon R_2, η_z and η_{xy} were calculated using the obtained results for cross-validation. **d)** Distributions of parameters for the explicit model of motions. The mean values of parameters are given on every panels when relevant. The populations p_6 obtained from the MD analysis is indicated by the red arrow. The exchange rates are expressed in s^{-1}.

Ile-36 Ile-36 is the isoleucine residue sampling the most conformations, with 7 out of the 9 possible conformations being populated in the MD trajectory. Only 2 have populations higher than 10 % such that we fixed the values of the population of the other 5 conformers to their MD values and we only considered exchange with the most populated state (rotamer 6). Carbon R_1 and σ^{NOE} are well reproduce by the 7-rotamer state exchange model (Fig. 4.19a,b). Carbon R_2 are under-estimated using this explicit model of motions which cannot be interpreted as a sign of fast chemical exchange from the magnetic-field evolution of the difference between

experimental and calculated rates. This might be indicative of a miss-characterization of the spectral density function at low frequencies, which could explain the deviations between the MF and explicit model for carbon R_1 at low field. Still, cross-correlated cross-relaxation rates are correctly predicted from the result of this analysis (Fig. 4.19c). Despite the large number of free parameters in the MCMC procedure, we can consider that the parameters distribution are narrow for the majority of them (Fig. 4.19d). The population of rotamer 6 is 10 % lower compared to the MD value. Interestingly, the exchange rates are about one order of magnitude lower than the exchange rates obtained for the other residues. It can be noted that a 2-rotamer state jump model (between rotamer 6 and 9) does not correctly reproduce carbon R_2 and σ^{NOE} (Appendix Fig. F.13), showing that the collected relaxation rates are particularly sensitivite to the presence of rotamers with small populations.

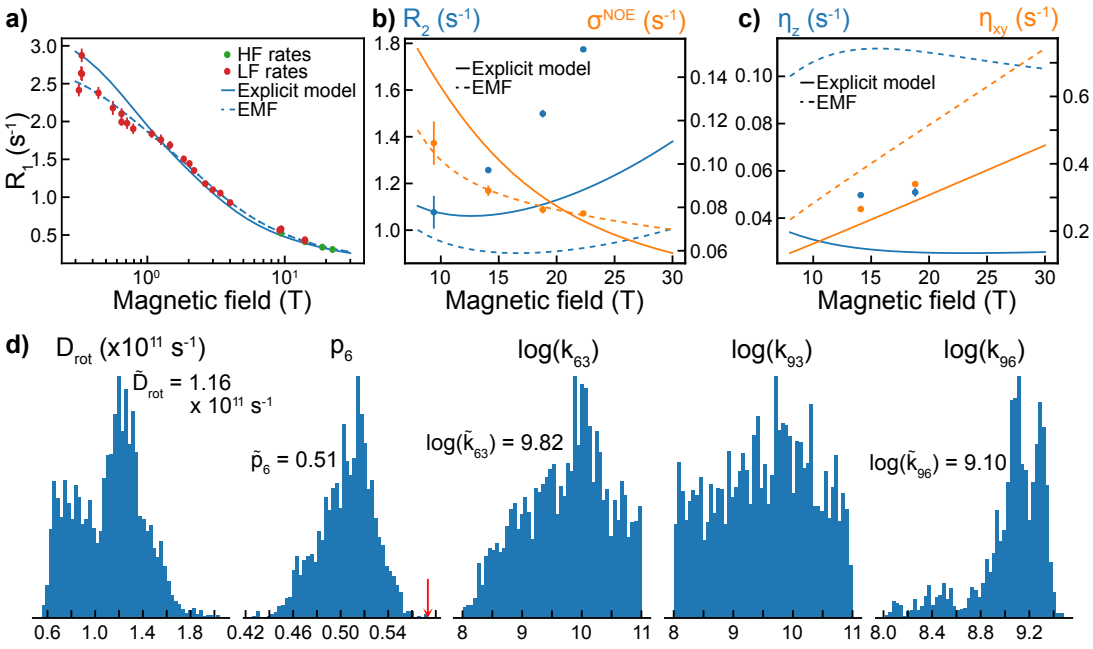

Figure 4.20: Analysis of relaxation rates for Ile-44 using a 3-rotamer jump model. Carbon R_1 (**a**), R_2 and carbon-proton σ^{NOE} (**b**) and longitudinal and transverse cross-correlated cross-relaxation rates (**c**) as a function of the magnetic field. The results from the EMF analysis are shown in dash lines in each panel. Only carbon R_1 and carbon-proton σ^{NOE} were used in each analysis while carbon R_2, η_z and η_{xy} were calculated using the obtained results for cross-validation. **d)** Distributions of parameters for the explicit model of motions. The mean values of parameters are given on every panels when relevant. The populations p_6 obtained from the MD analysis is indicated by the red arrow. The exchange rates are expressed in s^{-1}.

Ile-44 In the case of Ile-44, carbon R_2 cannot be used in the analysis due to chemical exchange contributions (Appendix Fig. E.1) [21]. For this reason, the CSA factor was fixed to $\alpha_{CSA} = 0.8$, in the range of the values found for the other isoleucines and in the litterature [131]. When analyzing carbon R_1 and carbon-proton σ^{NOE}, distributions of the population for rotamer 3 is ill-defined. We fixed it to the value given by the MD trajectory (11 %). The carbon R_1 and carbon-proton σ^{NOE} are not well reproduced by the chosen model of motion (Fig. 4.20a,b). In particular, low-fields R_1 deviations are indivative of miss-characterization of motions with time-scales in the low nanosecond range. This might arise form the fact that this surface-exposed residue undergoes significant libration motions of its C-C bonds, as suggested by the large χ_1 distribution (Appendix Fig. F.8). On the other hand, η_z and η_{xy} are better reproduced by this model of motions while carbon R_2 show a clear contribution from chemical exchange, in agreement with our previous study (Fig. 4.20b,c). Parameters distributions obtained from the MCMC procedure are broad (Fig. 4.20d), but an averaged value can still be identified for the population of rotamer 6, and is in good agreement with the MD value (51 % for NMR *vs* 57 % for MD). In addition, the diffusion constant for methyl rotation is one order of magnitude larger than for the other residues, which is consistent with the fact that Ile-44 methyl rotation is not hindered by the proximity of other atoms of the protein.

Discussion In this section, we have re-analyzed the HRR data recorded on Ile-δ1 methyl-groups of Ubiquitin using explicit models of motions introduced in the previous sections, and results from MD simulations and DFT calculations. Overall, all relaxation rates used in the MCMC procedure are nicely reproduced. Parameters distributions can be broad and sometimes ill-defined, but these often can be rationalized by the presence of rotamer states with a small populations. Rotamer populations obtained from the analysis of the NMR relaxation rates are in good agreement with the MD values for 4 out of the 7 isoleucine residues (3, 30, 44 and 61). In addition to the potential miss-sampling in MD simulation, the differences observed for the remaining 3 can be explained by the fact that DFT calculations were performed for an isoleucine in water and CSA tensors were transposed to isoleucine residues in the protein, neglecting the effects of all nearby nuclei. The scaling factor α_{CSA} was introduced to account for these effects, under the assumptions that the relative difference in CSA values between each states remained the same and that the orientations of the CSA tensors was unchanged. These two hypotheses need to be validated by computing the CSA tensors on the whole Ubiquitin. Rotamer populations for isoleucine side-chains in Ubiquitin have been determined from two other methods: scalar coupling constants, leading to χ_1 populations [239], and chemical shifts, giving χ_1 and

χ_2 distributions [229]. Our combined NMR and MD analysis is in good agreement with the χ_1 distributions obtained from scalar couplings measurements but significantly differs from the results of chemical shifts, except for Ile-3 (Table 4.7). The reason for the differences between the 3 studies needs to be investigated.

Table 4.7: Populations of χ_1 angles determined from the combined analysis of NMR relaxation and MD trajectory (this study), scalar coupling constants (SC) [239] and chemical shifts (CS) [229].

	$\chi_1 = 60$ deg			$\chi_1 = 180$ deg			$\chi_1 = 300$ deg		
Ile	NMR + MD	SC	CS	NMR + MD	SC	CS	NMR + MD	SC	CS
3	0.84	0.47	0.88	0.05	0.21	0.07	0.11	0.32	0.05
13	0.22	0.24	0.34	0.0	0.01	0.0	0.78	0.75	0.66
23	0.0	0.04	0.12	0.0	0.07	0.0	1.0	0.89	0.88
30	0.0	0.0	0.04	0.0	0.01	0.0	1.0	0.99	0.96
36	0.08	0.0	0.32	0.13	0.10	0.03	0.79	0.90	0.65
44	0.0	0.03	0.14	0.0	0.06	0.02	1.0	0.91	0.84
61	0.0	0.01	0.18	0.0	0.01	0.0	1.0	0.98	0.82

The calculated CSA-DD cross-correlated cross-relaxation rates η_z and η_{xy} using the parameters obtained from the MCMC procedure are in good agreement with the experimental data, and much better than in our initial MF analysis. This further suggests that side-chain motions cannot be accurately modeled using MF type of correlation functions. Among the rates that were collected, proton R_1 have not yet been considered. Systematic deviations were observed for these rates in our MF analysis and assigned to the contribution of DD with neighboring deuterium nuclei [19]. These deviations are still present in the analysis presented here (Fig. 4.21), and considering nearby deuterium nuclei might lead to a better correlation between calculated and measured rates. The framework presented here to build the spectral density function can better model the interaction between the methyl group and these nuclei compared to the MF.

We have shown in the previous sections that MF correlation function to account for methyl rotation can lead to miss-characterization of the methyl rotation diffusion coefficient

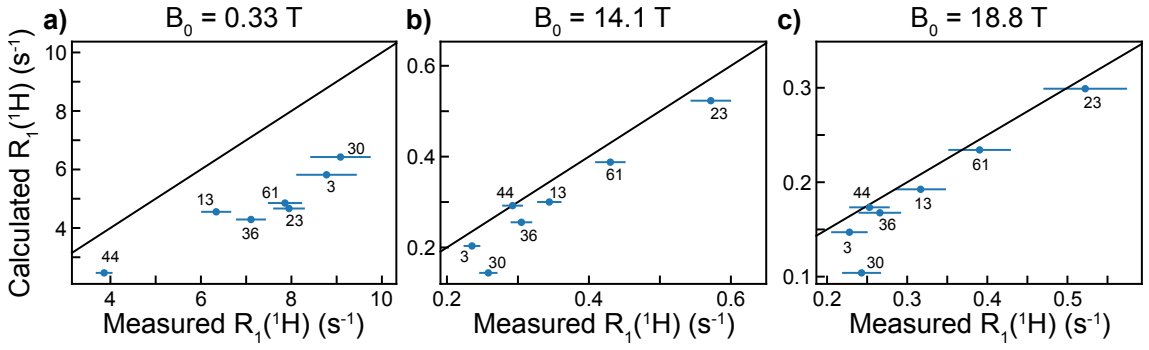

Figure 4.21: Correlations between measured and calculated proton longitudinal relaxation rates at 0.33 T (**a**), 14.1 T (**b**) and 18.8 T (**c**). Explicit model of motions was used to calculate the protons R_1.

(Fig. 4.8). However, calculated correlation time according to:

$$\tau_m^{\text{back}} = \frac{1}{1-\mathcal{S}_m^2} \sum_{\substack{b=-2 \\ b\neq 0}}^{2} \frac{1}{b^2 D_{rot}} \left[d_{b,0}(\beta_{CCH})\right]^2 , \tag{4.112}$$

correlates well with the MF-determined correlation time for most of the isoleucine residues (Fig. 4.22a). Similarly, the squared order parameters determined from the two approaches are in good agreement (Fig. 4.22b). The expected squared order parameter is calculated as:

$$\mathcal{S}^2 = \sum_{\alpha,\beta} p_\alpha p_\beta \mathcal{P}_2(\cos\theta_{\alpha,\beta}) \tag{4.113}$$

where the sums run over all the accessible states and $\theta_{\alpha,\beta}$ is the angle between the $C_{\gamma 1}$-$C_{\delta 1}$ bonds in rotamer states α and β. However, this does not relate to an accurate estimate of the conformational entropy. For isoleucine side-chains, the conformational entropy has been expressed as a function of the squared order parameter as [24]:

$$\frac{E_S}{k_B} = 2\left(1.95 + 1.55(1-\mathcal{S}^2)\right), \tag{4.114}$$

where the entropy is labeled E to avoid confusion from the squared order parameter and the subscript S indicates that it is calculated using order parameters. k_B is the Boltzmann constant. Since order parameters correlate well between the two approaches, so does conformational entropy calculated using Eq. 4.114 (blue circles in Fig. 4.22c). The analysis of HRR data presented here also allows us to calculate the conformational entropy from a model using the population

of each states:

$$\frac{E_P}{k_B} = -\sum_{\alpha} p_\alpha \log p_\alpha, \tag{4.115}$$

where the subscript P indicates that it is calculated using populations. The two entropies correlate with one another (orange circles in Fig. 4.22c), but the correlation coefficient is far from unity and equals 0.36. Thus, we cannot rule out the existence of a relationship between MF squared order parameters and conformational entropy of the form of Eq. 4.114, but this needs to be revisited. The reason for the disagreement between entropies calculated with Eq. 4.114 and Eq. 4.115 is unclear but can arise from the fact that the parametrization of Eq. 4.114 was only based on MD methods. Whether the relationship we find here between E_S and E_P is correct and stands for isoleucines residues in other proteins needs to be investigated in order to propose a correction to Eq. 4.114, or to favor analysis of relaxation data based on explicit models.

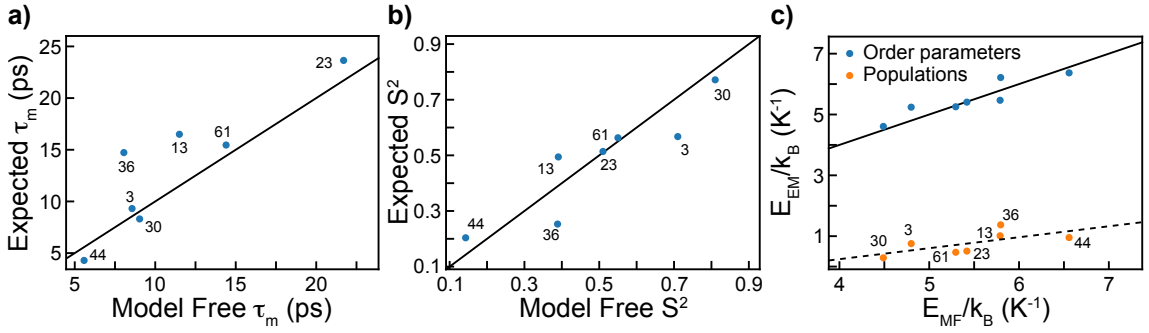

Figure 4.22: Correlations between parameters obtained from the analysis based on the MF and explicit models of spectral density functions. **a)** Correlation between the MF and calculated (Eq. 4.112) correlation times for methyl rotation . **b)** Correlation between the MF and calculated (Eq. 4.113) squared order parameters for C-C bond motions. The MF squared order parameters are either $\mathcal{S}_f^2$ (Ile-3, 23, 30, 61) or the product $\mathcal{S}_f^2\mathcal{S}_s^2$ (Ile-13, 36 and 44). **c)** Correlation between the conformational entropy calculated using Model Free (E_{MF}) or Explicit Model (E_{EM}) parameters. The entropy E_{MF} has been calculated using Eq. 4.114 (blue circles) and Eq. 4.115 (orange circles). The dash line has equation $y = 0.36x - 1.20$. In each pannel, the solid black lines are shown as a guide for perfect correlation, $y = x$.

4.7 Conclusion

This chapter started with a review of explicit models of correlation functions to study the internal dynamics in proteins, with a generalization of the wobbling in a cone model. We also calculated the correlation function in the case of rotamer jumps and rotamer-dependent methyl rotation. It must be noted that these models only apply to folded proteins, and potentially nucleic acids. We evaluated how these correlation functions compare with the MF approach. We found that the MF correlation function can lead to deviations in order parameters and correlation times in the case of instantaneous jumps between discrete positions. This suggests that the analysis of side-chains relaxation data requires explicit models of motions. In the last part of this chapter we used the models of correlation functions presented above to show that a relaxation mechanism is associated to the correlation between different CSA tensors of different rotamer states. We refer to it as the CSA rotamer-dependent relaxation mechanism. Its effects at high magnetic-fields might not be negligeable. DFT calculations performed on isoleucine in water show that CSA can vary by up to a factor *ca.* 2 between different rotamers. We re-analyzed our relaxation data collected on Ile-δ1 methyl groups of Ubiquitin in combination with MD simulations, and were able to better reproduce cross-correlated cross-relaxation rates. Our analysis leaves a number of questions:

- what are the reasons for the differences in rotamer populations obtained from different methods (MD only, MD and NMR, scalar couplings [239] and chemical shifts [229])? In our analysis, MD complements the NMR as the MD trajectory is used to constrain the model, while NMR provides a quantitative description of the dynamics, essentially populations and kinetics of exchange between rotamer states. Thus, questioning the agreement between each approach also questions the ability of computational methods (MD and DFT) to reproduce experimental data.

- what is the reason for the systematic deviation in proton longitudinal relaxation rate? We hypothesized here that the contribution from neighbouring deuterium nuclei can account for these deviations. This can be tested using the explicit models of correlation functions presented in this chapter.

- what is the reason for the systematic deviation in conformational entropy calculated either using squared order parameters or rotamer populations?

This later question is particularly critical as it has broad implications for the quantitative investigation of protein thermodynamics. In light of the complexity of the explicit models of

motions, obtaining an accurate picture of the thermodynamics properties from an MF analysis seems appealing. Indeed, even if the MF spectral density function does not reproduce cross-correlated cross-relaxation rates, the order parameters obtained from the analysis of longitudinal and transverse auto-relaxation rates, and DD cross-relaxation rates are in good agreement with the calculated order parameters from the analysis with explicit models of motions. This would suggest that the internal dynamics of isoleucine side-chains in Ubiquitin can still be characterized using the MF approach, although η_z and η_{xy} cannot be reproduced. Such conclusion have been challenged throughout this chapter and surely needs further validation.

General conclusion

During the 3 years of my PhD program, we have challenged the foundations of the relaxation theory in liquid state NMR based on results obtained from 'exotic' experiments. The research we performed constantly referred to the relaxation super-operator (Eq. 1.42). In the first chapter, we presented the basis of the BWR relaxation theory, and how we implemented it in a MATHEMATICA notebook called REDKITE. This tool was essential in order to carry most of the following projects. These can be summarized in three main axes.

We investigated relaxation properties of two types of spin system in 2F-NMR type of experiments. Methyl groups in Ubiquitin give rise to linewidths narrower than expected in the 2F version of the methyl **T**ransverse **R**elaxation-**O**ptimized **S**pectroscop**Y** (TROSY) experiment, and it was only by considering each transitions of the energy diagram independently from one another that we were able to reproduce experimental results. These theoretical considerations were mostly done to rationalize unexpected results, rather than propose a 2F counterpart to the methyl-TROSY pulse sequence. On the other hand, we presented the concept of 2F-TROSY and used computer simulations to show how it can lead to higher sensitivity and resolution in pairs of spins composed of one high-CSA nucleus. 2F-TROSY relies on the selection of slowly relaxing coherences at their optimal magnetic field in terms of relaxation by the use of a 2F-NMR spectrometer. Thus, the chemical shift of the nucleus which have high CSA contribution to relaxation is labeled at low field while the second nucleus chemical shift evolution leads to the signal detected at high field. The new generation of 2F-NMR spectrometer will most likely lead to an experimental validation of the theoretical predictions that were presented.

Next, we developped two approaches to analyse relaxation data recorded under shuttling. The first one, ICARUS, relies on the correction of the relaxometry relaxation rates to account for active cross-relaxation pathways while the sample is outside of the probe. We presented an application with the analysis of relaxation properties of Ile-δ1 methyl groups specifically labeled $^{13}C^1H^2H_2$ in the protein Ubiquitin. The second one, MINOTAUR, does not reproduce the relaxometry relaxation rates but rather the intensity decays so that this procedure does not need to correct experimental data. We showed that, for Ile-δ1 methyl groups in Ubiquitin, the two approaches give similar results.

Finally, we presented explicit models of motion, and compared them with the MF types of correlation functions. We showed that in the case of aliphatic side-chains, an analysis of relaxation data based on the MF can lead to a miss-representation of the motions. In addition, we showed that for a spin system undergoing exchange between positions with different CSA tensors, the correlation between the tensors of the different conformations is leading to a relaxation process. This effect cannot be taken into account by the MF types of correlation functions. For these reasons, we re-analysed our dataset recorded on iIle-δ1 methyl groups using a model of instantaneous jumps between discrete positions and the CSA tensors associated to each of these positions obtained from DFT calculations. We also used MD simulation results to build the models of correlation function. Overall, the explicit models of motions are reproducing well the relaxation rates, including the cross-correlated cross-relaxation rates, which was not the case in our initial MF analysis.

This later project has showed that NMR and MD have the ability to capture the complexity of motions in proteins, but efforts are still required to develop a general framework to reach a reliable description of the internal dynamics. Motions are complex and so are the models. Here, we chose to follow an approach where models were built according to the equilibrium properties obtained from the MD simulations, but deviations were observed between the NMR data and the MD predictions. At this point, we cannot identify the reason of these deviations, but these still do not undermine the potentiality of the combined analysis of NMR and MD data. Overall, it has become clear to me that our understanding of the relaxation theory, although powerful enough to analyse and predict results in standard experiments, is imperfect. The recent developments in other NMR spectroscopic techniques, and not only the ability to record datasets at low magnetic fields but also hyperpolarization methods for example, will certainly lead to an improved theory to unify the quantum description of the spin interactions and the geometric description of molecular motions.

Scientific contributions

Peer-reviewed articles

6. How wide is the window opened by high-resolution relaxometry on the internal dynamics of proteins in solution? Smith AA, Bolik-Coulon N, Ernst M, Meier BH, Ferrage F, *J. Biomol. NMR*, **75**, 119 (2021)

5. Two-field transverse relaxation-optimized spectroscopy for the study of large biomolecules - and *in silico* investigation, Bolik-Coulon N, Pelupessy P, Bouvignies G, Ferrage F, *J. Magn. Reson. O.*, **4-5**, 100007 (2020)

4. Theoretical and computational framework for the analysis of the relaxation properties of arbitrary spin systems. Application to high-resolution relaxometry, Bolik-Coulon N, Kadeřávek P, Pelupessy P, Dumez J-N, Ferrage F, Cousin SF, *J. Magn. Reson*, **313**, 106718 (2020)

3. Boosting the resolution of low-field ^{15}N relaxation experiments on intrinsically disordered proteins with triple-resonance NMR, Jaseňáková Z, Zapletal V, Padrta P, Zachrdla M, Bolik-Coulon N, Marquardsen T, Tyburn J-M, L Žídek, Ferrage F, Kadeřávek P, *J. Biomol. NMR*, **74**, 139, (2020)

2. Protein Dynamics from Accurate Low-Field Site-Specific Longitudinal and Transverse Nuclear Spin Relaxation, Kadeřávek P, Bolik-Coulon N, Cousin SF, Marquardsen T, Tyburn J-M, Dumez J-N, Ferrage F, *J. Phys. Chem. Lett.*, **10**, 5917, (2019)

1. Understanding the Methyl-TROSY Effect over a Wide Range of Magnetic Field, Bolik-Coulon N, Cousin SF, Kadeřávek P, Dumez J-N, Ferrage F, *J. Chem. Phys*, **150**, 224202 (2019)

Pre-PhD peer-reviewed articles

4. The Structure of SDS22 Provides Insights into the Mechanism of Heterodimer Formation with PP1, Choy MS, Bolik-Coulon N, Archuleta TL, Peti W, Page R, *Acta Crystallogr. F Struct. Biol. Commun.*, **74**, 817 (2018)

3. Time-Resolved Protein Side-Chain Motions Unraveled by High-Resolution Relaxometry and Molecular Dynamics Simulations, Cousin SF*, Kadeřávek P*, Bolik-Coulon N*, Gu Y, Charlier C, Carlier L, Bruschweiler-Li L, Marquardsen T, Tyburn JM, Brüschweiler R, Ferrage F, *J. Am. Chem. Soc.*, **140**, 13456-13465 (2018)

2. Structure and Dynamics of an Intrinsically Disordered Protein Region that Partially Folds upon Binding by Chemical-Exchange NMR, Charlier C, Bouvignies G, Pelupessy P, Walrant A, Marquant R, Kozlov M, De Ioannes P, Bolik-Coulon N, Sagan S, Cortes P, Aggarwal AK, Carlier L, Ferrage F, *J. Am. Chem. Soc.*, **139**, 12219 (2017)

1. Caspase-6 Undergoes a Distinct Helix- Strand Interconversion upon Substrate Binding, Dagbay KB, Bolik-Coulon N, Savinov SN, Hardy JA, *J. Biol. Chem.*, **292**, 4885 (2017)

Codes

2. ICARUS: https://figshare.com/articles/software/ICARUS/9893912

1. RedKite: https://figshare.com/articles/software/RedKite/11745111

Bibliography

[1] T. Liu, M. Leskes, W. Yu, A. J. Moore, L. Zhou, P. M. Bayley, G. Kim, and C. P. Grey *Science*, vol. 350, p. 530, 2015. (Cited on page ix.)

[2] P. C. Lauterbur *Nature*, vol. 242, p. 190, 1973. (Cited on page ix.)

[3] A. J. Weekley, P. Bruins, M. Sisto, and M. P. Augustine *J. Magn. Reson.*, vol. 161, p. 91, 2003. (Cited on page ix.)

[4] J.-H. Ardenkjaer-Larsen, G. S. Boebinger, A. A. Comment, S. Duckett, A. S. Edison, F. Engelke, C. Griesinger, R. G. Griffin, C. Hilty, H. Maeda, G. Parigi, T. Prisner, E. Ravera, J. van Bentum, S. Vega, A. Webb, C. Luchinat, H. Schwalbe, and L. Frydman *Angew. Chem. Int. Ed.*, vol. 54, p. 9162, 2015. (Cited on pages ix, 2 and 33.)

[5] G. Wagner, W. Braun, T. F. Havel, T. Schaumann, N. Go, and K. Wüthrich *J. Mol. Biol.*, vol. 196, p. 611, 1987. (Cited on page ix.)

[6] A. Sekhar and L. E. Kay *Annu. Rev. Biophys.*, vol. 48, p. 297, 2019. (Cited on page ix.)

[7] R. T. Anderson and L. E. Kay *Cell*, vol. 184, p. 577, 2021. (Cited on page ix.)

[8] `https://www.rcsb.org/stats/all-released-structures`. Accessed: 2021-03-31. (Cited on page ix.)

[9] D. D. Boehr, H. J. Dyson, and P. E. Wright *Chem. Rev.*, vol. 106, p. 3055, 2006. (Cited on page ix.)

[10] A. G. Palmer *Chem. Rev.*, vol. 104, p. 3623, 2004. (Cited on pages ix, 2 and 9.)

[11] C. Charlier, S. F. Cousin, and F. Ferrage *Chem. Soc. Rev.*, vol. 45, p. 2410, 2016. (Cited on pages ix, 82 and 83.)

[12] R. Wangsness and F. Bloch *Phys. Rev.*, vol. 89, p. 728, 1953. (Cited on pages x, 2, 9 and 31.)

[13] A. G. Redfield *IBM J. Res. Develop.*, vol. 1, p. 19, 1957. (Cited on pages x, 2, 9, 11 and 31.)

[14] A. G. Redfield *Advances in Magnetic and Optical Resonance*, vol. 1, p. 1, 1965. (Cited on pages x, 2, 9, 11 and 31.)

[15] G. Lipari and A. Szabo *J. Am. Chem. Soc.*, vol. 104, p. 4546, 1982. (Cited on pages x, xv, 3, 22, 30, 40, 60, 82, 83, 111, 116, 128, 138, 142, 151 and 153.)

[16] J. Cavanagh, W. J. Fairbrother, A. G. Palmer, M. Rance, and N. J. Skelton, *Protein NMR Spectroscopy: Principles and Practice*. Elsevier Academic Press, 2007. (Cited on pages x, 2, 7, 14, 16, 18, 20, 82, 108 and 205.)

[17] C. Charlier, S. N. Khan, T. Marquardsen, P. Pelupessy, V. Reiss, D. Sakellariou, G. Bodenhausen, F. Engelke, and F. Ferrage *J. Am. Chem. Soc.*, vol. 135, p. 18665, 2013. (Cited on pages xi, 3, 80, 82, 88, 105, 106, 116, 124 and 168.)

[18] I. Wolfram Research, "Mathematica," 2016. (Cited on pages xi, 9, 22, 31 and 107.)

[19] N. Bolik-Coulon, P. Kadeřávek, P. Pelupessy, J.-N. Dumez, F. Ferrage, and S. F. Cousin *J. Magn. Reson.*, vol. 313, p. 106718, 2020. (Cited on pages xi, 24, 28, 40, 60, 62, 81, 89, 94, 95, 97, 101, 107, 110, 163, 178 and 247.)

[20] C. Bengs and M. H. Levitt *Magn. Reson. Chem.*, vol. 56, p. 374, 2018. (Cited on pages xi, 3, 24, 25, 26, 31, 40 and 216.)

[21] S. F. Cousin, P. Kadeřávek, N. Bolik-Coulon, Y. Gu, C. Charlier, L. Carlier, L. Bruschweiler-Li, T. Marquardsen, J.-M. Tyburn, R. Brüschweiler, and F. Ferrage *J. Am. Chem. Soc.*, vol. 140, p. 13456, 2018. (Cited on pages xii, xiii, xvii, 3, 22, 42, 50, 55, 80, 81, 82, 83, 88, 89, 93, 95, 100, 104, 106, 108, 110, 111, 112, 113, 116, 139, 151, 159, 169, 177, 241, 242, 243 and 244.)

[22] P. Kadeřávek, N. Bolik-Coulon, S. F. Cousin, T. Marquardsen, J.-M. Tyburn, J.-N. Dumez, and F. Ferrage *J. Phys. Chem. Lett.*, vol. 10, p. 5917, 2019. (Cited on pages xiv, 4, 36, 80, 81, 96, 100, 102, 106 and 116.)

[23] D. Yang and L. E. Kay *J. Mol. Biol.*, vol. 263, p. 369, 1996. (Cited on pages xv, 3, 117, 139 and 152.)

[24] D.-W. Li and R. Brüschweiler *J. Am. Chem. Soc.*, vol. 131, p. 7226, 2009. (Cited on pages xv, 3, 117, 139, 152 and 179.)

[25] V. Tugarinov, Z. Liang, Y. E. Shapiro, J. H. Freed, and E. Meirovitch *J. Am. Chem. Soc.*, vol. 123, p. 3055, 2001. (Cited on pages xv, 3, 23, 116 and 138.)

[26] E. Meirovitch, Y. E. Shapiro, V. Tugarinov, Z. Liang, and J. H. Freed *J. Phys. Chem. B*, vol. 107, p. 9883, 2003. (Cited on pages xv, 116 and 117.)

[27] E. Meirovitch, Y. E. Shapiro, A. Polimeno, and J. H. Freed *J. Phys. Chem. A*, vol. 110, p. 8366, 2006. (Cited on pages xv, 3, 23, 83, 116 and 138.)

[28] E. Meirovitch, A. Polimeno, and J. H. Freed *J. Phys. Chem. B*, vol. 110, p. 20615, 2006. (Cited on pages xv and 116.)

[29] E. Meirovitch, Y. E. Shapiro, A. Polimeno, and J. H. Freed *J. Phys. Chem. B*, vol. 111, p. 12865, 2007. (Cited on pages xv, 83 and 116.)

[30] N. Salvi, A. Abyzov, and M. Blackledge *J. Phys. Chem. Lett.*, vol. 7, p. 2483, 2016. (Cited on pages xv and 116.)

[31] A. A. Smith, M. Ernst, S. Riniker, and B. H. Meier *Angew. Chem. Int. Ed*, vol. 58, p. 9383, 2019. (Cited on pages xv, 3, 116 and 137.)

[32] F. Kümmerer, S. Orioli, D. Larsen-Harding, F. Hoffmann, Y. Gavrilov, K. Teilum, and K. Lindorff-Larsen *BioRχiv*, doi:10.1101/2020.08.18.256024. (Cited on pages xv, 3 and 116.)

[33] A. A. Smith, N. Bolik-Coulon, E. Matthias, B. H. Meier, and F. Ferrage *J. Biomol. NMR*, vol. 75, p. 119, 2021. (Cited on pages xv, 3, 116 and 137.)

[34] P. Lunginbühl and K. Wüthrich *Prog. Nucl. Magn. Reson. Spectrosc.*, vol. 40, p. 199, 2002. (Cited on pages xv, 3, 22, 118 and 120.)

[35] K. Pervushin, R. Riek, G. Wider, and K. Wüthrich *Proc. Natl. Acad. Sci. USA*, vol. 94, p. 12366, 1997. (Cited on pages xviii, 4, 8, 31, 34, 36 and 59.)

[36] V. Tugarinov, P. M. Hwang, J. E. Ollerenshaw, and L. E. Kay *J. Am. Chem. Soc.*, vol. 125, p. 10420, 2003. (Cited on pages xviii, xix, 2, 4, 5, 8, 31, 34, 36, 38, 40, 42, 44, 46, 48, 50, 56, 59 and 127.)

[37] S. F. Cousin, P. Kadeřávek, B. Haddou, C. Charlier, T. Marquardsen, J.-M. Tyburn, P.-A. Bovier, F. Engelke, W. Maas, G. Bodenhausen, P. Pelupessy, and F. Ferrage *Angew. Chem. Int. Ed.*, vol. 55, p. 9886, 2016. (Cited on pages xviii, xix, 4, 35, 36, 37, 38, 45, 53, 58, 63, 74, 76, 80 and 102.)

[38] N. Bolik-Coulon, S. F. Cousin, P. Kadeřávek, J.-N. Dumez, and F. Ferrage *J. Chem. Phys.*, vol. 150, p. 224202, 2019. (Cited on pages xix, xx, 37, 38, 44, 45, 46, 47, 49, 51, 52, 56, 57, 59 and 76.)

[39] S. F. Cousin, C. Charlier, P. Kadeřávek, T. Marquardsen, J.-M. Tyburn, P.-A. Bovier, S. Ulzega, T. Speck, D. Wilhelm, F. Engelke, W. Maas, D. Sakellariou, G. Bodenhausen, P. Pelupessy, and F. Ferrage *Phys. Chem. Chem. Phys*, vol. 18, p. 33187, 2016. (Cited on pages xviii, 4, 35, 63, 68, 74, 80 and 102.)

[40] A. Boeszoermenyi, S. Chhabra, A. Dubey, D. L. Radeva, N. T. Burdzhiev, C. D. Chanev, O. I. Petrov, V. M. Gelev, M. Zhang, C. Anklin, H. Kovacs, G. Wagner, I. Kupor, K. Takeuchi, and H. Arthanari *Nat. Methods*, vol. 16, p. 333, 2019. (Cited on pages xx, 59, 60, 61, 62, 66, 67, 68, 69, 73, 75, 226 and 235.)

[41] N. Bolik-Coulon, P. Pelupessy, G. Bouvignies, and F. Ferrage *J. Magn. Reson. Open*, vol. 4-5, p. 100007, 2020. (Cited on pages xx, 59, 63, 67, 68, 69, 70, 71, 72, 73, 75, 227, 239 and 240.)

[42] J. C. Kendrew, G. Bodo, H. M. Dintzis, R. G. Parrish, and H. Wyckoff *Nature*, vol. 181, p. 662, 1958. (Cited on page 1.)

[43] M. P. Williamson, T. F. Havel, and K. Wüthrich *J. Mol. Biol.*, vol. 182, p. 295, 1985. (Cited on page 1.)

[44] Y. Cheng, N. Grigorieff, P. A. Penczek, and T. Walz *Cell*, vol. 161, p. 662, 1958. (Cited on page 1.)

[45] K. Kruger, P. J. Grabowski, A. J. Zaug, J. Sands, D. E. Gottschling, and T. R. Cech *Cell*, vol. 31, p. 147, 1982. (Cited on page 1.)

[46] C. Guerrier-Takada, K. Gardiner, T. Marsh, N. Pace, and S. Altman *Cell*, vol. 35, p. 849, 1983. (Cited on page 1.)

[47] M. J. Fedor and J. R. Williamson *Nat. Rev. Mol. Cell Biol.*, vol. 6, p. 399, 2005. (Cited on page 1.)

[48] S. Boeynaems, S. Alberti, N. L. Fawzi, T. Mittag, M. Polymenidou, F. Rousseau, J. Schymkowitz, J. Shorter, B. Wolozin, L. Van Den Bosch, P. Tompa, and M. Fuxreiter *Trends Cell Biol.*, vol. 28, p. 420, 2018. (Cited on page 1.)

[49] A. G. Larson and G. J. Narlikar *Biochemistry*, vol. 57, p. 2540, 2018. (Cited on page 1.)

[50] B. A. Gibson, L. K. Doolittle, M. W. G. Schneider, L. E. Jensen, N. Gamarra, L. Henry, D. W. Gerlich, S. Redding, and M. K. Rosen *Cell*, vol. 179, p. 1, 2019. (Cited on page 1.)

[51] P. E. Wright and H. J. Dyson *Nat. Rev. Mol. Cell Biol.*, vol. 16, p. 18, 2015. (Cited on page 1.)

[52] V. Tugarinov, V. Kanelis, and L. E. Kay *Nat. Protoc.*, vol. 1, p. 749, 2006. (Cited on pages 2, 34 and 127.)

[53] P. Gans, O. Hamelin, R. Sounier, I. Ayala, M. A. Durá, C. D. Amero, M. Noirclerc-Savoye, B. Franzetti, M. J. Plevin, and J. Boisbouvier *Angew. Chem. Int. Ed*, vol. 49, p. 1958, 2010. (Cited on pages 2 and 127.)

[54] G. Mas, J.-Y. Guan, E. Crublet, E. Colas Debled, C. Moriscot, P. Gans, G. Schoehn, P. Macek, and J. Boisbouvier *Sci. Adv.*, vol. 4, p. 1, 2018. (Cited on pages 2, 4 and 34.)

[55] G. Abramov, A. Velyvis, E. Rennella, L. E. Wong, and L. E. Kay *Proc. Natl. Acad. Sci. USA*, vol. 117, p. 12836, 2020. (Cited on pages 2 and 34.)

[56] M. Levitt, *Spin Dynamics: Basics of Nuclear Magnetic Resonance, 2cd edition.* Wiley, 2008. (Cited on pages 2, 13, 14, 17 and 71.)

[57] A. Abragam, *The Principles of Nuclear Magnetism.* Clarendon Press, 1983. (Cited on pages 2 and 10.)

[58] J. Kowalewski and L. Mäler, *Nuclear Spin Relaxation in Liquids: Theory, Experiments, and Applications.* Taylor & Francis, 2006. (Cited on pages 2, 10 and 82.)

[59] M. P. Nicholas, E. Eryilmaz, F. Ferrage, D. Cowburn, and R. Ghose *Prog. Nucl. Magn. Reson. Spectrosc.*, vol. 57, p. 111, 2010. (Cited on pages 2, 10 and 82.)

[60] J. W. Peng and G. Wagner *J. Magn. Reson.*, vol. 98, p. 308, 1992. (Cited on page 2.)

[61] J. W. Peng and G. Wagner *Biochemistry*, vol. 31, p. 8571, 1992. (Cited on page 2.)

[62] A. G. Redfield *Magn. Reson. Chem.*, vol. 41, p. 753, 2003. (Cited on pages 3, 80 and 82.)

[63] A. G. Redfield *J. Biomol. NMR.*, vol. 52, p. 159, 2012. (Cited on pages 3, 80, 82 and 87.)

[64] M. F. Roberts and A. G. Redfield *J. Am. Chem. Soc*, vol. 126, p. 13765, 2004. (Cited on pages 3 and 80.)

[65] M. F. Roberts, Q. Cui, C. J. Turner, D. A. Case, and A. G. Redfield *Biochemistry*, vol. 43, p. 3637, 2004. (Cited on page 3.)

[66] M. W. Clarkson, M. Lei, E. Z. Eisenmesser, W. Labeikovsky, A. Redfield, and D. Kern *J. Biomol. NMR.*, vol. 45, p. 217, 2009. (Cited on pages 3 and 80.)

[67] S. F. Cousin, P. Kadeřávek, N. Bolik-Coulon, and F. Ferrage, *Determination of Protein ps-ns Motions by High-Resolution Relaxometry*, vol. 1688, p. 169. Spinger, 2018. (Cited on pages 3, 80, 88, 89, 106 and 107.)

[68] F. Ferrage, *Protein Dynamics by 15N Nuclear Magnetic Relaxation*, vol. 831, p. 141. Spinger, 2012. (Cited on pages 3 and 87.)

[69] A. Jerschow *J. Magn. Reson.*, vol. 176, p. 7, 2005. (Cited on page 3.)

[70] I. Kuprov, N. Wagner-Rundell, and P. Hore *J. Magn. Reson.*, vol. 184, p. 196, 2007. (Cited on pages 3, 22, 24 and 26.)

[71] A. Polimeno and J. H. Freed *J. Phys. Chem.*, vol. 99, p. 10995, 1995. (Cited on pages 3, 23, 116 and 138.)

[72] V. Calandrini, D. Abergel, and G. R. Kneller *J. Chem. Phys.*, vol. 133, p. 145101, 2010. (Cited on pages 3, 83 and 138.)

[73] P. Calligari and D. Abergel *J. Phys. Chem. B*, vol. 116, p. 12955, 2012. (Cited on pages 3 and 138.)

[74] M. G. Clore, A. Szabo, A. Bax, L. E. Kay, P. C. Driscoll, and A. M. Gronenborn *J. Am. Chem. Soc.*, vol. 112, p. 4989, 1990. (Cited on pages 3, 22, 40, 83, 116, 138, 139, 151 and 153.)

[75] K. Lindorff-Larsen, R. B. Best, M. A. DePristo, C. M. Dobson, and M. Vendruscolo *Nature*, vol. 433, p. 128, 2005. (Cited on pages 3 and 116.)

[76] M. Salzmann, K. Pervushin, G. Wider, H. Senn, and K. Wüthrich *Proc. Natl. Acad. Sci. USA*, vol. 95, p. 13585, 1998. (Cited on page 4.)

[77] K. Pervushin, R. Riek, G. Wider, and K. Wüthrich *J. Am. Chem. Soc.*, vol. 120, p. 6394, 1998. (Cited on pages 4 and 59.)

[78] H. Shimizu *J. Chem. Phys.*, vol. 40, p. 3357, 1964. (Cited on pages 4, 8, 34 and 59.)

[79] M. Goldman *J. Magn. Reson.*, vol. 60, p. 437, 1984. (Cited on pages 4, 8, 10, 34 and 59.)

[80] S. Wimperis and G. Bodenhausen *Molec. Phys.*, vol. 66, p. 897, 1989. (Cited on pages 4, 8, 34 and 59.)

[81] J. Fiaux, E. B. Bertelsen, A. L. Horwich, and K. Wüthrich *Nature*, vol. 418, p. 207, 2002. (Cited on pages 4 and 34.)

[82] K. Loth, P. Pelupessy, and G. Bodenhausen *J. Am. Chem. Soc.*, vol. 127, p. 6062, 2005. (Cited on pages 4 and 34.)

[83] P. Kadeřávek, L. Strouk, S. F. Cousin, C. Charlier, G. Bodenhausen, T. Marquardsen, J.-M. Tyburn, P.-A. Bovier, F. Engelke, W. Maas, and F. Ferrage *ChemPhysChem*, vol. 18, p. 2772, 2017. (Cited on pages 4 and 36.)

[84] R. R. Ernst and W. A. Anderson *Rev. Sci. Instrumental.*, vol. 37, p. 93, 1966. (Cited on page 8.)

[85] L. G. Werbelow and A. G. Marshall *J. Magn. Reson.*, vol. 11, p. 299, 1973. (Cited on page 8.)

[86] A. Mittermaier and L. E. Kay *Science*, vol. 312, p. 224, 2006. (Cited on page 9.)

[87] A. Kumar, R. C. R. Grace, and P. K. Madhu *Prog. Nucl. Magn. Reson. Spectrosc.*, vol. 37, p. 191, 2000. (Cited on page 10.)

[88] C. Bengs and M. H. Levitt *J. Magn. Reson.*, vol. 310, p. 106645, 2020. (Cited on page 11.)

[89] J. H. Ardenkjaer-Larsen, B. Fridlund, A. Gram, G. Hansson, L. Hansson, M. H. Lerche, R. Servin, M. Thaning, and K. Golman *Proc. Natl. Accad. Sci. USA*, vol. 100, p. 10158, 2003. (Cited on pages 11 and 80.)

[90] A. Kumar, R. R. Ernst, and Wüthrich *Biochem. Biophys. Res. Commun.*, vol. 95, p. 1, 1980. (Cited on page 13.)

[91] M. G. Clore and A. M. Gronenborn *Curr. Opin. Chem. Biol.*, vol. 2, p. 564, 1998. (Cited on page 13.)

[92] G. B. Matson *J. Chem. Phys.*, vol. 65, p. 4147, 1976. (Cited on pages 13 and 38.)

[93] G. B. Matson *J. Chem. Phys.*, vol. 67, p. 5152, 1977. (Cited on pages 14 and 38.)

[94] F. A. L. Anet and D. J. O'Leary *Concept Magn. Reson.*, vol. 3, p. 193, 1991. (Cited on page 14.)

[95] D. Abergel and A. G. Palmer *ChemPhysChem*, vol. 5, p. 787, 2004. (Cited on page 14.)

[96] A. G. Palmer *J. Magn. Reson.*, vol. 241, p. 3, 2014. (Cited on page 14.)

[97] J. Kowalewski and L. Werbelow *J. Magn. Reson.*, vol. 128, p. 144, 1997. (Cited on page 15.)

[98] R. Paquin, P. Pelupessy, L. Duma, C. Gervais, and G. Bodenhausen *J. Chem. Phys.*, vol. 133, p. 034506, 2010. (Cited on page 15.)

[99] P. P. Man, "Quadrupolar interactions," in *Encyclopedia of Magnetic Resonance*, vol. 6, p. 3838, John Wiley & Sons, Ltd, 2011. (Cited on page 17.)

[100] L. J. Burnett and B. H. Muller *J. Chem. Phys*, vol. 55, p. 5829, 1971. (Cited on page 17.)

[101] A. Mittermaier and L. E. Kay *J. Am. Chem. Soc*, vol. 121, p. 10608, 1999. (Cited on pages 17 and 217.)

[102] G. Lipari and A. Szabo *J. Am. Chem. Soc.*, vol. 104, p. 4559, 1982. (Cited on pages 22, 82 and 138.)

[103] L. E. Kay and D. A. Torchia *J. Magn. Reson.*, vol. 95, p. 536, 1991. (Cited on pages 22 and 138.)

[104] B. Halle *J. Chem. Phys.*, vol. 131, p. 224507, 2009. (Cited on page 22.)

[105] R. Brüschweiler, X. Liao, and P. E. Wright *Science*, vol. 268, p. 886, 1995. (Cited on pages 22 and 138.)

[106] N. Tjandra, S. E. Feller, R. W. Pastor, and A. Bax *J. Am. Chem. Soc.*, vol. 117, p. 12562, 1995. (Cited on pages 22, 104, 122, 138 and 142.)

[107] L. K. Lee, M. Rance, W. J. Chazin, and A. G. Palmer *J. Biomol. NMR.*, vol. 9, p. 287, 1997. (Cited on pages 22, 122 and 138.)

[108] J. B. Hall and D. Fushman *J. Am. Chem. Soc.*, vol. 128, p. 7855, 2006. (Cited on pages 22 and 138.)

[109] X. Liao, D. Long, D.-W. Li, R. Brüschweiler, and V. Tugarinov *J. Phys. Chem. B*, vol. 116, p. 606, 2012. (Cited on pages 22, 41 and 138.)

[110] S. N. Khan, C. Charlier, R. Augustyniak, N. Salvi, V. Déjean, G. Bodenhausen, O. Lequin, P. Pelupessy, and F. Ferrage *Biophys. J.*, vol. 109, p. 988, 2015. (Cited on pages 23, 83 and 138.)

[111] V. Wong, D. A. Case, and A. Szabo *Proc. Natl. Acad. Sci. USA*, vol. 106, p. 11016, 2009. (Cited on pages 23, 116 and 155.)

[112] Y. Ryabov and D. Fushman *Magn. Reson. Chem.*, vol. 44, p. S143, 2006. (Cited on page 23.)

[113] Y. E. Ryabov and D. Fushman *J. Am. Chem. Soc.*, vol. 129, p. 3315, 2007. (Cited on page 23.)

[114] M. Novakovic, S. F. Cousin, M. J. Jaroszewicz, R. Rosenzweig, and L. Frydman *J. Magn. Reson.*, vol. 294, p. 169, 2018. (Cited on page 31.)

[115] C. A. Waudby and J. Christodoulou *BioRχiv*, doi:10.1101/2021.04.11.439328. (Cited on page 31.)

[116] V. Tugarinov, R. Muhandiram, A. Ayed, and L. E. Kay *J. Am. Chem. Soc.*, vol. 124, p. 10025, 2002. (Cited on page 34.)

[117] J. E. Ollerenshaw, V. Tugarinov, and L. E. Kay *Magn. Reson. Chem.*, vol. 41, p. 843, 2003. (Cited on page 34.)

[118] M. J. Plevin and J. Boisbouvier, *Isotope-Labelling of Methyl Groups for NMR Studies of Large Proteins*, ch. 1, pp. 1–24. Royal Society of Chemistry, 2012. (Cited on page 34.)

[119] G. Mas, E. Crublet, O. Hamelin, P. Gans, and J. Boisbouvier *J. Biomol. NMR*, vol. 57, p. 251, 2013. (Cited on page 34.)

[120] R. Rosenzweig and L. E. Kay *Annu. Rev. Biochem.*, vol. 83, p. 291, 2014. (Cited on page 34.)

[121] R. Sprangers and L. E. Kay *Nature*, vol. 445, p. 618, 2007. (Cited on page 34.)

[122] V. Tugarinov, R. Sprangers, and L. E. Kay *J. Am. Chem. Soc.*, vol. 129, p. 1743, 2007. (Cited on page 34.)

[123] J. Kitevski-LeBlanc, A. Fradet-Turcotte, P. Kukic, M. D. Wilson, G. Portella, T. Yumen, S. Panier, S. Duan, M. D. Canny, H. van Ingen, C. H. Arrowsmith, J. L. Rubinstein, M. Vendruscolo, D. Durocher, and L. E. Kay *eLife*, vol. 6, p. e23872, 2017. (Cited on page 34.)

[124] Z. Jaseňáková, V. Zapletal, P. Padrta, M. Zachrdla, N. Bolik-Coulon, T. Marquardsen, J.-M. Tyburn, L. Žídek, F. Ferrage, and P. Kadeřávek *J. Biomol. NMR*, vol. 74, p. 139, 2020. (Cited on pages 36 and 80.)

[125] A. J. Shaka, P. B. Barker, and R. Freeman *J. Magn. Reson.*, vol. 64, p. 547, 1985. (Cited on page 37.)

[126] L. G. Werbelow and D. M. Grant *J. Chem. Phys.*, vol. 63, p. 544, 1975. (Cited on pages 38, 41 and 84.)

[127] N. Muller, G. Bodenhausen, and R. R. Ernst *J. Magn. Reson.*, vol. 75, p. 297, 1987. (Cited on page 38.)

[128] L. E. Kay and T. Bull *J. Magn. Reson.*, vol. 99, p. 615, 1992. (Cited on page 38.)

[129] J.-N. Dumez, P. Hakansson, S. Mamone, B. Meier, G. Stevanato, J. T. Hill-Cousins, S. Singha Roy, R. C. Brown, G. Pileio, and M. H. Levitt *J. Chem. Phys.*, vol. 142, p. 044506, 2015. (Cited on pages 38 and 43.)

[130] D. Frueh *Prog. Nucl. Magn. Reson.*, vol. 41, p. 305, 2002. (Cited on pages 41, 83 and 151.)

[131] V. Tugarinov, C. Scheurer, R. Brüschweiler, and L. E. Kay *J. Biomol. NMR*, vol. 30, p. 397, 2004. (Cited on pages 46, 84, 160, 169 and 177.)

[132] V. Tugarinov and L. E. Kay *J. Am. Chem. Soc.*, vol. 129, p. 9514, 2007. (Cited on page 48.)

[133] V. Tugarinov, T. K. Karamanos, A. Ceccon, and M. G. Clore *ChemPhysChem*, vol. 21, p. 13, 2020. (Cited on page 48.)

[134] L. S. Batchelder, C. Niu, and D. Torchia *J. Am. Chem. Soc.*, vol. 105, p. 2228, 1983. (Cited on page 50.)

[135] V. Tugarinov, R. Sprangers, and L. E. Kay *J. Am. Chem. Soc.*, vol. 126, p. 4921, 2004. (Cited on page 53.)

[136] P. Virtanen, R. Gommers, T. E. Oliphant, M. Haberland, T. Reddy, D. Cournapeau, E. Burovski, P. Peterson, W. Weckesser, J. Bright, S. J. van der Walt, M. Brett, J. Wilson, K. Jarrod Millman, N. Mayorov, A. R. J. Nelson, E. Jones, R. Kern, E. Larson, C. Carey, İ. Polat, Y. Feng, E. W. Moore, J. Vand erPlas, D. Laxalde, J. Perktold, R. Cimrman, I. Henriksen, E. A. Quintero, C. R. Harris, A. M. Archibald, A. H. Ribeiro, F. Pedregosa, P. van Mulbregt, and Scipy 1.0 Contributors *Nat. Methods*, vol. 17, p. 261, 2020. (Cited on pages 55, 61, 108, 131 and 140.)

[137] J. J. Helmius and C. P. Jaroniec *J. Biomol. NMR*, vol. 55, p. 355, 2013. (Cited on pages 55 and 65.)

[138] K. Takeuchi, H. Arthanari, and G. Wagner *J. Biomol. NMR*, vol. 66, p. 221, 2016. (Cited on pages 59, 68 and 69.)

[139] B. Brutscher, J. Boisbouvier, A. Pardi, D. Marion, and J.-P. Simorre *J. Am. Chem. Soc.*, vol. 120, p. 11845, 1998. (Cited on page 59.)

[140] R. Riek, K. Pervushin, C. Fernández, M. Kainosho, and K. Wüthrich *J. Am. Chem. Soc.*, vol. 123, p. 658, 2001. (Cited on page 59.)

[141] M. Guéron, J. L. Leroy, and R. H. Griffey *J. Am. Chem. Soc.*, vol. 105, p. 7262, 1983. (Cited on page 59.)

[142] F. Nußbaumer, R. Plangger, M. Roeck, and C. Kreutz *Angew. Chem. Int. Ed.*, vol. 59, p. 17062, 2020. (Cited on pages 59 and 76.)

[143] P. Allard, M. Helgstrand, and T. Härd *J. Magn. Reson.*, vol. 134, p. 7, 1998. (Cited on page 61.)

[144] S. J. van der Walt, C. S. Colbert, and G. Varoquaux *Comput. Sci. Eng.*, vol. 13, p. 22, 2011. (Cited on pages 61 and 65.)

[145] C. R. Harris, K. J. Millman, S. J. van der Walt, R. Gommers, P. Virtanen, D. Cournapeau, E. Wieser, J. Taylor, S. Berg, N. J. Smith, R. Kern, M. Picus, S. Hoyer, M. H. van

Kerkwijk, M. Brett, A. Haldane, J. Fernández del RÍo, M. Wiebe, P. Peterson, P. Gérard-Marchant, K. Sheppard, T. Reddy, W. Weckesser, H. Abbasi, C. Gohlke, and T. E. Oliphant *Nature*, vol. 585, p. 357, 2020. (Cited on pages 61 and 65.)

[146] M. H. Levitt and L. Di Bari *Bull. Magn. Reson.*, vol. 16, p. 94, 1994. (Cited on pages 61, 65, 87 and 88.)

[147] T. O. Levante and R. R. Ernst *Chem. Phys. Lett.*, vol. 241, p. 73, 1995. (Cited on page 61.)

[148] K. Pervushin, G. Wider, and K. Wüthrich *J. Biomol. NMR*, vol. 12, p. 7, 1998. (Cited on pages 62, 69, 70, 71 and 236.)

[149] M. Ottiger and A. Bax *J. Am. Chem. Soc.*, vol. 120, p. 12334, 1998. (Cited on pages 68, 238 and 239.)

[150] A. Meissner, J. Ø. Duus, and O. W. Sørensen *J. Biomol. NMR*, vol. 10, p. 89, 1997. (Cited on pages 69 and 239.)

[151] D. Rovnyak *Concepts Magn. Reson. A*, vol. 47, p. e21473, 2019. (Cited on page 74.)

[152] K. E. Arntson and W. C. Pomerantz *J. Med. Chem.*, vol. 59, p. 5158, 2016. (Cited on page 76.)

[153] B. A. Klein and B. D. Sykes *J. Biomol. NMR*, vol. 73, p. 519, 2019. (Cited on page 76.)

[154] M. Carravetta, O. G. Johannessen, and M. H. Levitt *Phys. Rev. Lett.*, vol. 92, p. 153003, 2004. (Cited on page 80.)

[155] M. Carravetta and M. H. Levitt *J. Chem. Phys*, vol. 122, p. 214505, 2005. (Cited on page 80.)

[156] J. Milani, B. Vuichoud, A. Bornet, P. Miéville, R. Mottier, S. Jannin, and G. Bodenhausen *Rev. Sci. Instrum.*, vol. 86, p. 024101, 2015. (Cited on page 80.)

[157] S. Bowen and C. Hilty *Angew. Chem. Int. Ed.*, vol. 47, p. 5235, 2008. (Cited on page 80.)

[158] R. Kimmich and E. Anoardo *Prog. Nucl. Magn. Reson. Spectrosc.*, vol. 44, p. 257, 2004. (Cited on pages 80 and 87.)

[159] C.-Y. Chou, M. Chu, C.-F. Chang, and T.-h. Huang *J. Magn. Reson.*, vol. 214, p. 302, 2012. (Cited on page 80.)

[160] S. Korchak, K. Ivanov, A. Yurkovskaya, and H.-M. Vieth *J. Chem. Phys.*, vol. 133, p. 194502, 2010. (Cited on page 80.)

[161] M. Akke, R. Brüschweiler, and A. G. Palmer *J. Am. Chem. Soc.*, vol. 115, p. 9832, 1993. (Cited on pages 82 and 139.)

[162] V. Kasinath, K. A. Sharp, and J. A. Wand *J. Am. Chem. Soc.*, vol. 135, p. 15092, 2012. (Cited on page 82.)

[163] M. L. Verteramo, O. Stenstrom, M. M. Ignjatović, O. Caldaranu, M. A. Olsson, F. Manzoni, H. Leffler, E. Oksanen, L. D. T., U. J. Nilsson, U. Ryde, and M. Akke *J. Am. Chem. Soc.*, vol. 141, p. 2012, 2019. (Cited on pages 82 and 139.)

[164] Y. Wang, M. V. Jonggul Kim, G. Li, L. G. Ahuja, P. Aoto, S. S. Taylor, and V. Gianluigi *Nat. Comm.*, vol. 10, p. 799, 2019. (Cited on page 82.)

[165] M. Xie, L. Yu, L. Bruschweiler-Li, X. Xinyao, A. L. Hansen, and R. Brüschweiler *Sci. Adv.*, vol. 5, p. 1, 2019. (Cited on page 82.)

[166] S. Wardenfelt, X. Xiang, M. Xie, L. Yu, L. Bruschweiler-Li, and R. Brüschweiler *Angew. Chem. Int. Ed.*, vol. 60, 2021. (Cited on page 82.)

[167] A. Hsu, F. Ferrage, and A. G. Palmer *Biophys. J.*, vol. 115, p. 2301, 2018. (Cited on pages 83 and 138.)

[168] R. Ghose *Concepts Magn. Reson.*, vol. 12, p. 152, 2000. (Cited on page 87.)

[169] P. Pelupessy, F. Ferrage, and G. Bodenhausen *J. Chem. Phys.*, vol. 126, p. 134, 2007. (Cited on page 88.)

[170] D. Foreman-Mackey, D. W. Hogg, D. Lang, and J. Goodman *PASP*, vol. 125, p. 306, 2013. (Cited on pages 103, 107, 152 and 169.)

[171] O. F. Lange, N.-A. Lakomek, C. Farès, G. F. Schröder, K. F. A. Walter, S. Becker, J. Meiler, H. Grubmüller, C. Griesinger, and B. L. de Groot *Science*, vol. 320, p. 1471, 2008. (Cited on page 105.)

[172] Z. Liang and J. H. Freed *J. Phys. Chem. B*, vol. 103, p. 6384, 1999. (Cited on page 116.)

[173] Y. Ryabov, M. G. Clore, and C. D. Schwieters *J. Chem. Phys.*, vol. 136, p. 034108, 2012. (Cited on pages 116 and 155.)

[174] M. L. Gill and A. G. Palmer *J. Phys. Chem. B*, vol. 118, p. 11120, 2014. (Cited on page 116.)

[175] L. G. Werbelow and D. M. Grant *Advances in Magnetic and Optical Resonance*, vol. 9, p. 189, 1977. (Cited on page 120.)

[176] D. L. Favro *Phys. Rev.*, vol. 119, p. 53, 1960. (Cited on page 120.)

[177] D. E. Woessner *J. Chem. Phys.*, vol. 37, p. 647, 1962. (Cited on page 120.)

[178] W. A. Steele *J. Chem. Phys.*, vol. 38, p. 2411, 1963. (Cited on page 120.)

[179] W. T. Huntress *J. Chem. Phys.*, vol. 48, p. 3524, 1968. (Cited on page 120.)

[180] C. D. Kroenke, P. J. Loria, L. K. Lee, M. Rance, and A. G. Palmer *J. Am. Chem. Soc.*, vol. 120, p. 7905, 1998. (Cited on page 122.)

[181] D. Fushman, R. Xu, and D. Cowburn *Biochemistry*, vol. 38, p. 10225, 1999. (Cited on pages 122 and 168.)

[182] P. Dosset, J.-C. Hus, M. Blackledge, and D. Marion *J. Biomol. NMR*, vol. 16, p. 23, 2000. (Cited on page 122.)

[183] J. B. Hall and D. Fushman *J. Biomol. NMR*, vol. 27, p. 261, 2003. (Cited on page 122.)

[184] O. Walker, R. Varadan, and D. Fushman *J. Magn. Reson.*, vol. 168, p. 336, 2004. (Cited on pages 122 and 168.)

[185] D. Fushman, R. Varadan, M. Assfalg, and O. Walker *Prog. Nucl. Magn. Reson. Spectrosc.*, vol. 44, p. 189, 2004. (Cited on pages 122 and 168.)

[186] Y. E. Ryabov, C. Geraghty, A. Varshney, and D. Fushman *J. Am. Chem. Soc.*, vol. 128, p. 15432, 2006. (Cited on page 122.)

[187] J. Tropp *J. Chem. Phys.*, vol. 72, p. 6035, 1980. (Cited on page 124.)

[188] R. J. Witterbort and A. Szabo *J. Chem. Phys.*, vol. 69, p. 1722, 1978. (Cited on page 125.)

[189] F. Hoffmann, M. Xue, L. V. Schäfer, and F. A. A. Mulder *Phys. Chem. Chem. Phys*, vol. 20, p. 24577, 2018. (Cited on page 127.)

[190] F. Hoffmann, F. A. A. Mulder, and L. V. Schäfer *J. Phys. Chem. B*, vol. 122, p. 5038, 2018. (Cited on pages 127 and 166.)

[191] D. Wallach *J. Chem. Phys.*, vol. 47, p. 5258, 1967. (Cited on page 127.)

[192] K. Kinosita, S. Kawato, and A. Ikegami *Biophys. J.*, vol. 20, p. 289, 1977. (Cited on pages 128, 130 and 132.)

[193] M. P. Warchol and W. E. Vaughan *Advances in Molecular Relaxation and Interaction Processes*, vol. 13, p. 317, 1978. (Cited on pages 128, 129 and 130.)

[194] G. Lipari and A. Szabo *Biophys. J.*, vol. 30, p. 489, 1980. (Cited on page 128.)

[195] G. Lipari and A. Szabo *J. Chem. Phys.*, vol. 75, p. 2971, 1981. (Cited on page 128.)

[196] C. C. Wang and R. Pecora *J. Chem. Phys.*, vol. 72, p. 5333, 1980. (Cited on pages 128, 129, 130, 208, 210, 259 and 262.)

[197] A. Kumar and G. C. Levy *J. Chem. Phys.*, vol. 85, p. 485, 1986. (Cited on pages 129 and 130.)

[198] A. Kumar *J. Chem. Phys.*, vol. 91, p. 1232, 1989. (Cited on pages 129 and 130.)

[199] E. W. Hobson, *Spherical and Ellipsoidal Harmonics*. Cambridge University, London, 1931. (Cited on pages 130 and 208.)

[200] W. R. Smythe, *Static and Dynamic Electricity.* McGraw-Hill, New York, 1939. (Cited on pages 130 and 210.)

[201] H. F. Bauer *Math. Comput.*, vol. 46, p. 601, 1986. (Cited on pages 130 and 209.)

[202] A. A. Smith, E. Matthias, and B. H. Meier *J. Chem. Phys.*, vol. 148, p. 045104, 2018. (Cited on page 137.)

[203] A. A. Smith, E. Matthias, B. H. Meier, and F. Ferrage *J. Chem. Phys.*, vol. 151, p. 034102, 2019. (Cited on page 137.)

[204] D. M. Schneider, M. J. Dellwo, and A. J. Wand *Biochemistry*, vol. 31, p. 3645, 1992. (Cited on page 138.)

[205] A. M. Mandel, M. Akke, and A. G. Palmer *J. Mol. Biol*, vol. 246, p. 144, 1995. (Cited on page 138.)

[206] N. A. Farrow, O. Zhang, J. D. Forman-Kay, and L. E. Kay *Biochemistry*, vol. 34, p. 868, 1995. (Cited on page 138.)

[207] V. Z. Miloushev, F. Bahna, C. Ciatto, G. Ahlsen, B. Honig, L. Shapiro, and A. G. Palmer *Structure*, vol. 16, p. 1195, 2008. (Cited on page 138.)

[208] V. Calandrini, D. Abergel, and G. R. Kneller *J. Chem. Phys.*, vol. 128, p. 145102, 2008. (Cited on page 138.)

[209] A. V. Buevich and J. Baum *J. Am. Chem. Soc.*, vol. 121, p. 8671, 1999. (Cited on page 138.)

[210] A. V. Buevich, U. P. Shinde, M. Inouye, and J. Baum *J. Biomol. NMR*, vol. 121, p. 233, 2001. (Cited on page 138.)

[211] Z. Li, S. Raychaudhuri, and A. J. Wand *Protein Sci.*, vol. 5, p. 2647, 1996. (Cited on page 139.)

[212] M. S. Marlow, J. Dogan, K. K. Frederick, K. G. Valentine, and A. J. Wand *Nat. Chem. Biol.*, vol. 6, p. 352, 2010. (Cited on pages 139 and 153.)

[213] D. Yang, Y.-K. Mol, J. D. Forman-Kay, N. A. Farrow, and L. E. Kay *J. Mol. Biol.*, vol. 272, p. 790, 1997. (Cited on pages 139 and 152.)

[214] K. K. Frederick, M. S. Marlow, K. G. Valentine, and J. Wand *Nature*, vol. 448, p. 325, 2007. (Cited on pages 139 and 153.)

[215] O. Allnér, N. Floppe, and L. Nilsson *J. Phys. Chem. B*, vol. 119, p. 1114, 2015. (Cited on page 139.)

[216] G. Solomentsev, C. Diehl, and M. Akke *Biochemistry*, vol. 57, p. 1451, 2018. (Cited on page 139.)

[217] I. Nyqvist, E. Andersson, and J. Dogan *J. Phys. Chem. B*, vol. 123, p. 2882, 2019. (Cited on page 139.)

[218] G. Barbato, M. Ikura, L. E. Kay, R. W. Pastor, and A. Box *Biochemistry*, vol. 31, p. 5269, 1992. (Cited on page 142.)

[219] K. K. Frederick, K. A. Sharp, N. Warischalk, and J. A. Wand *J. Chem. Phys. B*, vol. 112, p. 12095, 2008. (Cited on pages 142, 143 and 144.)

[220] D. A. Case *J. Biomol. NMR*, vol. 15, p. 95, 1999. (Cited on page 159.)

[221] S. Tang and D. A. Case *J. Biomol. NMR*, vol. 38, p. 255, 2007. (Cited on page 159.)

[222] M. J. Frisch, G. W. Trucks, H. B. Schlegel, G. E. Scuseria, M. A. Robb, J. R. Cheeseman, G. Scalmani, V. Barone, B. Mennucci, G. A. Petersson, H. Nakatsuji, M. Caricato, X. Li, H. P. Hratchian, A. F. Izmaylov, J. Bloino, G. Zheng, J. L. Sonnenberg, M. Hada, M. Ehara, K. Toyota, R. Fukuda, J. Hasegawa, M. Ishida, T. Nakajima, Y. Honda, O. Kitao, H. Nakai, T. Vreven, J. A. Montgomery Jr., J. E. Peralta, F. Ogliaro, M. Bearpark, J. J. Heyd, E. Brothers, K. N. Kudin, V. N. Staroverov, R. Kobayashi, J. Normand, K. Raghavachari, A. Rendell, J. C. Burant, S. S. Iyengar, J. Tomasi, M. Cossi, N. Rega, J. M. Millam, M. Klene, J. E. Knox, J. B. Cross, V. Bakken, C. Adamo, J. Jaramillo, R. Gomperts, R. E. Stratmann, O. Yazyev, A. J. Austin, R. Cammi, C. Pomelli, J. W. Ochterski, R. L. Martin, K. Morokuma, V. G. Zakrzewski, G. A. Voth, P. Salvador, J. J. Dannenberg, S. Dapprich, A. D. Daniels, Ö. Farkas, J. B. Foresman, J. V. Ortiz, J. Cioslowski, and D. J. Fox, "Gaussian 09 Revision A.01," 2009. Gaussian Inc. Wallingford CT. (Cited on page 163.)

[223] C. Lee, W. Yang, and R. G. Parr *Phys. Rev. B*, vol. 37, p. 785, 1988. (Cited on page 163.)

[224] A. D. Becke *J. Chem. Phys.*, vol. 98, p. 5648, 1993. (Cited on page 163.)

[225] R. Ditchfield, W. J. Hehre, and J. A. Pople *J. Chem. Phys.*, vol. 54, p. 724, 1971. (Cited on page 163.)

[226] J. Tomasi, B. Mennucci, and R. Cammi *Chem. Rev.*, vol. 105, p. 2999, 2005. (Cited on page 163.)

[227] D. Zeroka and H. F. Hameka *J. Chem. Phys.*, vol. 43, p. 300, 1966. (Cited on page 164.)

[228] R. Ditchfield *J. Chem. Phys.*, vol. 56, p. 5688, 1972. (Cited on page 164.)

[229] L. Siemons, B. Uluca-Yazgi, R. B. Pritchard, S. McCarthy, H. Heise, and D. F. Hansen *Chem. Commun.*, vol. 55, p. 14107, 2019. (Cited on pages 164, 178 and 181.)

[230] H. J. C. Berendsen, D. van Der Spoel, and R. van Drunen *Comput. Phys. Commun.*, vol. 91, p. 43, 1995. (Cited on page 166.)

[231] E. Lindahl, B. Hess, and D. van der Spoel *J. Mol. Model.*, vol. 7, p. 306, 2001. (Cited on page 166.)

[232] D. van der Spoel, E. Lindahl, B. Hess, G. Groenhof, A. E. Mark, and H. J. C. Berendsen *J. Comput. Chem.*, vol. 26, p. 1701, 2005. (Cited on page 166.)

[233] B. Hess, C. Kutzner, D. van der Spoel, and E. Lindahl *J. Chem. Theory Comput.*, vol. 4, p. 435, 2008. (Cited on page 166.)

[234] S. Pronk, S. Páll, R. Schulz, P. Larsson, P. Bjelkmar, R. Apostolov, M. R. Shirts, J. C. Smith, P. M. Kasson, D. van der Spoel, B. Hess, and E. Lindahl *Bioinformatics*, vol. 29, p. 845, 2013. (Cited on page 166.)

[235] R. B. Best and G. Hummer *J. Phys. Chem. B*, vol. 113, p. 9004, 2009. (Cited on page 166.)

[236] K. Lindorff-Larsen, S. Piana, K. Palmo, P. Maragakis, J. L. Klepeis, R. O. Dror, and D. E. Shaw *Proteins*, vol. 78, p. 1950, 2010. (Cited on page 166.)

[237] A. J. Wand, J. L. Urbauer, R. P. McEvoy, and R. J. Bieber *Biochemistry*, vol. 35, p. 6116, 1996. (Cited on page 168.)

[238] R. Varadan, O. Walker, C. Pickart, and D. Fushman *J. Mol. Biol*, vol. 324, p. 637, 2002. (Cited on page 168.)

[239] J. J. Chou, D. A. Case, and A. Bax *J. Am. Chem. Soc.*, vol. 125, p. 8959, 2003. (Cited on pages 177, 178 and 181.)

[240] A. Gomes and J. Morgado *Math. Prob. Eng.*, vol. 13, p. 394654, 2013. (Cited on page 209.)

Appendices

Appendix A

Mathematical definitions

A.1 Spin angular momentum operators

Spin operators are angular momentum operators, and, as such, can be decomposed in a Cartesian basis as:

$$\hat{I} = \left(\hat{I}_x, \hat{I}_y, \hat{I}_z\right), \tag{A.1}$$

where $\hat{I}_x$, $\hat{I}_y$ and $\hat{I}_z$ satisfy the commutation relations:

$$[\hat{I}_x, \hat{I}_y] = i\hbar\hat{I}_z, \quad [\hat{I}_y, \hat{I}_z] = i\hbar\hat{I}_x, \quad [\hat{I}_z, \hat{I}_x] = i\hbar\hat{I}_y, \tag{A.2}$$

where $\hbar$ is the Planck constant devided by 2π, and the commutation between two operators $\hat{A}$ and $\hat{B}$ is defined as:

$$[\hat{A}, \hat{B}] = \hat{A}\hat{B} - \hat{B}\hat{A}. \tag{A.3}$$

The matrix representation of the operators $\hat{I}_x$, $\hat{I}_y$ and $\hat{I}_z$ is given by the Pauli matrices, written here for a spin-1/2:

$$I_x = \frac{1}{2}\begin{pmatrix} 0 & 1 \\ 1 & 0 \end{pmatrix}, \quad I_y = \frac{1}{2}\begin{pmatrix} 0 & -i \\ i & 0 \end{pmatrix}, \quad I_z = \frac{1}{2}\begin{pmatrix} 1 & 0 \\ 0 & -1 \end{pmatrix}. \tag{A.4}$$

Together with the identy operator $\hat{E}$, these operators form the Cartesian basis operators for a spin system composed of one spin-1/2. It is often more convenient to use the shift basis, written here in matrix representation:

$$\begin{aligned} E_0 = \frac{1}{\sqrt{2}}E = \frac{1}{\sqrt{2}}\begin{pmatrix} 1 & 0 \\ 0 & 1 \end{pmatrix}, \quad I^+ = I_x + iI_y = \begin{pmatrix} 0 & 1 \\ 0 & 0 \end{pmatrix}, \\ I^- = I_x - iI_y = \begin{pmatrix} 0 & 0 \\ 1 & 0 \end{pmatrix}, \quad I_0 = \sqrt{2}I_z = \frac{1}{\sqrt{2}}\begin{pmatrix} 1 & 0 \\ 0 & -1 \end{pmatrix}. \end{aligned} \tag{A.5}$$

In the case of two spin-1/2, the Cartesian basis is given by the combinations of direct products between one spin basis operator and the other. For example, the matrix representation of the operator $\hat{I}^+\hat{S}^-$ is:

$$I^+ \otimes S^- = \begin{pmatrix} 0 & 0 & 0 & 0 \\ 0 & 0 & 1 & 0 \\ 0 & 0 & 0 & 0 \\ 0 & 0 & 0 & 0 \end{pmatrix}. \tag{A.6}$$

See [16] for more details.

A.2 Spherical harmonics and Wigner rotation matrices

Rank-2 spherical harmonics are directly linked to Wigner matrices as:

$$\mathcal{D}^{(2)}_{m0}(\alpha,\beta,\gamma) = \sqrt{\frac{4\pi}{5}}\mathrm{Y}^*_{2m}(\beta,\alpha), \tag{A.7}$$

with:

$$\mathcal{D}^{(2)}_{mn}(\alpha,\beta,\gamma) = e^{-im\alpha}d^{(2)}_{mn}(\beta)e^{-in\gamma}, \tag{A.8}$$

where d_{mn} is the reduced Wigner matrix. From this definition (and the one of the reduced Wigner matrices), it follows:

$$\mathcal{D}^{(2)}_{mn}(\Omega) = (-1)^{-m-n}\mathcal{D}^{(2)*}_{-m-n}(\Omega). \tag{A.9}$$

The addition theorem relates rank-2 spherical harmonics to the second-order Legendre polynomial $\mathcal{P}_2(x) = \frac{3x^2-1}{2}$:

$$\mathcal{P}_2(\vec{x}\cdot\vec{y}) = \frac{4\pi}{5}\sum_{m=-2}^{2}\mathrm{Y}_{2m}(\vec{y})\mathrm{Y}^*_{2m}(\vec{x}) = \sum_{m=-2}^{2}\mathcal{D}^{(2)*}_{m0}(\vec{y})\mathcal{D}^{(2)}_{m0}(\vec{x}). \tag{A.10}$$

Wigner matrices can be decomposed into succesive rotations:

$$\mathcal{D}^{(2)}_{mn}(\Omega_{A\to B}) = \sum_{x_1,x_2,\dots x_k}\mathcal{D}^{(2)}_{mx_1}(\Omega_{A\to X_1})\mathcal{D}^{(2)}_{x_1x_2}(\Omega_{X_1\to X_2})\dots\mathcal{D}^{(2)}_{x_{k-1}x_k}(\Omega_{X_{k-1}\to X_k})\mathcal{D}^{(2)}_{x_kn}(\Omega_{X_k\to B}), \tag{A.11}$$

where $\Omega_{X_i\to X_j}$ is the Euler angle for transformation between frame X_i and frame X_j and the sums run from -2 to 2 for each frames X_i.
Wigner matrices can be normalized:

$$\int d\Omega\mathcal{D}^{L*}_{mn}(\Omega)\mathcal{D}^{L'}_{m'n'}(\Omega) = \frac{8\pi^2}{2L+1}\delta_{LL'}\delta_{mm'}\delta_{nn'}, \tag{A.12}$$

where δ is the Kronecker function. Finally, we have the following property:

$$\sum_{m=-2}^{2}\mathcal{D}^{(2)*}_{mn}(\alpha,\beta,0)\mathcal{D}^{(2)}_{mn'}(\alpha,\beta,0) = \delta_{nn'}. \tag{A.13}$$

It is worthwhile to specify the convention for Euler angle used throughout the presented projects. If we write an Euler angle set $\Omega = \{\alpha,\beta,\gamma\}$, for tranformation from a frame $\{O,x,y,z\}$ to $\{O',x',y',z'\}$ (the two frame origins can be different, which only yields a translation without affecting the rotations), α is the rotation angle around the Oz axis, β is the rotation angle about the new Ox axis (axis rotated by an angle α around the Oz axis), and γ is the rotation about the new Oz axis (after applying the two previous rotations, only the last one affecting the z-axis).
The reduced Wigner matrices are reported in Table A.1.

Table A.1: Reduced Wigner matrices d_{mn}.

	n				
	-2	-1	0	1	2
m					
-2	$\cos^4\frac{\beta}{2}$	$\frac{1}{2}\sin\beta(\cos\beta+1)$	$\sqrt{\frac{3}{8}}\sin^2\beta$	$-\frac{1}{2}\sin\beta(\cos\beta-1)$	$\sin^4\frac{\beta}{2}$
-1	$-\frac{1}{2}\sin\beta(\cos\beta+1)$	$\frac{1}{2}(2\cos\beta-1)(\cos\beta+1)$	$\sqrt{\frac{3}{2}}\sin\beta\cos\beta$	$-\frac{1}{2}(2\cos\beta+1)(\cos\beta-1)$	$-\frac{1}{2}\sin\beta(\cos\beta-1)$
0	$\sqrt{\frac{3}{8}}\sin^2\beta$	$-\sqrt{\frac{3}{2}}\sin\beta\cos\beta$	$\frac{1}{2}(3\cos^2\beta-1)$	$\sqrt{\frac{3}{2}}\sin\beta\cos\beta$	$\sqrt{\frac{3}{8}}\sin^2\beta$
1	$\frac{1}{2}\sin\beta(\cos\beta-1)$	$-\frac{1}{2}(2\cos\beta+1)(\cos\beta-1)$	$-\sqrt{\frac{3}{2}}\sin\beta\cos\beta$	$\frac{1}{2}(2\cos\beta-1)(\cos\beta+1)$	$\frac{1}{2}\sin\beta(\cos\beta+1)$
2	$\sin^4\frac{\beta}{2}$	$\frac{1}{2}\sin\beta(\cos\beta-1)$	$\sqrt{\frac{3}{8}}\sin^2\beta$	$-\frac{1}{2}\sin\beta(\cos\beta+1)$	$\cos^4\frac{\beta}{2}$

A.3 Legendre associated functions

A.3.1 Introduction on the Gamma function

The Gamma function is defined for all $z \neq 0$ by:

$$\Gamma(z) = \int_0^\infty e^{-t} t^{z-1} dt, \tag{A.14}$$

Numerical evaluation of the Gamma function is facilitated using the following property:

$$\Gamma(z+1) = z\Gamma(z), \quad z > 0. \tag{A.15}$$

We can then show that:

$$\Gamma(z+M) = (z+M-1)(z+M-2)\cdots(z+1)z\Gamma(z), \quad M \in \mathbb{N}. \tag{A.16}$$

In addition, when $n \in \mathbb{N}^*$, we have:

$$\Gamma(n) = (n-1)!. \tag{A.17}$$

A.3.2 Definition of Legendre associated functions

The analytical expression of the Legendre associated functions is given by [199, 196]:

$$\begin{aligned} m \geq 0: \; P^m_{\nu_{m,n}}(z) = (-1)^m \frac{\Gamma(\nu_{m,n}+m+1)}{\Gamma(\nu_{m,n}-m+1)} \frac{(1-z)^{m/2}}{2^m m!} \times \\ {}_2F_1(-\nu_{m,n}+m, \nu_{m,n}+m+1, m+1, \frac{1-z}{2}), \end{aligned} \tag{A.18}$$

and:

$$P^{-m}_{\nu_{-m,n}}(z) = (-1)^m \frac{\Gamma(\nu_{m,n}-m+1)}{\Gamma(\nu_{m,n}+m+1)} P^m_{\nu_{m,n}}(z), \tag{A.19}$$

where ${}_2F_1$ is the Hypergeometric function:

$${}_2F_1(\alpha,\beta,\gamma,z) = 1 + \frac{\alpha\beta}{\gamma}\frac{z}{1!} + \frac{\alpha(\alpha+1)\beta(\beta+1)}{\gamma(\gamma+1)}\frac{z^2}{2!} + \cdots. \tag{A.20}$$

We can use the Gamma function to write in a compact form:

$$\begin{cases} {}_2F_1(\alpha,\beta,\gamma,z) = 1, \quad \alpha = 0 \text{ or } \beta = 0, \\ {}_2F_1(\alpha,\beta,\gamma,z) = \displaystyle\sum_{k=0}^{\infty} \frac{\Gamma(\alpha+k)\Gamma(\beta+k)\Gamma(\gamma)}{\Gamma(\alpha)\Gamma(\beta)\Gamma(\gamma+k)} \frac{z^k}{k!}, \quad \alpha \neq 0 \text{ and } \beta \neq 0. \end{cases} \tag{A.21}$$

A.3.3 Roots of Legendre associated functions

Here, we show how the values of $\nu_{m,n}$ can be found. Different studies have already been published to report roots of the Legendre associated functions, and we do not aim here at proposing a new

method. We will detail the chosen methodology, which has been reported by H. Bauer [201]. It consists in solving for $\nu_{m,n}$ the following equation:

$$f(\nu_{m,n}, \beta_{cone}) = 0, \tag{A.22}$$

with:

$$f(\nu_{m,n}, \beta_{cone}) = \nu_{m,n} - m - \nu_{m,n}\cos\beta_{cone} + \sum_{n=1}^{+\infty} \frac{m!(\nu_{m,n}+m+1)^{(n-1)}(-\nu_{m,n}+m+1)^{(n-1)}}{n!(m+n)!} \times \sin^{2n}\frac{\beta_{cone}}{2}\left[(\nu_{m,n}^2 - m^2)(m-\nu_{m,n}+n) - \nu_{m,n}(m-\nu_{m,n})(m+n+\nu_{m,n})\cos\beta_{cone}\right], \tag{A.23}$$

where we have used the Pochhammer symbol $x^{(n)} = x(x+1)\cdots(x+n-1)$, and $x^{(0)} = 1$. In order to find the roots, from the lowest to the highest, we performed the regula falsi method [240] on intervals $\nu \in [k, k+0.1]$, $k \in \mathbb{Z}$, starting with $n = 0$, and implemented in Python. The sum in the definition of f was stopped at $n = 75$ (numerical evaluation of the factorial leads to overflows for larger sum limits).

In the frame of the study presented in this manuscript, only integer values of m from -4 to 4 are relevant. In addition, using Eq. A.19, it is straightforward to show that the roots obey the following usefull property:

$$\nu_{-m,n} = \nu_{m,n}, \tag{A.24}$$

such that we only need to consider values of $m \in \{0, 1, 2, 3, 4\}$. We have calculated the 5 first roots for angles $\beta_{cone} \in [0.01, \frac{\pi}{3}]$ (Fig. A.1).

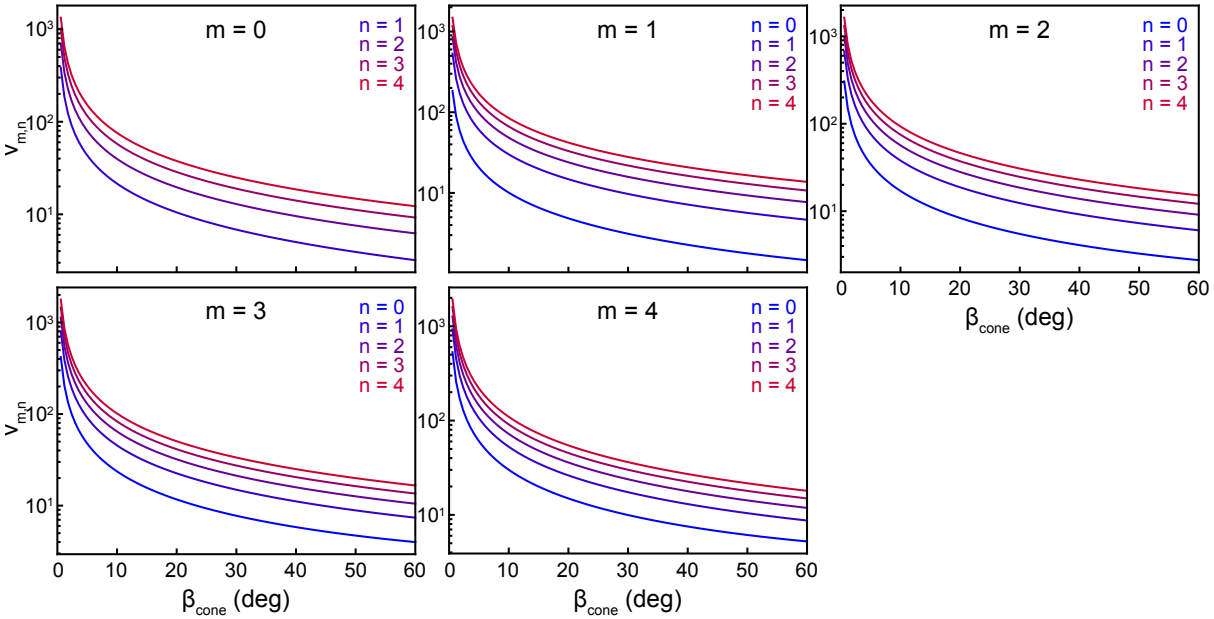

Figure A.1: Values of $\nu_{m,n}$ as a function of the cone semi-angle opening β_{cone} for $m = \{0, 1, 2, 3, 4\}$. In the case where $m = 0$, $\nu_{0,0} = 0$ for all cone semi-angle opening value.

A.3.4 Orthogonality of the Legendre associated functions

C. Wang and R. Pecora [196] reported the following result from W. Smythe [200], for $\nu_{m,n} \neq \nu_{m',n'}$:

$$\int_{\mu_0}^{1} P^{m}_{\nu_{m,n}}(\mu) P^{m'}_{\nu_{m',n'}}(\mu) d\mu = \frac{(\mu_0^2 - 1)\left[P^{m}_{\nu_{m,n}}(\mu_0) \left(\frac{dP^{m'}_{\nu_{m',n'}}(\mu)}{d\mu} \right)_{\mu=\mu_0} - P^{m'}_{\nu_{m',n'}}(\mu_0) \left(\frac{dP^{m}_{\nu_{m,n}}(\mu)}{d\mu} \right)_{\mu=\mu_0} \right]}{(\nu_{m,n} - \nu_{m',n'})(\nu_{m,n} + \nu_{m',n'} + 1)}. \tag{A.25}$$

Applied to the particular situation presented in this manuscript, that is using the boundary condition Eq. 4.44, this leads to:

$$\int_{\mu_{cone}}^{1} P^{m}_{\nu_{m,n}}(\mu) P^{m'}_{\nu_{m',n'}}(\mu) d\mu = \delta_{nn'} \delta_{mm'} H_{m,n}(\mu_{cone}), \tag{A.26}$$

where $\mu_{cone} = \cos \beta_{cone}$. Using Eq. A.19, it can be shown easily that:

$$\frac{P^{-m}_{\nu_{-m,n}}(\mu_1) P^{-m}_{\nu_{-m,n}}(\mu_2)}{H_{-m,n}(\mu_{cone})} = \frac{P^{m}_{\nu_{m,n}}(\mu_1) P^{m}_{\nu_{m,n}}(\mu_2)}{H_{m,n}(\mu_{cone})}, \tag{A.27}$$

where μ_1 and μ_2 are the cosine of two, potentially different, angles.

A result that will prove itself usefull is:

$$H_{0,0}(\mu_{cone}) = 1 - \mu_{cone}, \tag{A.28}$$

which is easily prooven after noticing that $\nu_{0,0} = 0$ and:

$$P^{0}_{\nu_{0,0}}(z) = 1. \tag{A.29}$$

Appendix B

RedKite implementation details

B.1 Variables names

Table B.1: Variable names used in RedKite.

Name	definition	User-defined?
Atoms	Table containing the spins present in the system and their associated labels	Yes
NumberofAtoms	number of spins considered	No
LF	vector orienting the System Frame in the Cartesian axis system	Yes
Coordinates	Table containing the position of the spins in the Cartesian axis system	Yes
CSAConsidered	Table filled with 1 (CSA is considered) or 0 (CSA is neglected)	Yes
$\delta_{csa}[i]$	value of the axially symmetric CSA associated with nucleus i	Yes
σlong$[i]$	value of the longitudinal component of an asymmetric CSA associated with nucleus i	Yes
σperp$[i]$	value of the orthogonal component of an asymmetric CSA associated with nucleus i	Yes
vectorNum$^{\text{"CSA"}}{}_i$	orientation of the principal axis of a symmetric CSA tensor for spin i	Yes
vectorNuml$^{\text{"CSA"}}{}_i$	orientation of the longitudinal component of a symmetric CSA tensor for spin i	Yes
vectorNump$^{\text{"CSA"}}{}_i$	orientation of the longitudinal component of a symmetric CSA tensor for spin i	Yes
$d_{\mathcal{Q}}[i]$	strength of the quadrupolar interaction for spin i	Yes
vectorNum$^{\text{"Quad"}}{}_i$	orientation of the quadrupolar interaction for spin i	Yes
opTDip	tensors associated with dipolar interactions	No
opTCSA	tensors associated with CSA interactions	No
opTQuad	tensors associated with quadrupolar interactions	No
opTDipFreq	frequencies associated to tensors OpTDip	No
opTCSAFreq	frequencies associated to tensors OpTCSA	No
opTQuadFreq	frequencies associated to tensors OpTQuad	No

Continued on next page

Table B.1 – continued from previous page

Name	definition	User-defined?
dDD[i, j]	dipolar coefficient for the interaction of spins i and j	No
$\Phi[i, j]$	vector linking spins i and j	No
Δ_i	symmetric CSA value in Hz: $\sqrt{2/3}\delta_{csa}[i]\omega[i]$	No
σln_i	longitudinal component of an asymmetric CSA value in Hz: $\sqrt{2/3}\sigma\text{long}[i]\omega[i]$	No
σpn_i	orthogonal component of an asymmetric CSA value in Hz: $\sqrt{2/3}\sigma\text{perp}[i]\omega[i]$	No
$\omega[i]$	Larmor frequency associated with spin i	No
AngleCSA[n, 1]	orientation of the longitudinal component of the CSA of spin i	No
AngleCSA[n, 2]	orientation of the orthogonal component of the CSA of spin i	No
		No
AngleQ[n, 2]	orientation of the quadrupolar interaction of spin i	
M	function depending on variables detailed in main text to perform the calculations	No
SpinTermOfInterest	Studied operator during the relaxation experiments	Yes

B.2 Tensor operators definitions

Table B.2: Tensor operators for the dipole-dipole interaction and associated frequency as written in RedKite. Tensors are of rank 2 and with coherence order q. The letter p refers to the decomposition of the tensors in the irreducible tensor operator basis. Tensors are written opTDip$[\{i_, j_\}, \{q, p\}]$ for the interaction between nuclei i and j. The associated frequencies are opTDipFreq$[\{i_, j_\}, \{q, p\}]$. We define $\omega[i] = -\gamma_i B_0$ in RedKite.

coherence order	p	Tensor	Frequency
2	0	$\frac{1}{2}$opI$[i, "+"]$.opI$[j, "+"]$	$\omega[i] + \omega[j]$
1	0	$-\frac{1}{2}$opI$[i, "z"]$.opI$[j, "+"]$	$\omega[j]$
1	1	$-\frac{1}{2}$opI$[i, "+"]$.opI$[j, "z"]$	$\omega[i]$
0	-1	$-\frac{1}{2\sqrt{6}}$opI$[i, "-"]$.opI$[j, "+"]$	$\omega[j] - \omega[i]$
0	0	$\frac{2}{\sqrt{6}}$opI$[i, "z"]$.opI$[j, "z"]$	0
0	1	$-\frac{1}{2\sqrt{6}}$opI$[i, "+"]$.opI$[j, "-"]$	$\omega[i] - \omega[j]$
-1	0	$\frac{1}{2}$opI$[i, "z"]$.opI$[j, "-"]$	$\omega[j]$
-1	1	$\frac{1}{2}$opI$[i, "-"]$.opI$[j, "z"]$	$\omega[i]$
-2	0	$\frac{1}{2}$opI$[i, "-"]$.opI$[j, "-"]$	$-\omega[i] - \omega[j]$

Table B.3: Tensor operators for the CSA interaction and associated frequency as written in RedKite. Tensors are of rank 2 and with coherence order q. Tensors are written opTCSA$[i_, \{q, 0\}]$ for the interaction between nuclei i and j. The associated frequencies are opTCSAFreq$[i_, \{q, 0\}]$. We define $\omega[i] = -\gamma_i B_0$ in RedKite.

coherence order	Tensor	Frequency
2	0	$2\omega[i]$
1	$-\frac{1}{2}$opI$[i, "+"]$	$\omega[i]$
0	$\frac{2}{\sqrt{6}}$opI$[i, "z"]$	0
-1	$\frac{1}{2}$opI$[i, "-"]$	$-\omega[i]$
-2	0	$-2\omega[i]$

Table B.4: Tensor operators for the quadrupolar interaction and associated frequency as written in RedKite. Tensors are of rank 2 and with coherence order q. Tensors are written opTQuad$[i_, \{q, 0\}]$ for the interaction between nuclei i and j. The associated frequencies are opTQuadFreq$[i_, \{q, 0\}]$. We define $\omega[i] = -\gamma_i B_0$ in RedKite.

coherence order	Tensor	Frequency
2	$\frac{1}{2}$opI$[i, "+"]$.opI$[i, "+"]$	$2\omega[i]$
1	$-\frac{1}{2}$(opI$[i, "z"]$.opI$[i, "+"]$	$\omega[i]$
	+opI$[i, "+"]$.opI$[i, "z"]$)	
0	$\frac{1}{\sqrt{6}}$(2opI$[i, "z"]$.opI$[i, "z"]$	
	−opI$[i, "x"]$.opI$[i, "x"]$	0
	−opI$[i, "y"]$.opI$[i, "y"]$)	
-1	$\frac{1}{2}$(opI$[i, "z"]$.opI$[i, "-"]$	$-\omega[i]$
	+opI$[i, "-"]$.opI$[i, "z"]$)	
-2	$\frac{1}{2}$opI$[i, "-"]$.opI$[i, "-"]$	$-2\omega[i]$

B.3 Hamiltonian in RedKite

We report here the definition of the Hamiltonian as written in RedKite. Constants are defined in Table B.1.
For the dipolar interaction:

$$\text{HDD[i\_, j\_, t\_] := } \sqrt{6}\ \text{dDD[Nuclei[[i, 2]],Nuclei[[j, 2]]] } \times \text{ Sum[} (-1)^m \text{ M[m, opTDipFreq[\{Nuclei[[i,1]],Nuclei[[j,1]]\},\{-m,k\}], t,}\Phi\text{[Nuclei[[i,2]], Nuclei[[j,2]]]] opTDip[\{Nuclei[[i,1]],Nuclei[[j,1]]\},\{-m,k\}], \{m, -2, 2\}], \{k, Min[0, Abs[m]-1], Min[1, 2 - Abs[m]]\}];}$$
$$\text{HDDtot[t\_] := Sum[HDD[i,j,t], \{i, 1,NumberofAtoms-1\}, \{j, i+1,NumberofAtoms\}];}$$

For the CSA interaction, in the case of an axially symmetric tensor:

$$\text{HCSA[t\_] := Sum[CSAConsidered[[n]] Sum[} (-1)^m \Delta_{\text{Nuclei}[[n,2]]} \text{ M[m, opTCSAFreq[Nuclei[[n,1]],\{-m,0\}], t,AngleCSA[[n, 1]]] opTCSA[Nuclei[[n,1]],\{-m,0\}], \{m, -2, 2\}], \{n, 1, NumberofAtoms\}];}$$

and for an asymmetric tensor:

$$\text{HCSA[t\_] := Sum[CSAConsidered[[n]] Sum[} (-1)^m \Big(\sigma\text{ln}_{\text{Nuclei}[[n,2]]} \text{ M[m, opTCSAFreq[Nuclei[[n,1]],\{-m,0\}], t,AngleCSA[[n, 1]]] + } \sigma\text{pn}_{\text{Nuclei}[[n,2]]} \text{ M[m, opTCSAFreq[Nuclei[[n,1]],\{-m,0\}], t,AngleCSA[[n, 2]]] } \Big) \text{ opTCSA[Nuclei[[n,1]],\{-m,0\}], \{m, -2, 2\}], \{n, 1, NumberofAtoms\}];}$$

and for the quadrupolar interaction:

$$\text{HQuad[i\_, t\_] := } \frac{d_{\mathcal{Q}}\text{[AtomsQuadConsidered[[}i\text{,2]]}}{\text{4QuantumNumberConsidered[[}i\text{]](2QuantumNumberConsidered[[}i\text{]]}-1)} \text{ Sum[}(-1)^k \text{ M[m, opTQuadFreq[Atoms[[i, 1]], \{-m, 0\}], t, AngleQ[[i]]] } V_k \text{ opTQuad[AtomsQuadConsidered[[n,2]],\{-m,0\}], \{m, -2, 2\}], \{k, -2, 2\}];}$$

B.4 Set up of RedKite for $^{13}C^1H^2H_2$-methyl groups with a vicinal deuterium

Here, we show the most important command lines used to calculate relaxation rates and relaxation matrix of a $\{^{13}C^1H^2H_2\}$-methyl group with a vicinal deuterium nucleus.

```
Nuclei = {{"13C","CA"}, {"1H", "HA"}, {"2H", "DA"}, {"2H", "DB"}, {"2H", "DC"}};
```

The deuterium DC is associated with the vicinal deuterium here. The *SetSpinSystem* [20] command is then run as explained in the section 1.3. We define the intermediate constants:

```
α = 109.47π/180;
aCH = π − α;
rCH = 1.115 × 10^−10;
rCD = 1.115 × 10^−10;
hCH = rCH × Cos[aCH];
hCD = rCD × Cos[aCH];
OH = Sqrt[rCD^2 − hCH^2];
OD = Sqrt[rCD^2 − hCD^2];
ryCD := rxyCDvic;
rzCD := rzCDvic;
```

before definition of the atoms coordinates:

```
Coordinates ={{0, 0, 0},
              {0, −OH, hCH},
              {(Sqrt[3]/2)OD, 2OD/2, hCD},
              {−(Sqrt[3]/2)OD, 2OD/2, hCD},
              {0, ryCD, rzCD};
```

The carbon-13 is set at the origin of the Cartesian axis system, the ^1H is in the *Oyz* plan, as is the vicinal deuterium, which position is determined by two unknown (later optimized) variables describing its position along axes *Oy* and *Oz* (ryCD and rzCD, respectively). The two deuterium nuclei of the methyl group are mirror image of one another with respect to the *Oyz* plane.
We define a SF with z-axis along the symmetry axis of the methyl group, *i.e.* the *Oz* axis:

```
SF = {0, 0, 1};
```

The orientation of the interactions relative to the SF is important when studying the dynamics of the methyl groups, in particular their rotation around the symmetry axis, and are used in the definition of the spectral density function.

We only consider the CSA for the carbon-13 nucleus, assumed to be axially symmetric:

$$\text{CSAConsidered} = \{1, 0, 0, 0, 0\};$$

with value CSAValue:

$$\delta_{csa}[1] = \text{CSAValue};$$

and oriented along the CC bond (*i.e.* the symmetry axis):

$$\text{vectorNum}_1^{\text{"CSA"}} = \{0,\ 0,\ 1\};$$

Finally, we consider the quadrupolar interaction of the methyl deuterium nuclei, but not for the vicinal deuterium [101]:

$$\begin{aligned} d_{\mathcal{Q}}[1] &= 0; \\ d_{\mathcal{Q}}[2] &= 0; \\ d_{\mathcal{Q}}[3] &= 167000 * 2 * \pi; \\ d_{\mathcal{Q}}[4] &= 167000 * 2 * \pi; \\ d_{\mathcal{Q}}[5] &= 0; \end{aligned}$$

and we define the orientations of the considered quadrupolar interactions:

$$\begin{aligned} \text{vectorNum}_3^{\text{"Quad"}} &= \text{Vec["CA", "DA"]}; \\ \text{vectorNum}_4^{\text{"Quad"}} &= \text{Vec["CA", "DB"]}; \\ \text{vectorNum}_5^{\text{"Quad"}} &= \{0,\ 0,\ 0\}; \end{aligned}$$

where the command *Vec* extracts the vector between the two entries (the two nuclei). In the following analytical expressions of relaxation rates, the intensity of the quadrupolar interaction will be labelled $\zeta_{\mathcal{Q}}$.

Appendix C

Analytical expressions of relaxation rates

C.1 Relaxation rates relevant for the methyl-TROSY

C.1.1 Notations

Table C.1: Spectral density functions used in the description of relaxation in a methyl group and associated values of $S^2_m(\theta_{\vec{i},\vec{j}})$ and $\mathcal{P}_2(\cos(\theta_{\vec{i},\vec{j}})$ for different interactions. $\mathcal{J}_{\mathrm{CCH}}$ and $\mathcal{J}_{\mathrm{CCHH}}$ are negative at all magnetic fields.

Notation	Correlation	Interactions	$S^2_m(\theta_{\vec{i},\vec{j}})$	$\mathcal{P}_2(\cos(\theta_{\vec{i},\vec{j}})$
$\mathcal{J}_{\mathrm{CC}}$	auto-correlation C-C	CSA	1	1
$\mathcal{J}_{\mathrm{CH}}$	auto-correlation C-H	DD	1/9	1
$\mathcal{J}_{\mathrm{HH}}$	auto-correlation H-H	DD	1/4	1
$\mathcal{J}_{\mathrm{HCH}}$	cross-correlation between two C-H pairs	DD/DD	1/9	-1/3
$\mathcal{J}_{\mathrm{HHH}}$	cross-correlation between two H-H pairs	DD/DD	1/4	-1/8
$\mathcal{J}_{\mathrm{CHH}}$	cross-correlation between a C-H_i and a H_i-H_j pair	DD/DD	1/6	1/2
$\mathcal{J}_{\mathrm{CHHH}}$	cross-correlation between a C-H_i and a H_j-H_k pair	DD/DD	1/6	-1/2
$\mathcal{J}_{\mathrm{CCH}}$	cross-correlation between the ^{13}C-CSA and a C-H pair	CSA/DD	-1/3	-1/3
$\mathcal{J}_{\mathrm{CCHH}}$	cross-correlation between the ^{13}C-CSA and a H-H pair	CSA/DD	-1/2	-1/2

C.1.2 Relaxation in the zero-quantum subspace

C.1.2.1 Auto-relaxation rates

$$
\begin{aligned}
R(ZQ^{\mathrm{A}}_{\mathrm{outer},1}) =& \frac{1}{8} d^2_{\mathrm{CH}} \left[8\mathcal{J}_{\mathrm{CH}}(0) + 9\mathcal{J}_{\mathrm{CH}}(\omega_{\mathrm{C}}) + 4\mathcal{J}_{\mathrm{CH}}(\omega_{\mathrm{C}} - \omega_{\mathrm{H}}) + 9\mathcal{J}_{\mathrm{CH}}(\omega_{\mathrm{H}}) + 12\mathcal{J}_{\mathrm{CH}}(\omega_{\mathrm{C}} + \omega_{\mathrm{H}})\right] \\
&+ \frac{1}{4} d^2_{\mathrm{CH}} \left[4\mathcal{J}_{\mathrm{HCH}}(0) + 3\mathcal{J}_{\mathrm{HCH}}(\omega_{\mathrm{C}}) + \mathcal{J}_{\mathrm{HCH}}(\omega_{\mathrm{C}} - \omega_{\mathrm{H}}) + 3\mathcal{J}_{\mathrm{HCH}}(\omega_{\mathrm{H}}) + 6\mathcal{J}_{\mathrm{HCH}}(\omega_{\mathrm{C}} + \omega_{\mathrm{H}})\right] \\
&- \frac{3}{2} d_{\mathrm{CH}} d_{\mathrm{HH}} \left[2\mathcal{J}_{\mathrm{CHH}}(0) + \mathcal{J}_{\mathrm{CHH}}(\omega_{\mathrm{H}}) + 2\mathcal{J}_{\mathrm{CHHH}}(0) - \mathcal{J}_{\mathrm{CHHH}}(\omega_{\mathrm{H}})\right] \\
&+ \frac{3}{4} d^2_{\mathrm{HH}} \left[3\mathcal{J}_{\mathrm{HH}}(0) + 4\mathcal{J}_{\mathrm{HH}}(\omega_{\mathrm{H}}) + 4\mathcal{J}_{\mathrm{HH}}(2\omega_{\mathrm{H}})\right] \\
&+ \frac{3}{4} d^2_{\mathrm{HH}} \left[3\mathcal{J}_{\mathrm{HHH}}(0) + 2\mathcal{J}_{\mathrm{HHH}}(\omega_{\mathrm{H}}) + 2\mathcal{J}_{\mathrm{HHH}}(2\omega_{\mathrm{H}})\right] \\
&+ \frac{1}{18} \sigma^2_C \omega^2_{\mathrm{C}} \left[4\mathcal{J}_{\mathrm{CC}}(0) + 3\mathcal{J}_{\mathrm{CC}}(\omega_{\mathrm{C}})\right] \\
&+ \frac{1}{3} d_{\mathrm{CH}} \sigma_C \omega_{\mathrm{C}} \left[4\mathcal{J}_{\mathrm{CCH}}(0) + 3\mathcal{J}_{\mathrm{CCH}}(\omega_{\mathrm{C}})\right] - 4 d_{\mathrm{HH}} \sigma_C \omega_{\mathrm{C}} \mathcal{J}_{\mathrm{CCHH}}(0) \\
R(ZQ^{\mathrm{A}}_{\mathrm{outer},2}) =& \frac{1}{8} d^2_{\mathrm{CH}} \left[8\mathcal{J}_{\mathrm{CH}}(0) + 9\mathcal{J}_{\mathrm{CH}}(\omega_{\mathrm{C}}) + 4\mathcal{J}_{\mathrm{CH}}(\omega_{\mathrm{C}} - \omega_{\mathrm{H}}) + 9\mathcal{J}_{\mathrm{CH}}(\omega_{\mathrm{H}}) + 12\mathcal{J}_{\mathrm{CH}}(\omega_{\mathrm{C}} + \omega_{\mathrm{H}})\right] \\
&+ \frac{1}{4} d^2_{\mathrm{CH}} \left[4\mathcal{J}_{\mathrm{HCH}}(0) + 3\mathcal{J}_{\mathrm{HCH}}(\omega_{\mathrm{C}}) + \mathcal{J}_{\mathrm{HCH}}(\omega_{\mathrm{C}} - \omega_{\mathrm{H}}) + 3\mathcal{J}_{\mathrm{HCH}}(\omega_{\mathrm{H}}) + 6\mathcal{J}_{\mathrm{HCH}}(\omega_{\mathrm{C}} + \omega_{\mathrm{H}})\right] \\
&- \frac{3}{2} d_{\mathrm{CH}} d_{\mathrm{HH}} \left[2\mathcal{J}_{\mathrm{CHH}}(0) + \mathcal{J}_{\mathrm{CHH}}(\omega_{\mathrm{H}}) + 2\mathcal{J}_{\mathrm{CHHH}}(0) - \mathcal{J}_{\mathrm{CHHH}}(\omega_{\mathrm{H}})\right] \\
&+ \frac{3}{4} d^2_{\mathrm{HH}} \left[3\mathcal{J}_{\mathrm{HH}}(0) + 4\mathcal{J}_{\mathrm{HH}}(\omega_{\mathrm{H}}) + 4\mathcal{J}_{\mathrm{HH}}(2\omega_{\mathrm{H}})\right] \\
&+ \frac{3}{4} d^2_{\mathrm{HH}} \left[3\mathcal{J}_{\mathrm{HHH}}(0) + 2\mathcal{J}_{\mathrm{HHH}}(\omega_{\mathrm{H}}) + 2\mathcal{J}_{\mathrm{HHH}}(2\omega_{\mathrm{H}})\right] \\
&+ \frac{1}{18} \sigma^2_C \omega^2_{\mathrm{C}} \left[4\mathcal{J}_{\mathrm{CC}}(0) + 3\mathcal{J}_{\mathrm{CC}}(\omega_{\mathrm{C}})\right] \\
&- \frac{1}{3} d_{\mathrm{CH}} \sigma_C \omega_{\mathrm{C}} \left[4\mathcal{J}_{\mathrm{CCH}}(0) + 3\mathcal{J}_{\mathrm{CCH}}(\omega_{\mathrm{C}})\right] + 4 d_{\mathrm{HH}} \sigma_C \omega_{\mathrm{C}} \mathcal{J}_{\mathrm{CCHH}}(0) \\
R(ZQ^{\mathrm{A}}_{\mathrm{central}}) =& \frac{1}{24} d^2_{\mathrm{CH}} \left[16\mathcal{J}_{\mathrm{CH}}(0) + 27\mathcal{J}_{\mathrm{CH}}(\omega_{\mathrm{C}}) + 12\mathcal{J}_{\mathrm{CH}}(\omega_{\mathrm{C}} - \omega_{\mathrm{H}}) + 27\mathcal{J}_{\mathrm{CH}}(\omega_{\mathrm{H}}) + 36\mathcal{J}_{\mathrm{CH}}(\omega_{\mathrm{C}} + \omega_{\mathrm{H}})\right] \\
&+ \frac{1}{12} d^2_{\mathrm{CH}} \left[-8\mathcal{J}_{\mathrm{HCH}}(0) - 9\mathcal{J}_{\mathrm{HCH}}(\omega_{\mathrm{C}}) + 6\mathcal{J}_{\mathrm{HCH}}(\omega_{\mathrm{C}} - \omega_{\mathrm{H}}) + 18\mathcal{J}_{\mathrm{HCH}}(\omega_{\mathrm{H}}) + 36\mathcal{J}_{\mathrm{HCH}}(\omega_{\mathrm{C}} + \omega_{\mathrm{H}})\right] \\
&- \frac{1}{2} d_{\mathrm{CH}} d_{\mathrm{HH}} \left[4\mathcal{J}_{\mathrm{CHH}}(0) + 3\mathcal{J}_{\mathrm{CHH}}(\omega_{\mathrm{H}})\right] + 2 d_{\mathrm{CH}} d_{\mathrm{HH}} \left[2\mathcal{J}_{\mathrm{CHHH}}(0) - 3\mathcal{J}_{\mathrm{CHHH}}(\omega_{\mathrm{H}})\right] \\
&+ \frac{3}{4} d^2_{\mathrm{HH}} \left[2\mathcal{J}_{\mathrm{HH}}(0) + 5\mathcal{J}_{\mathrm{HH}}(\omega_{\mathrm{H}}) + 2\mathcal{J}_{\mathrm{HH}}(2\omega_{\mathrm{H}})\right] \\
&+ \frac{3}{4} d^2_{\mathrm{HH}} \left[-2\mathcal{J}_{\mathrm{HHH}}(0) + \mathcal{J}_{\mathrm{HHH}}(\omega_{\mathrm{H}}) + 4\mathcal{J}_{\mathrm{HHH}}(2\omega_{\mathrm{H}})\right] \\
&+ \frac{1}{18} \sigma^2_C \omega^2_{\mathrm{C}} \left[4\mathcal{J}_{\mathrm{CC}}(0) + 3\mathcal{J}_{\mathrm{CC}}(\omega_{\mathrm{C}})\right]
\end{aligned}
$$

$$
\begin{aligned}
R(ZQ^{\Sigma\mathrm{E}}_{\mathrm{central}}) =& \frac{1}{24} d^2_{\mathrm{CH}} \left[8\mathcal{J}_{\mathrm{CH}}(0) + 27\mathcal{J}_{\mathrm{CH}}(\omega_{\mathrm{C}}) + 12\mathcal{J}_{\mathrm{CH}}(\omega_{\mathrm{C}} - \omega_{\mathrm{H}}) + 27\mathcal{J}_{\mathrm{CH}}(\omega_{\mathrm{H}}) + 36\mathcal{J}_{\mathrm{CH}}(\omega_{\mathrm{C}} + \omega_{\mathrm{H}})\right] \\
& - \frac{1}{12} d^2_{\mathrm{CH}} \left[4\mathcal{J}_{\mathrm{HCH}}(0) + 9\mathcal{J}_{\mathrm{HCH}}(\omega_{\mathrm{C}}) + 3\mathcal{J}_{\mathrm{HCH}}(\omega_{\mathrm{C}} - \omega_{\mathrm{H}}) + 9\mathcal{J}_{\mathrm{HCH}}(\omega_{\mathrm{H}}) + 18\mathcal{J}_{\mathrm{HCH}}(\omega_{\mathrm{C}} + \omega_{\mathrm{H}})\right] \\
& - \frac{1}{2} d_{\mathrm{CH}} d_{\mathrm{HH}} \left[2\mathcal{J}_{\mathrm{CHH}}(0) + 3\mathcal{J}_{\mathrm{CHH}}(\omega_{\mathrm{H}}) - 2\mathcal{J}_{\mathrm{CHHH}}(0) - 3\mathcal{J}_{\mathrm{CHHH}}(\omega_{\mathrm{H}})\right] \\
& + \frac{3}{4} d^2_{\mathrm{HH}} \left[\mathcal{J}_{\mathrm{HH}}(0) + 2\mathcal{J}_{\mathrm{HH}}(\omega_{\mathrm{H}}) + 2\mathcal{J}_{\mathrm{HH}}(2\omega_{\mathrm{H}})\right] \\
& - \frac{3}{4} d^2_{\mathrm{HH}} \left[\mathcal{J}_{\mathrm{HHH}}(0) + 2\mathcal{J}_{\mathrm{HHH}}(\omega_{\mathrm{H}}) + 2\mathcal{J}_{\mathrm{HHH}}(2\omega_{\mathrm{H}})\right] \\
& + \frac{1}{18} \sigma^2_C \omega^2_{\mathrm{C}} \left[4\mathcal{J}_{\mathrm{CC}}(0) + 3\mathcal{J}_{\mathrm{CC}}(\omega_{\mathrm{C}})\right]
\end{aligned}
$$

C.1.2.2 Cross-relaxation rates

$$
\begin{aligned}
R(ZQ^{\mathrm{A}}_{\mathrm{outer},1} \leftrightarrow ZQ^{\mathrm{A}}_{\mathrm{outer},2}) =& -\frac{3}{2} d^2_{\mathrm{HH}} \mathcal{J}_{\mathrm{HH}}(2\omega_{\mathrm{H}}) - 3 d^2_{\mathrm{HH}} \mathcal{J}_{\mathrm{HHH}}(2\omega_{\mathrm{H}}) \\
R(ZQ^{\mathrm{A}}_{\mathrm{outer},1} \leftrightarrow ZQ^{\mathrm{A}}_{\mathrm{central}}) =& \frac{\sqrt{3}}{4} d^2_{\mathrm{CH}} \mathcal{J}_{\mathrm{CH}}(\omega_{\mathrm{H}}) + \frac{\sqrt{3}}{2} d^2_{\mathrm{CH}} \mathcal{J}_{\mathrm{HCH}}(\omega_{\mathrm{H}}) - \frac{\sqrt{3}}{2} d_{\mathrm{CH}} d_{\mathrm{HH}} \left[2\mathcal{J}_{\mathrm{CHH}}(\omega_{\mathrm{H}}) + \mathcal{J}_{\mathrm{CHHH}}(\omega_{\mathrm{H}})\right] \\
R(ZQ^{\mathrm{A}}_{\mathrm{outer},1} \leftrightarrow ZQ^{\Sigma\mathrm{E}}_{\mathrm{central}}) =& \frac{3}{4\sqrt{6}} d^2_{\mathrm{CH}} \left[\mathcal{J}_{\mathrm{CH}}(\omega_{\mathrm{H}}) - \mathcal{J}_{\mathrm{HCH}}(\omega_{\mathrm{H}})\right] + \frac{9}{4\sqrt{6}} d^2_{\mathrm{HH}} \left[\mathcal{J}_{\mathrm{HH}}(\omega_{\mathrm{H}}) - \mathcal{J}_{\mathrm{HHH}}(\omega_{\mathrm{H}})\right] \\
& - \frac{\sqrt{6}}{2} d_{\mathrm{CH}} d_{\mathrm{HH}} \left[\mathcal{J}_{\mathrm{CHH}}(\omega_{\mathrm{H}}) - \mathcal{J}_{\mathrm{CHHH}}(\omega_{\mathrm{H}})\right] \\
R(ZQ^{\mathrm{A}}_{\mathrm{outer},2} \leftrightarrow ZQ^{\mathrm{A}}_{\mathrm{central}}) =& R(ZQ^{\mathrm{A}}_{\mathrm{outer},1} \leftrightarrow ZQ^{\mathrm{A}}_{\mathrm{central}}) \\
R(ZQ^{\mathrm{A}}_{\mathrm{outer},2} \leftrightarrow ZQ^{\Sigma\mathrm{E}}_{\mathrm{central}}) =& R(ZQ^{\mathrm{A}}_{\mathrm{outer},1} \leftrightarrow ZQ^{\Sigma\mathrm{E}}_{\mathrm{central}}) \\
R(ZQ^{\mathrm{A}}_{\mathrm{central}} \leftrightarrow ZQ^{\Sigma\mathrm{E}}_{\mathrm{central}}) =& \frac{\sqrt{2}}{3} d^2_{\mathrm{CH}} \left[\mathcal{J}_{\mathrm{CH}}(0) - \mathcal{J}_{\mathrm{HCH}}(0)\right] + \frac{3\sqrt{2}}{4} d^2_{\mathrm{HH}} \left[\mathcal{J}_{\mathrm{HH}}(0) - \mathcal{J}_{\mathrm{HHH}}(0)\right] \\
& + \sqrt{2} d_{\mathrm{CH}} d_{\mathrm{HH}} \left[\mathcal{J}_{\mathrm{CHHH}}(0) - \mathcal{J}_{\mathrm{CHH}}(0)\right]
\end{aligned}
$$

C.1.3 Relaxation in the double-quantum subspace

C.1.3.1 Auto-relaxation rates

$$
\begin{aligned}
R(DQ^{\mathrm{A}}_{\mathrm{outer},1}) =& \frac{1}{8} d^2_{\mathrm{CH}} \left[8\mathcal{J}_{\mathrm{CH}}(0) + 9\mathcal{J}_{\mathrm{CH}}(\omega_{\mathrm{C}}) + 2\mathcal{J}_{\mathrm{CH}}(\omega_{\mathrm{C}} - \omega_{\mathrm{H}}) + 9\mathcal{J}_{\mathrm{CH}}(\omega_{\mathrm{H}}) + 24\mathcal{J}_{\mathrm{CH}}(\omega_{\mathrm{C}} + \omega_{\mathrm{H}})\right] \\
& + \frac{1}{4} d^2_{\mathrm{CH}} \left[4\mathcal{J}_{\mathrm{HCH}}(0) + 3\mathcal{J}_{\mathrm{HCH}}(\omega_{\mathrm{C}}) + \mathcal{J}_{\mathrm{HCH}}(\omega_{\mathrm{C}} - \omega_{\mathrm{H}}) + 3\mathcal{J}_{\mathrm{HCH}}(\omega_{\mathrm{H}}) + 6\mathcal{J}_{\mathrm{HCH}}(\omega_{\mathrm{C}} + \omega_{\mathrm{H}})\right] \\
& + \frac{3}{2} d_{\mathrm{CH}} d_{\mathrm{HH}} \left[2\mathcal{J}_{\mathrm{CHH}}(0) + \mathcal{J}_{\mathrm{CHH}}(\omega_{\mathrm{H}}) + 2\mathcal{J}_{\mathrm{CHHH}}(0) - \mathcal{J}_{\mathrm{CHHH}}(\omega_{\mathrm{H}})\right] \\
& + \frac{3}{4} d^2_{\mathrm{HH}} \left[3\mathcal{J}_{\mathrm{HH}}(0) + 4\mathcal{J}_{\mathrm{HH}}(\omega_{\mathrm{H}}) + 4\mathcal{J}_{\mathrm{HH}}(2\omega_{\mathrm{H}})\right] \\
& + \frac{3}{4} d^2_{\mathrm{HH}} \left[3\mathcal{J}_{\mathrm{HHH}}(0) + 2\mathcal{J}_{\mathrm{HHH}}(\omega_{\mathrm{H}}) + 2\mathcal{J}_{\mathrm{HHH}}(2\omega_{\mathrm{H}})\right] \\
& + \frac{1}{18} \sigma^2_C \omega^2_{\mathrm{C}} \left[4\mathcal{J}_{\mathrm{CC}}(0) + 3\mathcal{J}_{\mathrm{CC}}(\omega_{\mathrm{C}})\right] \\
& + \frac{1}{3} d_{\mathrm{CH}} \sigma_C \omega_{\mathrm{C}} \left[4\mathcal{J}_{\mathrm{CCH}}(0) + 3\mathcal{J}_{\mathrm{CCH}}(\omega_{\mathrm{C}})\right] + 4 d_{\mathrm{HH}} \sigma_C \omega_{\mathrm{C}} \mathcal{J}_{\mathrm{CCHH}}(0)
\end{aligned}
$$

$$
\begin{aligned}
R(DQ^{\mathrm{A}}_{\mathrm{outer},2}) =& \frac{1}{8} d^2_{\mathrm{CH}} \left[8\mathcal{J}_{\mathrm{CH}}(0) + 9\mathcal{J}_{\mathrm{CH}}(\omega_{\mathrm{C}}) + 2\mathcal{J}_{\mathrm{CH}}(\omega_{\mathrm{C}} - \omega_{\mathrm{H}}) + 9\mathcal{J}_{\mathrm{CH}}(\omega_{\mathrm{H}}) + 24\mathcal{J}_{\mathrm{CH}}(\omega_{\mathrm{C}} + \omega_{\mathrm{H}})\right] \\
&+ \frac{1}{4} d^2_{\mathrm{CH}} \left[4\mathcal{J}_{\mathrm{HCH}}(0) + 3\mathcal{J}_{\mathrm{HCH}}(\omega_{\mathrm{C}}) + \mathcal{J}_{\mathrm{HCH}}(\omega_{\mathrm{C}} - \omega_{\mathrm{H}}) + 3\mathcal{J}_{\mathrm{HCH}}(\omega_{\mathrm{H}}) + 6\mathcal{J}_{\mathrm{HCH}}(\omega_{\mathrm{C}} + \omega_{\mathrm{H}})\right] \\
&+ \frac{3}{2} d_{\mathrm{CH}} d_{\mathrm{HH}} \left[2\mathcal{J}_{\mathrm{CHH}}(0) + \mathcal{J}_{\mathrm{CHH}}(\omega_{\mathrm{H}}) + 2\mathcal{J}_{\mathrm{CHHH}}(0) - \mathcal{J}_{\mathrm{CHHH}}(\omega_{\mathrm{H}})\right] \\
&+ \frac{3}{4} d^2_{\mathrm{HH}} \left[3\mathcal{J}_{\mathrm{HH}}(0) + 4\mathcal{J}_{\mathrm{HH}}(\omega_{\mathrm{H}}) + 4\mathcal{J}_{\mathrm{HH}}(2\omega_{\mathrm{H}})\right] \\
&+ \frac{3}{4} d^2_{\mathrm{HH}} \left[3\mathcal{J}_{\mathrm{HHH}}(0) + 2\mathcal{J}_{\mathrm{HHH}}(\omega_{\mathrm{H}}) + 2\mathcal{J}_{\mathrm{HHH}}(2\omega_{\mathrm{H}})\right] \\
&+ \frac{1}{18} \sigma^2_C \omega^2_{\mathrm{C}} \left[4\mathcal{J}_{\mathrm{CC}}(0) + 3\mathcal{J}_{\mathrm{CC}}(\omega_{\mathrm{C}})\right] \\
&- \frac{1}{3} d_{\mathrm{CH}} \sigma_C \omega_{\mathrm{C}} \left[4\mathcal{J}_{\mathrm{CCH}}(0) + 3\mathcal{J}_{\mathrm{CCH}}(\omega_{\mathrm{C}})\right] - 4 d_{\mathrm{HH}} \sigma_C \omega_{\mathrm{C}} \mathcal{J}_{\mathrm{CCHH}}(0) \\
R(DQ^{\mathrm{A}}_{\mathrm{central}}) =& \frac{1}{24} d^2_{\mathrm{CH}} \left[16\mathcal{J}_{\mathrm{CH}}(0) + 27\mathcal{J}_{\mathrm{CH}}(\omega_{\mathrm{C}}) + 6\mathcal{J}_{\mathrm{CH}}(\omega_{\mathrm{C}} - \omega_{\mathrm{H}}) + 27\mathcal{J}_{\mathrm{CH}}(\omega_{\mathrm{H}}) + 72\mathcal{J}_{\mathrm{CH}}(\omega_{\mathrm{C}} + \omega_{\mathrm{H}})\right] \\
&+ \frac{1}{12} d^2_{\mathrm{CH}} \left[-8\mathcal{J}_{\mathrm{HCH}}(0) - 9\mathcal{J}_{\mathrm{HCH}}(\omega_{\mathrm{C}}) + 6\mathcal{J}_{\mathrm{HCH}}(\omega_{\mathrm{C}} - \omega_{\mathrm{H}}) + 18\mathcal{J}_{\mathrm{HCH}}(\omega_{\mathrm{H}}) + 36\mathcal{J}_{\mathrm{HCH}}(\omega_{\mathrm{C}} + \omega_{\mathrm{H}})\right] \\
&+ \frac{1}{2} d_{\mathrm{CH}} d_{\mathrm{HH}} \left[4\mathcal{J}_{\mathrm{CHH}}(0) + 3\mathcal{J}_{\mathrm{CHH}}(\omega_{\mathrm{H}})\right] - 2 d_{\mathrm{CH}} d_{\mathrm{HH}} \left[2\mathcal{J}_{\mathrm{CHHH}}(0) - 3\mathcal{J}_{\mathrm{CHHH}}(\omega_{\mathrm{H}})\right] \\
&+ \frac{3}{4} d^2_{\mathrm{HH}} \left[2\mathcal{J}_{\mathrm{HH}}(0) + 5\mathcal{J}_{\mathrm{HH}}(\omega_{\mathrm{H}}) + 2\mathcal{J}_{\mathrm{HH}}(2\omega_{\mathrm{H}})\right] \\
&+ \frac{3}{4} d^2_{\mathrm{HH}} \left[-2\mathcal{J}_{\mathrm{HHH}}(0) + \mathcal{J}_{\mathrm{HHH}}(\omega_{\mathrm{H}}) + 4\mathcal{J}_{\mathrm{HHH}}(2\omega_{\mathrm{H}})\right] \\
&+ \frac{1}{18} \sigma^2_C \omega^2_{\mathrm{C}} \left[4\mathcal{J}_{\mathrm{CC}}(0) + 3\mathcal{J}_{\mathrm{CC}}(\omega_{\mathrm{C}})\right] \\
R(DQ^{\Sigma\mathrm{E}}_{\mathrm{central}}) =& \frac{1}{24} d^2_{\mathrm{CH}} \left[8\mathcal{J}_{\mathrm{CH}}(0) + 27\mathcal{J}_{\mathrm{CH}}(\omega_{\mathrm{C}}) + 6\mathcal{J}_{\mathrm{CH}}(\omega_{\mathrm{C}} - \omega_{\mathrm{H}}) + 27\mathcal{J}_{\mathrm{CH}}(\omega_{\mathrm{H}}) + 72\mathcal{J}_{\mathrm{CH}}(\omega_{\mathrm{C}} + \omega_{\mathrm{H}})\right] \\
&- \frac{1}{12} d^2_{\mathrm{CH}} \left[4\mathcal{J}_{\mathrm{HCH}}(0) + 9\mathcal{J}_{\mathrm{HCH}}(\omega_{\mathrm{C}}) + 3\mathcal{J}_{\mathrm{HCH}}(\omega_{\mathrm{C}} - \omega_{\mathrm{H}}) + 9\mathcal{J}_{\mathrm{HCH}}(\omega_{\mathrm{H}}) + 18\mathcal{J}_{\mathrm{HCH}}(\omega_{\mathrm{C}} + \omega_{\mathrm{H}})\right] \\
&+ \frac{1}{2} d_{\mathrm{CH}} d_{\mathrm{HH}} \left[2\mathcal{J}_{\mathrm{CHH}}(0) + 3\mathcal{J}_{\mathrm{CHH}}(\omega_{\mathrm{H}}) - 2\mathcal{J}_{\mathrm{CHHH}}(0) - 3\mathcal{J}_{\mathrm{CHHH}}(\omega_{\mathrm{H}})\right] \\
&+ \frac{3}{4} d^2_{\mathrm{HH}} \left[\mathcal{J}_{\mathrm{HH}}(0) + 2\mathcal{J}_{\mathrm{HH}}(\omega_{\mathrm{H}}) + 2\mathcal{J}_{\mathrm{HH}}(2\omega_{\mathrm{H}})\right] \\
&- \frac{3}{4} d^2_{\mathrm{HH}} \left[\mathcal{J}_{\mathrm{HHH}}(0) + 2\mathcal{J}_{\mathrm{HHH}}(\omega_{\mathrm{H}}) + 2\mathcal{J}_{\mathrm{HHH}}(2\omega_{\mathrm{H}})\right] \\
&+ \frac{1}{18} \sigma^2_C \omega^2_{\mathrm{C}} \left[4\mathcal{J}_{\mathrm{CC}}(0) + 3\mathcal{J}_{\mathrm{CC}}(\omega_{\mathrm{C}})\right]
\end{aligned}
$$

C.1.3.2 Cross-relaxation rates

$$
\begin{aligned}
R(DQ^{\mathrm{A}}_{\mathrm{outer},1} \leftrightarrow DQ^{\mathrm{A}}_{\mathrm{outer},2}) =& R(ZQ^{\mathrm{A}}_{\mathrm{outer},1} \leftrightarrow ZQ^{\mathrm{A}}_{\mathrm{outer},2}) \\
R(DQ^{\mathrm{A}}_{\mathrm{outer},1} \leftrightarrow DQ^{\mathrm{A}}_{\mathrm{central}}) =& \frac{\sqrt{3}}{4} d^2_{\mathrm{CH}} \mathcal{J}_{\mathrm{CH}}(\omega_{\mathrm{H}}) + \frac{\sqrt{3}}{2} d^2_{\mathrm{CH}} \mathcal{J}_{\mathrm{HCH}}(\omega_{\mathrm{H}}) + \frac{\sqrt{3}}{2} d_{\mathrm{CH}} d_{\mathrm{HH}} \left[2\mathcal{J}_{\mathrm{CHH}}(\omega_{\mathrm{H}}) + \mathcal{J}_{\mathrm{CHHH}}(\omega_{\mathrm{H}})\right] \\
R(DQ^{\mathrm{A}}_{\mathrm{outer},1} \leftrightarrow DQ^{\Sigma\mathrm{E}}_{\mathrm{central}}) =& \frac{3}{4\sqrt{6}} d^2_{\mathrm{CH}} \left[\mathcal{J}_{\mathrm{CH}}(\omega_{\mathrm{H}}) - \mathcal{J}_{\mathrm{HCH}}(\omega_{\mathrm{H}})\right] + \frac{9}{4\sqrt{6}} d^2_{\mathrm{HH}} \left[\mathcal{J}_{\mathrm{HH}}(\omega_{\mathrm{H}}) - \mathcal{J}_{\mathrm{HHH}}(\omega_{\mathrm{H}})\right] \\
& + \frac{\sqrt{6}}{2} d_{\mathrm{CH}} d_{\mathrm{HH}} \left[\mathcal{J}_{\mathrm{CHH}}(\omega_{\mathrm{H}}) - \mathcal{J}_{\mathrm{CHHH}}(\omega_{\mathrm{H}})\right] \\
R(DQ^{\mathrm{A}}_{\mathrm{outer},2} \leftrightarrow DQ^{\mathrm{A}}_{\mathrm{central}}) =& R(DQ^{\mathrm{A}}_{\mathrm{outer},1} \leftrightarrow DQ^{\mathrm{A}}_{\mathrm{central}}) \\
R(DQ^{\mathrm{A}}_{\mathrm{outer},2} \leftrightarrow DQ^{\Sigma\mathrm{E}}_{\mathrm{central}}) =& R(DQ^{\mathrm{A}}_{\mathrm{outer},1} \leftrightarrow DQ^{\Sigma\mathrm{E}}_{\mathrm{central}}) \\
R(DQ^{\mathrm{A}}_{\mathrm{central}} \leftrightarrow DQ^{\Sigma\mathrm{E}}_{\mathrm{central}}) =& \frac{\sqrt{2}}{3} d^2_{\mathrm{CH}} \left[\mathcal{J}_{\mathrm{CH}}(0) - \mathcal{J}_{\mathrm{HCH}}(0)\right] + \frac{3\sqrt{2}}{4} d^2_{\mathrm{HH}} \left[\mathcal{J}_{\mathrm{HH}}(0) - \mathcal{J}_{\mathrm{HHH}}(0)\right] \\
& - \sqrt{2} d_{\mathrm{CH}} d_{\mathrm{HH}} \left[\mathcal{J}_{\mathrm{CHHH}}(0) - \mathcal{J}_{\mathrm{CHH}}(0)\right]
\end{aligned}
$$

C.2 Relaxation rates for a ^{13}C-^{19}F spin pair

C.2.1 Notations

Table C.2: Spectral density functions used in the expressions of the relaxation rates for a ^{13}C-^{19}F group and values of $\theta_{\vec{A},\vec{B}}$. α_X: angle of the CSA tensor principal axis with the CF bond for nucleus X.

Notation	Correlation	Interaction	$\theta_{\vec{A},\vec{B}}$
$\mathcal{J}_{\mathrm{CF}}$	auto-correlation C-F or CSA auto-correlation	DD or CSA	0
$\mathcal{J}_{\mathrm{csa}}$	cross-correlation between homonuclear components of CSA tensor	$\sigma_{\parallel,i}/\sigma_{\perp,i}$	$\pi/2$
$\mathcal{J}_{\mathrm{CFF}_\parallel}$	cross-correlation between the ^{19}F longitudinal CSA and C-F	DD/$\sigma_{\parallel,F}$	α_{F}
$\mathcal{J}_{\mathrm{CFC}_\parallel}$	cross-correlation between the ^{13}C longitudinal CSA and C-F	DD/$\sigma_{\parallel,C}$	α_{C}
$\mathcal{J}_{\mathrm{CF}\sigma_\perp}$	cross-correlation between the orthogonal CSA and C-F	DD/$\sigma_{\perp,i}$	$\pi/2$
$\mathcal{J}_{\sigma_\parallel^F,\sigma_\parallel^C}$	cross-correlation between heteronuclear components of CSA tensor	$\sigma_{\parallel,F}/\sigma_{\parallel,C}$	$\alpha_{\mathrm{F}}-\alpha_{\mathrm{C}}$
$\mathcal{J}_{\sigma_\parallel^F,\sigma_\perp^C}$	cross-correlation between heteronuclear components of CSA tensor	$\sigma_{\parallel,F}/\sigma_{\perp,C}$	$\pi/2$
$\mathcal{J}_{\sigma_\perp^F,\sigma_\parallel^C}$	cross-correlation between heteronuclear components of CSA tensor	$\sigma_{\perp,F}/\sigma_{\parallel,C}$	$\pi/2$
$\mathcal{J}_{\sigma_\perp^F,\sigma_\perp^C}$	cross-correlation between heteronuclear components of CSA tensor	$\sigma_{\perp,F}/\sigma_{\perp,C}$	0

C.2.2 Auto-relaxation rates

$$
\begin{aligned}
\mathcal{R}_2(\mathrm{F}) =& \mathcal{R}(\hat{\mathrm{F}}_\mathrm{x}) = \mathcal{R}(\hat{\mathrm{F}}_\mathrm{y}) \\
=& \frac{d_{\mathrm{CF}}^2}{8}\left(4\mathcal{J}_{\mathrm{CF}}(0)+\mathcal{J}_{\mathrm{CF}}(\omega_\mathrm{F}-\omega_\mathrm{C})+6\mathcal{J}_{\mathrm{CF}}(\omega_\mathrm{C})+3\mathcal{J}_{\mathrm{CF}}(\omega_\mathrm{F})+6\mathcal{J}_{\mathrm{CF}}(\omega_\mathrm{F}+\omega_\mathrm{C})\right) \\
&+\frac{\omega_\mathrm{F}^2}{18}\left((\sigma_{\parallel,F}^2+\sigma_{\perp,F}^2)\left(4\mathcal{J}_{\mathrm{CF}}(0)+3\mathcal{J}_{\mathrm{CF}}(\omega_\mathrm{F})\right)+2\sigma_{\parallel,F}\sigma_{\perp,F}\left(4\mathcal{J}_{\mathrm{csa}}(0)+3\mathcal{J}_{\mathrm{csa}}(\omega_\mathrm{F})\right)\right) \\
\mathcal{R}_1(\mathrm{F}) =& \mathcal{R}(\hat{\mathrm{F}}_\mathrm{z}) \\
=& \frac{d_{\mathrm{CF}}^2}{4}\left(\mathcal{J}_{\mathrm{CF}}(\omega_\mathrm{F}-\omega_\mathrm{C})+3\mathcal{J}_{\mathrm{CF}}(\omega_\mathrm{F})+6\mathcal{J}_{\mathrm{CF}}(\omega_\mathrm{F}+\omega_\mathrm{C})\right) \\
&+\frac{\omega_\mathrm{F}^2}{3}\left((\sigma_{\parallel,F}^2+\sigma_{\perp,F}^2)\mathcal{J}_{\mathrm{CF}}(\omega_\mathrm{F})+2\sigma_{\parallel,F}\sigma_{\perp,F}\mathcal{J}_{\mathrm{csa}}(\omega_\mathrm{F})\right) \\
\mathcal{R}_2(\mathrm{C}) =& \mathcal{R}(\hat{\mathrm{C}}_\mathrm{x}) = \mathcal{R}(\hat{\mathrm{C}}_\mathrm{y}) \\
=& \frac{d_{\mathrm{CF}}^2}{8}\left(4\mathcal{J}_{\mathrm{CF}}(0)+\mathcal{J}_{\mathrm{CF}}(\omega_\mathrm{F}-\omega_\mathrm{C})+6\mathcal{J}_{\mathrm{CF}}(\omega_\mathrm{F})+3\mathcal{J}_{\mathrm{CF}}(\omega_\mathrm{C})+6\mathcal{J}_{\mathrm{CF}}(\omega_\mathrm{F}+\omega_\mathrm{C})\right) \\
&+\frac{\omega_\mathrm{C}^2}{18}\left((\sigma_{\parallel,C}^2+\sigma_{\perp,C}^2)\left(4\mathcal{J}_{\mathrm{CF}}(0)+3\mathcal{J}_{\mathrm{CF}}(\omega_\mathrm{C})\right)+2\sigma_{\parallel,C}\sigma_{\perp,C}\left(4\mathcal{J}_{\mathrm{csa}}(0)+3\mathcal{J}_{\mathrm{csa}}(\omega_\mathrm{C})\right)\right)
\end{aligned}
$$

$$
\begin{aligned}
\mathcal{R}_1(\mathrm{C}) =& \mathcal{R}(\hat{\mathrm{C}}_\mathrm{z}) \\
=& \frac{d_{\mathrm{CF}}^2}{4}\left(\mathcal{J}_{\mathrm{CF}}(\omega_\mathrm{F}-\omega_\mathrm{C})+3\mathcal{J}_{\mathrm{CF}}(\omega_\mathrm{C})+6\mathcal{J}_{\mathrm{CF}}(\omega_\mathrm{F}+\omega_\mathrm{C})\right) \\
&+\frac{\omega_\mathrm{C}^2}{3}\left((\sigma_{\parallel,C}^2+\sigma_{\perp,C}^2)\mathcal{J}_{\mathrm{CF}}(\omega_\mathrm{C})+2\sigma_{\parallel,C}\sigma_{\perp,C}\mathcal{J}_{\mathrm{csa}}(\omega_\mathrm{C})\right) \\
\rho_F =& \mathcal{R}(2\hat{\mathrm{F}}_\mathrm{x}\hat{\mathrm{C}}_\mathrm{z}) = \mathcal{R}(2\hat{\mathrm{F}}_\mathrm{y}\hat{\mathrm{C}}_\mathrm{z}) \\
=& \frac{d_{\mathrm{CF}}^2}{8}\left(4\mathcal{J}_{\mathrm{CF}}(0)+\mathcal{J}_{\mathrm{CF}}(\omega_\mathrm{F}-\omega_\mathrm{C})+3\mathcal{J}_{\mathrm{CF}}(\omega_\mathrm{F})+6\mathcal{J}_{\mathrm{CF}}(\omega_\mathrm{F}+\omega_\mathrm{C})\right) \\
&+\frac{\omega_\mathrm{F}^2}{18}\left((\sigma_{\parallel,F}^2+\sigma_{\perp,F}^2)\left(4\mathcal{J}_{\mathrm{CF}}(0)+3\mathcal{J}_{\mathrm{CF}}(\omega_\mathrm{F})\right)+2\sigma_{\parallel,F}\sigma_{\perp,F}\left(4\mathcal{J}_{\mathrm{csa}}(0)+3\mathcal{J}_{\mathrm{csa}}(\omega_\mathrm{F})\right)\right) \\
&+\frac{\omega_\mathrm{C}^2}{3}\left((\sigma_{\parallel,C}^2+\sigma_{\perp,C}^2)\mathcal{J}_{\mathrm{csa}}(0)+2\sigma_{\parallel,C}\sigma_{\perp,C}\mathcal{J}_{\mathrm{csa}}(0)\right) \\
\rho_C =& \mathcal{R}(2\hat{\mathrm{F}}_\mathrm{z}\hat{\mathrm{C}}_\mathrm{x}) = \mathcal{R}(2\hat{\mathrm{F}}_\mathrm{z}\hat{\mathrm{C}}_\mathrm{y}) \\
=& \frac{d_{\mathrm{CF}}^2}{8}\left(4\mathcal{J}_{\mathrm{CF}}(0)+\mathcal{J}_{\mathrm{CF}}(\omega_\mathrm{F}-\omega_\mathrm{C})+3\mathcal{J}_{\mathrm{CF}}(\omega_\mathrm{C})+6\mathcal{J}_{\mathrm{CF}}(\omega_\mathrm{F}+\omega_\mathrm{C})\right) \\
&+\frac{\omega_\mathrm{C}^2}{18}\left((\sigma_{\parallel,C}^2+\sigma_{\perp,C}^2)\left(4\mathcal{J}_{\mathrm{CF}}(0)+3\mathcal{J}_{\mathrm{CF}}(\omega_\mathrm{C})\right)+2\sigma_{\parallel,C}\sigma_{\perp,C}\left(4\mathcal{J}_{\mathrm{csa}}(0)+3\mathcal{J}_{\mathrm{csa}}(\omega_\mathrm{C})\right)\right) \\
&+\frac{\omega_\mathrm{F}^2}{3}\left((\sigma_{\parallel,F}^2+\sigma_{\perp,F}^2)\mathcal{J}_{\mathrm{csa}}(0)+2\sigma_{\parallel,F}\sigma_{\perp,F}\mathcal{J}_{\mathrm{csa}}(0)\right) \\
\lambda_{mq} =& \mathcal{R}(2\hat{\mathrm{F}}_\mathrm{x}\hat{\mathrm{C}}_\mathrm{x}) = \mathcal{R}(2\hat{\mathrm{F}}_\mathrm{y}\hat{\mathrm{C}}_\mathrm{y}) = \mathcal{R}(2\hat{\mathrm{F}}_\mathrm{y}\hat{\mathrm{C}}_\mathrm{x}) = \mathcal{R}(2\hat{\mathrm{F}}_\mathrm{x}\hat{\mathrm{C}}_\mathrm{y}) \\
=& \frac{d_{\mathrm{CF}}^2}{8}\left(3\mathcal{J}_{\mathrm{CF}}(\omega_\mathrm{C})+\mathcal{J}_{\mathrm{CF}}(\omega_\mathrm{F}-\omega_\mathrm{C})+3\mathcal{J}_{\mathrm{CF}}(\omega_\mathrm{F})+6\mathcal{J}_{\mathrm{CF}}(\omega_\mathrm{F}+\omega_\mathrm{F})\right) \\
&+\frac{\omega_\mathrm{F}^2}{18}\left((\sigma_{\parallel,F}^2+\sigma_{\perp,F}^2)\left(4\mathcal{J}_{\mathrm{CF}}(0)+3\mathcal{J}_{\mathrm{CF}}(\omega_\mathrm{F})\right)+2\sigma_{\parallel,F}\sigma_{\perp,F}\left(4\mathcal{J}_{\mathrm{csa}}(0)+3\mathcal{J}_{\mathrm{csa}}(\omega_\mathrm{F})\right)\right) \\
&+\frac{\omega_\mathrm{C}^2}{18}\left((\sigma_{\parallel,C}^2+\sigma_{\perp,C}^2)\left(4\mathcal{J}_{\mathrm{CF}}(0)+3\mathcal{J}_{\mathrm{CF}}(\omega_\mathrm{C})\right)+2\sigma_{\parallel,C}\sigma_{\perp,C}\left(4\mathcal{J}_{\mathrm{csa}}(0)+3\mathcal{J}_{\mathrm{csa}}(\omega_\mathrm{C})\right)\right) \\
\mathcal{R}_{CF} =& \mathcal{R}(2\hat{\mathrm{F}}_\mathrm{z}\hat{\mathrm{C}}_\mathrm{z}) \\
=& \frac{3d_{\mathrm{CF}}^2}{4}\left(\mathcal{J}_{\mathrm{CF}}(\omega_\mathrm{C})+\mathcal{J}_{\mathrm{CF}}(\omega_\mathrm{F})\right) \\
&+\frac{\omega_\mathrm{F}^2}{3}\left((\sigma_{\parallel,F}^2+\sigma_{\perp,F}^2)\mathcal{J}_{\mathrm{CF}}(\omega_\mathrm{F})+\sigma_{\parallel,F}\sigma_{\perp,F}\mathcal{J}_{\mathrm{csa}}(\omega_\mathrm{F})\right) \\
&+\frac{\omega_\mathrm{C}^2}{3}\left((\sigma_{\parallel,C}^2+\sigma_{\perp,C}^2)\mathcal{J}_{\mathrm{CF}}(\omega_\mathrm{C})+\sigma_{\parallel,C}\sigma_{\perp,C}\mathcal{J}_{\mathrm{csa}}(\omega_\mathrm{C})\right)
\end{aligned}
$$

C.2.3 Cross-relaxation rates

$$
\begin{aligned}
\sigma =& \mathcal{R}(\hat{\mathrm{F}}_\mathrm{z}\leftrightarrow\hat{\mathrm{C}}_\mathrm{z}) = \frac{d_{\mathrm{CF}}^2}{4}\left(6\mathcal{J}_{\mathrm{CF}}(\omega_\mathrm{F}+\omega_\mathrm{C})-\mathcal{J}_{\mathrm{CF}}(\omega_\mathrm{F}-\omega_\mathrm{C})\right) \\
\delta_F =& \mathcal{R}(\hat{\mathrm{F}}_\mathrm{z}\leftrightarrow 2\hat{\mathrm{F}}_\mathrm{z}\hat{\mathrm{C}}_\mathrm{z}) = d_{\mathrm{CF}}\omega_\mathrm{F}\left(\sigma_{\parallel,F}\mathcal{J}_{\mathrm{CFF}_\parallel}(\omega_\mathrm{F})+\sigma_{\perp,F}\mathcal{J}_{\mathrm{CF}\sigma_\perp}(\omega_\mathrm{F})\right) \\
\delta_C =& \mathcal{R}(\hat{\mathrm{C}}_\mathrm{z}\leftrightarrow 2\hat{\mathrm{F}}_\mathrm{z}\hat{\mathrm{C}}_\mathrm{z}) = d_{\mathrm{CF}}\omega_\mathrm{C}\left(\sigma_{\parallel,C}\mathcal{J}_{\mathrm{CFC}_\parallel}(\omega_\mathrm{C})+\sigma_{\perp,C}\mathcal{J}_{\mathrm{CF}\sigma_\perp}(\omega_\mathrm{C})\right)
\end{aligned}
$$

$$
\begin{aligned}
\eta_F =& \mathcal{R}(\hat{\mathrm{F}}_\mathrm{x} \leftrightarrow 2\hat{\mathrm{F}}_\mathrm{x}\hat{\mathrm{C}}_\mathrm{z}) = \mathcal{R}(\hat{\mathrm{F}}_\mathrm{y} \leftrightarrow 2\hat{\mathrm{F}}_\mathrm{y}\hat{\mathrm{C}}_\mathrm{z}) = \mathcal{R}(\hat{\mathrm{F}}^+ \leftrightarrow 2\hat{\mathrm{F}}^+\hat{\mathrm{C}}_\mathrm{z}) \\
=& \frac{d_\mathrm{CF}}{6}\omega_\mathrm{F}\left(\sigma_{\parallel,F}\left(4\mathcal{J}_{\mathrm{CFF}_\parallel}(0) + 3\mathcal{J}_{\mathrm{CFF}_\parallel}(\omega_\mathrm{F})\right) + \sigma_{\perp,F}\left(4\mathcal{J}_{\mathrm{CF}\sigma_\perp}(0) + 3\mathcal{J}_{\mathrm{CF}\sigma_\perp}(\omega_\mathrm{F})\right)\right) \\
\eta_C =& \mathcal{R}(\hat{\mathrm{C}}_\mathrm{x} \leftrightarrow 2\hat{\mathrm{F}}_\mathrm{z}\hat{\mathrm{C}}_\mathrm{x}) = \mathcal{R}(\hat{\mathrm{C}}_\mathrm{y} \leftrightarrow 2\hat{\mathrm{F}}_\mathrm{z}\hat{\mathrm{C}}_\mathrm{y}) \\
=& \frac{d_\mathrm{CF}}{6}\omega_\mathrm{C}\left(\sigma_{\parallel,C}\left(4\mathcal{J}_{\mathrm{CFC}_\parallel}(0) + 4\mathcal{J}_{\mathrm{CFC}_\parallel}(\omega_\mathrm{C})\right) + \sigma_{\perp,C}\left(4\mathcal{J}_{\mathrm{CF}\sigma_\perp}(0) + 3\mathcal{J}_{\mathrm{CF}\sigma_\perp}(\omega_\mathrm{C})\right)\right) \\
\mu_{mq} =& \mathcal{R}(2\hat{\mathrm{F}}_\mathrm{x}\hat{\mathrm{C}}_\mathrm{x} \leftrightarrow 2\hat{\mathrm{F}}_\mathrm{y}\hat{\mathrm{C}}_\mathrm{y}) = \mathcal{R}(2\hat{\mathrm{F}}_\mathrm{x}\hat{\mathrm{C}}_\mathrm{y} \leftrightarrow 2\hat{\mathrm{F}}_\mathrm{y}\hat{\mathrm{C}}_\mathrm{x}) \\
=& \frac{d_\mathrm{CF}^2}{8}\left(6\mathcal{J}_\mathrm{CF}(\omega_\mathrm{F} + \omega_\mathrm{C}) - \mathcal{J}_\mathrm{CF}(\omega_\mathrm{F} - \omega_\mathrm{C})\right) \\
&+ \frac{4}{9}\omega_\mathrm{F}\omega_\mathrm{C}\left(\sigma_{\parallel,F}\sigma_{\parallel,C}\mathcal{J}_{\sigma_\parallel^F,\sigma_\parallel^C}(0) + \sigma_{\parallel,F}\sigma_{\perp,C}\mathcal{J}_{\sigma_\parallel^F,\sigma_\perp^C}(0) + \sigma_{\perp,F}\sigma_{\parallel,C}\mathcal{J}_{\sigma_\perp^F,\sigma_\parallel^C}(0) + \sigma_{\perp,F}\sigma_{\perp,C}\mathcal{J}_{\sigma_\perp^F,\sigma_\perp^C}(0)\right)
\end{aligned}
$$

C.2.4 CSA tensor parameters

Table C.3: CSA tensor parameters as reported in Ref.[40] and TROSY operators. The parallel components of the CSAs lay in the aromatic ring plane at an angle α with respect to the C-F bond, while the perpendicular components are oriented perpendicular to this plane.

		^{19}F, ppm		^{13}C, ppm		α (deg)		TROSY operator	
Molecule		$\sigma_\parallel^F$	$\sigma_\perp^F$	$\sigma_\parallel^C$	$\sigma_\perp^C$	^{19}F	^{13}C	Fluorine	Carbon
2F-Phe	2-fluorophenylalanine	61	159	-113	48	3	0	$\hat{\mathrm{F}}^+ - 2\hat{\mathrm{F}}^+\hat{\mathrm{C}}_z$	$\hat{\mathrm{C}}^+ - 2\hat{\mathrm{F}}_z\hat{\mathrm{C}}^+$
2F-Trp	2-fluorotryptophan	70	159	-102	13	1	29	$\hat{\mathrm{F}}^+ - 2\hat{\mathrm{F}}^+\hat{\mathrm{C}}_z$	$\hat{\mathrm{C}}^+ - 2\hat{\mathrm{F}}_z\hat{\mathrm{C}}^+$
2F-Tyr	2-fluorotyrosine	65	167	-113	47	0	0	$\hat{\mathrm{F}}^+ - 2\hat{\mathrm{F}}^+\hat{\mathrm{C}}_z$	$\hat{\mathrm{C}}^+ - 2\hat{\mathrm{F}}_z\hat{\mathrm{C}}^+$
3F-Phe	3-fluorophenylalanine	80	137	-115	49	0	0	$\hat{\mathrm{F}}^+ + 2\hat{\mathrm{F}}^+\hat{\mathrm{C}}_z$	$\hat{\mathrm{C}}^+ - 2\hat{\mathrm{F}}_z\hat{\mathrm{C}}^+$
3F-Tyr	3-fluorotyrosine	43	157	-75	54	17	16	$\hat{\mathrm{F}}^+ - 2\hat{\mathrm{F}}^+\hat{\mathrm{C}}_z$	$\hat{\mathrm{C}}^+ - 2\hat{\mathrm{F}}_z\hat{\mathrm{C}}^+$
4F-Phe	4-fluorophenylalanine	81	139	-111	51	0	0	$\hat{\mathrm{F}}^+ + 2\hat{\mathrm{F}}^+\hat{\mathrm{C}}_z$	$\hat{\mathrm{C}}^+ - 2\hat{\mathrm{F}}_z\hat{\mathrm{C}}^+$
4F-Trp	4-fluorotryptophan	63	150	-98	39	10	11	$\hat{\mathrm{F}}^+ - 2\hat{\mathrm{F}}^+\hat{\mathrm{C}}_z$	$\hat{\mathrm{C}}^+ - 2\hat{\mathrm{F}}_z\hat{\mathrm{C}}^+$
5F-Trp	5-fluorotryptophan	79	113	-109	40	1	9	$\hat{\mathrm{F}}^+ + 2\hat{\mathrm{F}}^+\hat{\mathrm{C}}_z$	$\hat{\mathrm{C}}^+ - 2\hat{\mathrm{F}}_z\hat{\mathrm{C}}^+$
6F-Trp	6-fluorotryptophan	76	112	-108	45	9	0	$\hat{\mathrm{F}}^+ + 2\hat{\mathrm{F}}^+\hat{\mathrm{C}}_z$	$\hat{\mathrm{C}}^+ - 2\hat{\mathrm{F}}_z\hat{\mathrm{C}}^+$
7F-Trp	7-fluorotryptophan	54	146	-78	47	4	15	$\hat{\mathrm{F}}^+ - 2\hat{\mathrm{F}}^+\hat{\mathrm{C}}_z$	$\hat{\mathrm{C}}^+ - 2\hat{\mathrm{F}}_z\hat{\mathrm{C}}^+$

C.2.5 Field-dependence of the relaxation rates

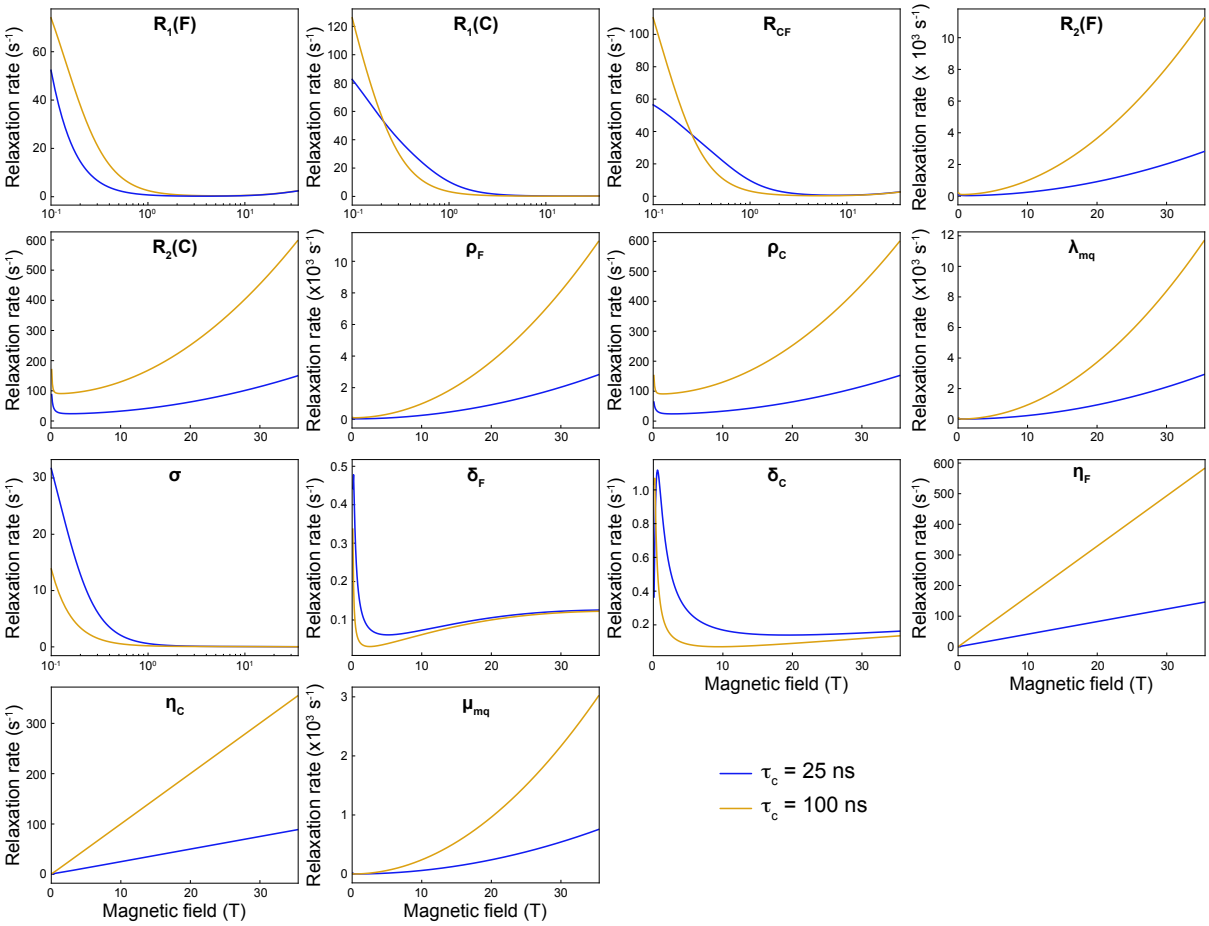

Figure C.1: Magnetic field variations of the relaxation rates of the fluorine and carbon operators forming the Liouville space of a ^{13}C-^{19}F nuclear spin pair for $\tau_c = 25\,\text{ns}$ (blue) and $\tau_c = 100\,\text{ns}$ (orange). Calculations were performed using the CSA tensor parameters for 3-fluorotyrosine. Figure reproduced from [41].

C.3 Relaxation rates relevant for $\{^{13}C^{1}H^{2}H_{2}\}$-methyl groups

C.3.1 Notations

Table C.4: Spectral density functions used in the description of relaxation in a $\{^{13}C^{1}H^{2}H_{2}\}$-methyl group.

Notation	Correlation	Interactions
$\mathcal{J}_{C}$	auto-correlation C-C	CSA
$\mathcal{J}_{\mathcal{Q}}$	auto-correlation C-D	quadrupolar
$\mathcal{J}_{CH}$	auto-correlation C-H	DD
$\mathcal{J}_{CD}$	intra-methyl auto-correlation C-D	DD
$\mathcal{J}_{HD}$	intra-methyl auto-correlation H-D	DD
$\mathcal{J}_{DD}$	intra-methyl auto-correlation D-D	DD
$\mathcal{J}_{CD_{vic}}$	auto-correlation C-D_{vic}	DD
$\mathcal{J}_{HD_{vic}}$	auto-correlation H-D_{vic}	DD
$\mathcal{J}_{DD_{vic}}$	auto-correlation D-D_{vic}	DD
$\mathcal{J}_{C,CH}$	cross-correlation between C-C and C-H	CSA/DD
$\mathcal{J}_{C,CD}$	cross-correlation between C-C and C-D	CSA/DD
$\mathcal{J}_{CD_1,CD_2}$	intra-methyl cross-correlation between two C-D pairs	DD/DD
$\mathcal{J}_{HD_1,HD_2}$	intra-methyl cross-correlation between two H-D pairs	DD/DD
$\mathcal{J}_{D_1D_{vic},D_2D_{vic}}$	cross-correlation between two D-D_{vic} pairs	DD/DD
$\mathcal{J}_{CH,HD}$	cross-correlation between C-H and H-D	DD/DD
$\mathcal{J}_{CH,CD}$	cross-correlation between C-H and C-D	DD/DD
$\mathcal{J}_{CD,HD}$	cross-correlation between C-D and H-D	DD/DD
$\mathcal{J}_{CD,DD}$	cross-correlation between C-D and D-D	DD/DD
$\mathcal{J}_{HD,DD}$	cross-correlation between H-D and D-D	DD/DD
$\mathcal{J}_{CD,\mathcal{Q}}$	auto-correlation C-D	DD/quadrupolar
$\mathcal{J}_{HD,\mathcal{Q}}$	cross-correlation H-D and C-D	DD/quadrupolar
$\mathcal{J}_{DD,\mathcal{Q}}$	cross-correlation D-D and C-D	DD/quadrupolar

C.3.2 Relaxation matrix

Operators in the secularized basis are:

$$\begin{aligned}\mathcal{B}_{\text{secularized}} = \Bigg\{ & \frac{\hat{C}_z}{3\sqrt{3}}, \frac{\hat{H}_z}{3\sqrt{3}}, \frac{2\hat{C}_z\hat{H}_z}{3\sqrt{3}}, \frac{\sqrt{2}\hat{C}_z\hat{H}_z\hat{D}_{1,z}}{3}, \frac{\sqrt{2}\hat{C}_z\hat{H}_z\hat{D}_{2,z}}{3}, \frac{\hat{C}_z\hat{D}_{1,z}}{3\sqrt{3}}, \frac{\hat{C}_z\hat{D}_{2,z}}{3\sqrt{3}}, \\ & \frac{\hat{D}_{1,z}}{6\sqrt{2}}, \frac{\hat{D}_{2,z}}{6\sqrt{2}}, \frac{\hat{C}_z\hat{D}_1^-\hat{D}_2^+}{4\sqrt{3}}, \frac{\hat{C}_z\hat{D}_1^+\hat{D}_2^-}{4\sqrt{3}}, \frac{\hat{C}_z\hat{D}_{1,z}\hat{D}_{2,z}}{2\sqrt{3}}, \frac{3\hat{C}_z\hat{D}_{1,z}\hat{D}_{1,z} - 2\hat{C}_z}{3\sqrt{6}}, \\ & \frac{3\hat{C}_z\hat{D}_{2,z}\hat{D}_{2,z} - 2\hat{C}_z}{3\sqrt{6}} \Bigg\}.\end{aligned} \tag{C.1}$$

The relaxation matrix in the basis $\mathcal{B}_{\text{secularized}}$ is:

$$\mathcal{R} = \begin{pmatrix}
R_1(^{13}\text{C}) & \sigma_{\text{CH}} & \eta_z^{\text{C}} & \kappa^{\text{C}} & \kappa^{\text{C}} & \eta_z^{\text{CD}} & \eta_z^{\text{CD}} & \sigma_{\text{CD}} & \sigma_{\text{CD}} & \lambda & \lambda & \nu_z & \mu & \mu \\
\sigma_{\text{CH}} & R_1(^1\text{H}) & 0 & \kappa^{\text{H}} & \kappa^{\text{H}} & 0 & 0 & \sigma_{\text{HD}} & \sigma_{\text{HD}} & 0 & 0 & 0 & 0 & 0 \\
\eta_z^{\text{C}} & 0 & R_{\text{CH}} & \kappa^{\text{CH}} & \kappa^{\text{CH}} & \delta & \delta & 0 & 0 & 0 & 0 & 0 & 0 & 0 \\
\kappa^{\text{C}} & \kappa^{\text{H}} & \kappa^{\text{CH}} & R_{\text{CHD}} & \kappa^{\text{CHD}} & \eta_z^{\text{CHD}} & 0 & \sigma_{\text{CHD}} & 0 & \lambda^{(1)} & \lambda^{(1)} & \nu_z^{(1)} & \mu^{(1)} & 0 \\
\kappa^{\text{C}} & \kappa^{\text{H}} & \kappa^{\text{CH}} & \kappa^{\text{CHD}} & R_{\text{CHD}} & 0 & \eta_z^{\text{CHD}} & 0 & \sigma_{\text{CHD}} & \lambda^{(1)} & \lambda^{(1)} & \nu_z^{(1)} & 0 & \mu^{(1)} \\
\eta_z^{\text{CD}} & 0 & \delta & \eta_z^{\text{CHD}} & 0 & R_{\text{CD}} & \kappa^{\text{CD}} & 0 & 0 & 0 & 0 & \nu_z^{(2)} & \mu^{(2)} & 0 \\
\eta_z^{\text{CD}} & 0 & \delta & 0 & \eta_z^{\text{CHD}} & \kappa^{\text{CD}} & R_{\text{CD}} & 0 & 0 & 0 & 0 & \nu_z^{(2)} & 0 & \mu^{(2)} \\
\sigma_{\text{CD}} & \sigma_{\text{HD}} & 0 & \sigma_{\text{CHD}} & 0 & 0 & 0 & R_{\text{D}} & \sigma_{\text{DD}} & \lambda^{(2)} & \lambda^{(2)} & \nu_z^{(3)} & \mu^{(3)} & 0 \\
\sigma_{\text{CD}} & \sigma_{\text{HD}} & 0 & 0 & \sigma_{\text{CHD}} & 0 & 0 & \sigma_{\text{DD}} & R_{\text{D}} & \lambda^{(2)} & \lambda^{(2)} & \nu_z^{(3)} & 0 & \mu^{(3)} \\
\lambda & 0 & 0 & \lambda^{(1)} & \lambda^{(1)} & 0 & 0 & \lambda^{(2)} & \lambda^{(2)} & R_{\text{CDD}}^{(1)} & \kappa^{\text{CDD}} & \nu_z^{(4)} & \mu^{(4)} & \mu^{(4)} \\
\lambda & 0 & 0 & \lambda^{(1)} & \lambda^{(1)} & 0 & 0 & \lambda^{(2)} & \lambda^{(2)} & \kappa^{\text{CDD}} & R_{\text{CDD}}^{(1)} & \nu_z^{(4)} & \mu^{(4)} & \mu^{(4)} \\
\nu_z & 0 & 0 & \nu_z^{(1)} & \nu_z^{(1)} & \nu_z^{(2)} & \nu_z^{(2)} & \nu_z^{(3)} & \nu_z^{(3)} & \nu_z^{(4)} & \nu_z^{(4)} & R_{\text{CDD}}^{(2)} & \mu^{(5)} & \mu^{(5)} \\
\mu & 0 & 0 & \mu^{(1)} & 0 & \mu^{(2)} & 0 & \mu^{(3)} & 0 & \mu^{(4)} & \mu^{(4)} & \mu^{(5)} & R & 0 \\
\mu & 0 & 0 & 0 & \mu^{(1)} & 0 & \mu^{(2)} & 0 & \mu^{(3)} & \mu^{(4)} & \mu^{(4)} & \mu^{(5)} & 0 & R
\end{pmatrix} \tag{C.2}$$

Note that numerical simulations were carried out in a reduced basis formed with elements $\frac{\hat{C}_z}{3\sqrt{3}}$, $\frac{\hat{H}_z}{3\sqrt{3}}$ and $\frac{2\hat{C}_z\hat{H}_z}{3\sqrt{3}}$ of the secularized basis.

C.3.3 Auto-relaxation rates

$$\begin{aligned}
R_1(^{13}C) =& \frac{1}{3}\Delta\sigma_C^2\omega_{\text{C}}^2\mathcal{J}_{\text{C}}(\omega_{\text{C}}) \\
&+\frac{1}{4}d_{\text{CH}}^2\left(\mathcal{J}_{\text{CH}}(\omega_{\text{C}} - \omega_{\text{H}}) + 3\mathcal{J}_{\text{CH}}(\omega_{\text{C}}) + 6\mathcal{J}_{\text{CH}}(\omega_{\text{C}} + \omega_{\text{H}})\right) \\
&+\frac{4}{3}d_{\text{CD}}^2\left(\mathcal{J}_{\text{CD}}(\omega_{\text{C}} - \omega_{\text{D}}) + 3\mathcal{J}_{\text{CD}}(\omega_{\text{C}}) + 6\mathcal{J}_{\text{CD}}(\omega_{\text{C}} + \omega_{\text{D}})\right) \\
&+\frac{2}{3}d_{\text{CD}_{\text{vic}}}^2\left(\mathcal{J}_{\text{CD}_{\text{vic}}}(\omega_{\text{C}} - \omega_{\text{D}}) + 3\mathcal{J}_{\text{CD}_{\text{vic}}}(\omega_{\text{C}}) + 6\mathcal{J}_{\text{CD}_{\text{vic}}}(\omega_{\text{C}} + \omega_{\text{D}})\right), \\
R_1(^1\text{H}) =& \frac{1}{4}d_{\text{CH}}^2(\mathcal{J}_{\text{CH}}(\omega_{\text{C}} - \omega_{\text{H}}) + 3\mathcal{J}_{\text{CH}}(\omega_{\text{H}}) + 6\mathcal{J}_{\text{CH}}(\omega_{\text{C}} + \omega_{\text{H}})) \\
&+\frac{4}{3}d_{\text{HD}}^2(\mathcal{J}_{\text{HD}}(\omega_{\text{D}} - \omega_{\text{H}}) + 3\mathcal{J}_{\text{HD}}(\omega_{\text{H}}) + 6\mathcal{J}_{\text{HD}}(\omega_{\text{D}} + \omega_{\text{H}})) \\
&+\frac{2}{3}d_{\text{HD}_{\text{vic}}}^2(\mathcal{J}_{\text{HD}_{\text{vic}}}(\omega_{\text{D}} - \omega_{\text{H}}) + 3\mathcal{J}_{\text{HD}_{\text{vic}}}(\omega_{\text{H}}) + 6\mathcal{J}_{\text{HD}_{\text{vic}}}(\omega_{\text{D}} + \omega_{\text{H}})),
\end{aligned}$$

$$
\begin{aligned}
R_{\mathrm{CH}} =& \frac{1}{3}\Delta\sigma_C^2\omega_{\mathrm{C}}^2\mathcal{J}_{\mathrm{C}}(\omega_{\mathrm{C}}) + \frac{3}{4}d_{\mathrm{CH}}^2\left(\mathcal{J}_{\mathrm{CH}}(\omega_{\mathrm{C}}) + \mathcal{J}_{\mathrm{CH}}(\omega_{\mathrm{H}})\right)\\
&+\frac{4}{3}d_{\mathrm{CD}}^2\left(\mathcal{J}_{\mathrm{CD}}(\omega_{\mathrm{C}}-\omega_{\mathrm{D}}) + 3\mathcal{J}_{\mathrm{CD}}(\omega_{\mathrm{C}}) + 6\mathcal{J}_{\mathrm{CD}}(\omega_{\mathrm{C}}+\omega_{\mathrm{D}})\right)\\
&+\frac{4}{3}d_{\mathrm{HD}}^2\left(\mathcal{J}_{\mathrm{HD}}(\omega_{\mathrm{H}}-\omega_{\mathrm{D}}) + 3\mathcal{J}_{\mathrm{HD}}(\omega_{\mathrm{H}}) + 6\mathcal{J}_{\mathrm{HD}}(\omega_{\mathrm{H}}+\omega_{\mathrm{D}})\right)\\
&+\frac{2}{3}d_{\mathrm{CD_{vic}}}^2\left(\mathcal{J}_{\mathrm{CD_{vic}}}(\omega_{\mathrm{C}}-\omega_{\mathrm{D}}) + 3\mathcal{J}_{\mathrm{CD_{vic}}}(\omega_{\mathrm{C}}) + 6\mathcal{J}_{\mathrm{CD_{vic}}}(\omega_{\mathrm{C}}+\omega_{\mathrm{D}})\right)\\
&+\frac{2}{3}d_{\mathrm{HD_{vic}}}^2\left(\mathcal{J}_{\mathrm{HD_{vic}}}(\omega_{\mathrm{H}}-\omega_{\mathrm{D}}) + 3\mathcal{J}_{\mathrm{HD_{vic}}}(\omega_{\mathrm{H}}) + 6\mathcal{J}_{\mathrm{HD_{vic}}}(\omega_{\mathrm{H}}+\omega_{\mathrm{D}})\right),\\
R_{\mathrm{CHD}} =& \frac{3}{16}\zeta_{\mathcal{Q}}^2\left(\mathcal{J}_{\mathcal{Q}}(\omega_{\mathrm{D}}) + 8\mathcal{J}_{\mathcal{Q}}(2\omega_{\mathrm{D}})\right) + \frac{1}{3}\Delta\sigma_C^2\omega_{\mathrm{C}}^2\mathcal{J}_{\mathrm{C}}(\omega_{\mathrm{C}})\\
&+\frac{2}{3}d_{\mathrm{DD}}^2(\mathcal{J}_{\mathrm{DD}}(0) + 3\mathcal{J}_{\mathrm{DD}}(\omega_{\mathrm{D}}) + 6\mathcal{J}_{\mathrm{DD}}(2\omega_{\mathrm{D}})) + \frac{3}{2}d_{\mathrm{CH}}^2(\mathcal{J}_{\mathrm{CH}}(\omega_{\mathrm{C}}) + \mathcal{J}_{\mathrm{CH}}(\omega_{\mathrm{H}}))\\
&+\frac{1}{12}d_{\mathrm{CD}}^2(11\mathcal{J}_{\mathrm{CD}}(\omega_{\mathrm{C}}-\omega_{\mathrm{D}}) + 9\mathcal{J}_{\mathrm{CD}}(\omega_{\mathrm{D}}) + 60\mathcal{J}_{\mathrm{CD}}(\omega_{\mathrm{C}}) + 66\mathcal{J}_{\mathrm{CD}}(\omega_{\mathrm{C}}+\omega_{\mathrm{D}}))\\
&+\frac{1}{12}d_{\mathrm{HD}}^2(11\mathcal{J}_{\mathrm{HD}}(\omega_{\mathrm{H}}-\omega_{\mathrm{D}}) + 9\mathcal{J}_{\mathrm{HD}}(\omega_{\mathrm{D}}) + 60\mathcal{J}_{\mathrm{HD}}(\omega_{\mathrm{H}}) + 66\mathcal{J}_{\mathrm{HD}}(\omega_{\mathrm{H}}+\omega_{\mathrm{D}}))\\
&+\frac{2}{3}d_{\mathrm{DD_{vic}}}^2(\mathcal{J}_{\mathrm{DD_{vic}}}(0) + 3\mathcal{J}_{\mathrm{DD_{vic}}}(\omega_{\mathrm{D}}) + 6\mathcal{J}_{\mathrm{DD_{vic}}}(2\omega_{\mathrm{D}}))\\
&+\frac{2}{3}d_{\mathrm{CD_{vic}}}^2(3\mathcal{J}_{\mathrm{CD_{vic}}}(\omega_{\mathrm{C}}) + \mathcal{J}_{\mathrm{CD_{vic}}}(\omega_{\mathrm{C}}-\omega_{\mathrm{D}}) + 6\mathcal{J}_{\mathrm{CD_{vic}}}(\omega_{\mathrm{C}}+\omega_{\mathrm{D}}))\\
&+\frac{2}{3}d_{\mathrm{HD_{vic}}}^2(3\mathcal{J}_{\mathrm{HD_{vic}}}(\omega_{\mathrm{H}}) + \mathcal{J}_{\mathrm{HD_{vic}}}(\omega_{\mathrm{H}}-\omega_{\mathrm{D}}) + 6\mathcal{J}_{\mathrm{HD_{vic}}}(\omega_{\mathrm{H}}+\omega_{\mathrm{D}})),\\
R_{\mathrm{CD}} =& \frac{3}{16}\zeta_{\mathcal{Q}}^2\left(\mathcal{J}_{\mathcal{Q}}(\omega_{\mathrm{D}}) + 4\mathcal{J}_{\mathcal{Q}}(2\omega_{\mathrm{D}})\right) + \frac{1}{3}\Delta\sigma_C^2\omega_{\mathrm{C}}^2\mathcal{J}_{\mathrm{C}}(\omega_{\mathrm{C}})\\
&+\frac{1}{4}d_{\mathrm{CH}}^2(\mathcal{J}_{\mathrm{CH}}(\omega_{\mathrm{C}}-\omega_{\mathrm{H}}) + 3\mathcal{J}_{\mathrm{CH}}(\omega_{\mathrm{C}}) + 6\mathcal{J}_{\mathrm{CH}}(\omega_{\mathrm{C}}+\omega_{\mathrm{H}}))\\
&+\frac{1}{4}d_{\mathrm{HD}}^2(\mathcal{J}_{\mathrm{HD}}(\omega_{\mathrm{H}}-\omega_{\mathrm{D}}) + 3\mathcal{J}_{\mathrm{HD}}(\omega_{\mathrm{D}}) + 6\mathcal{J}_{\mathrm{HD}}(\omega_{\mathrm{H}}+\omega_{\mathrm{D}}))\\
&+\frac{2}{3}d_{\mathrm{DD}}^2(\mathcal{J}_{\mathrm{DD}}(0) + 3\mathcal{J}_{\mathrm{DD}}(\omega_{\mathrm{D}}) + 6\mathcal{J}_{\mathrm{DD}}(2\omega_{\mathrm{D}}))\\
&+\frac{1}{12}d_{\mathrm{CD}}^2(11\mathcal{J}_{\mathrm{CD}}(\omega_{\mathrm{C}}-\omega_{\mathrm{D}}) + 9\mathcal{J}_{\mathrm{CD}}(\omega_{\mathrm{D}}) + 60\mathcal{J}_{\mathrm{CD}}(\omega_{\mathrm{C}}) + 66\mathcal{J}_{\mathrm{CD}}(\omega_{\mathrm{C}}+\omega_{\mathrm{D}}))\\
&+\frac{2}{3}d_{\mathrm{DD_{vic}}}^2(\mathcal{J}_{\mathrm{DD_{vic}}}(0) + 3\mathcal{J}_{\mathrm{DD_{vic}}}(\omega_{\mathrm{D}}) + 6\mathcal{J}_{\mathrm{DD_{vic}}}(2\omega_{\mathrm{D}}))\\
&+\frac{2}{3}d_{\mathrm{CD_{vic}}}(\mathcal{J}_{\mathrm{CD_{vic}}}(\omega_{\mathrm{C}}-\omega_{\mathrm{D}}) + 3\mathcal{J}_{\mathrm{CD_{vic}}}(\omega_{\mathrm{C}}) + 6\mathcal{J}_{\mathrm{CD_{vic}}}(\omega_{\mathrm{C}}+\omega_{\mathrm{D}})),\\
R_{\mathrm{D}} =& \frac{3}{16}\zeta_{\mathcal{Q}}^2(\mathcal{J}_{\mathcal{Q}}(\omega_{\mathrm{D}}) + 4\mathcal{J}_{\mathcal{Q}}(2\omega_{\mathrm{D}})) + \frac{2}{3}d_{\mathrm{DD}}^2(\mathcal{J}_{\mathrm{DD}}(0) + 3\mathcal{J}_{\mathrm{DD}}(\omega_{\mathrm{D}}) + 6\mathcal{J}_{\mathrm{DD}}(2\omega_{\mathrm{D}}))\\
&+\frac{1}{4}d_{\mathrm{CD}}^2(\mathcal{J}_{\mathrm{CD}}(\omega_{\mathrm{C}}-\omega_{\mathrm{D}}) + 3\mathcal{J}_{\mathrm{CD}}(\omega_{\mathrm{D}}) + 6\mathcal{J}_{\mathrm{CD}}(\omega_{\mathrm{C}}+\omega_{\mathrm{D}}))\\
&+\frac{1}{4}d_{\mathrm{HD}}^2(\mathcal{J}_{\mathrm{HD}}(\omega_{\mathrm{H}}-\omega_{\mathrm{D}}) + 3\mathcal{J}_{\mathrm{HD}}(\omega_{\mathrm{D}}) + 6\mathcal{J}_{\mathrm{HD}}(\omega_{\mathrm{H}}+\omega_{\mathrm{D}}))\\
&+\frac{2}{3}d_{\mathrm{DD_{vic}}}^2(\mathcal{J}_{\mathrm{DD_{vic}}}(0) + 3\mathcal{J}_{\mathrm{DD_{vic}}}(\omega_{\mathrm{D}}) + 6\mathcal{J}_{\mathrm{DD_{vic}}}(2\omega_{\mathrm{D}})),
\end{aligned}
$$

$$
\begin{aligned}
R^{(1)}_{\mathrm{CDD}} =& \frac{1}{48}\zeta_{\mathcal{Q}}^2(3\mathcal{J}_{\mathcal{Q}}(0)+5\mathcal{J}_{\mathcal{Q}}(\omega_{\mathrm{D}})+2\mathcal{J}_{\mathcal{Q}}(2\omega_{\mathrm{D}}))+\frac{3}{4}d_{\mathrm{DD}}\zeta_{\mathcal{Q}}(2\mathcal{J}_{\mathrm{DD},\mathcal{Q}}(0)+3\mathcal{J}_{\mathrm{DD},\mathcal{Q}}(\omega_{\mathrm{D}}))\\
&+\frac{1}{3}\Delta\sigma_C^2\omega_{\mathrm{C}}^2\mathcal{J}_{\mathrm{C}}(\omega_{\mathrm{C}})+\frac{1}{4}d_{\mathrm{CH}}^2(\mathcal{J}_{\mathrm{CH}}(\omega_{\mathrm{C}}-\omega_{\mathrm{H}})+3\mathcal{J}_{\mathrm{CH}}(\omega_{\mathrm{C}})+6\mathcal{J}_{\mathrm{CH}}(\omega_{\mathrm{C}}+\omega_{\mathrm{H}}))\\
&+\frac{1}{4}d_{\mathrm{DD}}^2(7\mathcal{J}_{\mathrm{DD}}(0)+18\mathcal{J}_{\mathrm{DD}}(\omega_{\mathrm{D}})+12\mathcal{J}_{\mathrm{DD}}(2\omega_{\mathrm{D}}))\\
&+\frac{1}{4}d_{\mathrm{HD}}^2(4\mathcal{J}_{\mathrm{HD}}(0)+\mathcal{J}_{\mathrm{HD}}(\omega_{\mathrm{H}}-\omega_{\mathrm{D}})+3\mathcal{J}_{\mathrm{HD}}(\omega_{\mathrm{D}})+6\mathcal{J}_{\mathrm{HD}}(\omega_{\mathrm{H}})+6\mathcal{J}_{\mathrm{HD}}(\omega_{\mathrm{H}}+\omega_{\mathrm{D}}))\\
&+\frac{1}{4}d_{\mathrm{CD}}^2(4\mathcal{J}_{\mathrm{CD}}(0)+5\mathcal{J}_{\mathrm{CD}}(\omega_{\mathrm{C}}-\omega_{\mathrm{D}})+3\mathcal{J}_{\mathrm{CD}}(\omega_{\mathrm{D}})+6\mathcal{J}_{\mathrm{CD}}(\omega_{\mathrm{C}})+30\mathcal{J}_{\mathrm{CD}}(\omega_{\mathrm{C}}+\omega_{\mathrm{D}}))\\
&+\frac{2}{3}d_{\mathrm{CD_{vic}}}(\mathcal{J}_{\mathrm{CD_{vic}}}(\omega_{\mathrm{C}}-\omega_{\mathrm{D}})+3\mathcal{J}_{\mathrm{CD_{vic}}}(\omega_{\mathrm{C}})+6\mathcal{J}_{\mathrm{CD_{vic}}}(\omega_{\mathrm{C}}+\omega_{\mathrm{D}}))-2d_{\mathrm{CD}}^2\mathcal{J}_{\mathrm{CD_1,CD_2}}(0)\\
&+\frac{2}{3}d_{\mathrm{DD_{vic}}}^2(5\mathcal{J}_{\mathrm{DD_{vic}}}(0)+9\mathcal{J}_{\mathrm{DD_{vic}}}(\omega_{\mathrm{D}})+6\mathcal{J}_{\mathrm{DD_{vic}}}(2\omega_{\mathrm{D}}))\\
&-\frac{1}{2}d_{\mathrm{HD}}^2(2\mathcal{J}_{\mathrm{HD_1,HD_2}}(0)+3\mathcal{J}_{\mathrm{HD_1,HD_2}}(\omega_{\mathrm{H}}))-\frac{4}{3}d_{\mathrm{DD}}^2(2\mathcal{J}_{\mathrm{D_1D_{vic},D_2D_{vic}}}(0)+3\mathcal{J}_{\mathrm{D_1D_{vic},D_2D_{vic}}}(\omega_{\mathrm{D}})),\\
R^{(2)}_{\mathrm{CDD}} =& \frac{3}{8}\zeta_{\mathcal{Q}}(\mathcal{J}_{\mathcal{Q}}(\omega_{\mathrm{D}})+4\mathcal{J}_{\mathcal{Q}}(2\omega_{\mathrm{D}}))+\frac{1}{3}\Delta\sigma_C^2\omega_{\mathrm{C}}^2\mathcal{J}_{\mathrm{C}}(\omega_{\mathrm{C}})\\
&+\frac{1}{4}d_{\mathrm{CH}}^2(\mathcal{J}_{\mathrm{CH}}(\omega_{\mathrm{C}}-\omega_{\mathrm{H}})+3\mathcal{J}_{\mathrm{CH}}(\omega_{\mathrm{C}})+6\mathcal{J}_{\mathrm{CH}}(\omega_{\mathrm{C}}+\omega_{\mathrm{H}}))\\
&+\frac{1}{2}d_{\mathrm{CD}}^2(\mathcal{J}_{\mathrm{CD}}(\omega_{\mathrm{C}}-\omega_{\mathrm{D}})+3\mathcal{J}_{\mathrm{CD}}(\omega_{\mathrm{D}})+6\mathcal{J}_{\mathrm{CD}}(\omega_{\mathrm{C}}+\omega_{\mathrm{D}})+12\mathcal{J}_{\mathrm{CD}}(\omega_{\mathrm{C}}))\\
&+\frac{1}{2}d_{\mathrm{HD}}^2(\mathcal{J}_{\mathrm{HD}}(\omega_{\mathrm{H}}-\omega_{\mathrm{D}})+3\mathcal{J}_{\mathrm{HD}}(\omega_{\mathrm{D}})+6\mathcal{J}_{\mathrm{HD}}(\omega_{\mathrm{H}}+\omega_{\mathrm{D}}))\\
&+\frac{1}{2}d_{\mathrm{DD}}^2(\mathcal{J}_{\mathrm{DD}}(0)+12\mathcal{J}_{\mathrm{DD}}(\omega_{\mathrm{D}})+6\mathcal{J}_{\mathrm{DD}}(2\omega_{\mathrm{D}}))\\
&+\frac{2}{3}d_{\mathrm{CD_{vic}}}^2(\mathcal{J}_{\mathrm{CD_{vic}}}(\omega_{\mathrm{C}}-\omega_{\mathrm{D}})+3\mathcal{J}_{\mathrm{CD_{vic}}}(\omega_{\mathrm{C}})+6\mathcal{J}_{\mathrm{CD_{vic}}}(\omega_{\mathrm{C}}+\omega_{\mathrm{D}}))\\
&+\frac{4}{3}d_{\mathrm{DD_{vic}}}(\mathcal{J}_{\mathrm{DD_{vic}}}(0)+3\mathcal{J}_{\mathrm{DD_{vic}}}(\omega_{\mathrm{D}})+6\mathcal{J}_{\mathrm{DD_{vic}}}(2\omega_{\mathrm{D}})),\\
R =& \frac{9}{16}\zeta_{\mathcal{Q}}^2\mathcal{J}_{\mathcal{Q}}(\omega_{\mathrm{D}})+\frac{1}{3}\Delta\sigma_C^2\omega_{\mathrm{C}}^2\mathcal{J}_{\mathrm{C}}(\omega_{\mathrm{C}})\\
&+\frac{1}{4}d_{\mathrm{CH}}^2(\mathcal{J}_{\mathrm{CH}}(\omega_{\mathrm{C}}-\omega_{\mathrm{H}})+3\mathcal{J}_{\mathrm{CH}}(\omega_{\mathrm{C}})+6\mathcal{J}_{\mathrm{CH}}(\omega_{\mathrm{C}}+\omega_{\mathrm{H}}))\\
&+\frac{3}{4}d_{\mathrm{CD}}^2(\mathcal{J}_{\mathrm{CD}}(\omega_{\mathrm{C}}-\omega_{\mathrm{D}})+3\mathcal{J}_{\mathrm{CD}}(\omega_{\mathrm{D}})+4\mathcal{J}_{\mathrm{CD}}(\omega_{\mathrm{C}})+6\mathcal{J}_{\mathrm{CD}}(\omega_{\mathrm{C}}+\omega_{\mathrm{D}}))\\
&+\frac{3}{4}d_{\mathrm{HD}}^2(\mathcal{J}_{\mathrm{HD}}(\omega_{\mathrm{H}}-\omega_{\mathrm{D}})+3\mathcal{J}_{\mathrm{HD}}(\omega_{\mathrm{D}})+6\mathcal{J}_{\mathrm{HD}}(\omega_{\mathrm{H}}+\omega_{\mathrm{D}}))\\
&+2d_{\mathrm{DD}}^2(\mathcal{J}_{\mathrm{DD}}(0)+3\mathcal{J}_{\mathrm{DD}}(\omega_{\mathrm{D}})+6\mathcal{J}_{\mathrm{DD}}(2\omega_{\mathrm{D}})\\
&+\frac{2}{3}d_{\mathrm{CD_{vic}}}^2(\mathcal{J}_{\mathrm{CD_{vic}}}(\omega_{\mathrm{C}}-\omega_{\mathrm{D}})+3\mathcal{J}_{\mathrm{CD_{vic}}}(\omega_{\mathrm{C}})+6\mathcal{J}_{\mathrm{CD_{vic}}}(\omega_{\mathrm{C}}+\omega_{\mathrm{D}}))\\
&+2d_{\mathrm{DD_{vic}}}^2(\mathcal{J}_{\mathrm{DD_{vic}}}(0)+3\mathcal{J}_{\mathrm{DD_{vic}}}(\omega_{\mathrm{D}})+6\mathcal{J}_{\mathrm{DD_{vic}}}(2\omega_{\mathrm{D}}).
\end{aligned}
$$

C.3.4 Cross-relaxation rates

Cross-relaxation rates with the operator $\hat{C}_z$ are:

$$\begin{aligned}
\sigma_{\mathrm{CH}} =& \frac{1}{4} d_{\mathrm{CH}}^2 (-\mathcal{J}_{\mathrm{CH}}(\omega_{\mathrm{C}} - \omega_{\mathrm{H}}) + 6\mathcal{J}_{\mathrm{CH}}(\omega_{\mathrm{C}} + \omega_{\mathrm{H}})), \\
\eta_z^{\mathrm{C}} =& \Delta\sigma_C \omega_{\mathrm{C}} d_{\mathrm{CH}} \mathcal{J}_{\mathrm{C,CH}}(\omega_{\mathrm{C}}), \\
\kappa^{\mathrm{C}} =& \sqrt{6} d_{\mathrm{CH}} d_{\mathrm{CD}} \mathcal{J}_{\mathrm{CH,CD}}(\omega_{\mathrm{C}}), \\
\eta_z^{\mathrm{CD}} =& 2\sqrt{\frac{2}{3}} d_{\mathrm{CD}} \Delta\sigma_C \omega_{\mathrm{C}} \mathcal{J}_{\mathrm{C,CD}}(\omega_{\mathrm{C}}), \\
\sigma_{\mathrm{CD}} =& \frac{1}{\sqrt{6}} d_{\mathrm{CD}}^2 (-\mathcal{J}_{\mathrm{CD}}(\omega_{\mathrm{C}} - \omega_{\mathrm{D}}) + 6\mathcal{J}_{\mathrm{CD}}(\omega_{\mathrm{C}} + \omega_{\mathrm{D}})), \\
\lambda =& \frac{2}{3} d_{\mathrm{CD}}^2 (\mathcal{J}_{\mathrm{CD_1,CD_2}}(\omega_{\mathrm{C}} - \omega_{\mathrm{D}}) + 6\mathcal{J}_{\mathrm{CD_1,CD_2}}(\omega_{\mathrm{C}} + \omega_{\mathrm{D}})), \\
\nu_z =& 4 d_{\mathrm{CD}}^2 \mathcal{J}_{\mathrm{CD_1,CD_2}}(\omega_{\mathrm{C}}), \\
\mu =& \frac{\sqrt{2}}{6} d_{\mathrm{CD}}^2 \left(-\mathcal{J}_{\mathrm{CD}}(\omega_{\mathrm{C}} - \omega_{\mathrm{D}}) + 6\mathcal{J}_{\mathrm{CD}}(\omega_{\mathrm{C}}) - 6\mathcal{J}_{\mathrm{CD}}(\omega_{\mathrm{C}} + \omega_{\mathrm{D}})\right).
\end{aligned}$$

Finally, other cross-relaxation rates are:

$$\begin{aligned}
\kappa^H =& \sqrt{6} d_{\mathrm{CH}} d_{\mathrm{HD}} \mathcal{J}_{\mathrm{CH,HD}}(\omega_{\mathrm{H}}), \\
\kappa^{\mathrm{CH}} =& -2\sqrt{\frac{2}{3}} d_{\mathrm{CD}} \Delta\sigma_C \omega_{\mathrm{C}} \mathcal{J}_{\mathrm{C,CD}}(\omega_{\mathrm{C}}), \\
\kappa^{\mathrm{CD}} =& 4 d_{\mathrm{CD}}^2 \mathcal{J}_{\mathrm{CD_1,CD_2}}(\omega_{\mathrm{C}}) - \frac{2}{3} d_{DD}^2 (\mathcal{J}_{\mathrm{DD}}(0) - 6\mathcal{J}_{\mathrm{DD}}(2\omega_{\mathrm{D}})), \\
\kappa^{\mathrm{CHD}} =& 4 d_{\mathrm{CD}}^2 \mathcal{J}_{\mathrm{CD_1,CD_2}}(\omega_{\mathrm{C}}) + 4 d_{\mathrm{HD}}^2 \mathcal{J}_{\mathrm{HD_1,HD_2}}(\omega_{\mathrm{H}}) - \frac{2}{3} d_{\mathrm{DD}}^2 (\mathcal{J}_{\mathrm{DD}}(0) - 6\mathcal{J}_{\mathrm{DD}}(2\omega_{\mathrm{D}})), \\
\kappa^{\mathrm{CDD}} =& -\frac{3}{4} d_{\mathrm{DD}}^2 \mathcal{J}_{\mathrm{DD}}(0), \\
\sigma_{\mathrm{HD}} =& \frac{1}{\sqrt{6}} d_{\mathrm{HD}}^2 (-\mathcal{J}_{\mathrm{HD}}(\omega_{\mathrm{H}} - \omega_{\mathrm{D}}) + 6\mathcal{J}_{\mathrm{HD}}(\omega_{\mathrm{H}} + \omega_{\mathrm{D}})), \\
\sigma_{\mathrm{DD}} =& \frac{2}{3} d_{\mathrm{DD}}^2 (-\mathcal{J}_{\mathrm{DD}}(0) + 6\mathcal{J}_{\mathrm{DD}}(2\omega_{\mathrm{D}})), \\
\sigma_{\mathrm{CHD}} =& \frac{3}{2} d_{\mathrm{CD}} d_{\mathrm{HD}} \mathcal{J}_{\mathrm{CD,HD}}(\omega_{\mathrm{D}}), \\
\eta_z^{\mathrm{CHD}} =& d_{CH} \Delta\sigma_C \omega_{\mathrm{C}} \mathcal{J}_{\mathrm{C,CH}}(\omega_{\mathrm{C}}), \\
\delta =& \sqrt{6} d_{\mathrm{CH}} d_{\mathrm{CD}} \mathcal{J}_{\mathrm{CH,CD}}(\omega_{\mathrm{C}}) - \frac{1}{\sqrt{6}} d_{\mathrm{HD}}^2 (\mathcal{J}_{\mathrm{HD}}(\omega_{\mathrm{H}} - \omega_{\mathrm{D}}) - 6\mathcal{J}_{\mathrm{HD}}(\omega_{\mathrm{H}} + \omega_{\mathrm{D}})), \\
\lambda^{(1)} =& \frac{1}{\sqrt{6}} d_{\mathrm{HD}}^2 (\mathcal{J}_{\mathrm{HD_1,HD_2}}(\omega_{\mathrm{H}} - \omega_{\mathrm{D}}) - 6\mathcal{J}_{\mathrm{HD_1,HD_2}}(\omega_{\mathrm{H}} + \omega_{\mathrm{D}})) \\
& + \frac{1}{\sqrt{6}} d_{\mathrm{HD}} d_{\mathrm{DD}} (2\mathcal{J}_{\mathrm{HD,DD}}(0) - 3\mathcal{J}_{\mathrm{HD,DD}}(\omega_{\mathrm{D}})), \\
\lambda^{(2)} =& -\frac{1}{\sqrt{6}} d_{\mathrm{CD}} d_{\mathrm{DD}} (2\mathcal{J}_{\mathrm{CD,DD}}(0) + 3\mathcal{J}_{\mathrm{CD,DD}}(\omega_{\mathrm{D}})), \\
\nu_z^{(1)} =& -\frac{1}{\sqrt{6}} d_{\mathrm{HD}}^2 (\mathcal{J}_{\mathrm{HD}}(\omega_{\mathrm{H}} - \omega_{\mathrm{D}}) - 6\mathcal{J}_{\mathrm{HD}}(\omega_{\mathrm{H}} + \omega_{\mathrm{D}})) + \sqrt{3} \left(d_{\mathrm{CH}} d_{\mathrm{CD}} \mathcal{J}_{\mathrm{CH,CD}}(\omega_{\mathrm{C}}) + d_{\mathrm{HD}} d_{\mathrm{DD}} \mathcal{J}_{\mathrm{HD,DD}}(\omega_{\mathrm{D}})\right),
\end{aligned}$$

$$
\begin{aligned}
\nu_z^{(2)} =& -2\sqrt{\frac{2}{3}}d_{\mathrm{CD}}\Delta\sigma_C\omega_{\mathrm{C}}\mathcal{J}_{\mathrm{C,CD}}(\omega_{\mathrm{C}}),\\
\nu_z^{(3)} =& \sqrt{6}d_{\mathrm{CD}}d_{\mathrm{DD}}\mathcal{J}_{\mathrm{CD,DD}}(\omega_{\mathrm{D}}),\\
\nu_z^{(4)} =& \frac{1}{2}d_{\mathrm{DD}}^2(\mathcal{J}_{\mathrm{DD}}(0)-3\mathcal{J}_{\mathrm{DD}}(\omega_{\mathrm{D}}))-\frac{3}{8}d_{\mathrm{DD}}\zeta_{\mathcal{Q}}(\mathcal{J}_{\mathrm{DD},\mathcal{Q}}(0)-3\mathcal{J}_{\mathrm{DD},\mathcal{Q}}(\omega_{\mathrm{D}})+6\mathcal{J}_{\mathrm{DD},\mathcal{Q}}(2\omega_{\mathrm{D}}))\\
&-\frac{3}{4}d_{\mathrm{CD}}^2\mathcal{J}_{\mathrm{CD_1,CD_2}}(\omega_{\mathrm{D}})-\frac{1}{4}d_{\mathrm{HD}}^2(\mathcal{J}_{\mathrm{HD_1,HD_2}}(\omega_{\mathrm{H}}-\omega_{\mathrm{D}})+3\mathcal{J}_{\mathrm{HD_1,HD_2}}(\omega_{\mathrm{D}})+6\mathcal{J}_{\mathrm{HD_1,HD_2}}(\omega_{\mathrm{H}}+\omega_{\mathrm{D}}))\\
&-\frac{2}{3}d_{\mathrm{DD_{vic}}}^2(\mathcal{J}_{\mathrm{D_1D_{vic},D_2D_{vic}}}(0)+3\mathcal{J}_{\mathrm{D_1D_{vic},D_2D_{vic}}}(\omega_{\mathrm{D}})+6\mathcal{J}_{\mathrm{D_1D_{vic},D_2D_{vic}}}(2\omega_{\mathrm{D}})),\\
\mu^{(1)} =& -\frac{\sqrt{3}}{4}d_{\mathrm{HD}}^2(\mathcal{J}_{\mathrm{HD}}(\omega_{\mathrm{H}}-\omega_{\mathrm{D}})-6\mathcal{J}_{\mathrm{HD}}(\omega_{\mathrm{H}}+\omega_{\mathrm{D}}))+\sqrt{3}d_{\mathrm{CH}}d_{\mathrm{CD}}\mathcal{J}_{\mathrm{CH,CD}}(\omega_{\mathrm{C}})\\
&-\frac{3\sqrt{3}}{4}d_{\mathrm{HD}}\zeta_{\mathcal{Q}}\mathcal{J}_{\mathrm{HD},\mathcal{Q}}(\omega_{\mathrm{D}}),\\
\mu^{(2)} =& -\frac{2}{\sqrt{3}}d_{\mathrm{CD}}\Delta\sigma_C\omega_{\mathrm{C}}\mathcal{J}_{\mathrm{C,CD}}(\omega_{\mathrm{C}}),\\
\mu^{(3)} =& \frac{\sqrt{3}}{12}d_{\mathrm{CD}}^2(\mathcal{J}_{\mathrm{CD}}(\omega_{\mathrm{C}}-\omega_{\mathrm{D}})-6\mathcal{J}_{\mathrm{CD}}(\omega_{\mathrm{C}}+\omega_{\mathrm{D}}))-\frac{3\sqrt{3}}{4}d_{\mathrm{CD}}\zeta_{\mathcal{Q}}\mathcal{J}_{\mathrm{CD},\mathcal{Q}}(\omega_{\mathrm{D}}),\\
\mu^{(4)} =& -\frac{\sqrt{2}}{4}d_{\mathrm{DD}}^2(2\mathcal{J}_{\mathrm{DD}}(0)+3\mathcal{J}_{\mathrm{DD}}(\omega_{\mathrm{D}}))-\frac{\sqrt{2}}{6}d_{\mathrm{CD}}^2(\mathcal{J}_{\mathrm{CD_1,CD_2}}(\omega_{\mathrm{C}}-\omega_{\mathrm{D}})+6\mathcal{J}_{\mathrm{CD_1,CD_2}}(\omega_{\mathrm{C}}+\omega_{\mathrm{D}}))\\
&+\frac{3}{8\sqrt{2}}d_{\mathrm{DD}}\zeta_{\mathcal{Q}}(\mathcal{J}_{\mathrm{DD},\mathcal{Q}}(0)+\mathcal{J}_{\mathrm{DD},\mathcal{Q}}(\omega_{\mathrm{D}})-2\mathcal{J}_{\mathrm{DD},\mathcal{Q}}(2\omega_{\mathrm{D}})),\\
\mu^{(5)} =& -\frac{1}{\sqrt{2}}d_{\mathrm{DD}}^2(\mathcal{J}_{\mathrm{DD}}(0)-6\mathcal{J}_{\mathrm{DD}}(2\omega_{\mathrm{D}}))+2\sqrt{2}d_{\mathrm{CD}}^2\mathcal{J}_{\mathrm{CD_1,CD_2}}(\omega_{\mathrm{C}})-\frac{3}{\sqrt{2}}d_{\mathrm{DD}}\zeta_{\mathcal{Q}}\mathcal{J}_{\mathrm{DD},\mathcal{Q}}(\omega_{\mathrm{D}}).
\end{aligned}
$$

Appendix D

Analysis of ^{13}C-^{19}F TROSY pulse-sequences

D.1 Single-Field TROSY experiment

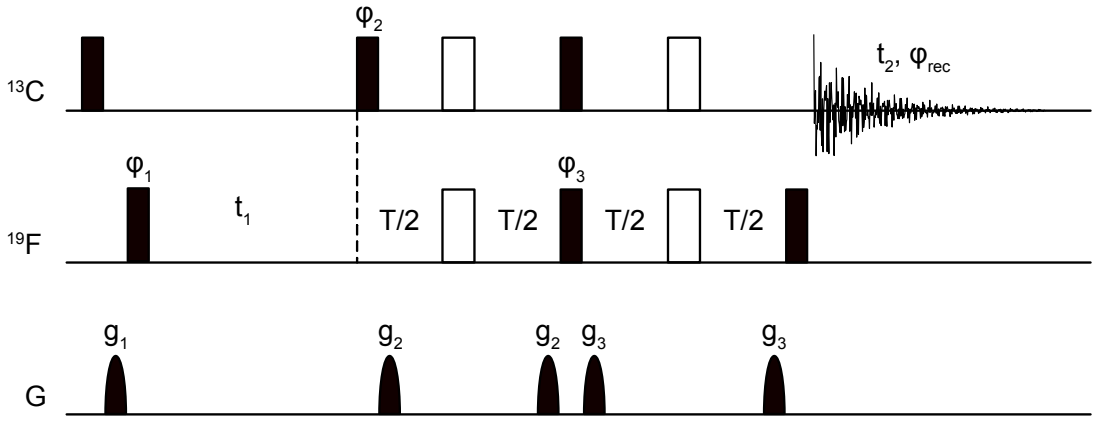

Figure D.1: Single-field TROSY pulse-sequence for ^{13}C-^{19}F aromatic groups. This sequence can be modified to include proton decoupling during the t_1 and t_2 evolution periods as detailed in the original publication [40]. Black narrow (resp. wide white) rectangles represent 90° (resp. 180°) pulses. Pulses are applied long the x-axis of the rotating frame if not otherwise stated. Phase cycles are as follows: φ_1=(y,-y,x,-x) , and φ_{rec}=(x,-x,-y,y). Pulses φ_2 and φ_3 select the TROSY component. In the case of the 3-fluorotyrosine, φ_2=y and φ_3=-y, while φ_2=-y and φ_3=-y for the 4-fluorophenylalanine. The indirect dimension is recorded in an Echo/Anti-Echo scheme by recording another set of experiment with following phases: φ_1=(-y,y,x,-x), φ_2=-y (3-fluorotyrosine) or φ_2=y (4-fluorophenylalanine), φ_3=y and the same receiver phase. The duration of the delay T=1/(2J). Gradient g_1 is a cleaning gradient and was simulated by setting the initial density operator to Fz only. Length of the gradients is 750 μs with amplitudes 24.75 G.cm^{-1} for g_2 and 27.5 G.cm^{-1} for g_3.

In the following, relaxation effects are neglected. The pulse sequence [40] is shown in Figure D.1. The first carbon pulse and gradient g_1 remove carbon polarization. After the pulse φ_1:

$$\begin{aligned}\hat{\mathrm{F}}_\mathrm{x} \xrightarrow{\Omega_F t_1 \hat{F}_z + 2\pi J_{CF} t_1 \hat{F}_z \hat{C}_z} & \hat{\mathrm{F}}_\mathrm{x} \cos(\Omega_F t_1)\cos(\pi J_{CF} t_1) + \hat{\mathrm{F}}_\mathrm{y} \sin(\Omega_F t_1)\cos(\pi J_{CF} t_1) \\ & + 2\hat{\mathrm{F}}_\mathrm{y}\hat{\mathrm{C}}_\mathrm{z} \cos(\Omega_F t_1)\sin(\pi J_{CF} t_1) - 2\hat{\mathrm{F}}_\mathrm{x}\hat{\mathrm{C}}_\mathrm{z} \sin(\Omega_F t_1)\sin(\pi J_{CF} t_1),\end{aligned} \tag{D.1}$$

where Ω_F is the offset frequency for the fluorine nucleus and J_{CF} the scalar-coupling constant between the carbon-13 and fluorine-19 nuclei. The **S**ingle **T**ransition-to-**S**ingle **T**ransition **P**olarization **T**ransfer (ST2-PT) block [148] converts these operators into observable carbon-13 magnetization (recall that the coupling constant is negative):

$$\begin{aligned}
&\hat{\mathrm{F}}_\mathrm{x} \xrightarrow{\frac{\pi}{2}\hat{C}_y} \hat{\mathrm{F}}_\mathrm{x} \xrightarrow{\pi\left(\hat{F}_x+\hat{C}_x\right)-\pi\hat{F}_z\hat{C}_z} -2\hat{\mathrm{F}}_\mathrm{y}\hat{\mathrm{C}}_\mathrm{z} \xrightarrow{\frac{\pi}{2}\left(\hat{C}_x-\hat{F}_y\right)} 2\hat{\mathrm{F}}_\mathrm{y}\hat{\mathrm{C}}_\mathrm{y} \xrightarrow{\pi\left(\hat{F}_x+\hat{C}_x\right)-\pi\hat{F}_z\hat{C}_z} 2\hat{\mathrm{F}}_\mathrm{y}\hat{\mathrm{C}}_\mathrm{y} \xrightarrow{\frac{\pi}{2}\hat{F}_x} 2\hat{\mathrm{F}}_\mathrm{z}\hat{\mathrm{C}}_\mathrm{y},\\
&\hat{\mathrm{F}}_\mathrm{y} \xrightarrow{\frac{\pi}{2}\hat{C}_y} \hat{\mathrm{F}}_\mathrm{y} \xrightarrow{\pi\left(\hat{F}_x+\hat{C}_x\right)-\pi\hat{F}_z\hat{C}_z} -2\hat{\mathrm{F}}_\mathrm{x}\hat{\mathrm{C}}_\mathrm{z} \xrightarrow{\frac{\pi}{2}\left(\hat{C}_x-\hat{F}_y\right)} 2\hat{\mathrm{F}}_\mathrm{z}\hat{\mathrm{C}}_\mathrm{y} \xrightarrow{\pi\left(\hat{F}_x+\hat{C}_x\right)-\pi\hat{F}_z\hat{C}_z} \hat{\mathrm{C}}_\mathrm{x} \xrightarrow{\frac{\pi}{2}\hat{F}_x} \hat{\mathrm{C}}_\mathrm{x},\\
&2\hat{\mathrm{F}}_\mathrm{x}\hat{\mathrm{C}}_\mathrm{z} \xrightarrow{\frac{\pi}{2}\hat{C}_y} 2\hat{\mathrm{F}}_\mathrm{x}\hat{\mathrm{C}}_\mathrm{x} \xrightarrow{\pi\left(\hat{F}_x+\hat{C}_x\right)-\pi\hat{F}_z\hat{C}_z} 2\hat{\mathrm{F}}_\mathrm{x}\hat{\mathrm{C}}_\mathrm{x} \xrightarrow{\frac{\pi}{2}\left(\hat{C}_x-\hat{F}_y\right)} 2\hat{\mathrm{F}}_\mathrm{z}\hat{\mathrm{C}}_\mathrm{x} \xrightarrow{\pi\left(\hat{F}_x+\hat{C}_x\right)-\pi\hat{F}_z\hat{C}_z} \hat{\mathrm{C}}_\mathrm{y} \xrightarrow{\frac{\pi}{2}\hat{F}_x} \hat{\mathrm{C}}_\mathrm{y},\\
&2\hat{\mathrm{F}}_\mathrm{y}\hat{\mathrm{C}}_\mathrm{z} \xrightarrow{\frac{\pi}{2}\hat{C}_y} 2\hat{\mathrm{F}}_\mathrm{y}\hat{\mathrm{C}}_\mathrm{x} \xrightarrow{\pi\left(\hat{F}_x+\hat{C}_x\right)-\pi\hat{F}_z\hat{C}_z} -2\hat{\mathrm{F}}_\mathrm{y}\hat{\mathrm{C}}_\mathrm{x} \xrightarrow{\frac{\pi}{2}\left(\hat{C}_x-\hat{F}_y\right)} -2\hat{\mathrm{F}}_\mathrm{y}\hat{\mathrm{C}}_\mathrm{x} \xrightarrow{\pi\left(\hat{F}_x+\hat{C}_x\right)-\pi\hat{F}_z\hat{C}_z} 2\hat{\mathrm{F}}_\mathrm{y}\hat{\mathrm{C}}_\mathrm{x} \xrightarrow{\frac{\pi}{2}\hat{F}_x} 2\hat{\mathrm{F}}_\mathrm{z}\hat{\mathrm{C}}_\mathrm{x}.
\end{aligned} \tag{D.2}$$

During the acquisition time t_2, the signal has the form:

$$\mathcal{S}^E_{y,x}(t_1,t_2) \propto \sin(\Omega_F t_1 - \pi J_{CF} t_1) e^{i(\Omega_C t_2 - \pi J_{CF} t_2)}, \tag{D.3}$$

where the notation $\mathcal{S}^E_{y,x}$ denotes the signal recorded for the set of phases $\varphi_1 = y$ and $\varphi_{\mathrm{rec}} = x$ during the echo part of the sequence. The second cycle ($\varphi_1 = -y, \varphi_{\mathrm{rec}} = -x$) produces the same FID. The last two cycles ($\varphi_1, \varphi_{\mathrm{rec}}$) lead to the signal:

$$\begin{aligned}
\mathcal{S}^E_{x,-y}(t_1,t_2) =& \mathcal{S}^E_{-x,y}(t_1,t_2),\\
\mathcal{S}^E_{x,-y}(t_1,t_2) \propto& -i\cos(\Omega_F t_1 - \pi J_{CF} t_1) e^{i(\Omega_C t_2 - \pi J_{CF} t_2)}.
\end{aligned} \tag{D.4}$$

In the "echo" linear combination, this leads to a signal of the form:

$$\begin{aligned}
\mathcal{S}^E(t_1,t_2) &= \sum_{(\varphi_1,\varphi_{\mathrm{rec}})^E} \mathcal{S}^E_{(\varphi_1,\varphi_{\mathrm{rec}})}(t_1,t_2),\\
&\propto -ie^{i(\Omega_F - \pi J_{CF})t_1} e^{i(\Omega_C - \pi J_{CF})t_2},
\end{aligned} \tag{D.5}$$

where the factor -i only introduces a -90° phase shift.
During the anti-echo acquisition, the ST2-PT block converts the operators into:

$$\begin{aligned}
\hat{\mathrm{F}}_\mathrm{x} &\xrightarrow{\mathrm{ST2PT}} 2\hat{\mathrm{F}}_\mathrm{z}\hat{\mathrm{C}}_\mathrm{y},\\
\hat{\mathrm{F}}_\mathrm{y} &\xrightarrow{\mathrm{ST2PT}} -\hat{\mathrm{C}}_\mathrm{x},\\
2\hat{\mathrm{F}}_\mathrm{x}\hat{\mathrm{C}}_\mathrm{z} &\xrightarrow{\mathrm{ST2PT}} \hat{\mathrm{C}}_\mathrm{y},\\
2\hat{\mathrm{F}}_\mathrm{y}\hat{\mathrm{C}}_\mathrm{z} &\xrightarrow{\mathrm{ST2PT}} -2\hat{\mathrm{F}}_\mathrm{z}\hat{\mathrm{C}}_\mathrm{x},
\end{aligned} \tag{D.6}$$

leading to signals:

$$\begin{aligned}
\mathcal{S}^{AE}_{(-y,x)}(t_1,t_2) &\propto \sin(\Omega_F t_1 + \pi J_{CF} t_1) e^{i(\Omega_C t_2 + \pi J_{CF} t_2)},\\
\mathcal{S}^{AE}_{(x,-y)}(t_1,t_2) &\propto i\cos(\Omega_F t_1 + \pi J_{CF} t_1) e^{i(\Omega_C t_2 + \pi J_{CF} t_2)},
\end{aligned} \tag{D.7}$$

where the exponent AE refers to the anti-echo acquisition of the sequence. Finally:

$$\mathcal{S}^{AE}(t_1, t_2) \propto ie^{i(\Omega_F + \pi J_{CF})t_1} e^{i(\Omega_C - \pi J_{CF})t_2}. \tag{D.8}$$

The Rance-Kay processing leads to the final spectrum with selection of the ^{19}F-TROSY component in the indirect dimension.

As detailed in section 2.3, the successive evolution during the **ST2PT!** (**ST2PT!**) under operators with drastically distinct relaxation properties (*i.e* single-quantum and multiple-quantum coherences) leads to a poor selection of the carbon-13 TROSY component (Fig. D.2).

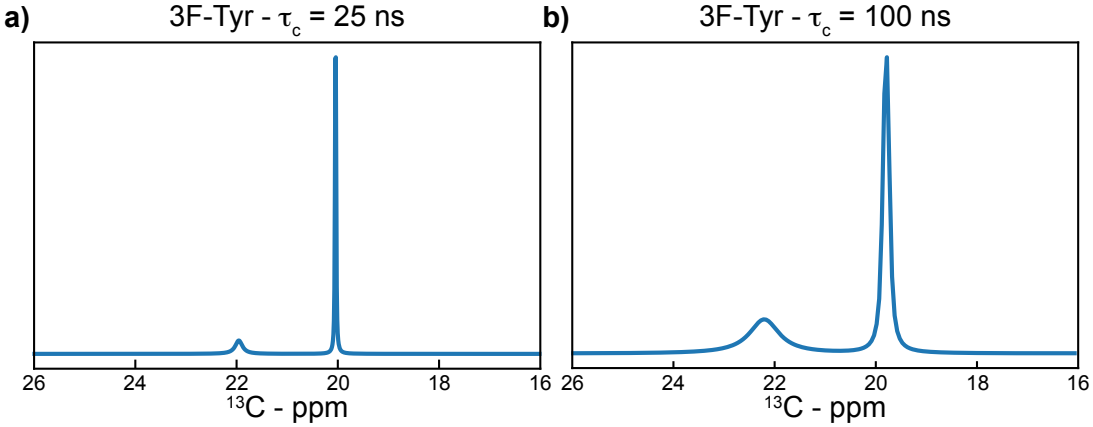

Figure D.2: The 1F-TROSY experiment does not perfectly select the carbon13 -TROSY peak. Carbon-13 cross-sections of two-dimensional spectra simulated with the 1F-TROSY pulse-sequence for 3F-Tyr with global tumbling correlation times $\tau_c = 25\,\text{ns}$ (**a**) and $\tau_c = 100\,\text{ns}$ (**b**).

D.2 Two-Field TROSY experiment

In the following derivation, relaxation effects are neglected. The pulse sequence is shown in Fig. 2.18. Polarization occurs at high field and the magnetization is stored and shuttled as $\hat{F}_z$ operator. Evolution in the Indirect dimension is performed in a semi-constant time fashion [149] such that scalar-coupling evolution is refocussed. The phase cycle on φ_2 allows selection of the cosine or sine evolving part, which is further transfered back to the $2\hat{F}_z\hat{C}_z$ operator for shuttling to high field. The first carbon-13 pulse creates anti-phase carbon magnetization, which further evolves under scalar coupling during a time T/2:

$$2\hat{\mathrm{F}}_\mathrm{z}\hat{\mathrm{C}}_\mathrm{z} \xrightarrow{\pi\hat{F}_x} -2\hat{\mathrm{F}}_\mathrm{z}\hat{\mathrm{C}}_\mathrm{z} \xrightarrow{\frac{\pi}{2}\hat{C}_x} 2\hat{\mathrm{F}}_\mathrm{z}\hat{\mathrm{C}}_\mathrm{y} \xrightarrow{\pi\left(\hat{F}_x+\hat{C}_x\right)-\frac{\pi}{2}\hat{F}_z\hat{C}_z} \frac{\sqrt{2}}{2}\left(2\hat{\mathrm{F}}_\mathrm{z}\hat{\mathrm{C}}_\mathrm{y}+\hat{\mathrm{C}}_\mathrm{x}\right). \tag{D.9}$$

The phase cycle on φ_3 and the use of two fluorine 180° pulses allow selection of the carbon-13 TROSY component.

$$\begin{aligned}
\varphi_3=\frac{\pi}{4}:\ \frac{\sqrt{2}}{2}\left(2\hat{\mathrm{F}}_\mathrm{z}\hat{\mathrm{C}}_\mathrm{y}+\hat{\mathrm{C}}_\mathrm{x}\right) &\xrightarrow{\varphi_3}\frac{\sqrt{2}}{2}\left[\frac{1}{2}\left(2\hat{\mathrm{F}}_\mathrm{z}\hat{\mathrm{C}}_\mathrm{x}+2\hat{\mathrm{F}}_\mathrm{z}\hat{\mathrm{C}}_\mathrm{y}\right)+\frac{\sqrt{2}}{2}2\hat{\mathrm{F}}_\mathrm{z}\hat{\mathrm{C}}_\mathrm{z}+\frac{1}{2}\left(\hat{\mathrm{C}}_\mathrm{x}+\hat{\mathrm{C}}_\mathrm{y}\right)-\frac{\sqrt{2}}{2}\hat{\mathrm{C}}_\mathrm{z}\right]\\
&\xrightarrow{\frac{\pi}{2}\hat{C}_y}\frac{\sqrt{2}}{2}\left[-\frac{1}{2}\left(2\hat{\mathrm{F}}_\mathrm{z}\hat{\mathrm{C}}_\mathrm{z}-2\hat{\mathrm{F}}_\mathrm{z}\hat{\mathrm{C}}_\mathrm{y}\right)+\frac{\sqrt{2}}{2}2\hat{\mathrm{F}}_\mathrm{z}\hat{\mathrm{C}}_\mathrm{x}-\frac{1}{2}\left(\hat{\mathrm{C}}_\mathrm{z}-\hat{\mathrm{C}}_\mathrm{y}\right)-\frac{\sqrt{2}}{2}\hat{\mathrm{C}}_\mathrm{x}\right],\\
\varphi_3=\frac{5\pi}{4}:\ \frac{\sqrt{2}}{2}\left(2\hat{\mathrm{F}}_\mathrm{z}\hat{\mathrm{C}}_\mathrm{y}+\hat{\mathrm{C}}_\mathrm{x}\right) &\xrightarrow{\varphi_3}\frac{\sqrt{2}}{2}\left[\frac{1}{2}\left(2\hat{\mathrm{F}}_\mathrm{z}\hat{\mathrm{C}}_\mathrm{x}+2\hat{\mathrm{F}}_\mathrm{z}\hat{\mathrm{C}}_\mathrm{y}\right)-\frac{\sqrt{2}}{2}2\hat{\mathrm{F}}_\mathrm{z}\hat{\mathrm{C}}_\mathrm{z}+\frac{1}{2}\left(\hat{\mathrm{C}}_\mathrm{x}+\hat{\mathrm{C}}_\mathrm{y}\right)+\frac{\sqrt{2}}{2}\hat{\mathrm{C}}_\mathrm{z}\right]\\
&\xrightarrow{\frac{\pi}{2}\hat{C}_y}\frac{\sqrt{2}}{2}\left[-\frac{1}{2}\left(2\hat{\mathrm{F}}_\mathrm{z}\hat{\mathrm{C}}_\mathrm{z}-2\hat{\mathrm{F}}_\mathrm{z}\hat{\mathrm{C}}_\mathrm{y}\right)-\frac{\sqrt{2}}{2}2\hat{\mathrm{F}}_\mathrm{z}\hat{\mathrm{C}}_\mathrm{x}-\frac{1}{2}\left(\hat{\mathrm{C}}_\mathrm{z}-\hat{\mathrm{C}}_\mathrm{y}\right)+\frac{\sqrt{2}}{2}\hat{\mathrm{C}}_\mathrm{x}\right].
\end{aligned} \tag{D.10}$$

Changing the receiver phase from -x to +x leads to the selection of the $2\hat{\mathrm{F}}_\mathrm{z}\hat{\mathrm{C}}_\mathrm{x}-\hat{\mathrm{C}}_\mathrm{x}$ operator before detection (*i.e.* the TROSY component). Reconstruction of the indirect dimension is done after Fourier transform of the direct dimension as:

$$\mathcal{S}(t_1,\omega_2)=\mathcal{S}_{\varphi_1=x}(t_1,\omega_2)+i\mathcal{S}_{\varphi_1=y}(t_1,\omega_2), \tag{D.11}$$

with $\mathcal{S}_{\varphi_1=k}(t_1,\omega_2)$ being the Fourier-transformed signal in the direct dimension recorded with phase $\varphi_1=k$.

D.3 Two-Field TROSY experiment with ST2-PT block

In this section, some results for an alternative 2F-TROSY pulse-sequence are detailed. In this pulse sequence (Fig. D.3), the **S**pin **S**tate **S**elective **E**xcitation (S3E) block [150] is replaced by a ST2-PT block [149]. This allows for a selection of both ^{13}C- and ^{19}-TROSY single-transitions. We refer to this experiment as 2F-ST2PT.

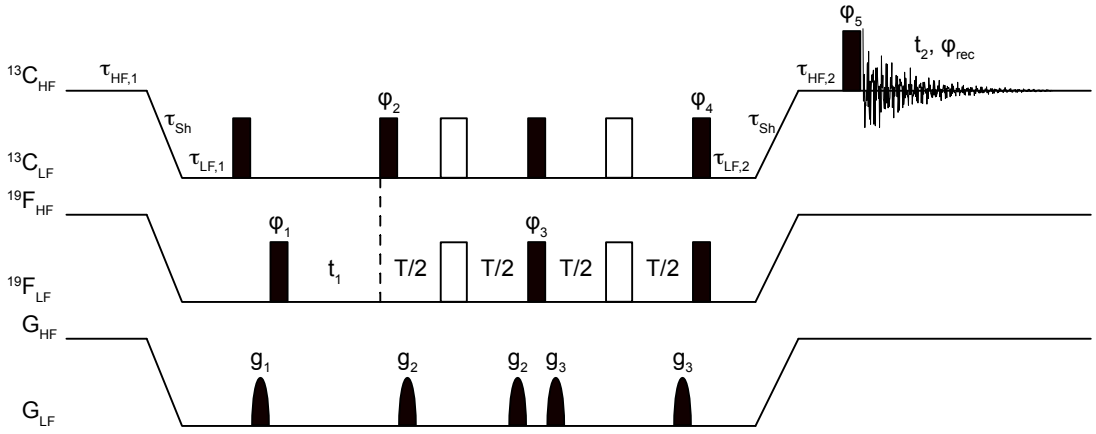

Figure D.3: Two-field TROSY pulse sequence with selection of both ^{19}F and ^{13}C-TROSY components in ^{13}C-^{19}F aromatic groups. Black narrow (respectively wide white) rectangles represent 90° (respectively 180°) pulses. Pulses are applied along the x-axis of the rotating frame unless otherwise stated. Phase cycles are as follows: φ_1 = (y,-y,x,-x, y,-y,x,-x), φ_4 = (x, x, x, x,y, y, y, y), φ_5 = (-x, -x, -x, -x,-y, -y, -y,-y) and φ_{rec} = (x,-x,-y,y,x,-x,-y,y). In order to select the TROSY peak, phases φ_2 and φ_3 have to be adjusted to either y and $-y$ for selection of $\hat{F}^+ - 2\hat{F}^+\hat{C}_z$ (3F-Tyr) or to $-y$ and $-y$ for selection of $\hat{F}^+ + 2\hat{F}^+\hat{C}_z$ (4F-Phe). Frequency discrimination in the indirect dimension is performed using the Echo/Anti-Echo acquisition scheme, with phases φ_1 = (-y,y,x,-x,-y,y,x,-x) and the phases φ_2 and φ_3 shifted by 180°. Length of the gradient g_2 and g_3 are the same as in the single-field experiment (750 μs, and 24.75 G.cm^{-1} and 27.5 G.cm^{-1} respectively). This pulse sequence can be modified to include proton decoupling during fluorine-19 and carbon-13 chemical shift evolution periods. The horizontal line breaks represent the shuttling periods from one field to the other. Time τ_{Sh} is the shuttling delay, $\tau_{HF,1}$ and $\tau_{LF,2}$ are waiting delays before shuttling and $\tau_{HF,2}$ and $\tau_{LF,1}$ are waiting delays after shuttling, as detailed in section 2.3. Figure reproduced from [41].

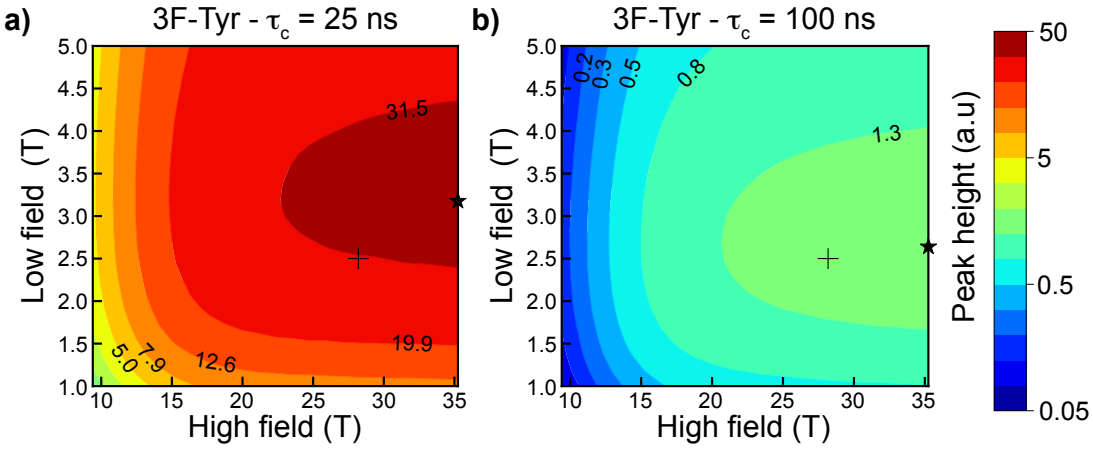

Figure D.4: Field optimization of the 2F-ST2PT experiment. Expected peak height for the 3F-Tyr for correlation times for global tumbling τ_c of 25 ns (**a**) and 100 ns (**b**). The highest peak-height position is indicated with a star. The optimal low-field remains the same as for the two-field experiment discussed in section 2.3 (2.5 T). Interestingly, the optimial high field is higher. This is due to an increase in the ^{19}F longitudinal relaxation rate (Fig. C.1) leading to a smaller recycling delay and hence lower experimental time. We simulated the experiment at the highest commercially available magnetic field at the time of writing (*i.e.* 28.2 T). Figure reproduced from [41].

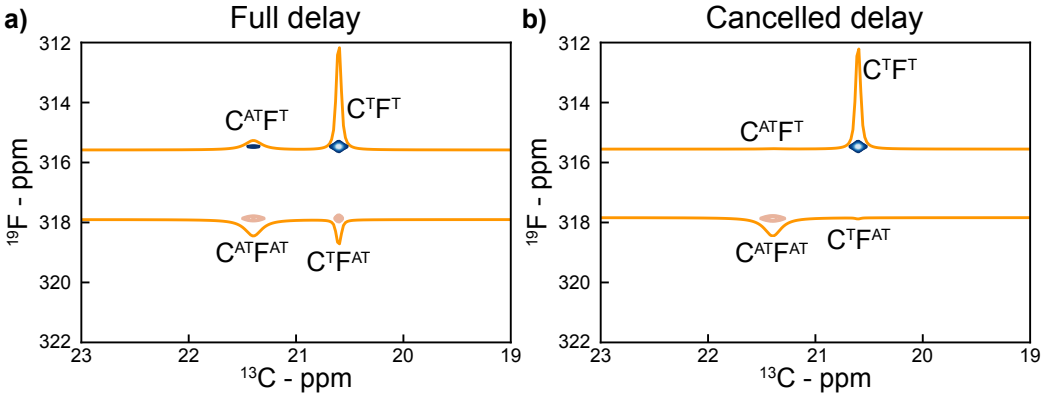

Figure D.5: The 2F-ST2PT leads to poor selection of the TROSY operators. 3F-Tyr spectra simulated with correct shuttling delays (**a**) and virtually cancelling shuttling (1 ms) and high-field stabilization (0 ms) delays (**b**). These simulations were performed for a global tumbling correlation time τ_c = 25 ns. Here, we show 15 contour levels starting from the maximum intensity and with a factor 1.2 between two consecutive levels. Peaks are labelled as Carbon-TROSY/-Fluorine TROSY ($C^{T}F^{T}$), Carbon anti-TROSY/Fluorine-TROSY ($C^{AT}F^{T}$), Carbon-TROSY/Fluorine anti-TROSY ($C^{T}F^{AT}$) and Carbon anti-TROSY/Fluorine anti-TROSY ($C^{AT}F^{AT}$). Figure reproduced from [41].

Appendix E

Results for the dynamics of ubiquitin methyl groups

E.1 Value of the parameters for isoleucine dynamics of ubiquitin

The results reported here were published by Cousin *et al.* [21] and are based on the analysis of high-resolution relaxometry data using a spectral density function accounting for an isotropic global tumbling motions (correlation time τ_c), the rotation of the methyl group (order parameter S^2_m and correlation time τ_m), and two modes of motions for the C-C bonds, one fast (correlation time S^2_f and correlation time τ_f) and one slow (order parameter S^2_s and correlation time τ_s):

$$\begin{aligned}\mathcal{J}(\omega,\theta_{\vec{i},\vec{j}}) = \frac{2}{5}\Big[&S^2_m(\theta_{\vec{i},\vec{j}})(S^2_f S^2_s L(\omega,\tau_c) + (1-S^2_f)L(\omega,\tau'_f) + S^2_f(1-S^2_s)L(\omega,\tau'_s)) \\ &+(\mathcal{P}_2[\cos(\theta_{\vec{i},\vec{j}})] - S^2_m(\theta_{\vec{i},\vec{j}}))(S^2_f S^2_s L(\omega,\tau'_m) + (1-S^2_f)L(\omega,\tau''_f) + S^2_f(1-S^2_s)L(\omega,\tau''_s))\Big],\end{aligned} \tag{E.1}$$

where $\theta_{\vec{i},\vec{j}}$ is the angle between the two interactions i and j, $L(\omega,\tau) = \tau/(1+(\omega\tau)^2)$ is the Legendre function, $\mathcal{P}_2(x) = (3x^2-1)/2$ is the second order Legendre polynomial and $S^2_m(\theta_{\vec{i},\vec{j}}) = \mathcal{P}_2[cos(\theta_{\vec{CC},\vec{i}})]\mathcal{P}_2[cos(\theta_{\vec{CC},\vec{j}})]$ where $\theta_{\vec{CC},\vec{i}}$ and $\theta_{\vec{CC},\vec{j}}$ are the angle between the C-C bond and the interactions i and j respectively.

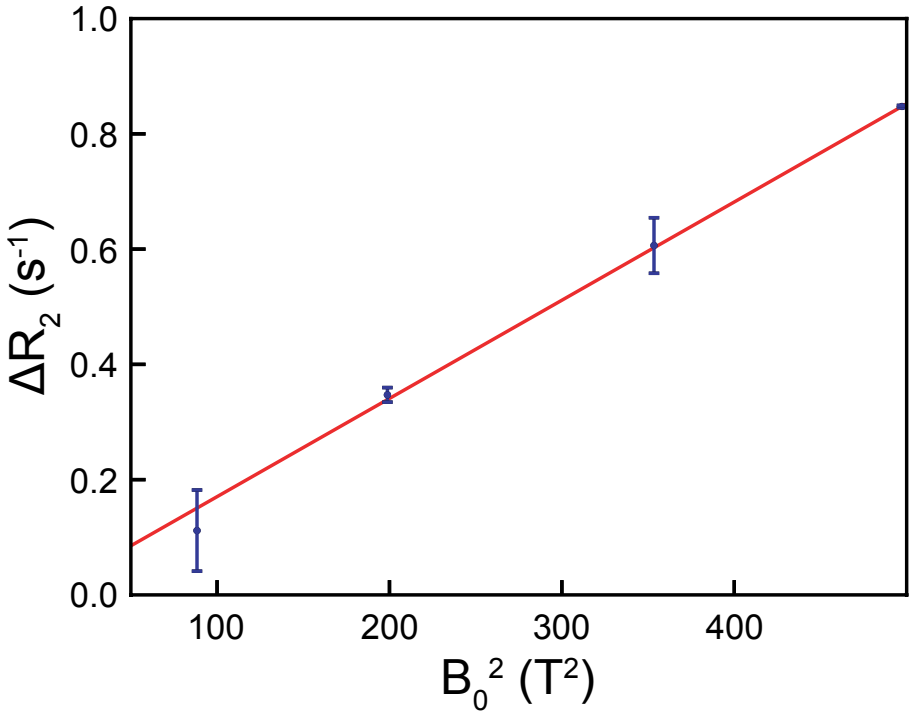

Figure E.1: Contribution of chemical exchange to the relaxation of carbon-13 $\delta 1$ nucleus of isoleucine 44 of Ubiquitin. The y-axis corresponds to the difference between the measured and calculated R_2 using ICARUS analysis without including these rates. Figure reproduced from [21].

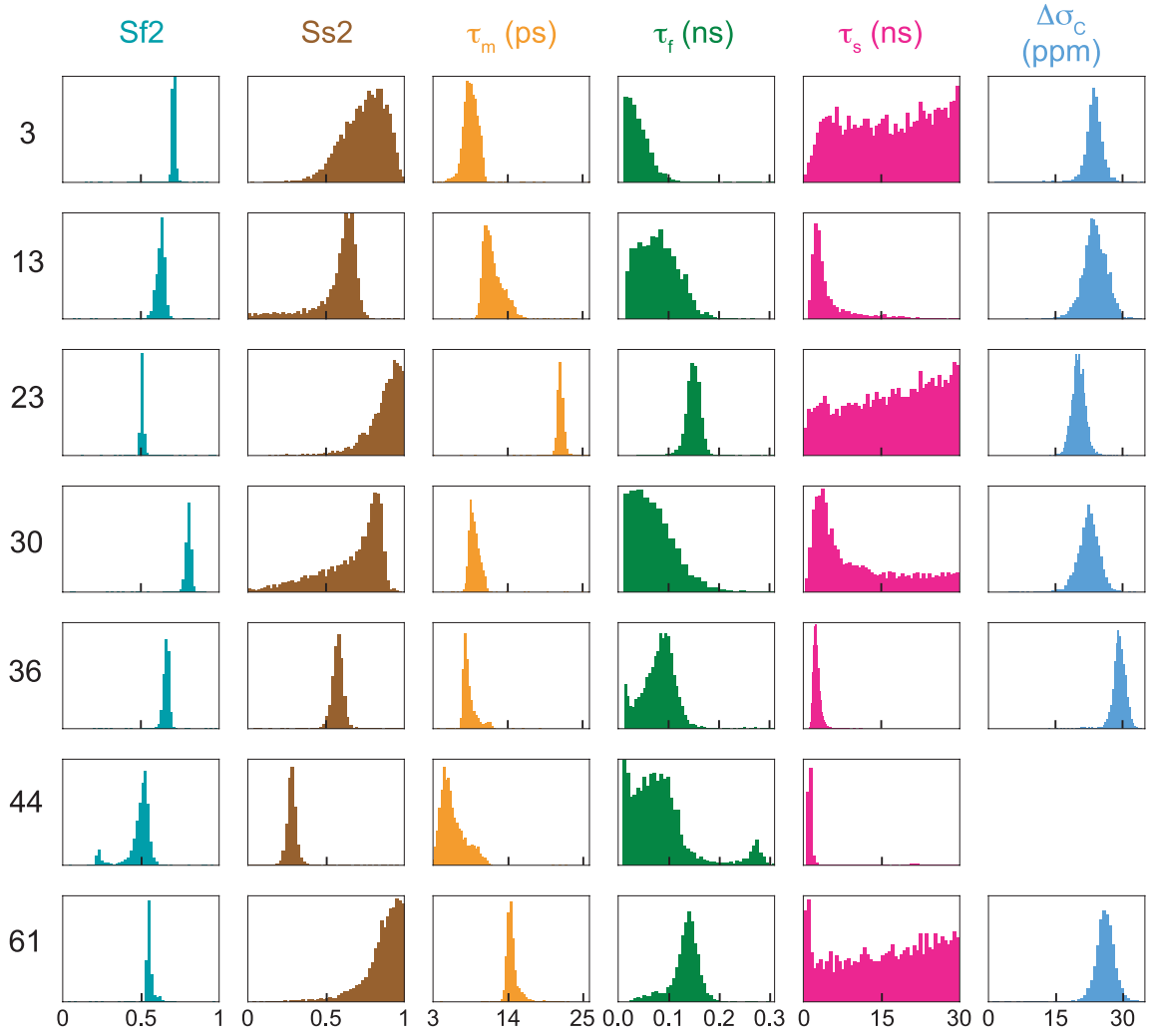

Figure E.2: Distribution of parameters of the dynamics after an MCMC procedure on corrected HRR rates using ICARUS and accurate high-field relaxation rates. Figure reproduced from [21].

Table E.1: Order parameters and correlation times for isoleucine $\delta 1$ methyl groups in Ubiquitin determined using HRR and ICARUS analysis [21]. τ_c was set to 5.028 ns. Chemical exchange is affecting transverse relaxation rates of Ile-44 and its CSA was set to 25.0 ppm.

	S_f^2			S_s^2			CSA (ppm)		
Residue	Median	$+\sigma$	$-\sigma$	Median	$+\sigma$	$-\sigma$	Median	$+\sigma$	$-\sigma$
3	0.71	0.01	0.01	0.76	0.12	0.15	23.8	1.57	1.43
13	0.63	0.02	0.03	0.62	0.06	0.15	23.9	2.53	2.33
23	0.51	0.01	0.01	0.90	0.07	0.12	20.1	1.36	1.37
30	0.81	0.01	0.02	0.74	0.10	0.30	22.5	2.05	2.19
36	0.67	0.02	0.02	0.58	0.03	0.03	29.4	1.28	1.19
44	0.51	0.03	0.05	0.28	0.02	0.03	Not fitted		
61	0.55	0.02	0.01	0.89	0.07	0.11	26.1	1.87	1.83

	τ_{met} (ps)			τ_f (ps)			τ_s (ns)		
Residue	Median	$+\sigma$	$-\sigma$	Median	$+\sigma$	$-\sigma$	Median	$+\sigma$	$-\sigma$
3	8.56	1.06	0.88	34.8	24.4	17.0	17.7	8.86	10.6
13	11.5	1.85	0.94	77.3	40.7	39.3	3.13	4.10	1.08
23	21.7	0.38	0.33	150	11.8	12.1	18.3	8.37	11.4
30	9.03	0.92	0.61	61.8	47.6	35.4	6.98	14.8	4.20
36	8.05	1.14	0.43	82.8	24.8	37.6	2.48	0.63	0.45
44	5.58	2.44	1.17	70.3	42.1	42.9	1.27	0.36	0.22
61	14.4	0.71	0.45	138	18.2	26.1	17.3	9.05	12.7

Table E.2: Median values and standard deviations for order parameters and correlation times for isoleucine $\delta 1$ methyl groups of Ubiquitin determined using HRR and a MINOTAUR analysis. τ_c was set to 5.028 ns. Chemical exchange is affecting transverse relaxation rates of Ile-44 and CSA was set to 25.0 ppm.

	S_f^2			S_s^2			CSA (ppm)		
Residue	Median	$+\sigma$	$-\sigma$	Median	$+\sigma$	$-\sigma$	Median	$+\sigma$	$-\sigma$
3	0.71	0.02	0.02	0.81	0.10	0.18	22.1	1.69	2.26
13	0.63	0.02	0.02	0.51	0.12	0.25	25.2	1.68	1.71
23	0.52	0.02	0.02	0.82	0.12	0.21	19.9	2.17	2.05
30	0.82	0.02	0.02	0.47	0.29	0.26	22.9	1.86	2.01
36	0.66	0.02	0.02	0.53	0.07	0.11	29.4	1.61	1.53
44	0.50	0.02	0.02	0.23	0.04	0.05	Not fitted		
61	0.57	0.02	0.01	0.84	0.10	0.17	25.0	1.57	1.41

	τ_{met} (ps)			τ_f (ps)			τ_s (ns)		
Residue	Median	$+\sigma$	$-\sigma$	Median	$+\sigma$	$-\sigma$	Median	$+\sigma$	$-\sigma$
3	8.40	0.83	0.63	40.0	25.5	16.3	19.6	7.19	10.3
13	11.3	0.90	0.48	84.5	21.0	27.2	5.44	4.98	2.39
23	21.9	0.50	0.39	139	13.7	16.8	17.8	8.42	11.3
30	9.21	0.69	0.52	59.4	38.2	30.6	16.3	8.68	10.3
36	9.21	0.58	0.31	94.9	22.6	26.4	3.50	1.76	0.99
44	6.06	1.35	0.73	58.6	19.2	22.7	1.62	0.28	0.26
61	14.7	0.36	0.29	121	12.8	14.9	17.6	8.53	10.4

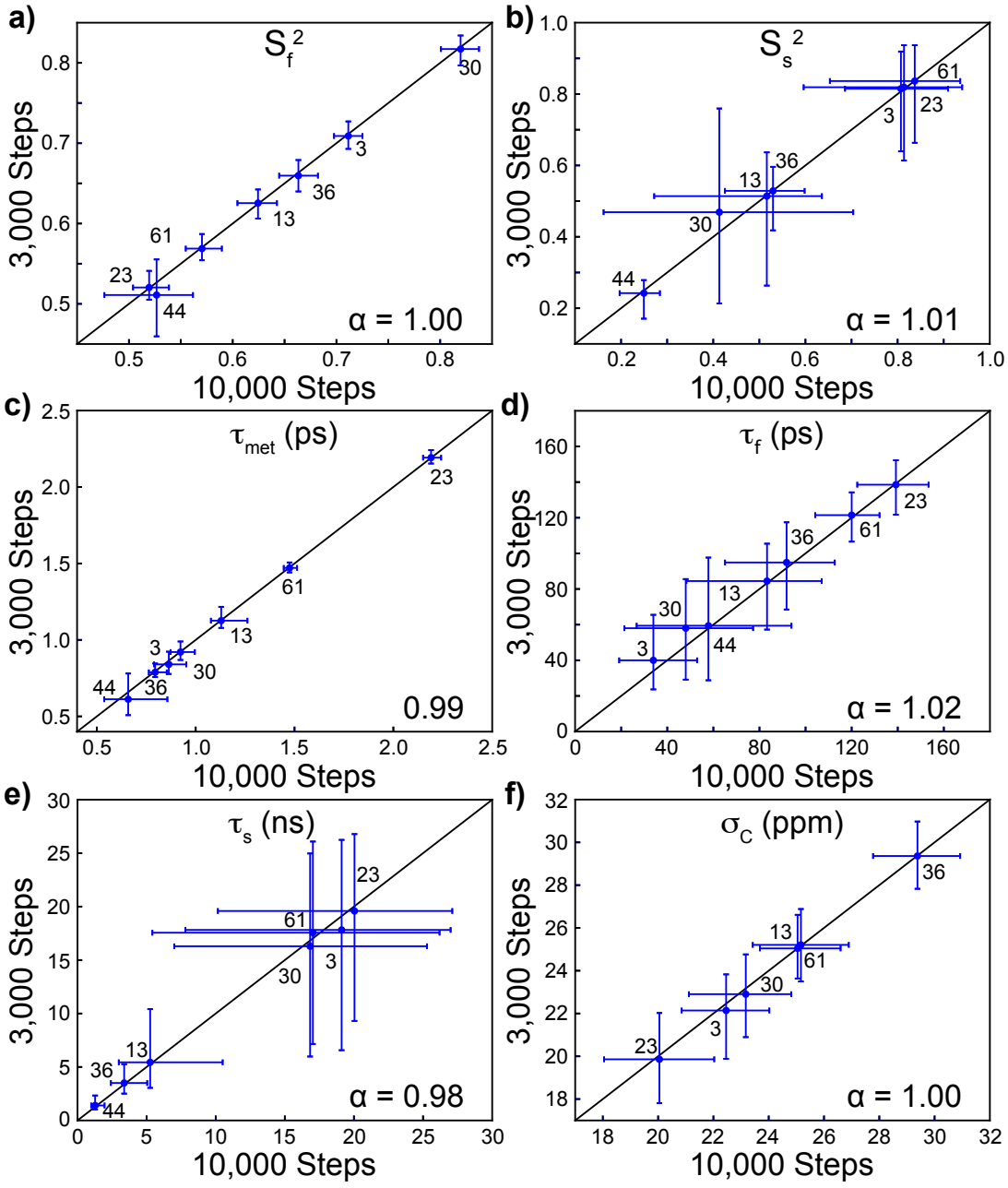

Figure E.3: Correlation between MINOTAUR analysis using 3,000 and 10,000 MCMC steps for S_f^2 (a), S_s^2 (b), τ_{met} (c), τ_f (d), τ_s (e) and the carbon-CSA (f). The solid black lines correspond to perfect correlation. α is the slope of the linear correlation function.

E.2 Experimental parameters

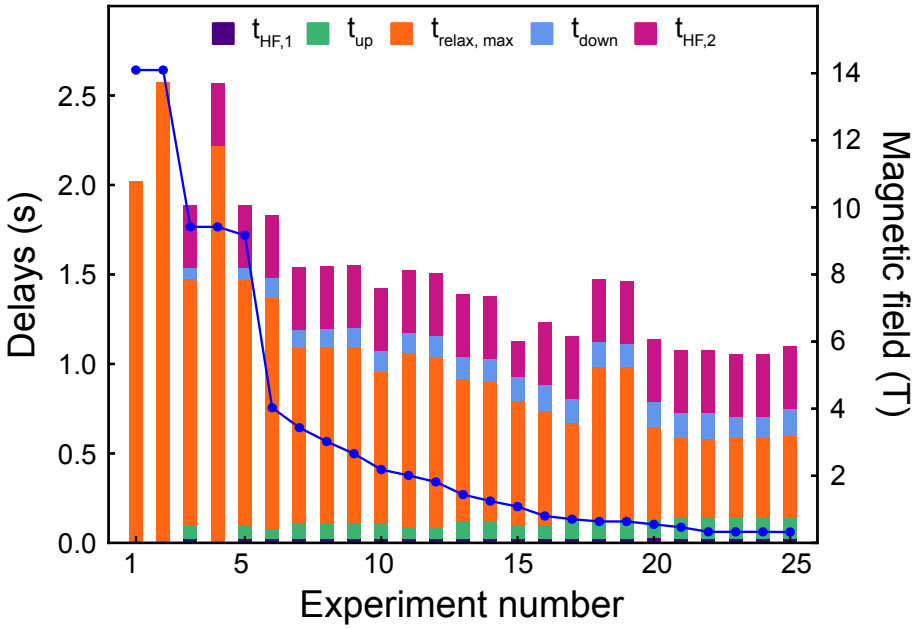

Figure E.4: Experimental delays for the 25 experiments used in the analysis of the dynamics of isoleucine-δ1-methyl groups of Ubiquitin, and ordered from the highest magnetic field at which relaxation takes place to the lowest. The time labels refer to the decomposition of the free-relaxation part of the pulse-sequence, as shown in Fig. 3.1. The blue curve (right y-axis) shows the variation of the magnetic field for each experiment (associated with an increase of shuttling height). Experiments 1, 2 and 4 were performed on high-field spectrometers, with no shuttle. Figure reproduced from [19].

E.3 Size-reduction of relaxation matrices by removing fast-relaxing operators

Here, we will show that fast-relaxing terms of a relaxation matrix can be discarded (as mentioned in Section 3.3.2 of the main text) in order to reduce the size of the relaxation matrix and save computational time. For the sake of simplicity, we consider a 2x2 Liouvillian:

$$\mathcal{L} = \begin{pmatrix} R_1 & \sigma \\ \sigma & R_1' \end{pmatrix}. \tag{E.2}$$

The characteristic polynomial of $\mathcal{L}$ is:

$$\det[\mathcal{L} - \lambda\mathcal{I}] = \lambda^2 - \lambda(R_1 + R_1') - \sigma^2 + R_1 R_1', \tag{E.3}$$

with $\mathcal{I}$ the identity matrix. The roots are given by:

$$\lambda_\pm = \frac{R_1 + R_1' \pm \sqrt{\Delta}}{2}, \tag{E.4}$$

with:

$$\Delta = R_1'^2 + R_1^2 - 2R_1 R_1' + 4\sigma^2. \tag{E.5}$$

Let's assume $R_1' \gg R_1, \sigma$. A first order approximation in R_1 and σ of $\sqrt{\Delta}$ leads to:

$$\sqrt{\Delta} \approx R_1'(1 - \frac{R_1}{R_1'}) = R_1' - R_1, \tag{E.6}$$

such that the eigenvalues of $\mathcal{L}$ are R_1 and R_1'. The associated eigenvectors approximate to $\{1, 0\}$ and $\{0, 1\}$ and the autorelaxation of the operator of interest can be considered mono-exponential with decay rate of R_1. The fast relaxing operator does not contribute to the relaxation of the slowly relaxing operator.

This can be verified by simulating the polarization decay. We will set $R_1 = 1\,s^{-1}$, $\sigma = 0.5\,s^{-1}$ and vary R_1'. We can compute the polarization decay (associated with the operator of interest with autorelaxation rate R_1) following Section 3.2.2.1 of the main text (Fig. E.5). The polarization decay can be fitted to a mono-exponential decay, and fitted relaxation rates are reported in Table E.3. It is clear that the fast relaxing operator has negligeable effects on the polarization decay when $R_1' \gg R_1$.

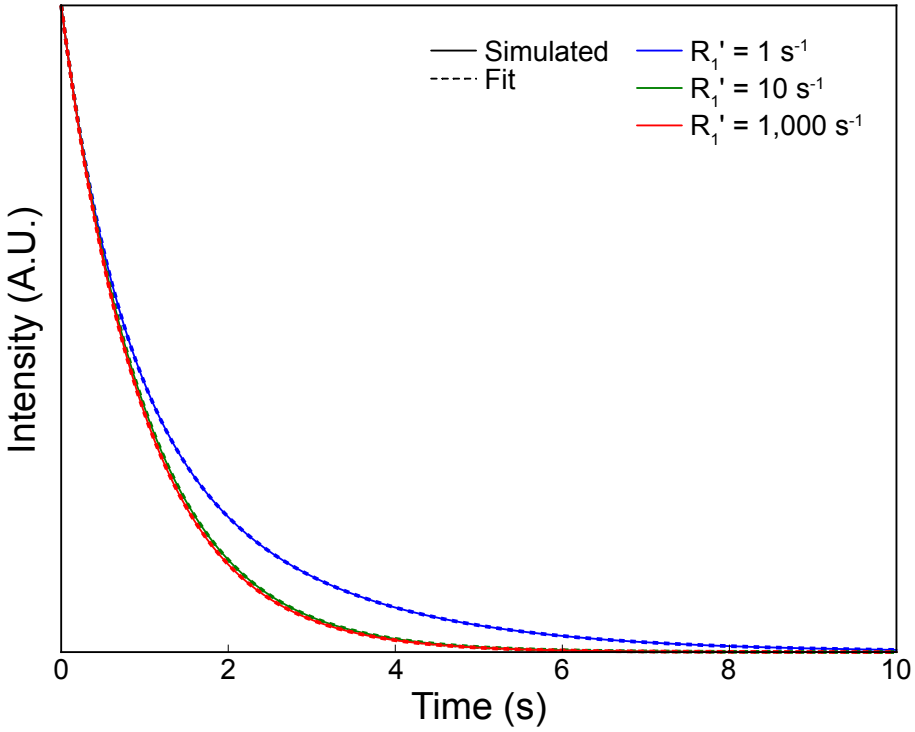

Figure E.5: Simulated polarization decay (plain) and exponential fit (dash) for different values of R_1' relaxation rates.

Table E.3: Fitted relaxation rates from the simulated polarization decay for different values of R_1'

R_1' (s^{-1})	fitted relaxation rate (s^{-1})
1	0.73
10	0.97
1,000	1.00

Appendix F

Detailed calculation of correlation functions

F.1 Correlation function global tumbling

F.1.1 Master equation

The Master equation for global tumbling has been written in the main text (section 4.3.1):

$$\frac{\partial}{\partial t}P(\Omega_{L,D},t) = -\sum_{j=x,y,z} D_{jj}L_j^2 P(\Omega_{L,D},t),$$

where D_{jj} is the jth component of the diagonalized diffusion coefficient tensor and L_j the associated angular momentum operator. Obtaining an expression for the correlation function requires first the diagonalization of the operator $\mathcal{D}_g = \sum_{j=x,y,z} D_{jj}L_j^2$. We express the operator in terms of raising and lowering operators:

$$\mathcal{D}_g = D_+L^2 + \frac{1}{2}D_-(L_+^2 + L_-^2) + (D_{zz} - D_+)L_z^2, \tag{F.1}$$

where:

$$\begin{aligned} D_\pm =& \frac{1}{2}(D_{xx} \pm D_{yy}), \\ L_\pm =& L_x \pm L_y. \end{aligned} \tag{F.2}$$

The eigen equation is written:

$$\mathcal{D}_g\Psi_n = E_n\Psi_n, \tag{F.3}$$

where the functions Ψ_n are expanded in terms of the normalized Wigner matrices:

$$\Psi_{L,\mu,\kappa}(\Omega) = \sum_k a_{\kappa,k}\sqrt{\frac{2L+1}{8\pi^2}}\mathcal{D}^L_{\mu,k}(\Omega). \tag{F.4}$$

Table F.1: Effect of the raising (L_+) and lowering (L_-) squared operators on the rank-2 Wigner matrices.

k	$L_+^2\mathcal{D}^{(2)}_{\mu,k}(\Omega)$	$L_-^2\mathcal{D}^{(2)}_{\mu,k}(\Omega)$
-2	$\sqrt{24}\mathcal{D}^{(2)}_{\mu,0}(\Omega)$	0
-1	$6\mathcal{D}^{(2)}_{\mu,1}(\Omega)$	0
0	$\sqrt{24}\mathcal{D}^{(2)}_{\mu,2}(\Omega)$	$\sqrt{24}\mathcal{D}^{(2)}_{\mu,-2}(\Omega)$
1	0	$6\mathcal{D}^{(2)}_{\mu,-1}(\Omega)$
2	0	$\sqrt{24}\mathcal{D}^{(2)}_{\mu,0}(\Omega)$

F.1.2 Calculation of the conditional probability

The following properties (in units of $\hbar$) will be used in constructing the linear combination of Wigner matrices that are eigenfunctions of the eigen equation (Eq. F.3):

$$\begin{aligned} L^2\mathcal{D}^L_{\mu,k}(\Omega) &= L(L+1)\mathcal{D}^L_{\mu,k}(\Omega), \\ L_z\mathcal{D}^L_{\mu,k}(\Omega) &= k\mathcal{D}^L_{\mu,k}(\Omega), \\ L_\pm\mathcal{D}^L_{\mu,k}(\Omega) &= \sqrt{(L\mp k)(L\pm k+1)}\mathcal{D}^L_{\mu,k\pm1}(\Omega). \end{aligned} \tag{F.5}$$

Using the above notations, the conditional probability (Eq. 4.10) is expressed as:

$$\begin{aligned} C_q^{aa'} = \int d\Omega_0 \int d\Omega P(\Omega_0)\mathcal{D}^{(2)*}_{qa}(\Omega_0)\mathcal{D}^{(2)}_{qa'}(\Omega)\times \\ \sum_{L,\mu,k,k',\kappa} \frac{2L+1}{8\pi^2} a_{\kappa,k}a_{\kappa,k'}\mathcal{D}^{L*}_{\mu,k}(\Omega_0)\mathcal{D}^{L}_{\mu,k'}(\Omega)e^{-E_{L,\mu,\kappa}t}. \end{aligned} \tag{F.6}$$

The orthogonality condition on the Wigner matrices (Eq. A.12) imposes $L = 2$ when calculating the integral. As a consequence, only 5 non-degenerate eigenfunctions are needed to solve Eq. F.1.1. With this simplication in hand, the eigenvalues and eigenfunctions of the components of the angular momentum operators are:

$$\begin{aligned} L^2\mathcal{D}^{(2)}_{\mu,k}(\Omega) &= 6\mathcal{D}^{(2)}_{\mu,k}(\Omega), \\ L_z^2\mathcal{D}^{(2)}_{\mu,k}(\Omega) &= k^2\mathcal{D}^{(2)}_{\mu,k}(\Omega). \end{aligned} \tag{F.7}$$

The effects of the raising and lowering squared operators are summed up in Table F.1.

It is then straightforward to find 3 eigenvectors:

$$\begin{aligned}
\mathcal{D}_g\sqrt{\frac{5}{8\pi^2}}\frac{\mathcal{D}^{(2)}_{\mu,1}(\Omega)+\mathcal{D}^{(2)}_{\mu,-1}(\Omega)}{\sqrt{2}} &= (5D_+ + 3D_- + D_{zz})\sqrt{\frac{5}{8\pi^2}}\frac{\mathcal{D}^{(2)}_{\mu,1}(\Omega)+\mathcal{D}^{(2)}_{\mu,-1}(\Omega)}{\sqrt{2}},\\
\mathcal{D}_g\sqrt{\frac{5}{8\pi^2}}\frac{\mathcal{D}^{(2)}_{\mu,1}(\Omega)-\mathcal{D}^{(2)}_{\mu,-1}(\Omega)}{\sqrt{2}} &= (5D_+ - 3D_- + D_{zz})\sqrt{\frac{5}{8\pi^2}}\frac{\mathcal{D}^{(2)}_{\mu,1}(\Omega)+\mathcal{D}^{(2)}_{\mu,-1}(\Omega)}{\sqrt{2}},\\
\mathcal{D}_g\sqrt{\frac{5}{8\pi^2}}\frac{\mathcal{D}^{(2)}_{\mu,2}(\Omega)-\mathcal{D}^{(2)}_{\mu,-2}(\Omega)}{\sqrt{2}} &= (2D_+ + 4D_{zz})\sqrt{\frac{5}{8\pi^2}}\frac{\mathcal{D}^{(2)}_{\mu,2}(\Omega)+\mathcal{D}^{(2)}_{\mu,-2}(\Omega)}{\sqrt{2}}.
\end{aligned} \tag{F.8}$$

Finding the remaining two requires more calculations. The initial step is to recognize that they have the form: $X(x_1,x_2) = x_1\sqrt{\frac{5}{8\pi^2}}\left(\mathcal{D}^{(2)}_{\mu,2}(\Omega)+\mathcal{D}^{(2)}_{\mu,-2}(\Omega)\right) + x_2\sqrt{\frac{5}{8\pi^2}}\mathcal{D}^{(2)}_{\mu,0}(\Omega)$, where x_1 and x_2 are two numbers to be found. The effect of opertor $\mathcal{D}_g$ on this eigenfunction is:

$$\begin{aligned}
\mathcal{D}_g X(x_1,x_2) =& x_1\sqrt{\frac{5}{8\pi^2}}\left(\mathcal{D}^{(2)}_{\mu,2}(\Omega)+\mathcal{D}^{(2)}_{\mu,-2}(\Omega)\right)\left[6D_+ + 4(D_{zz}-D_+) + \frac{\sqrt{24}}{2}D_-\frac{x_2}{x_1}\right]\\
&+ x_2\sqrt{\frac{5}{8\pi^2}}\mathcal{D}^{(2)}_{\mu,0}(\Omega)\left[6D_+ + \sqrt{24}D_-\frac{x_1}{x_2}\right].
\end{aligned} \tag{F.9}$$

Thus, $X(x_1,x_2)$ is an eigenvector if:

$$6D_+ + 4(D_{zz}-D_+) + \frac{\sqrt{24}}{2}D_-\frac{x_2}{x_1} = 6D_+ + \sqrt{24}D_-\frac{x_1}{x_2}, \tag{F.10}$$

which can be re-written:

$$x_2^2 - 2x_1^2 + 2\sqrt{\frac{2}{3}}\frac{D_{zz}-D_+}{D_-}x_1x_2 = 0. \tag{F.11}$$

The normalization condition for $X(x_1,x_2)$ to be an eigenvector gives:

$$2x_1^2 + x_2^2 = 1. \tag{F.12}$$

We set $x_1'^2 = 2x_1^2$ such that:

$$x_1'^2 + x_2^2 = 1. \tag{F.13}$$

We can find a number x such that:

$$x_1' = \sin\left(\frac{x}{2}\right),\ \ x_2 = \cos\left(\frac{x}{2}\right). \tag{F.14}$$

Inserting in Eq. F.11 leads to:

$$\cos^2(\frac{x}{2}) - \sin^2(\frac{x}{2}) + 2\frac{D_{zz}-D_+}{\sqrt{3}D_-}\sin\left(\frac{x}{2}\right)\cos\left(\frac{x}{2}\right) = 0. \tag{F.15}$$

We set $\alpha = \frac{\sqrt{3}D_-}{D_{zz}-D_+}$ and use trigonometric relationships to write:

$$\cos(x) + \frac{1}{\alpha}\sin(x) = 0, \tag{F.16}$$

Table F.2: Eigenvalues and eigenvectors for the operator associated to global tumbling. We define $\beta = \tan^{-1}\frac{\sqrt{3}D_-}{D_{zz}-D_+}$.

κ	E_κ	$\Psi_{2,\mu,\kappa}(\Omega) = \sum_k a_{\kappa,k}\sqrt{\frac{5}{8\pi^2}}\mathcal{D}^{(2)}_{\mu,k}(\Omega)$
1	$5D_+ + 3D_- + D_{zz}$	$\frac{1}{\sqrt{2}}\left(\mathcal{D}^{(2)}_{\mu,1}(\Omega) + \mathcal{D}^{(2)}_{\mu,-1}(\Omega)\right)$
2	$5D_+ - 3D_- + D_{zz}$	$\frac{1}{\sqrt{2}}\left(\mathcal{D}^{(2)}_{\mu,1}(\Omega) - \mathcal{D}^{(2)}_{\mu,-1}(\Omega)\right)$
3	$2D_+ + 4D_{zz}$	$\frac{1}{\sqrt{2}}\left(\mathcal{D}^{(2)}_{\mu,2}(\Omega) - \mathcal{D}^{(2)}_{\mu,-2}(\Omega)\right)$
4	$4D_+ + 2D_{zz} + 2\left[(D_{zz}-D_+)^2 + 3D_-^2\right]^{\frac{1}{2}}$	$\frac{1}{\sqrt{2}}\left(\mathcal{D}^{(2)}_{\mu,2}(\Omega) + \mathcal{D}^{(2)}_{\mu,-2}(\Omega)\right)\cos\frac{\beta}{2} + \mathcal{D}^{(2)}_{\mu,0}(\Omega)\sin\frac{\beta}{2}$
5	$4D_+ + 2D_{zz} - 2\left[(D_{zz}-D_+)^2 + 3D_-^2\right]^{\frac{1}{2}}$	$-\frac{1}{\sqrt{2}}\left(\mathcal{D}^{(2)}_{\mu,2}(\Omega) + \mathcal{D}^{(2)}_{\mu,-2}(\Omega)\right)\sin\frac{\beta}{2} + \mathcal{D}^{(2)}_{\mu,0}(\Omega)\cos\frac{\beta}{2}$

which yields:

$$x = -\tan^{-1}(\alpha), \tag{F.17}$$

and one set of solution to Eq. F.11:

$$x_1 = -\frac{1}{\sqrt{2}}\sin\left(\frac{\tan^{-1}(\alpha)}{2}\right), \quad x_2 = \cos\left(\frac{\tan^{-1}(\alpha)}{2}\right). \tag{F.18}$$

A second set of solution is obtained by choosing:

$$x_1' = -\cos\left(\frac{x}{2}\right), \quad x_2' = \sin\left(\frac{x}{2}\right), \tag{F.19}$$

which is a $\frac{\pi}{2}$-shift of the previous solution, and leads to:

$$x_1' = \frac{1}{\sqrt{2}}\cos\left(\frac{\tan^{-1}(\alpha)}{2}\right), \quad x_2' = \sin\left(\frac{\tan^{-1}(\alpha)}{2}\right). \tag{F.20}$$

The eigenvalues associated to these two eigenvectors can be calculated easily using Eq. F.9. The five eigenvectors and associated eigenvalues of Eq. F.3 are gathered in Table F.2 where we have defined $\beta = \tan^{-1}\frac{\sqrt{3}D_-}{D_{zz}-D_+}$.

When the molecule shows some symmetry properties, the angular momentum operator can have degenerate eigenfunctions. For example, if the molecule behaves as a cylinder (axial symmetry), then $D_{xx} = D_{yy}$, eliminating the L_+ and L_- part of Eq. F.1. The immediate consequence is that $D_- = 0$ and two of the three unique eigenvalues are doubly degenerate ($\kappa = 1$ and 2 on the one side, and $\kappa = 3$ and 4 on the other). When the diffusion tensor is isotropic, $D_{xx} = D_{yy} = D_{zz}$, all eigenvalues are degenerate and equal $6D$, usually refered to as the inverse of the global tumbling correlation time: $\tau_c = 1/(6D)$.

Static angle probability distribution It is clear from the form of the eigenvalues of the components of the angular momentum that one only needs to calculate the eigenfunction associated with the 0 eigenvalue in order to have a non-vanishing exponential term in Eq. 4.10 when calculating the limit with $t \to \infty$. It is obvious that such an eigenfunction has $L = 0$ (from the eigenvalues of L^2) and $k = 0$ (from the eigenvalues of L_z) such that it corresponds to $D^{(0)}_{0,0}(\Omega)$. Then:

$$P(\Omega_0) = \frac{1}{8\pi^2} D^{(0)}_{0,0}(\Omega_0)^2 = \frac{1}{8\pi^2}. \tag{F.21}$$

F.1.3 Integration of the correlation function for global tumbling

Using the integration in Eq. F.6:

$$\begin{aligned} C_{aa'}(t) = \int d\Omega_0 \int d\Omega \sum_{\mu=-2}^{2} \sum_{k=-2}^{2} \sum_{k'=-2}^{2} \sum_{\kappa=1}^{5} P(\Omega_0) \frac{5}{8\pi^2} a_{\kappa,k} a_{\kappa,k'} e^{-E_\kappa t} \times \\ \mathcal{D}^{(2)*}_{qa}(\Omega_0) \mathcal{D}^{(2)*}_{\mu k}(\Omega_0) \mathcal{D}^{(2)}_{qa'}(\Omega) \mathcal{D}^{(2)}_{\mu k'}(\Omega). \end{aligned} \tag{F.22}$$

We can use the property in Eq. A.9 to transform this equation into:

$$\begin{aligned} C_{aa'}(t) = & \frac{5}{64\pi^4} \sum_{\mu=-2}^{2} \sum_{k=-2}^{2} \sum_{k'=-2}^{2} \sum_{\kappa=1}^{5} a_{\kappa,k} a_{\kappa,k'} e^{-E_\kappa t} (-1)^{-k-k'} \times \\ & \int d\Omega_0 \mathcal{D}^{(2)*}_{qa}(\Omega_0) \mathcal{D}^{(2)}_{-\mu-k}(\Omega_0) \int d\Omega \mathcal{D}^{(2)}_{qa'}(\Omega) \mathcal{D}^{(2)*}_{-\mu-k'}(\Omega), \end{aligned} \tag{F.23}$$

where $P(\Omega_0)$ has been left out of the integrations as it is a constant of Ω_0. Looking at Table F.2 shows that $k + k'$ is always an even number such that $(-1)^{-k-k'} = 1$ for all k and k'. It immediately follows from the orthonormality condition (Eq. A.12) that:

$$C_{aa'}(t) = \frac{5}{64\pi^4} \sum_{\mu=-2}^{2} \sum_{k=-2}^{2} \sum_{k'=-2}^{2} \sum_{\kappa=1}^{5} a_{\kappa,k} a_{\kappa,k'} e^{-E_\kappa t} \delta_{q-\mu} \delta_{a-k} \delta_{a'-k'} \times \frac{8\pi^2}{5} \times \frac{8\pi^2}{5}, \tag{F.24}$$

where δ is the Kronecker-delta function. It simplifies into:

$$C_{aa'}(t) = \frac{1}{5} \sum_{\kappa=1}^{5} a_{\kappa,-a} a_{\kappa,-a'} e^{-E_\kappa t}. \tag{F.25}$$

From symmetry consideration, it follows that $a_{\kappa,-a} a_{\kappa,-a'} = a_{\kappa,a} a_{\kappa,a'}$ so that we find the result reported in the main text:

$$C_{aa'}(t) = \frac{1}{5} \sum_{\kappa=1}^{5} a_{\kappa,a} a_{\kappa,a'} e^{-E_\kappa t}.$$

F.2 correlation function for rotamer jumps

The strategy remains the same as presented in section 4.2, and used in the case of the global tumbling. The only difference is that integrals in Eq. 4.7 are replaced by discrete sums:

$$\langle \mathcal{D}^{(2)*}_{b,c}(\Omega_{J,SF},0)\mathcal{D}^{(2)}_{b',c'}(\Omega_{J,SF},t)\rangle = \sum_{\alpha=1}^{N}\sum_{\beta=1}^{N}\mathcal{D}^{(2)*}_{b,c}(\Omega_{J,SF_\alpha})\mathcal{D}^{(2)}_{b',c'}(\Omega_{J,SF_\beta})p^{eq}_{\alpha}p(\beta,t|\alpha,0), \quad \text{(F.26)}$$

where N is the number of accessible states, Ω_{J,SF_α} is the Euler angle for transformation from the jump frame to the system frame in rotamer α, p^{eq}_{α} is the equilibrium population of state α and $p(\beta,t|\alpha,0)$ is the conditional probability of finding the system in state β at time t when is was initially in state α at time $t=0$. The conditional probability is found by solving the Master equation presented in the main text (Eq 4.28):

$$\frac{\partial}{\partial t}p_i(t) = \sum_{j=1}^{N}\mathcal{R}_{ij}p_j(t),$$

where $p_i(t)$ is the population of state i at time t and $\mathcal{R}_{ij}$ is an element of the exchange matrix $\mathcal{R}$ and corresponds to the exchange rate from state j to i. The microscopic reversibility implies that:

$$\mathcal{R}_{ij}p^{eq}_j = \mathcal{R}_{ji}p^{eq}_i. \quad \text{(F.27)}$$

Diagonal elements of the exchange matrix are given by:

$$\mathcal{R}_{ii} = -\sum_{j\neq i}R_{ji}. \quad \text{(F.28)}$$

The boundary conditions associated to Eq. 4.28 are:

$$\begin{aligned} &(1)\ \ p(\beta,t=0|\alpha,0) = \delta_{\alpha\beta},\\ &(2)\ \ \lim_{t\to\infty}p(\beta,t|\alpha,0) = p^{eq}_{\beta}, \end{aligned} \quad \text{(F.29)}$$

Eq. 4.28 transforms into an eigen equation as follows:

$$RX = \lambda X. \quad \text{(F.30)}$$

The exchange matrix is in general not symmetric (it is only when equilibrium populations are equal) but can be transformed into a symmetric matrix $\widetilde{\mathcal{R}}$:

$$\begin{aligned} \widetilde{\mathcal{R}}_{ij} &= \sqrt{\frac{p^{eq}_j}{p^{eq}_i}}\mathcal{R}_{ij} = \sqrt{\mathcal{R}_{ij}\mathcal{R}_{ji}},\ \ i\neq j,\\ \widetilde{\mathcal{R}}_{ii} &= \mathcal{R}_{ii} = -\sum_{j\neq i}\mathcal{R}_{ji}. \end{aligned} \quad \text{(F.31)}$$

The eigen equation now reads:

$$\tilde{\mathcal{R}}\tilde{X} = \lambda\tilde{X}, \tag{F.32}$$

where:

$$\tilde{X_\alpha} = \frac{1}{\sqrt{p_\alpha^{eq}}} X_\alpha. \tag{F.33}$$

Since $\tilde{\mathcal{R}}$ is symmetric, its eigenvalues λ_n are all real and the associated eigenvectors $\tilde{X}^{(n)}$ are orthogonal. The conditional probability is written as in Eq. 4.10 such that, for the second condition in Eq. F.29 to be met, we must have $\lambda_0 = 0$ (we order the eigenvalues such that $|\lambda_n| \leq |\lambda_{n+1}|$). The associated eigenvector $\tilde{X}^{(0)}$ can be calculated as follows:

$$\begin{aligned}
\tilde{\mathcal{R}}\tilde{X}^{(0)} = 0 &\Leftrightarrow \sum_{j=1}^{N} \tilde{\mathcal{R}}_{ij}\tilde{X}_j^{(0)} = 0, \ \forall i \in [1, N], \\
&\Leftrightarrow \sum_{j\neq i} \tilde{\mathcal{R}}_{ij}\tilde{X}_j^{(0)} + \tilde{\mathcal{R}}_{ii}\tilde{X}_i^{(0)} = 0, \\
&\Leftrightarrow \sum_{j\neq i} \sqrt{\frac{p_i^{eq}}{p_j^{eq}}}\mathcal{R}_{ji}\tilde{X}_j^{(0)} - \sum_{j\neq i} \mathcal{R}_{ji}\tilde{X}_i^{(0)} = 0, \\
&\Leftrightarrow \sum_{j\neq i} \mathcal{R}_{ji}\left(\frac{1}{\sqrt{p_j^{eq}}}\tilde{X}_j^{(0)} - \frac{1}{\sqrt{p_i^{eq}}}\tilde{X}_i^{(0)}\right) = 0.
\end{aligned} \tag{F.34}$$

It follows that $\{\tilde{X}_n^{(0)}\} = \{\sqrt{p_n^{eq}}\}, \forall n \in [1, N]$ is an eigenvector associated to the eigenvalue $\lambda_0 = 0$.
The conditional probability can be written:

$$p(\beta, t|\alpha, 0) = A_{\beta,\alpha} \sum_{n=0}^{N-1} \tilde{X}_\alpha^{(n)}\tilde{X}_\beta^{(n)} e^{\lambda_n t}, \tag{F.35}$$

where $A_{\beta,\alpha}$ is a constant introduced to fullfill the conditions in Eq. F.29. The eigenvectors $\tilde{X}$ are orthogonal such that condition (1) is already met. In order to satisfy condition (2), we must have $A_{\beta,\alpha} = \frac{\sqrt{p_\beta^{eq}}}{\sqrt{p_\alpha^{eq}}}$:

$$p(\beta, t|\alpha, 0) = \sqrt{\frac{p_\beta^{eq}}{p_\alpha^{eq}}} \sum_{n=0}^{N-1} \tilde{X}_\alpha^{(n)}\tilde{X}_\beta^{(n)} e^{\lambda_n t}. \tag{F.36}$$

The correlation function Eq. F.26 is expressed as shown in the main text (Eq. 4.29):

$$\langle \mathcal{D}_{b,c}^{(2)*}(\Omega_{J,SF}, 0)\mathcal{D}_{b',c'}^{(2)}(\Omega_{J,SF}, t)\rangle = \sum_{\alpha=1}^{N}\sum_{\beta=1}^{N}\sum_{n=0}^{N-1} \mathcal{D}_{b,c}^{(2)*}(\Omega_{J,SF_\alpha})\mathcal{D}_{b',c'}^{(2)}(\Omega_{J,SF_\beta})\sqrt{p_\alpha^{eq}p_\beta^{eq}}\tilde{X}_\alpha^{(n)}\tilde{X}_\beta^{(n)} e^{\lambda_n t}. \tag{F.37}$$

F.3 Correlation function for diffusion on a cone

The correlation function is written as in the main text (Eq. 4.35):

$$C_{i,j}(t) = \frac{1}{5}\sum_{\kappa=1}^{5}\sum_{a,a'}\sum_{b,b'} a_{\kappa,a}a_{\kappa,a'}e^{-E_\kappa t}e^{i\alpha_{D,SF}(a-a')}d_{a,b}(\beta_{D,SF})d_{a',b'}(\beta_{D,SF})\times \\ \langle e^{i(b\gamma_{D,SF}(0)-b'\gamma_{D,SF}(t))}\rangle \mathcal{D}^{(2)*}_{b,0}(\Omega_{SF,i})\mathcal{D}^{(2)}_{b',0}(\Omega_{SF,j}).$$

We use the same approach as introduced in Section 4.2 to solve the ensemble average:

$$\langle e^{i(b\gamma_{D,SF}(0)-b'\gamma_{D,SF}(t))}\rangle = \int_0^{2\pi}\int_0^{2\pi} p(\gamma_0)p(\gamma,t|\gamma_0,0)e^{ib\gamma_0}e^{-ib'\gamma}d\gamma_0 d\gamma, \tag{F.38}$$

where $p(\gamma_0) = \frac{1}{2\pi}$ (all orientations are equi-probable), and the conditional probability is expressed as:

$$p(\gamma,t|\gamma_0,0) = \sum_n \varphi_n^*(\gamma_0)\varphi_n(\gamma)e^{-E_n t}, \tag{F.39}$$

where φ_n is the eigenfunction associated to the eigenvalue E_n of the rotation operator $D_{rot}L^2_{rot}$:

$$\frac{\partial}{\partial t}p(\gamma,t) = -D_{rot}L^2_{rot}p(\gamma,t) = D_{rot}\frac{\partial^2}{\partial\gamma^2}p(\gamma,t), \tag{F.40}$$

where D_{rot} is the rotational diffusion coefficient and L^2_{rot} is the angular momentum operator for rotation on a circle. Eigenfunctions and eigenvalues are given by:

$$\begin{aligned}\varphi_n(\gamma) &= \frac{1}{\sqrt{2\pi}}e^{in\gamma},\\ E_n &= D_{rot}n^2.\end{aligned} \tag{F.41}$$

Inserting in Eq. F.38 leads to:

$$\langle e^{i(b\gamma_{D,SF}(0)-b'\gamma_{D,SF}(t))}\rangle = \frac{1}{4\pi^2}\sum_n e^{-D_{rot}n^2 t}\int_0^{2\pi}\int_0^{2\pi} e^{i\gamma_0(b-n)}e^{-i\gamma(b'-n)}d\gamma_0 d\gamma, \tag{F.42}$$

which does not cancel out only for $n = b = b'$, and leads to the correlation function reported in the main text (Eq. 4.37):

$$\langle e^{i(b\gamma_{D,SF}(0)-b'\gamma_{D,SF}(t))}\rangle = \delta_{bb'}e^{-D_{rot}b^2 t}.$$

F.4 Correlation function wobbling in a cone

The correlation function has been written in the main text (Eq. 4.41):

$$C_{i,j}(t) = \frac{1}{5}\sum_{\kappa=1}^{5}\sum_{a,a'}\sum_{b,b'}\sum_{c,c'} a_{\kappa,a}a_{\kappa,a'}e^{-E_\kappa t}\langle \mathcal{D}^{(2)*}_{b,c}(\Omega_{WF,SF},0)\mathcal{D}^{(2)}_{b',c'}(\Omega_{WF,SF},t)\rangle \times \\ \mathcal{D}^{(2)*}_{a,b}(\Omega_{D,WF})\mathcal{D}^{(2)*}_{c,0}(\Omega_{SF,i})\mathcal{D}^{(2)}_{a',b'}(\Omega_{D,WF})\mathcal{D}^{(2)}_{c',0}(\Omega_{SF,j}).$$

The correlation function for wobbling is calculated by solving the Smoluchowski's equation (Eq. 4.42):

$$\frac{\partial}{\partial t}p(\Omega,t) = -D_W L_W^2 p(\Omega,t),$$

where D_W is the diffusion coefficient for the wobble motion and L_W^2 is the angular momentum operator (Eq. 4.43):

$$L_W^2 = -\frac{1}{\sin\theta}\frac{\partial}{\partial\theta}\left(\sin\theta\frac{\partial}{\partial\theta}\right) - \frac{1}{\sin^2\theta}\frac{\partial^2}{\partial\varphi^2},$$

with reflecting boundary condition at $\theta = \beta_{cone}$, with β_{cone} the cone semi-angle opening (Eq. 4.44):

$$\frac{\partial}{\partial\theta}p(\Omega,t)|_{\theta=\beta_{cone}} = 0.$$

F.4.1 Solving the Master equation

When solving Eq. 4.42, Wang and Pecora did not diagonalize the operator L_W^2, but their approach is mathematically the same [196]. For the sake of consistency, the diagonalization-based treatment is presented here. The eigen equation is written:

$$D_W L_W^2 c(\theta,\varphi) = Ec(\theta,\varphi). \tag{F.43}$$

We use the method of variable separation to write:

$$c(\theta,\varphi) = \Theta(\theta)\Phi(\varphi), \tag{F.44}$$

which yields:

$$-\frac{\Phi(\varphi)}{\sin\theta}\left[\frac{\partial}{\partial\theta}\sin\theta\frac{\partial}{\partial\theta}\right]\Theta(\theta) - \frac{\Theta(\theta)}{\sin^2\theta}\frac{\partial^2}{\partial\varphi^2}\Phi(\varphi) = \frac{E}{D_W}\Theta(\theta)\Phi(\varphi), \tag{F.45}$$

which leads to the following differential equation for Φ:

$$\frac{\partial^2}{\partial\varphi^2}\Phi(\varphi) \propto \Phi(\varphi). \tag{F.46}$$

Following the work of Wang and Pecora [196], we write the complete set of functions Φ as:

$$\Phi_m(\varphi) = A_m\cos(m\varphi) + B_m\sin(m\varphi), \tag{F.47}$$

where $m \in \mathbb{N}$, and A_n and B_m are coefficients associated to the eigenvalue m. It follows:

$$\frac{\partial^2}{\partial\varphi^2}\Phi_m(\varphi) = -m^2\Phi_m(\varphi), \tag{F.48}$$

and we can write the differential equation for Θ:

$$-\frac{1}{\sin\theta}\left[\frac{\partial}{\partial\theta}\sin\theta\frac{\partial\Theta}{\partial\theta}\right] + \frac{m^2}{\sin^2\theta}\Theta - \frac{E}{D_W}\Theta = 0. \tag{F.49}$$

We operate the following variable change: $\mu \to \cos\theta$:

$$2\mu\frac{\partial\Theta}{\partial\mu} - (1-\mu^2)\frac{\partial^2\Theta}{\partial\mu^2} + \frac{m^2}{1-\mu^2}\Theta - \frac{E}{D_W}\Theta = 0. \tag{F.50}$$

We now define $E = D_W\nu_m(\nu_m+1)$ to obtain:

$$(1-\mu^2)\frac{\partial^2\Theta}{\partial\mu^2} - 2\mu\frac{\partial\Theta}{\partial\mu} + \left(\nu_m(\nu_m+1) - \frac{m^2}{1-\mu^2}\right)\Theta = 0. \tag{F.51}$$

Solutions of the equations of the type Eq. F.51 for $\mu \in [0,1]$ are given by the Legendre associated functions $P^m_{\nu_m}$ of degree ν_m and order m. There are an infinite number of solutions and the eigenfunctions and eigenvalues are given by $P^m_{\nu_{m,n}}$ and $D_W\nu_{m,n}(\nu_{m,n}+1)$ respectively, where the $\nu_{m,n}$ fulfill the boundary condition Eq. 4.44. We choose the indices n such that $\nu_{m,n} < \nu_{m,n+1}$. The conditional probability $p(\Omega, t|\Omega_0, 0)$ is now given by:

$$p(\Omega,t|\Omega_0,0) = \sum_{m=0}^{+\infty}\sum_{n=0}^{+\infty} e^{-D_W\nu_{m,n}(\nu_{m,n}+1)t}(A_{m,n}\cos(m\varphi) + B_{m,n}\sin(m\varphi))P^m_{\nu_{m,n}}(\cos\theta), \tag{F.52}$$

where we explicitely show the dependence of the coefficients A and B in m and n.

F.4.2 Solving the boundary condition

The conditional probability is written in Eq. F.52 where the coefficients $A_{m,n}$ and $B_{m,n}$ still need to be calculated. For this, we first take a look at the conditional probability at time $t = 0$:

$$\begin{aligned} p(\Omega, t=0|\Omega_0,0) &= \delta(\mu-\mu_0)\delta(\varphi-\varphi_0), \\ &= \sum_{m=0}^{+\infty}\sum_{n=0}^{+\infty}(A_{m,n}\cos(m\varphi_0) + B_{m,n}\sin(m\varphi_0))P^m_{\nu_{m,n}}(\mu_0), \end{aligned} \tag{F.53}$$

where we set $\mu = \cos\theta$. Now, we can calculate the following two integrals:

$$\begin{aligned} I_c &= \int_{\mu_{cone}}^1 d\mu \int_0^{2\pi} d\varphi p(\Omega, t=0|\Omega_0,0)P^{m'}_{\nu_{m',n'}}(\mu)\cos m'\varphi, \\ I_s &= \int_{\mu_{cone}}^1 d\mu \int_0^{2\pi} d\varphi p(\Omega, t=0|\Omega_0,0)P^{m'}_{\nu_{m',n'}}(\mu)\sin m'\varphi. \end{aligned} \tag{F.54}$$

On one side, we have:

$$\begin{aligned} I_c &= \int_{\mu_{cone}}^{1} d\mu \int_0^{2\pi} d\varphi \delta(\mu-\mu_0)\delta(\varphi-\varphi_0) P^{m'}_{\nu_{m',n'}}(\mu)\cos m'\varphi = P^{m'}_{\nu_{m',n'}}(\mu_0)\cos m'\varphi_0, \\ I_s &= \int_{\mu_{cone}}^{1} d\mu \int_0^{2\pi} d\varphi \delta(\mu-\mu_0)\delta(\varphi-\varphi_0) P^{m'}_{\nu_{m',n'}}(\mu)\sin m'\varphi = P^{m'}_{\nu_{m',n'}}(\mu_0)\sin m'\varphi_0. \end{aligned} \tag{F.55}$$

On the other side, we can write:

$$\begin{aligned} I_c &= \sum_{m,n} \int_{\mu_{cone}}^{1} P^{m'}_{\nu_{m',n'}}(\mu) P^{m}_{\nu_{m,n}}(\mu) d\mu \times \int_0^{2\pi} d\varphi (A_{m,n}\cos(m\varphi) + B_{m,n}\sin(m\varphi))\cos m'\varphi, \\ I_s &= \sum_{m,n} \int_{\mu_{cone}}^{1} P^{m'}_{\nu_{m',n'}}(\mu) P^{m}_{\nu_{m,n}}(\mu) d\mu \times \int_0^{2\pi} d\varphi (A_{m,n}\cos(m\varphi) + B_{m,n}\sin(m\varphi))\sin m'\varphi. \end{aligned} \tag{F.56}$$

Using the property Eq. A.26, we have:

$$\begin{aligned} I_c &= H_{m',n'}(\mu_{cone}) \times \int_0^{2\pi} d\varphi (A_{m',n'}\cos(m\varphi) + B_{m',n'}\sin(m'\varphi))\cos m'\varphi, \\ I_s &= H_{m',n'}(\mu_{cone}) \times \int_0^{2\pi} d\varphi (A_{m',n'}\cos(m\varphi) + B_{m',n'}\sin(m'\varphi))\sin m'\varphi. \end{aligned} \tag{F.57}$$

After simple integration, we now have:

$$\begin{aligned} I_c &= \varepsilon\pi H_{m,n'}(\mu_{cone}) A_{m,n'}, \\ I_s &= \pi H_{m,n'}(\mu_{cone}) B_{m,n'}. \end{aligned} \tag{F.58}$$

where:

$$\varepsilon = \begin{cases} 2, & m = 0 \\ 1, & m = \{1,2\} \end{cases}. \tag{F.59}$$

By identification with Eq. F.55, we can express the two coefficients $A_{m,n}$ and $B_{m,n}$:

$$\begin{aligned} A_{m,n} &= \frac{\cos m\varphi_0}{\varepsilon\pi H_{m,n}(\mu_{cone})} P^{m}_{\nu_{m,n}}(\mu_0), \\ B_{m,n} &= \frac{\sin m\varphi_0}{\pi H_{m,n}(\mu_{cone})} P^{m}_{\nu_{m,n}}(\mu_0). \end{aligned} \tag{F.60}$$

F.4.3 Expression of the conditional probability

The conditional probability can now be written:

$$p(\Omega, t|\Omega_0, 0) = \sum_{m=-\infty}^{+\infty} \sum_{n=0}^{+\infty} X_{m,n}, \tag{F.61}$$

where we define:

$$X_{m,n} = e^{-D_W \nu_{m,n}(\nu_{m,n}+1)t} \frac{P^{m}_{\nu_{m,n}}(\mu) P^{m}_{\nu_{m,n}}(\mu_0)}{\pi H_{m,n}(\mu_{cone})} \left(\frac{\cos m\varphi_0}{\varepsilon} \cos m\varphi + \sin m\varphi_0 \sin m\varphi \right). \tag{F.62}$$

We have:

$$X_{0,n} = \frac{1}{2}\frac{P^0_{\nu_{0,n}}(\mu)P^0_{\nu_{0,n}}(\mu_0)}{\pi H_{0,n}(\mu_{cone})}e^{-D_W\nu_{0,n}(\nu_{0,n}+1)t} \tag{F.63}$$

and, for $m \neq 0$:

$$X_{m,n} = e^{-D_W\nu_{m,n}(\nu_{m,n}+1)t}\frac{P^m_{\nu_{m,n}}(\mu)P^m_{\nu_{m,n}}(\mu(0))}{\pi H_{m,n}(\mu_{cone})}\left(\cos m\varphi_0\cos m\varphi + \sin m\varphi_0 \sin m\varphi\right). \tag{F.64}$$

We can write:

$$\cos m\varphi_0\cos m\varphi + \sin m\varphi_0\sin m\varphi = e^{im\varphi}\left(e^{-im\varphi_0} + i\sin m(\varphi-\varphi_0)\right), \tag{F.65}$$

so that, after using Eq. A.27 and Eq. A.24, we can write:

$$\begin{aligned} X_{m,n} &= e^{-D_W\nu_{m,n}(\nu_{m,n}+1)t}\frac{P^m_{\nu_{m,n}}(\mu)P^m_{\nu_{m,n}}(\mu_0)}{\pi H_{m,n}(\mu_{cone})}e^{im\varphi}\left(e^{-im\varphi_0} + i\sin m(\varphi-\varphi_0)\right), \\ X_{-m,n} &= e^{-D_W\nu_{m,n}(\nu_{m,n}+1)t}\frac{P^m_{\nu_{m,n}}(\mu)P^m_{\nu_{m,n}}(\mu_0)}{\pi H_{m,n}(\mu_{cone})}e^{-im\varphi}\left(e^{im\varphi_0} - i\sin m(\varphi-\varphi_0)\right). \end{aligned} \tag{F.66}$$

Including negative values of m in the sum Eq. F.61 let the sinus terms cancel with one another. Including the $m<0$ terms in Eq. F.61 is possible as $X_{-m,n} = X_{m,n}$, as seen using Eq. F.64. We can write:

$$p(\Omega,t|\Omega_0,0) = \frac{1}{2}\sum_{m=-\infty}^{+\infty}\sum_{n=0}^{+\infty} e^{-D_W\nu_{m,n}(\nu_{m,n}+1)t}\frac{P^m_{\nu_{m,n}}(\mu)P^m_{\nu_{m,n}}(\mu_0)}{\pi H_{m,n}(\mu_{cone})}e^{im\varphi}e^{-im\varphi_0}. \tag{F.67}$$

The factor $1/2$ comes from the equality $X_{-m,n} = X_{m,n}$ and the extension of the sum on the index m from $-\infty$ to $+\infty$, and the expression of $X_{0,n}$ (Eq. F.63). C. Wang and R. Pecora introduced the pseudo-spherical harmonics [196]:

$$Y^m_{\nu_{m,n}}(\Omega) = \frac{1}{\sqrt{2\pi H_{m,n}(\mu_{cone})}}P^m_{\nu_{m,n}}(\mu)e^{im\varphi}, \tag{F.68}$$

and wrote the conditional probability in a compact form:

$$p(\Omega,t|\Omega_0,0) = \sum_{m=-\infty}^{+\infty}\sum_{n=0}^{+\infty} e^{-D_W\nu_{m,n}(\nu_{m,n}+1)t}Y^m_{\nu_{m,n}}(\Omega)Y^{m*}_{\nu_{m,n}}(\Omega_0). \tag{F.69}$$

F.4.4 Initial angle probability

The initial angle probability can easily be found with geometric arguments. We prefer to use the limit definition (Eq. 4.11). The conditional probability does not cancel out when $t\to\infty$ only for $\nu_{m,n}=0$, that is $m=n=0$:

$$p(\Omega_0) = Y^0_0(\Omega)Y^0_0(\Omega_0) = \frac{P^0_0(\mu)P^0_0(\mu_0)}{2\pi H_{0,0}(\mu_{cone})}. \tag{F.70}$$

It is then straightforward to show:

$$\begin{cases} p(\Omega_0) = \dfrac{1}{2\pi(1-\mu_{cone})}, \;\; \theta_0 \in [0, \beta_{cone}], \\ p(\Omega_0) = 0, \;\; \theta_0 > \beta_{cone}. \end{cases} \tag{F.71}$$

F.5 Additional figures

F.5.1 Contribution of each motion to the relaxation

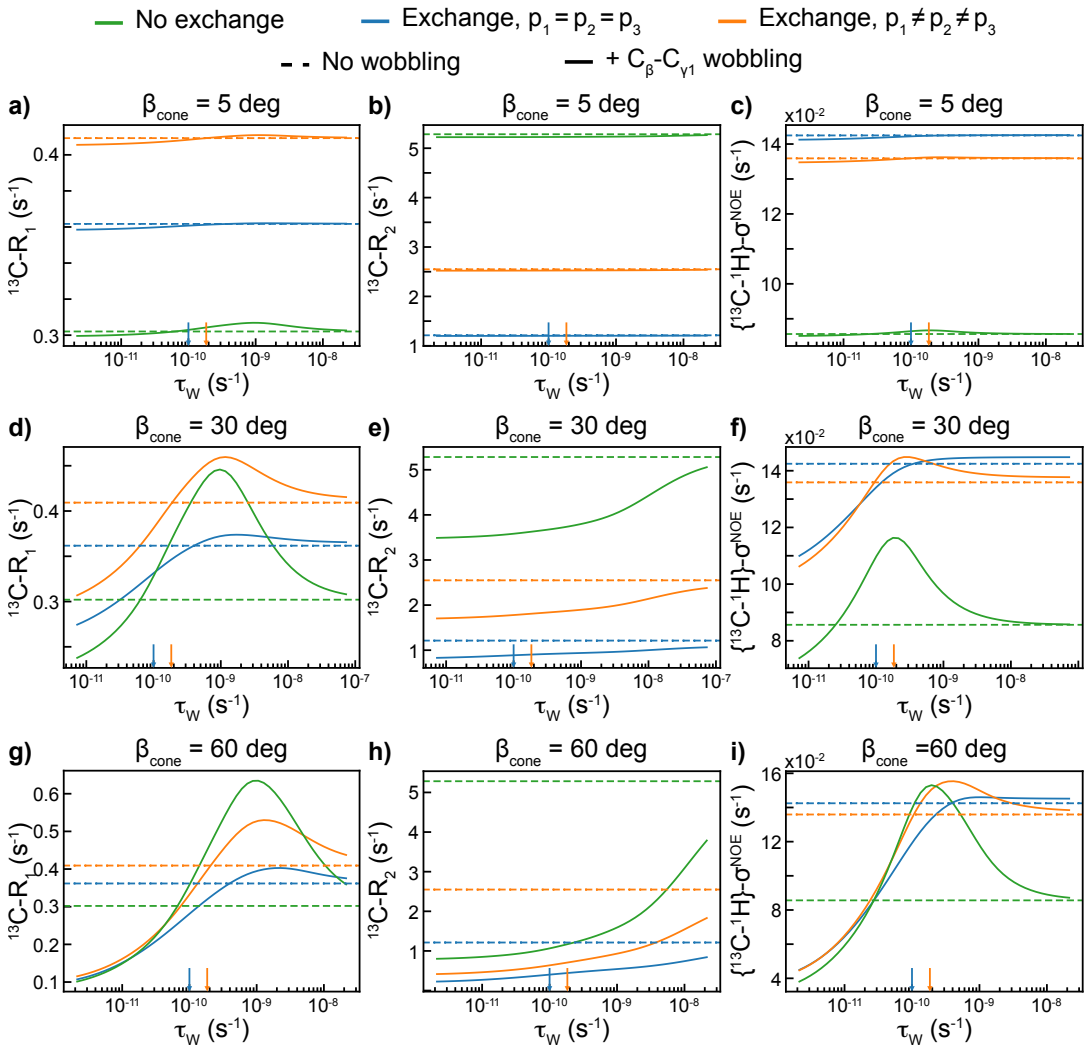

Figure F.1: Contribution of rotamer jump and wobbling in a cone motions to relaxation rates. Carbon R_1 (**a**, **d**, **g**), R_2 (**b**, **e**, **h**) and carbon-proton σ^{NOE} (**c**, **f**, **i**) at 14.1 T in a $^{13}C^1H^2H_2$ methy group for a protein of global tumbling correlation time $\tau_c = 10\,\mathrm{ns}$. Dashed horizontal lines show the value of the relaxation rates without wobbling. Relaxation rates calculated in the abscence of rotamer jumps are shown in green. In the presence of rotamer jumps, the case where all rotamer populations are equal (blue) and unequal (orange) are distinguish. In this later case, populations are $p_1 = 0.7$, $p_2 = 0.2$ and $p_1 = 0.1$. Calculations are shown as a function of the correlation time for wobbling, a function of the wobbling diffusion constant and cone semi-angle opening β_{cone}, while the diffusion constant is varied from 10^6 to $10^{10}\,\mathrm{s}^{-1}$. The blue and orange vertical arrows indicate the values of the correlation time for rotamer jumps, when populations are equal and unequal respectively.

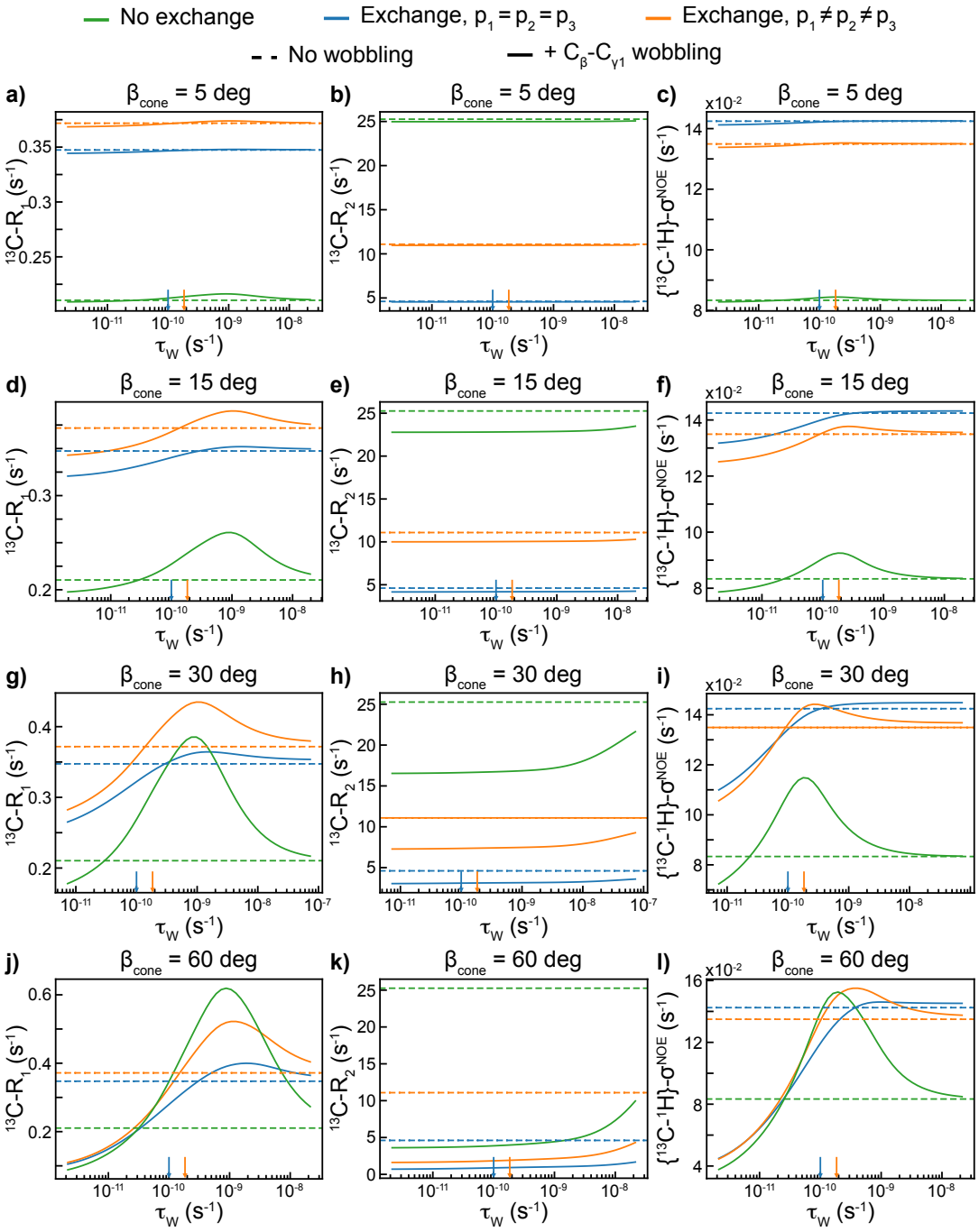

Figure F.2: Same as Fig. F.1 for a protein of global tumbling correlation time $\tau_c = 50\,\text{ns}$.

F.5.2 Model Free analysis with multiple internal motions

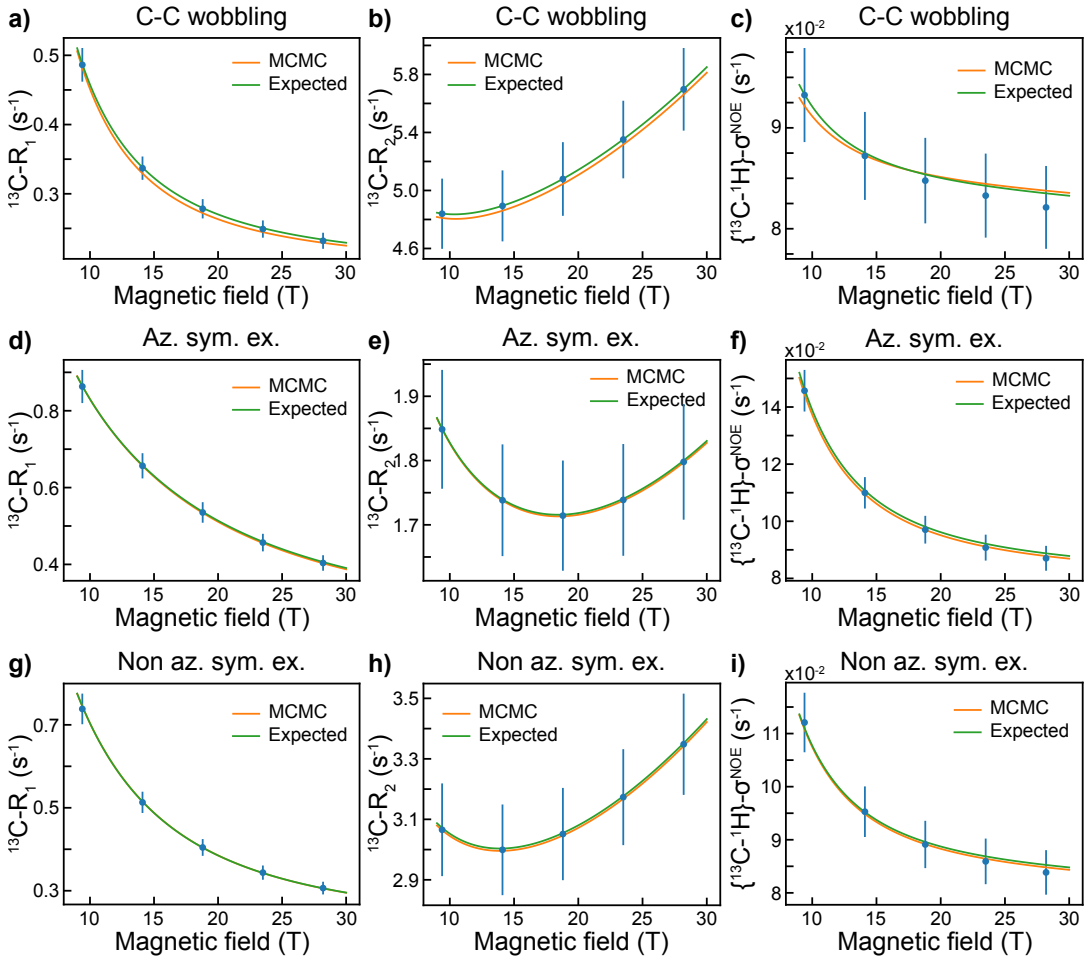

Figure F.3: Model Free analysis of relaxation rates in the presence of two internal motions. Carbon-13 longitudinal (**a**, **d**, **g**) and transverse (**b**, **e**, **h**), and carbon-proton DD (**c**, **f**, **i**) relaxation rates calculated assuming isotropic overall tumbling (global tumbling correlation time $\tau_c = 10\,\mathrm{s}^{-1}$), methyl rotation and C-C wobbling (**a**-**c**), azymutal symmetric rotamer jumps (**d**-**f**) or non-azymutal symmetric jumps (**g**-**h**).

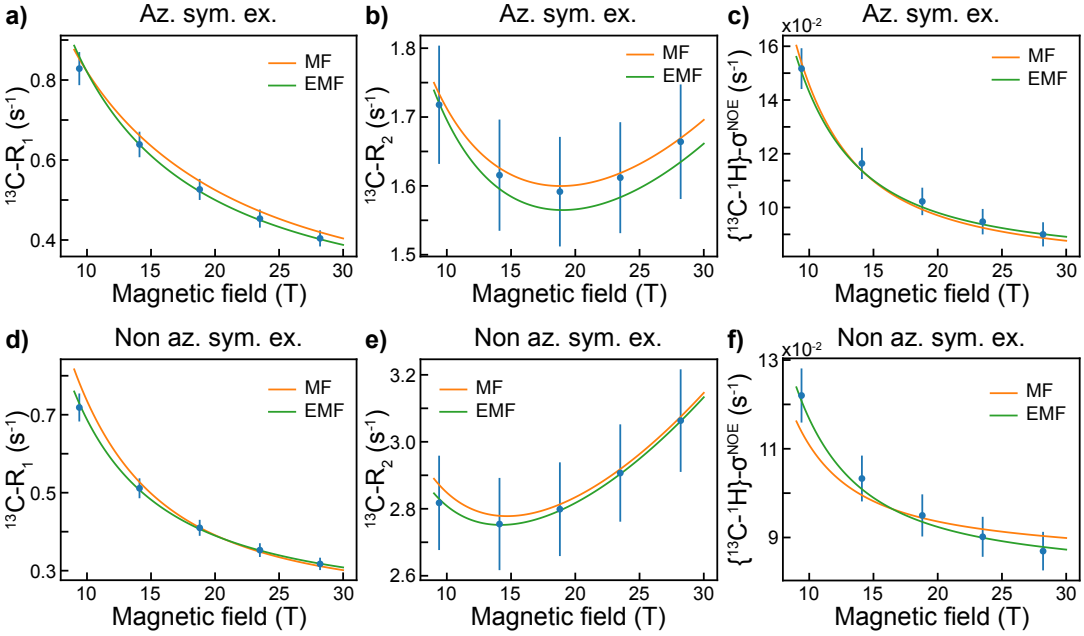

Figure F.4: Model Free and Extended Model Free analyses of relaxation rates in the presence of three internal motions. Carbon-13 longitudinal (**a**, **d**) and transverse (**b**, **e**), and carbon-proton DD (**c**, **f**) relaxation rates calculated assuming isotropic overall tumbling (global tumbling correlation time $\tau_c = 10\,\mathrm{s}^{-1}$), methyl rotation, C-C wobbling and azymutal symmetric rotamer jumps (**a**-**c**) or non-azymutal symmetric jumps (**d**-**f**).

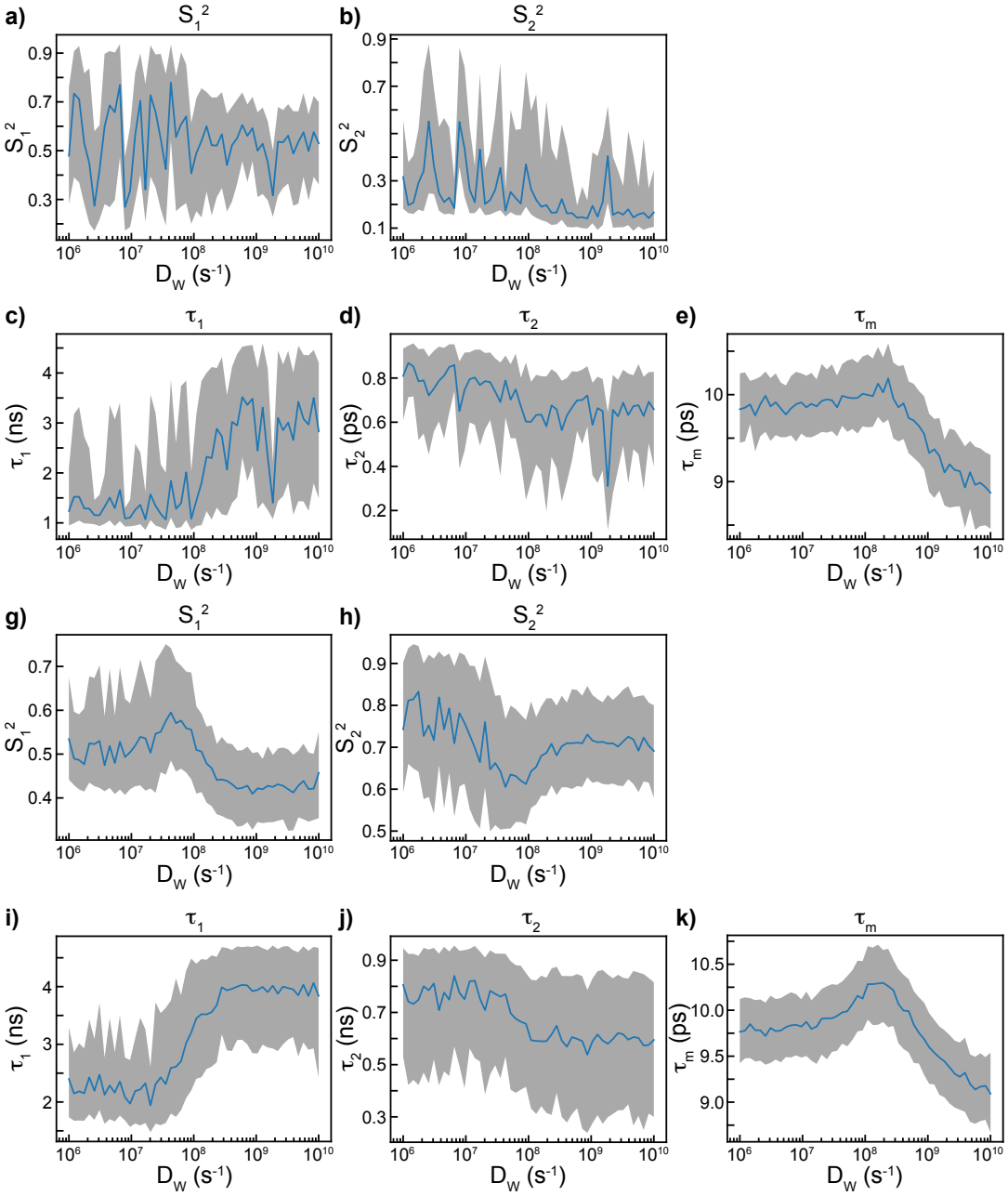

Figure F.5: Evolution of the EMF parameters obtained after a MCMC analysis as a function of the diffusion coefficient for wobling, in the case where three internal motions are considered. Results for azymutal symmetric rotamer jumps are presented in a-e, and for non-azymutal symmetric rotamer jumps in f-k. The blue line shows the mean of the parameter and the grey area the parameter distribution obtained after a MCMC analysis of the relaxation rates. Points are connected by a solid line for visual clarity.

F.5.3 Rotamer-dependent CSA tensors and relaxation

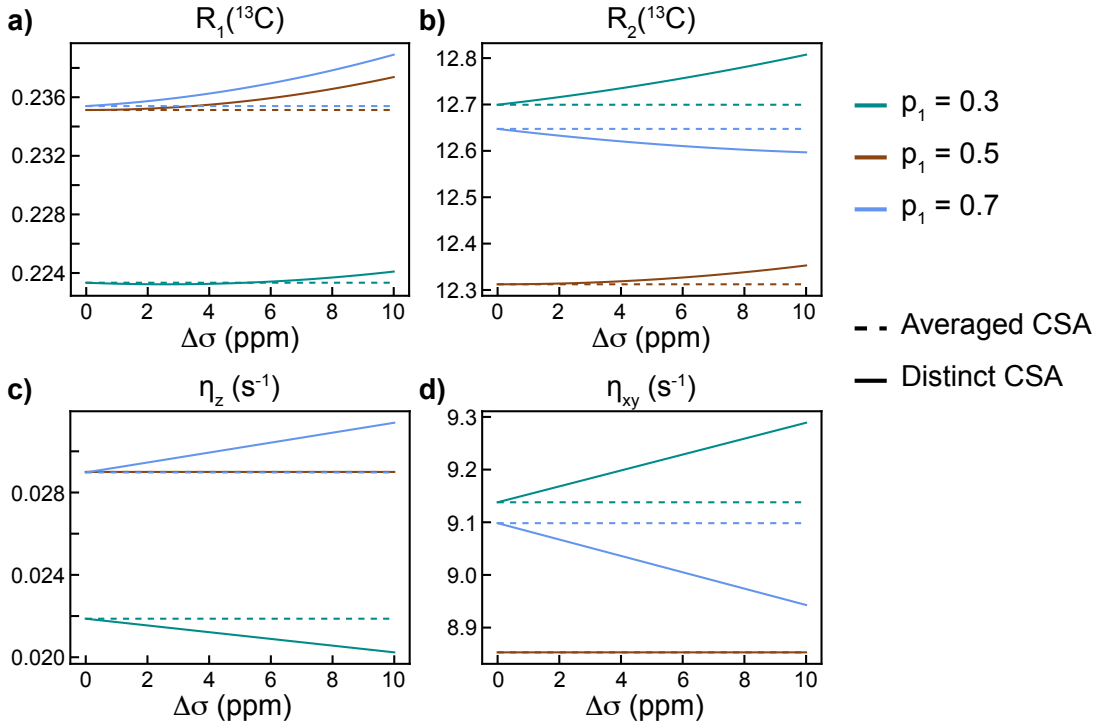

Figure F.6: Highlighting the CSA rotamer-dependent relaxation mechanism at 1.2 GHz. Evolution of the carbon-R_1 (**a**), carbon-R_2 (**b**), and carbon longitudinal (**c**) and transverse (**d**) cross-correlated cross-relaxation rate for a methyl group exchanging between two rotamer positions as a function of the difference between the CSA of the two rotamers. Calculations are performed for three equilibrium position for the state 1 and by either considering a population-averaged CSA value (dash) or distinct CSA tensors (solid).

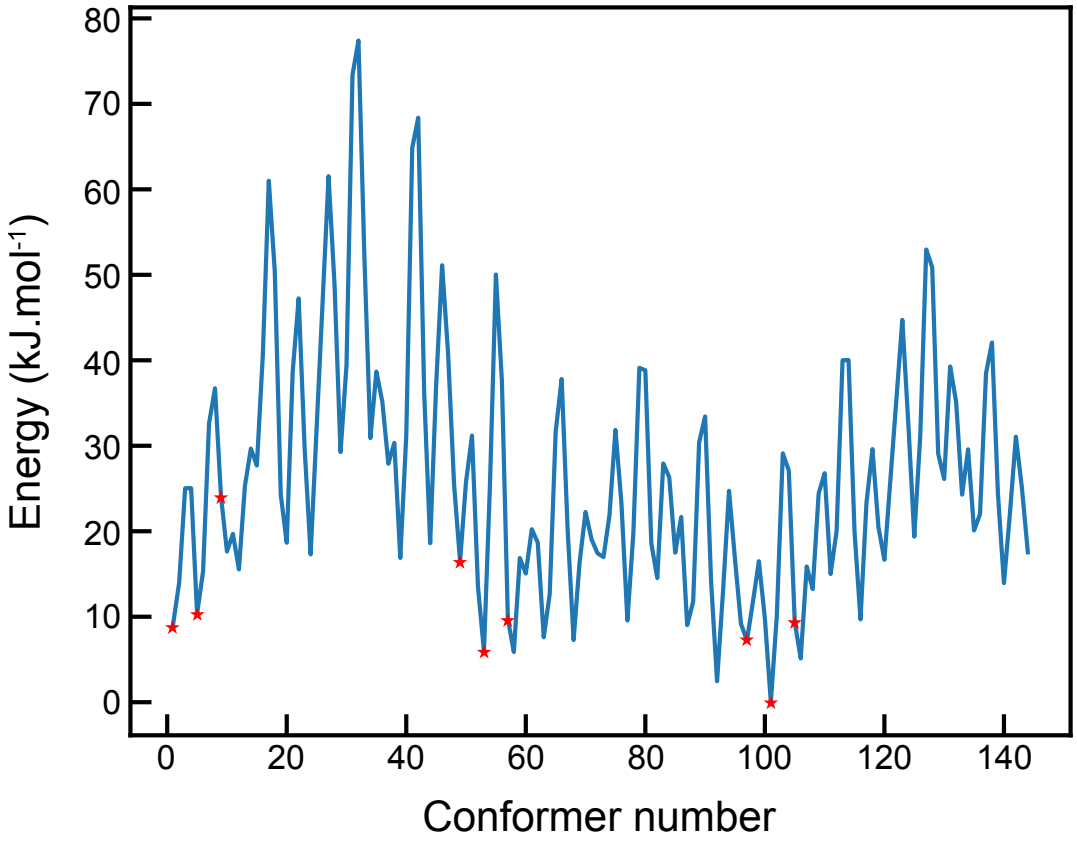

Figure F.7: Energies of the 144 conformations of an isoleucine amino acid in water and calculated using DFT. The conformation with the lowest energy (conformation 101) defines the reference point. The 9 selected rotamers are indicated with the red stars

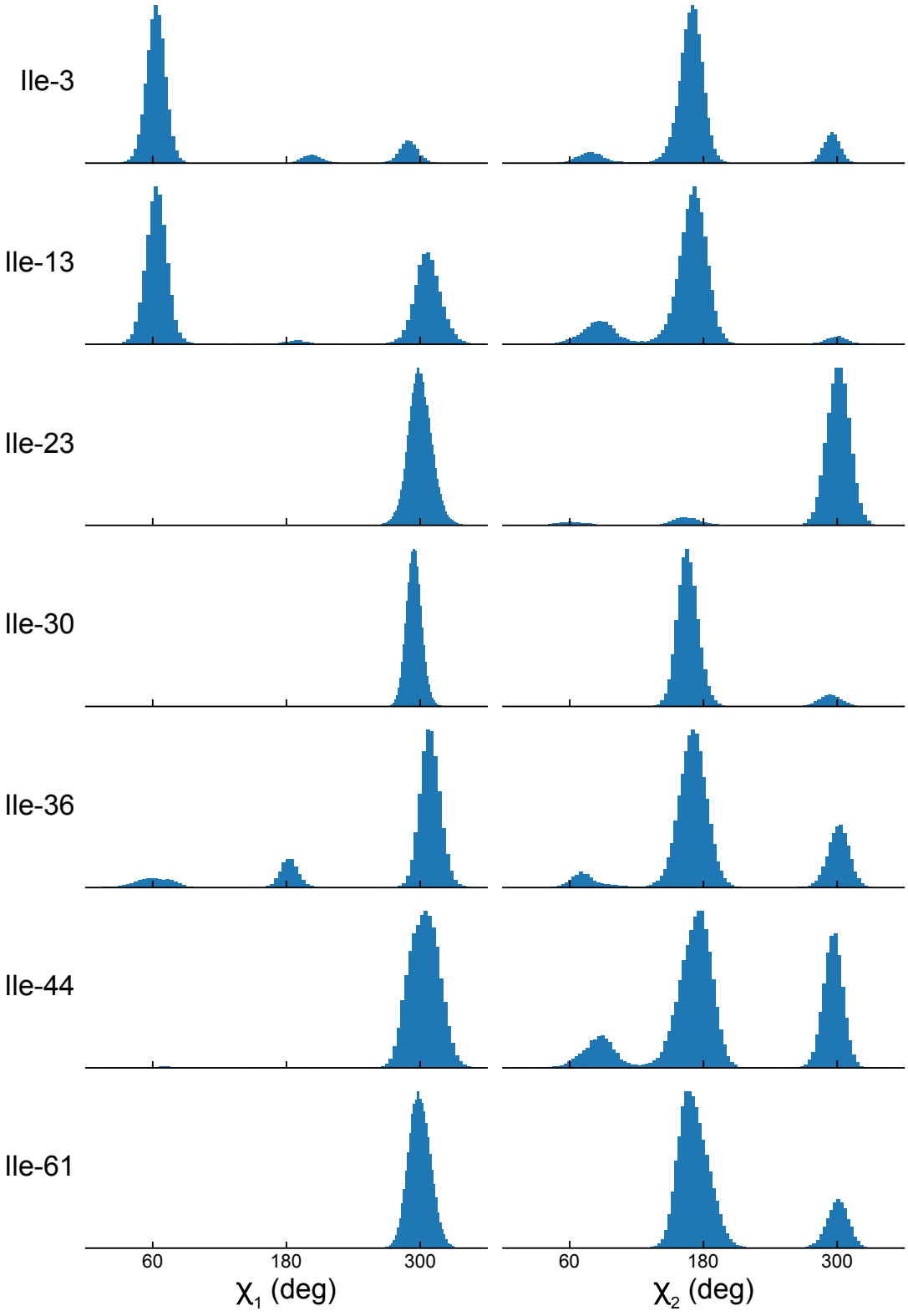

Figure F.8: Distribution of χ_1 and χ_2 angles for Ubiquitin isoleucine side-chains from the MD simulation.

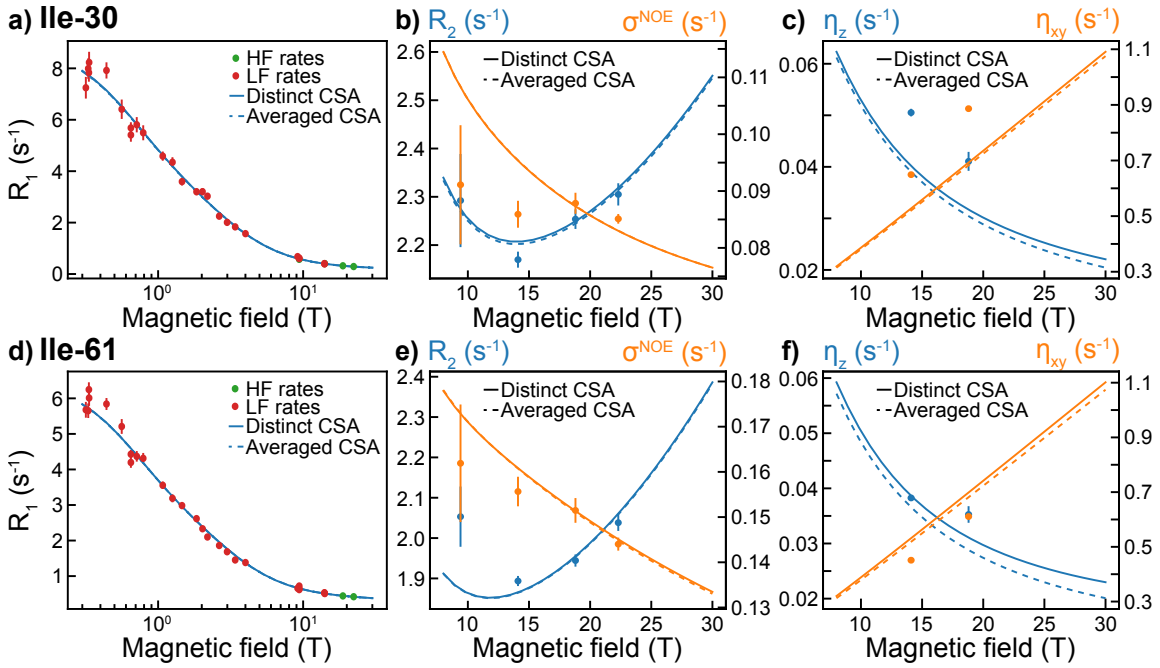

Figure F.9: Contribution from the CSA rotamer-dependent relaxation mechanism. Analysis of relaxation rates for Ile-30 and Ile-61 using a 2-rotamer exchange model (rotamer 4 and 9). Carbon R_1 (**a**), R_2 and carbon-proton σ^{NOE} (**b**) and longitudinal and transverse cross-correlated cross-relaxation rates (**c**) as a function of the magnetic field. Only carbon R_1, R_2 and carbon-proton σ^{NOE} were used in each analysis while η_z and η_{xy} were calculated using the obtained results for cross-validation. Calculation were performed either using distinct CSA tensors in each rotamer (plain) or the population-averaged value (dash).

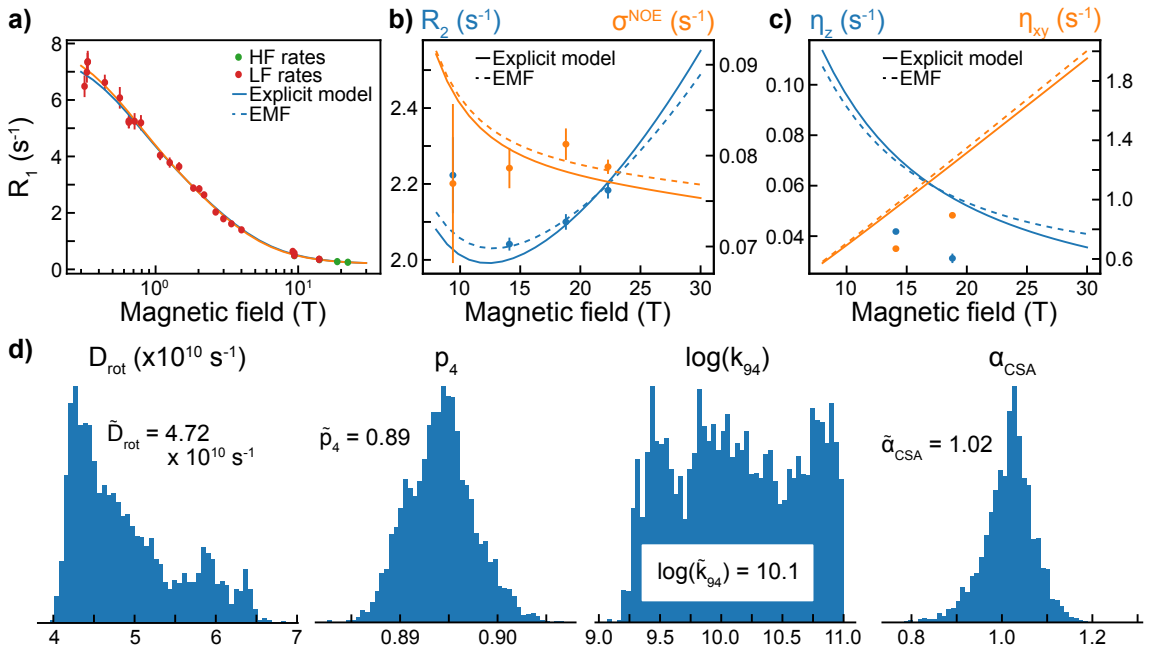

Figure F.10: Analysis of relaxation rates for Ile-3 using a 2-rotamer jump model (rotamer 4 and 9). Carbon R_1 (**a**), R_2 and carbon-proton σ^{NOE} (**b**) and longitudinal and transverse cross-correlated cross-relaxation rates (**c**) as a function of the magnetic field. The results from the EMF analysis are shown in dash lines in each panel. Only carbon R_1, R_2 and carbon-proton σ^{NOE} were used in each analysis while η_z and η_{xy} were calculated using the obtained results for cross-validation. **d)** Distributions of parameters for the explicit model of motions. The mean values of parameters are given on every panels. The jump rate k_{94} is expressed in s^{-1}.

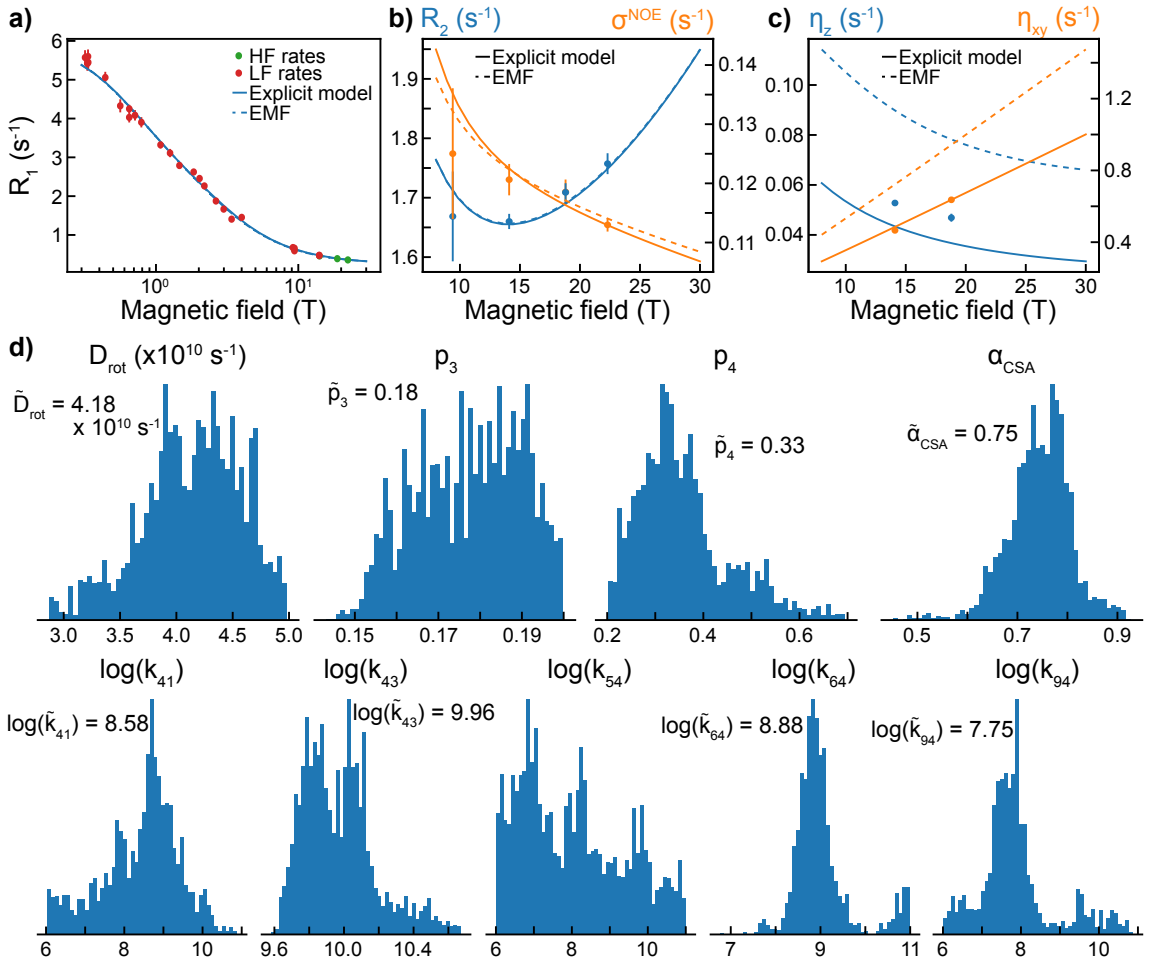

Figure F.11: Analysis of relaxation rates for Ile-13 using a 6-rotamer jump model (rotamer 1, 3, 4, 5, 6, and 9). Carbon R_1 (**a**), R_2 and carbon-proton σ^{NOE} (**b**) and longitudinal and transverse cross-correlated cross-relaxation rates (**c**) as a function of the magnetic field. The results from the EMF analysis are shown in dash lines in each panel. Only carbon R_1, R_2 and carbon-proton σ^{NOE} were used in each analysis while η_z and η_{xy} were calculated using the obtained results for cross-validation. **d)** Distributions of parameters for the explicit model of motions. The mean values of parameters are given on every panels. All jump rates are expressed in s^{-1}. In the model, populations of rotamers 1, 5 and 9 were fixed to their MD values (respectively 2 %, 1 % and 3 %) and all jump rates fixed to 10^{-10} except exchange rates involving rotamer 4 which is predicted to be the most populated rotamer from the MD simulation.

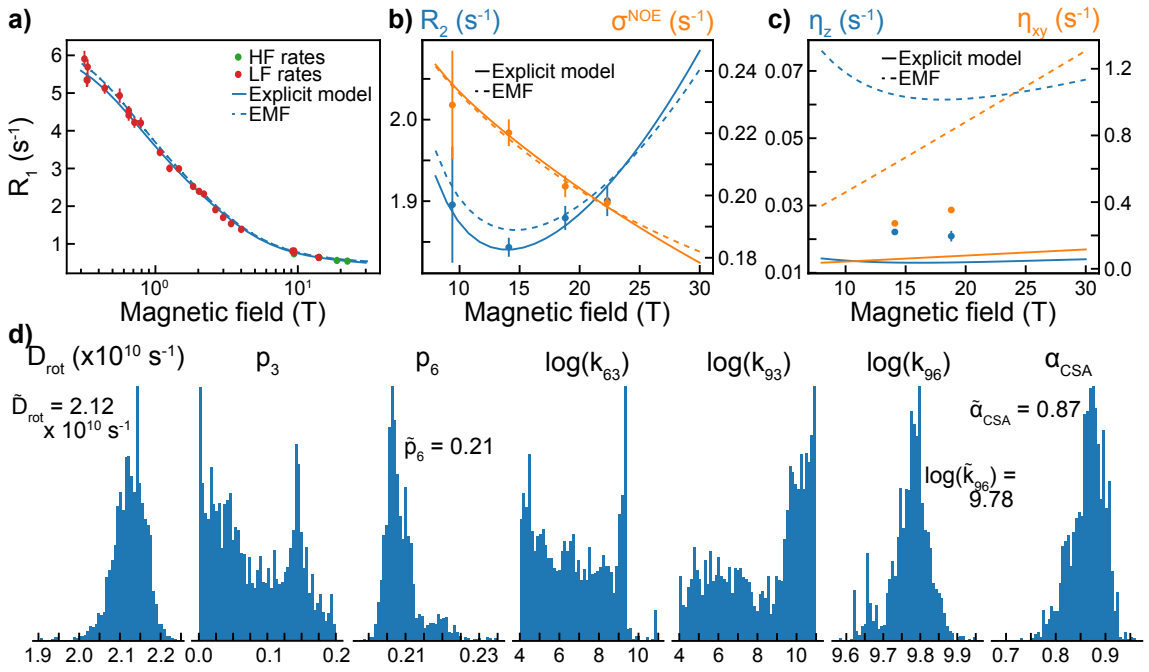

Figure F.12: Analysis of relaxation rates for Ile-23 using a 3-rotamer jump model (rotamer 3, 6 and 9). Carbon R_1 (**a**), R_2 and carbon-proton relaxation rates (**b**) and longitudinal and transverse cross-correlated cross-relaxation rates (**c**) as a function of the magnetic field. The results from the EMF analysis are shown in dash lines in each panel. Only carbon R_1, R_2 and carbon-proton σ^{NOE} were used in each analysis while η_z and η_{xy} were calculated using the obtained results for cross-validation. **d)** Distributions of parameters for the explicit model of motions. The mean values of parameters are given on every panels. The exchange rates are expressed in s^{-1}.

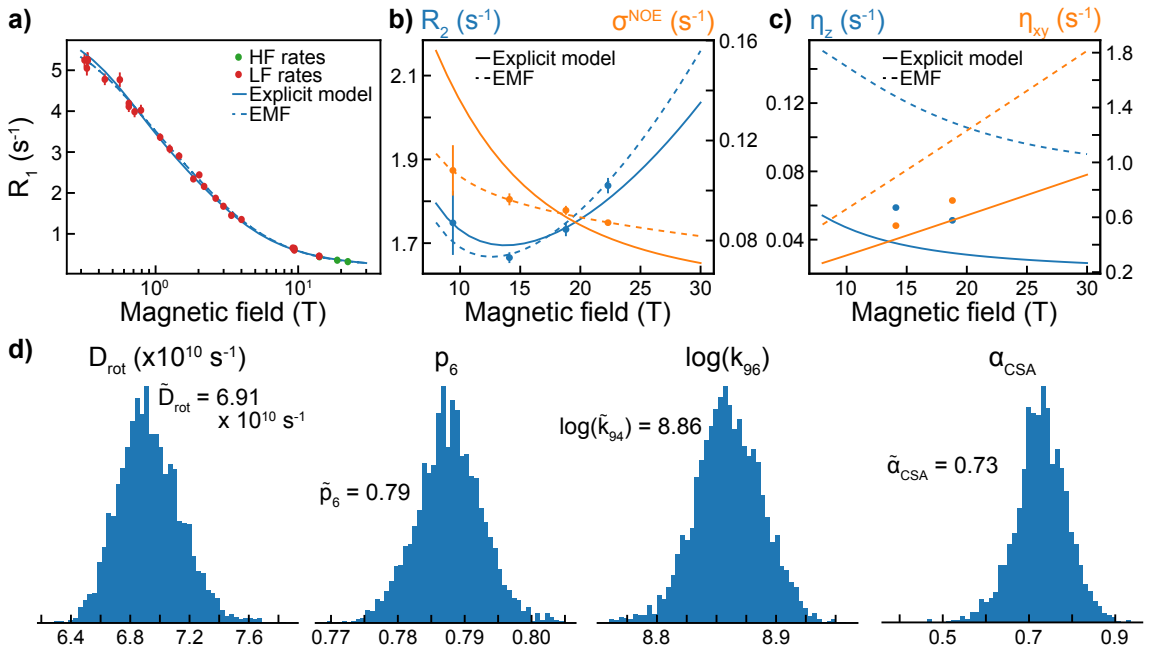

Figure F.13: Analysis of relaxation rates for Ile-36 using a 2-rotamer jump model (rotamer 6 and 9). Carbon R_1 (**a**), R_2 and carbon-proton σ^{NOE} (**b**) and longitudinal and transverse cross-correlated cross-relaxation rates (**c**) as a function of the magnetic field. The results from the EMF analysis are shown in dash lines in each panel. Only carbon R_1, R_2 and carbon-proton σ^{NOE} were used in each analysis while η_z and η_{xy} were calculated using the obtained results for cross-validation. **d)** Distributions of parameters for the explicit model of motions. The mean values of parameters are given on every panels. The exchange rates are expressed in s^{-1}.

F.6 Additional tables

Table F.3: Values of χ_1 and χ_2 angles obtained after DFT optimization of isoleucine structures, and defining the 9 rotamers, and Euler angles $\varphi_{J,R}$ and $\theta_{J,R}$ defining the orientation of the rotamer frame in the jump frame.

	χ_1 (deg)		χ_2 (deg)			
Rotamer	Theoretical	DFT	Theoretical	DFT	$\varphi_{J,R}$ (deg)	$\theta_{J,R}$ (deg)
1	60	55.58	60	56.70	105.33	103.74
2	180	178.08	60	53.63	228.21	108.71
3	300	291.44	60	59.22	199.06	101.55
4	60	59.88	180	173.85	135.10	5.80
5	180	180.25	180	172.19	249.12	7.65
6	300	295.36	180	177.00	211.35	4.97
7	60	63.59	300	289.81	172.20	92.98
8	180	184.40	300	287.02	127.09	91.56
9	300	296.95	300	295.15	241.33	100.43

Table F.4: Populations of each Isoleucine rotamer states in the MD trajectory of Ubiquitin.

Rotamer	Ile-3	Ile-13	Ile-23	Ile-30	Ile-36	Ile-44	Ile-61
1	0.05	0.02	0.0	0.0	0.0	0.0	0.0
2	0.02	0.0	0.0	0.0	0.05	0.0	0.0
3	0.0	0.12	0.03	0.0	0.01	0.11	0.0
4	0.79	0.55	0.0	0.0	0.05	0.0	0.0
5	0.03	0.01	0.0	0.0	0.08	0.0	0.0
6	0.0	0.26	0.06	0.92	0.58	0.57	0.81
7	0.0	0.0	0.0	0.0	0.03	0.0	0.0
8	0.0	0.0	0.0	0.0	0.0	0.0	0.0
9	0.12	0.03	0.92	0.08	0.19	0.31	0.18

RÉSUMÉ

La relaxation des spins nucléaires est un phénomène fondamental en Résonance Magnétique Nucléaire (RMN). Au cours d'une expérience, elle conduit à des pertes de polarisation affectant la qualité des spectres. Afin de développer de nouvelles séquences d'impulsion, il est essentiel de prendre en compte ses effets, voire de les optimiser, comme dans le cas des expériences de type TROSY (Transverse Relaxation Optimized SpectroscopY). Après une brève introduction à la théorie de la relaxation en phase liquide, nous détaillons comment cette théorie a été implémentée dans le but de calculer efficacement les vitesses de relaxation d'un grand nombre de systèmes de spins.

La théorie de la relaxation nous a permis de comprendre le spectre de groupes méthyl dans la protéine Ubiquitine, et enregistré avec une évolution zéro quantum à bas champs et une détection à haut champs en utilisant un spectromètre RMN à deux champs. Cela nous a conduit à étendre le champ d'application de la théorie du methyl-TROSY. Par ailleurs, nous avons introduit le concept de TROSY a deux-champs. Il repose non seulement sur la sélection d'opérateur de spin ayant des propriétés de relaxation favorables, mais également sur la sélection adéquate des champs magnétiques pour l'évolution sous l'effet du déplacement chimique tout en conservant la sensibilité des hauts champs pour la détection.

La mesure des vitesses de relaxation, constitue un outil de choix pour la caractérisation de la dynamique sur des échelles de temps allant de la pico- à la seconde, et plus. Nous présentons ici des outils pour analyser la dépendance en champs magnétique de vitesses de relaxation enregistrées sur une large gamme de champs magnétiques. Enfin, nous présentons quelques modèles de mouvements prenant en compte la nature des mouvements dans les protéines. En particulier, nous montrons l'existence d'un mécanisme de relaxation associé à des différences de CSA (Chemical Shift Anisotropy) dans les chaînes latérales aliphatiques.

MOTS CLÉS

Résonance Magnétique Nucléaire, Relaxation, Dynamique des protéines, RMN multi-champ

ABSTRACT

Nuclear spin relaxation is a fundamental phenomenon in Nuclear Magnetic Resonance (NMR). During the course of an experiment, it leads to polarization losses that can be detrimental to the spectrum quality. Taking spin relaxation into account when developing NMR pulse sequences appears essential, and can reveal itself beneficial as shown in TRansverse Optimized SpectroscopY (TROSY) type of experiments. After a brief introduction to nuclear spin relaxation theory in liquid, we will detail how it has been implemented to efficiently compute relaxation rates of arbitrary spin systems.

Nuclear spin relaxation theory has been used to understand the spectrum of methyl groups in the protein Ubiquitin recorded with zero-quantum evolution at low field and signal detection at high field using a two-field NMR spectrometer. This led us to extend the methyl-TROSY theory beyond the its original conditions of application. In addition, we introduced the concept of two-field TROSY which relies not only on the selection of spin quantum operators with favorable relaxation properties, but also on the proper selection of the magnetic field for chemical shift labeling while retaining high-field high-sensitivity detection.

Relaxation measurements report on dynamic properties over timescales ranging from pico- to seconds and more is unique. Here, we present tools to analyze the field-dependence of relaxation rates recorded while moving the sample inside the bore of the spectrometer to extend the range of available magnetic fields. Finally, we discuss models of motions adapted to the nature of internal motions in protons. We reveal the existence of a rotamer Chemical Shift Anisotropy (CSA) dependent relaxation mechanism in aliphatic side-chains.

KEYWORDS

Nuclear Magnetic Resonance, Nuclear spin relaxation, Protein dynamics, Multiple-field NMR